Serbian Microscopy Society | Српско Друштво за Микроскопију

MCM2019

PROCEEDINGS

from the

14th MULTINATIONAL CONGRESS ON MICROSCOPY

September 15–20, 2019, Belgrade, Serbia

PROCEEDINGS

from the

14th MULTINATIONAL CONGRESS ON MICROSCOPY

SEPTEMBER 15–20, 2019, BELGRADE, SERBIA

TITLE:

Proceedings from the 14th Multinational Congress on Microscopy, September 15–20, 2019, Belgrade, Serbia

PUBLISHERS:

University of Belgrade, Institute for Biological
Research "Siniša Stanković", National Institute of Republic of Serbia

Serbian Society for Microscopy, Serbia

FOR PUBLISHERS:

Dr. Mirjana Mihailović
Dr. Jasmina Grbović Novaković

EDITORS:

Dr. Jasmina Grbović Novaković
Dr. Nataša Nestorović
Dr. Dragan Rajnović

ISBN 978-86-80335-11-7

PRINT:

Knjigoveznica i kartonaža Grbović M. Milica, M. Gorkog 43, Beograd 11000, Serbia
30 e-copies

Copyright © 2019
by Institute for Biological Research "Siniša Stanković" and others contributors.

All rights reserved. No part of this publication may be reproduced, in any form or by any means, without permission in writing from the publisher

We are honored to host for the first time the Multinational Congress of Microscopy (MCM2019) in Serbia. The aim of MCM conferences is to become a worldwide forum for discussion on different application of various microscopical techniques for both experts and young researchers. MCM conferences have always been a good instrument for establishment of new liaisons between laboratories interested in similar projects. Trade exhibitions also helped to gain insight into the newest development of microscopy

MCM2019 is jointly organized by 8 societies: Austrian Society for Electron Microscopy (ASEM), Croatian Microscopy Society (CMS), Czechoslovak Microscopy Society (CSMS), Hungarian Society for Microscopy (HSM), Italian Society of Microscopical Sciences (SISM), Serbian Society for Microscopy (SSM), Slovenian Society for Microscopy (SDM) and Turkish Society for Electron Microscopy (TEMD)

The bit of history

Extracted from the "Opening lecture" given at the 10th Multinational Congress on Microscopy (Urbino, 4-7 September 2011) by Giuseppe Arancia,, Department of Technology and Health, Italian National Institute of Health Past President and Honorary Member of the Italian Society of Microscopical Sciences.

"In 1990, some representatives of the Italian, Hungarian, Austrian, Yugoslavian and Czechoslovak Societies for Electron Microscopy began to have contacts in order to evaluate the possibility of organizing jointly a multinational congress on electron microscopy. The inspirer reasons of this idea were, mainly, the substitution of a number of small congresses in neighboring countries with a single multinational meeting with the aim of increasing the scientific level and reducing the organizing costs, and to favor interactions and exchange of information and experiences among researchers operating in different countries."

Conference chairs
Dragan Rajnović
Nataša Nestorović
Jasmina Grbović Novaković

COMMITEES AND BOARDS

CHAIRS/LOC

Jasmina Grbovic Novakovic
Center of Excellence CONVINCE, VINCA Institute of Nuclear Sciences, University of Belgrade, Belgrade, Serbia

Natasa Nestorovic
Institute for Biological Research "Sinisa Stankovic", University of Belgrade, Belgrade, Serbia

Dragan Rajnovic
Faculty of Technical Sciences, University of Novi Sad, Novi Sad, Serbia

International Organizing Committee

Gerd Leitinger
Medical University of Graz, Graz, Austria

Bernardi Johannes
Vienna University of Technology, Vienna, Austria

Goran Kovacevic
University of Zagreb, Zagreb, Croatia

Andreja Gajovic
Rudjer Boskovic Institute, Zagreb, Croatia

Bela Pecz
Institute of Technical Physics and Materials Science of Hungarian Academy of Sciences, Budapest, Hungary

Kristof Zoltan
Eotvos Lorand University, Budapest, Hungary

Elisabeta Felcieri
University of Urbino Carlo Bo, Urbino, Italy

Roberto Balboni
CNR Institute for Microelectronics and Microsystems, Bologna, Italy

Dusan Chorvat
International Laser Center, Bratislava, Slovak Republic

Vladislav Krzyzanek
Institute of Scientific Instruments of the Czech Academy of Science, Brno, Czech Republic

Rok Kostanjsek
University of Ljubljana, Ljubljana, Slovenia

Saso Sturm
Jozef Stefan Institute, Ljubljana, Slovenia

Serap Arbak
Acıbadem Mehmet Ali Aydınlar University, Istanbul, Turkey

Servet Turan
Eskisehir Technical University, Eskisehir, Turkey

Jasmina Grbovic Novakovic
VINCA Institute of Nuclear Sciences, University of Belgrade, Belgrade, Serbia

Natasa Nestorovic
Institute for Biological Research "Sinisa Stankovic", University of Belgrade, Belgrade, Serbia

Dragan Rajnovic, Faculty of Technical Sciences, University of Novi Sad, Novi Sad, Serbia

SESSIONS AND CHAIRS

INSTRUMENTATION AND TECHNIQUES

IT1 - Advances in sample preparation techniques

Evolution of the sample preparation methods and instrumentation runs parallel with the evolution of modern microscopy and image processing. Resolution and other capabilities of microscopes are solidly improving, setting new requirements for the preparation process. This session focuses on recent developments in sample preparation methods ranging from Focused Ion Beam (FIB) to ultramicrotomy, including various applications in different disciplines of science and technology.

Chairs:
György Zoltán Radnóczi, Centre for Energy Research, Hungarian Academy of Sciences, Budapest Hungary
Meltem Sezen, Nanotechnology Research and Application Center, Sabanci University, Turkey

IT2 - 3D imaging, image processing, and phase-related techniques

Light, electron and x-ray techniques will be included in this session for all cases of using serial sectioning, or/and phase rather than amplitude imaging, or/and computational methods for data acquisition, analysis and 3-D visualization. Contributions are welcome in any area of holography, diffraction imaging, tomography, nano-CT and micro-CT, confocal microscopies (multiphoton and electron), differential phase contrast imaging, structured illumination, and exit-wave reconstruction for the case of biological as well as non-biological samples. This section/symposium is anticipated also as a forum to discuss computational methods for processing large complex datasets in all kinds of microscopies and spectroscopies with the aim of improving spatial and temporal resolution, as well as precision and contrast for visualization of various types structural information.

Chairs:
Ognjen Milat, Institute of Physics, Zagreb, Croatia
Thomas Heuser, Vienna Bio Center, Vienna, Austria

IT3 - Diffraction techniques and spectroscopy

The session addresses methodology and implementation of electron diffraction and spectroscopy in characterization of various materials. Topics include contributions based on transmission and backscatter electron diffraction including diffraction tomography, and analytical techniques such as energy dispersive X-ray spectrometry, electron energy loss spectrometry, energy filtering, and cathodoluminescence. Contributions related to innovative/emerging techniques in electron diffraction and spectroscopies are highly encouraged.

Chairs:
Mariana Klementova, Institute of Physics CAS, Prague, Czech Republic
Miran Čeh, Center for Electron Microscopy and Microanalysis, Jozef Stefan Institute, Ljubljana, Slovenia

IT4 - Correlative, and super-resolution microscopy

The session addresses new methodologies and advanced applications of correlative microscopies ranging from advanced light microscopy, electron microscopy and scanning probe microscopies. We will lay a particular focus on new developments in combining and correlating microscopy signals from the same specimen, which could open a new route to understand structure-property relations in biosciences and materials research. Contributions from all areas of microscopy including new data analysis methods are welcome.

Chairs:
Ferdinand Hofer, Institut für Elektronenmikroskopie und Nanoanalytik, TU Graz, Graz,Austria
Kristof Kovacs, Pannonia University, Veszprem, Hungary

IT5 - In situ and environmental microscopy

In situ electron microscopy has experienced a great rate of advancement in both techniques and instrumental capabilities over the last decade being a subject of increasing impact in life and materials sciences. The goal of the Symposium is to bring together an interdisciplinary group of scientists from materials science, chemistry, physics and the fields of biology, to highlight newly developed instrumental capabilities and experimental techniques for studying dynamic processes in functional materials and biological systems under realistic or near realistic conditions. The symposium is planned to cover, although is not restricted to, the following areas: in situ experiments spanning from nanoparticle nucleation and growth, studies of material transformations, catalysis, corrosion, and mechanical testing to aspects of correlative microscopy of biological processes; and in-operando experiments, such as batteries and other devices – all at high spatial- and time-domain resolution

Chairs:
Sašo Šturm, Department for Nanostructured Materials, Jozef Stefan Institute, Ljubljana, Slovenia
Kónya Zoltán, Dept. of Applied and Environmental Chemistry, University of Szeged, Szeged, Hungary

IT6 - Advances in instrumentation and techniques (SEM, TEM, SPM, etc.)

This session intends to cover recent advances in all fields of electron microscopy, but also including scanning probe related techniques. The focus is mainly on the instrumentation developments and related advances in methodology. The session includes aberration correction and other resolution/contrast improvements for TEM and SEM, low voltage EM techniques, analytical methods, as well as all exciting new ideas on electron and probe microscopy.

Chairs:
Daniel Kiener, Department Materialphysik, Universität Leoben, Leoben, Austria
Vladislav Krzyzanek, Institute of Scientific Instruments CAS, Brno, Czech Republic

LIFE SCIENCES

LS1 - Live cell imaging, and intracellular dynamics
Nowadays, a number of technologies make it possible to analyze biological processes directly in living organisms and cells, with the ultimate goal to localize and describe in vivo the dynamics of cell metabolic

pathways. Live cell imaging allows following cell populations, individual cells or specific molecules within complex living tissues and organs, while light and electron microscopy offer the possibility to assemble snapshots of events to obtain the dynamic pattern. This symposium will focus on the visualization and analysis of dynamic cell processes using various microscopy techniques, as well as on using experimental tools (e.g., optogenetics and novel probes) for monitoring cellular and tissue events

Chairs:
Manuela Malatesta, Verona University, Italy
Pavel Hozak, Institute of Molecular Genetics CAS, Prague, Czech Republic

LS2 - Structure and imaging of biomolecules

Imaging of cellular and subcellular structures at the microscopic level is essential for the understanding important biological processes. Advanced microscopy techniques such as conventional confocal, lightsheet, multiphoton and super-resolution (STED) microscopes allow visualization of the dynamic processes on a time-based manner. The use of fluorescence is advantageous in labeling the multiple structures and thus permits visualization of the interactions between cellular structures. Furthermore, the structure of individual biomolecules can be addressed by cryo-electron microscopy (cryo-EM) techniques. In this session, the advantages and disadvantages of using advanced microscopy techniques for detecting biomolecules and determining their structure will be discussed.

Chairs
Sevinc Inan, Dep. of Histology and Embryology, Izmir University of Economics, Izmir, Turkey
Tea Pavkov-Keller, Institute of Molecular Biosciences (IMB), University of Graz, Graz, Austria

LS3 - Microscopic applications in symbiotic interactions, plants, microorganisms, and environmental sciences

Microscopic techniques have wide application in biological and environmental sciences. Light microscopy has recently experienced an incredible increase in technology and methods development, enabling use in study cellular features and architectures, molecular movement and protein localization, as well as morphology of microscopic specimens and samples. Electron microscopy techniques have revolutionized studies of cellular ultrastructures and organelles, with a special contribution of ESEM which is designed for imaging specimens in their natural state. Modern environmental studies utilize microscopy to study symbiotic interactions, biofilms, and anthropogenic interventions and their impacts on the environment. This session is aimed to present novel achievements in microscopic applications in botany, microbiology and environmental sciences.

Chairs:
Hrvoje Fulgosi, Division of Molecular Biology, Ruđer Bošković Institute, Zagreb, Croatia
Sonja Duletić Laušević, Faculty of Biology, University of Belgrade, Belgrade, Serbia

LS4 - Neuroscience and histopathology

Neuroscience and neuroscientists are among the first beneficiaries of the amazing development of imaging techniques in both light and electron microscopy. Super-resolution techniques have reached <20 nm resolution, due to fast imaging systems we can follow intercellular processes in situ, and the number of

publications involving the use of the Nobel-prize awarded ultra-cryo electron microscopy is rapidly increasing. This session wants to offer a range of lectures including topics of histopathology, in which classical and state-of-the art microscopic techniques contributed to significant discoveries in the field of neuroscience.

Chairs:
Agnes Kittel, Institute of Experimental Medicine, Hungarian Academy of Sciences, Budapest, Hungary
Gerd Leitinger, Gottfried Schatz Research Center, Medical University of Graz, Graz, Austria

LS5 - High-resolution microscopy in life sciences

Fluorescent microscopy is a well-established method for the non-invasive measurements of cell structures and processes; however, its resolution is limited. Popularization of super-resolution imaging techniques, with superior resolution, has allowed us to probe in detail cell structures that were previously only in domain of electron microscopy. In the field of electron microscopy, advancements in detectors, image processing and reconstruction software make possible currently to study larger biological structures at near atomic-resolution, understand their molecular dynamics and functions. Nonetheless, different types of microscopies are complementary and together can lead to new biological insights. The focus of this session will be to present recent discoveries in cell/tissue structure and function using advanced microscopy techniques.

Chairs:
Jernej Jorgačevski, Medical Faculty, University of Ljubljana, Ljubljana, Slovenia
Marie Vancová, Biology Centre CAS, Ceské Budějovice, Czech Republic

LS6 - Nanomaterials in biology and medicine

The use of nanobiotechnology in human health has been increased in recent years. Drug carrier nanoparticles with their wide range of uses and advantages are promising approaches for the treatment of many diseases. Engineered nanomaterials are made to be attracted only by diseased cells and not by normal cells. These materials allow early detection and treatment of many diseases. One of the most challenging tasks in the fields of microscopic sciences is to visualize and identify the complex interaction of nanomaterials with biological material and correlate them with specific cellular functions in physiology and pathology. The topics of the session are: carbon-based, metal-based nanomaterials and nanoparticles such as, chitosan, alginate, polymeric micelles, cellulose, liposomes, dendrimers, inorganic nanoparticles, nanocrystals, metallic nanoparticles, quantum dots, protein and polysaccharides. The evaluation of cell death in the nanosystems as disease therapy; nanotoxicology mechanisms evaluations; advantages of nanoparticles and their role in oxidative stress are important topics to be addressed in this session.

Chairs:
Serap Arbak, Dep. of Histology and Embriology, Acibadem Mehmet Ali Aydinlar University, Turkey
Stefania Meschini, ISS, Roma, Italy

LS7 - Multidisciplinary approaches for medical and biological sciences

In biological and medical research, multidisciplinary approaches have become of great importance and interest for the scientific community. This session is focused on multiple applications and translational research in this field. Oral and poster presentations from biotechnology, biomedicine, diagnostics, and relat-

ed multidisciplinary studies, are cordially invited. Researches obtained by using microscopical and imaging techniques, as well as technological innovations, are particularly welcome.

Chairs:
Elisabetta Falcieri, Urbino University, Italy
Melek Ozturk, Dep. of Medical Biology, Istanbul University, Istanbul, Turkey

LS8 - Emerging and miscellaneous topics in life sciences

Microscopic methods are rapidly advancing, offering new technologies to address novel problems in biological and biomedical research. This panel is initially intended for emerging topics that may not match directly to other sessions. The session will remain open for late breaking submissions until the end of August 2019. However, the latter submissions will be
assigned as poster presentations.

Chairs:
Jana Nebesářová, Biology Centre CAS, Ceské Budějovice, Czech Republic
Nela Puškaš, School of Medicine, University of Belgrade, Belgrade, Serbia

MATERIAL SCIENCES

MS1 - Metals, alloys and intermetallics

Importance of metals, alloys and intermetallic in everyday life cannot be stressed enough and the research aimed at the discovery of new compounds as well tailoring of the existing ones is currently at the forefront of materials science. The only way of improving desiring properties, such as extreme strength accompanied with the low weight and endurance in the robust atmospheric conditions, superior electrical and thermal conductivity, self-healing properties and so on, is by full elucidation of the crystal structure of materials. And what better way of understanding the structure than through the use of electron microscopy? This session will address, but is not limited to, the following topics: phase transformations, high-entropy alloys, shape memory alloys, energy and gas storage alloys, advanced alloys for transportation industry, new alloying materials used in medicine, ultrafast cooled materials, new alloys for corrosive environment, materials for solar cells and LEDs, catalytic materials based on intermetallics, intermetallic matrix composites.

Chairs:
Matjaž Godec, Institute of Metals and Technology, University of Ljubljana, Ljubljana, Slovenia
Željko Skoko, Faculty of Science, University of Zagreb, Zagreb, Croatia

MS2 - Nanoscale, nanostructured, and carbon based materials

With the advent of nanoscience and nanotechnology, various electron microscopy techniques became indispensable in structural and chemical characterization and local property measurements of materials for nanotechnology, such as nanoparticles, one-dimensional structures (nanowires, nanotubes, nanorods), layered structures and heterostructures. This symposium is focused on the application of electron microsco-

py techniques in determination of structure and chemical composition of materials for nanotechnology on nano and atomic scale.

Chairs:
Andreja Gajović, Division of Materials Physics, Ruđer Bošković Institute, Zagreb, Croatia
Sanja Milošević Govedarović, Vinča Institute of Nuclear Sciences, University of Belgrade, Belgrade, Serbia

MS3 - Thin films, coatings, surfaces and interfaces

Thin films, coatings, and interfaces such as optical thin films and coatings, energy production related coatings, biomedical and biological thin films, thermal and environmental barrier coatings, electrical and magnetic coatings, component coatings for automotive, aerospace and manufacturing applications play important role in our daily life. Regardless of the application field, all thin films and coatings have in common that their properties depend on chemical and phase composition, crystalline structure, texture, microstructure, interface properties, and surface related properties. The goal of this session is to provide information on the relationship between the listed factors, and functional properties and processing of thin films, coatings, and interfaces. Contributions from all fields where thin films, coatings, and interfaces play vital role are welcome. Besides interfaces in thin film and coating systems, interfaces between different phases and grains are also covered by the session.

Chairs:
Aleksandar Miletić, Faculty of Technical Sciences, University if Novi Sad, Novi Sad, Serbia
Regina Ciancio, IOM-CNR TASC, Trieste, Italy

MS4 - Ceramics, composites, cultural heritage materials, rocks and minerals

The session covers microscopy of wide range of materials including ceramics, composites, cultural heritage materials, rocks and minerals. Learning materials' phenomena from macroscopic down to the atomic scale to reconstruct reaction sequences and phase transformations in rocks, or man made historical and modern functional materials, utilizing microscopy and spectroscopy methods. Papers covering discovery of minerals and polytypes, phase transitions, exsolutions, topotaxial replacements and orientation relations studies, studies related to ceramic or composite textures, interfaces and grain growth phenomena, and finally, contributions investigating cultural heritage materials and preservation treatments are cordially invited. The session also invites discussion of sample preparation, as one of the crucial steps for microscopy observations

Chairs:
Aleksander Rečnik, Department for Nanostructured Materials, Jozef Stefan Institute, Ljubljana, Slovenia
Snežana Vučetić, Faculty of Technology, University of Novi Sad, Novi Sad, Serbia

MS5 - Polymers, biomaterials, and soft materials

The session invites contributions concerning current research on both fundamental and applied aspects of polymers, biomaterials and soft materials. It will address, but is not limited, to the topics of: molecules on surfaces (including films and supramolecular architectures); physical/chemical properties of polymeric films, surfaces and interfaces; polymeric matrix; polymeric/molecular nanostructured systems; colloidal systems (such as polymer self-assembled systems, micelles, beads and foams). Molecular systems

should be investigated by state-of-the-art microscopy techniques (TEM, SEM, SPM, LM). Technological applications of such materials in organic electronic devices, organic sensors and active surfaces, for instance, are encouraged.

Chairs:
Cristiano Albonetti, CNR, Bologna, Italy
Suzana Šegota, Ruđer Bošković Institute, Zagreb, Croatia

MS6 -Semiconductors, devices, and magnetic materials

Even after several decades of theoretical and applied research, Semiconductors, Electronic devices and Magnetic materials are still an important field of study. This is due to both the variety of industrial application as well as the theoretical opportunities offered by such materials in understanding the structure of matter. Moreover, the continuous scaling down of the size of structures and devices requires updated instrumentation and skills able to investigate samples at the nanometric or atomic level. This session welcomes contributions on morphological, structural and analytical characterization of semiconductor and magnetic materials and devices. This includes (but it is not limited to) classic semiconductors, wide-gap materials, heterostructures, dielectrics and materials for interconnects, magnetic materials as well as their applications, as in devices for micro- and nano-electronics. All contribution should emphasize the role of microscopy in the characterization of the materials

Chairs:
János Lábár, Center for Energy Research, Hungarian Academy of Sciences, Budapest, Hungary
Roberto Balboni, CNR, Bologna, Italy

MS7 - Materials for energy harvesting, production, storage, and catalysis

Advanced energy related materials and catalytic ones encounter worldwide a growing demand. This session demonstrates that cutting edge microscopy methods are necessary to comprehend their properties and tailor the materials for sustainable future.

Chairs:
Peter Karnthaler, Faculty of Physics, University of Vienna, Vienna, Austria
Sandra Kurko, Vinča Institute of Nuclear Sciences, University of Belgrade, Belgrade, Serbia

MS8 - Emerging and miscellaneous topics in material sciences

The session covers different topic in materials science. The session includes new developments, new strategies and interdisciplinary topics. The talks will be focused on hierarchy materials, self-healing materials, biomaterials, self-reporting materials and other emerging and miscellaneous topics in material sciences.

Chairs:
Alena Michalcova, The Department of Metals and Corrosion Engineering, University of Chemistry and Technology in Prague, Prague, Czech Republic
Servet Turan, Eskisehir Technical University, Eskisehir, Turkey

TABLE OF CONTENTS

PLENARY LECTURES

ATOMISTIC PHENOMENA IN NANOSTRUCTURES FOR ENERGY RELATED APPLICATIONS
Velimir R. Radmilović 22

QUANTUM SORTING: A NEW PARADIGM OF QUANTUM MEASUREMENT IN ELECTRON MICROSCOPY
Vincenzo Grillo 23

ANATOMY AND PHYSIOLOGY OF THE NUTRITIONAL SYSTEM
Saverio Cinti 24

USING OFF-AXIS ELECTRON HOLOGRAPHY TO MEASURE MAGNETIC PROPERTIES OF MATERIALS
András Kovács, Jan Caron, P. Diehle, Fengshan Zheng, Thibaud Denneulin, Dongsheng Song, Rafal E Dunin-Borkowski 28

MICROSCOPING THE AMOEBOID CELL MOTILITY
Igor Weber 30

QUANTITATIVE CS CORRECTED STEM OF LOCAL STRUCTURES IN LEAD-FREE FERROELECTRICS
Goran Drazic, Andreja Bencan, Hana Ursic, Maja Makarovic, Matej Komelj, Tadej Rojac, Dragan Damjanovic 31

INSTRUMENTATION AND TECHNIQUES

IT1 – ADVANCES IN SAMPLE PREPARATION TECHNIQUES

ION SAMPLE PREPARATION FOR MICROANALYSIS IN EARTH SCIENCE
Andrey Kudryavtsev, Evgeny Vasilev, Olga Telnova, John Marshall 35

BROAD ION BEAM CROSS SECTION PREPARATION ON NITROCARBURISED AND OXIDISED STEEL SAMPLES TO CORRELATE MICROSTRUCTURE AND TRIBOLOGICAL BEHAVIOUR
Johannes Rattenberger, Stefan Mitsche, Harald Fitzek, Igor Velkavrh, Alexander Diem, Hartmuth Schroettner . 37

NEW APPROACHES TO SBF-SEM SPECIMEN PREPARATION
Eva Ďurinová, Jan Langhans, Jana Nebesářová 39

SURFACE ZEOLITE·S STUDY IN SUGAR-ENRICHED SOLUTIONS
Rumenka Markoska, Vedrana Spada, Krešimir Pavelić, Sandra Kraljević Pavelić 40

ON THE COMBINED USE OF FIB AND PIPS FOR TEM SAMPLE PREPARATION FROM ACTINIDES MATERIALS FOR NUCLEAR APPLICATIONS
Alessandro Benedetti, Thierry Wiss, Oliver Dieste and Emanuele De Bona 42

IT2 – 3D IMAGING, IMAGE PROCESSING, AND PHASE-RELATED TECHNIQUES

PROJECT „PATTERN“ – AN OPEN ACCESS ONLINE TOOL FOR SPATIAL ANALYSIS OF IMMUNOLABELING IN ELECTRON MICROSCOPY
Dominik Pinkas, Erik Vlcak, Vlada Philimonenko, Jiri Janacek, Jakub Novak, Marcel Jirina, Pavel Hozak 45

ANALYTICAL ELECTRON TOMOGRAPHY OF METALLIC SAMPLES
Cornelia Trummer, Francisca Mendez-Martin, Gerald Kothleitner, Georg Haberfehlner 46

TOWARD AN ELECTROSTATIC OAM SORTER
Paolo Rosi, Amir Tavabi, Alberto Roncaglia, Giulio Pozzi, Enzo Rotunno, Matteo Zanfrognini, Stefano Frabboni, Rafal Durnin Burkoski, Vincenzo Grillo. 48

COMPARISON OF COLLAGEN DISTRIBUTION BETWEEN KERATOCONUS AND NORMAL HUMAN CORNEAL STROMA USING SECOND HARMONIC GENERATION MICROSCOPY
Mehmet Serif Aydin, Olgu Enis Tok, Aylin Kilic, Cihan Bilge Kayasandik, Cafer Tanriverdi, Burcu Nurozler Tabakci, Gurkan Ozturk. 50

MAKING A 3D MODEL OF MERINO WOOL FIBRE WITH PHOTOGRAMMETRIC PROCESSING OF SEM IMAGES
Mirjam Leskovšek, Urška Stankovič Elesini, Anja Škerjanc, Marko Vrabec, Helena Gabrijelčič Tomc. 53

QUANTITATIVE THREE-DIMENSIONAL MICROSTRUCTURE DESCRIPTION OF POROUS NANO-SIZED CERMET ANODES FOR SOFC USING FIB NANOTOMOGRAPHY
Gregor Kapun, Marjan Marinšek, Tina Skalar, Endre Majorovits, Franci Merzel, Miran Gaberšček, Sašo Šturm . 56

DIGITAL OPTICAL HOLOGRAPHIC MICROSCOPE; INTERFEROMETRIC STUDY OF THIN FILM DELEMINATION BUCKLING PATTERNS
Ognjen Milat, Nazif Demoli 58

IT3 – DIFFRACTION TECHNIQUES AND SPECTROSCOPY

CRYSTAL STRUCTURE DETERMINATION USING *OPERANDO* AND *IN SITU* ELECTRON DIFFRACTION TOMOGRAPHY
Karakulina OM, Batuk M, Hendrickx M, Abakumov AM, Hadermann J. 61

AUTOMATIC PROCESSING OF A LARGE NUMBER OF ELECTRON DIFFRACTION PATTERNS IN THE TEM
János L. Lábár, Z. Fogarassy 62

DONWILHELMSITE – A NEW MINERAL FROM THE MOON
Mariana Klementova, Lukas Palatinus, Jörg Fritz, Ansgar Greshake, Richard Wirth, Vera Assis Fernandes, Ludovic Ferrière 64

ANALYTICAL ELECTRON MICROSCOPY: RECENT ADVANCES AND NEW APPLICATIONS
Ferdinand Hofer, Mihaela Albu, Werner Grogger, Georg Haberfehlner, Daniel Knez, Judith Lammer, Franz-Philipp Schmidt, Gerald Kothleitner. 66

VIBRATIONAL STEM-EELS SIMULATIONS AT ATOMIC RESOLUTION
Paul M. Zeiger, Ján Rusz. 68

STRUCTURE AND PROPERTIES OF NOVEL 1D SELF-ORGANIZED TIO_2 NANOTUBES DEPOSITED BY MOS_2 AND CDS VIA ATOMIC LAYER DEPOSITION
Jan Michalicka, Raul Zazpe, Hanna Sopha, Alexander Tesfaye, Milos Krbal, Jan Prikryl, Ludek Hromadko, Thierry Djenizian, Jan M. Macak. 70

IT4 – CORRELATIVE, AND SUPER-RESOLUTION MICROSCOPY

CORRELATIVE RAMAN MICROSCOPY, SEM AND EDX – EXAMPLES OF APPLICATION AND BEST PRACTICE
Harald Fitzek, Ruth Schmidt, Manfred Nachnebel, Claudia Mayrhofer, Armin Zankel, Hartmuth Schroettner 72

MICROBIOLOGICALLY INFLUENCED CORROSION (MIC) OF STEEL – A STUDY USING CORRELATIVE SEM, EDX AND RAMAN MICROSCOPY
Thomas Planko, Harald Fitzek, Stefanie Eichinger, Johannes Rattenberger, Hartmuth Schroettner. 74

ALPHA-SYNNUCLEIN AFFECTS DIFFERENTLY THE INTERNAL AND EXTERNAL LEAFLET OF THE LIPID MEMBRANES
Samira Jadavi, Silvia Dante, Annalisa Relini, Alberto Diaspro, Claudio Canale. 77

UNEXPECTED ASYMMETRY IN THE AGGREGATION OF PARTIALLY LABELED PEPTIDES REVEALED BY STED-AFM CORRELATIVE NANOSCOPY
Claudio Canale, Michela Cosentino, Paolo Bianchini, Alberto Diaspro, ... 78

MEASURING THE TEMPERATURE HOMOGENEITY ACROSS FIB LAMELLAE FOR *IN SITU* TEM EXPERIMENTS VIA RAMAN SCATTERING IN CRYSTALLINE SILICON
Robert Krisper, Harald Fitzek, Evelin Fisslthaler, Werner Grogger. 79

IT5 – IN SITU AND ENVIRONMENTAL MICROSCOPY

IN-SITU/EX-SITU ATOMIC-RESOLUTION STUDY ON METALLIC AND OXIDE NANOCRYSTALLINE MATERIALS
Zaoli Zhang, Jinming Guo, Yonhui Zheng 82

IN SITU TEM OF ELECTRON BEAM INDUCED NANOCRYSTALLIZATION OF WC AND W
Stefan Noisternig, Ursula Ludacka, Christian Rentenberger, H. Peter Karnthaler 84

NANOPATTERNING SILVER: TARGETED OXIDATION WITH AN ELECTRON BEAM
Huaping Sheng, He Zheng, Shuangfeng Jia, Maria K. Y. Chan, Tijana Rajh, Jianbo Wang, Jianguo Wen, Jürgen Eckert, Christoph Gammer. 86

MICRON-SCALE CHARACTERIZATION OF TWINNING AND DISLOCATION SLIP IN MAGNESIUM SINGLE-CRYSTALS BY ADVANCED SEM IN-SITU TECHNIQUES
Kristián Máthis, Petr Harcuba, Dávid Ugi, Michal Knapek, František Chmelík, Péter Ispánovity, István Groma 88

TEMPERATURE-INDUCED CATIONIC DIFFUSION TO REGULATE THE PHASE TRANSITION IN VO2 FILM
Yonghui Zheng, Zhuo Chen, Qinqin Shao, Yan Cheng, Yunbin He, Zaoli Zhang 89

THERMOSALIENT BEHAVIOR IN ORGANIC ALLOY OF 1,2,4,5-TETRABROMOBENZENE AND 1,2,4,5-TETRACHLOROBENZENE.
Teodoro Klaser, Željko Skoko 91

IN SITU OBSERVATION OF PRECIPITATE GROWTH AND DECOMPOSITION IN ALCU4 DURING HEAT TREATMENT VIA ANALYTICAL STEM
Evelin Fisslthaler, Robert Krisper, Werner Grogger 92

IT6 – ADVANCES IN INSTRUMENTATION AND TECHNIQUES (SEM, TEM, SPM, ETC.)

NANOSCALE STRAIN MAPPING IN METALLIC GLASSES DURING *IN SITU* DEFORMATION
Christoph Gammer, Thomas C. Pekin, Colin Ophus, Andrew M. Minor, Jürgen Eckert 96

ADVANCED TECHNIQUES FOR LOW- AND VERY-LOW ENERGY SEM USING REFLECTED AND TRANSMITTED SIGNALS
Ilona Müllerová, Benjamin Daniel, Ivo Konvalina, Luděk Frank, Eliška Materna Mikmeková 98

QUANTUM EXPERIMENTS IN THE TEM: REALIZING UNITARY OPERATORS USING QUADRUPOLES
Stefan Löffler, Peter Schattschneider 100

MAGNETIC DIFFERENTIAL PHASE CONTRAST IMAGING AT ATOMIC SCALE
Ján Rusz, Alexander Edström, Axel Lubk 103

IMPROVEMENTS IN ENVIRONMENTAL SCANNING ELECTRON MICROSCOPY – UNIVERSAL PRESSURE SCANNING ELECTRON MICROSCOPY (UPSEM)
Johannes Rattenberger, Harald Fitzek, Hartmuth Schroettner, Ferdinand Hofer. 104

ASSESSING THE THICKNESS ERROR RATE OF QUANTITATIVE STEM MEASUREMENTS
Radim Skoupy, Vladislav Krzyzanek. 107

SEM-EDS ANALYSIS OF GOLD MERCAPTOTRIAZOLE CRYSTALS (AU-MT)
Silvana Dimitrijević, Stevan Dimitrijević, Aleksandra Ivanović. 110

ADVANCED APPROACH TO SCANNING-TRANSMISSION TOMOGRAPHY IN THE SEM
V. Morandi, M. Ferroni, P. Maccagnani, L. Masini, A. Migliori, L. Ortolani, M. Donarelli, A. Signoroni, M. Savardi 111

INVESTIGATION IN THE EFFECTS OF EXERCISE ON THE TESTICULAR MORPHOLOGY, CELL PROLIFERATION AND BLOOD TESTIS BARRIER IN THE HIGH FAT DIET-INDUCED OBESITY
Merve Acikel Elmas, Ozlem Bingol Ozakpinar, Meltem Kolgazi, Goksel Sener, Serap Arbak, Feriha Ercan 113

CORRELATIVE ANALYSIS OF DUST PARTICLES BY SEM, EDXS AND RAMAN
Manfred Nachtnebel, Andrea Steitz, Ute Munoz-Czerny, Johannes Mantler, Gerhard Gruell, Hartmuth Schroettner. 115

LIFE SCIENCES

LS1 – LIVE CELL IMAGING, AND INTRACELLULAR DYNAMICS

SINGLE-MOLECULE TRACKING REVEALS DISTINCT BEHAVIORS OF EPIGENETIC MODIFIERS TET1 AND TET2 IN LIVE EMBRYONIC STEM CELLS
Joel Ryan, Philipp Messer, Christopher Mulholland, Don C. Lamb, Heinrich Leonhardt. 120

THE IMMOBILE MOVEMENT
Marco Biggiogera, Lorena Zannino, Stella Siciliani 121

COMBINED TWO PHOTON EXCITATION FLUORESCENCE AND THIRD HARMONIC GENERATION IMAGING OF REDOX RATIO FOR MONITORING METABOLIC STATE OF LIVE CELLS OF FUNGUS *PHYCOMYCES BLAKESLEEANUS*
Tanja Pajić, Katarina Stevanović, Nataša Todorović, Aleksandar Krmpot, Mihailo Rabasović, Branislav Jelenković, Miroslav Živić. 122

A NEW HOLOTOMOGRAPHIC MICROSCOPE FOR MONITORING APOPTOTIC CELL BEHAVIOR IN VIVO: A PRELIMINARY STUDY
Sara Salucci, Michela Battistelli, Francesca Sbrana, Debora Burini, Sabrina Burattini, Paolo Giovanninetti, Elisabetta Falcieri. 123

FIXATION-INDUCED CELL BLEBBING: HOW TO MINIMIZE A LOSS OF SOLUBLE PROTEINS FROM CELLS?
Pavel Hozák, Margarita Sobol, Lukáš Pastorek 125

EFFECTS OF MILD OZONISATION ON THE DYNAMICS OF LIPID DROPLETS IN ADIPOSE-DERIVED STEM CELLS AND MATURE ADIPOCYTES
Manuela Costanzo, Barbara Cisterna, Flavia Carton, Viviana Covi, Gabriele Tabaracci, Manuela Malatesta . . . 126

IMPACT OF ENDOTHELIAL LIPASE MODIFIED HDL ON ENOS TRAFFICKING AND ACTIVITY IN ENDOTHELIAL CELLS
Snježana Radulović, Benjamin Gottschalk, Pablo Zardoya Laguardia, Irene Schilcher, Markus Trieb, Dagmar Kratky, Gunther Marsche, Wolfgang F. Graier, Kurt Schmidt, Saša Frank. 128

LS2 – STRUCTURE AND IMAGING OF BIOMOLECULES

THE ADVANTAGES AND LIMITATIONS OF ADVANCED IMAGING FOR BIOLOGICAL STRUCTURES IN LIVE AND FIXED CELLS
Sercin Karahuseyinoglu, MD 130

ARCHITECTURE AND MODULAR ASSEMBLY OF THE SULFOLOBUS S-LAYER REVEALED BY ELECTRON CRYO-TOMOGRAPHY
Lavinia Gambelli, Benjamin Meyer, Mathew McLaren, Kelly Sanders, Tessa E.F. Quax, Vicki Gold, Sonja-Verena Albers, Bertram Daum 131

MODE OF ACTION OF MEMBRANE-ACTIVE COMPOUNDS: A BIOPHYSICAL STUDY COMBINING ELECTRON AND FLUORESCENCE MICROSCOPY ON LIFE BACTERIA
Nermina Malanovic, Ayse Ön, Karl Lohner 132

ULTRASTRUCTURAL ARRANGEMENT OF CADHERIN DIMERS AT CELL-CELL ADHESION SITES REVEALED BY ELECTRON TOMOGRAPHY
Walter A. Kaufmann, Christoph Sommer, Mateusz Dobrychlop, Ludek Lovicar, Carl-Philipp Heisenberg, Mateusz Sikora 133

REGIOSELECTIVE PARA-CARBOXYLATION OF CATECHOLS BY A PRENYLATED FLAVIN DEPENDENT DECARBOXYLASE
Stefan E. Payer, Stephen A. Marshall, Natalie Bärland, Xiang Sheng, Tamara Reiter, Andela Dordic, Georg Steinkellner, Christiane Wuensch, Susann Kaltwasser, Janet Vonck, Karl Gruber, Kurt Faber, Fahmi Himo, David Leys, Silvia M. Gluecka, Tea Pavkov-Keller 135

WORTMANNIN INDUCED APOPTOSIS VIA AUTOPHAGY INHIBITION IN 4T1 BREAST CANCER CELL LINE
Elgin Turkoz Uluer, Pinar Kilicaslan Sonmez, Damla Akogullari, Sevinc Inan 136

PROTECTIVE EFFECT OF MELATONIN ON THE MORPHOLOGY OF TESTIS TISSUE OF DIET-INDUCED OBESE RATS: MICROSCOPICAL AND BIOCHEMICAL INVESTIGATIONS
Nilsu Atay, Merve Açıkel Elmas, Hande Yapışlar, Özlem Bingöl Özakpınar, Fikriye Uras, Serap Arbak 139

LS3 – MICROSCOPIC APPLICATIONS IN SYMBIOTIC INTERACTIONS, PLANTS, MICROORGANISMS, AND ENVIRONMENTAL SCIENCES

MICROSCOPY AND PALYNOLOGY SIDE BY SIDE - CASE STUDY OF PALAEOENVIRONMENTAL CONDITIONS IN THE PAST ON THE AREA OF CENTRAL CROATIA
Dario Hruševar, Koraljka Bakrač, Slobodan Miko, Nikolina Ilijanić, Ozren Hasan, Božena Mitić 142

MICROSCOPIC TECHNIQUES AS AN EXPEDIENT TOOL FOR BINDING SCIENCE AND ART
Željko Savković, Nikola Unković, Miloš Stupar, Jelena Vukojević, Milica Ljaljević Grbić 143

A FIRST PROOF OF AN EARLY MECHANICAL COUPLING AND BIOFILM FORMATION IN DILUTE BACTERIAL SUSPENSIONS
Kostanjšek Rok, Sretenovič Simon, Stojković Biljana, Dogša Iztok, Poberaj Igor, Stopar David..... 144

APPLICATION OF SCANNING ELECTRON MICROSCOPY FOR EXAMINATION OF INFECTED TISSUES
Tereza Juříková, Dominika Luptáková, Helena Marešová, Andrea Palyzová, Anton Škríba, Jiří Novák, Olga Kofroňová, Miloš Petřík, Vladimír Havlíček, Oldřich Benada 146

SCREENING OF SURFACE MUSTARD SEEDS MORPHOLOGY BY SEM (SCANNING ELECTRON MICROSCOPY) AND OPTICAL MICROSCOPY BEFORE AND AFTER CONVENTIONAL AND MODERN EXTRACTION TECHNIQUES
Ivana Vrca, Josipa Šćurla, Azra Đulović, Tea Bilušić, Ivica Blažević..... 149

THE EFFECTS OF IONIZING RADIATION ON THE CELL WALL OF MICROALGAE *CHLORELLA SOROKINIANA* – TEM STUDY
Jelena Danilović Luković, Bernd Zechmann, Snežana Vojvodić, Jelena Bogdanović Pristov, Marina Stanić, Jon Pittman, Ivan Spasojević..... 152

MICROMORPHOLOGICAL TRAITS OF *MICROMERIA GRAECA* (L.) BENTH. EX RCHB. (LAMIACEAE) LEAF GLANDULAR TRICHOMES OF *IN VITRO* PROPAGATED PLANTS
Mirjana Janjanin, Svetlana Tošić, Dragana Stojičić, Bojan Zlatković, Snežana Budimir, Branka Uzelac 154

PHENOTYPIC CELL PLASTICITY OF *TRICHOPLAX ADHAERENS* SCHULZE, 1883 (PLACOZOA) AFTER TREATMENT WITH ETHANOL AND *PRUNUS SPINOSA* L. ETHANOL EXTRACT
Loretta Guidi, Federica Semprucci, Maria Balsamo, Daniele Fraternale, Mariastella Colomba, Silvio Cecchini, Eleonora Grassi, Lucia Cesaroni, Sabrina Burattini, Maria Cristina Albertini..... 157

IMAGING FTIR MICROSCOPY – TECHNIQUE FOR RAPID SCREENING OF PLANT CELL WALLS
Jasna Simonović Radosavljević, Jasna Stevanic, Daniela Đikanović, Aleksandra LJ. Mitrović, Lennart Salmén, Ksenija Radotić..... 159

THE SEM OBSERVATION IN FOUR PLUM GENOTYPES (*PRUNUS DOMESTICA* L.)
Milena Đorđević, Radosav Cerović, Dragan Nikolić, Sanja Radičević, Ivana Glišić, Nebojša Milošević..... 162

ALBEDO AND FLAVEDO FROM *"LIMONCELLA OF MATTINATA"*: MORPHOLOGICAL AND CHEMICAL DATA
S. Burattini; L. Di Patria; L. Potenza; R. Saltarelli; D. Burini; E. Falcieri; P. Gobbi; L. Valentini; D. Sisti; V. Stocchi; G. Annibalini, E. Barbieri..... 164

SCANNING ELECTRON MICROSCOPY-A SENSITIVE TOOL IN PORIFERA DETERMINATION
Stefan Andjus, Božica Vasiljević, Vladimir Lazović, Momir Paunović 166

GIMME SHELTER: GRAPEVINE PINOT GRIS VIRUS IN DEFORMED ENDOPLASMIC RETICULUM
Laura Pagliari, Giulia Tarquini, Sara Buoso, Alberto Loschi, Paolo Ermacora, Gregor Kapun, Rita Musetti ... 168

THE USE OF FLUORESCENCE MICROSCOPY FOR CLASSIFICATION OF POLLEN GRAINS
Mira Stanković, Jasna Simonović Radosavljević, Daniela Djikanović, Dragica Spasojević, Ksenija Radotić..... 171

DISTINCTION BETWEEN SPECIFIC IONIC AND OSMOTIC ASPECTS OF THE ULTRASTRUCTURAL CHANGES INDUCED BY SALT STRESS ON ETIOPLASTS AND THEIR GREENING
Roumaissa Ounoki, Adél Sóti, Annamária Kósa, Beata Mysliwa-Kurdziel, Katalin Solymosi 174

LS4 – NEUROSCIENCE AND HISTOPATHOLOGY

MICU1 CONTROLS CRISTAE JUNCTION AND SPATIALLY ANCHORS MITOCHONDRIAL CA2+ UNIPORTER COMPLEX
Benjamin Gottschalk, Christiane Klec, Gerd Leitinger, Eva Bernhart, Rene Rost, Helmut Bischof, Corina Madreiter-Sokolowski, Snjezana Radulovic, Emrah Eroglu, Wolfgang Sattler, Markus Waldeck-Weiermair, Roland Malli, Wolfgang F. Graier 177

STUDYING THE COMPLEX ROLES OF MICROGLIA WITH HIGH RESOLUTION IMAGING AND MICROGLIA MANIPULATION APPROACHES
Ádám Dénes 178

ELECTRON MICROSCOPIC ANALYSIS OF NEUROSECRETORY GRANULES IN THE NEUROBLASTOMAS OF PAEDIATRIC PATIENTS
Tamara Kravic-Stevovic, Tamara Martinovic, Darko Ciric, Gordana Samardzija, Sofija Jovanović, Djuricic Slavisa, Djokic Dragomir,Vujic Dragana, Vladimir Bumbasirevic 180

DEVELOPMENTAL PROGRAMMING: IMACT OF PRENATAL EXPOSURE TO DEXAMETHASONE ON GONADOTROPIC CELLS IN FEMALE RAT OFFSPRING
Nataša Ristić, Nataša Nestorović, Milica Manojlović-Stojanoski, Svetlana Trifunović, Branka Šošić-Jurjević, Branko Filipović, Verica Milošević..... 182

ADRENAL GLAND FUNCTIONING IN MALE AND FEMALE OFFSPRING FROM DX TREATED MOTHERS
Milica Manojlović-Stojanoski, Nataša Nestorović, Nataša Ristić, Svetlana Trifunović, Branko Filipović, Branka Šošić-Jurjević, Verica Milošević..... 185

THE EFFECTS OF EXPERIMENTALLY-INDUCED SEPSIS ON FOLLICULOGENESIS IN RAT OVARY
Müge Taşdemir, Tuğba Ekiz Yılmaz, Mehmet Kaya, Nadir Arıcan, Bülent Ahıshalı..... 188

ULTRASTRUCTURAL FEATURES OF MITOCHONDRIA IN LYMPHOCYTES OF PATIENTS WITH DIABETES MELLITUS TYPE 2
Tamara Martinovic, Darko Ciric, Tamara Kravic-Stevovic, Andjelija Stankovic, K. Lalic, I. Rasulic, Vladimir Bumbasirevic 190

THE EFFECTS OF ANAX IMPERATOR ADIPOKINETIC HORMONE ON THE EXPRESSION OF BRAIN-DERIVED NEUROTROPHIC FACTOR IN A RAT GLIOMA CELL LINE
Sibel Doğan, Sibel Köktürk, Oğuz Mutlu, Fatma Kaya Dağıstanlı, Elif Gelenli Dolanbay, Emel Usta, Feride Özdemir 193

NACHR A7 EFFECTS EXPRESSION OF SYNAPTIC TRANSLATION CONTROL PROTEINS CPEB3 AND NGDN IN HIPPOCAMPAL ORGANOTYPIC SLICE CULTURE
Irem L. Atasoy, Selma Yılmazer, Erdinç Dursun, Duygu Gezen-Ak . . . 195

DOES THE CO2 THAT IS USED IN HORIZONTAL INCUBATORS SUFFICIENTLY CLEAN? THE EFFECTS OF IN-LINE FILTERS IN EMBRYO DEVELOPMENT
Oktay Arda, Ebru Öztürk Öksüz, Murat Başar . . . 196

AUTOPHAGY ANALYSIS IN LYMPHOCYTES OF PATIENTS WITH TYPE 2 DIABETES MELLITUS AND HYPERLIPIDEMIA
Darko Ciric, Tamara Martinovic,Vladimir Bumbasirevic, Aleksa Zivkovic, Ankica Jankovic, K. Lalic, I. Rasulic, Tamara Kravic-Stevovic . . . 197

A NOVEL TYPE OF MICROGLIA-NEURON INTERACTION AND THE ROLE OF P2Y12 RECEPTORS
Balázs Pósfai, Csaba Cserép, Rebeka Fekete, Anett D. Schwarcz, Katinka Ujvári, Nikolett Lénárt, Barbara Orsolits, Zsófia I. László, Zsolt Lele, István Katona, Ádám Dénes . . . 199

HISTOPATHOLOGICAL EVALUATION OF SKIN DIMPLE IN FIBULAR HEMIMELIA
Salih Marangoz, Salime Pelin Ergüven, Basak Isildar, Mehmet Kaymakoglu, Guney Yilmaz . . . 202

IMMUNOFLUOROSCENT ANALYSIS OF C6 GLIOMA CELL LINES AFTER PACLITAXEL TREATMENT
Aleksandar Mirčić, Mihajlo Bošnjak, Vladimir Trajković, Vladimir Bumbaširević . . . 203

EFFECTS OF Δ-9 TETRAHYDROCANNABINOL ON THE SMALL INTESTINE ALTERED BY HIGH FRUCTOSE DIET
Alisa Bahar Beydogan, Isildar Basak, Zeynep Mine Coskun, Ece Koyuturk, Meral Koyuturk, Sema Bolkent . . . 205

THE EFFECTS OF MAGNESIUM SULFATE ON CYCLOPHOSPHAMIDE INDUCED OVARIAN DAMAGE: FOLLICULOGENESIS
Tuğba Ekiz Yılmaz, Müge Taşdemir, Mehmet Kaya, Nadir Arıcan, Bülent Ahıshalı . . . 207

LS5 – HIGH-RESOLUTION MICROSCOPY IN LIFE SCIENCES

SUPER-RESOLUTION MICROSCOPY REVEALED UNIQUE ORGANIZATION OF MICROTUBULES IN TUNNELING MEMBRANE NANOTUBES
Nataša Resnik, Tim Prezelj, Giulia Maria Rita De Luca, Erik Manders, Roman Polishchuk, Peter Veranič, Mateja Erdani Kreft . . . 210

HIGH-RESOLUTION DETECTION AND DYNAMICS OF POISED HUMAN RIBOSOMAL GENES
Klara Weipoltshammer, Sylvia Laffer, Luc Snyers, Christian Schöfer . . . 211

MOLECULAR INTERACTIONS BETWEEN BORRELIA ADHESINS AND EXTRACELLULAR MATRIX
Martin Strnad, Yoo Jin Oh, Marie Vancová, Peter Hinterdorfer, Ryan OM Rego . . . 212

INVERTEBRATE EPITHELIA MORPHOGENESIS: INTEGRATION OF EXTRACELLULAR MATRIX, CYTOSKELETON AND CELL JUNCTIONS IMAGING
Polona Mrak, Urban Bogataj, Jasna Štrus, Nada Žnidaršič . . . 213

THREE DIMENSIONAL RECONTRUCTION OF THE FEEDING APPARUTUS OF UNFED NYMPH *IXODES RICINUS*
Marie Vancová, Tomáš Bílý, Jana Nebesářová . . . 216

WEST-NILE VIRUS AND MOSQUITO-ONLY FLAVIVIRUS ARE BOTH INFECTING HUMAN NEUROBLASTOMA CELL LINE CULTIVATED ON PET MEMBRANES
Marko Kolenc, Mateja Poljšak-Prijatelj, Miša Korva . . . 217

LS6 – NANOMATERIALS IN BIOLOGY AND MEDICINE

NANOCARRIERS FOR NEUROMUSCULAR DISEASES
Manuela Malatesta . . . 220

CALCIUM PHOSPHATE NANOPARTICLES: SECOND GENERATION NON-VIRAL VECTORS
Feray Bakan . . . 222

BACTERIAL SURFACE-LAYER PROTEINS AND THEIR SECRETS
Markus Eder, Andela Dordic, Theo Sagmeister, Elisabeth Damisch, Djenana Vejzovic, Lavinia Gambelli, Walter Keller, Janet Vonck, Bertram Daum, A. Palva, T. Pavkov-Keller . . . 223

LOW ENERGY STEM: NEW TOOL FOR VISUALIZATION OF NANOPARTICLES CONJUGATED WITH BIOMOLECULES
Nebesarova Jana, Frank Luděk, Patak Aleš, Ďurinová Eva, Vancova Marie . . . 225

AUTOPHAGY AND CELL DEATH ROLE IN THE NANOMATERIALS BIODISTRIBUTION AND DEGRADATION
Maria Condello, Evelin Pellegrini, Gloria D'Avack, Stefania Meschini . . . 227

HYALURONIC ACID-BASED NANOCOMPLEXES AS AN INNOVATIVE THERAPEUTIC TOOL TO TREAT MYOTONIC DYSTROPHY
Mathieu Repellin, Flavia Carton, Federico Boschi, Andrea Albano, Giovanna Lollo, Manuela Malatesta . . . 229

TESTING NANOCARRIERS IN VITRO: ARE ALWAYS CULTURED CELLS A RELIABLE REFERENCE SYSTEM?
Manuela Costanzo, Federica Vurro, Laura Calderan, Federico Boschi, Ilaria Andreana, Silvia Arpicco, Barbara Stella, Manuela Malatesta . . . 231

HYPERTHERMIC NANOCARRIERS FOR BIOMEDICAL APPLICATIONS
Federica Vurro, Silvia Mannucci, Davide Prosperi, Massimiliano Perduca, Concepción Jiménez López, Alice Busato, Marco Gerosa, Stefano Tambalo, Maria Rosaria Marinozzi, Federico Boschi, Manuela Malatesta, Laura Calderan . . . 233

ALCIAN BLUE STAINING TO STUDY NANOPARTICLE-CELL INTERACTIONS AT TRANSMISSION ELECTRON MICROSCOPY
Flavia Carton, Mathieu Repellin, Giovanna Lollo, Manuela Malatesta . . . 235

MICROSCOPIC EVIDENCE OF THE PRIMARY ASTROCYTES' MORPHOLOGICAL DIFFERENTIATION AND MIGRATION INSIDE POROUS POLY-L-LACTIC ACID 3D SCAFFOLDS
Maria Antonietta Di Bella, Francesco Carfì Pavia, Valerio Brucato, Valeria Blanda, Francesca Zummo, Ilenia Vitrano, Carlo Maria Di Liegro, Giulio Ghersi, Italia Di Liegro, Gabriella Schiera . . . 237

MICROSTRUCTURE ANALYSIS OF POROUS MULTILAYERED CORE/SHELL SILICA PARTICLES FOR IMMOBILIZATION OF LIPASE
Milan P. Nikolić, Vladimir V. Srdić, Slobodanka S. Nikolić, Katarina Pavlović, Aleksa Maričić . . . 238

LS7 – MULTIDISCIPLINARY APPROACHES FOR MEDICAL AND BIOLOGICAL SCIENCES

DRUG RESISTANCE IN CANCER AND ITS OVERCOMING
Maria Condello, Evelin Pellegrini, Stefania Meschini . . . 242

CENTRIOLAR SATELLITES ARE REQUIRED FOR THE BIOGENESIS AND FUNCTION OF THE CENTROSOME/CILIUM COMPLEX
Elif N. Firat-Karalar . . . 244

BIOMECHANICAL FINGERPRINT OF DISEASE: APPLICATION OF ATOMIC FORCE MICROSCOPY TO CELL AND TISSUE MECHANICS
Gabriele Ciasca, Massimiliano Papi, Cristina Rossi, Fabio De-Giorgio, Angelo Minnella, Eleonora Minelli, Matteo Nardini, Alberto Mazzini, Marco De Spirito . . . 245

CHARACTERIZATION OF EXTRACELLULAR VESICLES FROM IN VITRO AND IN VIVO ORIGINS WITH ELECTRON MICROSCOPY
Samo Hudoklin, Nataša Resnik, Rok Romih . . . 247

ELECTRON MICROSCOPY AS A HELPFUL TOOL FOR VIRUS VACCINE DEVELOPMENT AGAINST PRRSV2
Susanne Richter, Tatjana Sattler, Jasmin Fertey, Boris Hartmann, Adi Steinrigl, Viskam Wijewardana, Richard Kangethe, Giovanni Cattoli, Sebastian Ulbert, Friedrich Schmoll . . . 250

RESVERATROL RECOVERS THE BETA CELL MASS, ISLET MORPHOLOGY AND APOPTOSIS IN FRUCTOSE-FED STREPTOZOTOCIN INDUCED RODENT DIABETES
Fatma Kaya Dagistanli, Ayşe Seda Akdemir, Merve Anapali, Turgut Ulutin, Melek Ozturk 254

VARIOUS MICROSCOPIC TECHNIQUES FOR TRACING CANCER UROTHELIAL CELLS IN MOUSE BLADDER TUMOR MODEL
Andreja Erman, Gregor Kapun, Sara Novak, Mojca Pavlind, Goran Dražić, Damjana Drobnec, Peter Veranič 257

MELATONIN FAILS TO PROTECT CARDIAC MITOCHONDRIA IN SIRTUIN 1 HETEROZYGOUS MICE PLACED ON A HIGH FAT DIET
Alessandra Stacchiotti, Raquel Garcia-Gomez, Antonio Lavazza, Maria Monsalve, Rita Rezzani 259

THE EFFECT OF SEEDING IN PROGRAMMED SLOW FREEZING OF IMMATURE TESTICULAR
Gülnaz Kervancıoğlu, Elif Kervancıoğlu Demirci, Şule Çetinel 261

THE EFFECTS OF TRIFOLIUM PRATENSE L. ON THE EXPRESSION OF LEUKEMIA INHIBITORY FACTOR IN THE ISHIKAWA CELL LINE
Emel Usta, Sibel Doğan, Havva Atar, Hatice Çölgeçen, Gamze Tanrıverdi, Feride Özdemir, Sibel Köktürk 263

AN INNOVATIVE BIOREACTOR FOR SKIN EXPLANTS MODEL
Enrica Cappellozza, Laura Calderan, Manuela Malatesta . . 265

INVESTIGATION IN THE EFFECTS OF EXERCISE ON THE TESTICULAR MORPHOLOGY, CELL PROLIFERATION AND BLOOD TESTIS BARRIER IN THE HIGH FAT DIET-INDUCED OBESITY
Merve Acikel Elmas, Ozlem Bingol Ozakpinar, Meltem Kolgazi, Goksel Sener, Serap Arbak, Feriha Ercan 267

PRENATAL DEXAMETHASONE TREATMENT AFFECTS GONADOTROPIC CELLS IN ADULT MALE AND FEMALE RATS
Nataša Nestorović, Milica Manojlović-Stojanoski, Nataša Ristić, Svetlana Trifunović, Branko Filipović, Branka Šošić-Jurjević, Verica Milošević. 269

NEGATIVE EFFECTS ON ENDOMETRIUM OF CLOMIPHENE CITRATE TREATMENT CAN BE PREVENTED WITH RESVERATROL?
Olgu Enis Tok, Pınar Özcan, Mukaddes Eşrefoğlu 272

ALTERATION IN BUCCAL MUCOSAL CELLS DUE TO THE EFFECT OF SMOKING CIGARETTE AND PERIODONTITIS BY ASSESSING GENETIC AND HISTOPATHOLOGIC DAMAGE
Köroğlu P, Alkan B 275

MORPHO-FUNCTIONAL EFFECTS OF ELECTRONIC CIGARETTE IN LUNG AND TRACHEA
Sabrina Burattini, Silvia Cirillo, Fabio Vivarelli, Vladimiro Cardenia, Maria Teresa Rodriguyez-Estrada, Eleonora Turrini, Moreno Paolini, Elisabetta Falcieri, Carmela Fimognari, Donatella Canistro 276

COMPARISON OF BASAL MEMBRANE THICKNESS OF GRANULOSA CELLS IN PCOS
Suleyman Erol, Selim Zirh, Gokce Nur Ari, Cemile Merve Seymen, Gulnur Take Kaplanoglu, Sevda Muftuoglu . . . 278

IMMUNOGOLD LABELLING OF VITAMIN D RECEPTOR AND ULTRASTRUCTURAL CHARACTERISATION OF METABOLIZING ENZYMES IN LIPID DROPLETS IN THE RAT LIVER
Natalija Filipović, Ivana Bočina, Ivana Restović, Nives Kević, Maximilian Grobe, Genia Kretzschmar, Tomislav Mašek, Marija Vitlov Uljević, Katarina Vukojević, Mirna Saraga-Babić, Ana Vuica. 281

MORPHOLOGICAL EVALUATION OF NATURAL ANTIOXIDANTS PROTECTIVE EFFECT IN DRUG-INDUCED C2C12 MYOTUBES ATROPHY
Debora Burini, Sabrina Burattini, Davide Curzi, Giovanni Zappia, Pietro Gobbi, Elisabetta Falcieri, Sara Salucci 283

INHIBITION OF CELLULAR ENERGY PRODUCTION IN TREATMENT OF CANCER INOCULATED TO HAMSTERS
Dušica J. Popović, Dušan Lalošević, Kosta J. Popović, Dejan Miljković, Ivan Čapo, Jovan K. Popović 285

NITROGLYCERIN INDUCES METFORMIN ANTICANCER EFFECT ON FIBROSARCOMA IN HAMSTERS
Kosta J. Popović, Dušica J. Popović, Dušan Lalošević, Dejan Miljković, Ivan Čapo, Jovan K. Popović 287

CORRELATION OF LIGHT- AND TRANSMISSION ELECTRON MICROSCOPY WITH NANOSIMS
Reipert S, Schintlmeister A, Legin AA, Volland J-M, Cyran N, Peredes G, Goldammer H, Eckhard M, Wagner M, Lichtscheidl I 290

LS8 – EMERGING AND MISCELLANEOUS TOPICS IN LIFE SCIENCES

QUANTITATIVE SCANNING-FREE CONFOCAL FLUORESCENCE MICROSCOPY FOR THE CHARACTERIZATION OF FAST DYNAMIC PROCESSES IN LIVE CELLS
Aleksandar J. Krmpot, Stanko N. Nikolić, Sho Oasa, Dimitrios K. Papadopoulos, Marco Vitali, Makoto Oura, Shintaro Mikuni, Per Thyberg, Simone Tisa, Masataka Kinjo, Lennart Nilsson, Lars Terenius, Rudolf Rigler, Vladana Vukojević 293

BENEFITS AND LIMITATIONS OF SCANNING ELECTRON MICROSCOPY AND RAMAN SPECTROSCOPY IN MICROBIOLOGICAL RESEARCH
Kamila Hrubanova, Vladislav Krzyzanek, Jana Nebesarova, Filip Ruzicka, Zdenek Pilat, Ota Samek. . . . 296

LINE-FRAP: A FAST TECHNIQUE TO DIFFERENTIATE BETWEEN THE DIFFUSION RATES OF FAST DIFFUSING MOLECULES FROM IN VITRO TO *IN VIVO*
Dr. Debabrata Dey, Shir Marciano, Prof. Gideon Schreiber 299

QUANTIFYING ORGANIZATION OF COLLAGEN FIBERS IN THE UNINVOLVED HUMAN COLON MUCOSA 10 CM AND 20 CM AWAY FROM THE MALIGNANT TUMOR
Sanja Despotović, Novica Milićević, Živana Milićević, Aleksandar Krmpot, Mihailo Rabasović, Aleksandra Pavlović, Vladimir Živanović 300

MICROSCOPY IN DAIRY SCIENCE: KEY HINTS FOR PRODUCT UNDERSTANDING AND TECHNOLOGY IMPROVEMENT
Paolo D'Incecco, Veronica Rosi, Luisa Pellegrino 303

VESICULAR TRAFFIC RELATED PROTEINS IN SUPERFICIAL UROTHELIAL CELLS OF URINARY BLADDER CANCER
Daša Zupančič, Samo Hudoklin, Rok Romih 307

ULTRASTRUCTURE OF TRAUMATIC RESIN DUCT FORMATION IN *CUPRESSUS SEMPERVIRENS* L. IN RESPONSE TO THE ATTACK OF THE FUNGUS *SEIRIDIUM CARDINALE* (WAG.) SUTTON & GIBSON
Alessio Papini, Salvatore Moricca, Roberto Danti, Corrado Tani, Isabella Posarelli, Sara Falsini, Gianni Della Rocca 310

EFFECTS OF MONOBENZYL ETHER OF HYDROQUINONE ON 3T3 MOUSE FIBROBLAST VIABILITY AND ULTRASTRUCTURE
Aslı Erdoğan, Hasan Serdar Mutlu, Sibel Doğan, Tuğba Kotil 312

SOY EXTRACT-DEPENDENT MODIFICATIONS OF THE PITUITARY SOMATOTROPHS IN RATS: STEREOLOGICAL, HISTOLOGICAL AND FUNCTIONAL STUDY
Svetlana Trifunović, Milica Manojlović-Stojanoski, Nataša Nestorović, Nataša Ristić, Branko Filipović, Branka Šošić-Jurjević, Verica Milošević. 315

THE ROLE OF P-IRE1 IN THE PATHOGENESIS OF ENDOMETRIOSIS: THE CONTRUBITION OF PERITONEAL FLUID
Tuğba Ekiz Yılmaz, Başak Işıldar, Altay Gezer, Duygu Kankaya, Cevriye Cansız Ersöz, Umit Kayışlı, Elif Güzel. . 318

EFFECTS OF KNOCK-DOWN OF ADHESIVE PROTEINS ON THE ULTRASTRUCTURE OF ADHESIVE VESICLES IN THE FLATWORM MINONA ILEANAE
Willi Salvenmoser, Robert Pjeta, Teresa Hofer, Michael W. Hess, Peter Ladurner 320

ELECTROPORATION: NEW STRATEGY TO IMPROVE THE DRUG UPTAKE AND OVERCOME THE TUMOR RESISTANCE
Maria Condello, Gloria D'Avack, Stefania Meschini 322

MATERIAL SCIENCES

MS1 – METALS, ALLOYS AND INTERMETALLICS

ANALYSIS OF INCLUSIONS IN STEELS: A CORRELATVE APPROACH
Barbara Šetina Batič, Jaka Burja, Matjaž Godec..... 326

SINGLE-STEP PREPARATION OF THE MIXED-METAL OXIDES FROM THE VERSATILE OXALATE PRECURSORS – CHARACTERIZATION AND PROPERTIES
Marijana Jurić, Lidij Androš Dubraja, Jasminka Popović, Lidija Kanižaj..... 327

MICROSTRUCTURE AND PROPERTIES OF AL-FE-MM-MG-SI ALLOY PREPARED BY POWDER METALLURGY
Alena Michalcová, Anna Knaislová, Zdeněk Kačenka, Jan Zábrodský, Ivo Marek 328

CHARACTERIZATION OF NANO-SIZED PARTICLES IN 14%CR OXIDE DISPERSION STRENGTHENED (ODS) STEEL USING CLASSICAL AND FRONTIER MICROSCOPY METHODS
Yael Templeman, Sergey Rogozhkin, Artem Khomich, Aleksander Nikitin, Malki Pinkas, Louisa Meshi..... 329

PRECIPITATION BEHAVIOR IN AN INTERMETALLIC FULLY LAMELLAR TIAL ALLOY
Michael Burtscher, Martin Schloffer, Daniel Kiener, Helmut Clemens, Svea Mayer..... 332

A MICROSTRUCTURE DEVELOPMENT DURING INTERCRITICAL ANNEALING OF DUCTILE IRON – THE DUAL PHASE AUSTEMPERED DUCTILE IRONS
Petar Janjatovic, Dragan Rajnovic, Olivera Eric Cekic, Sebastian Balos, Leposava Sidjanin..... 335

EFFECTS OF ALLOYING ELEMENTS ON THE MICROSTRUCTURE OF TI-AL-SI ALLOYS
Anna Knaislová, Vendula Šimůnková, Pavel Novák, Filip Průša 338

IN SITU TEM FRACTURE EXPERIMENTS ON ULTRAFINE GRAIN CHROMIUM AT RT: DISLCOATIONS PROCESSES AND TOUGHNENING MECHANISMS
Inas Issa, Anton Hohenwarter, Reinhard Fritz, Daniel Kiener 340

DISTRIBUTION OF DISLOCATIONS ON THE LÜDERS BAND FRONT DURING COLD DEFORMATION IN STEEL
M. Matvija, S. Rešković, T. Brlić 343

EVALUATION OF FRACTURE TOUGHNESS AND RECRYSTALLIZATION BEHAVIOUR OF ULTRAFINE GRAINED TUNGSTEN WIRES
Vladica Nikolić, Manuel Pfeifenberger, Anton Hohenwarter, Reinhard Pippan 346

HOMOGENEITY IN SUPERCONDUCTING NB3SN WIRES: EXPLORING THE ROUTES TOWARDS HIGH-PERFORMANCE BENDING MAGNETS FOR THE CERN FUTURE CIRCULAR COLLIDER
Alice Moros, Mattia Ortino, Stefan Löffler, Maxim Alekseev, Anastasia Tsapleva, Pavel Lukyanov, Ildar M. Abdyukhanov, Victor Pantsyrny, Bernardo Bordini, Amalia Ballarino, Simon C. Hopkins, Michael Stöger-Pollach, Johannes Bernardi, Michael Eisterer ... 349

ELECTRON MICROSCOPY ANALYSIS OF FLASH-ANNEALED CUZR BASED BULK METALLIC GLASS
Christoffer Müller, Christian Ebner, Christoph Gammer, Konrad Kosiba, Benjamin Escher, Simon Pauly, Jürgen Eckert, Christian Rentenberger..... 351

INTERACTION OF PICOSECOND ND:YAG LASER IRRADIATION WITH TI-13NB-13ZR ALLOY SURFACE IN AIR AND ARGON ATMOSPHERE
Slađana Laketić, Marko Rakin, Miloš Momčilović, Jovan Ciganović, Đorđe Veljović, Ivana Cvijović-Alagić ... 354

MICROSTRUCTURE AND FRACTURE ANALYSIS OF T6 TREATED HYPEREUTECTIC AL-13.5SI ALLOY FOR IC ENGINE COMPONENTS
Darko Vuksanovic, Vanja Asanovic, Zorica Cvijovic, Jelena Scepanovic, Dragan Radonjic 357

CRACK DEVELOPMENT AT IN-SITU TENSILE TESTING
Martin Bystrianský, Ludmila Kučerová, Jan Hajšman ... 360

EFFECT OF PARTICLE SIZE TIO2 FLUX IN A-TIG WELDING
Miroslav Dramicanin, Sebastian Balos, Petar Janjatovic, Dragan Rajnovic, Savka Adamovic..... 362

PROPERTIES OF THE FEAL20SI20-MOX (X=5, 10, 15, 20 WT.%) ALLOY PREPARED BY MECHANICAL ALLOYING AND COMPACTED VIA SPS
Filip Průša, Andrea Školáková, Jiří Lietavec..... 366

THE EFFECT OF NI AND MO ADDITION ON MICROSTRUCTURE AND PROPERTIES OF FE-AL-SI ALLOYS
Andrea Školáková, Olga Proshchenko, Filip Průša..... 367

FRICTION STIR SPOT WELDING OF MULTIPLE ULTRATHIN SHEETS OF ALUMINIUM-MAGNESIUM ALLOY
Danka Labus Zlatanovic, Sebastian Balos, Jean Pierre Bergmann, Michael Grätzel, Dragan Rajnovic, Tobias Köhler, Leposava Sidjanin..... 368

MICROSTRUCTURE AND PHASE CONSTITUTION OF NEAR-CO2FESI HEUSLER ALLOY
Jiří Buršík, Yvonna Jirásková 371

MS2 – NANOSCALE, NANOSTRUCTURED, AND CARBON BASED MATERIALS

LOW-ENERGY ELECTRON MICROSCOPY OF 2D GRAPHENE-HEXAGONAL BORON NITRIDE HETEROSTRUCTURES
Marin Petrović..... 373

DYNAMIC ACOUSTIC MODULATION OF QUANTUM LIGHT EMISSION FROM GAN/INGAN NANOWIRE QUANTUM DOTS
Snežana Lazić, Žarko Gačević, Enrique Calleja 374

FORMATION AND MICROSTRUCTURE REGULATION OF ULTRA-STRONG NANOCRYSTALLINE TUNGSTEN NANOFOAMS BY REVERSE PHASE DISSOLUTION
Mingyue Zhao, Inas Issa, Manuel J. Pfeifenberger, sMichael Wurmshuber, Daniel Kiener..... 375

MICROSTRUCTURAL CHARACTERIZATION OF ZINC TIN OXIDE (ZN2SNO4) PARTICLES SYNTHESIZED VIA HYDROTHERMAL SYNTHESIS TO BE USED IN SPUTTER TARGET
Umut Savacı, Cem Aciksari, Emel Ozel, Ender Suvacı, Servet Turan 377

SCATTERING-TYPE SCANNING NEAR-FIELD OPTICAL MICROSCOPY AND SPECTROSCOPY FOR NANOSCALE CHEMICAL ANALYSIS
Adrian Cernescu, Sergiu Amarie, Jan Vávra..... 379

THE STRUCTURE ANALYSIS METHODS FOR SYNTHETIZED DIAMONDS CONSOLIDATION AND FRACTALS CHARACTERIZATION
Sandra Veljkovic, Vojislav V. Mitic, Goran Lazovic, Vesna Paunovic, Markus Mohr, Hans Fecht 380

REDUCED GRAPHENE OXIDE-CHITOSAN FLEXIBLE NANOCOMPOSITE FOR EFFICIENT BACTERIA CAPTURE AND PHOTOTHERMAL ABLATION
Milica Budimir, Alexandre Barras, Duska Kleut, Rabah Boukherroub, Biljana Todorovic Markovic..... 381

REDUCTION OF GRAPHENE OXIDE AND GRAPHENE QUANTUM DOTS USING NASCENT HYDROGEN: INVESTIGATION OF MORPHOLOGICAL AND STRUCTURAL CHANGES
Svetlana Jovanovic, Olaf C. Haenssler, Milica Budimir, Duška Kleut, Jovana Prekodravac, Biljana Todorovic Markovic..... 382

MS3 – THIN FILMS, COATINGS, SURFACES AND INTERFACES

ATOMIC RESOLUTION IMAGING OF EPITAXIAL STRAIN DRIVEN PHENOMENA IN COMPLEX OXIDES
César Magén..... 384

AN INVESTIGATION ON THE EFFECTS OF THICKNESS ON GROWTH, STRUCTURE AND PROPERTIES OF RF MAGNETRON SPUTTERED ITO COATINGS
Andrius Subacius, Etienne Bousser, Bill Baloukas, Steve Hinder, Mark Baker, Duc-The Ngo, Claus Rebholz, Allan Matthews 385

IMPACT OF OXYGEN VACANCIES ON ELECTRONIC PROPERTIES OF ANATASE THIN FILMS
Daniel Knez, Goran Dražić, Sandeep Kumar Chaluvadi, Pasquale Orgiani, Regina Ciancio 386

ORIENTATION DEPENDENCE OF METASTABLE-ALN STABILITY IN GRADIENT CRN/ALN MULTILAYERS REVEALED BY HRTEM
Zhuo Chen, David Holec, Matthias Bartosik, Paul H. Mayrhofer, Zaoli Zhang, ... 387

SI NANOCRYSTAL GROWTH IN A-SI:H THIN FILMS AND MULTILAYERS AT VARIOUS CONDITIONS AND SURROUNDING MATERIALS BY TEM AND XRD STUDY
Rostislav Medlín, Pavol Šutta, Pavel Calta. 389

PHASE DISTRIBUTION AND ORIENTATION ANALYSIS WITH EBSD FOR DIFFERENT CONCENTRATIONS IN ELECTROLESS NI-B COATINGS
Erdem Kılıçaslan, Mehmet Uysal, Hatem Akbulut 390

QUANTITATIVE LOW-VOLTAGE WDS ELECTRON-PROBE MICROANALYSIS OF PMN-PT THIN FILMS PREPARED BY PULSED-LASER DEPOSITION
Zoran Samardžija, Urška Gabor, Matjaž Spreitzer 392

STUDY OF THIN PLASMA-POLYMER FILM GROWTH UNDER DUSTY PLASMA CONDITIONS
Vilma Bursikova, Vojtěch Homola, Štěpánka Bittnerová, Roman Přibyl, Petr Tomšej, Monika Stupavská, Anna Charvatova Campbell, Petr Klapetek, Jiří Buršík, Vratislav Perina. 395

FUNCTIONALIZED MAGNETITE NANOPARTICLES FOR DRUG LOADING, RELEASE, AND DELIVERY OF POORLY SOLUBLE ACTIVE BIOMOLECULES
Lucija Mandić, Anja Sadžak, Suzana Šegota 397

PLASMA ELECTROLYTIC OXIDATION OF ZN ALLOY IN ALUMINATE ELECTROLYTE
Sergey Karpushenkov, Hanna Maltanava, Aliaksandr Mikhailau, Sergey Poznyak, Larisa Karpushenkava, Kiryl Yasakau, Stevan Stojadinović, Rastko Vasilić 398

OPTIMISATION OF BATIO3 THIN FILMS PREPARED BY MAGNETRON SPUTTERING FOR SENSOR AND SOLAR CELL USE
Mario Bohač, Krunoslav Juraić, Ivana Panžić, Andreja Gajović 399

OXIDATIVE STRESS IN MODEL MEMBRANES: PROTECTION VIA FLAVONOID EMBEDDED NANOPARTICLES
Anja Sadžak, Lucija Mandić, Suzana Šegota 400

DEMYSTIFYING THE COMPOSITION AND THICKNESS OF LONG-LASTING COMMERCIALLY AVAILABLE TOOL COATINGS BY THE USE OF MICROSCOPY
Sara Hawi, Saurav Goel 401

MS4 – CERAMICS, COMPOSITES, CULTURAL HERITAGE MATERIALS, ROCKS AND MINERALS

THE MICROSTRUCTURE AND TEXTURE OF SPINEL REACTION LAYERS AROUND CORUNDUM: EFFECTS OF REACTION INTERFACE ORIENTATION
Gerlinde Habler, Roman Schuster, Chen Li, Lisa Baldwin, Petr Jeřábek, Rainer Abart 405

PRECESSION ELECTRON DIFFRACTION: APPLICATION TO VARIOUS CERAMIC COMPOSITES
Umut Savaci, Servet Turan. 408

TEM/MD INVESTIGATION INTO THE DYNAMICS OF SHI INDUCED TRACK FORMATION IN INSULATORS
Jacques O'Connell, Ruslan Rymzhanov, Nikita Medvedev, Vladimir Skuratov, Alexander Volkov 409

THE SYNERGY OF POLARIZED TRANSMITTED LIGHT MICROSCOPY AND SCANNING ELECTRON MICROSCOPY IN MINERALOGICAL-PETROLOGICAL INVESTIGATIONS OF CULTURAL HERITAGE OBJECTS
Kristina Šarić, Vesna Matović, Suzana Erić 411

USE OF OPTICAL MICROSCOPY, SEM AND EDS ANALYSIS FOR INVESTIGATION OF HISTORICAL PAINT LAYERS
Snežana Vučetić, Olivera Brdarić, John Milan van der Bergh, Bojan Miljević, Jonjaua Ranogajec. 414

SCANNING (SEM) AND TRANSMISSION ELECTRON MICROSCOPY (TEM) IN CULTURAL HERITAGE
Sabrina Burattini, Elisabetta Falcieri, Laura Baratin 416

THE NANOSCALE ORIGIN OF CHATOYANCY IN CHRYSOBERYL FROM PRATINHAS, BRAZIL
Sandra Drev, Aleksander Rečnik, Matjaž Mazaj, Nina Daneu. 418

MICROSTRUCTURAL CHARACTERIZATIONS OF K0.5BI0.5TIO3-BATIO3-NA0.5BI0.5TIO3 TEXTURED LEAD-FREE PIEZOELECTRIC CERAMICS
Umut Savaci, Ceren Aşkın, H. Şule Tetik, İsmail Şahin, Gürol Özarslan, A. Murat Avcı, Servet Turan, Ender Suvacı. 421

EBSD AND STEM ANALYSIS OF CYCLIC TWINS IN SNO_2 CERAMICS DOPED WITH COO AND NB_2O_5
Nina Daneu, José Alberto Padrón Navarta, Fabrice Barou, Goran Dražić, Sara Tominc, Aleksander Rečnik . . 422

OPTIMIZATION OF CARBON NANOTUBE CONTENT OF ASPHALT NANO COMPOSITES WITH REGARD TO RESISTANCE TO PERMANENT DEFORMATION
Emmanuel Gadzama Hamatu 425

MS5 – POLYMERS, BIOMATERIALS, AND SOFT MATERIALS

NANOMECHANICS OF BIOMATERIALS: VESICLES AND BIOPOLYMERS
Francesco Valle. 428

MECHANICAL PROPERTIES ON CELLULAR AND MOLECULAR LEVEL, AFM STUDY
Jan Pribyl 429

DIRECT VISUALIZATON OF LIPID-POLYMER STRUCTURES BY CRYO-TEM
Aleksander Foryś, Maria Chountoulesi, Natassa Pippa, Stergios Pispas, Costas Demetzos, Barbara Trzebicka . . 430

POLYMERIZATION SHRINKAGE-STRESS-RELATED DENTAL CUSP DEFORMATION ASSESSED BY DIGITAL HOLOGRAPHY
Evgenije Novta, Tijana Lainović, Dušan Grujić, Dejan Pantelić, Larisa Blažić, ... 433

FORMATION OF CALCIUM PHOSPHATES ON TIO_2 NANOTUBES IN THE PRESENCE OF ALBUMINE: INSIGHT IN FORMATION OF MULTIFUNCTIONAL NANOCOMPOSITES
Ina Erceg, Atiđa Selmani, Maja Dutour Sikirić 435

POROUS CERAMIC SCAFFOLDS WITH BIOACTIVE COMPOUNDS FOR BONE TISSUE ENGINEERING
Vera Lukasova, Michala Rampichova, Jana Dorazilova, Premysl Stastny, Radek Sedlacek, Martin Trunec, Milan Krticka, Lucy Vojtova. 438

POLYESTERAMIDE NANOFIBROUS SCAFFOLDS FOR BONE TISSUE ENGINEERING
Karolina Vocetkova, Radek Divin,, Vera Sovkova, Veronika Blahnova, Vera Lukasova, Evzen Amler, Karolina Rehakova, Jiri Brozek, Eva Filova 440

COLLAGEN TYPE I SCAFFOLD COATED WITH NATURE INSPIRED POLYMER
Veronika Blahnová, Katarína Kacvinská, Lucy Vojtová, Eva Filová, ... 441

EXAMINING HYDROGEL STRUCTURE USING FREEZING METHODS, CRYO SEM IMAGING AND IMAGE ANALYSIS
Katerina Adamkova, Kamila Hrubanova, Monika Trudicova, Petr Sedlacek, Vladislav Krzyzanek 442

NANOSCALE CHARACTERIZATION IN A MULTIPHASIC POLYMERIC SYSTEM - MORPHOLOGY@MECHANICAL PROPERTY@CHEMICAL COMPOSITION COMPLEMENTARY STUDIES.
Marco Casinelli 445

TRANSMISSION-ELECTRON-MICROSCOPY CHARACTERIZATION OF NANODEBRIS PARTICLES FROM THE WEAR OF A BIOCOMPATIBLE CERAMIC-ON-CERAMIC ARTIFICIAL HIP PART
Darja Feizpour, Monika Jenko, Borut Pompe, Boštjan Kocjančič, Matjaž Godec, Drago Dolinar 446

POLYESTERAMIDE NANOFIBERS FOR SKIN TISSUE ENGINEERING
Věra Sovková, Karolína Vocetková, Radek Divín, Karolína Řeháková, Jiří Brožek, Eva Filová, Evžen Amler 453

MS6 – SEMICONDUCTORS, DEVICES, AND MAGNETIC MATERIALS

CONFINEMENT EFFECTS IN SEMICONDUCTING NANOSTRUCTURES REVEALED WITH STEM-EELS
Giovanni Bertoni, Rosaria Brescia, Quentin Ramasse, Clive Downing, Valeria Nicolosi, Luca De Trizio, Javad Shamsi, Stefano Toso, Dmitry Baranov, Liberato Manna. . 450

ANALYSIS OF EXTENDED DEFECTS IN HIGH DOSE PROTON BOMBARDED GAAS USING CS-CORRECTED STEM
Johannes Neethling, Jaco Olivier, Arno Janse van Vuuren 453

SEGREGATION OF CA TOWARDS THE COMPRESSIVE STRAIN INTERFACE OF AN EPITAXIAL GROWN BISMUTH FERRITE THIN FILM
U. Haselmann, G. Haberfehlner, D. Knez, M. N. Popov, L. Romaner, A. Ghasemi, Z. L. Zhang, ... 456

DIRECT ATOMIC IDENTIFICATION OF CATION MIGRATION INDUCED GRADUAL CUBIC-TO-HEXAGONAL PHASE TRANSITION IN GE2SB2TE5
Yonghui Zheng, Yong Wang, Tianjiao Xin, Yan Cheng, Rong Huang, Pan Liu, Min Luo, Zaoli Zhang, Shilong Lv, Zhitang Song, Songlin Feng 459

ROLE OF DY DIFFUSION IN SINTERED ND-FE-B HARD MAGNETS
Kristina Žagar Soderžnik, András Kovács, Martial Duchamp, Andraž Kocjan, Rafal E. Dunin-Borkowski, Joachim Mayer, Spomenka Kobe. . . . 461

ANALYTICAL ELECTRON MICROSCOPY OF HALF-HEUSLER THERMOELECTRIC ALLOYS
Jiří Buršík, Gerda Rogl, Peter Rogl 462

MS7 – MATERIALS FOR ENERGY HARVESTING, PRODUCTION, STORAGE, AND CATALYSIS

INVESTIGATION ON THE EFFECT OF HYDROGEN ON DISLOCATION PATTERNS IN HIGH-STRENGTH STEELS USING ELECTRON CHANNELLING CONTRAST IMAGING IN THE SCANNING ELECTRON MICROSCOPE
Stefan Zaefferer, Dayong An, Yuchen Shan. 464

ELECTROCHEMICAL APPROACHES TO DESIGN MATERIALS FOR POTENTIAL SENSING AND ENERGY RELATED APPLICATIONS
Lidija D. Rafailović, Christoph Gammer, Tomislav Trišović, Christian Rentenberger, Aleksandar Z. Jovanović, Igor A. Pašti, H. Peter Karnthaler. 466

TEM CHARACTERIZATION OF SOME SENSITIVE MATERIALS BASED ON MGH2 AND NANOPOROUS CARBONS
Pavel Markov, Diana Nihtianova, Boyko Tsyntsarski, Eli Grigorova 468

TEM METHODS FOR CHARACTERIZATION OF ENCAPSULATED METAL NANOPARTICLES WITHIN ZEOLITES FRAMEWORK VIA 2D TO 3D TRANSITION
Michal Mazur, Yuyan Zhang, Martin Kubů, Jiří Čejka. . . . 470

CALCIUM MANGANITE COATINGS FROM CHEMICALLY SYNTHESIZED POWDERS
Jelena Macan, Anamarija Havliček, Suzana Kralj, Ivana Panžić, Miran Čeh, Andreja Gajović 472

ELECTRON MICROSCOPY AS AN ESSENTIAL TOOL IN ELECTROCHEMISTRY: ASSESSING THE SURFACE MORPHOLOGY OF AL ELECTRODES
David Moser, Sandra Steiner, Bernhard Gollas, Gerald Kothleitner, ... 475

STRUCTURAL STUDY BY CS-CORRECTED ELECTRON MICROSCOPY OF LUMINESCENT INDIUM-ZINC OXIDES
J. García-Fernández, A. Torres-Pardo, J. Bartolomé, A. Cremades, J. Ramírez-Castellanos, J. M. González-Calbet, ... 476

IDENTICAL LOCATION TEM FOR THE STUDY OF CATALYST MATERIALS: FROM SINGLE ATOMS TO NANOPARTICLES
Francisco Ruiz-Zepeda, Matija Gatalo, Primož Jovanovič, Davide Menga, Tim-Patrick Fellinger, Léonard Jean Moriau, Andraž Pavlišič, Nejc Hodnik, Marjan Bele, Goran Dražić, Miran Gaberšček 477

ROLE OF LATTICE OXYGEN CONTENT IN THE CO OXIDATION ACTIVITY OF THE BA-FE-O SYSTEM
Aurea Varela, Isabel Gómez-Recio, Achraf el Hadri, María Hernando, Marina Parras, Juan J. Delgado, José J. Calvino, José M. González-Calbet 478

STRUCTURAL SINGULARITIES IN 2H-RELATED BANIO PHASES
D. Gutiérrez-Martín, M. Hernando, A. Torres-Pardo, J. M. González-Calbet, A. Varela, M. Parras 479

SURFACE DECORATED TIO2 NANOTUBES FOR PHOTOCATALYTIC APPLICATION
Vedran Kojić, Marko Rukavina, L. Radetić, Ivana Grčić, Andreja Gajović 480

ELECTRON MICROSCOPY STUDY OF NANOCRYSTALLINE WURTZITE ZNS PRODUCED VIA A CO-PRECIPITATION TECHNIQUE AND ITS PYROELECTRIC CERAMICS PROCESSED BY 2-STEP-PRESSURELESS SINTERING
Radenka Krsmanović Whiffen, Loris Pietrelli, Luciano Pilloni, Giuseppe Magnani, Elena Salernitano, Selene Grilli, Francesca Mazzanti, Amelia Montone. 482

MICROSTRUCTURE AND THERMAL BEHAVIOR OF MG-V THIN FILMS FOR SOLID STATE HYDROGEN STORAGE
T. Pantić, K. Zagar Soderžnik, S. Šturm, S. Drev, A. Mitrović, S. Kurko, B. Paskaš Mamula, N. Novaković, J. Grbović Novaković, I. Milanović, S. Milosević Govedarović. . 484

MS8 – EMERGING AND MISCELLANEOUS TOPICS IN MATERIAL SCIENCES

PHOTOCROMIC MOLECULAR PROBES FOR PHOTOACOUSTIC MICROSCOPY
Francesco Garzella, Paolo Bianchini, Alberto Diaspro, Ranieri Bizzarri, Barbara Storti, Cristiano Viappiani 488

POLLEN *IN VITRO* GERMINATION, VIABILITY AND MORPHOLOGY OF BLACK CHOKEBERRY CULTIVAR 'ARONIA NERO' (*ARONIA MELANOCARPA* (MICHX.) ELLIOT)
Milena Đorđević, Svetlana M. Paunović, Mira Milinković, Radosav Cerović, Dragan Nikolić 491

ELECTROCHEMICAL SENSORS BASED ON PHYROPYILITE
Anđela Mitović, Tijana Patnić, Sivana Dimitrijević, Aleksandra Ivanović, Nikola Novaković, Sandra Kurko, Sanja Milošević Govedarović, Jasmina Grbović Novaković 494

PLENARY LECTURES

ATOMISTIC PHENOMENA IN NANOSTRUCTURES FOR ENERGY RELATED APPLICATIONS

VELIMIR R. RADMILOVIĆ[1,2]

[1] Serbian Academy of Sciences and Arts, Belgrade, Serbia; [2] Nanotechnology and Functional Materials Center, Faculty of Technology and Metallurgy, University of Belgrade, Serbia

This study demonstrates nanostructure enhancement in both, thermal and electrical properties in functional oxide polytypoid nanowires for energy related applications. A novel method, which controls both, structure and chemical composition at nanoscale, was used to produce polytypoid nanowires. Due to the decoupling of certain electrical and thermal properties, these polytypoid nanowires, which contain low dimensional periodic compositional and structural features, are ideal model systems for studying thermoelectric phenomena at atomic scale. The concept of structure control at atomic level is in agreement with the theoretical prediction that it is possible to increase the material-dependent figure of merit, $zT=S^2\sigma T/\kappa$ (S - Seebeck coefficient, σ - electrical conductivity, κ - thermal conductivity coefficient, T - absolute temperature). This can be achieved by using nanoscale materials, attributed to electronic band structure changes due to the quantum confinement effect, which increases the Seebeck coefficient, and enhances interface phonon scattering, which brings down the thermal conductivity coefficient. It appeared that control of lattice phonon transport contribution is essential in improving thermoelectric properties of functional oxide nanowires. Aberration corrected transmission electron microscopy was used to perform a detailed structural analysis of these nanowires at atomic level, based on which we propose that the aperiodic superlattice structure is generated through a defect-assisted solid-state diffusion. One of the greatest advantages of this novel synthesis is the ability to tune the nanoscale features of the polytypoid wires by simply adjusting the amount of metal precursor with appropriate annealing procedure in oxygen atmosphere. These new oxide thermoelectric nanostructures exhibited a two to three orders of magnitude increase in figure of merit, due to hindering of phonon propagation, while preserving good electrical conductivity.

QUANTUM SORTING: A NEW PARADIGM OF QUANTUM MEASUREMENT IN ELECTRON MICROSCOPY

VINCENZO GRILLO
CNR-NANO, Modena, Italy

The methodological and instrumental research in electron microscopy is a very vital and flourishing field of research. Important innavations have regarded the correction of spherical aberrations and the improvement down to meV scale of the EELS energy resolution. However a completely new prospective on electrons in microscopy has arisen from the introduction of electron vortex beams and more general of beam shaping [1][2]. These concepts, very familiar to light optics community, are quite unusual for electron microscopy. But what is the actual use of these new tools?

Beam shaping can be used to correct the spherical aberration, measure the off-axis component of the magnetic field, produce new form of interferometry and new forms of lensing.

However we introduce here the idea and the application of a new beam control configuration that should allow for a paradigm change in the microscopy measurements.

This device is the Orbital Angular Momentum (OAM) sorter [3][4]. Using a combination of electrostatic phase elements we can produc, directly of the screen of the microscope or in a spectrometer, a spectrum of the OAM distribution of a given wavefunction. In a quantum language this is an alternative representation of a wave alternative to position (imaging) and momentum (diffraction) and promises to open a new world of measurements: plasmon mode analysis, EMCD (magnetic dichroism) and protein analysis are just a few examples.

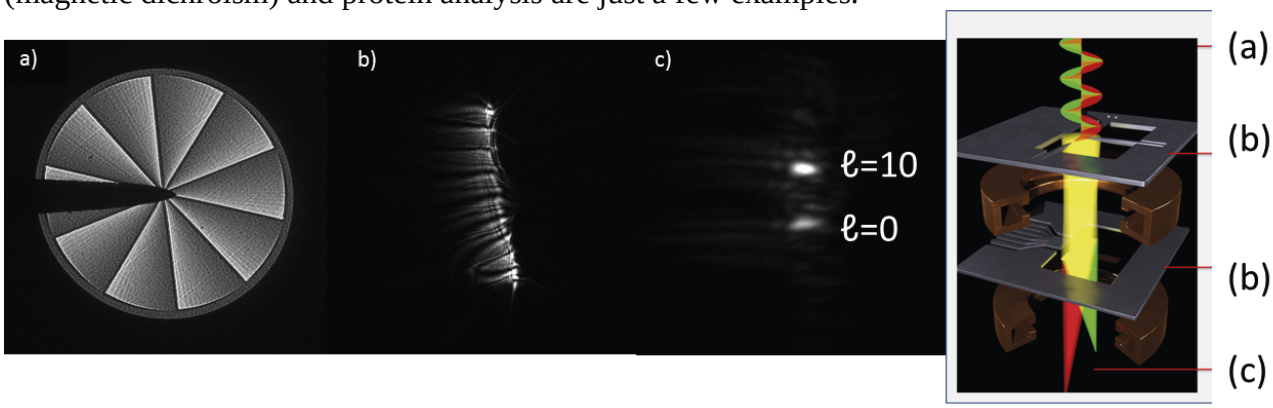

Figure 1. Evolution of a test wavefunction in a sorter from the initial wave (a) trough the coordinate tranformation (b) to the final spectrum (c). The scheme of the 3 elements is also shown.

Figure 1 shows an example of working OAM sorter acting on a test beam. The final spectrum shows that the beam can be written as a quantum superpostion of OAM states with ℓ=10 and ℓ=0 (the OAM is here equal to ℓ times the plank constant ħ).

These data are obtained from QSORT personnel and not only the author. This work is supported by Q-SORT, a project funded by the European Union's Horizon 2020 Research and Innovation Program under grant agreement No. 766970.

References

[1] J. Verbeek , H Tian., P. Schattschneider Nature 467 (2010) 301
[2] V. Grillo et al. Optics Express 25 (2017) 21851
[3] V.Grillo, A.H. Tavabi et al. Nature Comm. 8, 15536 (2017)
[4] B. McMorran, T.R. Harvey, M.P.J. Lavery, New Journal of Physics 19, 023053 (2017)

ANATOMY AND PHYSIOLOGY OF THE NUTRITIONAL SYSTEM

SAVERIO CINTI
Dep. of Exp. and Clin. Med.-Center of Obesity; Polytechnic University of Marche, Ancona, Italy

Anatomy of Adipose Tissues

The term adipocyte refers to the anatomical feature of cells able to contain relevant amounts of lipids regardless their function. It is widely accepted that two very different cell types can be defined as adipocytes: white and brown adipocytes.

White adipocytes and white adipose tissue (WAT)

White adipocytes are large (about 70-140 microns) spherical cells containing a unilocular lipid droplet in their cytoplasm that form about 90% of the cell volume. The spherical shape is the best geometrical form allowing maximal volume in minimal space, thus supporting the main goal of this cell: a reservoir of energy able to guarantee energy distribution to the rest of organism during intervals between meals (1). Lipids contained into white adipocytes are triglycerides, i.e. highly energetic molecules that represent the ideal fuel for the activity of heart. Brain must also be served during fasting and this condition induces white adipocytes to secrete asprosin a protein able to induce hepatic glucogenesis, thus providing fuel for brain (2) . White adipose tissue (WAT) is also the main site of production of leptin (3). Leptinemia is positively correlated with the total amount of fat contained in the body. When fat is scarce and does not guarantee for survival during fasting, low leptinemia induces a strong stimulus for food search and intake (in collaboration with asprosin).

Brown adipocytes and brown adipose tissue (BAT)

Brown adipocytes are smaller than white adipocytes (about 1/3) and lipid droplets are small and numerous (multilocular). The reason for this lipid arrangement is that mitochondria of these cells are able to burn fatty acids to produce heat (4). The large lipid-cytoplasm surface contact due to the multilocular arrangement and the presence of the uncoupling protein 1 (UCP1) on the inner membrane of large and packed with laminar cristae mitochondria are key factors for their thermogenic activity. Cold exposure induces a noradrenergic stimulus, trought sympathetic nervous system, for ß3 adrenergic receptors of brown adipocytes. The adrenergic signalling induces two main consequences: UCP1 synthesis and activation (5). Mitochondria oxidize fatty acids that result in formation of a proton gradient between the external and internal compartments of mitochondria. UCP1 is inserted in the membrane forming the laminar cristae and separating the two compartments. In coupled cells (without UCP1) the proton gradient is used to form ATP using the energy of proton flux trough the enzymatic channel formed by ATPase that is also present on mitochondria cristae. In brown adipocytes UCP1 acts as a protonophore offering an alternative way to protons to reach the mitochondria internal compartment and thus uncoupling the oxidation of fatty acids from ADP phosphorylation. The net result of this uncoupling process is the heat production derived from the inevitable side effect of fatty acids oxidation. Because the total amount of fatty acids oxidized in the large and numerous mitochondria is relevant the heat production assumes a physiologic role allowing survival of mammals in quite cold climate. The vascular and nerve supply to WAT and BAT is quite different. In humans WAT and BAT have the same morphologic and functional characteristics described above.

The Adipose Organ

Our anatomical studies showed that adipose tissues are contained in a dissectible organ: the adipose organ (6). This organ is contained in two compartments of the body: subcutaneous and visceral. The subcutaneous part forms a continuous layer between cutis and muscles. The visceral part is contained in mediastinum, abdomen and pelvis. In small mammals many of these depots are composed by a mixed population of BAT and WAT and accurate quantitative studies on mice maintained in warm environment (28°C) have shown that BAT is the prevalent tissue (about 60%) in obesity resistant strain Sv129, while WAT is the prevalent tissue (about 80%) in obesity prone strain C57/BL6 (B6). In adult humans the adipose organ is mainly composed by WAT but remnants of metabolically active BAT are found mainly in the supraclavicular area (in close proximity with aorta arch branches) (7).

Plasticity of the Adipose Organ

A true organ can be defined as follows: an anatomically dissectible composed by at least two different tissues with reciprocal cooperative functions able to concur for a unitary functional purpose. For example, a widely accepted structure that is considered as an organ is the stomach. This organ fulfils the above reported definition: it is dissectible, it is formed by several tissues (i.e.: muscles and mucosae) and the cooperation for digestion is evident. The adipose organ is dissectible, composed by WAT and BAT having distinct several functions. Our data suggest that the reciprocal cooperative aspect of WAT and BAT consist in their ability to convert each other reversibly in physiologic conditions (transdifferentiation). As a matter of fact, several data showed that in different occasions the adipose organ is able to became more brown (browning) or more white (whitening). Detailed analyses of browning in the two different strains mentioned above (Sv129 and B6) showed that after ten days of cold exposure the total number of adipocytes contained in the adipose organ did not change in both strains, the BAT component increased in both and the WAT component decreased in both. Interestingly the decrease of WAT was in both equivalent to the increase in BAT suggesting a direct conversion of WAT in BAT as several other experiments have shown before(8). Of note, a recent paper supported the reversible transdifferentiation phenomenon by lineage tracing experiments.

The clearest data showing the reverse phenomenon (BAT whitening) in physiological condition is offered by aging and obesity. BAT whitening due to aging is probably due to reduced sympathetic activity as shown by a prompt browning of whitened BAT after cold exposure of old rats and by a clear BAT whitening in beta less mice, but the physiologic whitening can be that occurring when a chronic excess of calorie intake induces energy storing in BAT. The organism in fact cannot refuse the precious energetic molecules because a fasting period cannot be excluded a priori.

Thus, a converging body of evidences seem to suggest that a mature cell, under a physiologic stimulus can reversibly change its phenotype and function. In order to further support this new basic cellular property, we found another striking example in the adipose organ: mammary gland.

The Pink Adipocyte (PAT)

The mammary gland is a true gland only during pregnancy and lactation because the glandular part of it (milk-producing alveoli) develop only in these periods and disappear after the end of lactation. The alveolar cells seems to derive mainly from a direct conversion of adipocytes. All alveolar epithelial cells of late pregnancy, immunoreactive for the milk protein WAP (Whey Acidic Protein) and the nuclear transcription factor ELF5 (E74-Like Factor5, key regulator of alveologenesis), have impressive amount of lipids (unilocular vacuole) in cytoplasm that make their morphology very similar to unilocular adipocytes.

The term adipocyte implies simply a parenchymal cell of adipose organ rich in lipids whatever is its function, thus we called these epithelial cells pink adipocytes because the colour of the organ during pregnancy is pink (9). Electron microscopy studies, BrdU experiments, immunohistochemistry

data on serial sections and lineage tracing and explants experiments support the reversible white to pink conversion and also the pink to brown conversion (10-12). Brown to pink conversion has not been jet demonstrated but a brown to myoepithelial conversion was recently found by another lab (13).

Thus, the transdifferentiation seems to be a basic physiologic property of adipose organ acting to allow the best distribution of energy for different needs: thermogenesis (brown), nutrition of the body (white), nutrition of pups (pink).

The concept of Nutritional System

The adipose organ collaborates with digestive organs for the vital homeostatic mechanism of humans: nutrition (14). Both adipose (leptin, asprosin) and digestive (Ghrelin, PYY^{3-36}, Insulin) organs produce hormones able to influence the mammal's behaviour for pivotal activities finalized to nutrients search, intake and distribution. Low levels of leptinemia informs brain of poor energy storage and induces a strong stimulus for food search and intake . Thus leptin action on limbic system assume a primary importance in driving the very primitive behaviour to survive. But leptin stimulus is not the only one, because together with food search it is necessary the intake of food and the recent discovery of asprosin led new light on this aspect .

Post-prandial BAT thermogenesis is stimulated by intestinal products such as bile acids and secretin and BAT produced factors such as FGF21 influence digestive aspects.

Finally, intestinal microbiota implements the intestinal-adipose organ functional link.

Histopathology of the Adipose Organ

Adipose tissues of obese animals and humans are infiltrated by macrophages. Infiltration creates a low-grade chronic inflammation of considerable importance because it determines insulin resistance that leads to type 2 diabetes (15). Our laboratory has shown that both human and murine obese hypertrophic adipocytes die thus producing particularly large cellular residues (Fig. 1). The macrophages surround the debris and form characteristic histopathological figures that we have called CLS (crown-like-structures) (16, 17). Subsequent studies have shown that hypertrophic visceral adipocytes die earlier than those of the subcutaneous and therefore have a lower critical death size, justifying the greater morbidity of visceral fat accumulation, well known since early clinical studies [4].

Conclusions

Thus, the cooperation between adipose organ and digestive organs seem to delineate a complex system able to coordinate the most important basic behaviour and function for survival: food search and intake. After the intake food must be absorbed (intestine) and transformed into useful energetic molecules that must be stored and distributed to the rest of the organism in the intervals between meals (adipose organ). Furthermore, the energy distribution must be delivered to new-borns in order to guarantee the species survival and pink adipocytes (mammary alveolar cells) derived from WAT conversion during pregnancy and lactation seem to serve this important function of the system.

All these data on adipose organ anatomy, physiology and plasticity allow a better understanding of its histopathology and this knowledge is necessary for future strategies of prevention and treatment of obesity and related disorders: i.e. a very widely diffused and important pathology (18).

References

[1] Cinti S. Obesity, Type2 Diabetes and The Adipose Organ2018.
[2] Romere C, Duerrschmid C, Bournat J, Constable P, Jain M, Xia F, et al. Asprosin, a Fasting-Induced Glucogenic Protein Hormone. Cell. 2016;165(3):566-79.
[3] Friedman J. The long road to leptin. J Clin Invest. 2016;126(12):4727-34.
[4] Cinti S. Adipose Organ Development and Remodeling. Compr Physiol. 2018;8(4):1357-431.
[5] Cinti S. UCP1 protein: The molecular hub of adipose organ plasticity. Biochimie. 2017;134:71-6.
[6] Cinti S. The Adipose Organ: Kurtis, Milan; 1999.

[7] Zingaretti MC, Crosta F, Vitali A, Guerrieri M, Frontini A, Cannon B, et al. The presence of UCP1 demonstrates that metabolically active adipose tissue in the neck of adult humans truly represents brown adipose tissue. FASEB J. 2009;23(9):3113-20.
[8] Cinti S. Adipocyte differentiation and transdifferentiation: plasticity of the adipose organ. J Endocrinol Invest. 2002;25(10):823-35.
[9] Cinti S. Pink Adipocytes. Trends Endocrinol Metab. 2018;29(9):651-66.
[10] Morroni M, Giordano A, Zingaretti MC, Boiani R, De Matteis R, Kahn BB, et al. Reversible transdifferentiation of secretory epithelial cells into adipocytes in the mammary gland. Proc Natl Acad Sci U S A. 2004;101(48):16801-6.
[11] De Matteis R, Zingaretti MC, Murano I, Vitali A, Frontini A, Giannulis I, et al. In vivo physiological transdifferentiation of adult adipose cells. Stem Cells. 2009;27(11):2761-8.
[12] Giordano A, Perugini J, Kristensen DM, Sartini L, Frontini A, Kajimura S, et al. Mammary alveolar epithelial cells convert to brown adipocytes in post-lactating mice. J Cell Physiol. 2017;232(11):2923-8.
[13] Li L, Li B, Li M, Niu C, Wang G, Li T, et al. Brown adipocytes can display a mammary basal myoepithelial cell phenotype in vivo. Mol Metab. 2017;6(10):1198-211.
[14] Cinti S. Anatomy and physiology of the nutritional system. Mol Aspects Med. 2019.
[15] Weisberg SP, McCann D, Desai M, Rosenbaum M, Leibel RL, Ferrante AW, Jr. Obesity is associated with macrophage accumulation in adipose tissue. J Clin Invest. 2003;112(12):1796-808.
[16] Cinti S, Mitchell G, Barbatelli G, Murano I, Ceresi E, Faloia E, et al. Adipocyte death defines macrophage localization and function in adipose tissue of obese mice and humans. J Lipid Res. 2005;46(11):2347-55.
[17] Giordano A, Murano I, Mondini E, Perugini J, Smorlesi A, Severi I, et al. Obese adipocytes show ultrastructural features of stressed cells and die of pyroptosis. J Lipid Res. 2013;54(9):2423-36.
[18] Giordano A, Frontini A, Cinti S. Convertible visceral fat as a therapeutic target to curb obesity. Nat Rev Drug Discov. 2016;15(6):405-24.

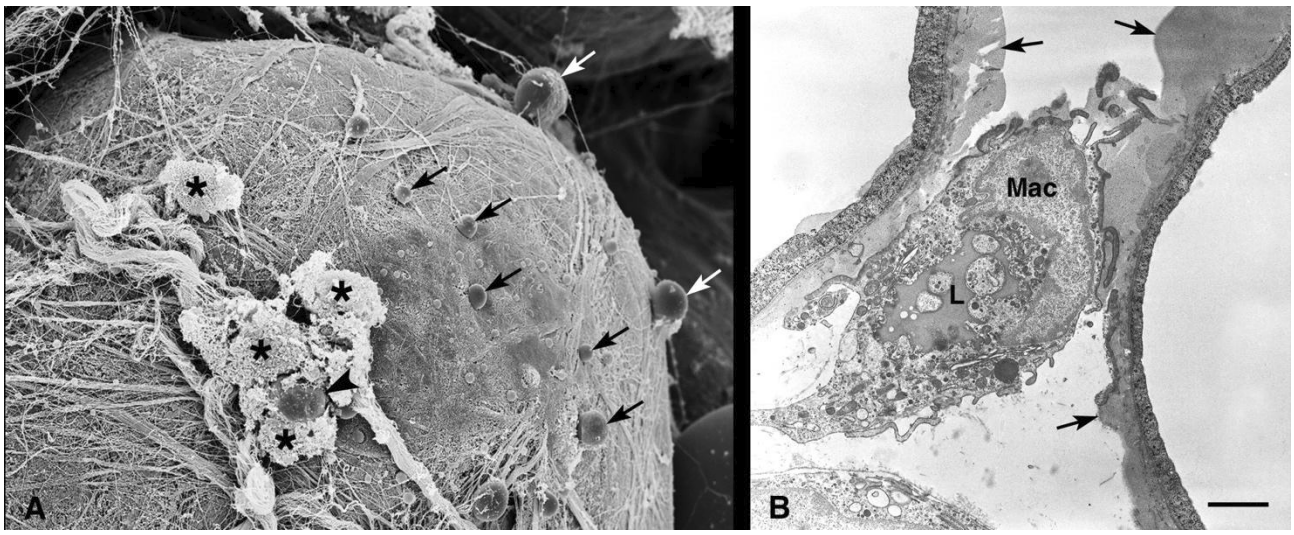

Fig 1. Extrusion of lipid droplets by degenerating adipocytes into the visceral fat of a db/db obese mouse. By HR-SEM, (A) a degenerating adipocyte is releasing several small lipid droplets (arrows) into the extracellular space. An extruded lipid droplet (arrowhead) is surrounded by some macrophages (asterisks). Note the numerous collagen fibrils covering the surface of the degenerating adipocyte. In (B), TEM shows lipid droplets being cleared by a macrophage (Mac) in an area where two adjacent degenerating adipocytes are extruding lipid droplets (arrows). Note the large lipid droplet (L) in the macrophage cytoplasm. Scale bar: 4.2 µm for (A); 1.8 µm for (B). This figure was originally published in the Journal of Lipid Research. Giordano A, Murano I, Mondini E, Perugini J, Smorlesi A, Severi I, Barazzoni R, Scherer PE, Cinti S. Obese adipocytes show ultrastructural features of stressed cells and die of pyroptosis. J. Lipid Res. J Lipid Res. 2013 Sep; 54(9):2423-36. © the American Society for Biochemistry and Molecular Biology or © the Author(s).

USING OFF-AXIS ELECTRON HOLOGRAPHY TO MEASURE MAGNETIC PROPERTIES OF MATERIALS

ANDRÁS KOVÁCS[1], JAN CARON[1], P. DIEHLE[2], FENGSHAN ZHENG[1], THIBAUD DENNEULIN[1], DONGSHENG SONG[1] AND RAFAL E DUNIN-BORKOWSKI[1]

[1] Enst Ruska-Centre for Microscopy and Spectroscopy with Electrons, Peter Grünberg Institute, Forschungszentrum Jülich, Jülich, Germany; [2] Fraunhofer Institute for Microstructure of Materials and Systems, Halle, Germany

Off-axis electron holography (EH) is one of the most powerful technique that directly measures the phase shift of the electron wave that has interacted with the electromagnetic fields of an electron transparent sample in the transmission electron microscope (TEM). It can be used to measure quantitatively the magnetic properties of materials with high spatial resolution. The introduction of high brightness electron guns, improved specimen holders with external stimuli, spherical aberration corrections, direct electron detectors, image analysis and image simulation have resulted in dramatic improvements in the spatial, phase resolutions and ability to interpret the often very complex magnetic states of nanostructures. Here, we describe the magnetic field measurements in the TEM, recent experimental results of magnetic field characterization of nanostructures, soft and hard magnetic alloys and magnetic skyrmions and give an outlook to possible future developments in methodology developments.

Off-axis EH is based on the use of an interference of an object wave that passed through a region of interest on the sample with another part of the same electron wave that usually passed through vacuum. An electron holographic interference pattern is generated by applying positive voltage to the biprism that is positioned one of the conjugated image plane of the microscope. In this work, off-axis EH measurements were performed using a high-brightness gun, spherical aberration corrected TEM operated at 300 kV. The magnetic field-free environment around the sample is obtained by turning off the conventional objective lens of the microscope and using, instead the transfer lens of the aberration corrector. A magnetic field is applied to the specimen using a combination of the sample tilt and small excitation of the objective lens. Electron holograms are recorded using a direct electron counting camera taking advantage of its high speed and improved phase noise characteristics.

Figure 1 shows an example of quantitative magnetic measurements of Bloch skyrmions in B20-type FeGe thin film. To generate skyrmions, the sample was cooled below the magnetic transition temperature in the presence of a small magnetic field (100 mT) using a liquid nitrogen filled TEM holder as the magnetic transition temperature of this material is 278 K. The magnetic contribution to the phase alone was obtained by repeating the experiment at room temperature and evaluating the difference between the phase images recorded at the two temperatures. Figure 1a shows the magnetic phase shift image of Bloch skyrmions recorded at 200 K in the presence of 400 mT out-of-plane magnetic field applied using the objective lens of the microscope [2]. The magnetic phase is proportional to the in-plane component of the magnetic induction within and around the specimen integrated in the electron beam direction. The induction map can be generated by adding contours to the image by evaluating the cosine of a chosen multiple of the phase. The horizontal and and vertical derivatives can also be used to generate colours that shows the field directions. Figure 1b shows the magnetic induction map of Bloch skyrmions generated from the magnetic phase image. In addition, the magnetic phase shift can be used to calculate the projected in-plane magnetization applying a model-based iterative reconstruction algorythm. Figure 1c,d shows the results of the magnetization calculation of a Bloch skyrmion, which can serve to analyse the field distribution and characteristic properties of magnetic objects [3]. The measured magnetization is approximately 110 kA/m at 200 K, which is in a reasonable agreement with the bulk value considering the three-dimensional magnetic field distribution of a Bloch skyrmion in a thin film.

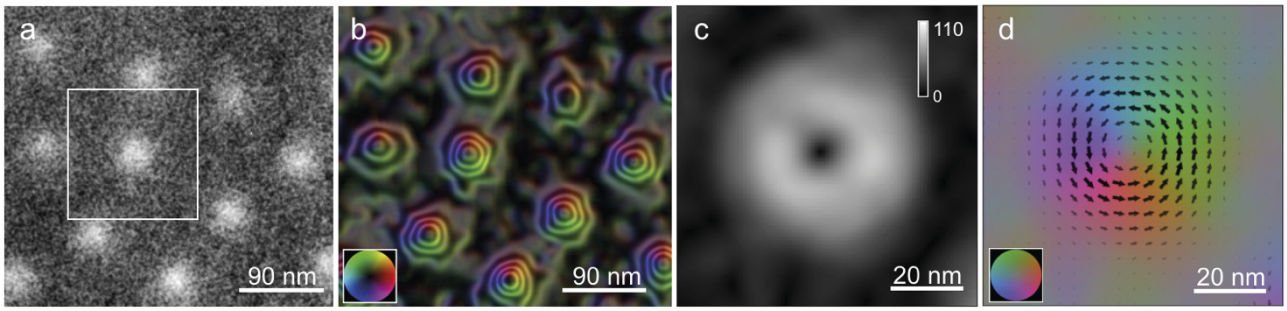

Figure 1. Magnetic imaging of Bloch skyrmions in B20-type FeGe thin film. a) Magnetic phase shift map recorded at 200 K in the presence of 400 mT applied perpendicular to the sample. b) The corresponding magnetic induction map of the skyrmions is visualized by adding colors and contours with a spacing of $2\pi/64=0.098$ rad. c) Projected in-plane magnetisation of a single skyrmion marked in (a) calculated using a model-based iterative reconstruction algorithm. The scale is in kA/m. d) The corresponding vector map of the recovered projected magnetisation.

Acknowledgements

We are grateful to T. Almeida, J. Arbiol, S. Blügel, M. Charilaou, P. Diehle, L. Kibkalo, N. Kiselev, Z.-A. Li, D. Meertens, J. Nogues, C. Panagopoulos, W. Pieper, L. Pierobon, K.G. Pradeep, J. Shah, K. Shibata, A. Soumyanarayan, Y. Tokura, K. Zagar-Soderznik for contribution to this work.

References

[1] A. Kovács and R.E. Dunin-Borkowski, Handbook of Magnetic Materials, vol. 27, p.59-153 (Ed. E. Brueck, Elsevier), 2018
[2] K. Shibata et al., Physical Review Letters 118 (2017) 087202
[3] A. Kovács et al., Applied Physics Letters 111 (2017) 192410

MICROSCOPING THE AMOEBOID CELL MOTILITY

IGOR WEBER
Ruđer Bošković Institute, Division of molecular biology, Zagreb, Croatia

Transition from mesenchymal to amoeboid cell migration is a hallmark of tumor metastasis. Genuine amoeboid motility is most appropriately studied in amoeba such as *Dictyostelium*. The core motility mechanisms conserved from amoebozoa to mammals are based on fast remodeling of the actin cytoskeleton regulated by small GTPases. I will present a retrospective of a quarter century of cell motility research in *Dictyostelium* and give an overview of the contemporary evolution of digital microscopy techniques with the focus on live cell imaging [1-15].

References

[1] Weber I., Wallraff E., Albrecht R., Gerisch G. (1995). Motility and substratum adhesion of Dictyostelium wild-type and cytoskeletal mutant cells: a study by RICM/bright-field double-view image analysis. J. Cell Sci. 108, 1519-1530.
[2] Weber I., Albrecht R. (1997). Image processing for combined bright-field and reflection interference contrast video microscopy. Comput. Programs Biomed. 53, 113-118.
[3] Weber I., Gerisch G., Heizer C., Murphy J., Badelt K., Stock A., Schwartz J.-M., Faix, J. (1999). Cytokinesis mediated through the recruitment of cortexillins into the cleavage furrow. EMBO J. 18, 586-594.
[4] Weber I. (1999). Computer-assisted morphometry of cell-substratum contacts. *Croatian Med. J.* 40, 334-339.
[5] Medalia O., Weber I., Frangakis A.S., Nicastro D., Gerisch G., Baumeister W. (2002). Macromolecular architecture in eukaryotic cells visualized by cryoelectron tomography. *Science* 298, 1209-1213.
[6] Weber I. (2003). Reflection interference contrast microscopy. *Methods Enzymol.* 361, 34-47.
[7] Weber I. (2006). Is there a pilot in a pseudopod? *Eur. J. Cell Biol.* 85, 915-924.
[8] Gerisch G., Weber I. (2007). Toward the structure of dynamic membrane-anchored actin networks: an approach using cryo-electron tomography. *Cell Adhes. Migration* 1, 145-148.
[9] Weber I. (2011). Interference Reflection Microscopy. In: Encyclopedia of Life Sciences (ELS), Zheng, Yixian (ed.). Chichester: John Wiley & Sons, Ltd, pp. 1-6.
[10] Filić V., Marinović M., Faix J., Weber, I. (2012). A dual role for Rac1 GTPases in the regulation of cell motility. *J. Cell Sci.* 125, 387-398.
[11] Antolović V., Marinović M., Filić V., Weber, I. (2014). A simple optical configuration for cell tracking by dark-field microscopy. *J. Microbiol. Meth.* 104, 9-11.
[12] Ramalingam N., Franke C., Jaschinski E., Winterhoff M., Lu Y., Brühmann S., Junemann A., Meier H., Noegel A.A., Weber I., Zhao H., Merkel R., Schleicher M., Faix J. (2015). A resilient formin-derived cortical actin meshwork in the rear drives actomyosin-based motility in 2D-confinement. *Nat. Commun.* 6: 8496.
[13] Marinović M., Šoštar M., Filić V., Antolović V., Weber I. (2016). Quantitative imaging of Rac1 activity in *Dictyostelium* cells with a fluorescently labelled GTPase-binding domain from DPAKa kinase. *Histochem. Cell Biol.* 146, 267-279.
[14] Junemann A., Filić V., Winterhoff M., Nordholz B., Litschko C., Schwellenbach H., Stephan T., Weber I., Faix J. (2016). A Diaphanous-related formin links Ras signaling directly to actin assembly in macropinocytosis and phagocytosis. *Proc. Natl. Acad. Sci. USA* 113, E7464-E7473.
[15] Marinović M., Mijanović L., Šoštar M., Vizovišek M., Junemann A., Fonović M., Turk B., Weber I., Faix J., Filić V. (2019). IQGAP-related protein IqgC suppresses Ras signaling during large-scale endocytosis. *Proc. Natl. Acad. Sci. USA* 116(4): 1289-1298.

QUANTITATIVE CS CORRECTED STEM OF LOCAL STRUCTURES IN LEAD-FREE FERROELECTRICS

GORAN DRAZIC[1,2,3], ANDREJA BENCAN[2,3], HANA URSIC[2,3], MAJA MAKAROVIC[2,3], MATEJ KOMELJ[3,4], TADEJ ROJAC[2,3] AND DRAGAN DAMJANOVIC[5]

[1] Department of Materials Chemistry, National Institute of Chemistry, Ljubljana, Slovenia; [2] Electronic Ceramics Department, Jozef Stefan Institute, Ljubljana, Slovenia; [3] Jožef Stefan International Postgraduate School, Ljubljana, Slovenia; [4] Department for Nanostructured Materials, Jozef Stefan Institute, Ljubljana, Slovenia; [5] Group for Ferroelectrics and Functional Oxides, Swiss Federal Institute of Technology - EPFL, Route Cantonale, Lausanne, Switzerland

Ferroelectric materials in thin-film or bulk forms are technologically very important and are used for decades in electronic, electro-mechanical and optical devices. This class of materials, often having a perovskite structure, undergoes spontaneous polarisation below some critical temperature (Tc, Curie temperature) where non-centrosymmetric (paraelectric, normally cubic) structure transform to a centrosymmetric one (tetragonal, rhombohedral, orthorhombic or monoclinic). Upon transformation 2D topological defects are formed where two domains with different direction of polarisation come into contact, called domain walls (DW). DWs may form along various crystallographic planes, depending on crystal symmetry, may accumulate different ionic or electronic point defects, and may be pinned by different defects like dislocations or grain boundaries. Under external electric field the spontaneous polarisation of ferroelectric materials can be reversed and the domain walls can move. The DW dynamics and consequently the final macroscopic properties are influenced by the DW local structure and the presence of various point defects accumulated at or near the wall. Most of these structural features are the result of the material synthesis and have detrimental effect on the DW properties, such as electrical conductivity. Controlling those features could be directly utilizable in the so-called "domain-wall nanoelectronics" [1, 2, 3] or may indirectly influence the functional response of polycrystalline ferroelectrics [4]. To make further progress in tailoring the DW properties, in-depth understanding of the structural details of DWs on the nano and atomic scales are needed.

Using elaborated quantification methodologies based on ADF and ABF STEM images the atom columns shifts from the original positions can be measured within few pm precision, and from comparison of experimental atom column intensities with calculated ones the presence and concentration of cation vacancies can be very precisely determined [5].

As a continuation of our recently published work on domain-wall conductivity in $BiFeO_3$ [5] where we explained the extrinsic nature of the DW conduction mechanism dominated by the accumulation of charged defects (Bi vacancies and Fe^{4+}) at the DWs we report in this presentation that through different material processing conditions (temperature, atmosphere, and cooling rates) the type and concentration of defects at DWs may be controlled and the local DW structure, thickness, unit-cell distortions across the wall and consequently the DW conductivity can be tailored. By constructing displacements maps from STEM images, we identified the DW type (charged/non-charged) and compared the point defects accumulation differences at DW regarding the type. The observed domain structures and point defects clustering were correlated with DFT calculations. Some interesting in- and ex- situ biasing experiments will be explained and the DW dynamics discussed and commented.

In the second part of the presentation the direct experimental evidence of the existence of polar nano regions in paraelectric state of barium titanate based ferroelectric materials will be introduced and discussed. It was recently found that some ferroelectric materials exhibit unusual types of electro-mechanical and electro-thermal coupling in their paraelectric state, which should be

forbidden by their centric symmetry. Origins of this phenomena are not yet well understood. It was shown with indirect evidences that $BaTiO_3$ cubic phase exhibits local and macroscopic breaking of nominal centric symmetry and exhibits local and global polarization. It was assumed that both are linked to presence polar nano regions [6].

A direct visualisation of polar nano-regions in paraelectric phase of $BaTiO_3$ (BT with Tc at 130 °C) and $(Ba_{0.6}Sr_{0.4})TiO_3$ (BST, with Tc at 0°) by measuring oxygen atoms displacement regarding to Ba and Ti sub-lattices will be presented. We also correlate the chemical composition fluctuations (Ba/Sr ratio) in BST with possible appearance of polar nano-regions. Data were obtained from ABF and ADF images, acquired with Cs probe-corrected STEM using heating sample holder in the temperature range from RT to 300 °C. Results show that in paraelectric state BT and BST Ba or (Sr, Ba), Ti and O atom columns are displaced in a coherent way, and forming noncubic few nm sized clusters. Based on shifts of Ti and O sub-lattices we confirm that those regions are polar and possess symmetry, which could even be lower than tetragonal.

Possible origins of polar nano-regions and the correlation between the presence of polar nano-regions and chemical composition fluctuations (in the case of BST) and lattice strain will be explained and discussed.

Throughout the lecture the techniques and approaches used during quantitative Cs-corrected STEM analysis, such as fast collection of frame stacks to minimize the effect of the specimen drift and scanning nonlinearity, estimation of the influence of sample thickness, defocus values, etc. on the quality of results will be described and discussed in details.

References

[1] J. Seidel et al., Nat. Mater. 8 (2009), p. 229
[2] P. Sharma et al., Sci. Adv. 3 (2017), e1700512
[3] G. Catalan et al., Rev. Mod. Phys. 84 (2012), p. 119
[4] T. Rojac et al., Adv. Funct. Mater. 25 (2015), p. 2099
[5] T. Rojac et al., Nat. Mat. 16 (2017), p. 322
[6] H. Sina et al., J. Appl. Phys. 9 (2016), p. 119

INSTRUMENTATION AND TECHNIQUES

IT1

Advances in sample preparation techniques

CHAIRPERSONS:

György Zoltán Radnóczi, Meltem Sezen

INVITED LECTURE

Ion sample preparation for microanalysis in Earth science

ANDREY KUDRYAVTSEV[1], EVGENY VASILEV[2], OLGA TELNOVA[3] AND JOHN MARSHALL[4]

[1] TESCAN Ltd., Saint-Petesburg, Russia; [2] Saint-Petersburg Mining University, Saint-Petersburg, Russia; [3] IG Komi SC UB RAS, Syktyvkar, Russia; [4] School of Ocean and Earth Science, Southampton, United Kingdom

Since the EBSD information comes from depth of few tens of nanometers the most critical issue of the EBSD measurement is the surface quality. The ion beam can gently polish surface as for EBSD so for cutting any ingomogenious solid samples in order to create a new surface for imaging and microanalysis. Therefore ion sample preparation is presented as the most promissing, well defined and precise, universal and succesful method for preparation of a wide range of materials with the purpose of microanalysis such as EDS, EBSD and TKD. Paleontological objects are one of the most fragile samples in the surfase preparation for any investigation. Another type of “extrimely hard” materials for surfase preparation is diamond. Ion polishing can significantly improve the surface quality in both cases.

1. Ion polishing for EBSD analysis of natural diamonds.

High surface quality on series of mechanically polished natural diamonds was achived using broad ion beam (BIB) or in the other words by a near parallel Ar^+ ion beam source (see. Fig. 1 left). Only BIB technique allow us to treat and polish large samples up to 12 mm in diameter (see. Fig. 1 right). Ion Ar^+ polishing was carry out by 1 keV beam energy with 4 degree inlcine during 30 min. This type of surface preparation allows us to reveal the cases of misorientation of the structure and the split of diamond crystals into subgrains. We have shown that this effect are more often than it is usually assumed [1]. We showed also cases of cracking, disorientation and regeneration of diamond crystals by EBSD maping of classic polycrystalline diamond. We have identified 60° twins with a thickness of 60-600 nm, in plastically deformed crystals. At the intersection of twins, <110> etching channels (Rose channels) are observed in some cases. Thus, the EBSD method allows one to obtain new data on the real structure of even such a well-studied mineral as the diamond is.

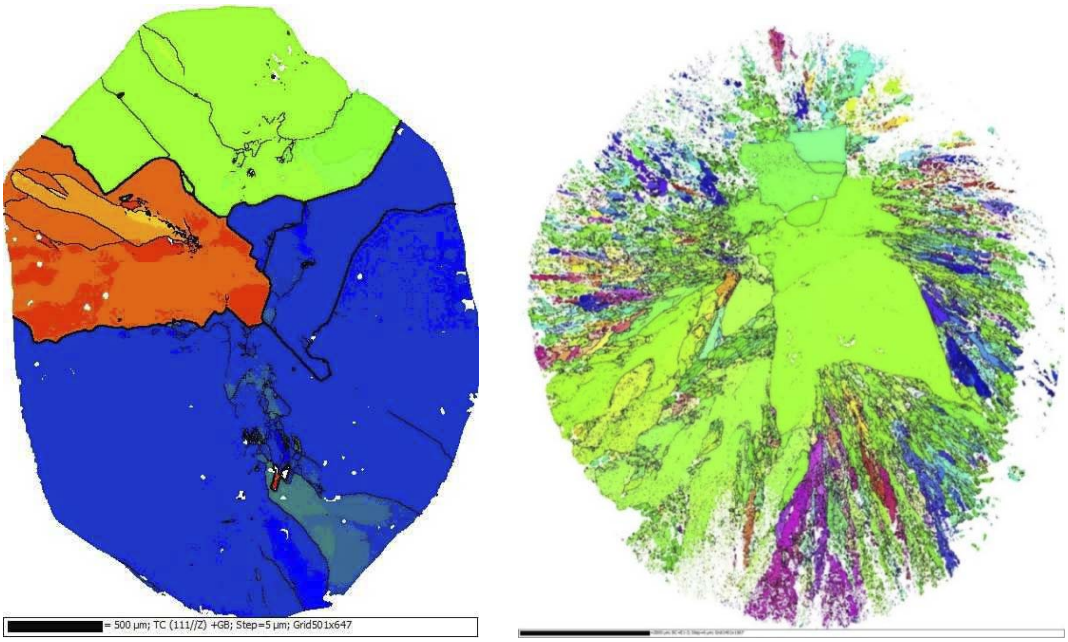

Fig.1. Texture component map (111//Z) of diamond surface (left) and large area polishing of diamond in IPF Z coloure (right).

2. Ion slope cutting of Devonian micro- and megaspores.

Studying the morphology and ultrathin structure of spores *in situ* in various phylogenetic lines of Paleozoic plants and comparing them with dispersed ones is necessary information in reconstructions of plant communities of the Earth past history. However the time consuming and sophisticated sample preparation with high probability of failure mainly for paleontological samples have laed us to use the ion milling tecniquies. Studying of inner fine structure and microanalysis inside these spores was done after ion beam cutting. These Devonian micro- and megaspores were collected in the Pease Bay formation in the northeastern part of Scotland (these collection is compiled by the University of Southgemtom University J. Marshall, United Kingdom).

Slope cut of a megaspores 1200 um in diameter was performed by 8 keV of Ar^+ ion beam with 30 degree incline during 2.5 hours (see. Fig.2 left). For local ion cutting of a microspore 100 um in diameter the liquid metall source of Ga^+ was used with 30 keV of focused ion beam (FIB) at 90 degrees (see. Fig.2 right). The use of FIB and BIB thechniques allows one to study the micro and nanosculpture of a sporoderm surface, the number of its layers and their ultrathin structure. These results are in a good agreeement with a preliminary TEM analysis and can be obtained in the framework of ion sample preparation techniques [2].

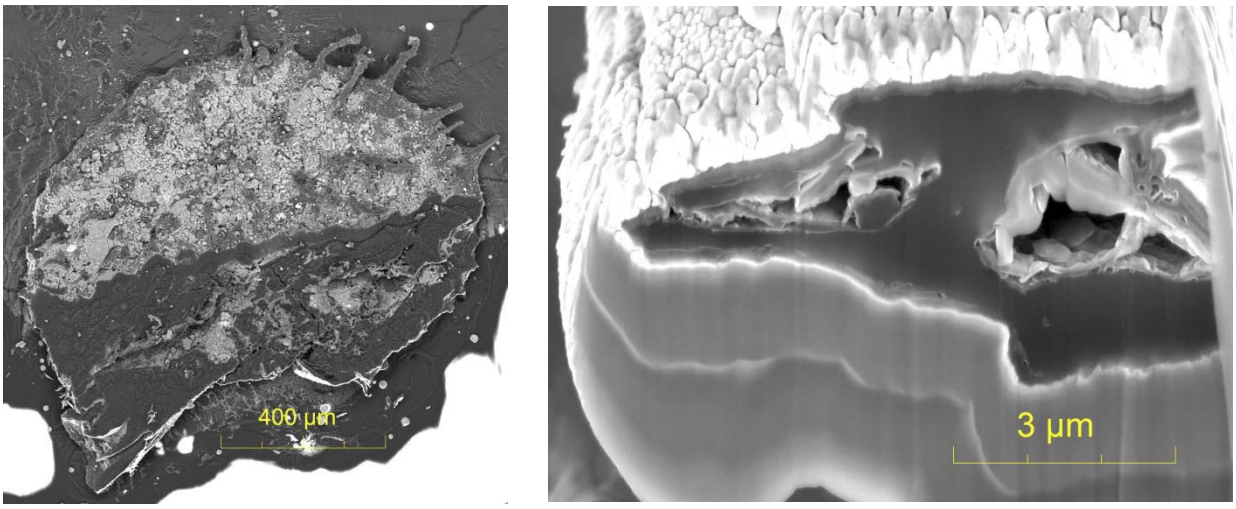

Fig. 2. BIB 30° slope cut of megaspore - *Archaeotriletes* Naumova (left) and 90° FIB cross-section of microspores edge - *Curriculomonoletes orbis* McLean et Neves (right).

References

[1] Y. L. Orlov, The mineralogy of diamond, New York: Wiley and Sons, (1977) 235.
[2] D. McLean, R. Neves, Review of Palaeobotany and Palynology, 126 (2003) 153–162.

Broad Ion Beam Cross Section Preparation on Nitrocarburised and Oxidised Steel Samples to Correlate Microstructure and Tribological Behaviour

JOHANNES RATTENBERGER[1], STEFAN MITSCHE[1,2], HARALD FITZEK[1], IGOR VELKAVRH[3], ALEXANDER DIEM[3] AND HARTMUTH SCHROETTNER[1,2]

[1] Graz Centre for Electron Microscopy - ZFE, Graz, Austria; [2] Graz University of Technology, Institute of Electron Microscopy and Nanoanalysis - FELMI, Graz, Austria; [3] V-Research GmbH, Dornbirn, Austria

A widespread technique to increase the surface hardness of metal components is nitrocarburising. In this thermochemical process nitrogen and carbon diffuse into the surface of ferrous materials, which increases the hardness, wear resistance, fatigue strength, low adhesion and corrosion resistance of tools and engineering parts operating under unlubricated or boundary lubrication conditions [1-3]. It is often applied to inexpensive, easily machined low carbon steel to impart the surface properties of more expensive and difficult to work grades of steel.

In this work 31CrMoV9 (1.8519) steel samples were initially treated by salt bath- (SNC), gas- (GNC) and plasma-nitrocarburising (PNC) and afterwards oxidised for increased corrosion protection. The surface as well as the cross section of these samples were analysed using optical- and Scanning Electron Microscopy (SEM), Energy-Dispersive X-ray Spectroscopy (EDX) and Electron Backscatter Diffraction (EBSD) to get detailed information about the surface topography, the microstructure, the crystallography and the chemical composition.

From a microscopy point of view the cross section preparation is very challenging. On the one hand, the interesting regions are at the edge of the samples and rounding due to embedding could provide misleading information. On the other hand, the nanoporosity of the surface modified areas can easily be smeared by using a conventional sample preparation (embedding, grinding and polishing). For these reasons the broad ion beam technique (Gatan Ilion) was used for cross section preparation. To guarantee an artefact-free cross section and to avoid changes in nanoporosity the sample was cooled during preparation and prepared from the backside to avoid redeposition (see Figures 1 and 2).

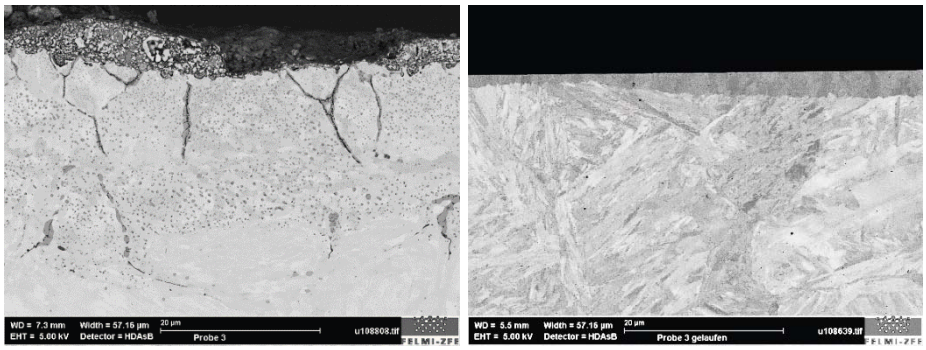

Figure 1. Backscatter electron micrograph of a PNC modified sample
left: prior to tribological tests; middle: after tribological tests

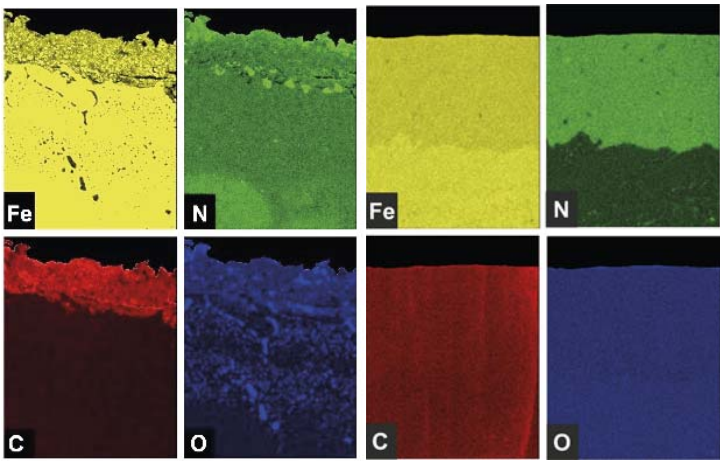

Figure 2. EDX mapping of a PNC modified sample for carbon, oxygen, iron and nitrogen image width 4.8 µm; left: prior to tribological tests; right: after tribological tests

Following these analyses tribological tests for characterisation of wear and frictional behaviours were performed under unlubricated sliding conditions. Results show that, although different nitrocarburising processes yield very similar hardness profiles and compound layer thicknesses, their surface morphology and oxide layer properties can be significantly different. On SNC samples, the thickest oxide layers were formed, which had a different chemical composition than those formed on GNC and PNC samples. Furthermore, SNC samples provided the highest wear resistance and only on these samples, the oxide layers were not removed during tribological testing. It is thus possible that a correlation between the oxide properties and the favourable tribological behaviour of the SNC samples exists.

References

[1] Y. E. Kalay, Y.Kuru, E. Unalan, Int. J Hydrogen Energy, 12 (2015) 915–920
[2] E.J. Mittemeijer, Fundamentals of nitriding and nitrocarburizing, in: J. Dossett, G.E. Totten (Eds.), ASM Handbook, Steel Heat Treating Fundamentals and Processes, vol. 4A, ASM International, Ohio, USA, 2013
[3] C.-M. Karamboiki, A. Mourlas, P. Psyllaki, J. Sideris, Influence of microstructure on the sliding wear behavior of nitrocarburized tool steels, Wear 303 (1–2) (2013) 560–568

New Approaches To SBF-SEM Specimen Preparation

EVA ĎURINOVÁ[1,2], JAN LANGHANS[1] AND JANA NEBESÁŘOVÁ[1,2]

[1] Laboratory of Electron Microscopy, Institute of Parasitology, Biology Centre CAS in České Budějovice, Czech Republic; [2] Institute of Physics, Faculty of Science, University of South Bohemia in České Budějovice, Czech Republic

Serial block-face scanning electron microscopy (SBF SEM) uses an ultramicrotome installed inside the microscope to cut away ultrathin slices and a backscatter detector to scan each newly exposed layer of the specimen. Such arrangement brings the possibility to acquire a series of images allowing reliable and precise volume reconstruction. Sample preparation procedures for SBF-SEM are derived from standard protocols used in transmission electron microscopy. Generally, it is a time-consuming process with enlarged number of contrasting, fixing or washing steps. We attempted to innovate a common SBF-SEM specimen preparation protocol.

We applied and evaluated several modifications to a protocol originally based on the Deerinck et al. method. [1] Firstly, we focused on enhancing OsO_4 penetration into the sample and thus reducing sample charging during visualization in SEM. The insufficiently penetrated OsO_4 in a standardly prepared sample can be seen in figure 1. The tested modifications included change of chemicals, incubation times or temperatures during contrasting steps. Secondly, a table-size milling cutter was introduced as a less time-demanding alternative to an ultramicrotome in trimming the sample into a desired shape. Apart from a time reduction we also evaluated the effect of shape on the conductivity and charging in SEM.

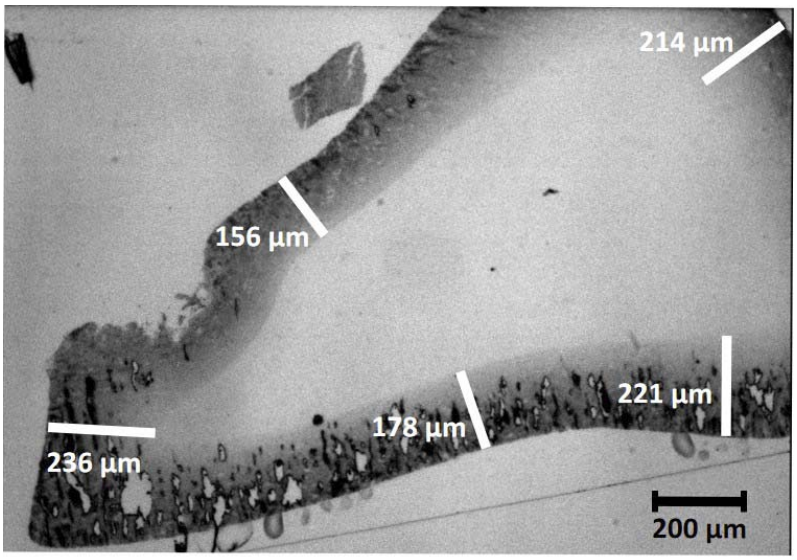

Figure 1. Section of a mouse brain tissue prepared by a standard protocol and visualised in an optical microscope. The decreasing contrast toward the middle of the sample is visible.

References

[1] Deerinck, T. J., Bushong, E. A., Thor, A., Ellisman, M. H.: NCMIR methods for 3D EM: A new protocol for preparation of biological specimens for serial block face scanning electron microscopy. Microscopy, 6–8 (2010).

Surface zeolite's study in sugar-enriched solutions

RUMENKA MARKOSKA[1*], VEDRANA SPADA[3], KREŠIMIR PAVELIĆ[1,2], SANDRA KRALJEVIĆ PAVELIĆ[1]

[1] University of Rijeka, Department of Biotechnology, Centre for High-throughput technologies, Rijeka, Croatia; [2] University "Juraj Dobrila" Pula, Croatia; [3]Research Center for Materials of Region of Istria METRIS, Croatia

The zeolite clinoptilolite is an alumosilicate material used in many industries and has also medical applications due to its safety in applications *in vivo*. Due to its crystalline structure with pores and cavities, it is an ion-exchanger that may be useful for certain detoxification purposes in animals and humans. This and other biological effects documented in the scientific literature so far, are most probably related to physio-chemical structure of clinoptilolite materials, especially to the surface properties. We therefore, present herein the surface study of the different clinoptilolite materials by a simple approach of monitoring the surface changes upon interaction of clinoptilolite-materials with sugar solutions. For this purpose, we prepared suspensions of different zeolites, namely synthetic zeolite A and three clinoptilolite materials prepared by different micronization methods TMAZ, PMA and PMAO2. Glucose solution was added to the zeolite suspension at concentration of 40g/L at room temperature. The samples were analysed by use of the Scanning Electron Microscope (SEM) microscope and the results show a dramatic change in the surface area appearance of zeolites in glucose-enriched solutions due to glucose adsorption that differed among tested micronized materials. The Energy Dispersive X-Ray Spectroscopy (EDS) analyses showed that the observed surface structure is mainly composed by oxygen and carbon. This behavior and chemical composition will be systematically analyzed in future experiments.

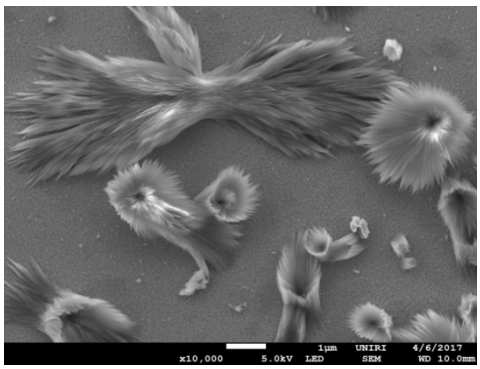

Figure 1. Synthetic zeolite A pre-treated water suspension

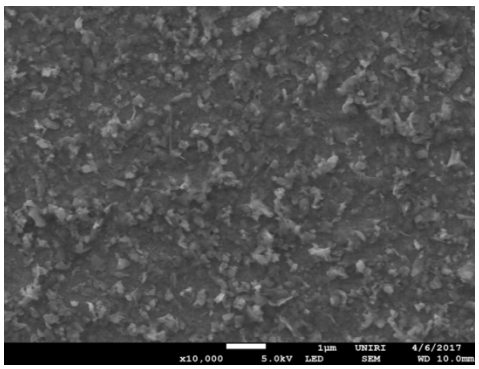

Figure 2. Zeolite clinoptilolite material TMAZ pre-treated water suspension

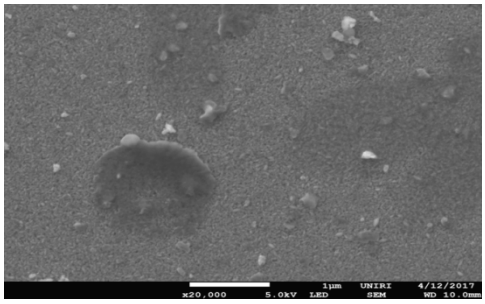

Figure 3. Zeolite clinoptilolite material PMA pre-treated water suspension

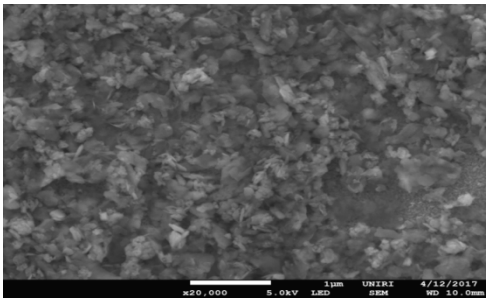

Figure 4. Zeolite clinoptilolite material PMAO2 pre-treated water suspension

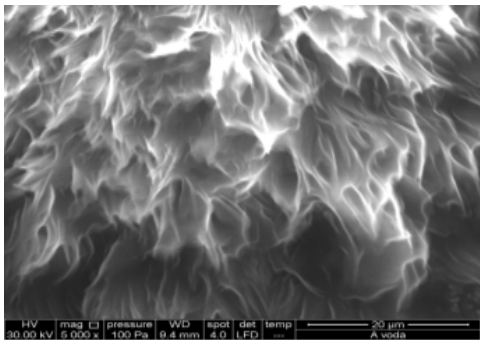

Figure 5. Synthetic zeolite A pre-treated water suspension upon addition of glucose

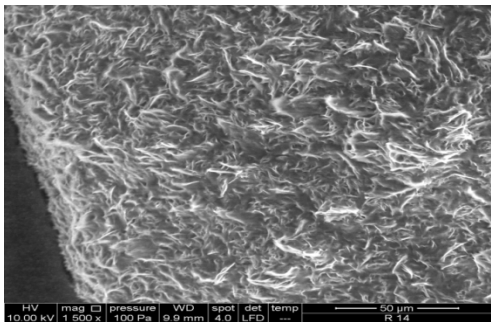

Figure 6. Clinoptilolite material TMAZ pre-treated water suspension upon addition of glucose

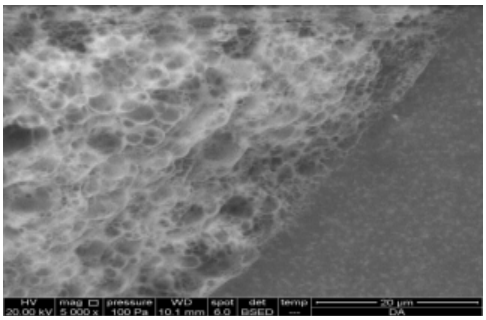

Figure 7. Clinoptilolite material PMA pre-treated water suspension upon addition of glucose

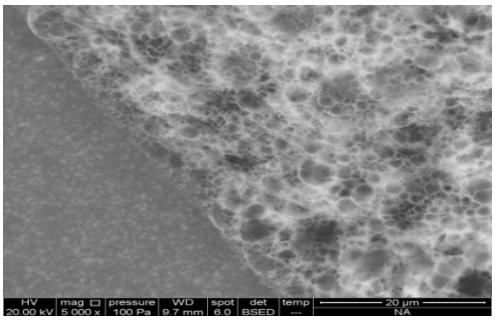

Figure 8. Clinoptilolite material PMAO2 pre-treated water suspension upon addition of glucose

References

[1] S.Kraljević Pavelić et al. Microporous and Mesoporous Materials 249 (2017) 146-156.
[2] María Francisco et al. Chemical Engineering Journal 172 (2011) 184–190.
[3] Peng Bai, J. Ilja Siepmann, Michael W. Deem. AIChE Journal 59(9) (2013) 3523-3529

On the combined use of FIB and PIPS for TEM sample preparation from actinides materials for nuclear applications

ALESSANDRO BENEDETTI[1], THIERRY WISS[1], OLIVER DIESTE[1] AND EMANUELE DE BONA[1]
[1] European Commission, Joint Research Centre, Karlsruhe, Germany

A deep knowledge of the way materials properties change under irradiation is of paramount importance, in order to predict the behavior of structural materials, cladding and fuels for Nuclear Power Plants (NPP). TEM characterization represents a powerful method in this sense, allowing one to detect structural changes with nanometer scale spatial precision. This is particularly true when the FIB *in situ* lift-out technique for sample preparation is used; another advantage of FIB as compared to conventional methods is the possibility to work with greatly reduced specimen mass as compared to conventional 3 mm samples, thus significantly reducing the amount of radiation emitted and the complexity of safety measures.

However, since irradiation invariably produces a wide variety of defects in the material, it is fundamental to ensure that TEM sample preparation does not introduce artefacts such as gallium implantation, surface amorphisation and, more importantly, crystal defects which can be confused with irradiation damage. [1]. These drawbacks are generally minimised by performing a careful final cleaning at low energy of the lamella; unfortunately, for actinides such as UO2 and ThO2 this approach is not enough to guarantee defect free TEM samples, as the relatively high atomic mass of the U atoms implies that they can trigger a cascade effect inside the material once knocked out of the original lattice position [2].

We present here an alternative method, based on the combined use of FIB and PIPS techniques. Much longer than usual (approx. 150 um) lamellas are first extracted from the substrate in the usual way, attached to a grid and polished at high (30 kV) energy. The grid is then transferred to the PIPS and milled at low angles and decreasing voltages till electron transparency.
In this way, we combine the FIB spatial precision and high efficiency with the relatively low damage introduce by the PIPS, since the latter employs a very large and defocused beam compared to the former.

A marked decrease in terms of defect density is observed for monocrystalline UO_2 TEM samples prepared in this way, when compared to analogous samples prepared by conventional FIB (Fig. 1); in particular, very few dislocations loops are observed.
On the other hand, only a minor fraction of the lamella was thin enough for TEM analysis, indicating that the PIPS experimental parameters (incidence angle, final energy, grid positioning) need to be optimised through careful tuning.

As a further step, we have extended the method to more representative materials, such as UO2 pellets prepared via Spark Plasma Sintering (SPS), which allows full densification in a much shorter time and at lower temperatures as compared to conventional sintering [3]. The materials were implanted with He^+ at energies on the MeV scale, to produce very high levels of damage in a relatively short time and without activating the samples.

Preliminary results agree with theoretical predictions, indicating the sample preparation method does not introduce artefacts in the material.

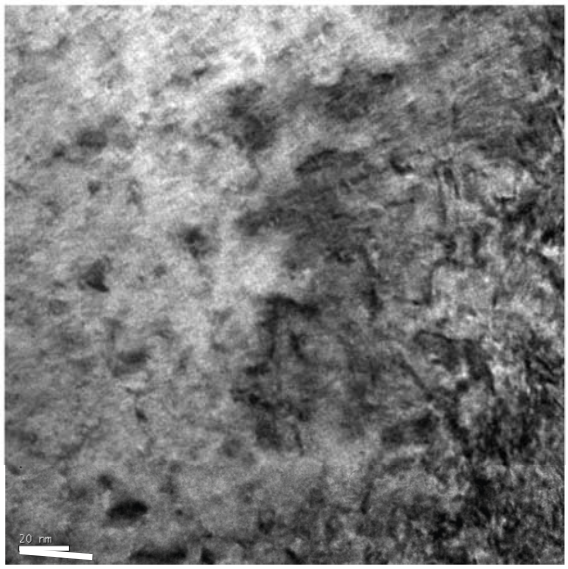

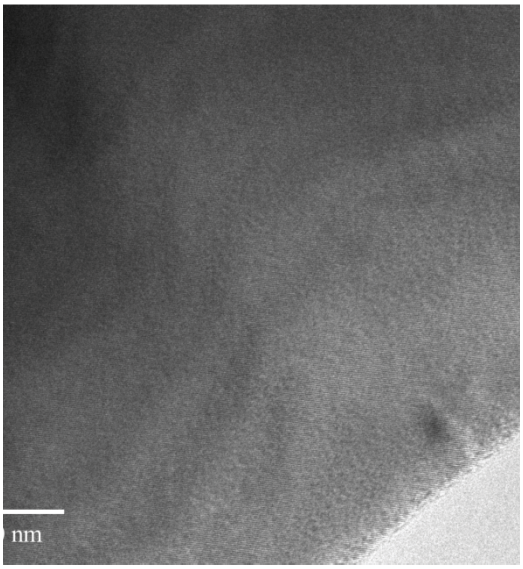

References

[1] F. Hofmann, E. Tarleton, R. J. Harder, N. W. Phillips, P.-W. Ma, J. N. Clark, I. K. Robinson, B. Abbey, W. Liu, C. E. Beck, Nature Scient. Reports, 7 (2017) article number: 45993.

[2] T. Wiss, *Radiation effects in UO2*, in: Comprehensive Nuclear Materials, Vol. 2 (2012) 465-480, Elsevier Science Amsterdam, NL

[3] L. Balice, D. Bouëxière, M. Cologna, A. Cambriani, J.- F. Vigier, E. De Bona, G. D. Sorarù, C. Kübel, O. Walter, K. Popa, Journ. Nucl. Mat. 498 (2018) 307-313

IT2

3D imaging, image processing, and phase-related techniques

CHAIRPERSONS:

Ognjen Milat, Thomas Heuser

INVITED LECTURE

Project „Pattern“ – an open access online tool for spatial analysis of immunolabeling in electron microscopy

DOMINIK PINKAS[1], ERIK VLCAK[1], VLADA PHILIMONENKO[1,2], JIRI JANACEK[3], JAKUB NOVAK[4], MARCEL JIRINA[4], PAVEL HOZAK[1,2]

[1] Institute of Molecular Genetics ASCR v.v.i., Electron Microscopy Core Facility, Prague, Czech Republic; [2] Institute of Molecular Genetics ASCR v.v.i., Department of Biology of the Cell Nucleus, Prague, Czech Republic; [3] Institute of Physiology ASCR v.v.i., Department of Biomathematics, Prague, Czech Republic; [4] Czech Technical University in Prague, Faculty of Information technology, Department of Theoretical Computer Science, Prague, Czech Republic

Evaluation of immunolabelling in EM often lacks unbiased quantitative approach. We are developing an easy-to-use online tool for semi-automatic multi-stage analysis of immunolabeling on EM images spanning particle detection and classification, mathematical and statistical evaluation and visualization of results. This builds on previous work of A. Philimonenko et al. [1] and C. Schofer et al. [2]. The tool detects basic particles (“big” and “small” spheres) automatically; results of detection and identification can be manually reviewed and edited. Spatial relations can be analysed in 2D and 3D microscopic data and along linear structures such as membranes and filaments. The tool uses pair correlation and pair cross-correlation functions for clustering and colocalization evaluation with results presented both numerically and graphically. Labelled structures are visualised via mapping and their spatial relations to other structures or particles are further evaluated as shown by V. Philimonenko et al. [3]. Statistical significance of detected patterns will be calculated and presented in a comprehensive way without the need for deep insight into statistical analysis. All results and respective settings can be exported. Particle coordinates can be kept on the server for prolonged periods of time to be reused with new settings or compared to new datasets. Projects can be shared with colleagues. For routine analysis, useful results should be available in just a few clicks.

The tool is currently in test phase. It will be provided to the broad scientific community in open access mode by the IMG within the Czech-BioImaging research infrastructure. The tool emphasizes convenience and understandability of the interface and will provide detailed explanations of all results, steps, values and options. The platform is modular and can be expanded with more capabilities in the future.

This project is supported by MEYS CR (LM2015062), OPVVV (CZ.02.1.01/0.0/16_013/0001775), IMG grant (RVO: 68378050) and TACR (TE01020118) grants.

References

[1] Philimonenko, A. A., Janáček J. and Hozák P. "Statistical evaluation of colocalization patterns in immunogold labeling experiments." Journal of structural biology 132.3 (2000): 201-210.
[2] Schöfer, C., Janáček, J., Weipoltshammer, K., Pourani, J., & Hozák, P. (2004). Mapping of cellular compartments based on ultrastructural immunogold labeling. Journal of structural biology, 147(2), 128-135.
[3] Philimonenko, V. V., Philimonenko, A. A., Šloufová, I., Hrubý, M., Novotný, F., Halbhuber, Z., ... & Hozák, P. (2014). Simultaneous detection of multiple targets for ultrastructural immunocytochemistry. Histochemistry and cell biology, 141(3), 229-239.

Analytical electron tomography of metallic samples

CORNELIA TRUMMER[1], FRANCISCA MENDEZ-MARTIN[2], GERALD KOTHLEITNER[1,3] AND GEORG HABERFEHLNER[1,3]

[1] Graz Centre for Electron Microscopy, Graz, Austria; [2] Department of Materials Science, Montanuniversität Leoben, Austria; [3] Institute of Electron Microscopy and Nanoanalysis, Graz University of Technology, Steyrergasse 17, 8010 Graz, Austria

The central piece of materials science is the need to understand and modify the structure and composition of materials. To understand the relation between structure, morphology and chemical makeup and mechanical, electrical and thermal properties of metals and alloys, conventional two-dimensional (2D) projection images recorded via transmission electron microscopy (TEM) are often insufficient. To go beyond these limitations, three-dimensional (3D) nano-analysis of internal morphology, as well as information about chemical composition is indispensably required. The expansion into 3D space can be done by STEM tomography, but for measuring elemental distributions, spectroscopic methods are essential.[1] For the combination of tomography with spectroscopic methods, spectrum images (SIs) are recorded. Ideally several signals, such as HAADF (Figure 1,a), electron energy-loss spectra (EELS) (Figure 1,b) and X-ray spectra (EDX) (Figure 1,c) can be acquired simultaneously. [1,2] These can be used to reconstruct 3D chemical maps from each element in the material.

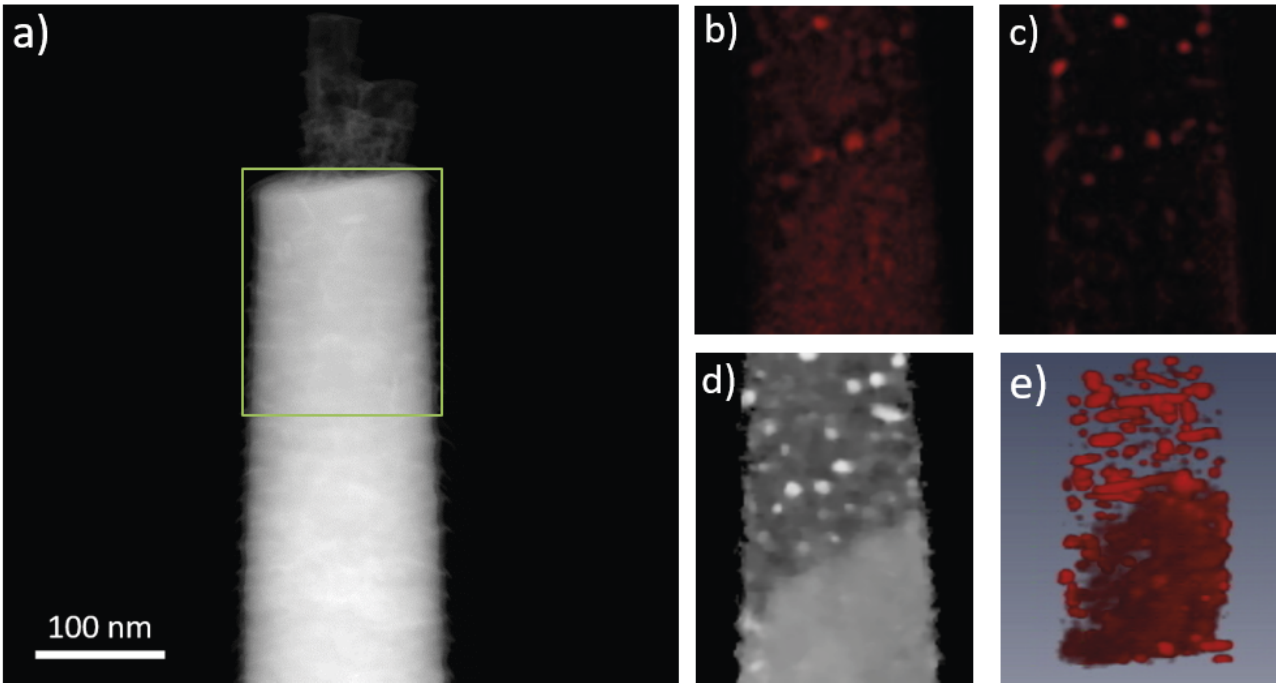

Figure 1. a) Example of an HAADF image of a steel tip. The green rectange marks the SI area b) Analytical EELS signal of nickel L-edge in steel c) Analytical EDS signal of nickel K-lines d) one slice through reconstruction of the nickel signal e) Visualization of nickel with the software Avizo®

In this work, we investigate steel and nickel-base alloy (Inconel® 718) by electron tomgraphy to reveal shape and composition of different types of precipitates within the materials. For electron tomography samples in the form of sharp needles are ideal, which we fabricated by electropolishing. This is an electrochemical sample preparation method, which shapes rectangular

conductive samples into sharp needle-shaped samples and is commonly used for atom probe tomography (APT). [3]

The acquisition of the tilt series of the metal needle is done by tilting the sample about a single axis, acquiring projections at equal angular increments. For reconstruction of the dataset, we employ variational modelling and multi-channel regularization techniques within the software Graptor – a Python/OpenCL reconstruction tool [5,6]. This method is based on two main ideas: First, within the reconstruction, each dataset is regularized either with a total generalized variation (TGV) term, which favors piecewise constant and linear reconstructions, leading to sharp and gradual interfaces within the reconstructions. Second, the different elemental maps and the ADF data are linked together, to favor similar interface locations for the different reconstructions. This provides superior reconstructions compared to conventional methods, like weighted back projection or SIRT, but also compared to other total-variation based methods, which do not employ the correlation between different signals. Additionally, we will discuss the possibilities of correlating electron tomography with atom probe tomography, by investigating the same sample with the two techniques to combine their advantages and compensate for shortcomings of each methods. [1].

In summary, this work focuses on the determination of the morphology and analytical information of different metals and alloys by analytical electron tomography and by adding information from APT, to understand materials properties. The combination of these techniques can provide detailed understanding of the morphology and compositional information of metals and alloys.

Acknowledgements

We acknowledge the financial support by the Austrian Federal Ministries for Transport, Innovation and Technology (BMVIT).

This project has received funding from the European Union's Horizon 2020 research and innovation programme under grant agreement No. 823717 – ESTEEM3.

References

[1] Ercius, P., Alaidi, O., Rames, M. J. & Ren, G. Electron Tomography: A Three-Dimensional Analytic Tool for Hard and Soft Materials Research. *Adv. Mater.* 27, 5638–5663 (2015).

[2] Haberfehlner, G., Orthacker, A., Albu, M., Li, J. & Kothleitner, G. Nanoscale voxel spectroscopy by simultaneous EELS and EDS tomography. *Nanoscale* 6, 14563–14569 (2014).

[3] Wang, Y., Zeng, Y., Qu, N. & Zhu, D. Note: Electrochemical etching of cylindrical nanoprobes using a vibrating electrolyte. *Rev. Sci. Instrum.* 86, 2013–2016 (2015).

[4] Levin, B. D. A. *et al.* Nanomaterial datasets to advance tomography in scanning transmission electron microscopy. *Sci. Data* 3, 1–11 (2016).

[5] Huber, R., Haberfehlner, G., Holler, M. & Bredies, K. Total Generalized Variation regularization for multi-modal electron tomography. 1–38

[6] Huber R., Holler M. and Bredis K., Graptor [Software],Zenodo, 2019, DOI: 10.5281/zenodo.2586204.

Toward an electrostatic OAM sorter

PAOLO ROSI[1], AMIR TAVABI[2], ALBERTO RONCAGLIA[4], GIULIO POZZI[2], ENZO ROTUNNO[3], MATTEO ZANFROGNINI[3], STEFANO FRABBONI[2], RAFAL DURNIN BURKOSKI[2], VINCENZO GRILLO[3]

[1] Modena e Reggio Emilia, Modena, Italy; [2] Ernst Ruska-Centre for Microscopy and Spectroscopy with Electrons, ForschungszentrumJülich, Germany; [3] CNR-Istituto Nanoscienze, Modena, Italy; [4] CNR-IMM, centro CNR, Bologna, Italy

1. Introduction

The OAM sorter is a useful approach for the measurement of OAM for light [1]. The same device is now under study for electrons [2,3]. The prospect is that it is going to drastically change the measurement paradigm in electron microscopy.

We proved already a working sorting system by holographic means, but building an equivalent device based on electrostatic lenses is a very difficult tasks that requires modeling of fields, propagations in the microscope and design of MEMS devices. It pays off in its application in measuring plasmon resonances, magnetization properties of materials and proteins structures due to its intrinsic higher efficiency with respect to the holographic approach.

2. Methods

The electrostatic OAM sorter devices have been realized on MEMS chips by means of optical lithography at the CNR-IMM institute. The devices, once fabricated, have been polished and reshaped by FIB milling to remove leftovers from the etching process and reach the desired tip shape. Finite elements simulations have been carried out, alongside analitical calculations, to design the best performing device (Figure 1.a and b).

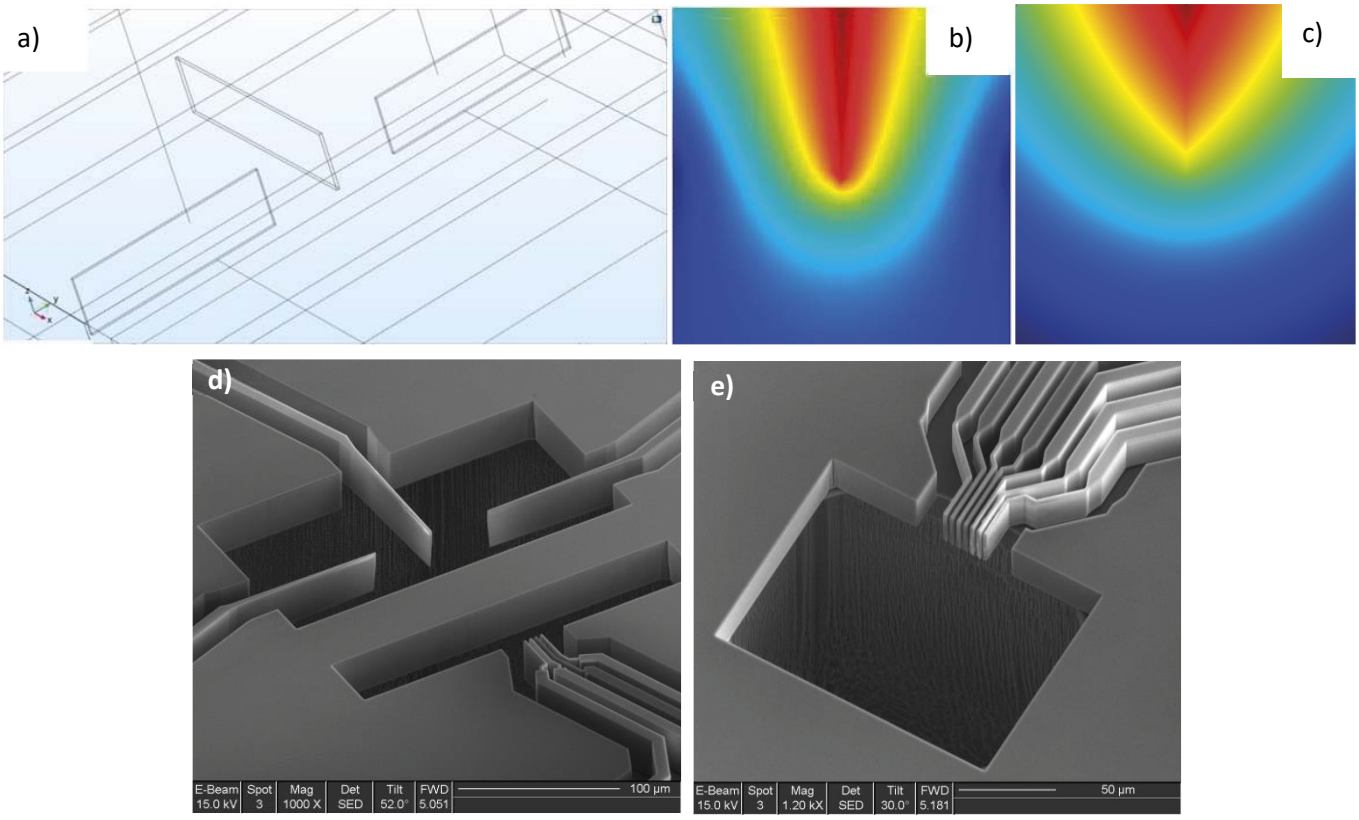

Figure 1. a) and b) show the modelled tip design and the phase of the central tip

3. Results

By means of electron holography we measured the phase produced by the sorting objects. And in a more recent experiment we were also able to obtain a very well defined OAM spectrum of an incoming electron vortex beam.

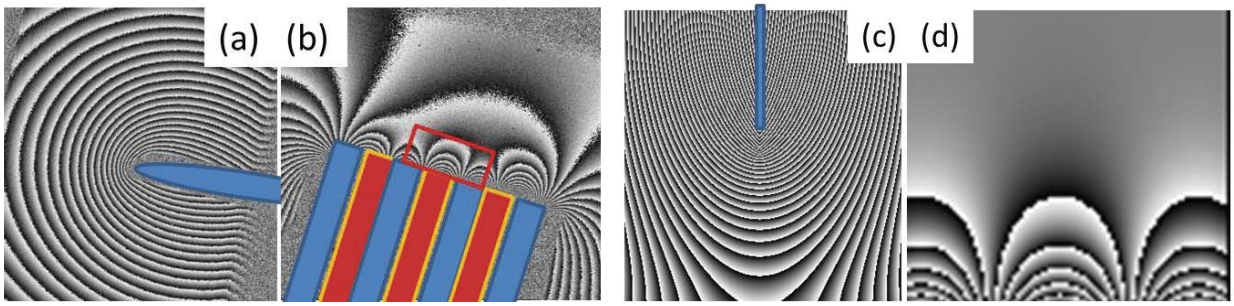

Figure 2. a) and b) show the experimental phase of the two sorting elements, respectively S1 and S2;while c) and d) show the ideal phase of the two.

With simulation it has been possible to predict that in the ideal working conditions the electrostatic phase plates that we design should reach an OAM resolution of 1 ħ, and indeed already in preliminary experiments, were not all the parameters have been perfectly tuned we have been able to achieve an OAM resolution of 1.5-2 ħ.

4. Conclusions

In conclusion here we show the promising experimental and theoretical results toward the realization of an OAM sorter to be introduced inside an electron microscope.

The device promises to be an important advance in electron microscopy and to improve our understanding of plasmonic and magnetic structure.

References

[1] G. C. Berkhout, M. P. Lavery *et al* Phys. Rev. Lett. **105**, 153601 (2010).
[2] B. McMorran, TR Harvey, MPJ Lavery, New Journal of Physics **19**, 023053 (2017)
[3] V.Grillo, A.H. Tavabi *et al*, Nature Comm. **8**, 15536 (2017)

Comparison of collagen distribution between keratoconus and normal human corneal stroma using second harmonic generation microscopy

MEHMET SERIF AYDIN[1], OLGU ENIS TOK[1,2], AYLIN KILIC[3], CIHAN BILGE KAYASANDIK[4], CAFER TANRIVERDI[3], BURCU NUROZLER TABAKCI[3], GURKAN OZTURK[1,5]

[1] Regenerative and Restorative Medicine Research Center (REMER), Istanbul Medipol University, Istanbul, Turkey; [2] Department of Histology and Embryology, International School of Medicine, Istanbul Medipol University, Istanbul, Turkey; [3] Department of Ophthalmology, School of Medicine, Istanbul Medipol University, Istanbul, Turkey; [4] Department of Computer Engineering, School of Natural Sciences and Engineering, Istanbul Medipol University, Istanbul, Turkey; [5] Department of Physiology, International School of Medicine, Istanbul Medipol University, Istanbul, Turkey

1.Introduction

In this study, we investigated the horizontal arrangement and organization of human corneal collagen bundles in the stroma between keratoconus and normal human cornea by second harmonic generation (SHG) imaging.

The corneal stroma is mainly composed of collagen and changes in collagen structure can lead to visual impairment and various corneal diseases. The corneal stroma contains collagen of types I, V, VI, XII, and XIV, and the collagen fibrils align with the same orientation to form lamellae[1]. Second harmonic generation (SHG) imaging is a form on non-linear optical microscopy that allows for the visualization of fibrillar collagen in situ[2]. A key advantage of this approach is that it allows evaluation of the structural characteristics of collagen lamellae in 3-dimensional in intact cornea.

Keratoconus is a relatively common condition characterized by progressive corneal protrusion and thinning that result in reduced visual acuity[3] (Figure 1). Although various bioactive molecules have been implicated in its pathogenesis, the mechanisms responsible for the development of keratoconus have remained unclear. In previous studies using SGH in keratoconus, 3D characteristics of collagen lamellae were evaluated[3], less lamellar interweaving and loss of lamellae were revealed[4].

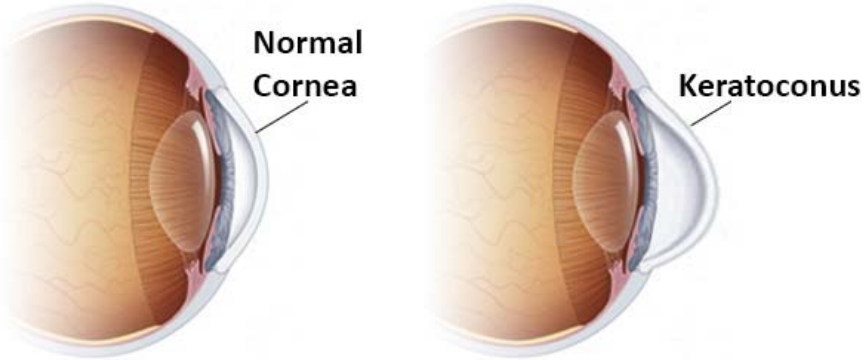

Figure 1. Illustration of normal and keratoconic cornea.

2. Material and Methods

We obtained 6 normal human total cornea specimens from the eye bank (Beyoğlu Eye Bank, Istanbul, Turkey) and 3 keratoconic cornea at the time of penetrating keratoplasty performed at Istanbul Medipol University Hospital. The cornea tissue was immediately fixed overnight at 4°C in 4% paraformaldehyde, washed with phosphate-buffered saline (PBS), mounted with the corneal surface parallel to the scanning plane on a petri dish in PBS and imaged. Second harmonic generation imaging was performed using a Zeiss 7 MP microscope (Carl Zeiss, Jena,

Germany) equipped with dual Ti:Sapphire multiphoton lasers (Coherent Chameleon Vision II and Ultra, Coherent, Santa Clara, CA) (Figure 2). 820 nm wavelength was used for second harmonic image generation. Forward and backward SHG signals were simultaneously acquired using a 20x/1.0 N Plan-Apochromat water immersion with a 1.8 mm working distance, image sizes were 1024 × 1024 pixels, 400–600 µm thick image stacks were acquired with a z-step size of 1.0, extending from the surface of Descemet's membrane to that of Bowman's layer. In order to quantify the irregularity of the collagen bundle layout, we used image analysis method describe by Park et al[6].

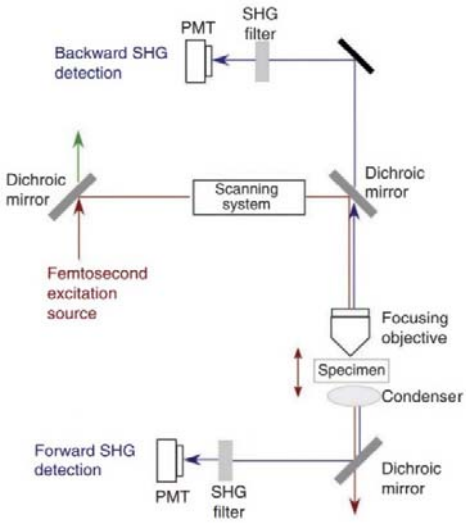

Figure 2. Schematic of the optical layout of the SHG microscope, showing the optical components before the scan head and the detection pathways (Optimized from Chen et al[5]).

3. Results and Conclusion

Both forward and backward scatter images were taken from all samples by SGH imaging. Backward scatter SHG imaging is noninvasive but the signal intensity is lower compared with forward scatter SHG imaging. Therefore, forward scatter image was used in the analysis. In normal cornea, irregular connective tissue forms thick bundles of collagen interweaving in three dimensions, while keratoconus collagen fibers are irregular and loss of collagen bundles according to plot analysis. In addition, the collagen bundles were curved in the keratoconus (Figure 3).

As a result, by SGH imaging we observed that the corneal stroma of the keratoconus is disrupted due to the disorganization of the bundles of collagen and forming a loose structure.

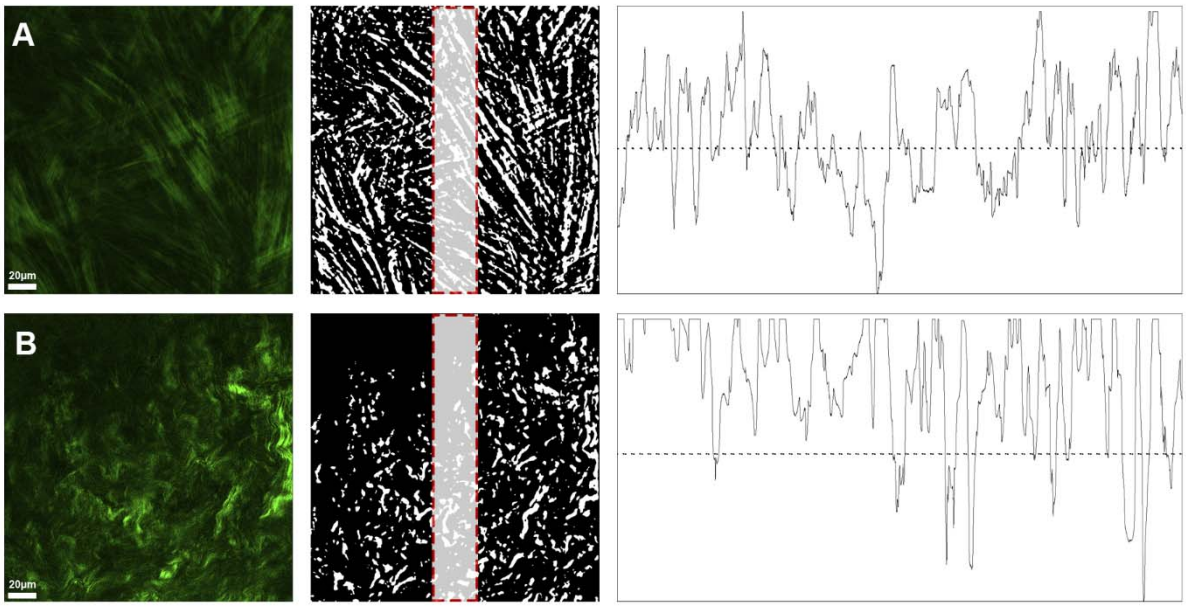

Figure 3: The collagen bundle arrangement (green) in corneal lamella was shown. Forward scatter image of normal **(A)** and keratoconic cornea **(B)**. SGH images were processed by ImageJ with sequential application of bandpass filter and binary conversion. The crossing density was measured at the vertical center of the image and each black and white conversion is plotted as a peak in the graph. The number of peaks crossing the median cut-off value (dotted line) of signal intensity is counted and represents the irregularity of collagen bundle arrangement pattern.

4. References

[1] I. Drubaix, J.M. Legeais, N. Malek-Chehire. Collagen synthesized in fluorocarbon polymer implant in the rabbit cornea. Exp Eye Res, 62 (1996) 367–376

[2] A. Quantock, M. Winkler, G.J. Parfitt, R.D. Young, D.J. Brown, C. Boote, J.V Jester. From nano to macro: studying the hierarchical structure of the corneal extracellular matrix. Exp Eye Res, 133 (2015) 81–99

[3] N. Morishige, R. Shin-gyou-uchi, H. Azumi, H. Ohta, Y. Morita, N. Yamada, K. Kimura, A. Takahara, K. Sonoda. Quantitative analysis of collagen lamellae in the normal and keratoconic human cornea by second harmonic generation imaging microscopy. Investigative Ophthalmology & Visual Science December, 55 (2014) 8377-8385

[4] N. Morishige, A.J. Wahlert, M.C. Kenney. Second-harmonic imaging microscopy of normal human and keratoconus cornea. Invest Ophthalmol Vis Sci., 48 (2007) 1087–1094

[5] X. Chen, O. Nadiarynkh, S. Plotnikov, P.J. Campagnola. Second harmonic generation microscopy for quantitative analysis of collagen fibrillar structure. Nature Protocols, 7 (2012) 654-669

[6] C.Y. Park, J.K. Lee, R.S. Chuck. Second harmonic generation imaging analysis of collagen arrangement in human cornea. Invest Ophthalmol Vis Sci., 56 (2015) 5622-5629

Making a 3D model of merino wool fibre with photogrammetric processing of SEM images

MIRJAM LESKOVŠEK, URŠKA STANKOVIČ ELESINI, ANJA ŠKERJANC, MARKO VRABEC AND HELENA GABRIJELČIČ TOMC
Faculty of Natural Sciences and Engineering, University of LjubljanaSlovenia

1. Introduction

As generally known, scanning electron microscopy (SEM) provides insight into the surface topography of small 3D objects (micron fragments). Specimens can be observed from different vantage points by changing the angle and by rotation of the observation table on which specimen is mounted. Several recent studies employed photogrammetric processing of SEM images to derive 3D models of micro objects for research purposes in the fields of biology, chemistry, geology, etc. [1-3]. Multi-view, or Structure-from-motion photogrammetry uses a number of overlapping SEM images captured from different viewpoints around the object, to create a 3D point cloud and a triangulated polygonal surface with photographic texture, representing the shape of the object. The resulting surface models are extremely accurate and topologically complex (highly detailed), appropriate not only for inspection and visualization, but also for further processing, analysis, measurements, and application of 3D technologies as printing, simulations, animation etc. [4]. The non-invasive nature of this approach and the capability of acquisition and reconstruction on a micro and even on a nanoscale are the main benefits of the methodology. The main challenge in the experimental is setting the parameters of image acquisition, which are crucial for the quality of the 3D reconstruction and depend on a type of the object under the inspection.
The objective of the research was to study the possibility of application of a simple and non-invasive 3D surface photogrammetric reconstruction using captured overlapped SEM images of merino wool fibre. The goal was to define optimal acquisition settings that could be used for efficient image capture and photogrammetric model generation, and to define the framework for employing geometric and topological analysis and metrics on the derived 3D models.

2. Experimental

In research, the SEM microscope, model 6060 LV (Jeol) was used. This model of SEM allows to capture photos at a table tilt ranging from -10° to 70°, with full plane rotation of the specimen (360°) at a 45° rotation step. From preliminary tests we decided to tilt the sample from -10 ° to 65 ° in 5 ° steps, and to rotate the sample in 45 ° steps at full plane rotation (Figure 1). The primary electron beam was generated at 10 kV voltage. The photos were taken at 2.000× magnification of the sample.
A series of overlapping photos was captured in tagged image file format (TIFF) and processed with the Agisoft Metashape photogrammetric reconstruction software. Photogrammetric reconstruction is highly automated and includes identification of keypoints in individual images, matching the keypoints between the images, determining the camera positions relative to the object, and calculating the 3D coordinates of recognizable points on the object, resulting in a dense point cloud representing the geometry of the object in a relative but metrically correct coordinate space. Finally, a polygonal mesh is generated from the point cloud, and a photographic texture is assembled from the captured images and projected onto the polygonal surface model for added realism.
For visualization, 3D surface models were exported to Meshlab, an open source platform for the analysis, measuring, editing and processing of 3D triangular meshes. The meshes were inspected topologically, geometrically and texturally. Moreover, the metric system enabled 3D comparison of geometric difference between 3D models.

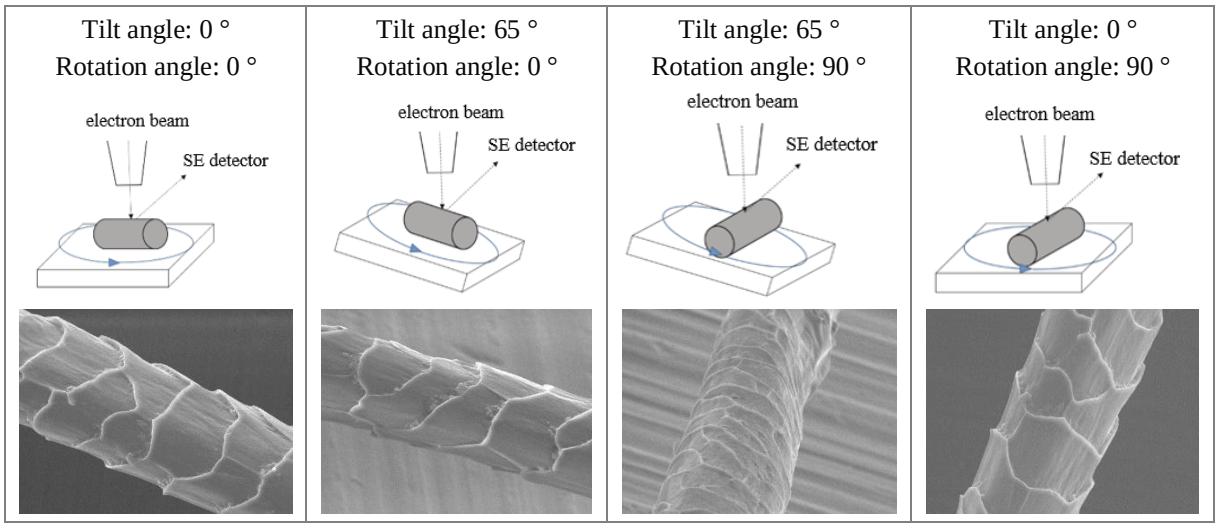

Figure 1. SEM images of merino wool fibre at different rotation and tilt angle (mag. 2.000×)

3. Results with discussion

The level of detail (LOD), expressing the accuracy of representation of the merino wool fibre, was strongly affected by the acquisition parameters set on the SEM microscope. The spatial extent of our derived 3D photogrammetric models is limited with the object coverage that the rotating sample table can provide. In particular, the parts of the wool fibres that were resting on the rotating table are not possible to reconstruct with this method. The resulting raw 3D models therefore have an open mesh topology in the shape of a cylinder (Figure 2). Moreover, the parts of the fibres closest to the table could only be imaged at highly oblique angles due to the limitations in table rotation. Consequently, these parts of the models showed significant degradation in reconstruction quality and had to be discarded in subsequent surface editing.

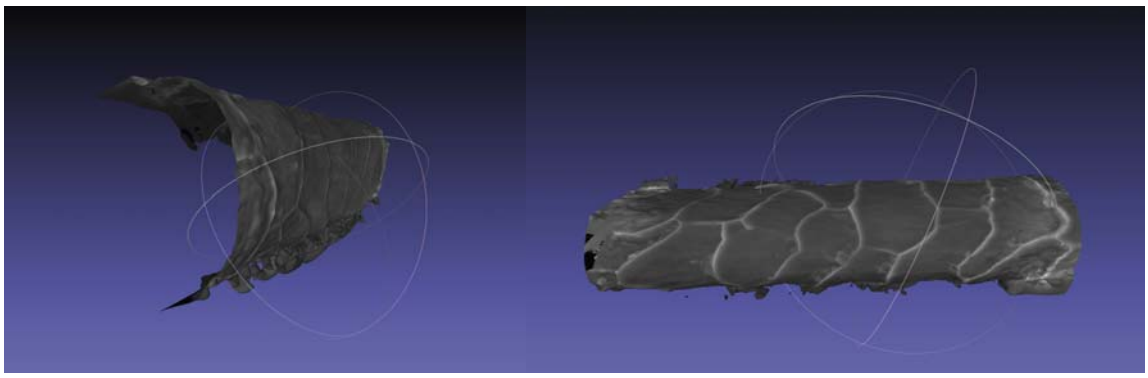

Figure 2. Front and side view of the wool fibre 3D reconstruction.

The quality of resulting photogrammetric 3D models was generally very good, showing no topological artefacts such as duplicate faces and duplicated vertices, unreferenced vertices, zero area faces and non-manifold edges. The only detected artefact of the method was occasional occurrence of self-intersecting surfaces, which is controlled both by the SEM acquisition parameters and the photogrammetric modelling procedure. Different realisations of the wool fibre model were compared in Meshlab by inspecting the errors and checking the distances between

model meshes. In Figure 2 front and side view of a fibre model is presented, pointing out the details in geometry and texture. Figure 3 emphasizes topological artefacts which required subsequent mesh correction in order to provide topological accuracy for the further use of the 3D model.

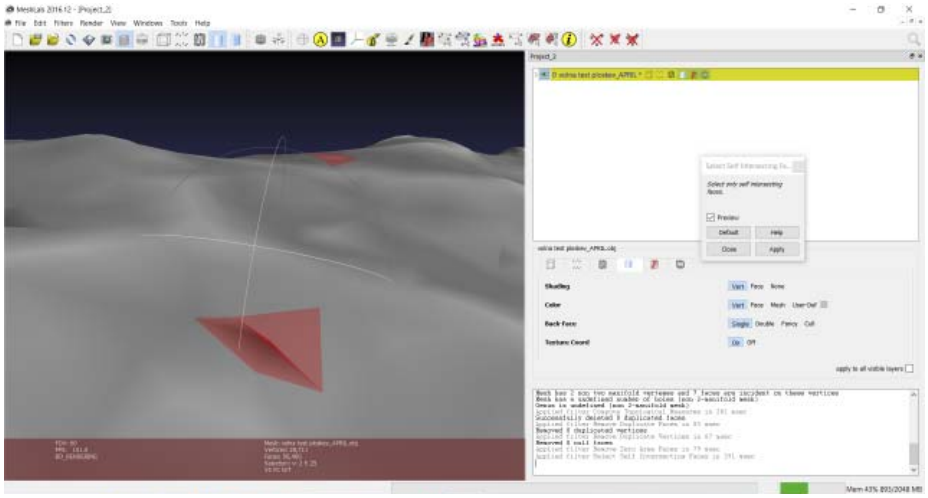

Figure 3. Topology artefacts in a 3D mesh, self intersecting faces.

4. Conclusion

Our results demonstrate that combining SEM imagery and the Structure-from-motion photogrammetric workflow provides a valuable 3D reconstruction approach. The technique is completely non-invasive and does not require any specific specimen preparation, that an ordinary SEM user would not be able to cope with. The only downside of the method is the time-consuming procedure of rotating the specimen, required to provide sufficient spatial coverage of the imagery. Photogrammetric reconstruction provides an accurate geometrical and textural 3D representation of investigated objects. Derived 3D geometrical models require little topological editing and are suitable for metric examination and for further use such as 3D printing.

5. References

[1] C. L. Gontard, R. Schierholz, S. Yu, J. Cintas, R. E. Dunin-Borkowski, Ultramicroscopy, 169(2016), 80–88
[2] A.D. Ball, P.A. Job, A.E.L. Walker, J Microsc. 267(2) (2017) 214–226
[3] C. Lionel, C. L. Gontard, M. Batista, J. Salguero, J. Calvino, Scientific Reports 8, 11000 (2018)
[4] M. Eulitz , G. Reiss, J Struct Biol. 191(2) (2015) 190–6

Quantitative three-dimensional microstructure description of porous nano-sized cermet anodes for SOFC using FIB nanotomography

GREGOR KAPUN[1,2], MARJAN MARINŠEK[4], TINA SKALAR[4], ENDRE MAJOROVITS[5], FRANCI MERZEL[1], MIRAN GABERŠČEK[1], SAŠO ŠTURM[3]

[1] National Institute of Chemistry, Ljubljana, Slovenia; [2] Center of Excellence on Nanoscience and Nanotechnology – Nanocenter, Ljubljana, Slovenia; [3] Jozef Stefan Institute, Ljubljana, Slovenia; [4] University of Ljubljana, Faculty of Chemistry and Chemical Technology, Ljubljana, Slovenia; [5] Carl Zeiss Microscopy GmbH, ZEISS Gruppe, Oberkochen, Germany

Porous nano-sized Ni-SDC cermets are commonly used anode material in contemporarily solid oxide fuel cell (SOFC) energy conversion system. The most important requirements for efficient electro-oxidation at the anode are: i) high catalytic activity for fuel electro-oxidation, ii) chemical-, morphological- and dimensional-stability, iii) electronic- and ionic-conductivity, iv) open porosity and v) tortuosity. Many of those properties can be determined by detailed anode microstructure analysis [1]. For this purpose, it is crucial to establish quantitative relationship between primary microstructural parameters, which can be adjusted during material processing, with the higher order topological features that control the electrochemical performance of the anode. In porous cermets critical topological features such as connectivity, TPB density and the tortuosity of transport pathways within the pores can only be established based on a detailed 3D microstructural information.

In this work we present quantitative three-dimensional microstructure description of nano-sized Ni-SDC cermets, fabricated at various sintering conditions, using FIB (focused ion beam) nanotomography. Porous Ni-SDC cermets were fabricated with co-sintering of NiO-SDC pressed pellets at various temperatures and reduced to Ni-SDC functional anodes. The samples were specially prepared for microscopy and serial sectioned using a fully automated slicing procedure with active drift correction algorithms and auto focusing routine to obtain a series of low-loss BSE images with 5 nm reproducible step. Advanced image processing algorithms were developed and applied directly to image data volume. Individual phases were labelled using python assisted 3D watershed segmentation algorithm. After phase separation, the entire probed volume was reconstructed and visualized as presented in Figure 1. Volume fractions, porosity, feature sizes and their size distributions were calculated directly from 3D reconstructed microstructure [2]. A high quality tetrahedral grid was generated with triangular aproximations and used for specific surface areas (SSA) and specific interface areas (SIA) calculations. Segmented 3D data cube was used for grain connectivity analysis, TPB density and tortuosity calculations [3]. Active and inactive TPB's were identified as ilustrated in Figure 2 and quantitatively evaluated using "in house" programing algorithm based on the centroid method. In a final stage, gas transport streamlines and absolute gas permeabilities were simulated through porous network. The simulation results for the case of methane gas at typical fuel cell operating condions are visualy presented in Figure 3.

The presented analytical approach will serve as a tool for detailed quantitative microstructural description of various porous nano-sized SOFC anode cermets. The detailed three-dimensional microstructural data will be used to optimize their fabrication process in direction to achieve highly-efficient and durable electrodes.

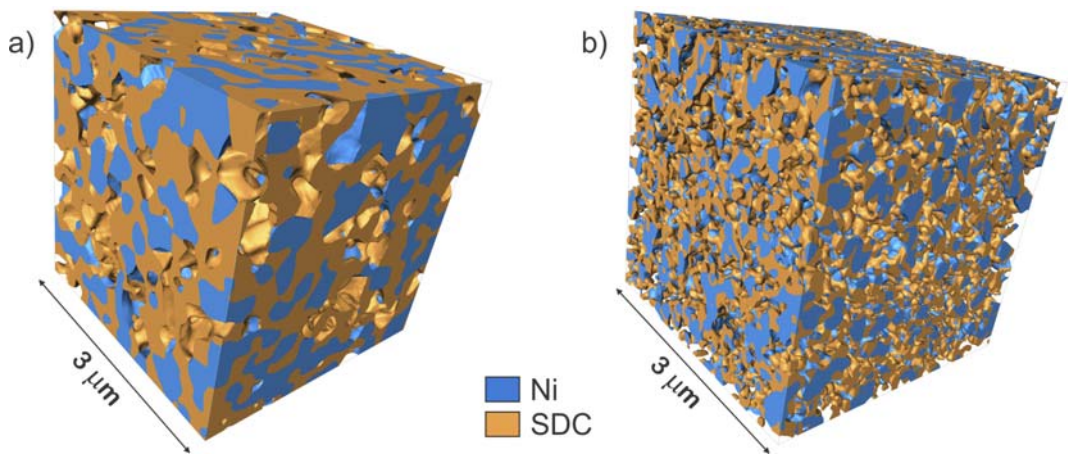

Figure 1. 3D reconstruction of porous Ni-SDC cermet sintered at a) 1400 °C and b) 1200 °C

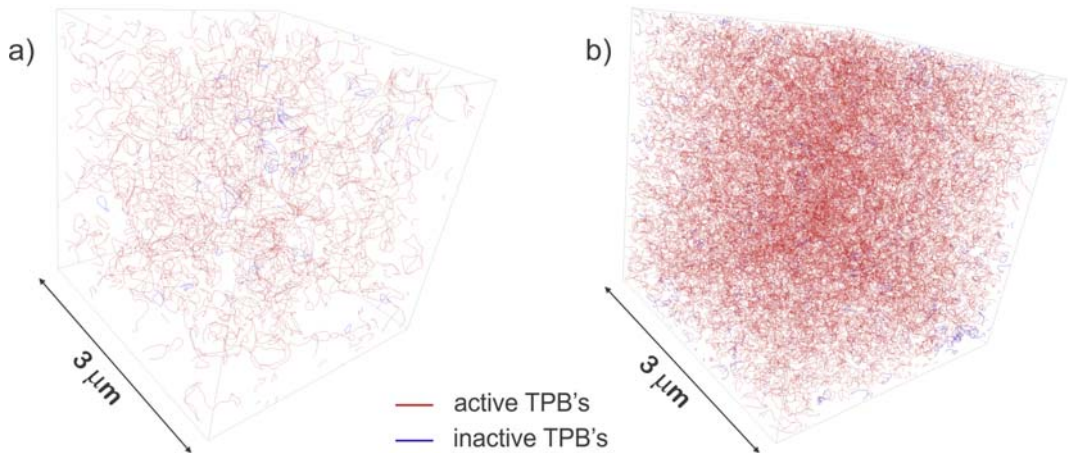

Figure 2. 3D distributions of active TPB's (red) and inactive TPB's (blue) for the case of Ni-SDC cermet sintered at a) 1400 °C and b) 1200 °C

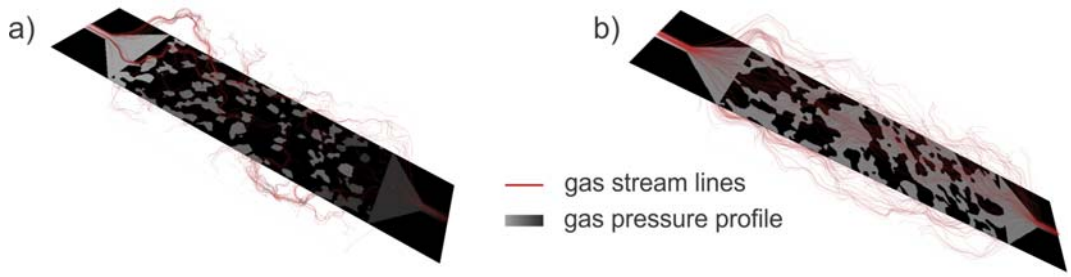

Figure 3. Simulations of absolute permeability throughout the complex porous structure with visualization of gas stream lines and pressure profiles for the case of Ni-SDC cermet sintered at a) 1400 °C and b) 1200 °C

References

[1] J. Zhu, Z. Lin, Appl. Energy, 2018, 231, 22-28
[2] J. A. Taillona, C. Pellegrinelli, Y. L. Huang, Ultramicroscopy, 2018, 184, 24-38
[3] Lu, X., Heenan, T. M. M., Bailey, J. J., Li, T., Li, K., Brett, D. J. L., & Shearing, P. R. Journal of Power Sources, 2017, 365, 210–219

Digital optical holographic microscope; interferometric study of thin film delemination buckling patterns

OGNJEN MILAT AND NAZIF DEMOLI
Institute of Physics, Zagreb, Croatia

A home-made Digital Optical Holographic Microscope (DOHM) [1] was used for the interferometric study of morphology and topography of buckling patterns in residually compressed thin film during or after its delamination from the substrate. A number of buckling patterns such as disordered surface wrinkles, regular herringbone, straight-sided or telephone cord (TC) buckles and circular blisters [2, 3], Figure 1., has been studied and analysed. Delamination usually starts as straight-sided linear wrinkle, but then deviate to the "telephone cord" periodic wavy geometry due to the fact that the compressive residual stress in the film is biaxial. In general, morphology and topography of buckling patterns can be characterized, by scanning electron microscopy, mechanical or laser-scanning profilometry, optical interferometry, or (depending on scale) by using an atomic force microscope [4, 5].

Our Digital Optical Holographic Microscope is based on an adapted commercial metallurgical instrument (rather old brand Leitz Metallux II) by setting up a number of sophisticated extensions. This set-up provides simultaneous and/or alternative white-light and/or monochromatic illumination; coupled pair of CCD cameras enables acquisition of the corresponding images of the very same area of a specimen. This enables traditional microscopic imaging in succession with holographic imaging and the real time optical reconstruction as well as interferometric processing and correlation of acquired digital images. Figure 2. displays white light microscopic images in correlation with holographic interferometry data ($\lambda/2$ fringes).

White-light microscopy of top surface of highly compressed tungsten thin film clearly reveals (at lower magnification: <500X) lateral morphology of the buckling patterns, Figure 1. At higher magnification (>500X) reduction of focus depth affects imaging contrast, so that the lateral as well as vertical wrinkles` features can hardly be observed and measured down to submicron precisions, as it is represented in Figure 2(a, b, c). By imaging and optical processing in holographic mode of our DOHM, one can display interferometric fringes patterns that reveal buckling features with lateral and vertical precision: $\Delta l \approx \Delta h \approx 0.3$ µm, Figure 2(d, e, f). Correlation of traditional microscopy and holographic interferometry provides topography data in optical and digital format that can be used as a basis for quantitative 3-D modelling of TC buckling morphology and associated stress-strain mechanics of thin films.

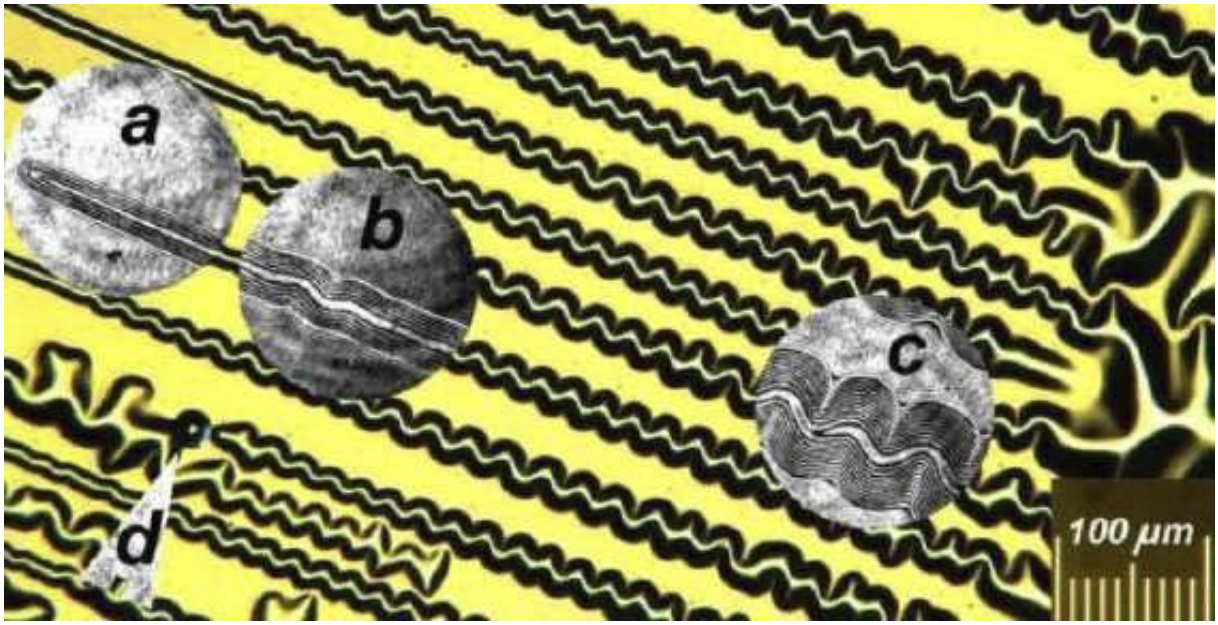

Figure 1. Buckling patterns of W-thin film on substrate revealing straight-sided and „telephon-corde“ (TC) morphologies (insets a, b, c), as well as disordered surface wrinkles (right) and a circular blister (arrowhead d); medium magnification (200X) top view image (white-light microscopy mode). Insets represent interferometric fringes (magnification 500X) recorded and processed by monochromatic-light holography mode.

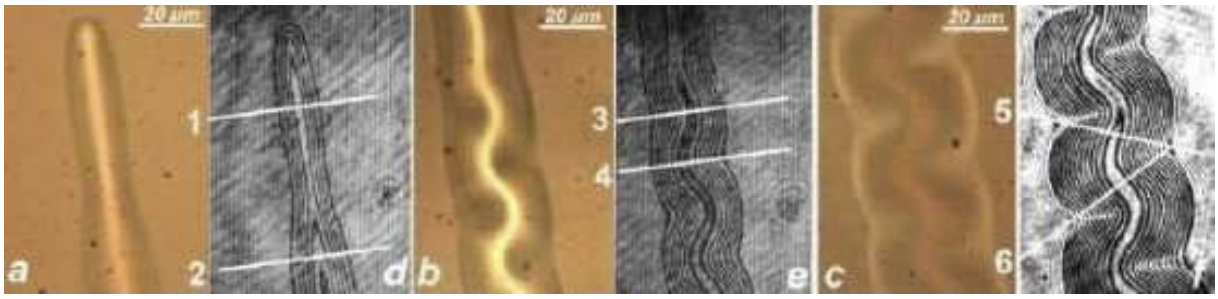

Figure 2. Correlative images (a, b, c) and corresponding interferometric fringes patterns (d, e, f) of straight and TC delamination buckless of thin W-film as recorded in microscopy mode, and by reconstruction and processing of holographic images. White lines (1 to 6) indicate traces for height profile characterization. Consecutive dark fringes reveal lines of constant height in steps of 0.3 µm. Magnification 1000X.

References:

[1] N. Demoli and O. Milat, not to be published yet.
[2] L.B. Freund and S. Suresh in „Thin Film Materials“, Cambridge University Press, 2003, pp 86-153
[3] J.W. Hutchinson, M.D. Thouless and E.G. Liniger, Acta Metall. Mater. 40 (1992), 295308
[4] J.-Y. Faou, G. Parry, S. Grachev and E. Berthel, Phys. Rev. Lett. 108 (2012) 116102
[5] M.W. Moon, H.M. Jenssen, J.W. Hutchinsion, K.H. Oh, and A.G. Evans Journal of the Mechanics and Physics of Solids 50 (2001) 2351-3159

IT3
Diffraction techniques and spectroscopy

CHAIRPERSONS:

Mariana Klementova, Miran Čeh

INVITED LECTURE

Crystal structure determination using *operando* and *in situ* electron diffraction tomography

KARAKULINA OM[1], BATUK M[1], HENDRICKX M[1], ABAKUMOV AM[1,2], HADERMANN J[1]

[1] EMAT, Department of Physics, University of Antwerp, Belgium; [2] Centre for Energy Science and Technology, Skoltech, Skolkovo Institute of Science and Technology, Moscow, Russia

Quantitative electron diffraction in the form of electron diffraction tomography has been used for about a decade now to solve and refine structures of different types of compounds. It is based on reconstructing the three dimensional reciprocal space with minimal dynamic diffraction effects, to allow using the intensities for direct structure solution and even precise and accurate refinement of the coordinates.

Recently, the focus in our research group has turned to trying to refine structures from *operando* data obtained using an electrochemical cell or a gas environment cell. Up until now, X-ray (XRD) and neutron diffraction (ND) are typically applied for *operando* tracking of structural changes during reactions, however, they can only be usefully applied as powder diffraction, since the single crystals needed for X-ray and neutron diffraction are too large to be active for most of the targeted reactions, such as redox reactions. *Operando* electron diffraction would allow obtaining single crystal data from submicron sized materials during ongoing reactions in realistic environments (instead of the high vacuum of the microscope), but it has not yet been reported in literature. For gas environments, nanoparticles have been tracked in literature to observe their changes in size or morphology, or the addition or removal of a single atom to the surface, but no crystal structure determinations were yet done. For an electrochemical reactions, due to the thick liquid layer, it is impossible to image the structure at high resolution and only low magnification tracking was done.

Recently, we published the determination of the structure of charged $LiFeO_4$ (thus $FePO_4$) from *in situ* obtained data, to show the potential of in situ electrochemistry TEM [1]. $LiFePO_4$ was chosen for the proof-of-concept as it is one of the few materials for which the structure of the charged compound is well known from neutron diffraction experiments, and simple. Using an *in situ* electrochemistry holder filled with 1M LiF_6/DMC and LiFePO4 drop-casted on the electrodes, we charged the material inside the TEM and could refine the cell parameters, atom coordinates and occupancy of the lithium position of the charged compound, in good agreement with the structure from literature. However, we encountered many problems that will still need to be handled before the experiments can become *operando*.

In this talk, I will discuss the potential of in situ/operando electron diffraction tomography, but also the problems that still need to be overcome.

References

[1] O.M. Karakulina et al. Chem. Mater. 28 (2016) 7578; S.S. Fedotov et al., JSSC 242 (2016) 70; D. Mikhailova et al. Inorg. Chem. 55 (2016) 7079; O.A. Drozhzhin, Electrochim. Acta 191 (2016) 149; S.S. Fedotov, Chem. Mater. 28 (2016) 411; O.M. Karakulina et al., Nano Letters 18 (2018) 6286

Automatic processing of a large number of electron diffraction patterns in the TEM

JÁNOS L. LÁBÁR[1], Z. FOGARASSY[1]
[1] MTA EK MFA, Budapest

1. Introduction

Modern STEMs can record a large number of diffraction patterns, one from each pixel of a scanned area. The electron probe is usually focused to a nearly parallel beam of nanometric diameter for such studies. Many of these studies do not require precession and special additional hardware is not needed in such studies (although simultaneous precession with additional hardware may be advantageous in certain cases). The information obtained from that set of diffraction patterns depends on the fact if the scanned sample region was crystalline or amorphous. Phase maps and orientation distributions are obtained from the spot patterns and electron pair distribution function (ePDF) analysis is performed on the amorphous patterns to obtain nearest neighbors as an example. Automatic processing of the huge number of patterns is a challenge in both cases and the steps of the automatic procedure depend on the type of patterns (crystalline spots vs. amorphous rings) and the information to be deciphered. We report here a new computer program that processes the spot patterns, where the number of patterns to be processed in a single session depends only on the power of the processing computer (size of memory and speed).

2. Crystalline spot patterns

Due to the nanometric probe size, any of the spot patterns is typically dominated by spots from one or two grains, provided the sample is thin enough to prevent overlapping many grains in the beam direction. For successful application of the method it is assumed that the diffraction patterns are collected from samples, whose thichness in not more than a few times larger than the average grain size. Identification of the crystalline phase and of the orientation is based on template matching in a similar way as also described in [1]. The procedure is implemented within the ProcessDiffraction program [2]. The Template for a given phase contains calculated diffraction patterns for each independent orientations. The number of necessary orientations depends on the crystal symmetry of the given phase. In the present version of the program, only cubic patterns are calculated. The independent orientations are represented by a double-triangular part of the stereographic projection: [001]-[101]-[111]-[011]. That region includes both right-handed and left-handed variants. A spot in the diffraction pattern is represented by 3 numbers: its angular distance from the direct beam, its azimuthal angle (related to the same but arbitrary starting angle) and intensity. Intensity includes the structure factor (kinematic in the present version) and the deviation from the Ewald-sphere (calculated up to a pre-specified length of the relrod, which is determined by the sample thickness). During Template-matching the Template is azimuthally rotated to find the measured diffraction spots. The best-matching phase in the best-matching orientation is assigned to the given measured diffraction as a solution. Even in case of overlapping patterns (from two or three grains within the excited volume) ususally there is a dominant one, which is found as a solution, only the quality of the fit will be reduced for such patterns.

Logically distinct steps are used to structure the program into menu-driven functional units. First the measured diffraction must be calibrated (primary beam energy, camera length, pixel size) and the center of the pattern must also be located (in pixel numbers). It is assumed that the pattern center only makes a minor movement between patterns of the same set. The origin of this possible slight movement might be the scanning of the beam. This minor movement is tracked and corrected for automatically during automatic processing. Next, Templates are generated for all of the phases to be considered. Template-matching assignes a phase and an orientation to a given diffraction pattern (that corrsponds to a pixel of a scanned image) and this result is saved. Visualization in the

next step starts from these saved results and includes several options. The identified orientation of a phase can be plotted on the sterographic projection. Integration of the direct beam region in each pattern is used to produce a virtual bright field (VBF) image. Asignment of intensites to image points is done according to the scanning-parameters (number of lines and columns) of the experiment. Similarly, a virtual image, corresponding to the one recorded by a high-angle annular dark-field detector (VHHADF) can also be calculated by integrating the intensities in the measured pattern along a belt that excludes the central region. On the same scanning image the quality of the fit or the uniquness of the olution can also be visualized. Phase maps are rendered similarly.

3. Experimental

Experimental patterns are recorded on a C_s-corrected FEI Themis TEM, operated at 200 keV. The corrector is in the imaging part and the probe is not corrected. The size of the C2 aperture is 20 µm, to ensure small-sized, nearly parallel illumination. The patterns are recorded on a 4k*4k CETA CMOS camera controlled by the TIA rpogram. The presentation will provide examples of application of the new program.

References

[1] E.F. Rauch and L. Dupuy, Archives of Metallurgy and Materials, 50 (2005) 87-99
[2] J.L. Lábár, Ultramicroscopy 103 (2005) 237–249

Donwilhelmsite – a new mineral from the Moon

MARIANA KLEMENTOVA[1], LUKAS PALATINUS[1], JÖRG FRITZ[2], ANSGAR GRESHAKE[3], RICHARD WIRTH[4], VERA ASSIS FERNANDES[3,5] AND LUDOVIC FERRIÈRE[6]

[1] Institute of Physics of the Czech Academy of Sciences, v.v.i., Prague, Czechia; [2] Saalbau Weltraum Projekt, Heppenheim, Germany; [3] Museum für Naturkunde Berlin, Berlin, Germany; [4] Helmholtz-Zentrum Potsdam - Deutsche GeoForschungsZentrum, Potsdam, Germany; [5] University of Manchester, Williamson Building, Manchester, UK; [6] Natural History Museum, Burgring 7, A-1010 Vienna, Austria

The new mineral "donwilhelmsite" [1], calcium aluminium silicon oxide (CAS) phase, formed in shock melt pockets in the lunar meteorite Oued Awlitis 001. The meteorite is classified as an anorthositic lunar melt rock [2]. Shock melt pockets 100 µm in size of roughly anorthitic chemical composition contain bundles of up to 20 µm long and less than 1 µm wide needle-shaped crystals (Fig 1).

A lamella was cut out of the thick section NHMV-O104 with a focused ion beam (FIB) to study the structure of needle-like donwilhelmsite crystals. The sample was investigated by Precession Electron Diffraction Tomography (PEDT) using a Philips CM 120 TEM (LaB6, 120kV) equipped with a NanoMEGAS precession unit DigiStar and an Olympus SIS CCD Veleta (2048x2048 pixel) camera. The data were collected from -50° to +50° with a step of 1° and a precession angle of 1°. The data were processed in the PETS software. Structure solution and refinement were performed in the computing program package Jana2006. Donwilhelmsite structure was solved by the charge flipping algorithm using the program Superflip, and refined using dynamical approach [3].

Eight datasets (Fig. 2) were collected with average lattice parameters a = 5.44(1) Å, c = 12.76(3) Å, space group $P6_3/mmc$. The structure is identical to the one of synthetic crystals experimentally produced at pressures of >15 GPa and temperatures of >1550 K by Gautron et al. [4]. The structure comprises M1 octahedral sheets that contain Al and Si (Fig. 2). These are intercalated with two M2-octahedra occupied by Al, one larger site occupied by Ca coordinated by 12 oxygen atoms, and two Al-tetrahedra with 50% occupancy. The structure was refined dynamically to R1(obs) = 8.98%. The chemical composition derived from the structure model is $CaAl_4Si_2O_{11}$, which is in good agreement with chemical composition of $Ca_{1.02}Al_{3.92}Si_{2.06}O_{11}$ obtained experimentally.

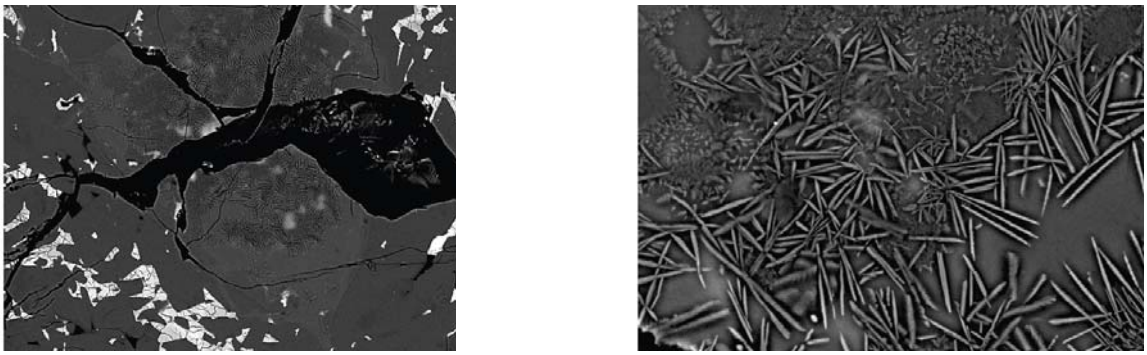

Figure 1. Backscattered-electron (BSE) images of a polished and carbon coated thick section of Oued Awlitis 001. (a) shock melt pocket, (b) needle-like crystals of donwilhelmsite.

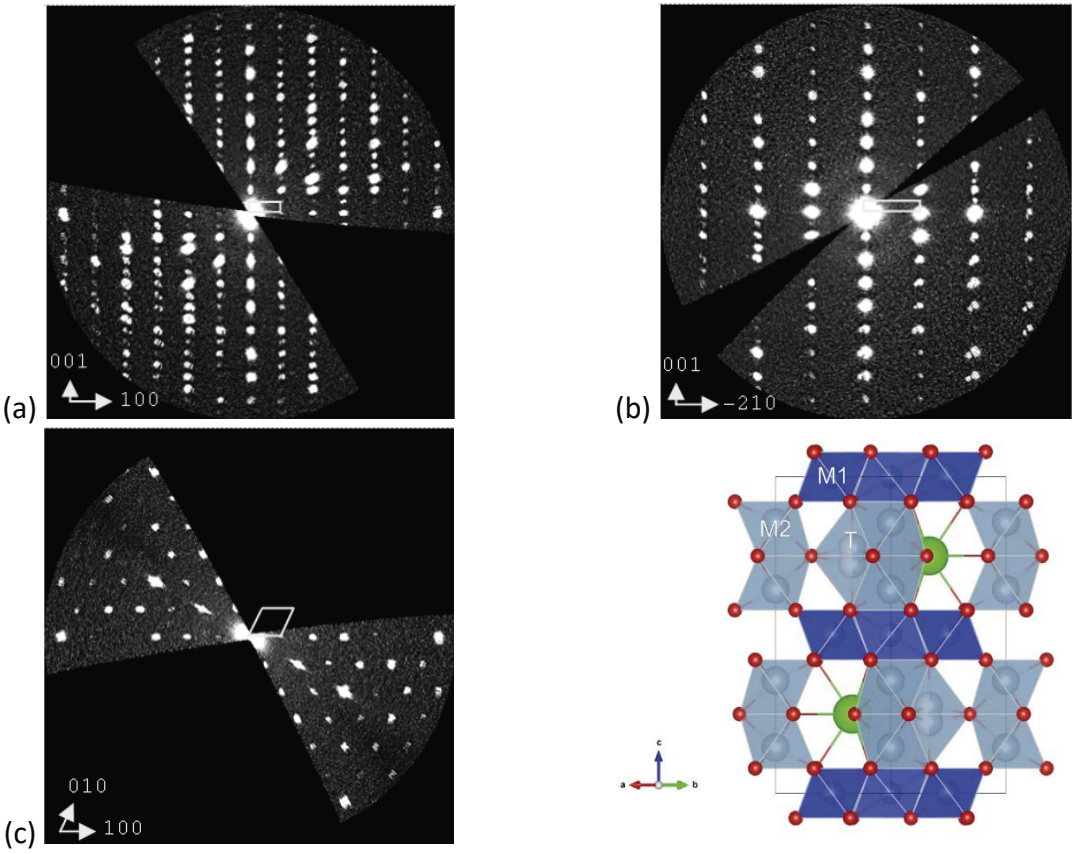

Figure 2. PEDT experiment. Reciprocal space sections (a,b,c). Structure of donwilhelmsite (d). Structure is composed of octahedral (M1) layers (dark blue) occupied by Al and Si in 1:2 ratio and interlayer containing octahedral position M2 (grey) fully occupied by Al, tetrahedral position T (grey) half occupied by Al, and cavity occupied by Ca (green).

References

[1] J. Fritz et al., European Journal of Mineralogy 31 (2019) 201.
[2] A. Ruzicka et al., Meteoritics & Planetary Science 52 (2017) 1014.
[3] L. Palatinus et al., Acta Crystallogr. A 71 (2015) 235.
[4] L. Gautron et al., Physics and Chemistry of Minerals 27 (1999) 47.
[5] The authors acknowledge funding from the Czech Ministry of Education, Youth and Sports (project LM2015087).

INVITED LECTURE

Analytical Electron Microscopy: Recent Advances and New Applications

FERDINAND HOFER[1,2], MIHAELA ALBU[2], WERNER GROGGER[1,2], GEORG HABERFEHLNER[1], DANIEL KNEZ[1,2], JUDITH LAMMER[2], FRANZ-PHILIPP SCHMIDT[3] AND GERALD KOTHLEITNER[1,2]

[1] Institute for Electron Microscopy and Nanoanalysis, Graz University of Technology, Graz, Austria; [2] Graz Centre for Electron Microscopy, Graz, Austria; [3] Fritz-Haber-Institute, Max-Planck-Society, Berlin, Germany

Scanning transmission electron microscopy (STEM) has proven to be an indispensable method for mapping the location and identity of atoms in complex materials. The introduction of spherical aberration correction paved the way for atomic resolution imaging by means of high-angle annular dark field (HAADF) and annular bright field (ABF) detectors and recently also differential phase contrast (DPC) imaging [1]. Additionally, an aberration corrected STEM enables atomic-resolution mapping of the individual elements in a material thus allowing a unique correlation of structural and chemical information by means of electron energy-loss spectrometry (EELS) and energy dispersive X-ray spectrometry (EDS).

1. Quantitative elemental mapping

However, quantification of atomic resolution elemental maps on an absolute scale remains a challenge. In most cases elemental maps recorded at atomic resolution have been only interpreted in a qualitative way. This situation changed with the novel simultaneous acquisition of EELS and X-ray signals and the careful consideration of the geometry of X-ray detectors [2], thus enabling elemental quantification in terms of volumetric densities [3]. Absolute scale quantification comparisons between experiment and quantum mechanical calculations revealed the number of atoms in the individual atom columns e.g. in $SrTiO_3$, but this is only possible if all scattering processes are fully considered [4]. Since a few years, elemental mapping has been extended to the third dimension by combining electron tomography methods with simultaneous EELS and EDX spectroscopies revealing voxel spectroscopy data at the nanoscale [5]. Advancing electron tomography to atomic resolution now even reveals the 3D atomic positions in core/shell nanoparticles [6].

2. The new electron energy-loss spectrometry

Here we will concentrate on new developments in EELS instrumentation: Around 15 years ago we saw the hype with the monochromated STEM-EELS instruments of the first generation, which allowed to acquire EELS spectra with an energy-resolution down to 150 meV. This development was extremely important for studying surface plasmons on noble metal nanoparticles and nanostructures by taking advantage of the electron microscope's unbeaten high spatial resolution. In the meanwhile, STEM-EELS is the main microscopic method for imaging of surface plasmons starting with Au and Ag nanoparticles [7] via flat nanostructures [8] to 3D nanoscale mapping of coupled plasmonic nanoparticles [9]. Recently, we could gain a quantitative understanding of the light coupling of dark plasmonic modes by simultaneous EELS and cathodoluminescence (CL) spectroscopy [10]. A new generation of a monochromated microscopes was introduced in 2014 and now these instruments deliver an energy resolution in the sub-20 meV regime. It gives access to a range of new and unique experiments hitherto impossible on any other electron microscope: vibrational spectroscopy with a nm-sized probe or even smaller [11].

Another important improvement for EELS comes with the introduction of direct-electron-detectors which can be attached to EELS-spectrometers and energy-filters [12]. We will show that the improved detective quantum efficiency enables low-dose elemental mapping of radiation sensitive organic matter, trace element analysis and higher signal-to-noise ratios for high energy ionization edges [13].

3. New application examples

Finally, we will describe two new applications of analytical STEM at atomic resolution. Firstly, we will describe the quantitative analysis of interstitial Sr atom colums in silicon by combining STEM and DFT simulations [14] and secondly the diffusion defining atomic-scale spinodal decomposition within nanoprecipitates in an Al-alloy [15].

Acknowledgements

This project has received funding from the European Union's Horizon 2020 research and innovation programme under grant agreement No. 823717 – ESTEEM3 and from the "Zukunftsfonds Steiermark" of the Provincial Government of Styria.

References

[1] M.Lohr, R. Schregle, M. Jetter, C. Wächter, T. Wunderer, F. Scholz, J. Zweck, Ultramicroscopy 117 (2012) 7-14.
[2] J. Kraxner, M. Schäfer, O. Röschel, G. Kothleitner, G. Haberfehlner, M. Paller, W. Grogger, Ultramicroscopy 172 (2017) 30-39.
[3] G. Kothleitner, W. Grogger, M. Dienstleder, F. Hofer, Microsc.Microanal. et al., Microsc. Microanal. 20 (2014) 678-686.
[4] G. Kothleitner, M.J. Neish, N.R. Lugg, S.D. Findlay, W. Grogger, F. Hofer, L.J. Allen, Phys. Rev. Lett. 112 (2014) 085501, 1-5.
[5] G. Haberfehlner, A. Orthacker, M. Albu, J. Li and G. Kothleitner, Nanoscale 6 (2014) 14563-9.
[6] G. Haberfehlner, P. Thaler, D. Knez, A. Volk, F. Hofer, W.E. Ernst, G. Kothleitner, Nature Comm. 6 (2015) 8779, 1-6.
[7] B. Schaffer, U. Hohenester, A. Trügler, F. Hofer, Phys.Rev. B79 (2009) 041401, 1-4.
[8] F.-P. Schmidt, H. Ditlbacher, U. Hohenester, A. Hohenau, F. Hofer, J.R. Krenn, Nat. Comm. 5 (2014) 3604, 1-6.
[9] G. Haberfehlner, A. Trügler, F.-P. Schmidt, A. Hörl, F. Hofer, U. Hohenester, G. Kothleitner, Nano Lett. 15 (2015) 7726-7730.
[10] F.-P. Schmidt, A. Losquin, F. Hofer, A.Hohenau, J.R. Krenn, M. Kociak, ACS Photonics 5 (2018) 861-866.
[11] O.L. Krivanek, T.C. Lovejoy, N. Dellby, T. Aoki, R.W. Carpenter, P. rez, E. Soignard, J. Zhu, P.E. Batson, M.J. Lagos, R.F. Egerton, P.A. Crozier, Nature 514 (2014) 209-212.
[12] J.A. Hart, A.C. Lang, A.C. Leff, P. Longo, C. Trevor, R.D. Twesten, M.S. Taheri, Sci. Rep. 7 (2017) 8243, 1-14.
[13] S.F. Höfler, G. Haberfehlner, T. Rath, G. Kothleitner, F. Hofer, G. Trimmel, submitted to J. Mat. Chem. A.
[14] M. Albu, A. Pal, C. Gspan, R.C. Picu, F. Hofer, G. Kothleitner, Sci. Rep. 6 (2016) 31635, 1-7.
[15] A. Orthacker, G. Haberfehlner, J. Tändl, M.C. Poletti, B. Sonderegger, G. Kothleitner, Nat. Mat. 17 (2018) 1101-1107.

Vibrational STEM-EELS simulations at atomic resolution

PAUL M. ZEIGER, JÁN RUSZ
Department of Physics and Astronomy, Uppsala University, Uppsala, Sweden

We have investigated the potential of the so-called "delta thermostat" [1] for vibrational Scanning Transmission Electron Microscopy Electron Energy Loss Spectroscopy (STEM-EELS) simulations. The phonon-loss processes are thereby modeled within the frozen phonon approximation by a combination of Molecular Dynamics (MD) and elastic multislice calculations. The method was applied to the simulation of a 15 nm flake of hexagonal boron-nitride (hBN).

Vibrational spectroscopy in the electron microscope became only possible a few years ago after incremental advances in several components of EELS instrumentation and the development of new monochromators [2]. It was noted back then that the phonon-EELS signal contains both low- and high-resolution components [2-4]. In a recent paper by Hage et al it was demonstrated on hBN, that spectral mapping of atomic structure using the phonon sector in EELS is possible [5]. They found suitable detector positions in order to exploit the high-resolution component of the vibrational EELS for atomic resolution STEM images. Their results show furthermore that high angle phonon scattering carries atomic scale information and that this contrast is somewhat lost in low angle phonon scattering. These findings are supported by computer simulations using the quantum excitation of phonons (QEP) model [6], in which the atomic vibrations are treated by means of an Einstein model. The Einstein model neglects correlations of the motion of atomic nuclei, since each atom is modeled to vibrate independently from all other atoms.

The second important development, that enabled this work, happened in the field of Molecular Dynamics (MD) simulations. Stochastic thermostats based on the Langevin equation and the Generalized Langevin Equation (GLE) can be tailored for a range of applications, such as improving the sampling efficiency of Path-Integral MD simulations and modelling Nuclear Quantum Effects at low cost [7]. One interesting flavor of these thermostats is the so-called delta thermostat, which allows to heat only those normal modes, whose frequencies lie within a narrow interval around a selected peak frequency.

Within the frozen phonon approximation, the image or diffraction pattern (DP) including phonon scattering is an incoherent average over elastic electron scattering images or DPs calculated using the thermally distorted structure "snapshots". The key idea of our work lies in the generation of the structure snapshots: instead of an Einstein model the delta thermostat is used in a MD simulation. By "scanning" the peak frequency of the delta thermostat over the phonon-loss region, N structure snapshots, corresponding to atomic displacements τ_n of the heated phonon modes are generated. These snapshots are subsequently used as inputs for elastic electron scattering simulations utilizing the multislice method. This procedure yields a set of exit wave functions Ψ for each frequency. In the spirit of Ref. [4], the phonon signal (the intensity due to phonon scattering) is computed from these exit wave functions as the difference of the incoherently averaged intensity and the intensity of the coherently averaged exit wave functions, i.e.,

$$I_{phonon}(x_\perp, z) = \frac{1}{N}\left[\sum |\Psi(x_\perp, z, \tau_n)|^2 - \left|\sum \Psi(x_\perp, z, \tau_n)\right|^2\right],$$

where $x_\perp$ is the position in the image plane and z is the thickness at which the signal is considered. Using this procedure, the phonon-loss sector in EELS is simulated and it is possible to match the frequency or energy of a phonon mode with the predicted electron intensity. Given a suitable inter-

atomic potential for the MD simulation, our method should improve upon the simulations in Ref. [5] by taking into account correlations between atomic vibrations.

The main results of our work are summarized in Figure 1. Two spectra of the phonon-loss region for a dark field (DF) detector, one for the beam centered on an atomic column and one centered on a "hole" of the hBN structure, are shown in Fig. 1a. A clear difference in intensity between both spectra is observed, leading to atomic scale contrast in Fig. 1b), which shows a STEM image in which the intensity of a pixel is the integral over the phonon-loss sector for the corresponding beam position. The contrast of 0.55 agrees well with the contrast of 0.52 reported in Ref. [5]. Figure 1c) shows spectra for a bright field (BF) detector at the same beam positions as in Fig. 1a). It is evident that the difference between on column and off column spectra is substantially smaller in the BF than in the DF case. This leads to a much lower contrast in the tentative BF image in Fig. 1d) and in agreement with Ref. [5]. The lack of hexagonal symmetry apparent in the BF image is most likely caused by not yet reaching full convergence by averaging over 48 structure snapshots. Phonon impact scattering is only a tiny fraction of the total elastic scattering cross-section (~10^{-4}) in the bright field and reaching full convergence is thus computationally demanding.

In summary we have found good agreement in image contrast between our results and those of Ref. [5] but the tentative BF image is distinctly different from the simulated BF image of Ref. [5].

We acknowledge funding from Swedish Research Council and Swedish National Infrastructure for computing (SNIC) at the NSC center (computer cluster Tetralith).

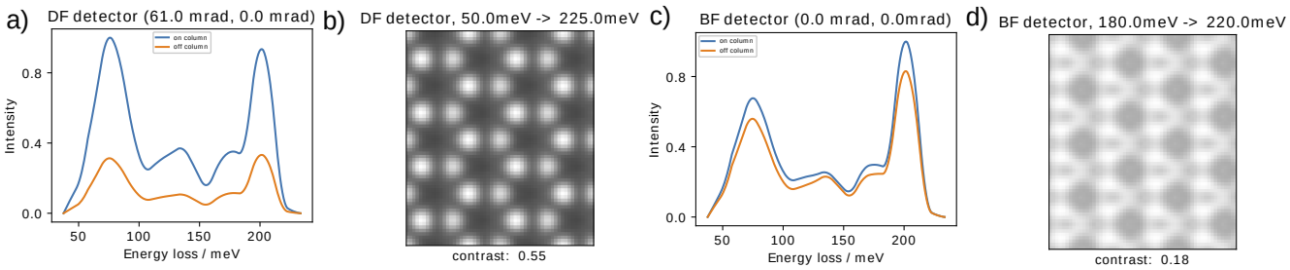

Figure 1: Visualization of the main results of this work: a) phonon-EELS spectrum with detector in DF position. b) STEM-image with detector in DF position, c) phonon-EELS spectrum in BF position, c) STEM-image with detector in BF position.

References

[1] M. Ceriotti, M. Parrinello, Procedia Comput. Sci. 1, 1607 (2010)
[2] O. L. Krivanek, T. C. Lovejoy, N. Dellby, T. Aoki, R. W. Carpenter, P. Rez, E. Soignard, J. Zhu, P. E. Batson, M. J. Lagos, R. F. Egerton, P. A. Crozier, Nature 514 (2014), p. 209
[3] C. Dwyer, Phys. Rev. B 89, 054103 (2014)
[4] C. Dwyer, T. Aoki, P. Rez, S. L. Y. Chang, T. C. Lovejoy, and O. L. Krivanek, Phys. Rev. Lett. 117, 256101 (2016)
[5] F. S. Hage, D. M. Kepaptsoglou Q. M. Ramasse, L. J. Allen, Phys. Rev. Lett. 122, 016103 (2019)
[6] B. D. Forbes, A. V. Martin, S.D. Findlay, A. J. D'Alfonso, L. J. Allen, Phys. Rev. B 82, 104103 (2010)
[7] M. Ceriotti, G. Bussi, M. Parrinello, J. Chem. Theory Comput. 6, 1170 (2010)

Structure and Properties of Novel 1D Self-organized TiO_2 Nanotubes Deposited by MoS_2 and CdS via Atomic Layer Deposition

JAN MICHALICKA[1], RAUL ZAZPE[1,2], HANNA SOPHA[1,2], ALEXANDER TESFAYE[3], MILOS KRBAL[2], JAN PRIKRYL[2], LUDEK HROMADKO[2], THIERRY DJENIZIAN[3], JAN M. MACAK[1,2]

[1] Central European Institute of Technology, Brno University of Technology, Brno, Czech Republic; [2] Center of Materials and Nanotechnologies, Faculty of Chemical Technology, University of Pardubice, Pardubice, Czech Republic; [3] Mines Saint-Etienne, Center of Microelectronics in Provence, Department of Flexible Electronics, Gardanne, France

The self-organized TiO_2 nanotube layers have attracted considerable scientific and technological interest over the past 15 years, motivated by the range of applications including photo-catalysis, solar cells, hydrogen generation and biomedical uses **[1]**. The synthesis of 1D TiO_2 nanotube structure of high aspect ratio is carried out by a conventional electrochemical anodization of Ti sheet.

One of the major issues to extend the functional range of nanotubes is to coat homogenously tube interiors by a suitable secondary material to tailor surface properties and expand the application portfolio of these unique 1D layers.

The poster will focus in recent successes in the coatings of the TiO_2 nanotube arrays via the atomic layer deposition (ALD). In particular, it will be presented properties of:

A) Homogeneously decorated TiO_2 nanotubes with ultrathin 2D MoS_2 nanosheets by the ALD, which were used for the first time for Li-ion batteries anodes [2]. When employed as anodes for Li-ion batteries, the MoS_2-decorated TiO_2 nanotube layers show a superior performance compared to their pristine counterparts with more than 50 % higher areal capacity and ~70 % higher gravimetric capacity.

B) Homogeneously deposited TiO_2 nanotubes with few nm thin layer of CdS light absorber, which revealed a strong influence on the light absorption profile within the CdS/TiO_2 heterostructure and on sub bandgap tail of CdS within the TiO_2 nanotubes. As a result it showed up nearly 80 % trapped photons converted into electrons. All these aspects make this heterostructure very promising for the next generation of highly performing solar cells [3].

Both created heterostructures will be demonstrated via SEM and STEM-HAADF imaging and via STEM-EDX elemental mapping with use of a quadrant SUPER-X spectrometer, as a powerful tool to thoroughly analyze deposited structures.

References:

[1] J. M. Macak et al., *Curr. Opin. Solid State Mater. Sci.*, 1-2 (2007) 3.
[2] H. Sopha et al., *FlatChem*, in press.
[3] R. Zazpe et al., *Nanoscale*, 35 (2018)

IT4

Correlative, and super-resolution microscopy

CHAIRPERSONS:

Ferdinand Hofer, Kristof Kovacs

INVITED LECTURE

Correlative Raman microscopy, SEM and EDX – examples of application and best practice

HARALD FITZEK[1], RUTH SCHMIDT[1,2], MANFRED NACHNEBEL[1], CLAUDIA MAYRHOFER[1], ARMIN ZANKEL[2] AND HARTMUTH SCHROETTNER[1,2]

[1] Graz Centre for Electron Microscopy, Graz, Austria; [2] Institute of Electron Microscopy and Nanoanalysis, NAWI Graz, Graz University of Technology, Austria

Recent years have seen the introduction of commercially available systems that integrate fully capable Raman microscopes with scanning electron microscopes (SEM) [1]. This opens up the exciting possibilities of combining high resolution SEM and elemental analysis by energy dispersive X-ray spectroscopy (EDX) with chemical mapping by Raman microscopy for a broad audience from fundamental research to industry.

When it comes to correlative Raman-SEM, in addition to having the equipment it is also necessary to have experience with both measurement techniques. On one hand, both techniques have specific requirements with regards to sample preparation, which need to be carefully arranged if a sample is prepared for correlative measurements. On the other hand, the interpretation of the results on a complex sample usually requires experience in SEM-EDX and especially in Raman microscopy. On top of that, issues specific to the combination of the two techniques such as carbon contamination and chemical deterioration by the electron beam [2] or correct correlation of measurements with significantly different resolution and contrast mechanism need to be considered. In addition, the full performance of the Raman microscope can only be achieved in a “off axis” setup as shown in figure 1, which further complicates the instrument operation, as the sample has to be moved precisely between the two measurement positions. To sum up a lot needs to be considered in correlative Raman-SEM-EDX microscopy and some general best practices guidelines are very helpful for anybody venturing into this field of research.

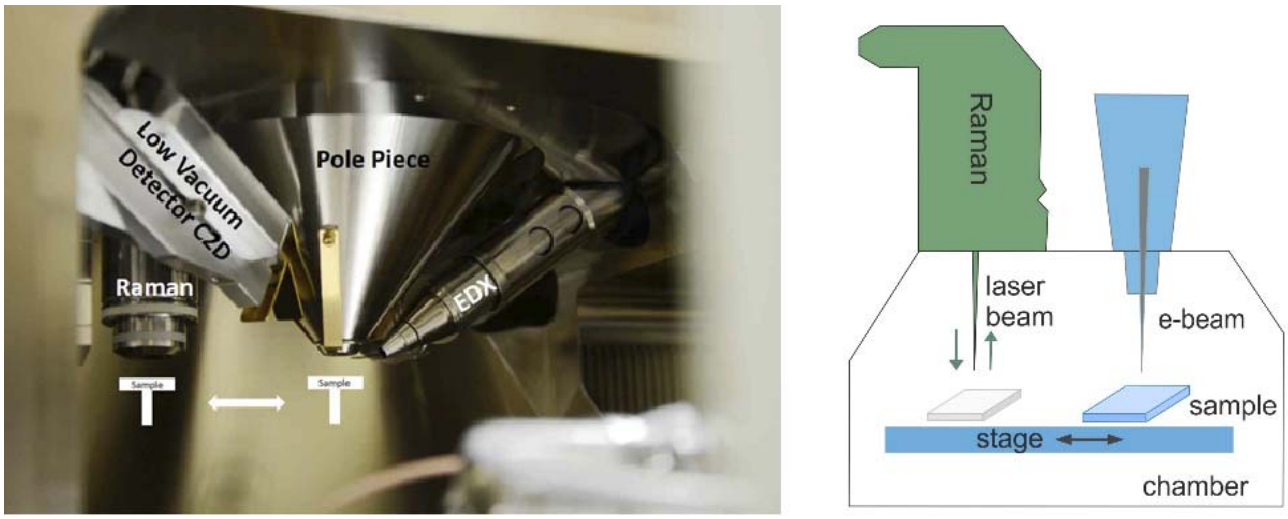

Figure 1: Left: Image of the sample chamber and detectors in a combined SEM-EDX-Raman (Zeiss Sigma 300 VP; Oxford X-Max 80; WITec RISE); Right: Schematic Drawing of the “off axis” setup and sample movement for correlative measurements.

Our institute has extensive experience with both SEM-EDX and Raman microscopy in fundamental research as well as in cooperation with partners from industry. In 2017, a combined SEM-EDX-Raman (Zeiss Sigma 300 VP; Oxford X-Max 80; WITec RISE) was installed at our institute. Since then a broad range of samples has been investigated, a particularly exotic example of which, a meteorite, is shown in figure 2. Other types of samples that have been investigated include metal-oxides, inclusions in metals, metal-organic compounds, pharmaceuticals, polymers, organic-inorganic compounds and diverse particles (from micro to nano). Using some of these examples, we would like to outline general benefits of the addition of Raman microscopy to the established combination of SEM and EDX, such as readily available information about hydrogen bonds or the possibility to identify organic compounds. Additionally we would like to point out specific benefits with regards to the concrete examples shown, such as using the superior depth of focus of the SEM to guide Raman point measurements on a rough surface or confirming a difference in chemical composition that can only be inferred from the contrast in the SEM image. On top of that, the most important considerations concerning sample preparation and the limitations that arise from them will be discussed. Furthermore, some best practices guidelines to avoid problems that can occur due to beam damage by both the laser and electron beam will be presented.

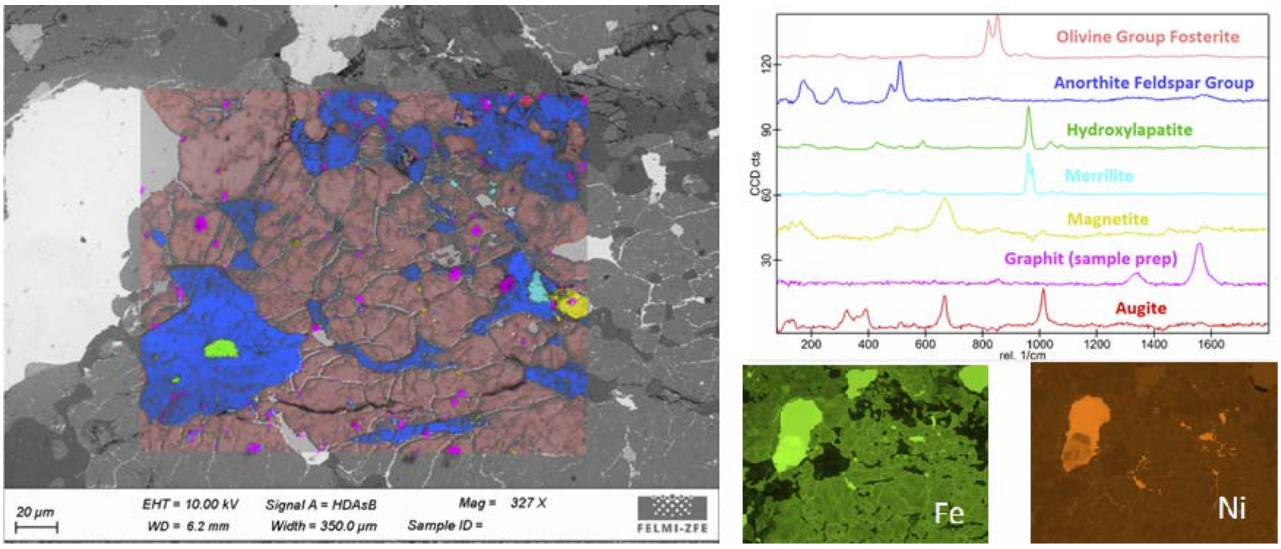

Figure 2: Correlative Raman-SEM-EDX of a meteorite. Left: SEM (BSE) image with an overlay of a Raman mapping, the phases are shown in the same color as the spectra on the right. Note that the metallic phases (bright parts in the BSE image) cannot be identified by Raman microscopy. Right (top): Raman spectra with the identification of the phases. Right (bottom): Complementary EDX spectrum identifying the composition of the metallic phases.

References

[1] C. Cardell, I. Guerra, TrAC, 77 (2016) 156-166.
[2] D. Lau, A. E. Hughes, T. H. Muster, T. J. Davis, A. M. Glenn, Microsc. Microanal., 16-1 (2010) 13-20

Microbiologically influenced corrosion (MIC) of steel – a study using correlative SEM, EDX and Raman microscopy

THOMAS PLANKO[1], HARALD FITZEK[1], STEFANIE EICHINGER[3], JOHANNES RATTENBERGER[1] AND HARTMUTH SCHROETTNER[1,2]

[1] Graz Centre for Electron Microscopy, Graz, Austria; [2] Institute of Electron Microscopy and Nanoanalysis, NAWI Graz, Graz University of Technology, Austria; [3] Institute of Applied Geosciences, Graz University of Technology, Graz, Austria

Direct costs due to corrosion worldwide amount to 3% and in some countries up to 5% of the GDP (gross domestic product) [1][2]. Secondary cost like production losses or efficiency loss can be much higher [3]. Apart from these enormous costs and the economic consequences, in many areas, corrosion represents a very high safety risk (e.g. aircraft and pipelines). Microbiologically influenced corrosion (MIC) is responsible for 20% of all corrosion damage [4]. In this context, there is great interest in understanding MIC especially, since it has been shown that some microbes slow down the rate of corrosion [5], while others speed it up [6]. It is important to note that one of the difficulties in understanding MIC is that the composition of bacterial cultures and biofilms can vary greatly [7]. This makes any newly discovered composition an interesting topic to study.

During experiments in the Koralmtunnel, a bacterial strain was found, whose main mass consists of iron-oxidizing gallionella ferruginea, sulfur-oxidizing thiothrix and methanotrophic bacteria. In figure 1, the typical corrosion structures of the dominating bacteria is shown. This bacterial strain causes MIC and as a result a biofilm is formed (figure 1).

Figure 1: Left: SEM-image of typical microbial corrosion structures measured on a powder sample from the experimental setup in the Koralmtunnel (Right). The red mucus in the pipes is a biofilm, formed by the bacterial strain.

To study the effects of this strain, various steel samples, with different composition and roughness, a 3D printed steel, and three pipes (copper, lead, steel) were placed in the experimental setup (figure 1, right). Both a macroscopic and microscopy analysis of the samples is performed. On the macroscopic side, the average corrosion rates are determined by etching in accordance with Standard G1-03 [8] and the pitting corrosion rate is determined using infinite focus microscopy.

On the microscopic side a novel technique that combine Raman imaging with scanning electron microscopy (SEM) and energy dispersive X-Ray spectroscopy (EDX) (Zeiss Sigma 300 VP; Oxford X-Max 80; WITec RISE) is applied. The correlative Raman microscopy complements the established SEM-EDX combination with information about chemical bonds and oxidation states. An example of a correlative SEM-EDX-Raman measurement of a powder sample from the experimental setup is shown in figure 2. The Raman spectra shows hematite and biotic maghemite. The EDX-mappings shows the distribution of iron, oxygen, silicon and calcium.

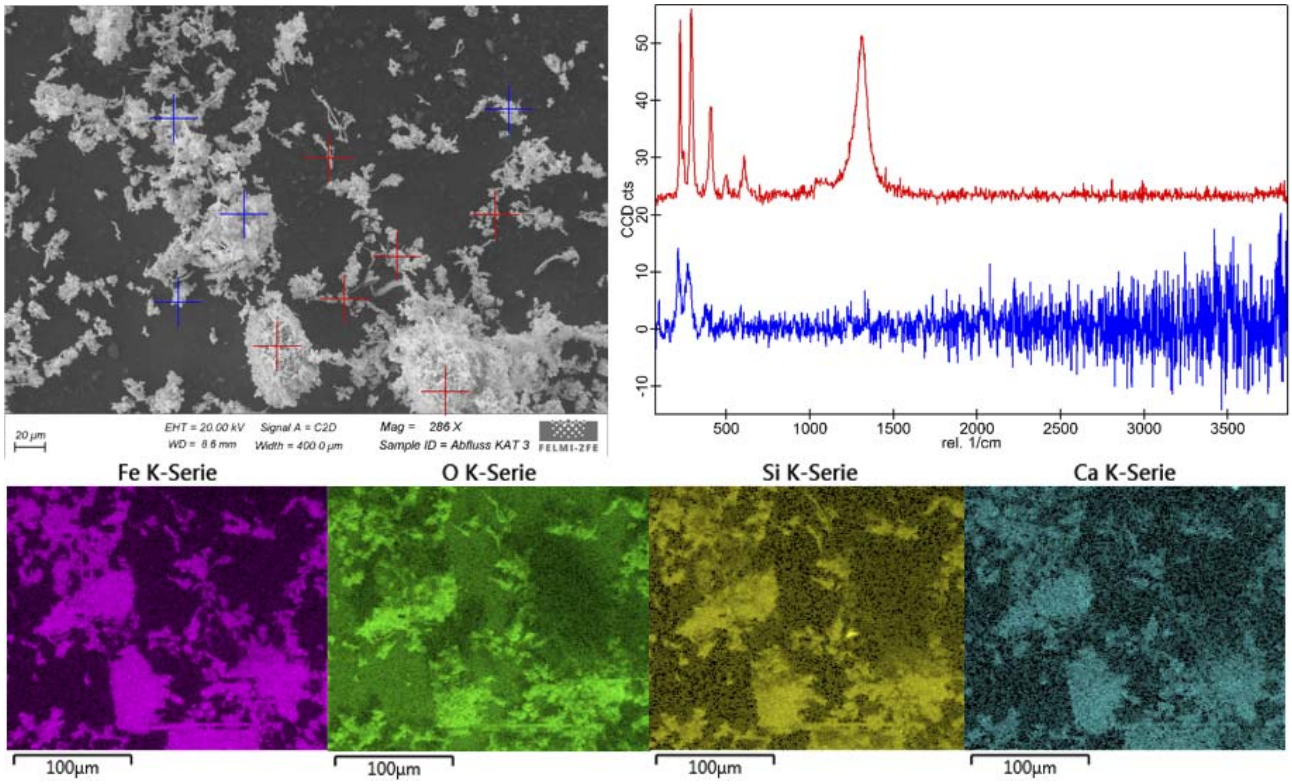

Figure 2: Top: Left (top): SEM-image with Raman positions; Right (top): Raman spectrum: red → hematite; blue → biotic maghemite; Bottom: EDX-mappings

To quantify the influence of MIC on the corrosion rate and separate the corrosion products of regular corrosion and MIC, a reference measurement with equal samples is necessary. This was done by removing the bacteria strain by a filter method from the water. The water from the Koralmtunnel without the bacteria strain was then filled in a reactor, which was positioned in the tunnel as well to ensure comparable environmental conditions, and the flow rate was simulated by means of a magnetic stirrer [9]. Both, the original samples and the reference samples (Figure 3) were weighed before the experiment and placed in the appropriate experimental setup for 3 weeks. Thereafter, the corroded material was removed by etching according to standard G1-03 [8] and the material loss of the samples was compared.

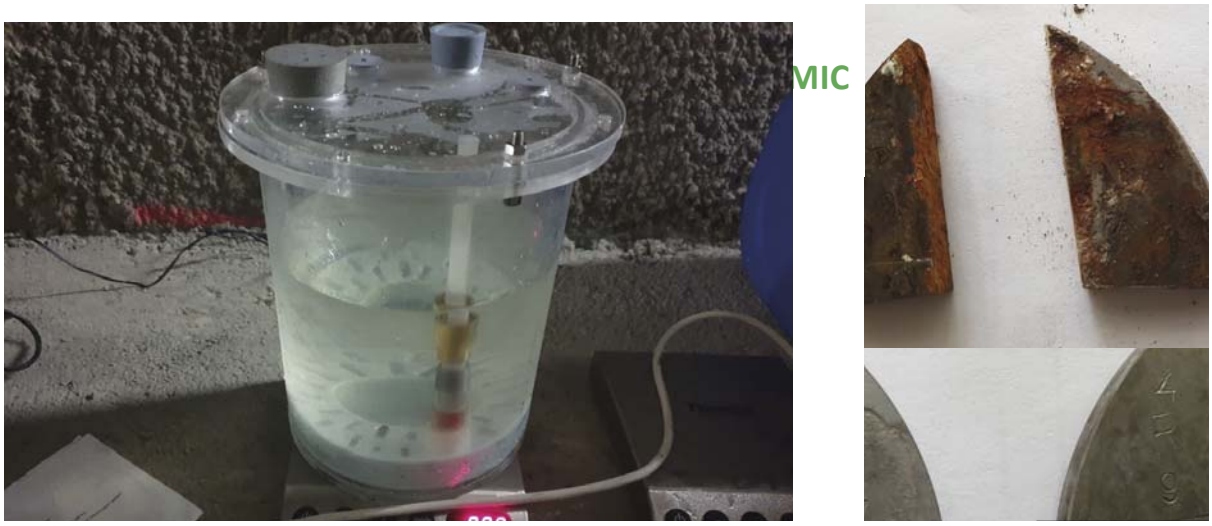

Figure 3: Left: Experimental setup for reference measurement. The flow rate was simulated by means of a magnetic stirrer, with a rotation speed of 800 revolutions per minute. Right: Equal steel with equal roughness. MIC: Sample after MIC; Ref: Reference sample after Corrosion without MIC; MIC (etched): MIC-Sample after etching; Ref (etched): Reference-sample after etching;

In this contribution both the influence of MIC on the corrosion rates and the microscopic composition of the corrosion products as measured by correlative SEM-EDX-Raman will be discussed. A special focus will be on the specific benefits of the correlative SEM-EDX-Raman approach for the analysis of corrosion.

References

[1] Hays, George F. "Now is the Time." *World Corrosion Organization* (2010).
[2] Biezma, M. V., and J. R. San Cristobal. "Methodology to study cost of corrosion." *Corrosion engineering, science and technology* 40.4 (2005): 344-352.
[3] Wendler-Kalsch, Elsbeth, and Hubert Gräfen. *Korrosionsschadenkunde*. Springer-Verlag, 2012.
[4] Javaherdashti, Reza. "A review of some characteristics of MIC caused by sulfate-reducing bacteria: past, present and future." *Anti-corrosion methods and materials* 46.3 (1999): 173-180.
[5] Dubiel, M., et al. "Microbial iron respiration can protect steel from corrosion." *Appl. Environ. Microbiol.* 68.3 (2002): 1440-1445.
[6] Javed, M. A., et al. "Effect of sulphate-reducing bacteria on the microbiologically influenced corrosion of ten different metals using constant test conditions." *International Biodeterioration & Biodegradation* 125 (2017): 73-85.
[7] Beech, Iwona B., and Jan Sunner. "Biocorrosion: towards understanding interactions between biofilms and metals." *Current opinion in Biotechnology* 15.3 (2004): 181-186.
[8] Standard, A. S. T. M. "G1-03 (Reapproved 2017)." *Standard Practice for Preparing, Cleaning, and Evaluating Corrosion Test Specimens (West Conshohocken, PA: ASTM International).*
[9] Halász, Gábor, et al. "Vortex flow generated by a magnetic stirrer." *American Journal of Physics* 75.12 (2007): 1092-1098.

Alpha-synnuclein affects differently the internal and external leaflet of the lipid membranes

SAMIRA JADAVI[1,2], SILVIA DANTE[1], ANNALISA RELINI[2], ALBERTO DIASPRO[1,2] AND CLAUDIO CANALE[2]

[1] Department of Nanophysics, Istituto Italiano di Tecnologia, Genova, Italy; [2] Department of Physics, University of Genova, Italy

Abstract

Peptides and proteins possess an inherent tendency to convert from their native functional states into intractable amyloid aggregates. This phenomenon is associated with a range of increasingly common human disorders, including Alzheimer and Parkinson's diseases, type II diabetes, and a number of systemic amyloidosis [1]. Amyloid toxicity is associated to the interaction between aggregates of protein and cell membrane in particular with the lipid part of the cell membrane. By simplifying the system, it is possible to systematically study the interaction of such protein aggregates with lipid membranes.

Atomic Force Microscopy (AFM) is an approach to study topographical changes at the nanoscale including local biomechanical properties. As well, AFM is powerful biophysical approach for the study of planar supported lipid bilayers (SLB) of variable composition as membrane model systems[2]. In the current work we used a protocol that has been developed for preparing defect-free planar bilayers with the coexistence of both fluid and gel lipid phases [3]. In particular, we employed two different lipid mixtures, mimicking the composition of both the external and internal leaflet of the neuronal cell membranes. The main difference between the two mixtures is the localization of the lipid head-group negative charge, confined in the gel phase and in the fluid phase for external and internal membrane, respectively. Among all the possible amyloidosis, here we focus on Parkinson's disease (PD). We found that the interaction with α-synuclein, the main peptide involved in PD, induced significant damages in SLBs with different extent in the two investigated lipid mixtures. These results highlighted the fine interplay between protein aggregates characteristic and membrane composition and organization as a key factor in the cytotoxicity of amyloid aggregates.

References

[1] F. Chiti, C. M. Dobson, Annu. Rev. Biochem, 2017. 86:27-68.
[2] S. J. Attwood, Y. Choi, Z. Leonenko, Int. J. Mol. Sci, 2013, 14, 3514-3539
[3] R. Oropesa-Nuñez, S. Seghezza, S. Dante, A. Diaspro, R. Cascella, C. Cecchi, M. Stefani, F. Chiti and C. Canale, Oncotarget, 2016; 7:44991-45004.

Unexpected asymmetry in the aggregation of partially labeled peptides revealed by STED-AFM correlative nanoscopy

CLAUDIO CANALE[1], MICHELA COSENTINO[2], PAOLO BIANCHINI[2] AND ALBERTO DIASPRO[1,2]

[1] Physics Dept., University of Genova, Italy; [2] Nanophysics Dept., Istituto italiano di Tecnologia, Genova, Italy

In the last decays, new approaches pave the way to super-resolution (SR) microscopy. SR microscopy goes beyond the diffraction limit [1], providing spatial resolution in the order of the nanometer scale. The use of SR offers new insights into biological processes at the, hitherto inaccessible, molecular scale [2]. Since almost all the SR techniques are based on fluorescence [3-4], it is clear the great role played by the fluorophore and by the labeling technique. An optimal molecular dye must provide high brightness, stability, and specificity. While the first two properties are associated with the molecular structure of the fluorochrome itself, the former depends on the approach that is exploited for the recognition and binding of a molecular target. Moreover, the dye must not influence the biological processes under investigation. Different labeling approaches are available and are nowadays very standard procedures. On the other hand, a direct assessment of the efficiency and homogeneity of the labeling, as well as of the influence that the fluorescent tag has on the molecular activity, is not readily achievable. We investigated the formation process of amyloid aggregates, from monomeric insulin, Aβ1-42 and Aβ1-40 by using AFM-STED correlative nanoscopy.

We induced the in-vitro aggregation of insulin and Aβ1-42, and we used standard and well-consolidated methods for protein labeling. We demonstrated that the aggregation process of all the peptides depends on the presence of the fluorescent dye. In particular, the labeled peptides are not stochastically contributing to the formation of the amyloid fibrils, but they tend to assemble only in a fraction of aggregates, while a significant group of fibrils is completely unlabeled. This result suggests the coexistence of two simultaneous aggregation processes, producing well distinct aggregates. These new findings generate a warning: only a fraction of the products derived from in vitro aggregation can be imaged by fluorescence techniques [5].

AFM-STED correlative nanoscopy is a unique instrument that can provide direct control of the fluorophore distribution within the sample, working at the molecular scale. Furthermore, it can detect the presence of unpredictable effects induced by the dye molecules on intermolecular processes.

References

[1] Y. E. Kalay, Y.Kuru, E. Unalan, Int. J Hydrogen Energy, 12 (2015) 915–920
[1] E. Abbe, Arch. für mikroskopische Anat. 9 (1873) 413–418
[2] A. Diaspro, Nanoscopy and multidimensional optical fluorescence *microscopy*. Chapman and Hall/CRC (2010)
[3] S. W. Hell, J. Wichmann, Opt. Lett. 19 (1994) 780–782
[4] E. Betzig *et al.*, Science 313 (2006) 1642–1645
[5] M. Cosentino, C. Canale, P. Bianchini and A. Diaspro, Sci. Adv., 5 (2019) eaav8062

Measuring the Temperature Homogeneity Across FIB Lamellae for *In Situ* TEM Experiments via Raman Scattering in Crystalline Silicon

ROBERT KRISPER[1,2], HARALD FITZEK[1], EVELIN FISSLTHALER[1], WERNER GROGGER[1,2]
[1] Graz Centre for Electron Microscopy, Graz, Austria; [2] Institute of Electron Microscopy and Nanoanalysis, Graz University of Technology,Graz, Austria

In all *in situ* heating experiments, an accurate reading of the applied temperature as driving force for phase transitions and other effects is the basis for retrieving interpretable and reliable results. For the MEMS heater chip manufactured by DENSsolutions, a four-point probe resistive measurement of the heating spiral tunes the temperature with an accuracy of more than 95 % [1]. However, as the thermal contact between heater chip and specimen is usually not well defined, methods to measure the actual sample temperature locally in a TEM are the focal point of ongoing research. These include recording alterations in parallel beam electron diffraction patterns of Au nanoparticles [2], plasmon peak shifts in EELS for Aluminium nanoparticles [3] or applying Raman spectroscopy to Silicon particles [1].

Unlike distinct particles adhering to an electron transparent SiN_x membrane, a mounted FIB lamella is in better thermal contact with bulkier parts of the heater chip membrane. With this study, we take an approach towards measuring the temperature distribution across such a lamella via recording the shift of the Raman-active LO mode in Silicon. We carried out the measurements using a Zeiss Sigma 300 VP (*variable pressure*) SEM with an integrated WITec Raman confocal microscope to simulate vacuum conditions inside a TEM (figure 1). The spectrometer laser features a wavelength of 532 nm and adjustable output power settings, which we set to 0.11 mW to obtain a reasonable signal while not excessively contributing to the heating of the chip (as seen with 1.0 mW). A DENSsolutions Wildfire™ heater chip in combination with a custom-built holder (figure 1) for contacting the former in SEM, FIB and AFM applications provided the primary temperature stimulus.

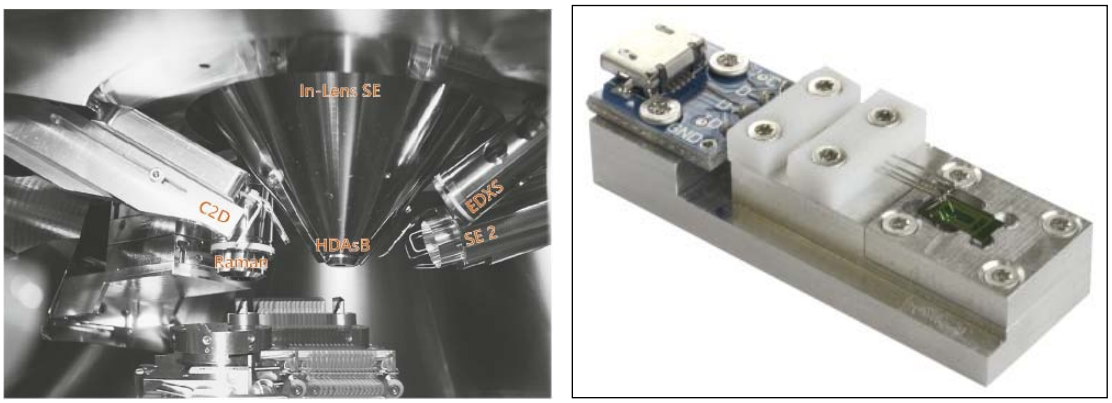

Figure 1. Left: Specimen chamber of the Zeiss Sigma 300 VP SEM installed at FELMI-ZFE, which features a WITec Raman confocal microscope alongside other detectors. Right: Custom-built holder to use TEM heater chips in (Raman-)SEM, FEBID, and AFM applications and for correlative microscopy, here combined with a DENSsolutions Wildfire™ S3 used in our experiments.

We recorded the Raman peak shift over a temperature series from 25 °C to 800 °C at 0.11 mW laser power and up to 1000 °C at 1.0 mW respectively, and fitted the data using the theoretical model suggested by Balkanski *et al.* [4] for calibration (figure 2). The stability of the spectrometer, the quality of the fit and the small standard deviation obtained from time series measurements result in a statistical uncertainty of $\Delta T = \pm 2$ °C. Possible systematic errors arise due to parameters which shift

Raman peaks but are challenging to control during a heating experiment (mechanical stress within the lamella [5]) or during the manufacturing of the specimen (nanocrystallinity of the sample [6]). Figure 3 therefore depicts the relative temperature homogeneity at a nominal temperature set point of 800 °C across a 6.2 µm long scan line in Si on a FIB lamella instead of an absolute temperature value. Clearly, temperatures in the centre of the lamella are homogeneous with respect to statistical uncertainty, but 10 K to 20 K lower than close to the fixation points on the heater chip.

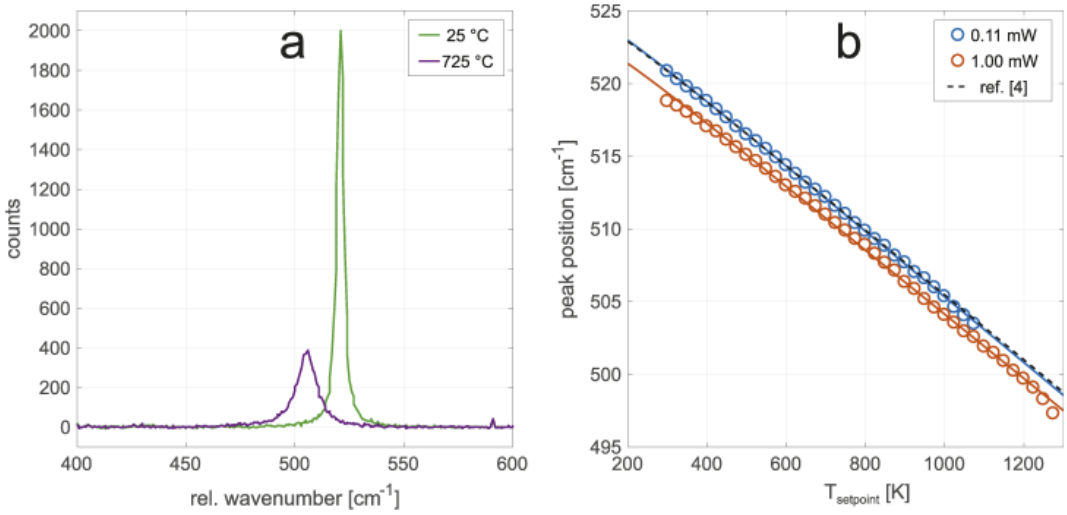

Figure 2. a) Measured shift of the Raman active LO mode in Si between heater set points of 25 °C and 725 °C. b) Calibration measurements for different laser powers. The dashed line shows reference data using the model from [4] for three-phonon scattering.

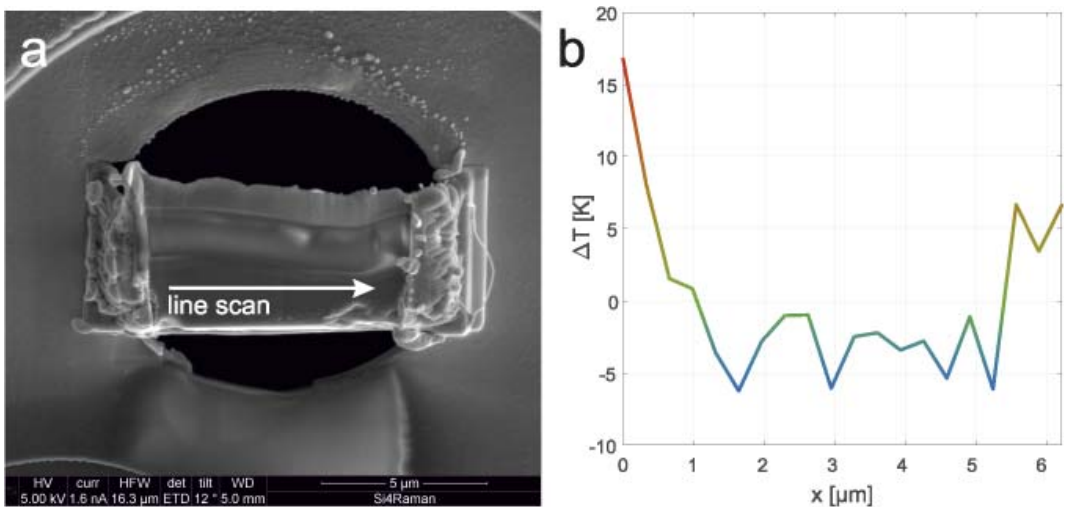

Figure 3. a) FIB lamella (Si, oxide layer, Pt) on a DENSsolutions Wildfire™ S3 heater chip (tilted view) after measurements. Raman line scan in Si along the indicated distance. b) Temperature homogeneity across the FIB lamella based on the calibration model and the Raman mode shift at a nominal set point of 800 °C.

References

[1] J. T. van Omme et al., Ultramicroscopy, 192 (2018) 14–20
[2] F. Niekiel et al., Ultramicroscopy, 176 (2017) 161–169
[3] B. K. Miller et al., Microscopy and Microanalysis, 24(S1) (2018) 1924–1925
[4] M. Balkanski et al., Physical Review B, 28(4) (1983) 1928–1934
[5] E. Anastassakis et al., Solid State Communications, 8 (1970) 133–138
[6] G. Viera et al., Journal of Applied Physics, 90 (2001) 4175–4183

IT5
In situ and environmental microscopy

CHAIRPERSONS:

Sašo Šturm, Kónya Zoltán

INVITED LECTURE

In-situ/ex-situ atomic-resolution study on metallic and oxide nanocrystalline materials

ZAOLI ZHANG[1], JINMING GUO[1] AND YONHUI ZHENG[1]
[1] Erich Schmid Institute, Austrian Academy of Sciences, Leoben, Austria

Recent development in *in-situ* experimental methods such as heating, biasing and straining has largely advanced our understanding about the materials interior structure and property relationship, and also enabled us to gain insights into such correlation at the atomic scale [1]. In this talk, two examples of our recent studies using the *in-situ* heating and biasing will be presented.

First example will be metallic nanocrystalline materials, which obtained via severe plastic deformation. Nanostructure materials have received unprecedented attention since they exhibit extremely high strength compared to coarse-grain bulk materials. The main issue on the nanocrystalline materials is its thermal stability [2]. *In-situ* experiments on the thermal stability of nanocrystalline materials not only help clarifying the structural evolution in details, but also can be used to correlate the structure changes with the macroscopic property. Here, Cu-based alloys, i.e. Cu-Cr [3] and Cu-Fe [4] are investigated by *in-situ* HRTEM experiments.

The evolution of structural and chemical composition in nanostructured materials with temperature was tracked in *real-time*. The results showed that: (i) it showed that the nanostructured materials are not only subjected to a structural change but also to chemical composition fluctuations upon annealing. This destabilization process in the nanostructured materials can initiate at a very low temperature while the grain sizes remain unaltered. (ii) The r*eal-time* chemical composition measurement exhibits the elemental concentration variation with annealing temperature (as seen in **Figure1**). This allows further analyzing the dynamic behavior in nanocrystalline materials in details, i.e. deducing the instantaneous diffusion coefficients and studying the interface sharpening phenomenon. The availability of *in-situ* composition profiles enables us to directly evaluate the excess vacancy concentration in nanocrystalline materials created by severely plastic deformation.

Furthermore, (iii) it is found that the thermal stability of nanocrystalline materials changes with the impurity level (i.e. oxygen) in nanostructured materials. Single-phase Cu-Fe supersaturated solid solution using powders precursors which contain a different amount of oxygen is given to demonstrate a total different behavior upon annealing. Firstly, nanometer-scale oxides form, and then upon heating a decomposition of supersaturated solid solution is observed [3]. It displays a dissimilar behavior compared to Cu-Cr during *in-situ* heating. **Figure2** shows the atomic-resolution structural evolution by *in-situ* HRTEM imaging.

The second example is regarding a prototype correlated electron material, vanadium oxide (VO_2), which is a potential candidate for optical, electrical and multi-responsive sensor applications. It shows a distinct reversible structural phase transition, namely metal-insulator transition at around room temperature (343 K). A Ti-doped VO_2 film on TiO_2 substrate annealed is used in the present study. Apart from *ex-situ* experiments and atomic resolution spectroscopy analysis, *in-situ* heating and biasing experiments were carried out to reveal the structural change characteristics in details as well as associating them with the electrical properties. It is noted that the structural anisotropy and structural defects induced by the cationic diffusion is relevant to the measured property [5, 6].

References

[1] H. Zheng et al, Frontiers of *in situ* electron microscopy, MRS Bulletin, 40 (2015)12-18
[2] R.Z. Valiev *et al.*, Mater. Res. Lett., 4(2016) 1–21.
[3] Z.L. Zhang *et al.*, Acta Materialia **138** (2017) 42-51.
[4] J. Guo *et al.*, Nature communications, **9** (2018)946.
[5] Y. Zheng *et al.*, the 14th MCM, Sept. 15-20, 2019, Belgrade, Serbia.
[6] The authors (Y.Z. and Z.Z.) would like to acknowledge the financial support by the Austrian Academy of Sciences via the 'Innovation funds'.

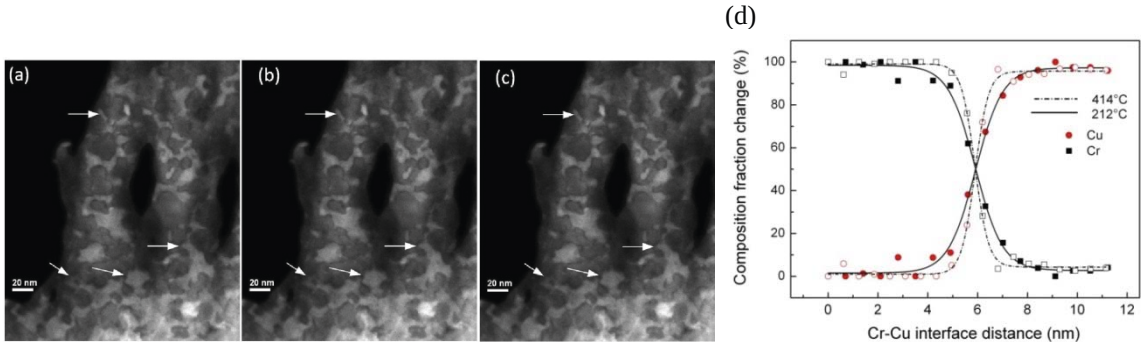

Figure1. (a) (b) and (c): HAADF STEM image demonstrating the nanocrystalline structural evolution process; (a) 25°C, (b) 212°C, (c) 414 °C. Particular locations labeled by arrows. (d) Elemental profile crossing one typical Cr-Cu interface.

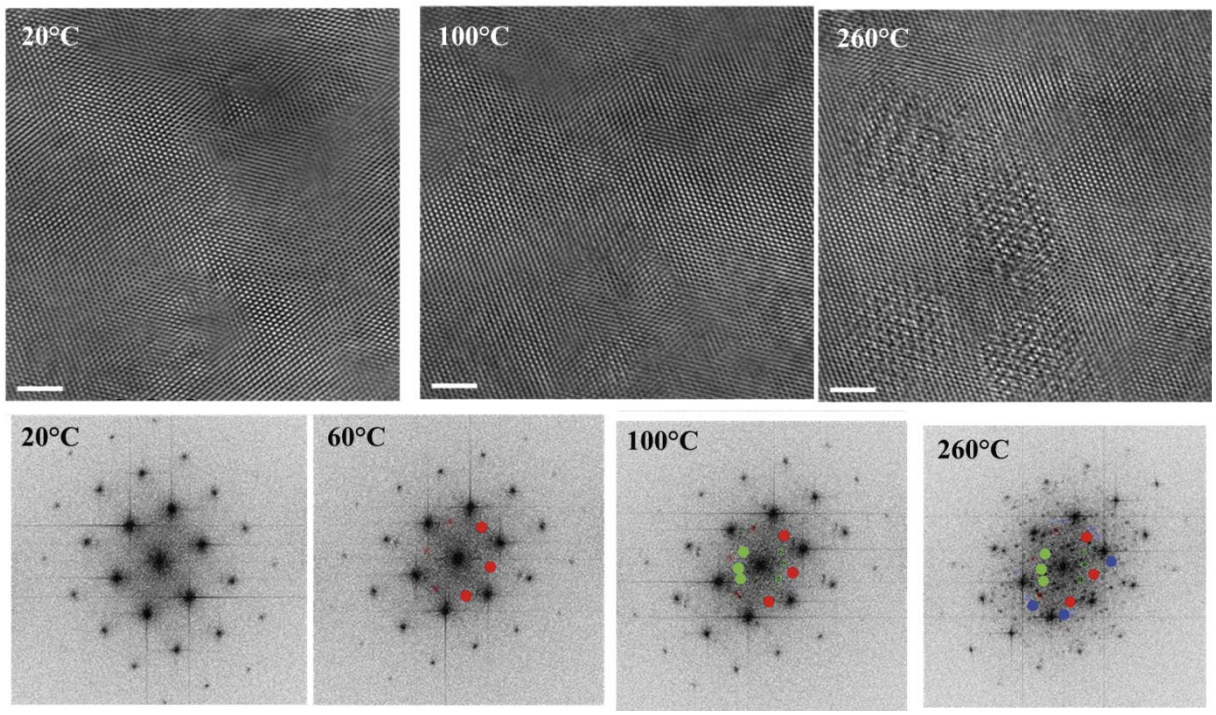

Figure2. Upper**:** *In-situ* HRTEM observations on the oxidation and decomposition of Cu-Fe supersaturated solid solution after severe deformation. Heating from 20°C, 100°C to 260°C, the oxidation starts at 60°C while the decomposition occurs at 260°C. The scale bar is 2 nm. Lower: FFT from 20°C, 60°C, 100°C to 260°C. The red, green and blue spots in FFTs correspond to Cu oxide, Fe oxides and pure Fe, respectively.

In situ TEM of electron beam induced nanocrystallization of WC and W

STEFAN NOISTERNIG, URSULA LUDACKA, CHRISTIAN RENTENBERGER AND H. PETER KARNTHALER

University of Vienna, Faculty of Physics, Physics of Nanostructured Materials, Vienna, Austria

Nanocrystals of WC are receiving scientific attention since they are considered for potential applications as supporting material for platinum catalysts. Usually WC is prepared by solid state reaction of W with graphitic C at temperatures above 1000 °C or by gas solid reactions.

In this study we co-evaporate W and C on a thin film of amorphous C or SiN (about 2 or 5 nm thick, respectively). Electron beam physical vapor deposition was used to make an amorphous layer of W and C with a thickness of about 6 nm. For the electron irradiation, in situ observation and structural characterization two instruments were used: a dedicated STEM (probe corrected) and a (S)TEM (image corrected) operating in TEM or STEM mode.

The intermixing of W and C in the deposited amorphous layer was confirmed by EDX analysis and its amorphous structure by FFT of high resolution transmission electron microscope images (HRTEM) and diffraction patterns. A limited specimen area (between 25 and 2500 nm²) was exposed to an intense electron irradiation using different electron dose rates (between $10^5$and 10^7electrons per nm² and second). The crystallization of the irradiated area starts after a few minutes and is completed after 5 to 20 minutes depending on the dose rate (cf. the HRTEM image in fig.1). For the structural analysis of the WC crystals in addition the method of high angle annular dark field (HAADF) imaging was used revealing the presence of different WC phases with $WC_{0.82}$ and W_2C dominating (cf. fig.2). A conformation of the WC phases was confirmed by matching the HAADF images with simulated images.

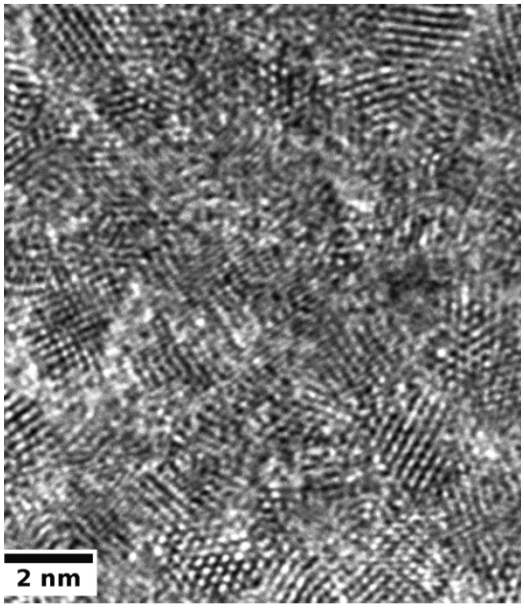

Figure 1. HRTEM image of nanocrystalline WC that was achieved by intense in situ electron irradiation of an amorphous layer (about 6 nm thick) of intermixed W and C.

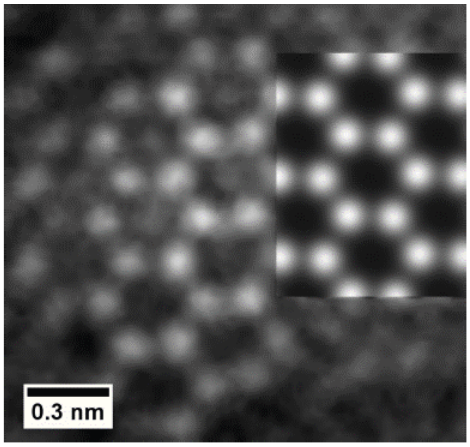

Figure 2. Structural analysis of the WC nanocrystals (cf. fig.1) by HAADF images. The inset shows an image simulation indicating that the structure is W_2C.

When the intense irradiation of the nanocrystals is continued it is quite remarkable that we observed a second phase transformation: As confirmed by in situ observations, WC nanocrystals convert to pure W also being nanocrystalline (cf. fig.3).

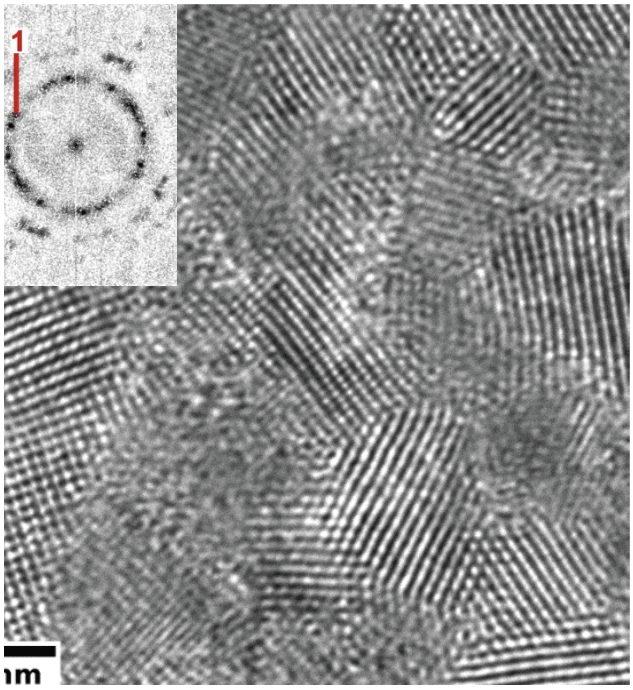

Figure 3. HRTEM image of metallic W nanocrystals. The second phase transformation from WC to pure W was again carried out in situ with intense electron irradiation. This transition is rather suprizing, since the binding energy of WC is quite high (about 10 eV). The FFT (cf. inset) shows the rings of bcc W; they are labeled 1, 2, 3 and 4 corresponding to the planes (110), (200), (211) and (220), respectively.

When explaining our findings one has to consider that the binding energy of WC is quite high (about 10 eV) [1]. This makes the probability of direct radiation displacement at 60 kV rather low. To investi-gate the influence of chemical etching we carried out in situ experiments at different pressures (at 10^{-10} and 10^{-7} mbar, respectively) by leaking in oxygen. It was found that the influence of the different pressures on phase transformations of the WC layer is but little. This is quite in contrast to our findings using a foil of pure amorphous carbon and applying the same pressures; in this case chemical etching is increased at the higher oxygen pressure. Therefore, it seems that other surface effects could be the cause for the observed phase transformation from nanocrystalline WC to pure W [2].

Acknowledgements
S. N. would like to thank Dr. C. Mangler for help with the STEM images taken on the Nion UltraStem. We would like to thank Prof. Jani Kotakoski for providing lab equipment. Financial support by the Austrian Science Fund (FWF): I1309 is acknowledged.

References
[1] V. G. Zavodinsky, Nanotechnologies in Russia, 5 (2010) 839 Energy, 2 (2012) 523
[2] R. F. Egerton, F. Wang and P. A. Crozier, Microscopy and Microanalysis, 12 (2006) 65

Nanopatterning silver: targeted oxidation with an electron beam

HUAPING SHENG[1,2,3], HE ZHENG[2], SHUANGFENG JIA[2], MARIA K. Y. CHAN[3], TIJANA RAJH[3], JIANBO WANG[2], JIANGUO WEN[3], JÜRGEN ECKERT[1,4] AND CHRISTOPH GAMMER[1].

[1] Erich Schmid Institute of Materials Science, Austrian Academy of Sciences, Leoben, Austria; [2] School of Physics and Technology, Center for Electron Microscopy, MOE Key Laboratory of Artificial Micro- and Nano-structures, and Institute for Advanced Studies, Wuhan University, China; [3] Center for Nanoscale Materials, Argonne National Laboratory, Argonne, USA; [4] Department of Material Science, Montanuniversität Leoben, Leoben, Austria

Nanostructure fabrication allowing precise control over dimension and location is of fundamental interest because of its potential utilization as a next-generation manufacture method for functional devices, such as quantum devices, light emitting devices, and nano-sensors. In general, possible nano-fabrication techniques can be classified into two categories: “top-down” approaches using nanolithography and etching techniques, and “bottom-up” approaches using chemical synthesis, self-assembly or targeted nano-deposition. However, neither of those techniques can fully control chemical reactions at the nanometer scale: “top-down” approaches provide good control over the location but do not allow for chemical reactions; “bottom-up” approaches can realize either chemical reactions or location precision, but not both simultaneously. Therefore, it is of great importance to develop an approach for the direct control of chemical reactions at nanoscale.

Ag has been proved subject to oxidation very easily when exposed to atomic O, while remaining stable in molecular O. A recent study by Sun *et al.* shows that the oxidation of Ag can be induced by ionizing O_2 using electron beam irradiation in an environmental gas cell, and elemental Ag will nucleate under intense electron-beam irradiation above a limit [1]. However, the precise control of the location and dimension is yet to be achieved for the oxidation reaction, which greatly limits the practical significance of this technique.

Inspired by the electron-beam-induced deposition (EBID), a “bottom-up” technique using a focused beam to decompose (metal-)organic gases, we combined the electron beam irradiation with chemical reactions to develop a new nanofabrication approach. Using this approach, we successfully fabricated patterned metal-oxide heterostructures on a Ag substrate [2].

In this abstract, we report recent progress in the nano-patterning of Ag_2O crystals in a Ag matrix. Through electron beam irradiation, Ag_2O crystals nucleate and grow from metallic Ag (Figure 1a). By making the electron-beam into a spindle shape and irradiating the Ag substrate for 40 minutes (Figure 1b), nanoscale Ag_2O phase was fabricated within the irradiated area showing exactly the same shape and size as the electron-beam (Figure 1c-d). X-ray energy dispersive spectroscopic (EDS) mapping results indicate the accumulation of additional Ag and O compared to the un-irradiated region (Figure 1e-f), which proves the surface diffusion of Ag atoms from adjacent areas and the occurrence of oxidation reactions. Taking another step further, DigitalMicrograph scripting was used for the precise control of a focused electron beam, thus enabling to irradiate several spots for a constant amount of time (Figure 1g). Figure 1h-j shows one of our preliminary results, where three spots have been irradiated. It can be seen that two Ag_2O nanodots with sizes down to 3 nm were fabricated in the Ag matrix, together with a hole. Therefore, the technique has the potential for controllable formation of arbitrary arrays of nanodots or nanorods.

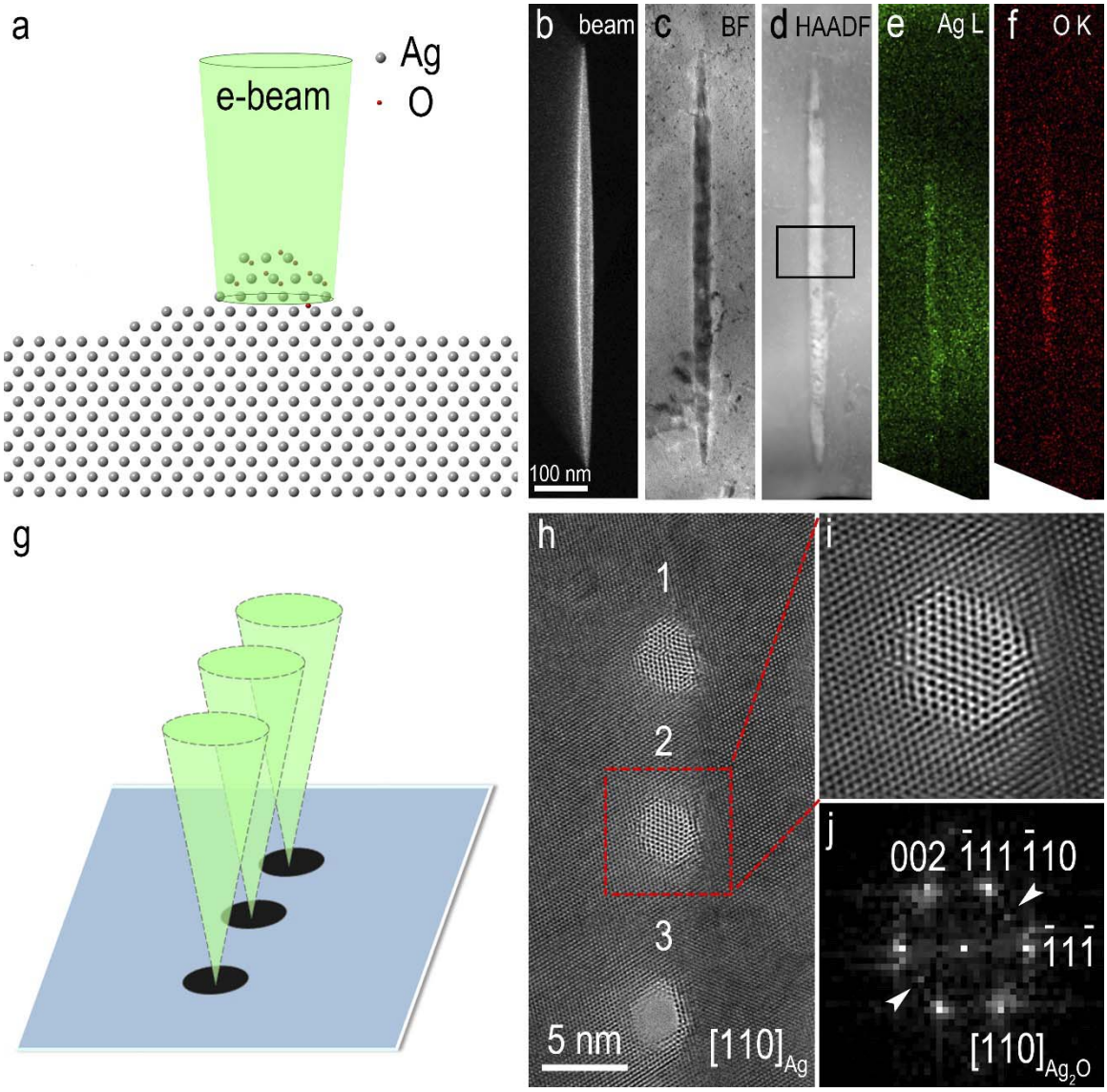

Figure 1. (a) Schematic illustration of the patterning experiments in Ag. (b-j) Preliminary results demonstrating the controlled formation of nanostructures.

References

[1] L. Sun, K. W. Noh, J.-G. Wen, S. J. Dillon, Langmuir, 27(2011) 14201–14206
[2] H. Sheng, H. Zheng, S. Jia, M. K. Y. Chan, T. Rajh, J. Wang, J. Wen, Nanoscale, 11(2019) 10756-10762

Micron-scale characterization of twinning and dislocation slip in magnesium single-crystals by advanced SEM in-situ techniques

KRISTIÁN MÁTHIS[1], PETR HARCUBA[1], DÁVID UGI[2], MICHAL KNAPEK[1], FRANTIŠEK CHMELÍK[1], PÉTER ISPÁNOVITY[2], ISTVÁN GROMA[2]

[1] Charles university, Prague, Czech Republic; [2] Eötvös Loránd University, Budapest, Hungary

A rare blend of combination of in-situ scanning electron microcopy (SEM) during deformation with simultaneous acoustic emission (AE) technique has been employed for study the deformation behavior of Mg micropillars. Unique in-situ micro-indentor which holds the sensitive accustic emmision sensor was developed. The combination of these two techniques enables to study the underlying physical processes with exceptional spatiotemporal resolution. It is shown that the stress drops on the deformation curves caused by size-effect are in perfect correlation with the acoustic emission events. AE and subsequent EBSD analysis alow us to distinguished between twinning and dislocation slip. The internal dynamics of the twinning and dislocation slip is discussed in detail using statistical analysis of the data.

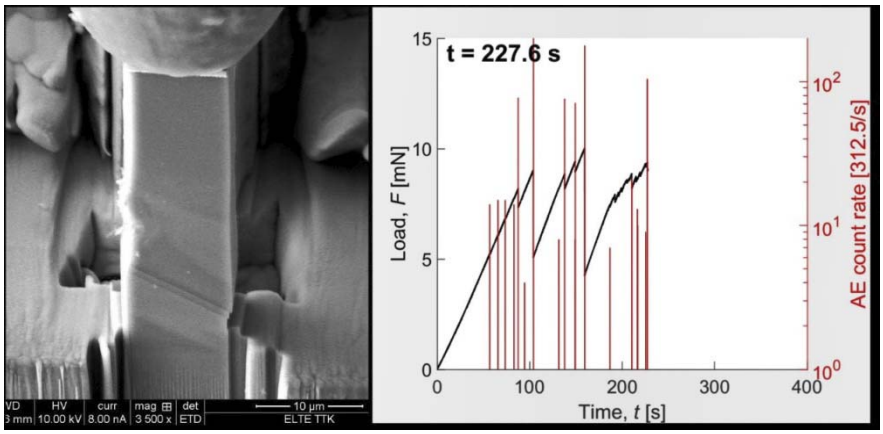

Figure 1. The style to be used for graphs.

Temperature-induced cationic diffusion to regulate the phase transition in VO_2 film

YONGHUI ZHENG[1], ZHUO CHEN[1], QINQIN SHAO[1], YAN CHENG[2], YUNBIN HE[3], AND ZAOLI ZHANG[1]

[1] Erich Schmid Institute of Materials Science, Austrian Academy of Science, Leoben, Austria; [2] Key Laboratory of Polar Materials and Devices (MOE), Department of Optoelectronics, East China Normal University, Shanghai, China; [3] Hubei Key Lab of Ferro & Piezoelectric Materials and Devices, School of Materials Science and Engineering, Hubei University, Wuhan. China

As a prototype correlated electron material (CEM), vanadium oxide (VO_2) is a fascinating functional potential candidate for strain-dominant, optical, electrical and multi-responsive sensor applications. This is mainly ascribed to its distinct reversible structural phase transition (SPT) between monoclinic (M, $P2_1/c$) and tetragonal phase (rutile structure, R, P4/mnm) around room temperature (343 K), accompanied with a metal-insulator transition (MIT)[1]. Generally, to fulfill specific smart devices, transition parameters of VO_2 material, e.g., transition temperature (T_c), hysteresis loop width (ΔT) need to be adjusted. Researchers have proposed several strategies to regulate the transition property of VO_2, such as elemental doping, stoichiometry engineering, strain field, and domain engineering. In addition to the above methods, it's found that there is a bit diffusion phenomenon between VO_2 film and TiO_2 substrate around several nanometers, and post thermal annealing in the solid solution (SS) of $V_{1-x}Ti_xO_2$ could drive a significantly cationic diffusion, resulting in spinodal decomposition (SD) alloy with recovery of MIT property[2,3]. Therefore, cationic diffusion under thermal annealing seems to be an alternative choice to modify the transition behavior of VO_2.

In this report, we found that cationic Ti diffusion induced by thermal annealing from the TiO_2 substrate could effectively regulate the T_c of VO_2 (~10K decreased) as shown in Figure 1. Dark-field (DF) transmission electron microscopy (TEM) images confirm confined M domains in the film after annealing via *in-situ* TEM, resulting in a higher domain boundary density. By using energy dispersive X-ray spectroscopy (EDS) technique, it reveals that the sharp Ti/V distribution plane on the interface of VO_2 film and TiO_2 substrate has disappeared after thermal annealing, and a high percentage of Ti atoms from TiO_2 substrate could diffuse into VO_2 film, which is characterized of a gradually decreasing Ti concentration gradient from substrate to the surface (around 100 nm) as shown in Figure 2. Advanced atomic EDS mapping results confirm that these diffusion Ti atoms still occupy the cationic site of VO_2. Furtherly, scanning transmission electron microscopy high-angle annular dark-field (STEM-HAADF) image was utilized to investigate the possible Ti migration pathway. Due to the strain stress[4] caused by the huge non-uniform Ti distribution inside the film, not only the formation of smaller M domains can be observed, but also the stacking fault lines (length can reach to 50 nm) along the low surface energy lattice plane will appear. Specifically, cationic atoms would occupy the interstitial sites of the VO_2 phase in these areas, and bond with the nearest oxygen atoms to form VO_6 octahedron, suggesting that the interstitial sites could act as the intermediate site during the cationic migration process [5].

Reference

[1] D. Lee, B. Chung, Y. Shi *et al.* Isostructural metal-insulator transition in VO_2. ***Science*** 362 (2018) 1037-1040.

[2] H. Paik, J. A. Moyer, T. Spila *et al.* Transport properties of ultra-thin VO_2 films on (001) TiO_2 grown by reactive molecular-beam epitaxy. ***Appl. Phys. Lett.*** 107 (2015) 163101.

[3] Z. Hiror, H. Hayamizu, T. Yoshida *et al.* Spinodal decomposition in the TiO_2–VO_2 system. ***Chem. Mater.*** 25 (2013) 2202-2210.

[4] Z. Yu, D. A. Muller and J. Silcox. Study of strain fields at a-Si/c-Si interface. ***J. Appl. Phys.*** 95 (2004) 3362.

[5] The authors (Y.Z. and Z.Z.) would like to acknowledge the financial support by the Austrian Academy of Sciences via the 'Innovation funds'.

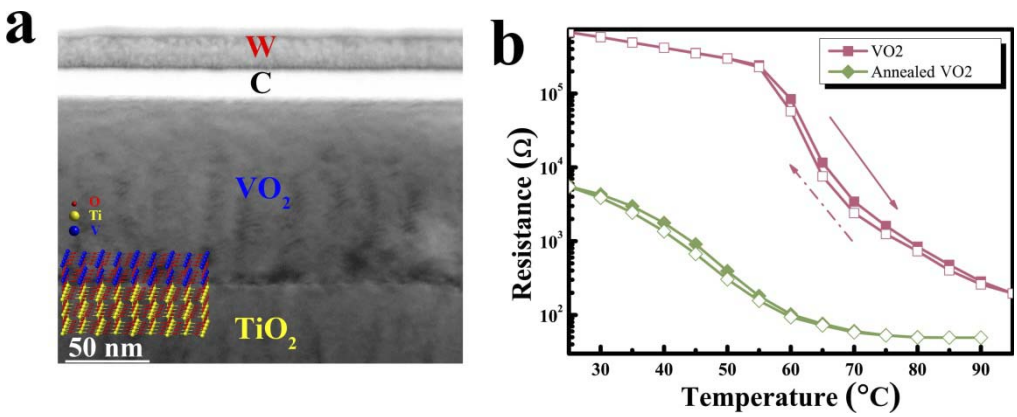

Figure 1 Thermal annealing regulates the structure transition behavior of VO_2. **a** cross-section bright field (BF) image, and the atomic model shows the orientation relationship between VO_2 film and the TiO_2 substrate. **b** sheet resistance versus temperature curves for VO_2 and annealed VO_2.

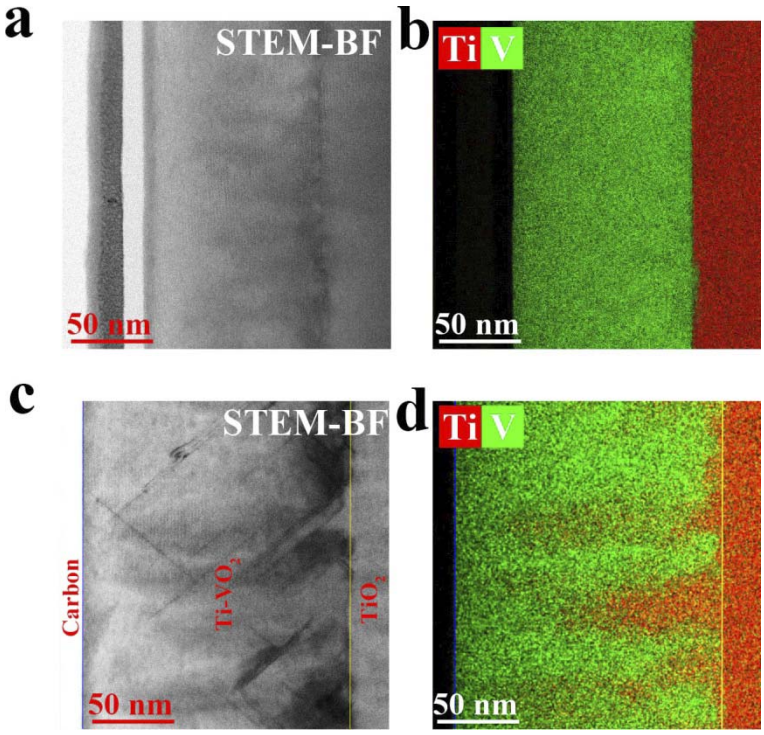

Figure 2 Nanostructure and nanoscale elemental distribution before and after thermal annealing. **a, b** STEM-BF image of VO_2 and the corresponding Ti/V elemental distribution in the VO_2 film and TiO_2 substrate. **c, d** STEM-BF image of annealed VO_2 and the corresponding Ti/V elemental distribution in the VO_2 film and TiO_2 substrate.

Thermosalient behavior in organic alloy of 1,2,4,5-tetrabromobenzene and 1,2,4,5-tetrachlorobenzene.

TEODORO KLASER[1], ŽELJKO SKOKO[1]
[1] Department of Physics, Faculty of Science, University of Zagreb, Croatia

Thermosalient materials are the ones that during heating/cooling undergo an energetic phase transition which is so sudden and abrupt that the crystals are ballistically projected to heights of several hundred times larger than their own dimensions. Apart from providing visually extremely attractive phenomenon, these materials have a tremendous technological potential as the future self-actuation device (nanoswitches, thermal sensors, artificial muscles, etc.)[1].
The majority of thermosalient crystals are organic compounds and several cases have been studied in great detail. Crystals of 1,2,4,5-tetrabromobenzene jump several centimeters during the phase transition from the low-temperature β-form to the high-temperature γ-form [2]. Hopping of the crystals happens at 45.0 °C for single crystals and at 45.5 °C for twinned crystals. Layered structures are characteristic for both forms, and the thermosalient effect is swayed by intermolecular Br···Br and C–H···Br interactions. During the phase transition there is a slight change in the dihedral angle between the neighboring rings which rotates the molecules, flattens the molecular stacks and generates strain in the crystal lattice, in turn causing the crystals to leap when the strain is released.
Here we present a systematic experimental study of the thermosalient effect in in 1,2,4,5-tetrabromobenzene and 1,2,4,5-tetrachlorobenzene organic alloys with in-situ hot stage microscopy, which enable us to study the effect on the thermosalient phenomenon of the variation of concentration of two compounds. Equilibrium relations in the system 1,2,4,5-tetrabromobenzene and 1,2,4,5-tetraclorobenzene have been studied from 93 to 460 K by D. Mondieig, et al. which have found seven two-phase regions and four single-phase fields corresponding to mixed crystalline solids [3].
Samples were prepared by crystallization from a solution of the two substances dissolved in ether, after which the solvent was evaporated under controlled conditions. We have synthetized crystals with different concentrations of 1,2,4,5-tetrabromobenzene and 1,2,4,5-tetraclorobenzene, ranging from 30% to 100% in molar mass of 1,2,4,5-tetrabromobenzene. Samples where then studied with hot stage microscope to characterize the thermosalinet behavior of this two mixed crystals. Resulting analysis shows that is present a threshold concentration for the activation of the jumping of crystals and also results a dependency of the temperature, at which phase transition occurs, from the concentration of the mixture.

References

[1] Skoko, Ž.; Zamir, S.; Naumov, P.; Bernstein, J. The Thermosalient Phenomenon. “jumping Crystals” and Crystal Chemistry of the Anticholinergic Agent Oxitropium Bromide. J. Am. Chem. Soc. 2010, 132 (40), 14191–14202.
[2] H. F. Lieberman; R. J. Davey, * and; Newsham, D. M. T. Br···Br and Br···H Interactions in Action: Polymorphism, Hopping, and Twinning in 1,2,4,5-Tetrabromobenzene. 2000.
[3] Mondieig, D., et al. "The system 1, 2, 4, 5-tetrachlorobenzene+ 1, 2, 4, 5-tetrabromobenzene. part l. Experimental phase diagram (93-460 K)." Thermochimica acta 177 (1991): 169-186.

In situ observation of precipitate growth and decomposition in $AlCu_4$ during heat treatment via analytical STEM

EVELIN FISSLTHALER[1], ROBERT KRISPER[1] AND WERNER GROGGER[2]

[1] Graz Centre for Electron Microscopy, Steyrergasse 17, 8010 Graz, Austria; [2] Institute of Electron Microscopy and Nanoanalysis, Graz University of Technology, Graz, Austria

Light alloys based on aluminum are used in a wide range of industries, from aerospace, building and construction to transportation systems. Their distinguishing quality is the combination of low weight, corrosion resistance and their property to alter hardness through temperature treatment.

An alloy formed from aluminum and copper can be strenghtend by age- or precipitation hardening. A widely used example is the Duralumin or 2000 series, which contains about 4% of copper in combination with additional dopants like manganese, silicon or magnesium. By a careful series of temperature treatments, the properties of such an alloy can be adjusted by the deliberate formation of a certain type of precipitate. [1]

Due to the importance of the exact nature of the dominant type of preciptiate, the comprehension of the processes occurring in these materials under temperature stress is of interest for the advancement and optimization of light alloys and the products formed from them. Initiation and progress of phase separation during the early stages of solid solution decomposition are still important questions in metallurgy. [2]

In order to describe transformations like these in detail, in situ transmission electron microscopy has become a widely used tool for the investigation of dynamic processes occuring on the micro- and nanoscale. Especially when combined with analytical methods like EDS or EELS, novel insights into precipitation can be gained by thorough interpretation of the observed events in the sample.

The material discussed in this study is an alloy formed from aluminum and 4% copper, with a small amount of Si and Mn. FIB lamellae were extracted from alloys with two distinct pre-treatments during fabrication and mounted on MEMS chips for a DENSsolutions Wildfire heating system. During the investigation in the TEM these samples were subjected to temperatures ranging from room temperature to 300°C. The system used for the experiments was a probe corrected FEI Titan³ G2 60-300 featuring a SuperX EDS system. Since the monitored processes are at least partially reversible, all investigations during the heating experiment have to be performed at the indicated temperature to ensure that no additional transformations occur during temperature fluctuations. As presented recently, EDS measurements with a SuperX can be performed at these temperatures with a Wildfire system without corrupting the EDS results. [3]

Figure 1 shows an overview tableau of HAADF images of a lamella from the AlCu4 F alloy at different temperatures: during the first heating steps, the Al_2Cu precipitates visibly grow (blue arrows), gathering the necessary Cu by diffusion from the matrix material. At 275°C they start to dissolve, as seen by the retreat of the grain boundary and by a total decomposition of parts or even whole precipitates. In parallel, a single Mn-rich grain starts to form from the matrix. The temperature ramp was stopped at 300°C due to the gradual decay of the bulk material of the lamella. During the subsequent cool down to 200°C, a slight growth can be seen in the large preciptiate at the left side (green arrows). The overall duration of the heating experiment was 390 min.

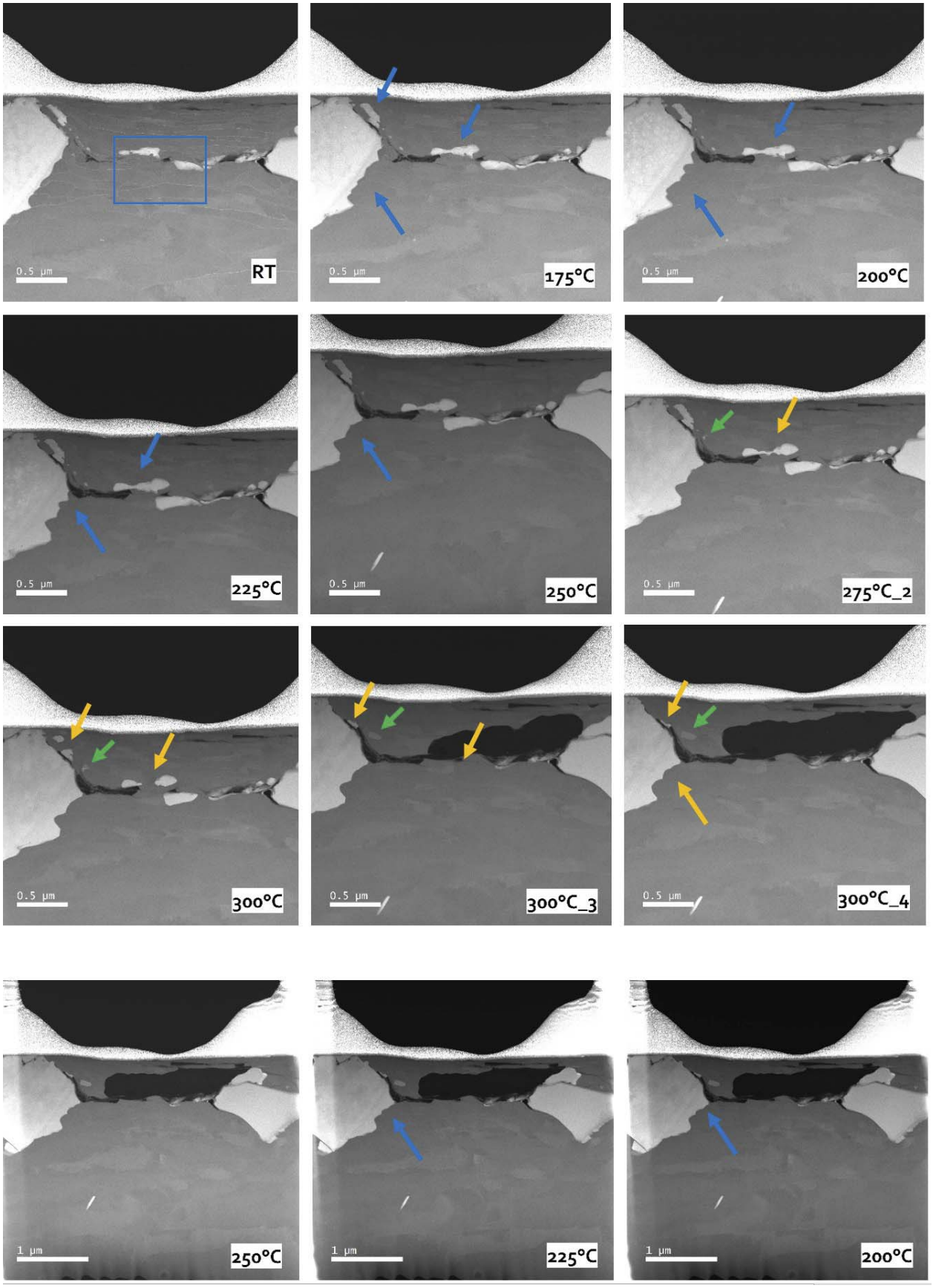

Figure 1. HAAFD images illustrating growth and decomposition of Al_2Cu precipitates in an AlCu4 alloy (Al with 4% Cu) during temperature treatment from room temperature up to 300°C, and from 300°C down to 200°C

Figure 2 presents a more detailed view of the two precipitates in the central area (indicated by the blue box): Precipitates grow and reshape during the first steps of the heating process; the obvious conversion from an agglomeration of smaller grains to a larger and more rounded shape is presumably driven by Ostwald ripening. [4] At 275°C, the precipitates start to dissolve in the surrounding matrix.

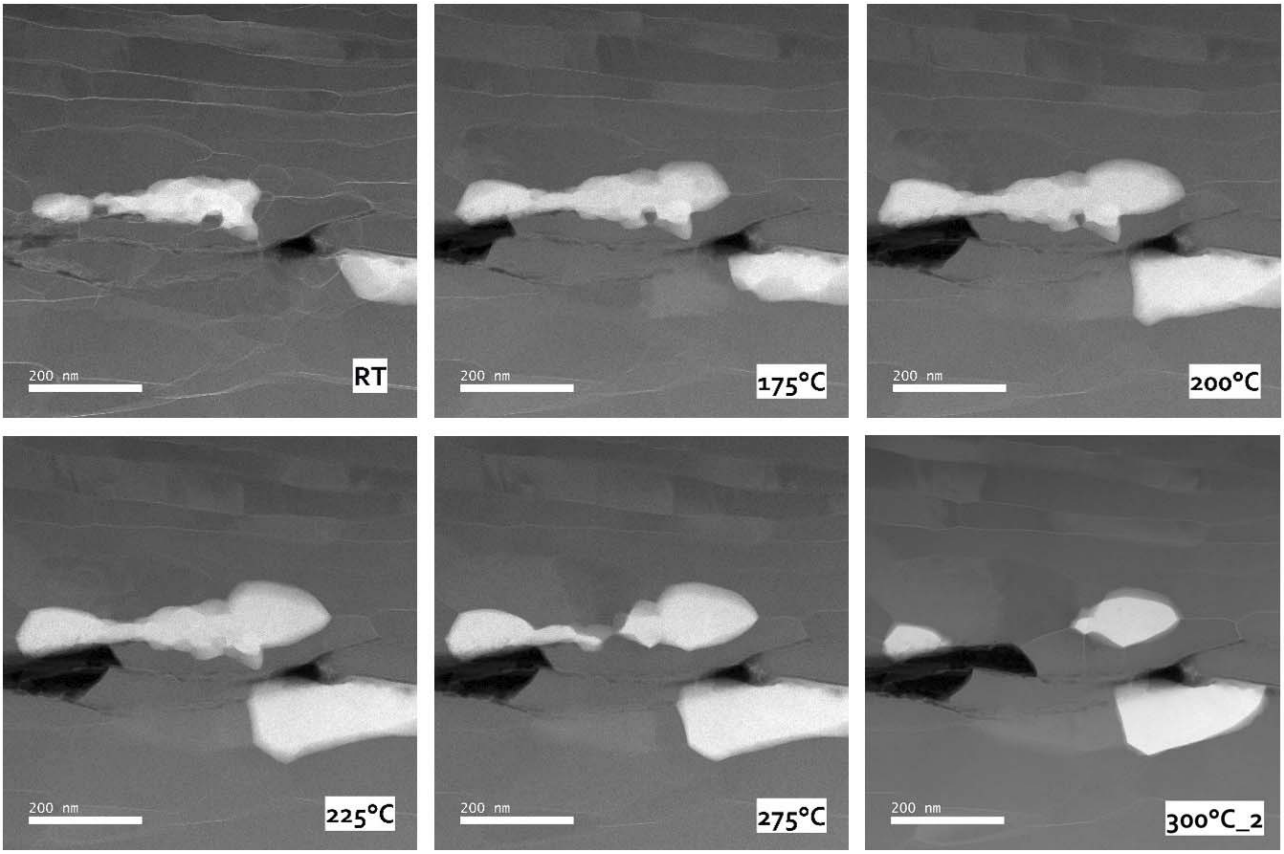

Figure 2. Growth and decomposition of the two precipitates shown in the center of the HAADF images in Figure 1

The "F" state of this type of alloy denotes the "as fabricated condition". This indicates that the material was cooled down slowly during fabrication, predominatly triggering the formation of Al_2Cu precipitates (θ-phase) distributed in the α-Al phase. Since different heat treatments during the fabrication process can lead to various other precipitate types, comparative TEM in situ study with several differently hardened AlCu alloys can provide novel insight into this widely used class of materials.

References

[1] M. F. Ashby, D. R. H. Jones, Engineering Materials, Volume 2, 2nd Edition (1998) 100-112

[2] M. Karlík, A. Bigot, B. Jouffrey, P. Auger, S. Belliot, Ultramicroscopy 98 (2004) 219-230

[3] R. Krisper, ICM19 (2018), publication in preparation

[4] I.M. Lifschitz, V.V. Slyozov, J. Phys. Chem. Solids, 19 (1/2) (1961), 35-50

IT6

Advances in instrumentation and techniques (SEM, TEM, SPM, etc.)

CHAIRPERSONS:

Daniel Kiener, Vladislav Krzyzanek

INVITED LECTURE

Nanoscale strain mapping in metallic glasses during *in situ* deformation

CHRISTOPH GAMMER[1], THOMAS C. PEKIN[2,3], COLIN OPHUS[2], ANDREW M. MINOR[2,3], JÜRGEN ECKERT[1,4]

[1]Erich Schmid Institute of Materials Science, Austrian Academy of Sciences, Leoben, Austria; [2] National Center for Electron Microscopy, Molecular Foundry, Lawrence Berkeley National Laboratory, Berkeley, USA; [3] Department of Materials Science and Engineering, University of California, Berkeley, USA; [4] Department of Materials Science, Montanuniversität Leoben, Austria

Metallic glasses (MGs) are an exciting new class of materials due to their unique mechanical properties, such as high strength and good wear resistance [1]. However, potential applications are hindered by their low ductility caused by the formation of shear bands causing catastrophic failure. While progress in the understanding of deformation localization was made using colloidal solids or molecular dynamics simulations [2], an experimental understanding of the fundamental deformation mechanisms in glasses is still lacking due to their disordered nature inhibiting direct imaging. Therefore, to study the deformation of metallic glasses at the nanoscale, *in situ* deformation is carried out inside a transmission electron microscope (TEM) using a Hysitron PI-95 Picoindenter. Samples for *in situ* deformation are made from bulk CuZr-based MG rods produced by suction-casting using focused ion beam machining.

Figure 1 shows the result from an *in situ* tensile test acquired in TEM bright-field mode. The sample is 200 nm thick. The corresponding load displacement curve shows elastic deformation followed by abrupt fracture with no indication of tensile plasticity. To obtain further information on the deformation behavior of the MG sample, we use scanning nanobeam electron diffraction to measure the local elastic strain during *in situ* deformation with nanometer resolution [3,4]. Figure 2 (left) shows the experimental procedure. An electron beam scans over the sample and for every probe position a full diffraction pattern is recorded using a fast electron detector. By fitting an ellipse to the first order diffraction ring a strain map can be determined. Figure 2 (right) shows the resulting strain maps obtained during continous loading. The strain in tensile direction and normal to it and the shear strain (ε_{xx}, ε_{xx}, ε_{xy}) are shown. During loading the strain in tensile direction as well as the compressive strain normal to it increase, while the shear strain reamains close to zero. In addition, the strain maps reveal significant inhomogeneities, showing the importance of measuring the local transient strain field [3].

In conclusion, we show an experimental setup capable of recording time-resolved strain maps with a spatial resolution down to 1 nm. The experimental measurement of local quantitative strain enables greater insight into the deformation processes in MGs on the nanoscale and yields the potential for direct comparison with atomistic simulations on similar size scales.

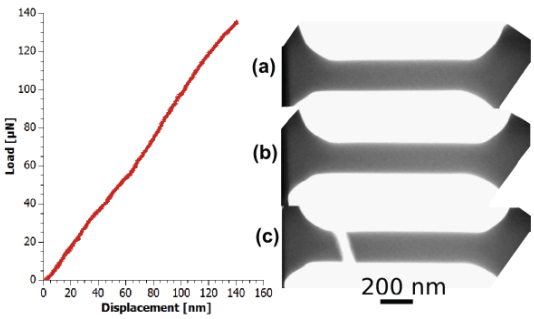

Figure 1. The stress-strain curve recorded during *in situ* TEM deformation of a metallic glass shows linear elastic elongation of the tensile specimen followed by fracture. Two frames corresponding to the initial state and the elongated state are shown in (a) and (b). After elongation the sample frac-tures abruptly and shows no ductility (c).

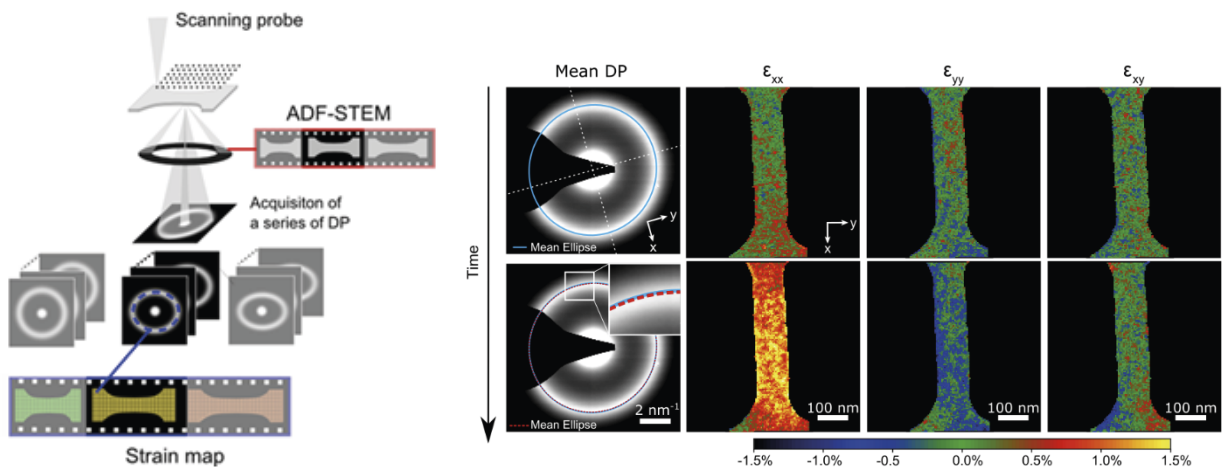

Figure 2. Experimental setup (left): A dog-bone shaped metallic glass sample is deformed *in situ* in the scanning transmission electron microscope (STEM) using a slightly converged electron beam. During scanning, a full diffraction pattern (DP), showing a characteristic amorphous ring, is acquired at every probe position. A best fit ellipse is computed for every DP and used to determine the local strain.
Result from the nanodiffraction maps recorded during *in situ* deformation (right): For visualization of the elliptic distortions, the mean DP is shown along with the best fit ellipse. The small distortion caused by the tensile strain can be seen when comparing the elipse detemined for the unstrained and strained cases. Full strain maps are computed by fitting the elliptic distortion for each individual DP and converting it to a strain tensor.

References

[1] M.F. Ashby, A.L. Greer, Scripta Mater. 54 (2006) 321.
[2] E.D. Cubuk et al., Science 358 (2017) 1033.
[3] C. Gammer, C. Ophus, T.C. Pekin, J. Eckert, A.M. Minor, Appl. Phys. Lett. 112 (2018) 171905.
[4] T.C. Pekin, J. Ding, C. Gammer, B. Ozdol, C. Ophus, M. Asta, R.O. Ritchie, A.M. Minor, Nature Comm.s 10 (2019) 2445.
[5] The authors acknowledge support of the European Research Council under the ERC Advanced Grant INTELHYB (grant ERC-2013-ADG-340025). Work at the Molecular Foundry was supported by the Office of Science, Office of Basic Energy Sciences of the U.S. Department of Energy under Contract No. DE-AC02-05CH11231

INVITED LECTURE

Advanced techniques for low- and very-low energy SEM using reflected and transmitted signals

ILONA MÜLLEROVÁ, BENJAMIN DANIEL, IVO KONVALINA, LUDĚK FRANK AND ELIŠKA MATERNA MIKMEKOVÁ

Institute of Scientific Instruments CAS, Brno, Czech Republic

There is a need for new diagnostic techniques to be developed for the study of new materials. The scanning low-energy electron microscope (SLEEM) equipped with a cathode lens in a specimen region [1] offers an innovative tool that enables samples at nanometre lateral resolution in both reflected (RE) and transmitted electrons (TE) to be seen. This diagnostics can be helpful for the study of freestanding graphene samples as well as other 2D materials. Interest in thin- and most notably 2D-materials is due to their unique physical properties that manifest when heat transport and charge is confined to a plane. Furthermore, layered 2D materials exhibit a combination of excellent electronic, mechanical, optical and thermal properties, which may substitute the commonly used materials in electronics, photonics, catalysis, biosensors, etc. and offer many innovative applications. 2D materials appear the most suitable candidates for the creation of a new generation of electronic devices, many examples of which have already been practically realized.

Figure 1 shows micrographs of commercial graphene (http://www.tedpella.com) prepared on a copper film using CVD technology, released and deposited on lacey carbon with eyes from the hundreds of nm up to a maximum of 2 µm in size, lying on a 300 mesh copper grid. A sample declared as 1LG, 2LG, and 3–5LG was used for the imaging in reflected as well as transmitted electron modes, at several primary beam energies of electrons. The RE signal was composed of both secondary and backscattered electron emission, accelerated in the cathode lens field toward the detector. In the RE frames, the maximum contrast between graphene layers and lacey carbon appears at 1 keV and decreases toward higher and lower energies due to extending and shortening information depth, respectively. While these images identify empty holes, they do not reveal thicker islands of graphene. In the TE mode, multilayer graphene islands are not visible above 100 eV. This fact underlines the suitability of very-low energy electron microscopy for the examination of 2D crystals. Challenges with regards to interpretation are presented by some details that invert their contrast more than once, see the arrow in the figure below. These probably arise from contaminations that become charged. The typically used counting of graphene layers with Raman spectroscopy confronts the issue of light optical imaging's low lateral resolution of. As SLEEM provides a much higher resolution, it is worth checking its selectivity for the same purpose.

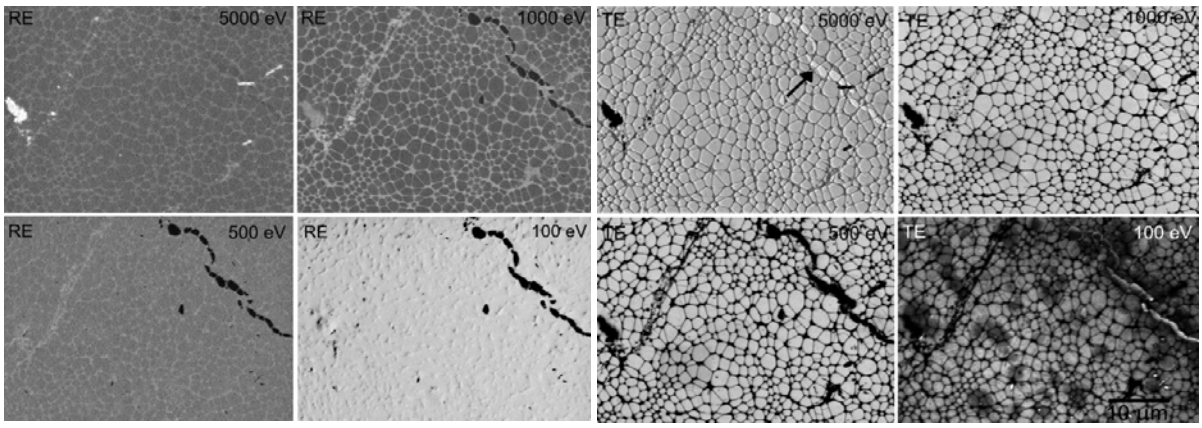

Figure 1. Freestanding graphene sample of 3 to 5 layers imaged in reflected and transmitted electrons at various low-energy landing electrons imaged in the SEM Magellan 400.

A Magellan 400 scanning electron microscope with standard vacuum condition ($5x10^{-4}$ Pa) in the specimen region was used for the contrast observation of individual atomic layers. A special procedure was developed to clean the specimen. The equilibrium between desorption and absorption on the specimen surface was ascertained before the imaging [3].

Two ultrahigh vacuum ($1x10^{-8}$ Pa) experimental set ups of SLEEM with a field emission gun are also used for the experiments, see Figure 2.

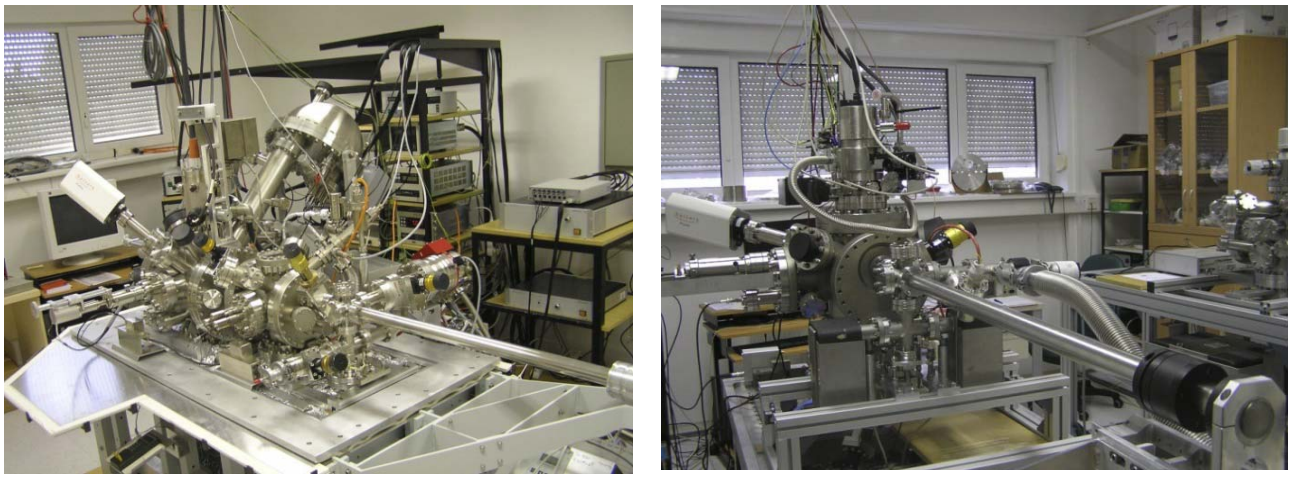

Figure 2. Experimental ultrahigh SLEEM vacuum (left) and SLEEM equipped with time-of- flight spectrometer (right).

The ultrahigh SLEEM vacuum is equipped with a detector for reflected, transmitted and Auger electrons. The ion cleaning and heating of the specimen are also available. The SLEEM with time-of- flight (TOF) spectrometer operating at energies below 100 eV was designed [4] to understand contrast formations at very low energies. The inelastic mean free path can be calculated from the measured transmitted signal to evaluate the thickness of very thin films of modern structures.

We found that the transmissivity of graphene layers for very slow electrons decreases, although an increase would be expected with respect to the IMFP “universal curve” [5]. Similarly, the IMFPs of Fe film on W (110) are much smaller in this energy range [6]. It can be assumed that the IMFP depends much less on energy than given by the “universal curve” and theoretical calculations. [7].

References

[1] I. Müllerová and L Frank, Advances in Imaging and Electron Physics **128** (2003) 309-443
[2] M. P. Seah and W. A. Dench, Surf. Interface Anal. **1** (1979) 0142-2421
[3] E. Materna Mikmeková et al, Journal of Electron Spectroscopy and Related Phenomena (2019) https://doi.org/10.1016/j.elspec.2019.06.005
[4] B. Daniel et al, In Sources, Interaction with Matter, Detection and Analysis of Low Energy Electrons (SIMDALEE2017). Book of Abstracts Wien: Technische Universität Wien (2017) 70
[5] L. Frank et al., Appl. Phys. Lett. **106** (2015) 013117
[6] R. Zdyb et al., Phys. Rev. B **87** (2013) 075436
[7] The authors acknowledge funding from the Technology Agency of the Czech Republic to the project: Centre of Competence - Electron microscopy, no TE01020118

Quantum Experiments in the TEM: Realizing Unitary Operators using Quadrupoles

STEFAN LÖFFLER[1] AND PETER SCHATTSCHNEIDER[1,2]
[1] USTEM, TU Wien, Austria; [2] Institute of Solid State Physics, TU Wien, Austria

Naturally, electrons are quantum objects. Despite this fact, in electron microscopy they are often treated in a (semi-)classical approach as point particles, or as simple waves when necessary. Only in relatively rare instances, their quantum nature is fully embraced. In this work, we propose a new, tunable scheme of using electrons to not only model but also eventually realize a simple quantum system.

The simplest (non-trivial) quantum system is the two-state system, which is well-known e.g. from quantum optics. All states in this system are composed of a coherent superposition of two basis states. In principle, any two independent states could serve as a basis. We will use the two Hermite-Gaussian (HG) modes $HG_{1,0} := |0\rangle$ and $HG_{0,1} := |1\rangle$ as basis states. These resemble orbitals with p character oriented in x and y directions, respectively (see fig. 1). Such HG beams can be created approximately in practice by using a Hilbert phase plate or an Aharonov-Bohm wire [1,2]. Since – apart from a global phase – all normalized, coherent superpositions of the two basis states can be written as

$$|\psi\rangle = \cos(\theta/2)\,|0\rangle + \sin(\theta/2)e^{i\varphi}\,|1\rangle,$$

all these states can be visualized on the Bloch sphere (see fig. 1) using the two angles θ and φ.

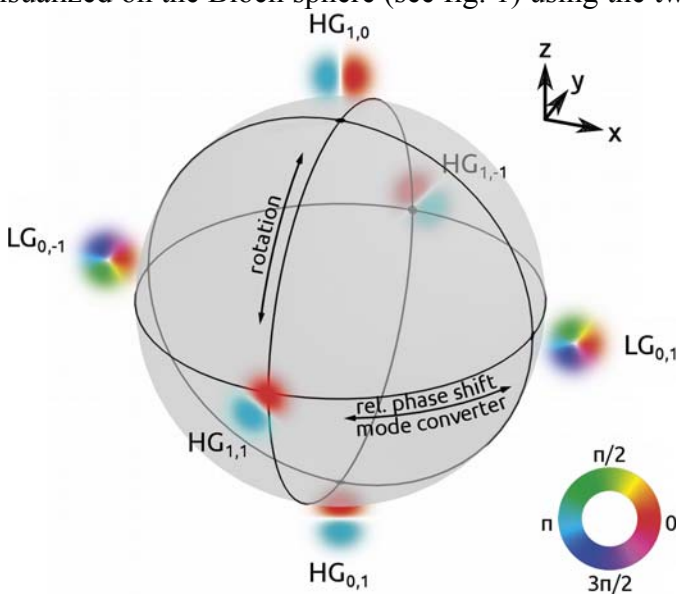

Figure 1. Bloch sphere showing the basis states $HG_{1,0}$ and $HG_{0,1}$ at the north and south pole, respectively, as well as several noteworthy related states. The phase is color-coded as depicted in the color wheel.

A crucial aspect of performing quantum experiments are operators. For instance, it is well known that all observables correspond to Hermitian operators: the (average) momentum of the beam corresponds to (the expectation value of) the momentum operators (typically measured in diffraction), while energy (as measured in EELS) corresponds to the Hamilton operator, etc. Just as Hermition operators correspond to observables, unitary operators correspond to basis transformations. In other words, they can be used to transform one state into another. The probably best-known example in electron microscopy is the lens, which can be used to transform an image in real space into a diffraction pattern in reciprocal space and vice versa.

For the two-state system considered here, all possible states lie on the Bloch sphere. Thus, all unitary operators correspond to rotations around the center of the sphere. It is straight-forward to see that rotations around the z axis correspond to changes of φ, i.e. changes of the relative phase between the two basis states. Similarly, rotations around the x axis correspond to changes of θ, i.e. the relative weights of the two basis states. Due to the nature of the basis chosen here, changes of θ simply mean a rotation of the coordinate system which is easily implemented. Changes of φ, on the other hand, require a relative phase shift of the horizontal component with respect to the vertical component. This can be achieved using two quadrupole lenses in a mode converter setup as depicted in fig. 2.

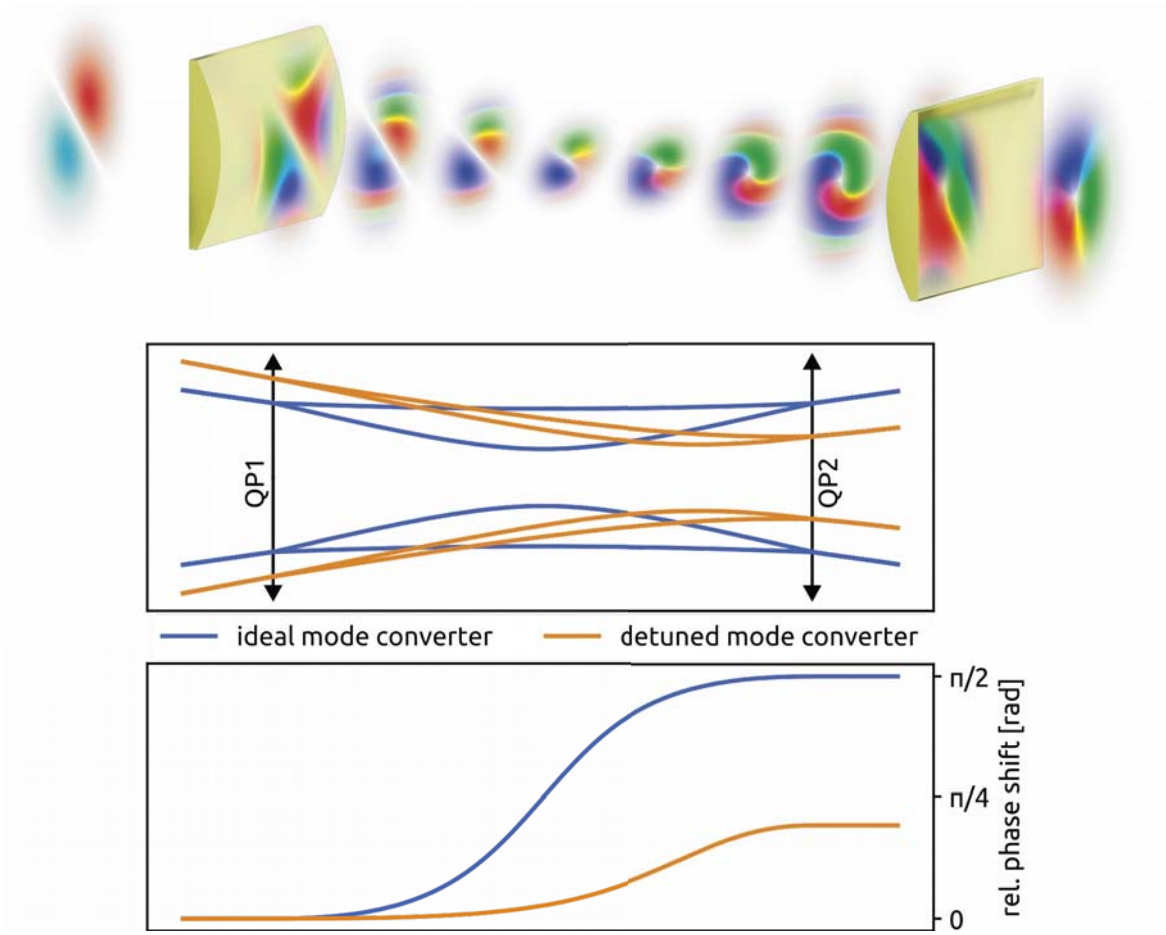

Figure 2. Top: schematic of a mode converter consisting of two quadrupole lenses to convert a $HG_{1,1}$ beam into a $LG_{0,1}$ vortex beam by producing a phase shift of π/2. The phase is color-coded as in fig. 1. Center: ray diagram for two different beam diameters/quadrupole excitations. In both cases, the horizontal and vertical components are identical before QP1 and after QP2, but are different in-between. Bottom: relative phase shift between the horizontal and vertical components as a function of position for the two different conditions.

It is well-known that quadrupoles focus in one direction while defocusing in the perpendicular direction [1,2]. Thus, one component (say, the horizontal one) goes through a focus, while the other one does not. A beam passing through the focus is subject to a phase shift. When comparing the pre-lens far-field with the post-lens far-field, this results in a phase shift of π. However, as the phase shift is continuous, it is smaller in the near field. This was notably used in practice to convert a $HG_{1,1}$ beam to an $LG_{0,1}$ Laguerre-Gaussian vortex beam carrying orbital angular momentum by imparting a relative phase shift of π/2 to the beam [1] – hence the name mode converter.

By carefully tuning the beam size, convergence, and the quadrupole excitation in relation to the quadrupole distance, one is able to implement any phase shift in the range (0, π) as shown exemplarily in fig. 2. Likewise, reversal of the quadrupole field allows for phase shifts in (-π, 0) by focusing the vertical component and defocusing the horizontal one. Care must of course be taken to end with a round, non-astigmatic beam which imposes conditions on the relation between the beam size/convergence and the quadrupole excitations [2]. The beam size and convergence angle can easily be tuned by existing round lens setups, so these conditions do not pose a problem in practice.

As rotations around both the x and the z axis of the Bloch sphere are feasible as described above, any point on the sphere can be reached by (at most) three rotations, e.g. by using the Euler angles and the rotation axis sequence z-x-z. Thus, any unitary operator can be realized by a setup employing two adjacent mode converters (with a total of four quadrupoles). This opens up many possibilities. For instance, it allows to always perform measurements in the corresponding Hermitian operator's eigenbasis by virtue of a tunable basis transformation. In addition, together with the possibility to entangle electrons by interaction [3,4], it may even pave the way for quantum computing experiments in the electron microscope.

References

[1] P. Schattschneider, M. Stöger-Pollach, J. Verbeeck, Phys Rev Lett, 109 (2012) 84801
[2] C. Kramberger, S. Löffler, T. Schachinger, P. Hartel, J. Zach, P. Schattschneider, submitted
[3] P. Schattschneider, S. Löffler, Ultramicroscopy 190 (2018) 39
[4] P. Schattschneider, S. Löffler, H. Gollisch, R. Feder, J El Spec Rel Phen (2019) in print

Acknowledgements

P.S. acknowledges financial support by the Austrian Sciene Fund (FWF) under grant P29687-N36.

Magnetic Differential Phase Contrast Imaging at Atomic Scale

JÁN RUSZ[1], ALEXANDER EDSTRÖM[2] AND AXEL LUBK[3]

[1] Dept. of Physics and Astronomy, Uppsala University, Sweden; [2] Materials Theory, ETH Zurich, Switzerland; [3] Institute for Solid State and Materials Physics, TU Dresden, Germany

Emergence of exotic magnetic behavior at nano-scale calls for magnetic characterization techniques capable to measure magnetism with sufficient spatial resolution. Scanning tunneling microscopy allows to measure magnetism with atomic spatial resolution, enabling fascinating insights into the atomic scale magnetism [1], however, this method is restricted to detection of properties of surface layers of atoms. Transmission electron microscope (TEM) appears to be a natural choice of an instrument to study magnetization inside materials, at atomic scale: it allows to focus illuminating electron probe to sub-atomic areas, while transmitting it through the sample. It is thus having the potential to obtain atomic-scale information from the bulk of the sample.

We will describe – from a theoretical perspective – a new technique with a potential to provide atomic-scale information about magnetism in samples. The technique is based on differential phase contrast imaging (DPC) at atomic resolution [2]. Recent simulations utilizing the Pauli multislice equation [3], which includes the interaction of the electron beam with microscopic magnetic field inside the sample, show that the diffraction patterns (ronchigrams) carry information about the projected microscopic magnetic fields at atomic scale [4]. Figure 1 shows an example result of simulations for ferromagnetic FePt crystal. The beam deflections due to microscopic magnetic fields are in the range between approximately 0.1% and 1% of the deflections due to microscopic electric fields, which is a comparatively weak signal. However, DPC measurements by their nature are very efficient per unit of electron dose, since a majority of elastically scattered signals are used to measure the beam deflection. Considering that EMCD signals [5] of strength about 1% have been detected [6] in the electron energy loss spectra, magnetic DPC at atomic resolution, which utilizes most of the elastically scattered electrons, could be a viable alternative for magnetic studies at atomic resolution.

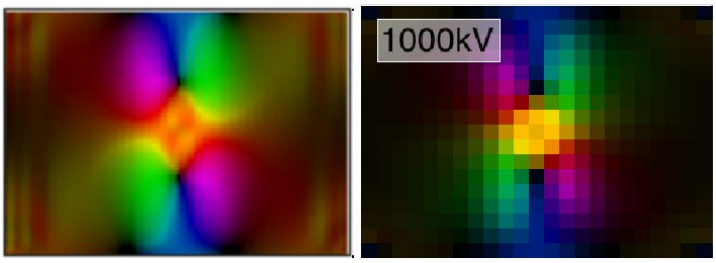

Figure 1. Left: Projected magnetization within a unit cell of FePt crystal with magnetization along the x-axis, which is parallel to crystallographic c-axis – the easy axis of magnetization of FePt. Right: Magnetic DPC image of 2.7nm thick FePt crystal calculated by Pauli multislice method for convergence semi-angle of 30mrad and acceleration voltage of 1000kV.

References

[1] A. Khajetoorians et al., Nature **467**, 1084 (2010).
[2] N. Shibata et al., Nature Physics **8**, 611 (2012).
[3] A. Edström, A. Lubk, J. Rusz, Phys. Rev. Lett. **116**, 127203 (2016).
[4] A. Edström, A. Lubk, J. Rusz, Phys. Rev. B **99**, 174428 (2019).
[5] P. Schattschneider et al., Nature **441**, 486 (2006).
[6] J. C. Idrobo et al., Adv. Struct. Chem. Imaging **2**, 5 (2016).

Improvements in Environmental Scanning Electron Microscopy – Universal Pressure Scanning Electron Microscopy (UPSEM)

JOHANNES RATTENBERGER[1], HARALD FITZEK[1], HARTMUTH SCHROETTNER[1,2] AND FERDINAND HOFER[1,2]

[1] Graz Centre for Electron Microscopy – ZFE, Graz, Austria; [2] Graz University of Technology, Institute of Electron Microscopy and Nanoanalysis – FELMI, Graz, Austria

The Environmental Scanning Electron Microscope (ESEM) enables the opportunity to investigate electrically insulating, biological and even wet samples without extensive sample preparation [1]. The imaging gas inside the sample chamber suppresses negative charging and prevents outgassing of the sample. This microscope technique opens new possibilities for electron microscopy. Wetting experiments can be performed by using water vapor as imaging gas and a cooling stage for the sample and catalytic processes can be investigated *in situ* by using a specific gas and a heating stage [2]. The negative side effect is the decreasing signal to noise ratio (SNR) with increasing chamber pressure. As a result, experiments must be done at lowest possible pressure (far away from reality), high electron energies (large interaction volume), long dwell times (poor time resolution for *in situ* experiments) and large electron beam currents (problematic for radiation sensitive samples).

However, research activities in the last few years have shown that state of the art microscopes are working far away from physical limits. The key to high image quality at high pressures is to reduce primary beam scattering as far as possible while maintaining ideal operation conditions for the secondary electron detector [3, 4].
In the Thermo Fisher Scientific (FEI) Quanta series ESEMs the gaseous environment in the sample chamber is separated by two Pressure Limiting Apertures (PLA) and a differential pumping system from the high vacuum inside the electron column. Nevertheless, Monte Carlo simulations and experimental results have shown that a lot of gas streams through the PLA upwards and a significant amount of electrons are lost for imaging even before the beam is entering the sample chamber [5]. The most straightforward way to improve image quality is to decrease the PLA diameter, which unfortunately also reduces the maximum available field of view.

In this work, a new pressure limiting aperture holder, based on Monte Carlo simualtions and experimental results, is presented which improves the high pressure performance of the microscope even at the same field of view. The direction of the upstreaming gas flow is redirected in a way to minimize the interaction with the primary electron beam. In figure 1 the additional stagnation gas thickness (aSGT), which represents the effective distance the electron beam must overcome inside the gaseous environment above the first PLA, can be seen for the original design (GSED) and different PLA diameters using the optimized aperture holder. It can be seen that the aSGT is about 1 mm shorter be using the optimized system even at the same PLA diameter of 500µm.

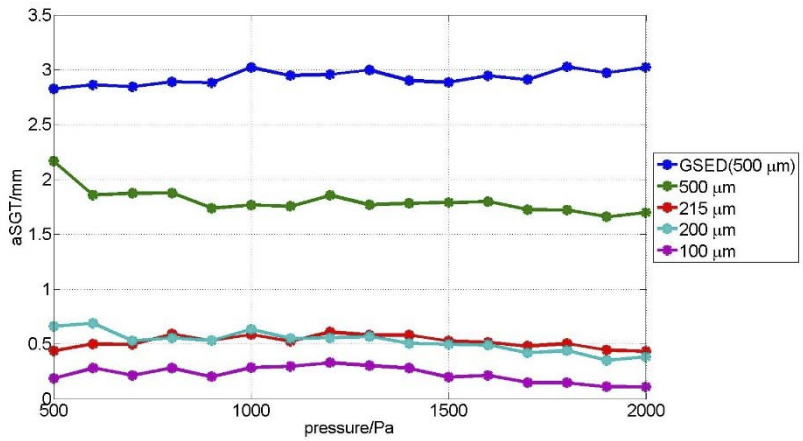

Figure 1. Additional Stagnation gas thickness as a function of chamber pressure for the original design (GSED) and different PLA diameter using the optimized aperture holder

Usually the secondary electron detector in ESEMs is a flat positively biased electrode positioned sideways or directly at the end of the pole piece. Secondary electrons are attracted and accelerated towards the detector and on their way collision ionization amplifies the signal. With increasing pressure, the amplification efficiency decreases because electrons do not gain enough energy between collisions to ionize the gas. However, nearby a needle detector with very small tip radius (R < 10 µm) the electric field is strong enough for amplification and by positioning the needle on the sample table it operates at ideal conditions regardless of pressure and working distance. A by-product of this design is that the conventional position of the backscatter electron detector at the end of the column is no longer blocked by the SE detector. In figure 2 the optimized design can be seen in comparison to the design of the Quanta series microscopes.

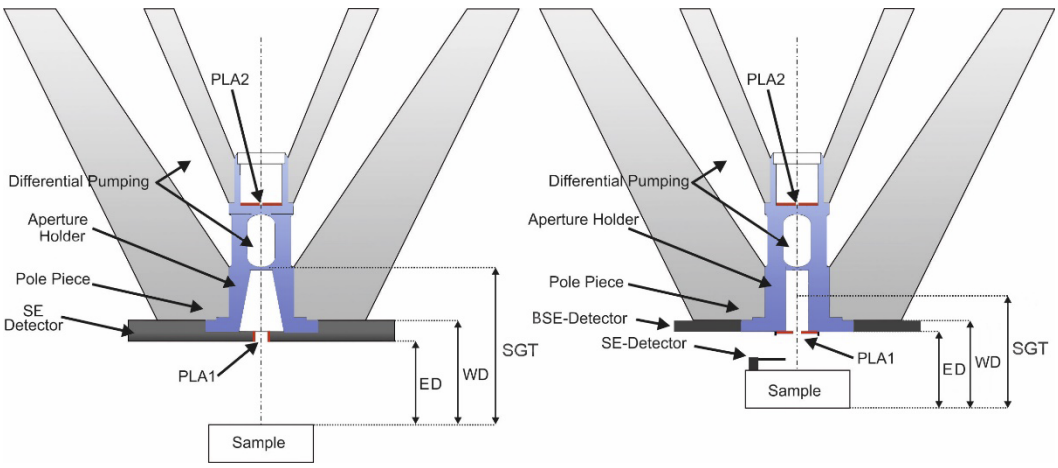

Figure 2. Comparison of the different designs (left: Quanta Series, right: ZFE [patent pending [6]]) (ED: environmental distance, WD: working distance, SGT: stagnation gas thickness, ED-SGT = aSGT additional stagnation gas thickness)

With this optimized high pressure design the limits of conventional ESEM technology can be crossed. Imaging at higher chamber pressures up to one atmosphere (see figure 3), investigations of pollen germination in water (wetting experiment at 16°C, Japanese sugi pine, Cryptomeria japonica, see figure 4) and much more is possible.

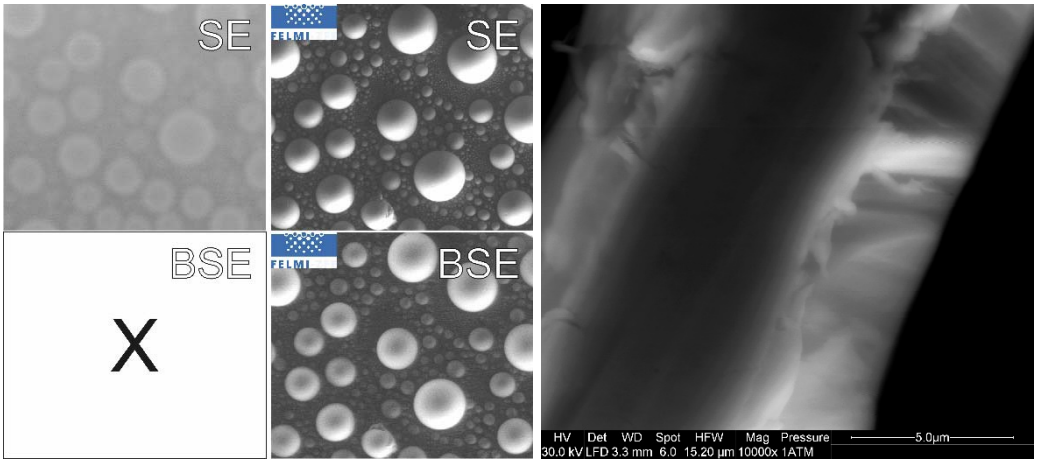

Figure 3. left: Overall performance comparison (5kV, 1500 Pa H_2O, 30 µs dwell time, 0.4 nA); right: Copper wire imaged at atmospheric pressure (30 µm PLA diameter, 30 kV)

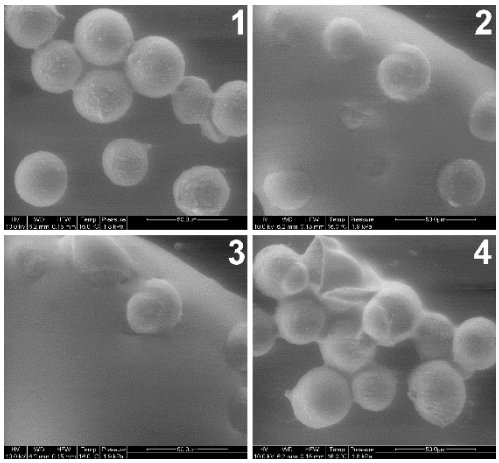

Figure 4. Pollen germination in water (Japanese sugi pine, 10keV, ~1800 Pa H_2O, 16°C)

References

[1] G.D. Danilatos, Adv. E.E.P., 71 (1988) 109-250
[2] Z.J. Wang et al., ACS Nano, Vol.9, No.2 (2015) 1506-1519
[3] H. Fitzek, H. Schroettner, J. Wagner, F. Hofer, J. Rattenberger, J. Microsc., 262 (2016) 85–91
[4] J. Rattenberger, H. Fitzek, H. Schroettner, Imaging & Microscopy, Vol 20 (2018) 38-40
[5] H. Fitzek, H. Schroettner, J. Wagner, F. Hofer, J. Rattenberger, J. Microsc., 260 (2015) 133–139
[6] J. Rattenberger, H. Fitzek, J. Wagner, H. Schroettner, European Patent No. 3231002

Assessing the thickness error rate of quantitative STEM measurements

RADIM SKOUPY AND VLADISLAV KRZYZANEK
Institute of Scientific Instruments of the CAS, Brno, Czech Republic

Quantitative scanning transmission electron microscopy (qSTEM) analysis is one of the few methods which provide determination of sample thickness in an electron microscope. We focus in more detail on the accuracy of such type of thickness determination. To compare individual detector segments and their accuracy we used – analogically to our previous work with a BSE signal [1] – a sample with a thickness known in each point – a latex nanosphere with a nominal diameter of 616 nm (S130-6, Agar Scientific, United Kingdom). We measured the diameter of 575 nm in the case of the shown particle (Fig. 1). The accurate diameter was assessed for each particle during the image processing.

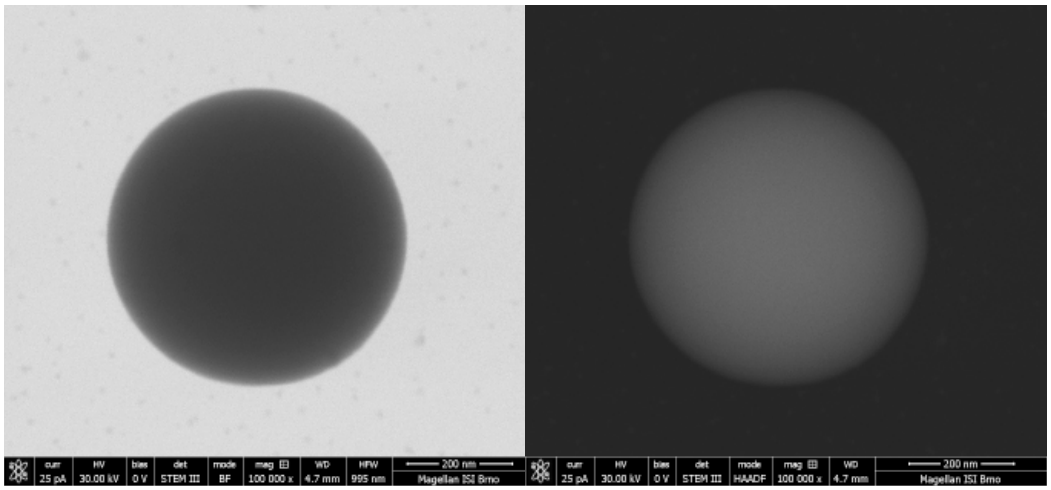

Figure 1. The latex nanosphere images captured simultaneously in BF and HAADF.

The Monte Carlo simulation, which plays a crucial role in assigning the correct sample thickness to the captured and normalized STEM signal intensity, was performed in Casino software [2] with appropriate settings (energy 30 keV, 200,000 e^- per point, total and partial cross section taken from Elsepa database [3], supporting thin carbon layer was taken into account). The simulated sample had a wedge shape with a maximum thickness of 800 nm and an angle of 5 °.

The influence of random shape changes and deformations can be suppressed by rotary averaging of individual particles (Fig. 2 left). In this step, a distance of each individual pixel from the center of the sphere is calculated. Then the pixels with distances in the chosen range are averaged. The advantage of this method is the absence of an interpolation error. However, a small amount of pixels in the middle of the particle causes a significantly higher noise in this area.

We found the highest accuracy in the case of the mean of both captured segments, where the estimated thickness corresponds with the theoretical one in the whole measured thickness range. Individual segments overestimate (BF) and underestimate (HAADF) the thickness in the high thickness region (Fig. 2 right).

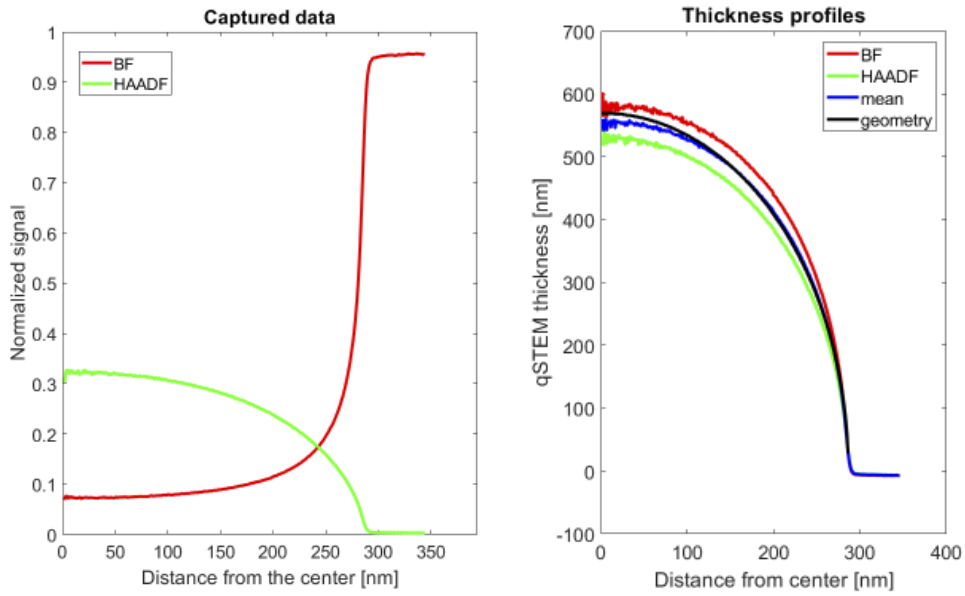

Figure 2. Captured data after rotationally averaging and signal normalization (left). Thickness of the sample estimated by quantitative STEM imaging in two different detector segments together with their mean and geometry (right).

We demonstrated the ability of quantitative low voltage STEM imaging to determine precisely the local thickness within a wide range of thicknesses up to approximately 600 nm in the case of a latex (polystyrene) sample. The proof was done at the sample of latex spherical nanoparticles that have relatively low density (composed of light elements – carbon and hydrogen). In the case of samples containing higher atomic elements, the penetration depth of the electron beam is much lower. Unfortunately, not all used segments gave us the same results. Both BF and HAADF segments brought results which corresponded with the reality of the sample – with a maximum error around 10 % (Fig. 3).

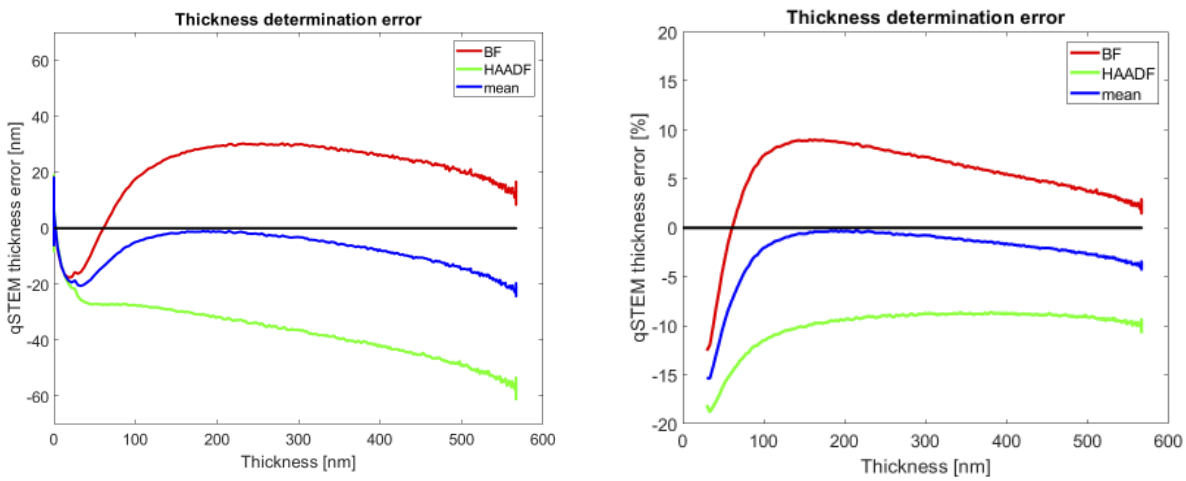

Figure 3. qSTEM thickness error dependency on the local geometrical thickness of the nanosphere. The error is determined absolutely in nanometers (left) and relatively in percent (right).

BF showed higher and HAADF brought lower thicknesses than those given by the geometry of the sample. However, it is possible to improve the accuracy of the method by simply averaging those curves. In the case of the "mean" curve the accuracy is better than 5 % in nearly all examined ranges of thicknesses. High errors in the range of thicknesses under 100 nm are caused by inaccurate detection of a nanosphere diameter, imperfect spherical shape and wedge shape of MC simulation body.

Acknowledgements
The research was supported by the Czech Science Foundation (project 17-15451S), the Ministry of Industry and Trade of the Czech Republic (project TRIO FV30271) and the Technology Agency of the Czech Republic (project TN01000008). R.S. is grateful to a ThermoFisher/CSMS scholarship for support.

References
[1] V. Krzyzanek, et al, Soft Matter 7 (2011) 7034-7041
[2] H. Demers et al, Scanning 33 (2011) 135-146
[3] F. Salvat, et al, Comput. Phys. Commun. 165 (2005) 157–190

SEM-EDS analysis of gold mercaptotriazole crystals (Au-MT)

SILVANA DIMITRIJEVIĆ[1], STEVAN DIMITRIJEVIĆ[2] AND ALEKSANDRA IVANOVIĆ[1]

[1] Mining and Metallurgy Institute Bor, Bor, Serbia; [2] Innovation Center Faculty of Technology and Metallurgy, University of Belgrade, Belgrade, Serbia

An electrolyte based on gold complex with mercaptotriazole was synthesized in a wide pH range from acid to alkaline (pH=2-12). After synthesis of the electrolyte, detailed characterization of the complex in liquid and solid state in the whole range of its stability was performed. Synthesized solutions of gold complex based on mercaptotriazole are vaporized at room temperature to dry in order to obtain and characterize Au-MT in the crystalline form. Optical microscopy showed that the crystals obtained from solutions of different pH values are different in color, size and homogeneity. The most homogeneous (according to size and color) and the smallest crystals were obtained from the electrolyte with pH=9. Scanning electron microscopy (SEM) with energy-dispersive spectrometry (EDS) crystals of the complex of gold with mercaptotriazole has shown that the crystals obtained at different pH values differ in shape, size and homogeneity. The most homogeneous and at the same time the smallest crystals are obtained from electrolytes at pH = 9.

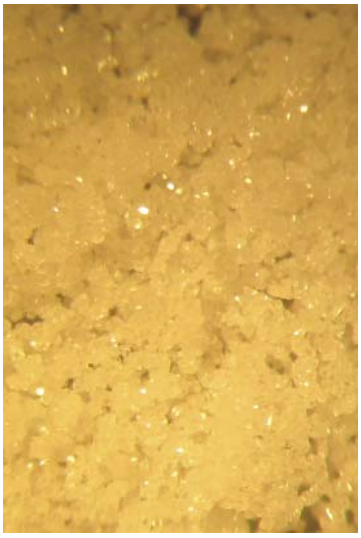

Figure 1. Au-MT crystals obtained from electrolytes at pH = 2, 4, 7 9 and 12

Advanced approach to Scanning-transmission tomography in the SEM

V. MORANDI[1], M. FERRONI[1,2], P. MACCAGNANI[1], L. MASINI[1], A. MIGLIORI[1], L. ORTOLANI[1], M. DONARELLI[2], A. SIGNORONI[2], M. SAVARDI[2]

[1] CNR-Microelectronic and Microsystems Institute, Bologna Section, Bologna, Italy; [2] Department of Information Engineering, University of Brescia, Italy

The implementation of electron tomography in the SEM operated in the scanning-transmission imaging mode (T-SEM) is here described and its application in both physical and materials sciences is presented to demonstrate the potential of the proposed approach. In the playground of three-dimensional reconstruction methods operated in the SEM platform, this approach complements the largely adopted serial-sectioning and slice-and-view reconstructions through imaging in the transmission mode and acquiring a series of projective images used to calculate the mass-distribution in space for the sample under investigation.
According to the complete workflow developed in TEM tomography, the acquisition scheme starts from a specific Si-based detection system for transmitted electrons that was fabricated and integrated with a sample rotating holder with the purpose to record a series of projection images taken at different tilt angles. The adaptation of the imaging strategy (beam energy, geometry, and combinations of sectors in the detector) fulfills the basic requirement of a monotonic variation of image contrast upon increase of the projected thickness and atomic number in the specimen. This allowed to retrieve the three-dimensional arrangement of the constituents by calculation of the tomogram and to perform an iterative refining of the reconstruction by exploiting the *a-priori* knowledge according to a compressive sensing approach [1].
The performance of the detector allowed to record the image series at suitable speed and limited dose, making the technique feasible and offering an effective complement to the FIB slice-and-view methods presently implemented in the SEM platform [2]. In particular, the materials science community presently addresses the characterization of nanosized heterostructures, basically formed by low-Z elements, which needs to be characterized in their spatial arrangement but are not suitable for embedding in hard media before serial sectioning by microtomy or FIB-sectioning. One example is given by the investigation of nanosized heterostructures formed by a combination of a graphene flakes which support the nanosized seeds for the growth of ZnO crystals.

We report on the image acquisition and tomographic reconstruction of graphene-ZnO nanorods hybrid structure. Such a sample is readily transparent to the electron beam for the T-SEM imaging (Fig. 1, left). The projection images have been recorded in dark-field (DF) imaging mode, attaining the highest STEM signal and visibility for the details at 27 keV beam energy. The 3D reconstruction of the sample, clearly presenting the arrangement of ZnO nanorods in Fig. 1-right has been achieved from 50 projections obtained through single-axis rotation with with 2° steps.

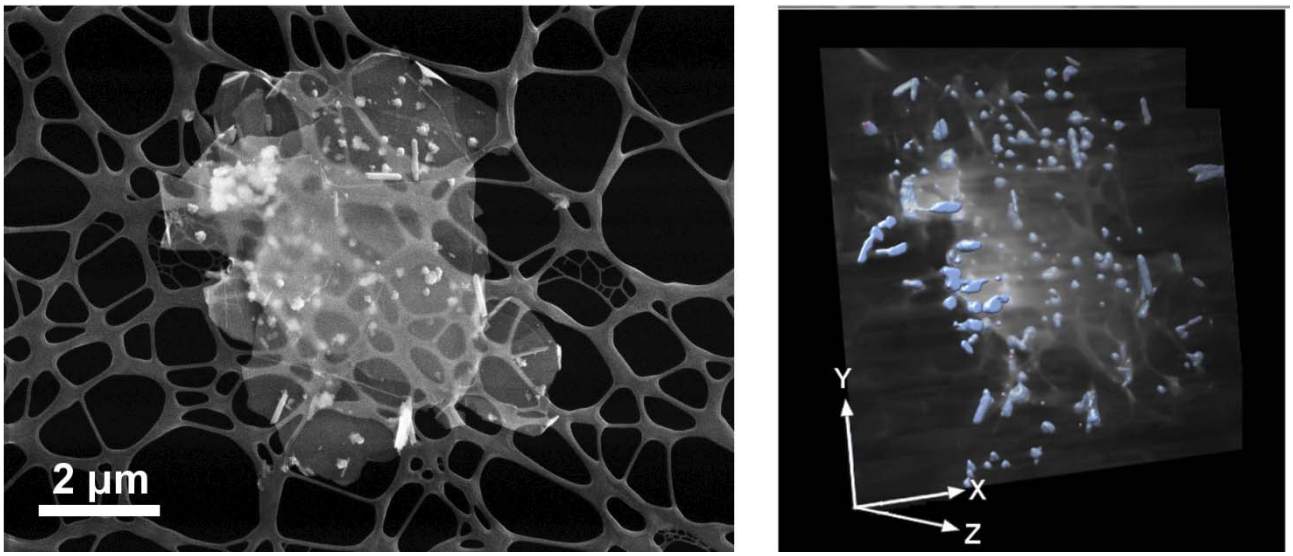

Figure 1. Left: secondary electrons SEM image of the graphene-ZnO hybrid structure.
Right: 3D reconstruction of the graphene-ZnO hybrid structure.

Compressed Sensing refinement was used as a complement of the reconstruction workflow; this proved effective in reducing the number of projections required to reconstruct the tomogram with adequate resolution. The utility was demonstrated in the reconstruction of bundles of collagen fibrils in a sample of biological tissue. The adopted imaging conditions were completely different and the refinement of the reconstruction was achieved by adapting the coefficents in the minimization of the residual function according to the compressed sensing approach. The details of the collagen fibrils, namely its periodical striation, was used to verify the capability of the algorithm to retrieve the finest details in the picture.
Also the experimental set up could benefit from the indications provided by the reconstruction and refinement algorithm, as a modification was exploited in order to improve acquisition strategy. The scheme of conical tilting has been exploited of an alternative projection scheme [4]. Departing from the conventional single axis tilting scheme, a conical tilt scheme was implemented in order to acquire a sequence of projection images through tilt-rotation of the sample under the electron beam. In this way, the Fourier space percentage covered in conical tilt is higher than in single-axis tilt geometry and the signal on the detector could be more rapidly optimized.

References

[1] M. Ferroni et al., Scientific Reports 6, (2016) 33354.
[2] Ferroni et al., *J. Phys.: Conf. Ser.* 644 (2015) 012012.
[3] Ferroni M et al., *J. Phys.: Conf. Ser.* 902 (2017) 012031.
[4] Zampighi G A et al., *Journal of Neuroscience* 28 (2008) 4151.

Investigation in the Effects of Exercise on the Testicular Morphology, Cell Proliferation and Blood Testis Barrier in the High Fat Diet-Induced Obesity

MERVE ACIKEL ELMAS[1], OZLEM BINGOL OZAKPINAR[2], MELTEM KOLGAZI[3], GOKSEL SENER[4], SERAP ARBAK[1], FERIHA ERCAN[5]

[1,5] Acibadem Mehmet Ali Aydinlar University Department of Histology and Embryology; [2] Marmara University School of Pharmacy, Deptartment of Biochemistry; [3] Acibadem Mehmet Ali Aydinlar University Department of Physiology; [4] Marmara University School of Pharmacy, Deptartment of Pharmacology; [5] Marmara University Department of Histology and Embryology

Background and Aim

Obese male population has been increased up 3 times in the last thirty years. The latest studies show that the obesity has negative affects on male fertility not only sperm quality but also physical and molecular structural defects in testis germ cells. Because of high fat diet consumption spermatogenic cycle in seminiferous epithelium is damaged by disruption of blood testis barrier integrity and which would be cause abnormal sperm production. Exercise could be defined as a rapid increase in energy consumption. The studies showed that exercise has a positive effect on sperm morphology, motility and function. However, the effects on blood testis barrier integrity, which played an important role in spermatogenesis, were not investigated. The aim of this study was to investigate the effects of execise on spermatogenic cell proliferation, blood testis barrier, inflammatory and oxidative markers and hormone levels in testes of high fat diet (HFD) induced obese rats.

Materials and Methods

Sprague Dawley male rats were fed with standard (STD group; 6% calories as fat) or HFD (HFD group; 45% calories as fat) for 18 weeks. Half of these animals were trained swimming exercise (STD+EXC and HFD+EXC groups; 1 hour a day, 5 days a week) for the last 6 weeks (Fig 1). Testis samples were evaluated by histological and ultrastructural methods. Cell proliferation, apoptosis and blood testis barrier was examined by histochemical methods. Lipid and hormone levels in blood serum and oxidative stress markers in tissue were examined by biochemically. All data were analyzed by statistically.

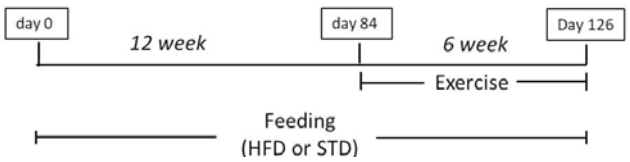

Figure 1. Experimental design

Results

Sertoli cells are affected by testosterone and FSH changes in HFD induced obesity. So Hypothalamus-pituitary-testis (HPT) axis could be unregulated and this situation which causes a change in signaling pathways that regulate the metabolism of Sertoli cells. A decrease in FSH and testosterone levels were observed in the HFD group while these hormone levels were increased in HFD+EXC group. Damaged tubules and apoptotic cells were increased and dilated intercellular areas were seen in HFD group. The number of proliferative cells and Sertoli cell tight junction protein immunoreactivity (ir) of ZO-1, Occludin and gap junction protein ir of Cx 43 were decreased in the HFD group. In this group, serum total cholesterol and triglyceride level, tissue MDA level and MPO activity increased, GSH level and SOD activity were decreased. All these histological and biochemical findings were ameliorated in HFD+EXC group. It was observed that high fat diet caused degeneration of testis morphology, altered blood testis barrier integrity and increased oxidative damage.

Conclusion

It is thought that exercise prevented testicular damage by regulating hormonal balance and testicular functions, reducing inflammation, regulating oxidant/antioxidant and cell proliferation/apoptotic balance, and also preserving blood-testicular barrier integrity.

References

[1] Linden MA, Pincu Y, Martin SA, Woods JA, Baynard T (2014) Moderate exercise training provides modest protection against adipose tissue inflammatory gene expression in response to high-fat feeding. *Physiol Rep* 2

[2] MacDonald AA, Herbison GP, Showell M, Farquhar CM (2010) The impact of body mass index on semen parameters and reproductive hormones in human males: a systematic review with meta-analysis. *Hum Reprod Update* 16: 293-311

[3] Palmer NO, Bakos HW, Fullston T, Lane M (2012a) Impact of obesity on male fertility, sperm function and molecular composition. *Spermatogenesis* 2: 253-263

[4] Palmer NO, Bakos HW, Owens JA, Setchell BP, Lane M (2012b) Diet and exercise in an obese mouse fed a high-fat diet improve metabolic health and reverse perturbed sperm function. *Am J Physiol Endocrinol Metab* 302: E768-80

Correlative analysis of dust particles by SEM, EDXS and Raman

MANFRED NACHTNEBEL[1], ANDREA STEITZ[2], UTE MUNOZ-CZERNY[3], JOHANNES MANTLER[4], GERHARD GRUELL[2], AND HARTMUTH SCHROETTNER[1,5]

[1] Graz Centre for Electron Microscopy, Graz, Austria; [2] Holzforschung Austia, Vienna, Austria; [3] Österreichisches Institut für Baubiologie und Bauökologie, Vienna, Austria; [4] Österreichischer Kachelofenverband, Vienna, Austria; [5] Institute of Electron Microscopy and Nanoanalysis, Graz, Austria

Dust is a complex mixture of organic and inorganic particles. Depending on the origin, these particles vary in size, shape and composition. Furthermore, they can cause respiratory irritation and allergies in humans. Thus for indoor air, dust has a great relevance to human health [1]. Due to its complex composition, analysis of dusts is done in this project by several institutes with methodical specializations.

Here the IBO (Österreichisches Institut für Baubiologie und Bauökologie) is dealing with the relationship between dust concentration and physiological parameters and the affection of various heating systems on the formation of dust. KOV´s (Österreichischer Kachelofenverband) task is the simulation of dust movement. The focus of HFA (Holzforschung Austia) is the development of both a representative discontinuous sampling method and an analysis routine of dust in indoor air. HFA and ZFE (Graz Centre for Electron Microscopy) are working closely together on the analysis of dust particles.

To obtain information about the different components of indoor dust, different techniques are used. At the HFA the combination of scanning electron microscopy (SEM) and energy dispersive X-ray spectroscopy (EDXS) is used to identify the elemental composition of the sampled dust. Figure 1 shows that a phase separation and the elemental composition of the different phases is easily accessible with this method.

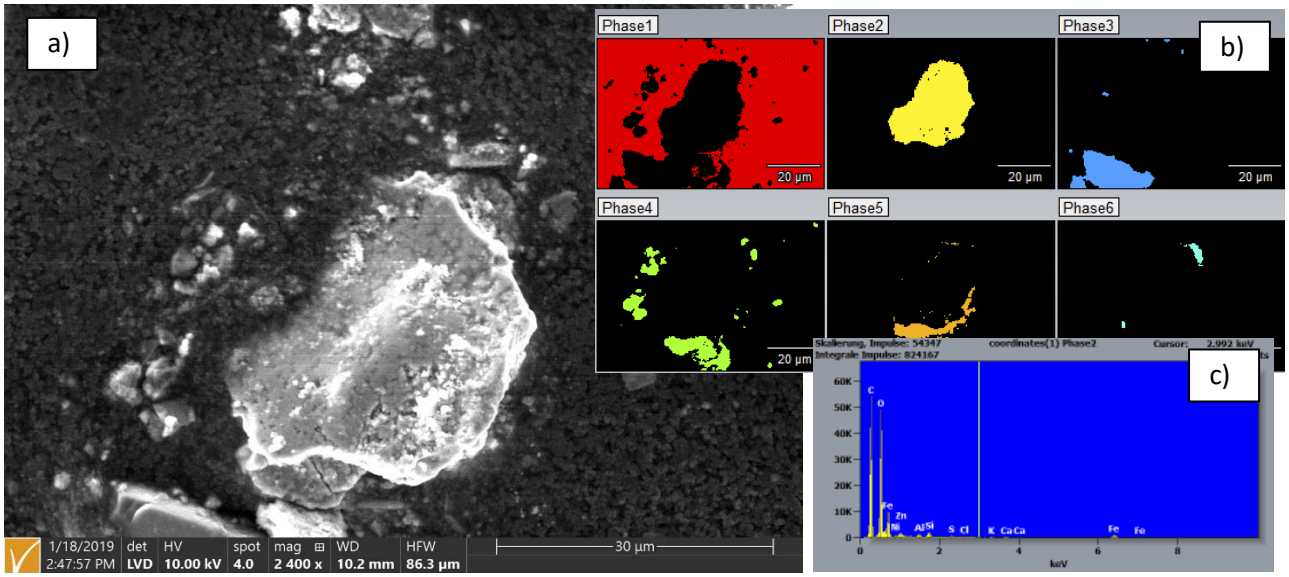

Figure 1. a) Secondary electron (SE) SEM image; b) different phases identified by EDXS; c) detailed elemental composition of phase2.

To reveal an even deeper insight into its components, correlative microscopy is performed at the ZFE. Here the so-called RISE (Raman imaging and scanning electron microscopy) is used [2]. Therewith the correlation of SEM, EDXS and Raman spectroscopy applied to the same particle or area under investigation is easily accessible. First investigations of sampled indoor dust already show the complexity of dust. Figure 2 shows that the EDXS result of the bright particle in the BSE (backscattered electron) SEM image center seems to reveal a quite homogeneous composition. However, correlative Raman spot-measurements demonstrate that this one particle has three different chemical components.

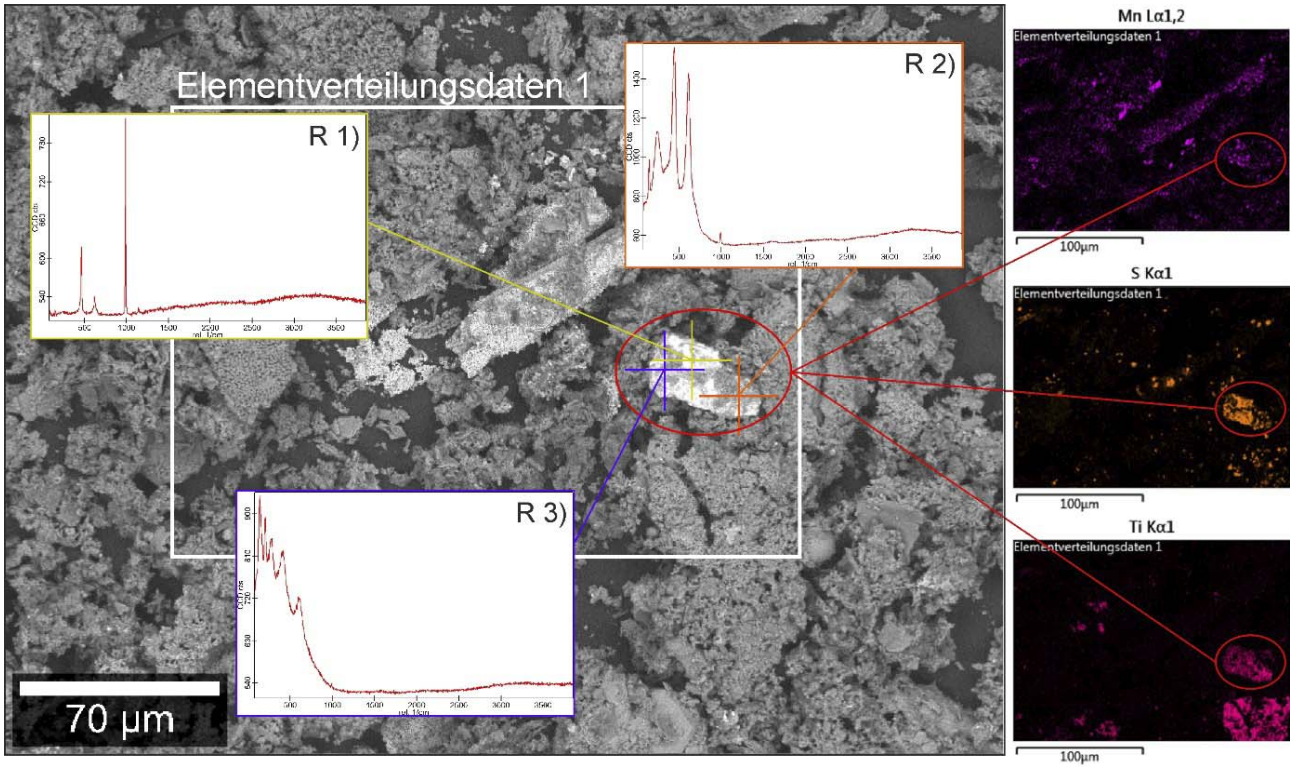

Figure 2. BSE SEM image shows a typical dust specimen after sampling. The EDXS results on the right side reveal an apparently homogeneous particle while the three Raman spot-measurements R 1) to R 3) reveal that it is composed of three different chemical compounds.

With the RISE system, the initially investigated center particle at Figure 1 was examined in more detail. Because of the surface roughness, two Raman spot-measurements of the iron rich particle were performed. Both Raman spectra were able to be identified as magnetite (Fe_3O_4), see Figure 3.

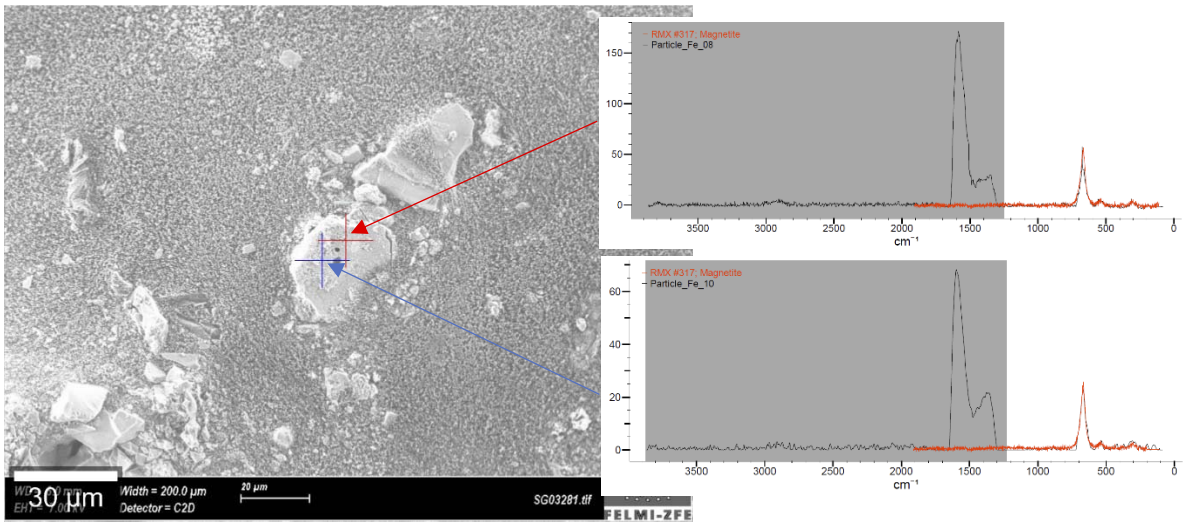

Figure 3. Two Raman spot-measurements of the same particle as in Figure 1 revealed the distinct identification of magnetite.

The goal of the overall project is to obtain a detailed understanding into indoor dust. With the comprehensive investigations reaching from determine physiological parameters, dust movement simulation to the detailed analysis with SEM, EDXS and Raman a deep insight into indoor dust composition and its impact on human wellbeing will be gained.

References

[1] J. W. Schaeffer *et al.*, Environmental Science and Technology, 06 (2017) 6430–6440
[2] R. Schmidt *et al.*, Macromolecular Symposia, 04 (2019), 384, 1800237–1800247

LIFE SCIENCES

LS1

Live cell imaging, and intracellular dynamics

CHAIRPERSONS:

Manuela Malatesta, Pavel Hozak

INVITED LECTURE

Single-molecule tracking reveals distinct behaviors of epigenetic modifiers Tet1 and Tet2 in live embryonic stem cells

JOEL RYAN[1], PHILIPP MESSER[2], CHRISTOPHER MULHOLLAND[1], DON C. LAMB[2], HEINRICH LEONHARDT[1]

[1] Department of Biology II and Center for Integrated Protein Science Munich (CIPSM), LMU Munich, Germany; [2] Department of Chemistry, LMU Munich, Germany

Chromatin modifications, such as DNA methylation (5mC), are epigenetic pathways which can mediate the long-term suppression of gene expression and as such is essential for embryonic development. The Ten-eleven translocation (TET) family of dioxygenases erase DNA methylation via the generation of oxidized cytosine derivatives such as hydroxymethylcytosine (hmC). TET1 has a dual role regulating gene expression in embryonic stem cells, where it acts as both a transcriptional activator and repressor.

The transcriptional and epigenetic functions depend on the mobility of TETs and their ability to find their targets in the nucleus. Here we use single-molecule tracking and raster image correlation spectroscopy with genome engineered embryonic stem cells to study the spatio-temporal organisation of Tet1 and Tet2 in the nuclei of live ESCs.

We show that Tet1 and Tet2 have markedly different kinetics which likely drive their contrasting functions. In naive and primed ESCs, Tet1 is mostly bound, and forms multivalent hubs which associate at euchromatin loci. In contrast, Tet2, while also localizing to euchromatin loci, is largely diffusive and less likely to form stable interactions in the nucleus.

Remarkably, these binding and diffusion behaviours appear to be independent of the methylation state of the genome, suggesting that the oxidative activity of TET proteins are transient events which are tightly regulated by their N-terminal domains. Taken together, we propose that Tet1 is targeted to promoters, tightly restricting its activity to these loci, whereas Tet2 more globally diffuses through the nucleus. We thus show for the first time physical evidence of distinct subnuclear kinetics of Tet1 and Tet2 in living ESCs and EpiLCs, at the single-cell and single-molecule level, which likely underlie the distinct roles of Tet1 and Tet2.

INVITED LECTURE

The immobile movement

MARCO BIGGIOGERA, LORENA ZANNINO AND STELLA SICILIANI
[1] Dipartimento di Biologia e Biotecnologie "L. Spallanzani", Università di Pavia, Pavia, Italy

The possibility of looking at a biological phenomenon *in vivo* has been exploited for several decades, starting with the first short movie in phase contrast of dividing cells. Nowadays, new cameras and super resolution techniques have approached the level of the single molecule visualization. It is indeed importat to follow a biological process during its development; however, there are some techniques, electron microscopy en vedette, in which this approach is impossible. Therefore, it is mandatory to study a complex process, developing in time, via a series of snapshots which can then be added in a logical succession. This long and complex process has been utilized for many years and complemented by autoradiography, immunocytochemistry and other techniques, finally creating a sort of virtual movie from a series of still-life pictures.

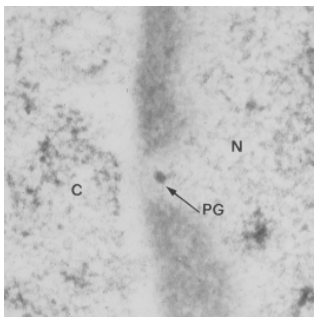

Figure 1. A perichromatin granule (PG) approaching a nuclear pore. N, nucleus; C, cytoplasm

We have made use of this method since the high resolution of EM is still unsurpassed. One exaple concerns the recuitment of S6 ribosomal protein to the nucleus, the assembly to rRNA into ribosomes and finally the export of the subunit to the cytoplasm [1]. We are currently studying the movement of mRNP particles along the perichromatin region [2] till their exit from the nucleus. In this context, we are also trying to pinpoint the timing of 5MeC production on RNA in relation to mRNA elongation and processing. Finally, we would like to improve this methodology by using electron tomography in order to have snapshot of time in a 3D space. We believe that no other technique could ensure such high resolution and we aim at providing a standard method to follow different processes inside the nucleus in an in vivo-like manner.

References

[1] B. Cisterna, D. Necchi, E. Prosperi, M. Biggiogera, FASEB J. fj.05-5278fje (2006)

[2] I. Masiello, S. Siciliani, M. Biggiogera, Histochem. Cell Biol. (2018) 150:227–233

Combined two photon excitation fluorescence and third harmonic generation imaging of redox ratio for monitoring metabolic state of live cells of fungus *Phycomyces blakesleeanus*

TANJA PAJIĆ[1], KATARINA STEVANOVIĆ[1], NATAŠA TODOROVIĆ[2], ALEKSANDAR KRMPOT[3], MIHAILO RABASOVIĆ[3], BRANISLAV JELENKOVIĆ[3] AND MIROSLAV ŽIVIĆ[1]

[1] Faculty of Biology, University of Belgrade, Serbia; [2] Institute for Biological Research, University of Belgrade, Serbia; [3] Institute of Physics, University of Belgrade, Serbia

Label-free two photon nonlinear microscopy is well established as a powerful tool for monitoring metabolic state of the various cell types due to its non-perturbative nature and fairly low phototoxicity, while application of third harmonic generation (THG) for three-dimensional (3D) cell and tissue microscopy was enabled more recently. THG occurs at structural interfaces, such as local transitions of the refractive index, most generally speaking at interfaces that are formed between aqueous interstitial fluids and lipid-rich structures. Here we present preliminary data obtained by capturing both THG and optical redox ratio signal from the same regions of the hyphae of *Phycomyces blakesleeanus*.

Label- free metabolic intravital microscopy through application of both THG and $NAD(P)H^+/FAD^+$ autofluorescence ratio was used in alternating sequence on the same field of view on a fungal cells of a model filamentous fungus *Phycomyces blakesleeanus*. The glass coverslip with collagen coating bearing unstained hyphae was mounted on custom built microscope. Laser beams for both imaging modalities were focused with the same objective lens, Zeiss Plan Neofluar 40x1.3. The autofluorescence of NAD(P)H was excited by Ti:Sa laser pulses at 730 nm, 160 fs duration and signal was collected through 479/40 filter, while for autofluorescence of FAD we used excitation by the same laser pulses at 860 nm, 160 fs duration and 530/43 filter.

For THG, we used 1040 nm, 200 fs pulses from Yb KGW laser, and detection was performed by PMT through Hoya glass UV filter with peak transmission at 340nm. As a control for perturbation of optical redox ratio, rothenone (complex I inhibitor) was applied in some experiments. Nile red staining was used to confirm that the brightest structures of round shape in THG images consist of lipids and probably represent lipid droplets that serve as energy deposits in hyphea.

A new holotomographic microscope for monitoring apoptotic cell behavior in vivo: a preliminary study

SARA SALUCCI[1], MICHELA BATTISTELLI[1], FRANCESCA SBRANA[2], DEBORA BURINI[1], SABRINA BURATTINI[1], PAOLO GIOVANNINETTI[2], ELISABETTA FALCIERI[1]

[1] Department of Biomolecular Sciences, Urbino University, Urbino; [2] IBF-CNR Genova Italy, Schaefer South-East Europe Srl

Holotomographic Microscopy (HT) represents a new approach to study cell behavior in different culture conditions.
HT, through optical diffraction tomography which reconstructs the 3D refractive index distribution of live cells, is able to investigate biological sistems by measuring in real time the volume of cells and subcellular components. In particular, structural and chemical informations, including dry mass, morphology, and dynamics of the cellular membrane, can be obtained. In this study, U937 monocytic cell lineage treated with apoptotic triggers [1] has been analysed *in vivo* with HT. Apoptosis represents indeed a cell model in which characteristic and reproducible cell changes have long been described by transmission electron microscopy (TEM, Figure 1A, B)
3D holotomographic images show the three-dimensional distribution of cell components, where the preservation of cytoplasm and nuclear structure in control condition (Figure 1C, E) appears clearly detectable. In treated cells (Figure 1 D-F), apoptotic features such as the modifications of plasma membrane, blebbing formation and the localisation of condensed chromatin, can be observed [2].
In addition, HT has permitted to monitor a chemical apoptotic compound inside of the cells, by identifying its site of action (observation in progress).
Therefore, HT, if compared to other conventional microscopical techniques, which present some limits and disadvantages, can be considered suitable to analyze cell biological processes without the need of cell markers, staining or the use high-intensity laser light. In conclusion, HT represents a noninvasive label-free light microscopy technology for investigating *in vivo* and in real time cell response against various stimuli.

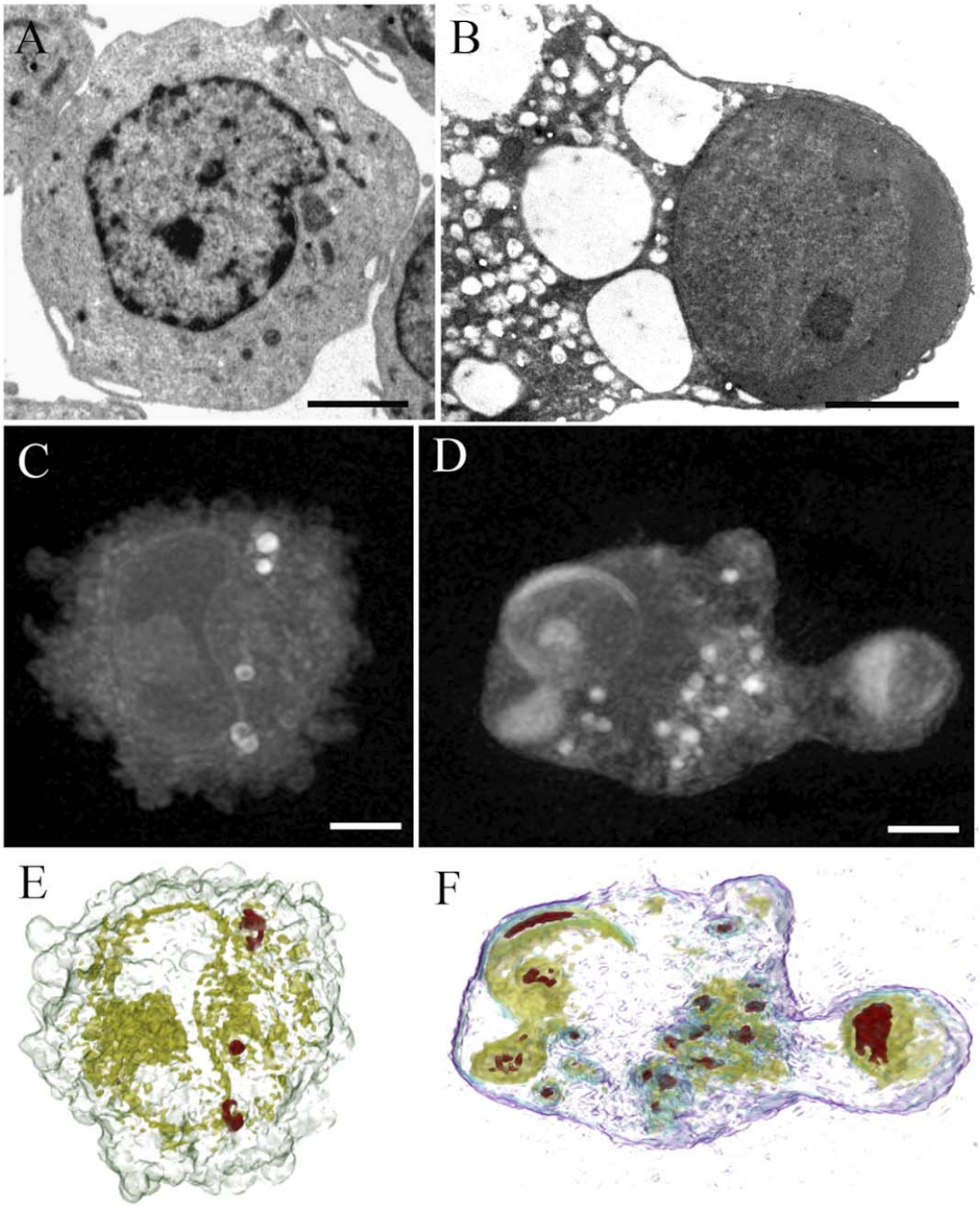

Figure 1. Control (A, C, E) and apoptotic (B, D, F) haemopoietic cells observed at TEM (A, B) and HT (C-F) in holographic (C, E) and 3D (D, F) modality. Bars: 2µm

References

[1] S. Salucci et al., Eur J Histochem, 12 (2018) 915–920

[2] S. Salucci et al., Int J Mol Sci, 15(2014) 6625-40

Fixation-induced cell blebbing: how to minimize a loss of soluble proteins from cells?

PAVEL HOZÁK[1,3], MARGARITA SOBOL[1], LUKÁŠ PASTOREK[1,2]

[1] Institute of Molecular Genetics, CAS, v.v.i., Department of Biology of the Cell Nucleus, Prague, Czech Republic; [2] Institute of Molecular Genetics, CAS, v.v.i., Electron Microscopy Core Facility, Prague, Czech Republic; [3] Institute of Molecular Genetics, CAS, v.v.i., Microscopy Centre, Prague, Czech Republic

In the course of the preparation of biological samples for various microscopy techniques, the first essential step is a fixation. Its efficiency is estimated by two main factors: the preservation of the cellular constituents and the suitability for further treatments like immunolabelling. However, till now the detailed mechanisms of the cell fixation are not fully understood and we rely mostly on empirical experiences. We concentrated here on the fixation-induced cell blebbing which is uselly missed, and searched for the way to minimize this deteriorating effect.
By means of different microscopy methods, we quantitatively assessed the loss of cytoplasmic content during the rupture of blebs. With holography microscopy time-lapse experiments, we found that the key points are the formation and rupture of blebs, and we discuss the possible mechanism of blebs appearance. Importantly, it was shown that up to 30% of soluble proteins can be lost from cytoplasm after the blebs rupture. Based on these data, we tested a wide range of fixation mixtures applied during different time intervals to minimize the loss of cytoplasmic proteins. Taking into account different quantitative parameters, we determined the optimal procedures to fix the cells. Finally, we provide some recommendations on the fixation protocols which are suitable for future experiments.

Keywords: formaldehyde fixation, blebbing, fixation artefacts, microscopy

We would like to thank for the financial support GACR (GA16-03346S, GA15-08738S); TACR (TE01020118); HFSP (RGP0017/2013); ERDF (CZ.1.05/1.1.00/02.0109, CZ.02.1.01/0.0/0.0/16 _013/0001775); CAS (JSPS-18-18); IMG (RVO:68378050). We acknowledge the Microscopy Centre - Light Microscopy Core Facility and Electron Microscopy Core Facility, IMG, CAS, Prague, Czech Republic, supported by MEYS (LM2015062), OPPK (CZ.2.16/3.1.00/21547), and (LO1419).

Effects of mild ozonisation on the dynamics of lipid droplets in adipose-derived stem cells and mature adipocytes

MANUELA COSTANZO[1], BARBARA CISTERNA[1], FLAVIA CARTON[1], VIVIANA COVI[2], GABRIELE TABARACCI[2] AND MANUELA MALATESTA[1]

[1] Department of Neurosciences, Biomedicine and Movement Sciences, Anatomy and Histology Section, University of Verona, Italy; [2] San Rocco Clinic, Montichiari (BS), Italy

1. Introduction

In the last decades, the medical use of gaseous ozone (O_3) has been progressively increasing as an alternative/adjuvant treatment for several diseases. In particular, low O_3 concentrations proved to induce the so-called eustress [1] by activating anti-oxidative response pathways [2] and stimulating cellular metabolism. In order to explore the potential of mild ozonisation in tissue regeneration and differentiation, we investigated the effects of low O_3 concentrations on lipid droplets (LDs) dynamics in human adipose-derived adult stem (hADAS) cells obtained from the stromal-vascular fraction of subcutaneous adipose tissue: the adipogenic process was monitored at early, intermediate and late differentiation steps in culture. Based on the obtained findings, we also investigated the effect of low O_3 concentrations on the LDs of mature adipocytes in the whole adipose tissue by treating murine fat explants maintained under *in vitro* conditions.

2. Materials and Methods

hADAS cells were isolated from the subcutaneous adipose tissue harvested by liposuction, and grown in adipogenic medium [3]. The cells were exposed to air (control), O_2 or to 5, 10 or 20 µg O_3/mL O_2 at early (6 days), intermediate (16 days) and late (20 days) differentiation steps, and the effects were evaluated 2 h and 24 h after gas exposure. After 6 days in differentiation medium, cell viability was estimated by the Trypan blue exclusion test 2 h and 24 h after gas treatment. 20 µg O_3/mL was found to significantly increase cell death, suggesting that excessive concentrations of O_3 induce the formation of high levels of reactive oxygen species: this concentration was therefore excluded from the subsequent experiments. Oil Red O staining was used to visualize LDs at light microscopy (LM). 2 h and 24 h after gas treatment, randomly selected cells grown in adipogenic medium were measured to evaluate the percentage of cytoplasmic area covered by LDs, the mean LD areas, and LD size distribution. 24 h after treatment, hADAS cells were processed for conventional morphology at transmission electron microscopy (TEM).

Mice were killed by over-anaesthesia, and the visceral adipose tissue was excised, cut in small (1-2 mm^3) pieces and placed in culture medium [4]. After 2 days, the samples were exposed to air, O_2, 10, 20 and 100 (as highly oxidizing condition) µg O_3/mL. The effects were evaluated 2 h and 24 h after gas exposure, processing the samples for the spectrophotometric evaluation of lactate dehydrogenase (LDH), or for scanning EM (SEM) and TEM.

3. Results and conclusions

In hADAS cells, exposure to 5 and 10 µg O_3 /mL proved to be safe at both short and long term post treatment. At day 6, hADAS cells contained a few small LDs, but cells exposed to 10 µg O_3/mL showed the highest values of mean LD area and lipid percentage. At day 16, hADAS cells contained numerous LDs (Figure 1a); in cells treated with O_2, 5µg or 10 µg O_3/mL, a decreased mean LD area was observed, while cells treated with 10 µg O_3/mL showed an increase in lipid percentage. At day 20, hADAS cells contained a large number of LDs; treatment with 10 µg O_3/mL significantly increased both the LD area and lipid percentage. No ultrastructural alterations were found in hADAS cells following ozonization, but LDs fusion was frequently observed (Figure 1b). In conclusion, the treatment with low O_3 concentrations proved to stimulate lipid accumulation

during the adipogenic differentiation *in vitro* of hADAS cells, without altering their differentiation process or ultrastructural cytoarchitecture.
In explanted adipose tissue, LDH evaluation revealed that both 10 and 20 µg O_3/mL induced a low cytotoxicity (below 3%) at 2 h in comparison to the control, while at 24 h no cytotoxic effect was observed as LDH did not increase. On the contrary, 100 µg O_3/mL treatment was expectedly very toxic at all time points. SEM revealed that control samples were always well preserved showing roundish adipocytes with smooth surfaces, while 10 and 20 µg O_3/mL induced a slight adipocyte wrinkling after 2 h from gas exposure. Accordingly, TEM showed small LDs budding from the large unilocular LD of mature adipocytes (Figure 1c), suggesting a delipidation process; however, no organelle damage was observed. In conclusion, the treatment with low O_3 concentrations probably induced a mild oxidative stress responsible for rapid LDH release and slight delipidation, but after 24 h from the gas exposure most alterations disappeared.
The results of these pilot experiments pave the way to further studies aimed at elucidating the effect of mild ozonisation on adipose tissue, in the attempt to design novel strategies for tissue regeneration/activation in reconstructive surgery and tissue engineering.

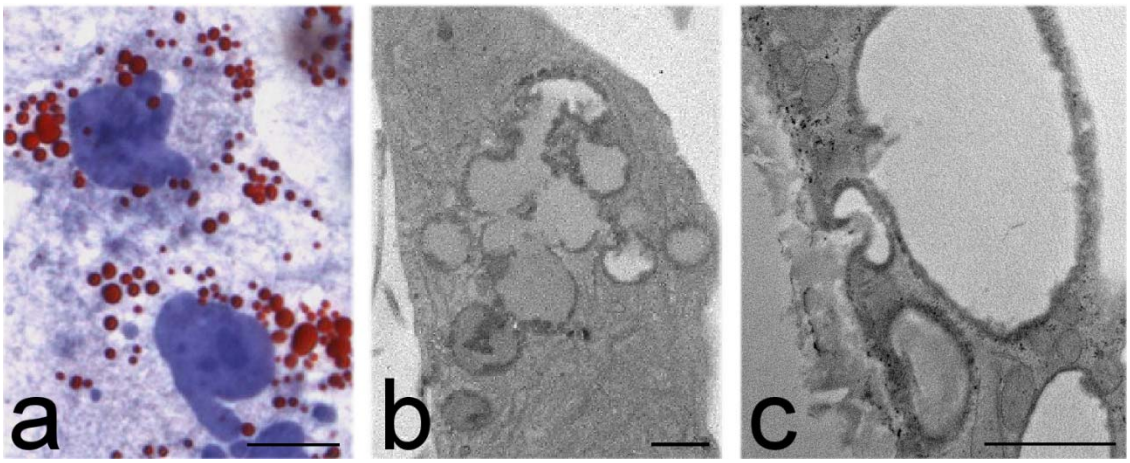

Figure 1. a,b) Differentiating hADAS cells at LM and TEM: a) LDs are stained with Oil Red O; b) LDs are fusing (modified from [3]). c) Mature murine adipocytes at TEM: small LDs occur in the cytoplasm as a result of the delipidation process. Bars: 20 µm (a), 2 µm (b,c).

4. Acknowledgments
This work was supported by the University of Verona (Joint Projects 2017).

References
[1] E. Niki, Arch. Biochem. Biophys., 595 (2016) 19–24
[2] M. Galiè, M. Costanzo, A. Nodari, F. Boschi, L. Calderan, S. Mannucci, V. Covi, G. Tabaracci, M. Malatesta, Free Radic. Biol. Med., 124 (2018) 114–121
[3] M. Costanzo, F. Boschi, F. Carton, G. Conti, V. Covi, G. Tabaracci, A. Sbarbati, M. Malatesta, Eur. J. Histochem., 62 (2018) 2969
[4] K. A. Carswell, M. J. Lee, S. K. Fried, Methods Mol. Biol., 806 (2012) 2013–2214

Impact of Endothelial Lipase Modified HDL on eNOS trafficking and activity in endothelial cells

SNJEŽANA RADULOVIĆ[1], BENJAMIN GOTTSCHALK[1], PABLO ZARDOYA LAGUARDIA[1], IRENE SCHILCHER[1], MARKUS TRIEB[2], DAGMAR KRATKY[1], GUNTHER MARSCHE[2], WOLFGANG F. GRAIER[1], KURT SCHMIDT[3], SAŠA FRANK[1]

[1] Gottfried Schatz Research Center, Molecular Biology and Biochemistry, Medical University Graz, Graz, Austria; [2] Otto Loewi Research Center, Division of Pharmacology, Medical University of Graz, Graz, Austria; [3] Institute of Pharmaceutical Sciences, University of Graz, Graz, Austria

Background and Aim

Endothelial lipase (EL) is an established determinant of structural and functional properties of HDL, a modulator of endothelial nitric oxide synthase (eNOS) trafficking and activity. We examined the impact of EL-modified HDL (EL-HDL) on eNOS.

Methods and Results

EL-HDL was isolated by ultracentrifugation from human serum incubated with EL-overexpressing HepG2 cells. Compared to control HDL, EL-HDL was smaller in size (NMR-spectroscopy) and exhibited altered lipid composition (mass spectrometry). Experiments in Ea.hy926 cells revealed a slower endocytosis rate of the ATTO-labelled EL-HDL and no colocalization of labelled EL-HDL or control HDL with eNOS-GFP. Cell membrane cholesterol content of Ea.hy926 cells (filipin staining and intensiometric widefield measurements) and cholesterol efflux from ^{3}H-cholesterol labelled Ea.hy926 cells exposed to EL-HDL were lower compared to control HDL. As revealed by confocal spinning disk and structured illumination microscopy, incubation of cells with EL-HDL resulted in a lower translocation of eNOS-GFP to the perinuclear region, a lower colocalization of eNOS-GFP with mitochondria and Golgi apparatus and a higher colocalization of eNOS-GFP with plasma membrane when compared to control HDL. Importantly, incubation of cells with EL-HDL resulted in a higher eNOS activity (conversion of L-[^{3}H]arginine into L-[^{3}H]citrulline), accompanied by increased Ser-1177 and decreased Thr-495 eNOS-phosphorylation. Myography measurements using mouse aortic rings revealed augmented eNOS-dependent vasorelaxing capacity of EL-HDL compared to control HDL.

Conclusion

EL-modification of HDL decreases HDL endocytosis accompanied by a decreased cell membrane cholesterol content and altered eNOS trafficking as well as increased eNOS activity and HDL vasorelaxing capacity.

LS2
Structure and imaging of biomolecules

CHAIRPERSONS:

Sevinc Inan, Tea Pavkov-Keller

INVITED LECTURE

The advantages and limitations of advanced imaging for biological structures in live and fixed cells

SERCIN KARAHUSEYINOGLU, MD

Asst. Prof. Koç University School of Medicine, Department of Histology & Embryology, Istanbul, Turkey; Co-director, Cellular and Molecular Imaging Center, Koç University Research Center for Translational Medicine (KUTTAM), Istanbul, Turkey

TOPIC

The microscopic imaging of cellular and subcellular structures is at utmost importance for understanding the scientific facts related to biological phenomena. As biological structures range from micron to nano scales, it is not always easy to identify each of them solely and separately. Advances in microscopy enables scientists to detect the intra and extra cellular biological structures more precisely and to visualize the dynamic processes on a time based manner. The focus of this presentation is to reveal the benefits of using advanced microscopy techniques, while demonstrating the possible disadvantages.

THE OBJECTIVES

Although electron microscopy has the highest resolving power for biological samples, use of fluorescence based system has the advantage of labeling of multiple structures at a time to enable the visualization of interactions between cellular structures. Live-cell imaging is another important advantage of fluorescence based systems. In order to reveal the advantages and limitations of microscopic imaging human mesenchymal stem cells, mouse blastocysts, human cell spheroids, spermatozoa, thick sections of brain tissue, cleared brain, zebrafish were labeled by multiple fluorochromes and/or fluorescent proteins to be visualized as fresh or fixed under conventional confocal, lightsheet, multiphoton and super-resolution (STED) microscopes. The thickness of the samples at z-axis varied from from 2000 to 2 micrometers and the samples were marked for structures at different sizes ranging from a couple of millimeters to 20-40 nm. Time-lapse imagings focused on visualization of fluorescent protein labeled structures in cells, organs and organisms for hours to days. To achieve a satisfactory result that produces the reliable and relevant information related to biology, experimental set up for imaging should be designed carefully to avoid the pitfalls of imaging.

INVITED LECTURE

Architecture and modular assembly of the Sulfolobus S-layer revealed by electron cryo-tomography

LAVINIA GAMBELLI[1,3], BENJAMIN MEYER[2], MATHEW MCLAREN[1,3], KELLY SANDERS[1,2], TESSA E.F. QUAX[2], VICKI GOLD[1,2], SONJA-VERENA ALBERS[2] AND BERTRAM DAUM[1,2]

[1] Living Systems Institute, University of Exeter, Exeter, United Kingdom; [2] College of Life and Environmental Sciences, University of Exeter, Exeter, United Kingdom; [3] College of Engineering, Mathematics and Physical Sciences, University of Exeter, Exeter, United Kingdom; [4] Institute of Biology II, Molecular Biology of Archaea, University of Freiburg, Freiburg, Germany

Surface protein layers (S-layers) often form the only structural component of the archaeal cell wall and are therefore important for cell survival. S-layers have a plethora of cellular functions including maintenance of cell shape, osmotic and mechanical stability, the formation of a semi-permeable protective barrier around the cell, cell-cell interaction, as well as surface adhesion. Despite the central importance of the S-layer for archaeal life, their three-dimensional architecture is still poorly understood. Here we present the first detailed 3D electron cryo-microscopy maps of archaeal S-layers from three different *Sulfolobus* species. We were able to pinpoint the positions and determine the structure of the two subunits SlaA and SlaB. We also present a model describing the assembly of the mature S-layer.

Mode of action of membrane-active compounds: a biophysical study combining electron and fluorescence microscopy on life bacteria

NERMINA MALANOVIC[1#], AYSE ÖN[1] AND KARL LOHNER[1]
[1] University of Graz, Institute of Molecular Biosciences, Biophysics Division, Graz, Austria

With increasing antimicrobial resistance worldwide discovering of novel drugs against multi-drug resistant (pathogenic) bacteria gained enormous research interest. Compounds that kill bacteria within minutes based on non-receptor-mediated mechanism like membrane perturbation as described for antimicrobial peptides are considered as promising candidates in preventing resistance development. In our studies we used such compounds to identify and characterize their membrane activity in order to design compounds with improved activity and specificity. Besides of their rapid killing of a wide variety of bacteria, they induce severe changes affecting membrane integrity of *Escherichia coli*, used in our studies as a model system for Gram-negative bacteria. *E. coli* is surrounded by two distinct membranes: The inner membrane is primarily composed of phospholipids (PL), whereas the outer membrane is characterized by a bilayer build up by PLs in the inner and lipopolysaccharides (LPS) in the outer leaflet. The effects observed with our compounds primarily include interaction with the inner membrane PLs inducing membrane permeabilization in model systems mimicking bacterial inner membranes. In agreement with the model systems, increased permeability and depolarization of the bacterial inner membrane and changes in membrane fluidity were observed using spectroscopic and microscopic techniques on life bacteria. Using ELMI we detected also alterations of cell morphology affecting *E. coli* inner but also outer membrane as well as the cytosolic compartment. In addition, neutralization of surface charge and antimicrobial susceptibility assay of mutants defective in production of full-length LPS confirmed multi-step interactions of such compounds.

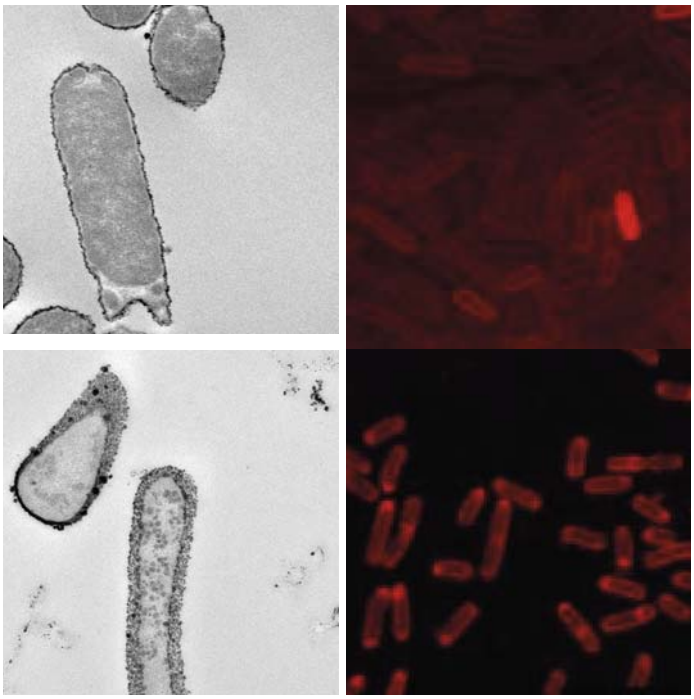

Figure 1. Membrane active compounds showing alterations of cellular morphology (left panels) and membrane fluidity using Nile Red (right panels) of *Escherichia coli*.

Ultrastructural arrangement of cadherin dimers at cell-cell adhesion sites revealed by electron tomography

WALTER A. KAUFMANN[1], CHRISTOPH SOMMER[1], MATEUSZ DOBRYCHLOP[2], LUDEK LOVICAR[1], CARL-PHILIPP HEISENBERG[1] AND MATEUSZ SIKORA[3]

[1] Institute of Science and Technology-Austria, Klosterneuburg, Austria; [2] Laboratory of Bioinformatics, Institute of Molecular Biology and Biotechnology, Adam Mickiewicz University, Poznan, Poland; [3] Theoretical Biophysics Group, Max Planck Institute for Biophysics, Frankfurt am Main, Germany

Early stage cadherin-containing cell-cell adhesion sites were studied in germ layer progenitor cells from Zebrafish after epoxy resin embedding. Such adhesion sites represent adherens junctions of different strength and size depending on cell type and cortical tension. Previous studies on cultured cells provided evidence that tension at adherens junctions promote cadherin clustering [1]. Here, we aimed to reveal the ultrastructural arrangement and quantity of cadherin molecules at cell-cell adhesion sites. We showed that changes in cortex tension affect the packing and topology of cadherin molecules at the junction sites interfaces, and that these clusters fuse upon myosin-II-dependent tension increase induced by lysophosphatidic acid treatment.

Progenitor cells from freshly dissociated dome-stage Zebrafish embryos were first allowed to form spontaneous contacts and adhere to carbon-coated sapphire disks. Samples were high-pressure frozen in the HPM-010 machine and freeze-substituted in the AFS1 device, both from Leica Microsystems. Samples were then Epon embedded, sliced at 70-250 nm thickness and mounted on formvar coated 200-line bar grids. They were observed under a JEM 2800 STEM (Jeol) operated at 200 kV in STEM bright-field and TEM mode, respectively. For recording of image tilt series in STEM mode, V3 Recorder and Magica Controller were employed (both System in Frontier Inc.). For TEM image recording, TVIPS TemCam XF416 and EMMENU software 5.0.10 were used (TVIPS GmbH). In either case, images were collected at 2° intervals between +/-74° of actual single tilt axis. Images were aligned by cross-correlation and 3D structure computed by weighted back-projection.

In order to extract the electron density maps of adherens junctions (Fig. 1A and B), progenitor cell plasma membranes were segmented using a U-Net architecture [2], a fully convolutional neural network (FCNN). A training set of 32x32px patches (n=852) of plasma membrane bilayer and background structures was manually annotated, and the FCNN was optimized with stochastic gradient descent. The trained network was used to predict the location of cell plasma membranes in the entire stack. A three-dimensional quadratic surface was fitted to each of the cell's plasma membranes and the density maps of enclosed regions were extracted, narrowed by the size of the protoplasmic membrane leaflet. Raw electron tomography stacks were denoised by 3D Gaussian filtering and rotated for rough horizontal junction alignment (Fig. 1C). Resulting density maps were segmented using the "segment map" feature available in the UCSF Chimera software to extract density segments corresponding to assemblies of cadherins. Quantitative content of cadherin dimers for each assembly was then assessed using macromolecular modeling software PyRy3D (www.genesilico.pl/pyry3d). Atomic structure of the protein was fitted to the density

segments in different number of copies in order to find a quality of fit threshold that could help estimate the content of cadherin dimers corresponding to each assembly (Fig. 1D).

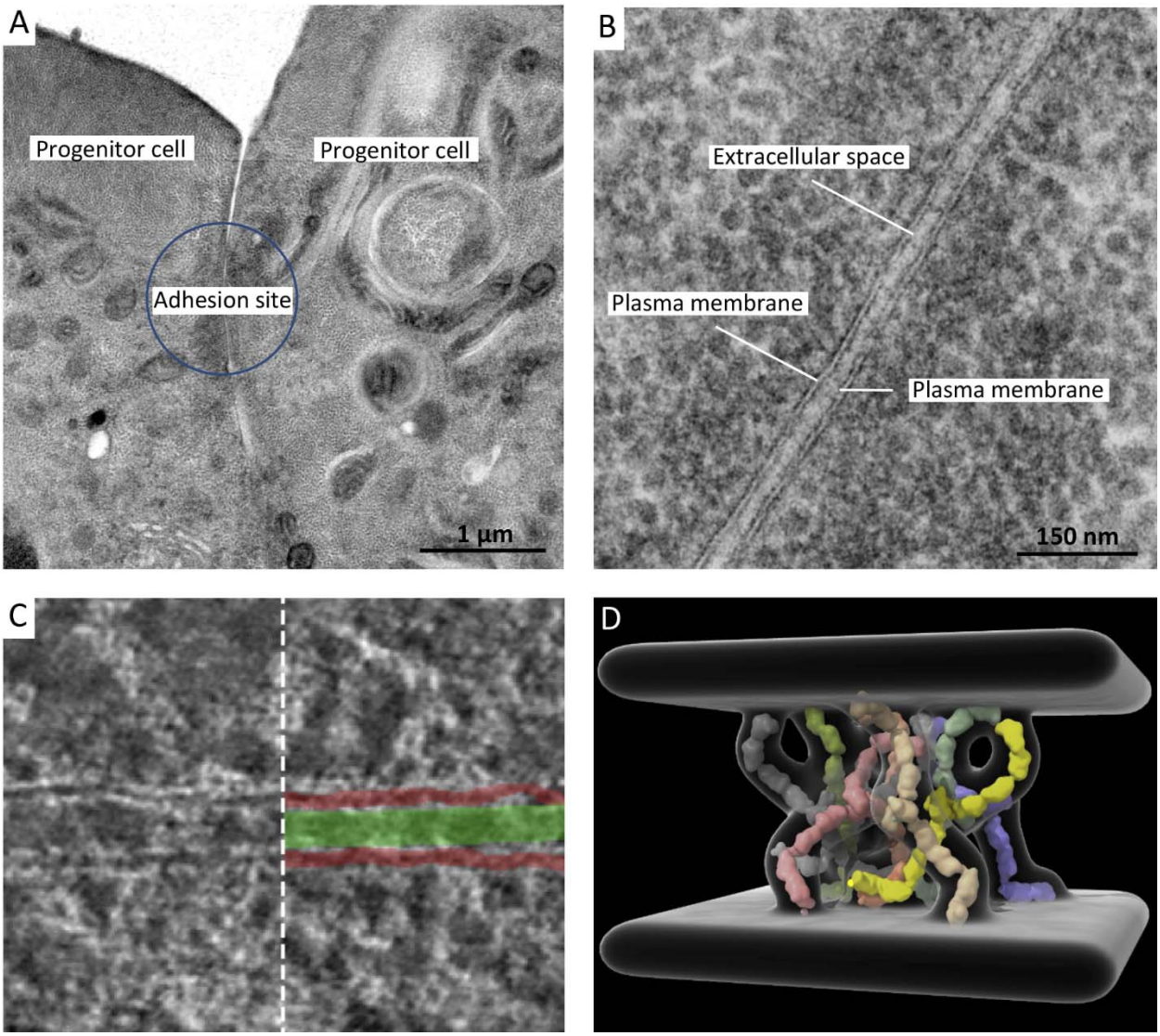

Figure 1A: Overview STEM image of an adhesion site between two progenitor cells. B: Cell-cell contact at higher magnification revealing the architecture of adherens junctions. C: Section through the tomographic reconstruction after post-processing indicating the predicted location of cell plasma membranes (red overlay) and enclosed region (extracellular space; green overlay). D: Synthetic density map of a predicted cadherin cluster derived from tomographic data with fitted cadherin atomic structure.

References

[1] W. Engl, B. Arasi, L. L. Yap, J. P. Thiery, V. Viasnoff. Nat Cell Biol, 16 (2014) 587-594
[2] T. Falk, D. Mai, R. Bensch, Ö. Çiçek, A. Abdulkadir, Y. Marrakchi, A. Böhm, J. Deubner, Z. Jäckel, K. Seiwald, A. Dovzhenko, O. Tietz, C. Dal Bosco, S. Walsh, D. Saltukoglu, T.L. Tay, M. Prinz, K. Palme, M. Simons, I. Diester, T. Brox, O. Ronneberger. Nat Methods, 16 (2019) 67-70

Regioselective para-Carboxylation of Catechols by a Prenylated Flavin Dependent Decarboxylase

STEFAN E. PAYER[1]*, STEPHEN A. MARSHALL[2]*, NATALIE BÄRLAND[3], XIANG SHENG[4], TAMARA REITER[1,5], ANDELA DORDIC[6], GEORG STEINKELLNER[5,6], CHRISTIANE WUENSCH[1,5], SUSANN KALTWASSER[3], JANET VONCK[3], KARL GRUBER[5], KURT FABER[1], FAHMI HIMO[4], DAVID LEYS[2], SILVIA M. GLUECKA[1], TEA PAVKOV-KELLER[6]

[1] Department of Chemistry, Organic & Bioorganic Chemistry, University of Graz, Austria; [2] Manchester Institute of Biotechnology, University of Manchester, UK; [3] Max-Planck Institute of Biophysics, Frankfurt/Main, Germany; [4] Department of Organic Chemistry, Arrhenius Laboratory, Stockholm University, Sweden; [5] Austrian Centre of Industrial Biotechnology (ACIB), Graz, Austria; [6] Institute of Molecular Biosciences, University of Graz, Austria; * Contributed equally

The utilization of CO2 as carbon source for organic syntheses meets the urgent demand of more sustainability in chemical production. Here we report on the enzyme-catalyzed para-carboxylation of catechols, employing 3,4-dihydroxybenzoic acid decarboxylases (AroY). The 4.6 Å cryo-EM and X-ray structures confirm AroY utilizes the recently discovered prenylated FMN cofactor (prFMN), and requires oxidative maturation to form the catalytically competent prFMNiminium species. The enzymes form hexameric assemblies, arranged as a trimer of dimers. Structural overlays between apo- and holo-AroY structures reveal two mobile loops and an open conformation for this group of enzymes. Combined with mutational studies and quantum chemical calculations, a reaction mechanism for the reversible decarboxylation involving a quinoid intermediate is proposed.

Acknowledgments: This work has been supported by the Austrian BMWFJ, BMVIT, SFG, Standortagentur Tirol and ZIT through the Austrian FFG-COMET-Funding Program. Financial support by the Austrian Science Fund (FWF, projects P26863 and P29432), the BBSRC grant BB/K017802/1 and a BBSRC iCASE studentship to S.A.M. is gratefully acknowledged. D.L. is a Royal Society Wolfson Merit Award holder.

References

[1] S.E.Payer, S.A. Marshall, N. Bärland, X. Sheng, T. Reiter, A. Dordic, G. Steinkellner, C. Wuensch, S. Kaltwasser, K. Fisher, S. E. J. Rigby, P. Macheroux, J. Vonck, K. Gruber, K. Faber, F. Himo, D. Leys, T. Pavkov-Keller* and S. M. Glueck*, *Angew Chem Int Ed Engl.* 2017; 56(44): 13893-7. doi:10.1002/anie.201708091

Wortmannin induced apoptosis via autophagy inhibition in 4T1 breast cancer cell line

ELGIN TURKOZ ULUER[1], PINAR KILICASLAN SONMEZ[1], DAMLA AKOGULLARI[1] AND SEVINC INAN[2]

[1] Manisa Celal Bayar University, Faculty of Medicine, Department of Histology and Embryology, Manisa, Turkey; [2] Izmir University of Economics, Faculty of Medicine, Department of Histology and Embryology, Izmir, Turkey

1. Introduction

Autophagy plays an important role in the responses of tumor cells to stress. Cells contribute to the survival of the cancer cell and its resistance to chemotherapy by disrupting cytoplasmic proteins to save energy and remove dangerous substances through autophagy [1]. The mTOR kinase pathway must be activated in order for the autophagy to be effective. The autofagosome is then formed by a series of molecular events involving MAP LC3 β lipid conjugation. The autophagosome matures by fusing with lysosomes to create autophagolysosomes where its selected cargo is degraded. The lysosome-associated membrane protein (LAMP) is essential for the fusion of autophagosomal-lysosome during autophagy [1,2]. In this study, we aimed to investigate the lysosomal pathway of autophagy of Wortmannin, which is a PI3K inhibitor in 4T1 mouse breast cancer cell line.

2. Material and Methods

4T1 mouse breast cancer cells were purchased from the American Type Culture Collection (ATCC) (Manassas, VA, USA) and cultured in Dulbecco's Modified Eagle Medium: Ham's F-12 medium (1:1) containing 10% fetal bovine serum (FBS), 1% penicillin-streptomycin, 0.5% Non-essential amino acids (NEAA), 1% L-glutamine at 37°C in a humidified incubator containing 5% CO_2.

Cytotoxicity of Wortmannin on 4T1 breast cancer cells was measured by the MTT assay. The assay was done in triplicate and the cytotoxicity effect and IC50 value of Wortmannin was analyzed. After the 4T1 breast cancer cells were plated into the 24-well cell culture plate, the IC50-determined Wortmannin dose (10nM) was added to each well. After 24 hours of incubation, cells were fixed with 4% paraformaldehyde. Cells were maintained for 15 minutes on ice in triton X-100 solution after washing with PBS and then they were treated with 3% H_2O_2 for 5 min to inhibit endogenous peroxidase activity. After washing with PBS, the cells were treated with 1 hour blocking solution. Cells were incubated overnight with the primary antibodies LAMP1 and MAP LC3 β. Then cells were incubated with anti-mouse biotin-streptavidin hydrogen peroxidase secondary antibody for 30 minutes. The cells were stained with DAB for 5 min to determine the visibility of the immunocytochemical reaction. After counterstaining with Mayer's hematoxylin, the cells were coated with the mounting medium.

In addition to determine cell death, terminal deoxynucleotidyl transferase dUTP nick end labeling (TUNEL) assay was used to evaluate apoptosis in 4T1 breast cancer cells. Cells were fixed with 4% paraformaldehyde for 30 min. Next, they were permeabilized with 0.1% Triton-X-100 for 2 min on ice. TUNEL staining was performed according to the manufacturer's instructions of ApopTag® Peroxidase In Situ Apoptosis Detection Kit (Millipore, Massachusetts, USA). Then the results were analyzed under a light microscope (OLYMPUS BX43, Tokyo, Japan) and the apoptotic cell number was determined per square millimeter. The results were evaluated statistically.

3. Results

In the immunocytochemical analysis of Wortmannin-treated 4T1 breast cancer cells, LAMP1 and MAP LC3 β immunostanings decreased significantly compared to the control group. As seen in these results, the decrease in the expression level of MAP LC3 β and LAMP1, which play a role in autophagosome formation, supports the inhibition of autophagy in Wortmannin on 4T1 breast cancer cells (Figure 1). According to TUNEL assay results the number of TUNEL positive cells was greater in the Wortmannin-treated group compared to the control group (Figure 1).

	LAMP1	**MAP LC3 B**	**TUNEL**
Control	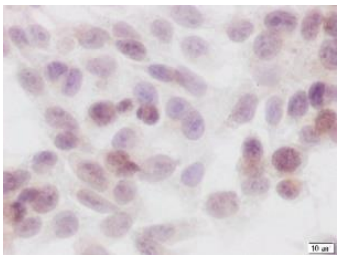	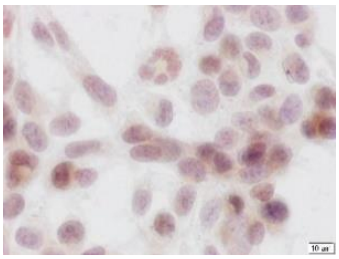	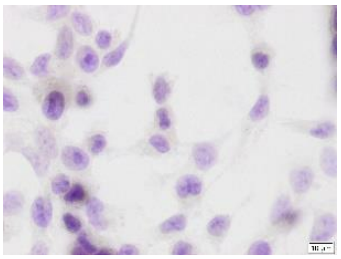
Wortmannin	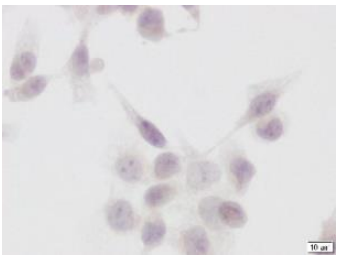	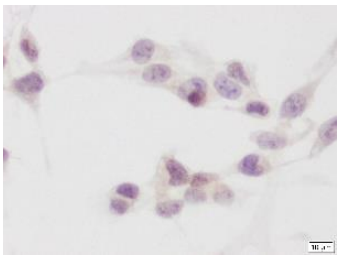	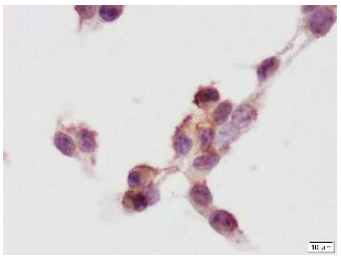

Figure 1. The immunocytochemistry stainings of LAMP1, MAP LC3 β and TUNEL assay of 4T1 mouse breast cancer cells.

4. Conclusion

Autophagy is the main mechanism for cell protein degradation. In cancer cells, autophagy has dual roles, both acting as a tumor suppressor and as a cell survival mechanism capable of promoting the growth of established tumors, avoiding the accumulation of damaged proteins and excess organelles [3]. In a study conducted with an early autophagy inhibitor effective on breast cancer cells, it was shown that LC3-II levels decreased in breast cancer cells in early autophagy inhibition [4]. In accordance with this, in our study, it was shown that MAP LC3 β expression levels were significantly reduced compared to the control group, supporting the inhibition of autophagy in 4T1 cells treated with Wortmannin.

The maturation of the autophagosome occurs by the fusion of the autophagolysosome with lysosomes, in which the selected cargo is degraded. In this process the lysosome-associated membrane protein (LAMP) is essential for the autophagosome lysosome fusion during autophagy [2]. In a study to investigate the effects of β-cypermethrin known to be a late-stage inhibitor of autophagy exposure to mouse macrophages, a reduction in LAMP1 expression was shown due to the late inhibition of autophagy [5]. In our study, a decrease in the level of LAMP1 expression in the Wortmannin-treated group was considered to be an indication of the late inhibition of autophagy.

Together, these findings suggest that Wortmannin, a PI3K inhibitor, affect the lysosomal pathway of autophagy and induce apoptotic cell death of breast cancer cells.

Therefore, further research is needed to elucidate the effect of Wortmannin on molecular signaling mechanisms involved in apoptotic cell death pathways and autophagy in cancer cell lines.

References

[1] Yu L, Chen Y, Tooze SA. Autophagy pathway: Cellular and molecular mechanisms. Autophagy. 2018;14(2):207-215. doi: 10.1080/15548627.2017.1378838.
[2] Babuta M, Furi I, Bala S, Bukong TN, Lowe P, Catalano D, Calenda C, Kodys K, Szabo G. Dysregulated autophagy and lysosome function are linked to exosome production via miR-155 in alcoholic liver disease. Hepatology. 2019 May 15. doi: 10.1002/hep.30766.
[3] Martini-Stoica H, Xu Y, Ballabio A, Zheng H. The Autophagy-Lysosomal Pathway in Neurodegeneration: A TFEB Perspective. Trends Neurosci. 2016 Apr;39(4):221-234. doi: 10.1016/j.tins.2016.02.002.
[4] Castagnola P, Bellese G, Birocchi F, Gagliani MC, Tacchetti C, Cortese K. Identification of an HSP90 modulated multi-step process for ERBB2 degradation in breast cancer cells. Oncotarget. 2016 Dec 20;7(51):85411-85429. doi: 10.18632/oncotarget.13392.
[5] He, B., Wang, X., Zhu, J., Kong, B., Wei, L., Jin, Y., & Fu, Z. (2019). Autophagy protects murine macrophages from β-cypermethrin-induced mitochondrial dysfunction and cytotoxicity via the reduction of oxidation stress. Environmental pollution, 250, 416-425. doi: 10.1016/j.envpol.2019.04.044

Protective effect of melatonin on the morphology of testis tissue of diet-induced obese rats: microscopical and biochemical investigations

NILSU ATAY[1], MERVE AÇIKEL ELMAS[1], HANDE YAPIŞLAR[2], ÖZLEM BINGÖL ÖZAKPINAR[3], FIKRIYE URAS[3], SERAP ARBAK[1]

[1] Acıbadem Mehmet Ali Aydınlar Univ.School of Medicine, Department of Histology and Embryology, Istanbul, Turkey; [2] Acıbadem Mehmet Ali Aydınlar University, School of Medicine, Department of Physiology, Istanbul, Turkey; [3] Marmara University, School of Pharmacy, Department of Biochemistry, Istanbul, Turkey

1. Background and Objective: It is known that obesity negatively affects male fertility [1]. There are many publications showing that melatonin supplementation, which play a role in the regulation of internal biological clock and energy metabolism and acts as an antioxidant agent, has beneficial effects on obesity and obesity-related complications [2]. The aim of this study is to investigate the effect of melatonin, a strong antioxidant, on the morphology and oxidative stress markers of testicular tissue of high fat diet induced obese rats, by histochemical, immunohistochemical and biochemical methods.

2. Materials and Methods: 32 Wistar albino male rats were fed with standard (STD group; 6% fat containing feed) or high fat diet (HFD group; 45% fat containing feed) for 13 weeks. Half of these animals were given melatonin (25 µg/ml) in drinking water. At the end of the experiments, testis tissues taken under deep anesthesia were prepared for routine light and electron microscopic examinations and biochemical analysis, blood samples taken from heart were prepared for biochemical analysis. Following hematoxylin-eosin (H&E) and periodic acid-Schiff (PAS) stainings, seminiferous tubules were scored as normal, regressive, degenerative and atrophic. ZO-1 and TUNEL immunohistochemistry were also applied to the tissue samples. Malondialdehyde, glutathione, IL-6 and TNF-α and SOD, testosterone, glucose, triglyceride, FSH, LH, and leptin levels were determined in tissue and blood serum samples. Animals were weighed regularly during the experiment and all data were analyzed statistically.

3. Results: Based on the histopathological scoring, regular seminiferous tubule morphology was observed in STD and STD+MEL groups. Increased number of regressive and degenerative tubules, impairment of basement membrane, and significant cell debris in the lumen of the seminiferous tubule were among the important morphological findings in HFD group. Seminiferous tubule reflected normal tubular morphology in HFD+MEL group. While ZO-1 immunoreactivity was higher in STD, STD+MEL and HFD+MEL groups, HFD group showed a weak ZO-1 immunoreactivity. TUNEL positive cells were few in STD, STD+MEL, HFD+MEL compared to HFD group. In HFD group, a prominent increase in glucose, triglyceride, MDA, leptin levels and significant decrease in GSH, FSH, LH and testosterone levels including SOD activity, were observed. In HFD+MEL group, all these histological and biochemical findings seemed to be ameliorated compared to the HFD group.

4.Conclusion: In conclusion, this study shows that obesity deteriorated seminiferous tubule structure by causing an oxidant effect and melatonin administration prevented testis tissue degeneration by reducing reactive oxygen species.

This study was supported by Acıbadem Mehmet Ali Aydınlar Univ. (No: 2017/01/11)

References

[1] W.J. Yan, Y. Mu, N. Yu, T.L. Yi, Y. Zhang, X.L. Pang, D. Cheng, J. Yang. J of Assisted Reproduction and Genetics, 32 (2015) 1097-1104.

[2] M. Koziróg, A.R. Poliwczak, P. Duchnowicz, M. Koter-Michalak, J. Sikora, M. Broncel. J of Pineal Research, 50 (2011)261-266.

LS3

Microscopic applications in symbiotic interactions, plants, microorganisms, and environmental sciences

CHAIRPERSONS:

Hrvoje Fulgosi, Sonja Duletić Laušević

INVITED LECTURE

Microscopy and palynology side by side - case study of palaeoenvironmental conditions in the past on the area of Central Croatia

DARIO HRUŠEVAR[1], KORALJKA BAKRAČ[2], SLOBODAN MIKO[2], NIKOLINA ILIJANIĆ[2], OZREN HASAN[2] AND BOŽENA MITIĆ[1]

[1] University of Zagreb, Faculty of Science, Department of Biology, Division of Botany, Zagreb, Croatia; 2 Croatian Geological Survey, Zagreb, Croatia

Palynology is an interdisciplinary scientific discipline related to the study of palynomorphs – microscopic structures between 5 and 500 micrometres in size. Palynology sensu stricto is a study of plants pollen and spores. However, its objects of interests are also fungal spores, algal cysts, and zoological remains – all microscopic organic structures which can be observed and analysed on 'pollen' slides [1, 2]. The role of a microscope in palynology is more than obvious – microscopic structures can be determined (or better said, interpreted) and counted only by the use of a light and/or electronic microscope. An electron microscope is significantly important in phylogenetic questions – e.g. the explanation of pollen/spores morphology and taxonomical level/relationships between plants [3]. However, in a paleoenvironmental analysis and reconstruction, a light microscope is routinely used. The focus of this lecture is on pollen, spores and non-pollen palynomorphs (fungal, algal and zoological micro remains), which are usually used to interpret the vegetation history and local changes in hydrological and trophic levels on a certain researched area. The sediment from the biggest mire in Croatia – Blatuša (central continental Croatia), which was cored during the year 2015 served as a case study. Namely, the peat is a very good palynomorphs trap, because its low pH values and reductive conditions allowed good preservation of palynomorphs. Except palynomorphs, in the 210 cm long core sediment of the Blatuša mire, charcoal particles were also detected and analysed, as evidence of fire activities. As the final result, the interpretation of vegetation dynamics and environmental changes during the Holocene period in the narrow area of Central Croatia was based on the analysis of 31.036 pollen palynomorphs (76 palynological taxa), 1.318 non-pollen palynomorphs and 13.970 charcoal particles [4]. According to the age-depth model, the environmental history of the researched area can be traced back to ~9800 cal yrs. before present. On the regional level, during the first thousand years pine (*Pinus*) dominated in the woodlands, later on succeeded by beech-alder (*Fagus-Alnus*) forests, which dominated most of the time, and only in the Modern Period was succeeded by hornbeam (*Carpinus*). Furthermore, on the local level the next transition was observed: from the sedge dominated mire, through the alder carr with peatland dominated vegetation, and again the sedge dominated mire. Primary anthropogenic indicators, like Cereal pollen, were for the first time observed quite late, in the 15th century. However, one century earlier secondary anthropogenic indicators have been frequent and continuously present in the pollen diagrams. To conclude, even though the high share of non-arboreal pollen type was observed from the 6th century AD (Migration Period), direct human impact on vegetation can only be traced from the Late Middle Ages to the middle of the 20th century.

References

[1] A. Traverse, Paleopalynology (2007) 1-16
[2] H. Halbritter, S. Ulrich, F. Grímsson, M. Weber, R. Zetter, M. Hesse, R. Buchner, M. Svojtka, A. Frosch-Radivo, Illustrated Pollen Terminology (2018) 4
[3] S. Blackmore, Bot. Macaronésica, 23 (1996) 21-24
[4] D. Hruševar, PhD Dissertation (2018) 1-177

INVITED LECTURE

Microscopic techniques as an expedient tool for binding science and art

ŽELJKO SAVKOVIĆ, NIKOLA UNKOVIĆ, MILOŠ STUPAR, JELENA VUKOJEVIĆ, MILICA LJALJEVIĆ GRBIĆ

Institute of Botany and Botanical Garden „Jevremovac", Faculty of Biology, University of Belgrade, Belgrade, Serbia

Keywords: biodeterioration, fungi, cultural heritage, *in situ* microscopy, SEM-EDS

Microbial growth and proliferation are one of the principal causes of cultural heritage objects deterioration. Investigation of structural and aesthetic alterations of artworks frequently entrenches micromycetes as the main culprits, making mycological investigations mandatory in conservation science. Since initial biodeterioration assessments include the study of structural change and identification of potential biodeteriogens, the application of adequate microscopic techniques is the first step in the complex study of degradation mechanisms. In recent years, development and application of *in situ* optical microscopy provides scientists with the opportunity to study the cultural heritage artifact at the site, which is especially important concerning masonry and monuments. Therefore, it represents a practical contemporary method for rapid detection of biological deteriogens present in both natural environment and on cultural heritage objects. Application of non-invasive adhesive tapes, sterile swabs and contact dip-slides allows further assessments via the usage of stereomicroscopy and standard optical microscopy which are essential for the accurate characterization of micromorphology of the isolated species. Finally, scanning electron microscopy coupled with energy dispersive spectrometer (SEM-EDS) provides a very detailed insight not only into morphological features of microorganisms and the colonized substrata but also gives information about chemical composition of the designated area. Hence, utilization of diverse microscopic techniques is indispensable in cultural heritage artworks survey, and its role cannot be disregarded in any trendsetting scientific research in this field.

References:

[1] N. Unković, M.L. Grbić, M. Stupar, Ž. Savković, A. Jelikić, D. Stanojević, J. Vukojević, Microsc. microanal., 22(2)(2016) 410-421.

[2] Ž. Savković, N. Unković, M. Stupar, M. Franković, M. Jovanović, S. Erić, K. Šarić, S. Stanković, I. Dimkić, J. Vukojević, M. Ljaljević Grbić, Int. Biodeter. Biodegr., 115 (2016) 212-223.

A first proof of an early mechanical coupling and biofilm formation in dilute bacterial suspensions

KOSTANJŠEK ROK[1], SRETENOVIČ SIMON[1], STOJKOVIĆ BILJANA[2], DOGŠA IZTOK[1], POBERAJ IGOR[3,4], STOPAR DAVID[1]

[1] Biotechnical Faculty, University of Ljubljana, Slovenia; [2] Medical Faculty, University of Ljubljana, Slovenia; [3] Faculty of Mathematics and Physics, University of Ljubljana, Slovenia; [4] Aresis d.o.o., Ljubljana, Slovenija

Introduction: It is a general perception that microbes can grow either in a planktonic form, or in a form of biofilm. The former occurs at lower cell densities and is characterized by an absence of mechanical interconnections between cells. Cells are therefore allowed to move independently and act as a dilute suspension. Biofilms on the other hand, are characterized by higher cell densities and intercellular mechanical interconnections enabled by a self-produced matrix of extracellular polymeric substances. Being most common form of bacterial communities, biofilms are capable of colonizing most of natural and artificial materials. As such, biofilms commonly interfere with biomedical and technological processes by changing the mechanical and chemical properties of the overgrown surfaces. To improve our understanding of the process of biofilm formation, we analyzed the possibility of a mechanical coupling of bacteria in dilute suspensions, much before cells become fully entrapped in the extracellular matrix of newly formed biofilm.

Materials and methods: We analyzed the presence of intracellular connections and microrheological parameters of bacteria in dilute suspension by optical tweezers Tweez 250si (Aresis) and CMOS camera UI-3370CP-M-GL (IDS Gmbh) mounted on invert light microscope Eclipse-Ti (Nikon). Presence, dynamics and composition of mechanical connections between cells were analyzed by FE-SEM JSM-7500F (Jeol), negatively contrasted samples examined by TEM CM-100 (Philips) and invert light microscope Observer Z1 (Zeiss) upgraded with a confocal system LSM 800 (Zeiss). The experiments were performed on several bacterial species (*Escherichia coli*, *Pseudomonas aeruginosa*, *Pseudomonas fluorescens*, *Pseudomonas stutzeri*, *Staphylococcus aureus*, *Vibrio ruber* and *Bacillus subtilis*) sampled at different time points after inoculation into a liquid growth medium. Biological origin of intracellular connections was examined on a set of mutated bacterial strains with knocked-out genes for individual components of extracellular matrix.

Results: By using optical tweezers, we detected long-range coordinated motion and mechanical coupling of bacterial pairs in dilute bacterial suspensions (Figure 1). TEM (Figure 2) and FE-SEM (Figure 3) analysis showed a gradual formation of extracellular matrix around bacterial cells, leading to their entrapment in the extracellular matrix. Although full entrapment of cells in the extracellular matrix and formation of biofilm occurs approximately 8 hours after inoculation, we observed the mechanical coupling between cells as soon as one hour after inoculation. The components connecting the cells much before the full formation of extracellular matrix comprise secreted bacterial polymers and cytoplasmic substances released from lysed cells. [1]

Discussion and conclusions: Our findings point to mechanical connections between bacteria in dilute bacterial suspensions, which is much earlier than previously expected. By fundamentally changing the view on bacterial interactions in dilute suspensions, our results shed a new light into understanding of biological processes related to biofilms, like their formation, diffusion of signal molecules and nutrients in them, origin of multicellularity and microbial physiology, with

a wide array of implications, including increased efficacy of antibiotic treatments, as well as reducing the formation of unwanted microbial aggregates in industry and natural environments.

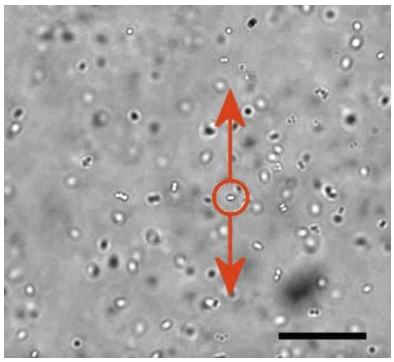

Figure 1. The principle of movement (arrows) of a single *B. subtilis* cell entrapped by optical tweezers (circle). Scale bar represents 15 µm.

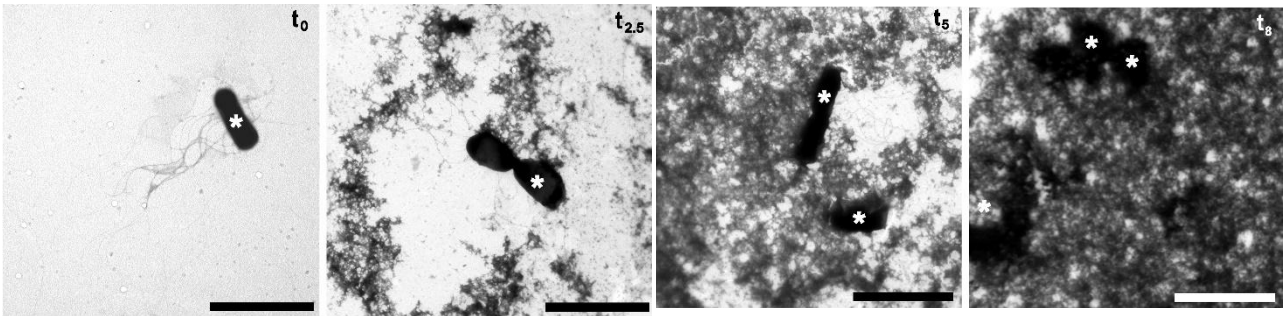

a **b** **c** **d**

Figure 2. Gradual formation of the extracellular network in *B. subtilis* culture. TEM micrographs depicting inoculated growth medium (t0) (a) and *B. subtilis* cells (asterisks) after 2.5 (b), 5 h (c), and 8 h (d) of incubation. Scale bars represent 3 µm.

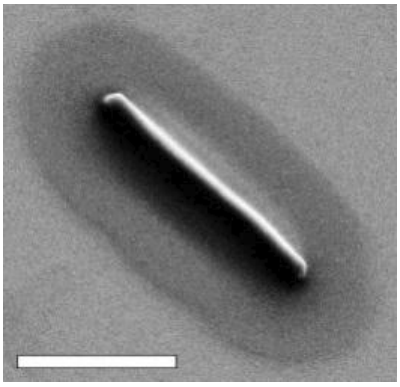

Figure 3. Extracellular matrix surrounding a single *B. subtilis* cell. Scale bar represents 3 µm.

Reference:
[1] S. Sretenovič, B. Stojković, I. Dogša, R. Kostanjšek, I. Poberaj, D. Stopar, Nature Comm, 8 (2017) 1-8

Application of Scanning Electron Microscopy for Examination of Infected Tissues

TEREZA JUŘÍKOVÁ[1,2], DOMINIKA LUPTÁKOVÁ[1], HELENA MAREŠOVÁ[1], ANDREA PALYZOVÁ[1], ANTON ŠKRÍBA[1], JIŘÍ NOVÁK[1], OLGA KOFROŇOVÁ[1], MILOŠ PETŘÍK[3], VLADIMÍR HAVLÍČEK[1] AND OLDŘICH BENADA[1]

[1] Institute of Microbiology, v.v.i., Academy of Sciences of the Czech Republic, Prague, Czech Republic; [2] Department of Genetics and Microbiology, Faculty of Science, Charles University, Prague, Czech Republic; [3] Institute of Molecular and Translational Medicine, Faculty of Medicine and Dentistry, Palacky University, Olomouc, Czech Republic

In these days, opportunistic pathogenic microorganisms represent a serious medical problem due to the growing number of immunocompromised patients. Fast and non-invasive diagnostics can decide on the survival of these patients. One of the dreaded bacteria is *Pseudomonas aeruginosa*. This Gram-negative bacterium is well known for being the causative agent of nosocomial infections and for its multidrug resistance. *P. aeruginosa* mainly attacks soft tissues, where it causes acute or chronic infections. In both cases, they may endanger life [1].

P. aeruginosa, like some other bacteria or fungi, produces siderophores, small iron-binding compounds that contribute to virulence. These molecules are species-specific and are detectable *in vitro* and *in vivo* in infected animals by mass spectrometry methods [2, 3]. The aim of our work is detection of *P. aeruginosa* by multimodal imaging. Using scanning electron microscopy (SEM), it is possible to characterize morphology of the bacteria in different growth phases *in vitro* (Figure 1.). SEM is also useful for detecting bacteria in infected lung tissue (Figure 2.). Pyoverdin, the main siderophore produced by *P. aeruginosa*, is detectable in the lungs using MALDI imaging mass spectrometry (MALDI-IMS).

Therefore we started to develop a methodological approach to combine these hard-to-combine methods – high resolution SEM and MALDI-IMS with resolution in the range tens of microns. However, tissue handling and sample preparation is problematic with respect to both analyses. While chemical fixation is generally required to preserve tissue structure for high resolution imaging, it can interfere with the signal of measured spectra by MALDI-IMS. A possible solution is to prepare consecutive sections of the non-fixed tissues to be used separately for multiple analyses [4]. Additional fixation of the tissue sections for SEM is then required. Gram staining is used to localize bacteria easily in the lung tissue sections. However, due to the light microscopy resolution limit, it is not possible to observe all morphological changes in the infected tissue. The bacterial biofilm formed in the lungs during infection is also hardly observable in histological samples.

We demonstrate a methodological approach for sample preparation, which is suitable for analyses of infected tissues in more modalities. Thereafter, data are correlated by analytical software [5]. By combining SEM and MALDI-IMS, it is possible to obtain complex information on the presence of bacteria and their metabolites in the infected tissue as well as the inflammatory response of the host in the infected rat model. Moreover, this approach can confirm the use of other mass spectrometry methods as fast and non-invasive diagnostic tools in the future [3].

Figures

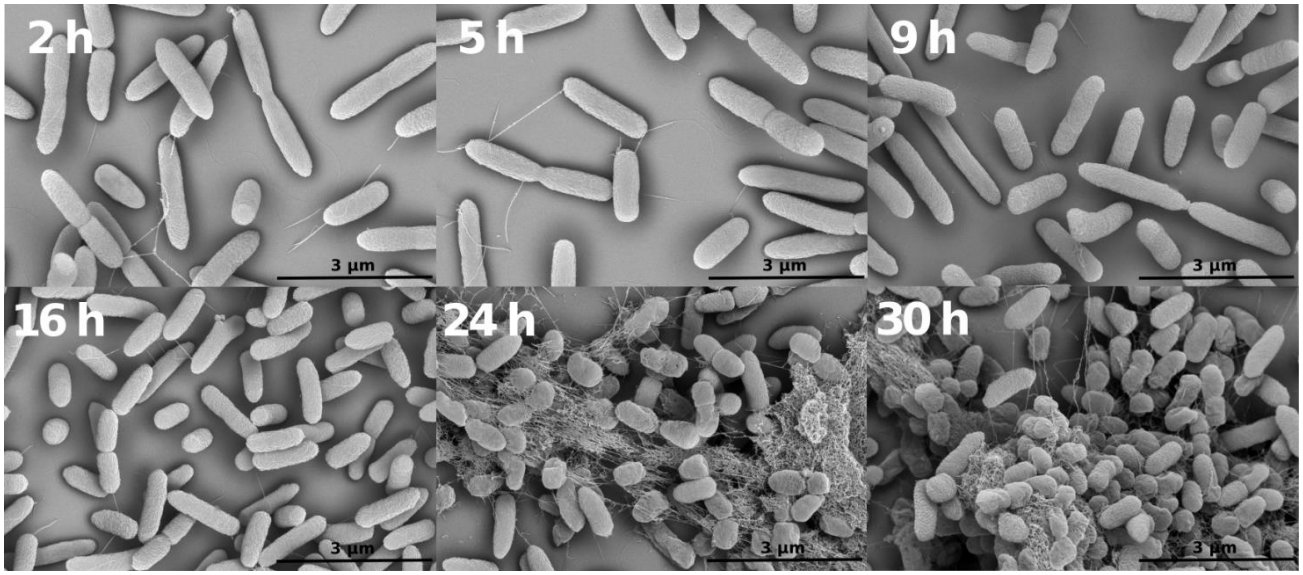

Figure 1. Different growth phases of *P. aeruginosa* in SEM. From 2 to 9 hours after inoculation, bacteria are motile with high doubling time. At the transition to the stationary phase (24 h), bacteria produce polysaccharides and associate into biofilm-like structure. After 30 h, bacterial cells are smaller and some of them are dead.

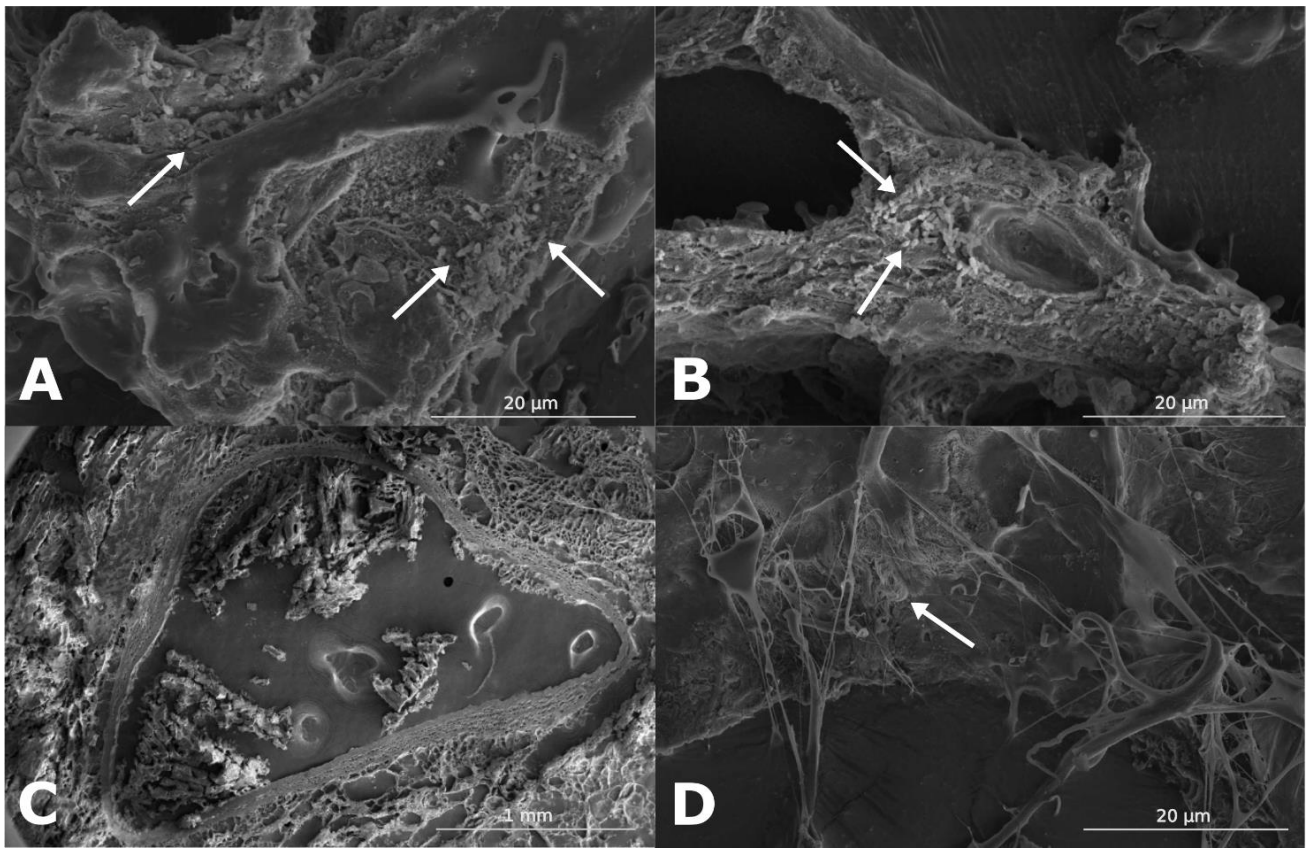

Figure 2. Post-fixed cryosections of infected lung tissue section in SEM. (A, B) *P. aeruginosa* (arrows) grows in biofilm-like structures. (C) Due to the additional fixation, it is possible to distinguish the morphological structures. (D) Tissue damage caused by inflammation, collagen fibers (arrow) are observable.

References

[1] M. F. Moradali, S. Ghods, B. H. Rehm, *Pseudomonas aeruginosa* lifestyle: A paradigm for adaptation, survival, and persistence, Front Cell Infect Microbiol, 7: 39 (2017)
[2] D. Luptáková, T. Pluháček, A. Palyzová, J. Přichystal, J. Balog, K. Lemr, I. Juránek, V. Havlíček, Meet interesting abbreviations in clinical mass spectrometry: from compound classification by REIMS to multimodal and mass spectrometry imaging (MSI), Acta virologica, 61 (2017) 353–360
[3] D. Luptáková, T. Pluháček, M. Petřík, J. Novák, A. Palyzová, L.Sokolová, A. Škríba, B. Šedivá, K. Lemr, V. Havlíček, Non-invasive and invasive diagnoses of aspergillosis in a rat model by mass spectrometry, Scientific Reports, 7: 16523 (2017)
[4] T. Pluhacek, M. Petrik, D. Luptakova, O. Benada, A. Palyzova, K. Lemr, V. Havlicek, *Aspergillus* infection monitored by multimodal imaging in a rat model, Proteomics, 16 (2016) 1785–1792
[5] J. Novák, L. Sokolová, L. Lemr, T. Pluháček, A. Palyzová, V. Havlíček, Batch-processing of imaging or liquid-chromatography mass spectrometry datasets and de novo sequencing of polyketide siderophores, BBA – Proteins and Proteomics, 1865 (2017) 768–775

Acknowledgment

This work was supported by the Ministry of Education, Youth and Sports of the Czech Republic (LO1509).

Screening of surface mustard seeds morphology by SEM (scanning electron microscopy) and optical microscopy before and after conventional and modern extraction techniques

IVANA VRCA[1], JOSIPA ŠĆURLA[2], AZRA ĐULOVIĆ[1], TEA BILUŠIĆ[1], IVICA BLAŽEVIĆ[1]
[1] Faculty of Chemistry and Technology, University of Split; [2] University of Split, Centre of Excellence STIM

The seeds of white (*Sinapis alba* L.), brown (*Brassica juncea* L.) and black mustard (*Brassica nigra* L.) are part of the Brassicaceae family known for the presence of glucosinolates (GSLs). In the plant, they coexist with an enzyme myrosinase, though separately stored in vacuoles of so-called S-cells. GSLs that are characteristic for these plants include sinalbin, gluconapin and sinigrin. When plant tissue is damaged, GSLs and enzyme myrosinase come into contact releasing unstable aglycones which spontaneously rearrange into a variety of reactive compounds, mainly isothiocyanates - responsible for the mustard flavour [1]. Sinalbin degrades and releases 4-hydroxybenzyl isothiocyanate, gluconapin releases but-3-enyl isothiocyanate, while sinigrin releases allyl isothiocyanate [2]. As a part of the mustard oils composition, the high content of lipid components is also present (20 – 30%).

The present study was designed to examine pore microstructure of mustard seeds (white, brown and black mustard) by optical (ZEISS AXIO Imager.A2m) and scanning electron microscopy (SEM) before and after using different extraction techniques. The SEM analysis of the mustard seeds was performed by JEOL JSM-5200 scanning electron microscope. The mustard seeds were examined at an accelerating voltage of 15 kV.

The techniques used for isolation were: conventional (Clevenger hydrodistillation and extraction with organic solvent after autolysis) and modern microwaves extraction techniques (Figure 1). The qualitative and quantitative composition of the main compounds were analysed using gas chromatography.

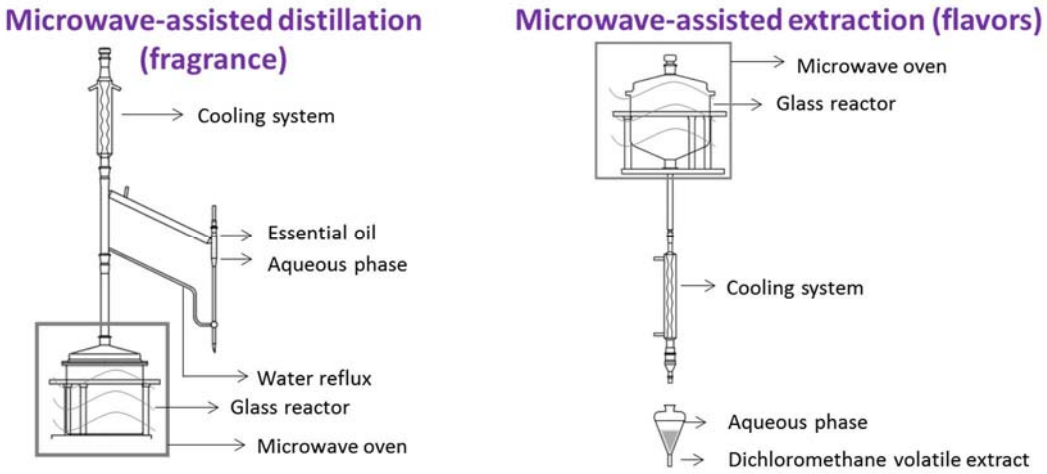

Figure 1. Scheme of microwave-assisted extraction system.

The seed coat is the interface between the embryo and the exterior environment, and it is a multifunctional organ that plays important role in embryo nutrition during seed development and in protection against pests and pathogens from the external environment afterwards [3].

Seed of brown mustard is spherical and coat captured with an optical microscope as viewed from the outer surface reminiscent of a golf ball (Figure 2). The surface contained a semiregular array of ridges with compartmented the seed coat to form a network that gave an almost honeycomb pattern [4].

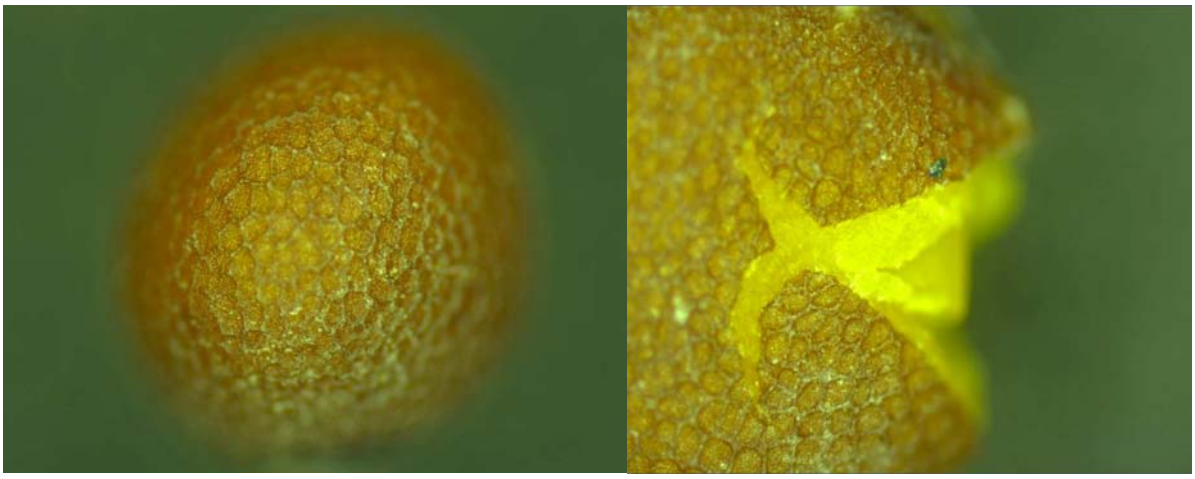

Figure 2. A 50x magnification images of brown mustard seed (untreated sample) taken trough an optical microscope.

Surface morphology scanned by SEM showed that the pores of white mustard seeds are significantly smaller than pores of brown and black mustard seeds (Figure 3).

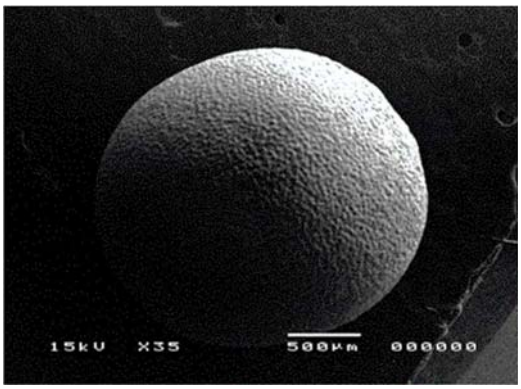

Figure 3. SEM image of white mustard seed (untreated sample).

Surface morphology also showed that tested sample has a compact pores microstructure throughout the whole sample (Figure 4).

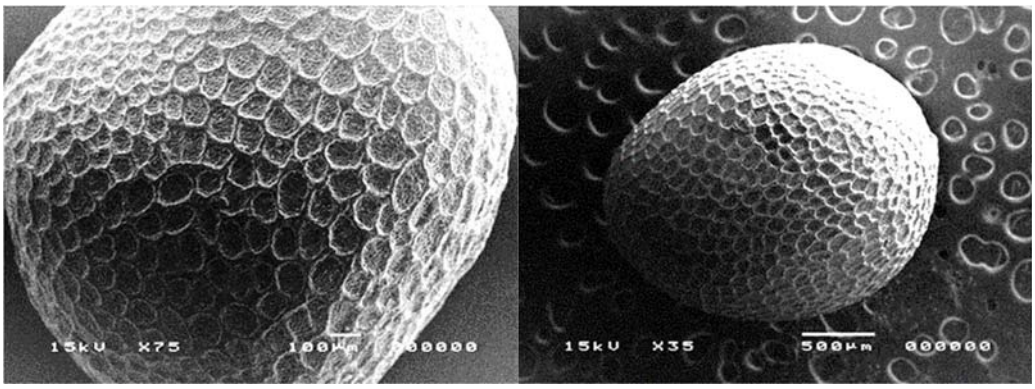

Figure 4. SEM images of brown and black mustard seed (untreated sample).

GC–MS results showed that allyl isothiocyanate was predominant compound in brown mustard seeds oil in MW distillate and Clevenger hydrodistillate (94.37% and 95.94%) and MW extract (95.20%),

while its concentration was lower in black mustard seeds oil (15.39% in Clevenger hydrodistillate) and in white mustard seeds oil (12.68% in MW extract).
But-3-enyl isothiocyanate was predominant compound in black mustard seeds oil (80.58% in Clevenger hydrodistillate), while its content was the lowest in CH_2Cl_2 extract after autolysis (0.82%).
The yields of essential oils after different extraction techniques are shown in the Table 1.

Table 1. The yields of essential oils after different extraction techniques

Clevenger hydrodistillate	**0.003 - 0.07%**
MW distillate	0.0001 - 0.002%
MW extract	0.003 - 0.013%
CH_2Cl_2 extract after autolysis	0.001 - 0.024%

It can be suggested that the amount of isothiocyanates released from the mustard seeds depended on different conditions applied (water content, microwaves, temperature), as well as a particle size of the mustard seed.

References

[1] V. Boscaro, L. Boffa, A. Binello, G. Amisano, S. Fornasero, G. Cravotto, M.Gallicchio, Molecules, 23(11) (2018) 3004.
[2] M. Tian, A. B. Hanley, M. W. J. Doods, K. Yaegaki, American Journal of Dentistry, 26 (4) (2013) 180-184.
[3] C. L. Zeng, J. B. Wang, A. H. Liu, X. M. Wu, Annals of Botany, 93 (2004) 555-566.
[4] R. A. Holley, B.E. Phipps-Todd, S. H. Yiu, Food Structure, 2(2) (1983) 143-151.

The effects of ionizing radiation on the cell wall of microalgae *Chlorella sorokiniana* - TEM study

JELENA DANILOVIĆ LUKOVIĆ[1,2], BERND ZECHMANN[3], SNEŽANA VOJVODIĆ1, JELENA BOGDANOVIĆ PRISTOV[1], MARINA STANIĆ1, JON PITTMAN[4], IVAN SPASOJEVIĆ[1]

[1] Life Sciences Department, Institute for Multidisciplinary Research, University of Belgrade, Serbia; [2] Department for Imunochemistry and Glycobiology, Institute for Application of Nuclear Energy INEP, University of Belgrade, Serbia; [3] Center for Microscopy and Imaging, Baylor University, Waco, TX, USA; [4] School of Earth and Environmental Sciences, University of Manchester, UK

1. Introduction

Microalgae are exposed to ionizing radiation from natural (*e.g.* radionuclides from soil and rocks) and anthropogenic sources (radioactive waste, nuclear power accidents, *etc*). However, there is a very limited amount of data on the mechanisms that microalgae employ in response/adaptation to radiation [1]. The aim of our study was to determine the effects of X-ray irradiation on the cell wall of *Chlorella sorokiniana*. Microalgal cell wall represents a dynamic multi-layer structure, which is both a barrier and the line of contact between unicellular algae and the surroundings [2].

2. Details of experiments

C. sorokiniana (CCAP 211/8K) culture was grown in 3N-BBM+V medium, at 22°C with a continuous photon flux of 120 µmol m^{-2} s^{-1} for 20 days, reaching stationary phase. Cultures were then exposed to X-rays at doses of 1, 2 and 5 Gy, left under the same conditions for additional 24 h, *C. sorokiniana* cells were collected by centrifugation (500 x g for 5 min) and fixed overnight at 4°C in 0.1M phosphate buffer (PB) (pH 7,2) containing 3% glutaraldehyde (SERVA, Germany) and 1% paraformalaldehyde (pH 6,9). Postfixation was performed with 1% osmium tetroxide (SERVA, Germany) in 0.1M PB (pH 7,2) for 2 h at room temperature. Samples were dehydrated in a graded acetone series and then embedded in resin for soft blocks (AGR1031, Agar Scientific, UK). Thin sections (0.07 mm), obtained with Leica UC7 ultramicrotome (Leica Microsystems, Germany), were stained with uranyl acetate and lead acetate and observed at 60 kV in a JEOL JEM-1010 TEM (JEOL, Japan). Characterisation of cell wall thickness was performed on TEM photographs using ImageJ (NIH). At least 25 cells with the nuclear mid-section for control and each examined dose were analysed on low (x7500) magnification. Thickness of the cell wall was measured at four points, (on x and y axis of the micrograph with 0 point at the cell's center), corresponding to the position of the small hand on the clock when it is set at 12h, 3h, 6h, 9h. In addition, gravimetry of isolated cell wall was performed. Isolation was conducted according to the previously described protocol that was slightly modified (starch was removed by amylase treatment of isolates) [3].

3. Results and discussion

TEM showed that cell wall of *C. sorokiniana* is composed of trilaminar sheath (TLS electron translucent line inserted between two electron dense lines; the outermost layer is a mature mother wall, while the thin inner layer is a daughter wall), and fibrilar cell wall. It is noteworthy that the obtained diameters for untreated microalgae were in accordance with available data [4]. The

analysis of TEM micrographs showed that there were no significant changes in the thickness of TLS for any of the used doses. However, the diameter of fibrillar wall was increased in response to irradiation for microalgae exposed to 1 Gy and 2 Gy. The thickness of cell wall in microalgae exposed to 5 Gy was not significantly different than in controls (Figure 1). A similar trend was observed by gravimetry of dry cell wall isolates normalized to biomass. It is important to note that no effects of radiation on biomass, at doses applied here, could be observed.

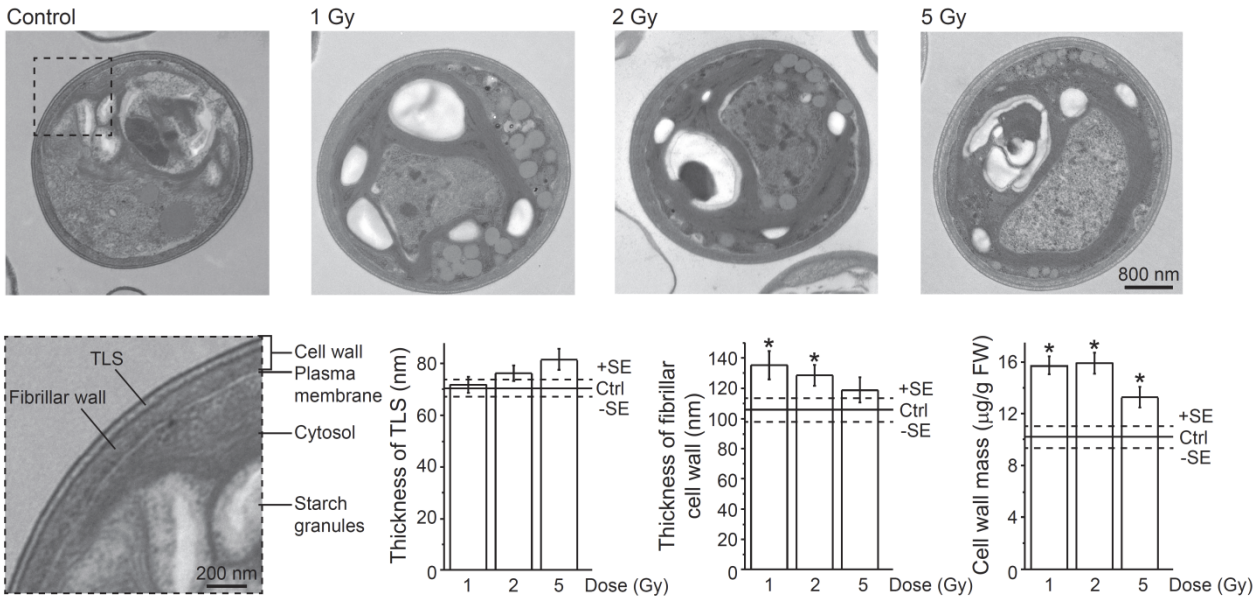

Figure 1. Representative TEM micrographs of *C.sorokiniana* cells and the analysis of cell wall parameters presented in graphs. Full and dashed lines in the graphs represent control (untreated microalgae) values ± standard error. * - statistically significant compare to controls ($p < 0.05$).

It appears that *Chlorella sorokiniana* responds promptly to ionizing radiation by fortifying its 'first line of defence'. The observed changes may be of particular interest for bioremediation, taking into account the capacity of cell wall to bind water-soluble metals, including radionuclides. In addition, cell wall may buffer the influx of reactive oxygen species that are generated in aqueous environment by ionizing radiation.

Acknowledgements
This work has been supported by NATO SPS Programme, Project number G5320.

References

[1] T. Gomes, L. Xie, D. Brede, O. C. Lind, K. A. Solhaug, B. Salbu, K. E. Tollefsen, Aquat Toxicol, 183 (2017) 1–10
[2] P. Baudelet, G. Ricochon, M. Linder, L. Muniglia, Algal Res, 25 (2017) 333–371
[3] J. Simonovic, J. Stevanic, D. Djikanovic, L. Salmen, K. Radotic, Cellulose 18 (2011) 1433–1440
[4] F. Martinez, C. Ascaso, M. I. Orus. Ann Bot, 67 (1991) 239–245

Micromorphological traits of *Micromeria graeca* (L.) Benth. ex Rchb. (Lamiaceae) leaf glandular trichomes of *in vitro* propagated plants

MIRJANA JANJANIN[1], SVETLANA TOŠIĆ[2], DRAGANA STOJIČIĆ[2], BOJAN ZLATKOVIĆ[2], SNEŽANA BUDIMIR[1] AND BRANKA UZELAC[1]

[1] Institute for Biological Research "Siniša Stanković",University of Belgrade, Serbia; [2] Department of Biology and Ecology, Faculty of Sciences and Mathematics, University of Niš, Serbia

1. Introduction

Plants of the genus *Micromeria* Benth. (Lamiaceae) are perennial herbs, subshrubs and shrubs distributed throughout the temperate belt [1]. *Micromeria* species are generally aromatic due to the presence of external glandular structures that produce essential oils, which serve to protect plants against herbivores and pathogens. This natural product isolated from a variety of *Micromeria* species was shown to exhibit antimicrobial, antifungal and antioxidant activities. Due to the socio-economic importance of the essential oil production, glandular trichomes of Lamiaceae species are among the most investigated secretory structures concerning their microporphology, ultrastructure, type and mode of secretion.

M. graeca (L.) Benth. ex Rchb. subsp. *graeca* is a perennial subshrub widely distributed in the Mediterranean area. The plant is pubescent, stout, 10-50 cm in height, has ovate to linear-lanceolate leaves with revolute margins, and flowers in spring. It is used in folk medicine in the Tyrrhenian part of the Basilicata region of southern Italy. This study aimed to record micromorphology and secretion of leaf glandular trichomes of *M. graeca* plants cultured under *in vitro* environmental conditions.

2. Experiment

Plant material – Shoots of wild-growing *M. graeca* plants, dissected into one-node stem segments, were used to establish *in vitro* cultures. Surface sterilized nodal segments were transferred to Murashige and Skoog (MS) culture medium [2] supplemented with 3% (w/v) sucrose, 0.7% (w/v) agar (Torlak, Belgrade) and 0.1% activated charcoal. Shoot multiplication was carried out on the same medium, by routine subculture performed in 5-week intervals.

Scanning electron microscopy (SEM) – For SEM analyses fresh leaves isolated from shoots cultured on MS medium were used. Leaf samples were coated with a thin layer of gold and palladium in a BAL-TEC SCD 005 sputter coater. Samples were examined with a JEOL JSM-6390 LV (JEOL, Tokyo, Japan) SEM operated at 15 kV.

Light microscopy (LM) – Micromorphological and histochemical analyses were performed on hand-sections of fresh leaves. Histochemical test using Sudan IV dye was applied for *in situ* detection of total lipids [3]. Sections were examined and photographed using a Zeiss Axiovert light microscope (Carl Zeiss GmbH, Göttingen, Germany).

3. Results and Discussion

Nodal segments of *M. graeca* cultured on MS medium developed non-branched axillary shoots (Fig. 1). SEM and LM investigations of regenerated plantlets indicated that two types of glandular trichomes, peltate and capitate, were present on their leaf surfaces (Figs. 2-10).

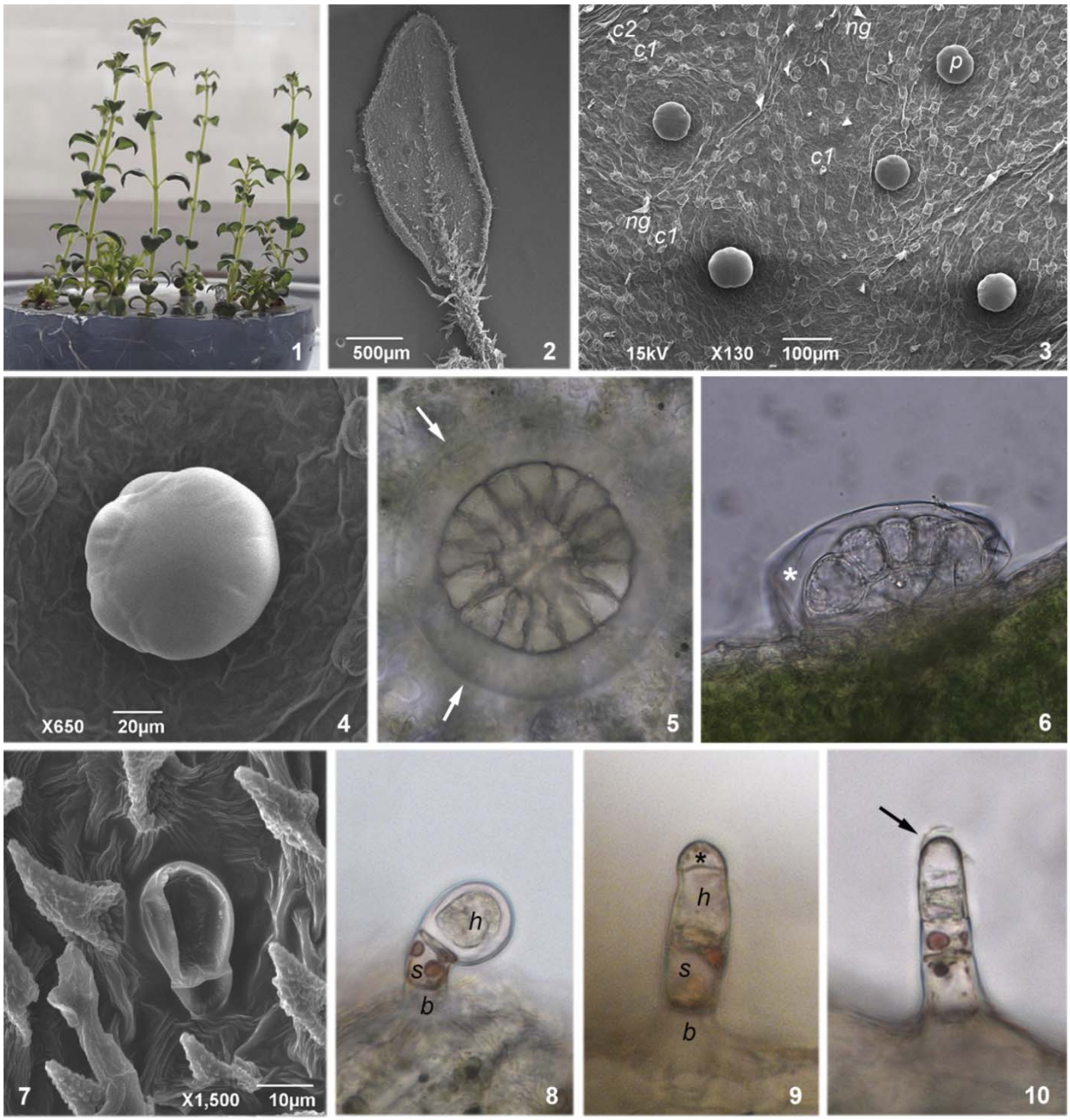

Figure 1. *In vitro* plantlets cultured on MS medium for 5 weeks, used for trichome characterization. Figure 2. Sparsely pubescent young lanceolate leaf with revolute margins. Figure 3. Micromorphology of the abaxial leaf surface of *in vitro* plantlets. Note sharply pointed non-glandular (*ng*) trichomes and two types of glandular trichomes, peltate (*p*) and capitate (*c1, c2*). Figure 4. Glandular head of developing peltate trichome on mature *in vitro* leaf, with its cuticle firmly attached to the secretory cell walls. Figure 5. Upper view of mature peltate trichome, with secretory cells arranged in two circles: peripheral, consisting of 16 cells, and central, composed of four cells. Note cuticular cap (*arrows*) detached from the head cell lateral walls. Figure 6. Mature peltate trichome with subcuticular storage cavity (*asterisk*), formed by detachment of the cuticle from the upper cell walls. Figure 7. Upper view of type I capitate trichome clinging to the leaf surface. Figure 8. Type I capitate trichome, with basal epidermal cell (*b*) and short unicellular stalk (*s*) subtending an oblong unicellular secretory head (*h*). Note lipophilic droplets within the stalk cell, after staining with Sudan IV. Figure 9. Type II capitate trichome, with conical basal cell (*b*), elongated stalk (*s*) and cylindrical unicellular secretory head (*h*). Note well-developed round subcuticular storage cavity (*asterisk*) atop the secretory cell. Figure 10. Type II capitate trichome with broken cuticle of the secretory cell. Note remnants of broken cuticle (*arrow*) attached to the secretory cell.

Peltate trichomes (Figs. 4-6) were more frequent on the abaxial leaf surface. They consisted of a broad basal cell, one wide stalk cell, and a glandular head comprising 12-16 peripheral and 4 centrally located secretory cells. On leaves of *in vitro* plantlets, mostly immature peltate trichomes, with cuticle firmly attached to the secretory cell walls, were observed (Fig. 4). During maturation, a storage cavity was formed by the separation of the cuticle from the secretory upper cell walls, rendering these trichomes spherical shape, characteristic of a peltate gland (Figs. 5, 6).

Two types of capitate trichomes could be distinguished on *M. graeca* leaves. Type I capitate trichomes were found on both adaxial and abaxial leaf side, positioned at an angle to the leaf surface (Figs. 7, 8). They were composed of one large basal epidermal cell, cutinized unicellular stalk and unicellular ellipsoidal head (Fig. 8). Cutinization of the stalk cell walls is presumed to prevent apoplastic backflow of trichome-produced compounds, which can be autotoxic to other parts of the plant.

Type II capitate trichomes (Figs. 9, 10) were observed on both adaxial and abaxial leaf surface, but appeared to be less frequent comparing to peltate and type I capitate trichomes. Type II capitate trichomes were composed of one conical basal cell, a stalk comprising two cells, and unicellular secretory head. In young trichomes small subcuticular storage cavity was present (Fig. 9). On mature leaves, their glands commonly had ruptured cuticle (Fig. 10).

Histochemical analysis revealed scarce lipophilic secretion of both peltate and capitate trichomes under *in vitro* conditions. Further optimization of *in vitro* culture conditions is needed in order to increase the production of secondary metabolites in *M. graeca* plantlets.

5. References

[1] C. Bräuchler, O. Ryding, G. Heubl. Willdenowia 38 (2008)
[2] T. Murashige, F. Skoog, Physiol Plant 15 (1962) 473–497
[3] W. A. Jensen, Botanical histochemistry. Freeman, San Francisco (1962)

6. Acknowledgment

This research was financially supported by the Ministry of Education, Science and Technological Development of the Republic of Serbia, Grant №. 173015 and 173030.

Phenotypic cell plasticity of *Trichoplax adhaerens* Schulze, 1883 (Placozoa) after treatment with ethanol and *Prunus spinosa* L. ethanol extract

LORETTA GUIDI, FEDERICA SEMPRUCCI, MARIA BALSAMO, DANIELE FRATERNALE, MARIASTELLA COLOMBA, SILVIO CECCHINI, ELEONORA GRASSI, LUCIA CESARONI, SABRINA BURATTINI AND MARIA CRISTINA ALBERTINI
Department of Biomolecular Sciences, University of Urbino, Urbino (PU), Italy

Prunus spinosa L. (Rosaceae) is a medicinal plant which contains a combination of bioactive phytochemicals and nutrients and is supposed to play very important biological activities [1,2]. *Trichoplax adhaerens* Schulze, 1883 (Placozoa), a non-bilaterian marine species, has the simplest body plan among metazoans. Only seven somatic cell types are organized into two pseudo-epithelial layers, a marginal cell cord, and an inner tridimensional network of star-shaped fiber cells [3,4,5,6]. Placozoa reproduce by binary fission with budding occurring only in unfavourable conditions [7]. Available data also show that sexual reproduction may take place in nature [8] and oocytes production is often observed, especially under stressful conditions [9]. In a recent study the possible effects of the treatment of *T. adhaerens* with *P. spinosa* ethanol extract or with only ethanol were investigated using Placozoa *in vivo* as a biological model to assess the natural extract bioactivity. Results highlighted clear differences in cell morphology between the untreated and the treated animals [10]. On this basis, the aim of this study was to further investigate the phenotypic cell plasticity of *T. adhaerens* in different experimental conditions [untreated (CTRLs), treated with ethanol (EtOH), treated with *Prunus spinosa* ethanol extract (P+EtOH)] through microscopical and ultrastructural TEM observations.

We found that untreated animals maintained a large and flattened body with irregular shape, whereas specimens treated with ethanol showed a much smaller body with rounded shape. Under TEM, we were able to deeply investigate the cell phenotypes and observed that the animals treated with ethanol showed a marginal cell cord much thicker than that of untreated ones, as composed of a higher number of cells (Fig. 1A-C). Moreover, beneath the cells of the marginal cord, we identified some peculiar cells looking different from any other placozoan cell type described so far. These cells are characterized by a well developed Golgi apparatus, numerous vesicles moderately electron-dense, and a basal body from which a flagellum arises (Fig. 1D-F). This finding supports a great phenotypic cell plasticity of *T. adhaerens* and emphasizes the need to further investigate the abundance of such cells in EtOH treated animals as well as to focus their ultrastructural details in order to confirm our present observations. Furthermore, since we noticed a high growth rate in EtOH group, in which reproduction by budding also took place thus confirming the existence of a stressful situation, the finding of these peculiar cells may suggest they originate as a response to sexual signals induced by unfavorable (i.e.EtOH treatment) experimental conditions. Indeed, the appearance of sexual reproduction in unfavourable life conditions is already known for a number of animals that usually reproduce by asexual modalities. Moreover, the observed growth rate in the EtOH group (higher than in P+EtOH group), seems to indicate that *Prunus spinosa* ethanol extract may exert a protective activity against ethanol effects.

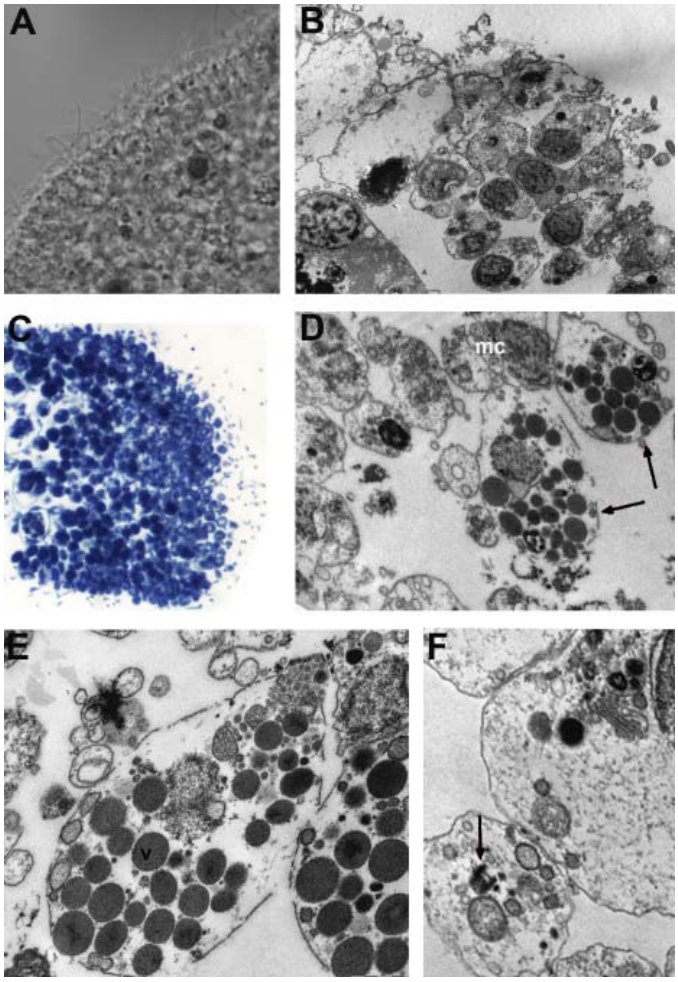

Figure 1. A,B: optical section and body cross-section of CTRLs showing the marginal zone formed by ovoidal, remarkably small cells. C,D: optical and electron body cross-section of EtOH treated animals showing the thick marginal cell cord (mc) and the peculiar cells (arrows) underneath. E,F: magnification of two peculiar cells in which are well visible the numerous vesicles (v) and the flagellum basal body (arrow).

Acknowledgements

This research was supported by DISB_ALBERTINI_PROGETTI_VALORIZZAZIONE_2017, CUP: H32F17000030005, from the University of Urbino Carlo Bo, Urbino (PU), Italy

References

[1] L. Barros, A. M. Carvalho, J. SaMorais, I.C.F.R. Ferreira, Food Chem, 120 (2010) 247-254
[2] Y. Avior, D. Bomze, O. Ramon, Y. Nahmias, Food & Funct, 4 (2013) 831-8443
[3] K.G. Grell, Z Morphol Tiere, 73 (1972) 297-314
[4] L. Guidi, M. Eitel, E. Cesarini, B. Schierwater, M. Balsamo, J Morphol, 272 (2011) 371-378
[5] C.L. Smith, F. Varoqueaux, M. Kittelmann, R.N. Azzam, B. Cooper, C.A. Winters, M. Eitel, D. Fasshauer, T.S. Reese, Curr Biol, 24 (2014) 1565-15727
[6] B. Schierwater, D. De Jong, R. DeSalle, Int J Biochem Cell Biol, 41 (2009) 370-379
[7] M. Thiemann, A. Ruthmann, Zoomorphology, 110 (1991) 165-174
[8] A.Y. Signorovitch, S.L. Dellaporta, L.W. Buss, PNAS, 102 (2005) 15518-15522
[9] M. Eitel, L. Guidi, H. Hadrys, M. Balsamo, B. Schierwater. PLoS One, 6 (2011) e19639
[10] M. C. Albertini, D. Fraternale, F. Semprucci, S. Cecchini, M. Colomba, M.B.L. Rocchi, D. Sisti, B. Di Giacomo, M. Mari, L. Sabatini, L. Cesaroni, M. Balsamo, L. Guidi, PeerJ, 7 (2019) e6789

Imaging FTIR microscopy – technique for rapid screening of plant cell walls

JASNA SIMONOVIĆ RADOSAVLJEVIĆ[1], JASNA STEVANIC[2], DANIELA ĐIKANOVIĆ[1], ALEKSANDRA LJ. MITROVIĆ[1], LENNART SALMÉN[2], KSENIJA RADOTIĆ[1]

[1] University of Belgrade, Institute for multidisciplinary research, Belgrade, Serbia; [2] RISE/ Innventia, Stockholm, Sweden

1. Introduction

Plant cell walls (CW) are the most abundant, renewable and biodegradable composite on Earth. Cell wall can also be considered as a nano-composite in which cellulose, lignin and hemicelluloses are interconnected in a specific manner. Biopolymers such as cellulose, hemicellulose and lignin, have wide applications in different industries, especially for biofuels and biomaterials [1,2]. By using imaging FTIR microscopy, run in transmission mode and at different polarisation modes (from 0° to 90°), it is possible to follow chemical variability and orientation of cell wall polymers [3]. The orientation of cellulose, xylan and lignin, as essential components of plants, were analysed by iFTIR with regard to the sample axis.

2. Materials and Methods

The purified isolated cell wall material was obtained from maple leaves (*A. platanoides*) by methanol extraction and subsequent purification using a series of solvents (1% Triton X-100, 1M sodium chloride, distilled water, methanol, acetone) [4].

FTIR microscopy measurements were carried out using a Spectrum Spotlight 400 FTIR Imaging System (Perkin Elmer Inc, Shelton, CT, USA). The area of interest was first displayed, using a visible CCD camera to locate the cell wall area, which was then irradiated using mid-IR light (Figure 1). The scanning was carried out in imaging mode using an array detector, providing a pixel resolution of 6.25 µm x 6.25 µm, a spectral resolution of 4 cm^{-1} and a spectral range from 1,800 to 720 cm^{-1}. IR scanning with a polarisation, where the incident IR radiation is polarised by a gold wire grid polariser, in our case, from 0° to 90° polarisation and in relation to the fibre orientation with intervals of 5° were carried out also. In this way, it is possible to investigate, for example, orientations of different polymers in a wood fibre. The IR spectra were processed by the software Spotlight 1.5.1, HyperView 3.2 and Spectrum 6.2.0 (Perkin Elmer Inc., Shelton, CT, USA) [3].

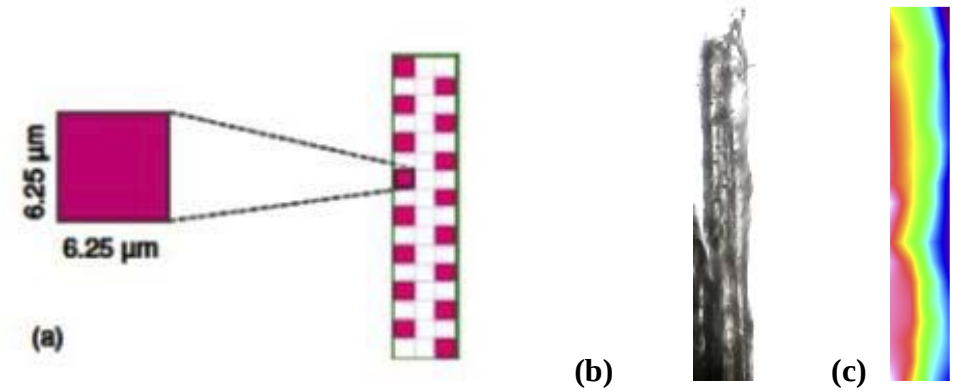

Figure 1. (a) shematic image of the linear array detector containing 16 MCT detectors, also showing one magnified pixel of a 6.25 µm x 6.25 µm, (b) visible image of a part of maple leaves cell wall, (c) IR full-spectral image of the sam part of maple leaves cell wall.

3. Results and Disscusion

From the in-depth study of polymer orientation, three areas from the sample (maple leaf) were selected. The transmission spectra were recorded from 0° to 90° polarisation modes. Figure 1 shows FTIR spectum of cell walls of maple leaves in the region 800–1800 cm^{-1}. Spectral signals related to absorptions from cellulose, xylan and lignin can be identified.

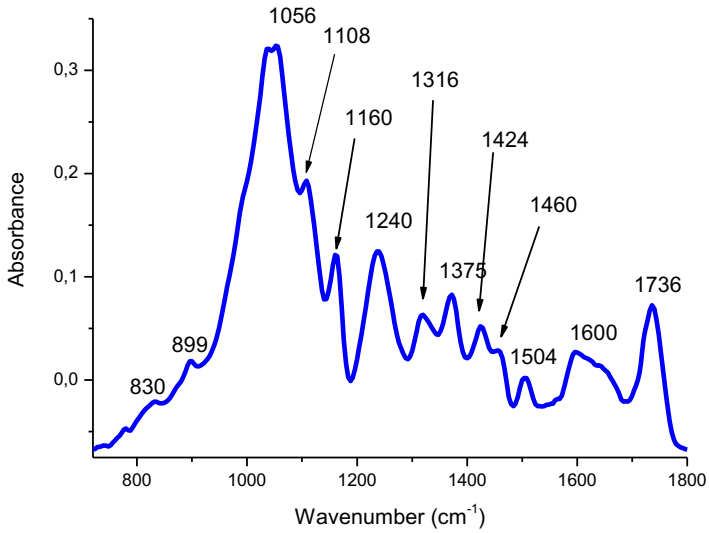

Figure 2. Average absorbance spectrum of maple leaves cell wall.

The relative absorbance spectra are presented (Figure 2) as specific absorption peaks (RA = (I_p – I_{min}) / (I_{max} – I_{min})$RA = \frac{(I_P - I_{min})}{(I_{max} - I_{min})}$) where RA is relative absorbance, I_p is intensity of the absorbed IR radiation at a given angle of the polarisation, I_{max} is maximal intensity observed for a given vibration and I_{min} is minimal intensity observed for a given vibration. These relative absorbance values were presented in relation to the angle of the incident IR polarisation (from 0° to 90°).

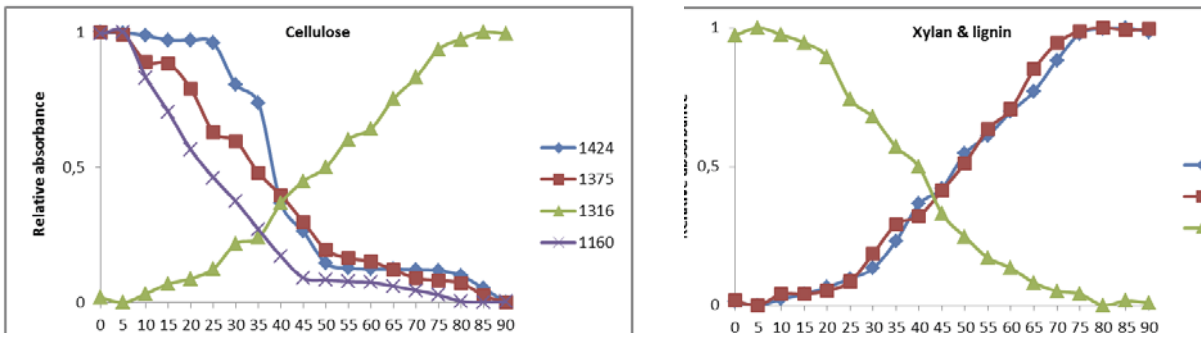

Figure 3. The relative absorbance of IR specific absorption wavenumbers plotted against the polarisation angle for the different polymers (cellulose - left, xylan & lignin – right) for maple leaves.

It is evident (Figure 3 left) that the three cellulose peaks (1160 cm^{-1},1375 cm^{-1} and 1424 cm^{-1}) [3–5] had high absorption levels at low polarisation angles, which is a consequence of a more parallel orientation of the corresponding groups to the CW longitudinal axis. The fourth cellulose peak (the perpendicular signal at 1316 cm^{-1}) had the greatest intensity at a high polarisation angle, due to the perpendicular orientation of the corresponding group (Figure 3 left). For the xylan, the characteristic band signals (1244 cm^{-1}, 1736 cm^{-1}) [5–7] increased with an increase in the polarisation angle. Due to the parallel orientation of these side groups in xylan, an orientation parallel to the longitudinal CW axis is indicated (Figure 3 right). For the lignin, the characteristic band signal (1517 cm^{-1}) [8,9] decreased with an increase in the polarisation angle (Figure 3 right), indicating that lignin is organised in parallel with the longitudinal CW axis.

4. Conclusion

It has been shown that xylan is oriented in parallel to the cellulose and more or less parallel to the axis of a cell wall, in isolated CW fragments from maize leaves. There was also a clear indication of lignin orientation parallel to the longitudinal CW axis. This means that all of these components show strong anisotropic behaviour and organisation.

Acknowledgement

This work was supported by Ministry of Education, Science and Technological development of Republic Serbia (Project no. 173017, 45012) and COST Action FP0802.

References

[1] M. Pauly, K. Keegstra, Plant J, 54 (2008) 559–568

[2] A.J. Ragauskas, C.K. Williams, B. H. Davison, *et al.*, Science, 311 (2006) 484–489

[3] J. S. Stevanic, L. Salmén, Holzforschung, 63 (2009) 497–503

[4] M. Chen, A.J. Sommer, J.W. McClure, Phytochem. Anal, 11 (2000) 153–159

[5] R.H. Marchessault, Pure Appl. Chem, 5 (1962) 107–129

[6] R.H. Marchessault, C. Y. Liang, J. Polym. Sci, 59 (1962) 357–378

[7] M. Åkerholm, B. Hinterstoisser, L. Salmén, Carbohydr. Res, 339 (2004) 569–578

[8] R.H. Atalla, U.P. Agarwal, Science, 227 (1985) 636–638

[9] O. Faix, Holzforschung, 45 (1991) 21–27

The SEM observation in four plum genotypes (*Prunus domestica* L.)

MILENA ĐORĐEVIĆ[1], RADOSAV CEROVIĆ[2], DRAGAN NIKOLIĆ[3], SANJA RADIČEVIĆ[1], IVANA GLIŠIĆ[1], NEBOJŠA MILOŠEVIĆ[1]

[1] Fruit Research Institute, Čačak, Serbia; [2] University of Belgrade, Innovation Centre at Faculty of Technology and Metallurgy, Belgrade, Serbia; [3] Faculty of Agriculture, University of Belgrade, Serbia

1. Introduction

In systematic approach, *Prunus domestica* L. (European plum) belongs to the family *Rosaceae* L. and it is an important fruit species, interesting for various forms of industrial and domestic processing, and for fresh consumption [1]. Examination of the pollen morphological structure is of great significance in taxonomy, phylogeny due to the fact that the pollen grains have a definitive size, structure and shape for each species, genus and family. Pollen grain at the time of its maturity has a three-layer coating: an exine, an intina and a pollen coat [2] According to the Hebda and Chinnappa [3], in most of the genera in the subfamilies of *Prunoideae*, *Maloideae* and *Spiroideae*, pollen grains are tricolpate, with large perforations in the furrow between the ridge. Major plant breeding programme in the Fruit Research Institute, Čačak, was to breeding new cultivars of European plum using autochthonous and introduced genotypes as the parental combinations within the planned hybridization. This program produced 'Čačanska Najbolja' (1975) and 'Pozna Plava' (1980). 'Hanita' and 'Presenta' were cultivars, introduced at the University of Hohenheim, Germany.

2. Material and methods

The study was conducted on four plum genotypes ('Čačanska Najbolja', 'Čačanska Lepotica', 'Hanita' and 'Presenta') growing in the experimental plum orchard near Čačak, Serbia. For the SEM study, samples were mounted directly on metallic stubs using double-sided adhesive tape and coated with gold in a sputtering chamber (BAL-TEC SCD 005 Sputter Coater). Observation of the prepared samples was carried out with a scanning electron microscope (SEM) JEOL JSM-7100F (Tokyo, Japan) at 15 kV.

3. Results

Based on the analysis conducted by SEM, all pollen grains can be characterized as isopolar, radially symmetric with three colpate apertures (Table 1). In equatorial view pollen grains are eliptical and in polar view are round (Figure 1). The pattern of the exine of the investigated plum cultivars was striate, with longitudinal ridges (Figure 2). Apart from the width, the other morphological characteristics of the pollen had the highest values in the 'Pozna Plava'. 'Hanita' had the smallest value of all the examined morphological characteristics of pollen grain. Also, when examining the parameters of the exine ornamentation, except for the number of ridges per 100 μm^2 of the equatorial regions, the highest values were observed in the 'Pozna Plava'. Pollen grains in 'Hanita' showed the highest number of ridges in 100 μm^2 of exine.

Table 1. Morphological characteristics of pollen grains in plum (*Prunus domestica* L.) cultivars.

Cultivar	Pollen lengh (µm)	Pollen width (µm)	Lenght/width ratio	Colpus lengh (µm)	Colpus width (µm)	Mesocolpium width (µm)

*Mean values follower by different lower-case letters in colums represent significant difference at P≤0,05 according LSD test

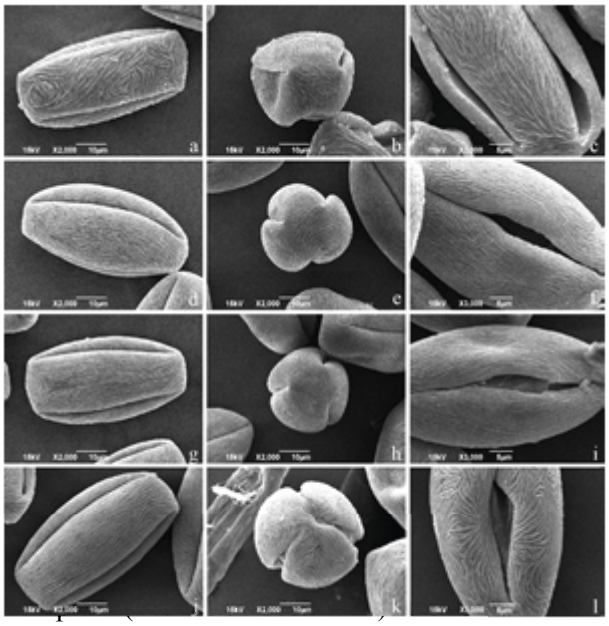

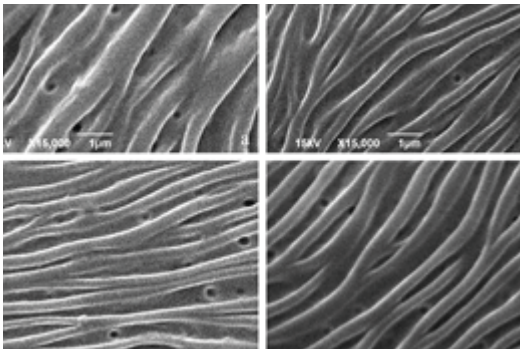

ure 2. Pollen exine in plum (*Prunus domest*
L.) cultivars: a) 'Pozna Plava'; b) 'Čačanska
Najbolja'; c) 'Hanita'; d) 'Presenta'.

References

[1] I. Glišić, R. Cerović, N. Milošević, M. Đorđević, S. Radičević, Genetika, 44 (2012) 583–593
[2] A.F. Edlund, R. Swanson, D. Preuss, The Plant Cell, 16 (2004) S84–S97
[3] R.J. Hebda, C.C. Chinnappa, Acta Botanica Gallica, 141 (1994) 183-193

Albedo and Flavedo from *"Limoncella of Mattinata"*: morphological and chemical data

S. BURATTINI; L. DI PATRIA; L. POTENZA; R. SALTARELLI; D. BURINI; E. FALCIERI; P. GOBBI; L. VALENTINI; D. SISTI; V. STOCCHI; G. ANNIBALINI, E. BARBIERI
Department of Biomolecular Sciences, University of Urbino Carlo Bo, Campus Scientifico "E.Mattei", Urbino, Italy

Limoncella is the common name of a fruit tree of Rutaceae family, a rare and ancient Mediterranean variety of *Citrus* genus. The fruit is composed of flavedo (10 – 20%) and pulp (35 – 40%). Albedo is the spongy white layer underlying flavedo, a source of flavonoids (1,2) and usually food waste for the industries. Albedo, together with septum and core, constitutes 30-40% of the fruit weight.
In this study, albedo, particularly thick and sweet, and flavedo, were morphologically and chemically characterized.
Preliminary observations of fresh, dry and fixed albedo and flavedo samples, were carried out by means of a variety of microscopy approaches: light, fluorescence, transmission, scanning and environmental scanning electron microscopy (3). Semi-thin sections were stained with safranin, methylene blue, Azur II and basic fuchsin, to highlight and compare characteristic elements of the albedo and flavedo of this ancient fruit.
All morphological approaches allowed us to observe parenchymal cells with a considerable central vacuole. Elements of secondary lignified wall characteristic of the xylem were observed such us spiral tracheid, with regular pitting walls. Micro-analytical analyses showed that carbon, oxygen, chloride, potassium and calcium were associated to albedo and flavedo structures.
Further studies are necessary for a better biodiversity and eco-sustainability valorisation of the *Limoncella* biovar. In particular, its albedo, useful for recycling of organic waste in agriculture and food industries, and important source of flavonoids, deserves a new attention and highlighting.

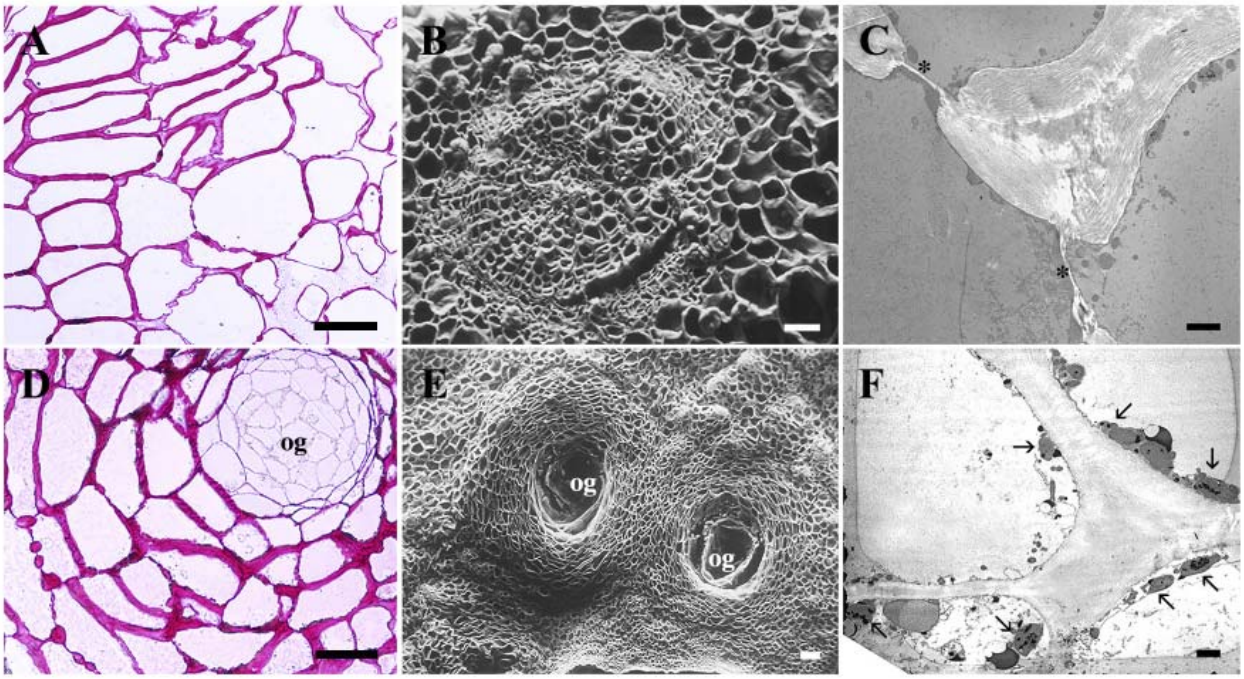

Figure 1 Light microscopy (A,D), SEM (B,E) and TEM (C,F) of albedo (A-C) and flavedo (D-F). Fibers and vessels in cross sections are visible (A-C). C, plasmodesmata structure (*). Oil glands (og) in flavedo area are present (D,E). In F, some plastids (⇦) in vessel cytoplasm are evident.
Bars: A, B = 50 µm; C,F = 0.25 µm; D, E = 100 µm.

References

[1] Y. Q. Liu, E. Heying, S. A. Tanumihardjo, Comp. Rev. Food Science Food Safety, 11 (2012) 530–545
[2] T. Inoue , A. Yoshinaga , K. Takabe , T. Yoshioka , K. Ogawa , M. Sakamoto , J. Azuma , Y. Honda, Phytochem Anal, 26 (2015) 105–110
[3] S. Burattini, M. Battistelli , S. Codenotti , E. Falcieri , A. Fanzani , S. Salucci, Acta Histochem, 118 (2016) 278–285

Scanning electron microscopy-a sensitive tool in Porifera determination

STEFAN ANDJUS[1], BOŽICA VASILJEVIĆ[1], VLADIMIR LAZOVIĆ[2], MOMIR PAUNOVIĆ[1]
[1] University of Belgrade, Institute of Biological Research „Siniša Stanković", Belgrade, Serbia;
[2] University of Belgrade, Institute of Physics, Belgrade, Serbia

Freshwater sponges belong to macrozoobenthic organisms with a worldwide distribution. European rivers and lakes, most generally, have been well analyzed for the presence of Porifera [1]-[5]. Some geographical areas, however, remain largely unexplored. Among these are West Balkan countries. The aim of the present study was to determine sponge species collected in Macedonia and Serbia based on the specific morphology of their mineral skeleton, using light and scanning electron microscopy (SEM). In total 122 specimens were collected and spicules were prepared by nitric acid technique [6]. Determination was mainly performed by observing sponge structures under light microscope. For fine analysis of sponge skeleton elements, in some cases, SEM was applied allowing measurements of these elements to be done for an accurate species determination (Figure 1.).

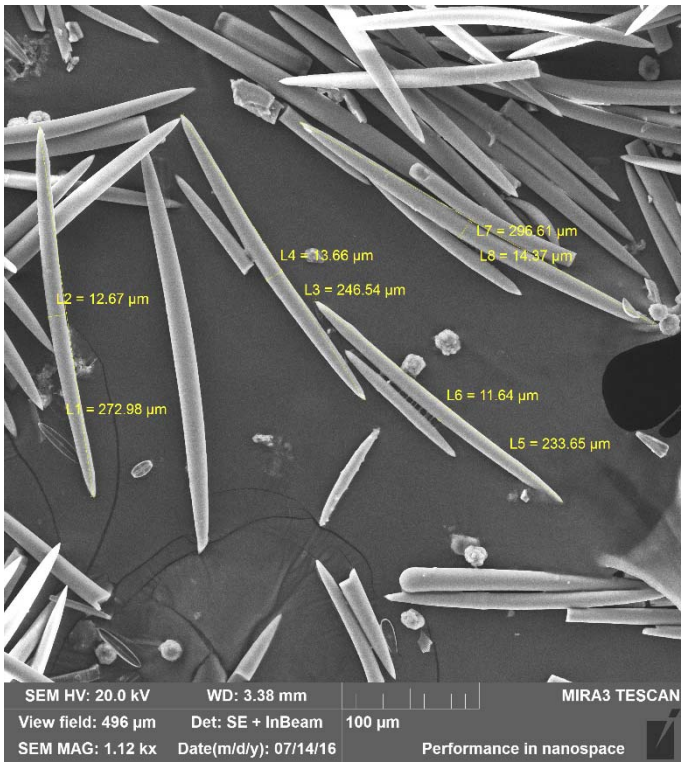

Figure 1. SEM image of spicules (megascleres) of *E. fragilis* with measured lengths and widths

As revealed by the length and width of sponge spicules, as well as their shape, among the collected specimens the following species have been identified: in Serbia- *Spongilla lacustris* Linnaeus, 1758, *Eunapius fragilis* (Leidy, 1851), *Ephydatia fluviatilis* (Linnaeus, 1759), *Ephydatia muelleri* (Lieberkühn, 1856), and *Trochospongilla horrida* Weltner, 1893; in Macedonia *S. lacustris*, *E. fluviatilis*, *S stankovici* Arndt 1937, *Spongilla carteri* Bowerbank, 1863 and *Ochridaspongia rotunda* (Arndt 1937). In conclusion, SEM made possible an efficient assessment of fine sponge skeletal structure needed for species identification.

References

[1] J. Gugel. Life cycles and ecological interactions of freshwater sponges (Porifera, Spongillidae) in the River Rhine in Germany. Limnol Manag Inl Waters. 2001;31(3):185–98

[2] I. Dröscher, J. Waringer. Abundance and distribution of freshwater sponges (Spongillidae) in Danube floodplain waters near Vienna, Austria. Dep Freshw Ecol Vienna Univ. 2007;52(6)

[3] K. A. Økland, J. Økland. Freshwater sponges (Porifera: Spongillidae) of Norway: distribution and ecology. Hydrobiologia [Internet]. 1996;330(1):1–30. Available from: http://dx.doi.org/10.1007/BF00020819

[4] T. Roovere, A. Lopp, T. Reintamma, A. Kuusksalua, E. Richelle-Maurerc, M. Kelvea. Freshwater sponges in Estonia: genetic and morphological identification. In: Hillar A, Virve K, editors. Proceedings of the Estonian Academy of Sciences, Biology and Ecology. Estonian Academy Publishers; 2006. p. 216–27

[5] R. Manconi, R. Pronzato. Global diversity of sponges (Porifera: Spongillina) in freshwater. Hydrobiologia. 2008;595(1):27–33.

[6] R. Manconi, R. Pronzato. Phylum Porifera. In: James TH, Christopher RD, editors. Thorp and Covich's Freshwater Invertebrates: Ecology and General Biology: Fourth Edition [Internet]. 4th ed. Academic Press; 2016 [cited 2019 May 25]. p. 133–57

Gimme shelter: Grapevine Pinot Gris virus in deformed endoplasmic reticulum

LAURA PAGLIARI[1], GIULIA TARQUINI[1], SARA BUOSO[1], ALBERTO LOSCHI[1], PAOLO ERMACORA[1], GREGOR KAPUN[2], RITA MUSETTI[1]

[1] Department of Agricultural, Food, Environmental and Animal Sciences, University of Udine, Italy;
[2] Center of Excellence on Nanoscience and Nanotechnology – Nanocenter, Ljubljana, Slovenia

Introduction.

Grapevine Pinot Gris (GPG) disease is associated to grapevine Pinot gris virus (GPGV), a positive-sense single-stranded RNA [(+)ssRNA] virus observed inside membrane-bound structures in the bundle sheath cells (BSCs) of the infected grapevines [1].

Usually, (+)ssRNA viruses modify host-cell membranes, to form inclusion bodies used as scaffolds for the assembly of viral replication complexes (VRCs). VCRs create an optimal environment for viral RNA synthesis and genome encapsidation, facilitating viral access to essential host resources and sheltering viral genome replication from host antiviral defences [2]. VRCs can derive from a variety of membranous organelles, but most of (+) ssRNA viruses studied to date usurped the endoplasmic reticulum (ER) [3].

Membrane-bound structures observed in BSCs of GPGV-infected grapevines [1] show a similar organization to those described in other virus-plant host interactions and assumed as deformed ER [4]. The association of the replicase protein with the host-cell ER reported for grapevine rupestris stem pitting-associated virus (GRSPaV), a virus belonging to the Betaflexiviridae family as GPGV [3], supports the hypothesis of a possible ER targeting by GPGV. In the present study, we investigated the identity of the GPGV-induced membranous structures. The combination of different microscopy techniques with molecular analysis provided functional information about the still poor investigated GPGV-grapevine interaction at ultrastructural level.

To understand if GPGV infection could interfere with ER-related pathways, the expression of *CALRETICULIN 3* (*CRT3α*, XM_010652325.2, and *CRT3β* XM_010650921.2), *CALNEXIN* (*CNXα*, XM_002273672.4, and *CNXβ*, XM_002277630.4) and *LUMINAL BINDING PROTEIN* 5 (*BIP5α*, XM_002263287.3, and *BIPβ*, XM_010664593.2) was analysed (Fig. 1). Since the expression of these genes is known to be induced by ER stress [5], they were used as marker of GPGV-ER interaction. Following GPGV infection, the above cited genes underwent to a significant upregulation by a factor varying from 2 to 3, with the sole exception of the gene *CRT3α*, whose transcription level was not altered (Fig. 1).

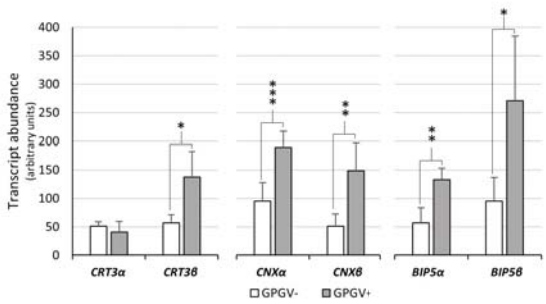

Figure 1. GPGV alters the expression of ER stress related genes.

TEM observations of epoxy resin-embedded samples confirmed the presence of membrane-bound structures in GPGV-infected BSCs, as previously reported ([1] and [6]). In London Resin White-embedded samples, anti luminal-binding protein (anti Bip) antibody localized the target protein in correspondence to ER in BSCs of healthy plants (Fig. 2A) and to the membrane-bound structures in BSCs of GPGV-infected samples (Fig. 2B). Anti- double-stranded RNA (anti dsRNA) antibody localized the intermediate of the viral replication only in correspondence to the putative deformed ER (Fig. 2D), failing to mark ER in healthy plants (Fig. 2C) or other cell compartements in infected BSC (Fig 2D). Considering ion beam scanning electron microscopy (FIB-SEM) analysis, 3D datasets were acquired (Fig. 2G-J): segmentation and 3D reconstruction are in progress (Fig. 2K).

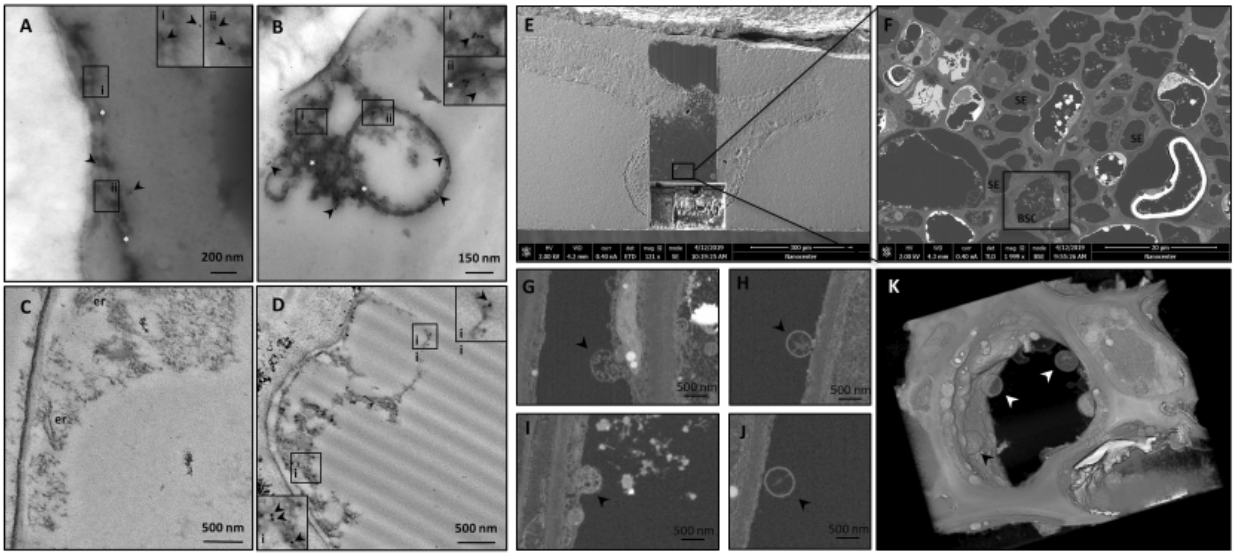

Figure 2. GPGV replicates in ER-derived membrane bound structures. A-B: Bip immunolocalization. C-D: dsRNA immunolocalization. E-F: individuation of the region of interest for FIB-SEM observations. G-H: individuation fo the membrane bound structures. K: 3D reconstruction.

Conclusions

In this study, we investigated on the identity of the GPGV-related membranous structures reported in GPGV-infected grapevine tissues ([1] and [6]). The specific localization of the ER-associated BiP identified the membranous structures as ER. The ER involvement in grapevine-GPGV interaction was confirmed by the change in the expression of different ER-stress related genes, as evidenced by RT-qPCR. FIB-SEM investigation will reveal the 3D organization of the ER-derived structures and their connections with the cytoplasmic environment. Finally, the association of the viral replication intermediate ds-RNA with the ER-derived structures indicated them as VRCs where GPGV replication occurs. Besides providing functional information about the still poor investigated GPGV-grapevine interaction, our results aim to help to achieve a better understanding of the microenvironment organization of grapevine viral replication complexes in their natural host.

References

[1] Tarquini G, Ermacora P, Bianchi GL, et al, Protoplasma 255 (2018) 923–935
[2] Heinlein M, Virology 479–480 (2105) 657–671
[3] Prosser SW, Xiao H, Li C, et al, J Gen Virol 96 (2015) 921–932
[4] Jiang J, Patarroyo C, Garcia Cabanillas D, et al, J Virol 89 (2015) 6695–6710
[5] Liu J-X, Howell SH New Phytol 211 (2016) 418–428
[6] Tarquini G, Zaina G, Ermacora P, et al, PLOS ONE 14 (2019) e0214010

The use of fluorescence microscopy for classification of pollen grains

MIRA STANKOVIĆ, JASNA SIMONOVIĆ RADOSAVLJEVIĆ, DANIELA DJIKANOVIĆ, DRAGICA SPASOJEVIĆ AND KSENIJA RADOTIĆ
Institute for Multidisciplinary Research, University of Belgrade, Serbia

1. Introduction

A large number of people suffer from a pollen allergy in all regions of the world [1]. In general, pollen allergens are considered a major risk factor for both seasonal allergic rhinitis and asthma [2]. Pollen grains show strong autofluorescence [3]. Fluorescence is non-destructive, sensitive, simple and fast method for analysis of fluorescent compounds contained in very low amounts in the samples [4]. The fluorescence microscopy and fluorescence spectroscopy, in combination with appropriate statistical methods, may provide useful fingerprints in pollen analysis [5].

2. Details of experiment

2.1. Pollen samples

Pollen samples were harvested from Serbian agricultural estate Radmilovac in the early spring 2018. The samples were packed in bags and stored in a freezer at -80 °C until analysis. We analyzed pollen samples of four different botanical species (*Amorpha fruticosa, Robinia pseudoacacia, Rhamnaceae and Rubus* L.).

2.2. Microscopic fluorescence image analysis

Fluorescent microscopic images were obtained by using Axio Observer Z1 Mikroskop, with AxioCamMR3 camera (8 bit per channel). Pollen samples were deposited on glass plates for the measurements. The same optics was used for all recordered pictures, in order to avoid chromatic aberations. The excitation/emission wavelengths were: 358/461 nm (49-DAPI), 488/510 nm (38 GFP), and 558/580 nm (DsRED), in the following text referred to as blue, green (38 GFP) and yellow, respectively. Series of images were captured for each sample, in order to create its representative image with a 10× objective lens. Each image was considered a matrix, where each element represents one pixel. The captured images (Figure 1) were analyzed using ImageJ program to provide the average red, green, and blue pixel values for the fluorescence intensity of each pollen grain selected in an image. Image analysis methods are quantitative tools for analyzing fluorescence and bright-field microscopy data.

a) 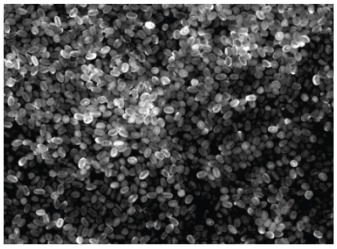 b) 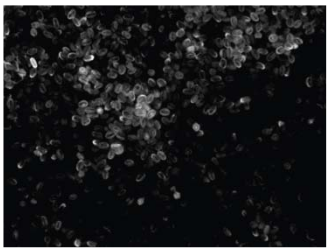 c) 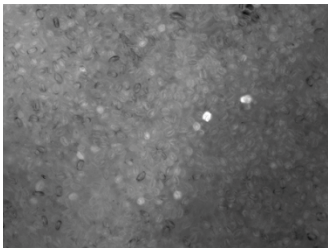

Figure 1. Microscopic fluorescence image for *Rhamnaceae* pollen grains through a) blue (49-DAPI), b) green (38 GFP), c) red color (DsRED) filters

2.3. Measurement of the fluorescence spectrum

Fluorescence spectra were collected using a Fl3-221 P Fluorolog spectrofluorimeter (Jobin-Yvon Horiba, Paris, France) equipped with a 450 W xenon lamp and a photomultiplier tube. All pollen samples were measured in a front-face configuration of the measuring cell. The illumination's incident angle was set to 22.5 °C, to minimize light reflections, scattered radiation and depolarization phenomena. The Reyleigh masking was applied in order to reduce Rayleigh scattering from the solid sample which limits the sensitivity and accuracy of the measurement. The fluorescence emission spectra in range from 350 to 600 nm, were recorded with excitation wavelengths of 330 to 430 nm. The integration time was 0.1 s, and the wavelength increment in excitation measurements was 5 nm, and emission increment was 1 nm. A spectral band width of 2 nm was employed for both the excitation and emission slits. The average of the 21 emission spectra recorded for various excitation wavelengths, for various pollen samples, are shown in the Figure 2.

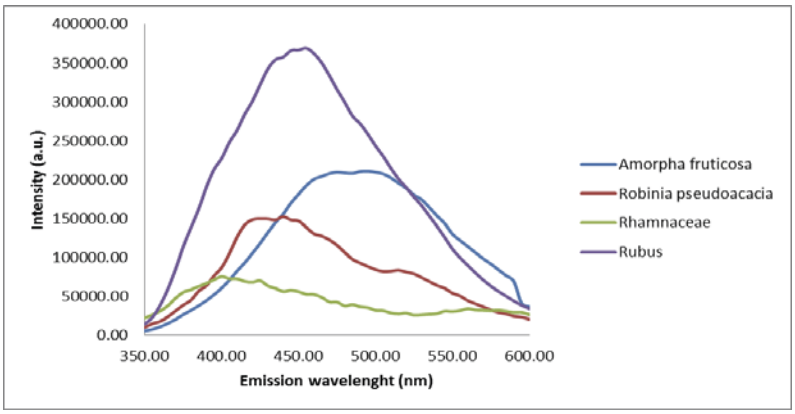

Figure 2. The average fluorescence emission spectra for different pollen samples

2.4. Statistical analysis

Principal Component Analysis (PCA) is a statistical method used to reduce the dimensionality of a data set whilst retaining the information content [6]. Principal Component Analysis (PCA) was performed using the CAMO Software AS package for The Unscrambler X 10.4. All data were group-scaled prior to PCA. The singular value decomposition algorithm (SVD) and a 0.95 confidence level for Q and Hotelling T2 limits for outliers were chosen.

For each sample the brightness results of microscopic fluorescence image or average of the 21 emission spectra recorded for various excitation wavelengths were used as input values in PCA, in order to take into account contribution of all fluorophores present in the sample. The results of PCA analysis are shown in the Figure 3.

3. Discussion

The PCA was used to classify pollen samples according to the differences in microscopic fluorescence and characteristic emission spectra. The scores and loadings plots obtained for pollen samples are shown in Figure 3. The PCA resulted in a two-component model which explains 98 % (microscopic fluorescence) and 99% (fluorescence emission spectra) of total variance. Based on brigtness data, *Amorpha fruticosa* was separated from the other investigated pollen samples along positive PC1, while *Robinia pseudoacacia* was separated along negative PC1. The discrimination of *Rubus* L. sample was along positive PC2, and of *Rhamnaceae* sample along negative PC2. PCA results for fluorescence emission spectra confirm separation of the pollen samples based on their characteristic emission maxima: *Amorpha fruticosa* at 480-520 nm, *Robinia pseudoacacia* and

Rubus L. at 420-470 nm, and *Rhamnaceae* at 350-420nm and 570-590nm (Figure 3B, Figure 2). The separation of the pollen samples was most probably due to their specific phenolic composition.

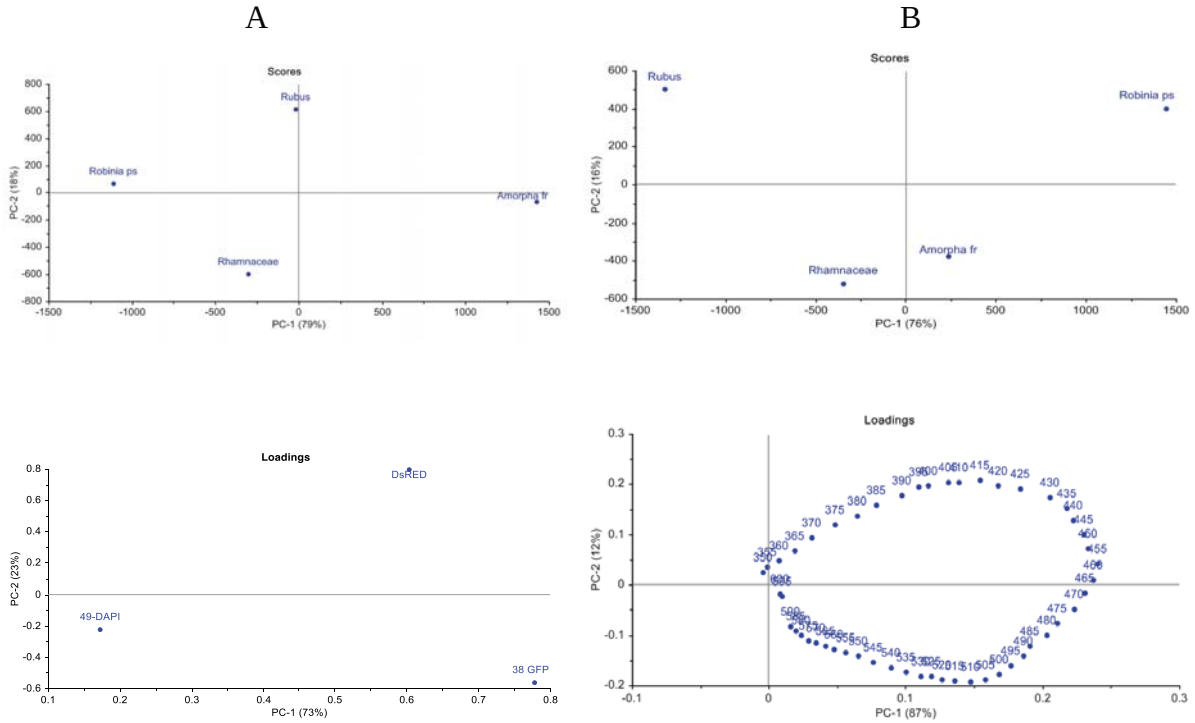

Figure 3. Principal component analysis of : (A) microscopic fluorescence and (B) the fluorescence emission spectra

4. Conclusions

In this pilot research, we showed that pollen autofluorescence varied between the pollen of the different botanical species. Our findings suggest that classification of pollen grains may be obtained based on their fluorescence images.

References

[1] https://www.allergy.org.au/patients/allergic-rhinitis-hay-fever-and-sinusitis/pollen-allergy

[2] G. D'Amato, L. Cecchi, S. Bonini, C. Nunes, I. Annesi-Maesano, H. Behrendt, G. Liccardi, T. Popov, P.van Cauwenberge Allergenic pollen and pollen allergy in Europe. Allergy 62 (2007) 976–990

[3] W. C. McCrone, and J. G. Delly, Ultraviolet (365 nm) and blue-violet fluorescence analysis of particles, In The Particle Atlas 4 (1973) Ann Arbor Science Publishers

[4] B. Valeur, Molecular fluorescence: Principles and applications 63 (2001)

[5] J. Sádecká , J. Tóthová, Fluorescence Spectroscopy and Chemometrics in the Food Classification - A Review. Czech, Journal of Food Sciences 25 (2007) 159-173

[6] G.L. Smith, Principal component analysis: an introduction Analytical Proceedings, 28 (1991) 150-151

Distinction between specific ionic and osmotic aspects of the ultrastructural changes induced by salt stress on etioplasts and their greening

ROUMAISSA OUNOKI[1], ADÉL SÓTI[1], ANNAMÁRIA KÓSA[1], BEATA MYSLIWA-KURDZIEL[2] AND KATALIN SOLYMOSI[1]

[1] Department of Plant Anatomy, Eötvös Loránd University, Budapest, Hungary; [2] Department of Plant Physiology and Biochemistry, Jagiellonian University, Krakow, Poland

Salt and drought stress represent increasingly threatening global problems for agriculture and food security. They strongly impact ion and water homeostasis of plants and plant metabolism, including the development and activity of the photosynthetic apparatus. Disturbances in plastid metabolism and photosynthesis strongly affect plant productivity and yield. In spite of this evident relationship, data about the effect of salt and osmotic (drought) stress on plastid structure and function are scarce. In addition, ultrastructural reports are also controversial, some of them show the swelling of the intrathylakoidal space in salt stressed plants, while others do not observe similar strong alterations in plastid structure. The molecular background of the observed swelling is also unclear – in case of drought or salt stress one would rather expect the shrinking of the water-containing lumen. In addition, salt stress affects plants in a complex way: its impact can be partly related to direct ion toxicity or to indirect effects related to salt-induced osmotic stress. Since several crops are sowed deep in the soil, it is evident that during the early phases of their germination their leaves are developing in the soil, deprived from light, and will get exposed to light only after they reached the surface.

Therefore, in this work we compared the effect of salt stress to isoosmotic (drought) stress induced by polyethylene glycol (PEG) on the etioplasts of wheat (*Triticum aestivum*). For this purpose we used excised leaf pieces obtained from the first leaves of 8-11-day-old wheat plants grown in complete darkness. Leaf pieces were floated on Hoagland solution (control), salt solution (600 mM NaCl:KCl 1:1 in Hoagland) or on PEG solution (isoosmotic amount of PEG dissolved in Hoagland) for 4-4,5 h in the dark, or in a second type of experiments were floated for 1.5 h in the dark and then illuminated with 50 µmol photons m^{-2} s^{-1} white light for 16 h.

Salt stress induced distinct and specific alterations in the organization of the pigment-protein complexes of etioplasts and of the etioplast inner membrane structure (as also revealed by stereographic analyses) in the dark. Similarly, salt stress treatment fully inhibited the etioplast-to-chloroplast transformation and chlorophyll biosynthesis. Granum development was only slightly delayed in the PEG treated plants, while it was almost completely inhibited under salt stress. Our data thus outline that the direct ionic component of the salt stress is more important than its osmotic component. Further investigations are necessary to elucidate more the molecular background of these processes.

Acknowledgements
This work was financed by the National Research, Development and Innovation Office (grant OTKA FK 124748), the János Bolyai Research Scholarship of the H.A.S. (to K.S.). The Ph.D. studies of R.U. are financed by Stipendium Hungaricum Scholarship of the Tempus Public Foundation.

LS4
Neuroscience and histopathology

CHAIRPERSONS:

Agnes Kittel, Gerd Leitinger

INVITED LECTURE

MICU1 controls cristae junction and spatially anchors mitochondrial Ca^{2+} uniporter complex

BENJAMIN GOTTSCHALK[1], CHRISTIANE KLEC[1], GERD LEITINGER[2], EVA BERNHART[1], RENE ROST[1], HELMUT BISCHOF[1], CORINA MADREITER-SOKOLOWSKI[1], SNJEZANA RADULOVIC[1,2], EMRAH EROGLU[1], WOLFGANG SATTLER[1], MARKUS WALDECK-WEIERMAIR[1], ROLAND MALLI[1,3] & WOLFGANG F. GRAIER[1]

[1] Gottfried Schatz Research Center, Molecular Biology and Biochemistry, Medical University of Graz, Austria; [2] Gottfried Schatz Research Center, Cell Biology, Histology and Embryology, Medical University of Graz, Austria; [3] BioTechMed Graz, Austria

Regulation of Ca^{2+} uptake is a crucial process for activation of mitochondria. Recently, core proteins (MICU1, MCU and EMRE) comprising the mitochondrial Ca^{2+} uniporter complex (MCUC) were identified, and this propelled investigations into its physiological workings. The current understanding of the MCUC complex is that the pore-forming proteins MCU and EMRE create a selective Ca^{2+} channel in the inner mitochondrial membrane (IMM), which is regulated by calcium-triggering mediated through the gatekeeping component MICU1. We present a new paradigm concerning the dynamics and spatial organization of these mitochondrial Ca^{2+} uptake components. By applying super-resolution structured illumination microscopy (SIM) to living cells, we were able to visualize MICU1, MCU, and EMRE spatial responses to Ca^{2+} mobilization at a sub-organellar level. We demonstrate that MICU1 is absent from cristae membranes owing to its quaternary structure and poly-lysine domain. Moreover, this exclusive localization of MICU1 is important for the stability of cristae junctions (CJ), cytochrome c release and the mitochondrial membrane potential. In contrast to MICU1, MCU and EMRE are homogeneously distributed at the inner mitochondrial membrane under resting conditions. However, upon cytoplasmic Ca^{2+} elevation MCU and EMRE dynamically accumulate at the IBM in a MICU1-dependent manner. Eventually, our findings unveil a so far unknown essential function of MICU1 in CJ stabilization and provide novel mechanistic insights of how sophistically MICU1 controls the MCU-Complex while maintaining the structural mitochondrial membrane framework.

INVITED LECTURE

Studying the complex roles of microglia with high resolution imaging and microglia manipulation approaches

ÁDÁM DÉNES
Momentum Laboratory of Neuroimmunology, Institute of Experimental Medicine, Hungarian Academy of Sciences, Budapest, Hungary

Introduction

The role of inflammation in common neurological disorders is increasingly recognised. Brain pathologies are associated with alterations in glial responses, BBB function and cerebral blood flow, which are markedly influenced by central and systemic inflammatory actions. Glial cells, particularly microglia emerge as major regulators of neuroinflammation with several currently unexplored roles in cerebrovascular responses, BBB function and leukocyte recruitment, which processes are shaped by both central inflammatory stimuli and circulating immune mediators. Understanding the molecular mechanisms underlying these interactions could pave the way for novel therapeutic approaches in brain diseases [1,2]. However, studying microglial actions is highly challenging due to their immediate reaction to even minor tissue disturbances, and the lack of microglia-specific manipulation approaches until recently. The rapidly growing body of tools to image or influence microglia greatly facilitates the understanding of microglial contribution to physiological and pathological processes in the brain.

Methods

Using selective microglia manipulation approaches, imaging, transgenic models and advanced microscopy, actions through which microglia shape neuronal activity and injury can be investigated. To this end, microglia-neuron interactions, neuronal calcium responses, blood brain barrier (BBB) injury and cerebral perfusion have been investigated in real time with two-photon-, widefield- and laser speckle contrast imaging after cerebral ischemia, infection and in other models of neuroinflammation. In line with this, high resolution anatomy with confocal laser scanning microscopy, STORM superresolution microscopy and transmission electron microscopy combined with electron tomography enabled us to investigate interactions between microglial processes and neurons, microvessels, or other elements of the neurovascular unit.

Results

Microglia react rapidly to neuronal injury following neurotropic virus infection or cerebral ischemia. Elimination of microglial cells, or blocking specific signalling pathways results in worse functional outcome and increased neuronal injury in mice (Fig. 1.) [3,4].

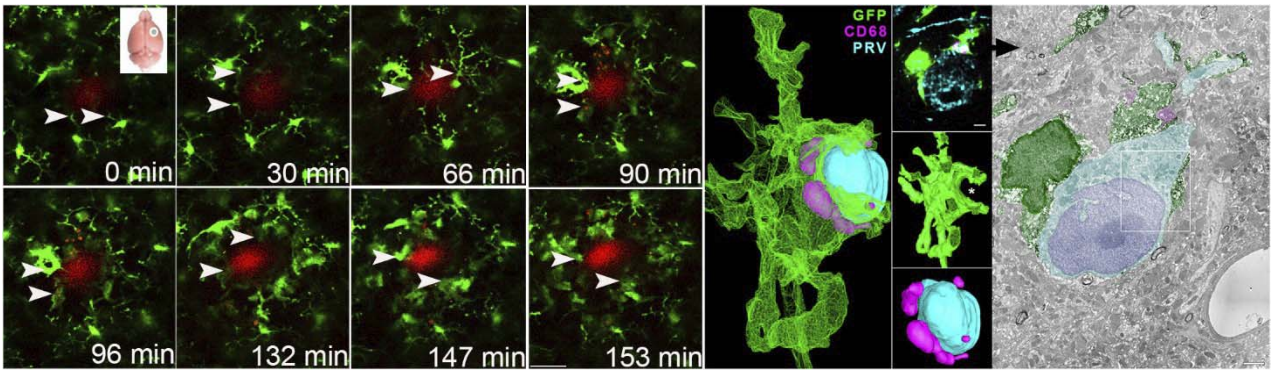

Figure 1. Microglial processes surround virus infected neurons.

We also show that in the neurovascular unit microglial processes establish direct contacts with different cell types and microglia play a previously unrecognised role in regulating cerebral blood flow under both physiological and pathological conditions. Real-time chemogenetic manipulation of microglia also shapes cerebral perfusion. In addition, microglia establish direct contacts with neuronal cell bodies termed as somatic junctions, which possess a unique ultrastructure [5]. Wide-range imaging data underpins the importance of these somatic junctions in both physiological and pathological processes (Fig. 2.)

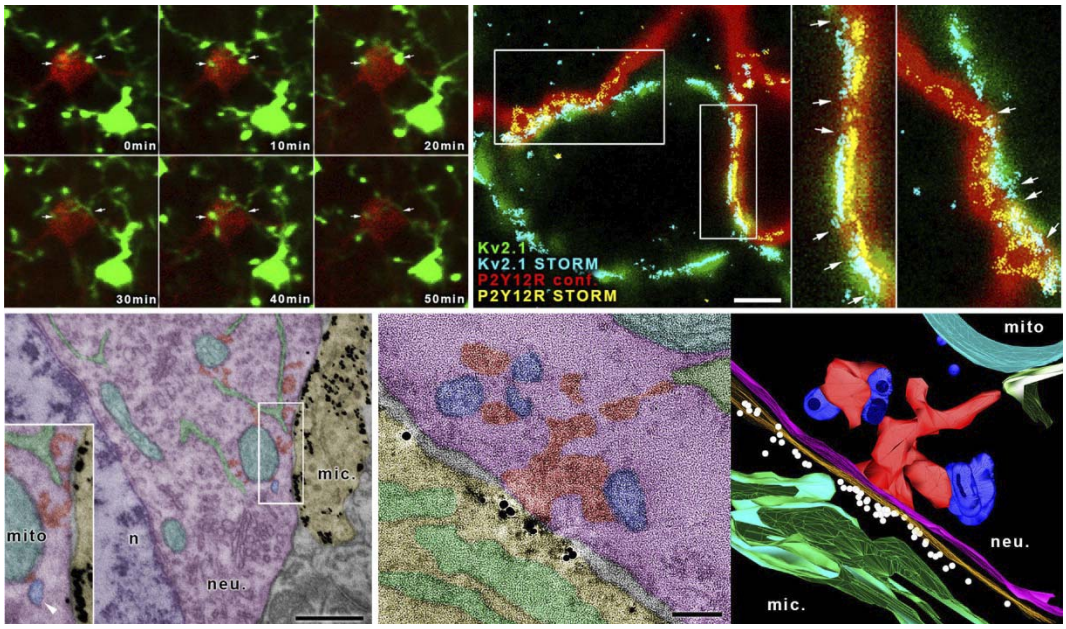

Figure 2. Microglial processes form somatic junctions with specialized areas of neuronal cell bodies

Discussion

Understanding the physiological role of microglia and their contribution to neuronal injury or cerebral blood flow is essential for the development of novel diagnostic and therapeutic tools in brain diseases.

References

[1] M. W. Salter, B. Stevens, *Nat Med*. 23, 1018-1027 (2017).
[2] R. Sankowski, S. Mader, S. I. Valdés-Ferrer, *Front Cell Neurosci.* 9:28 (2015).
[3] G. Szalay, B. Martinecz, N. Lénárt, et al. *Nat Commun*. 7:11499 (2016).
[4] R. Fekete, et al. *Acta Neuropathol.* 136, 461-482 (2018).
[5] C. Cserép, B. Pósfai, et al. *bioRxiv*. https://doi.org/10.1101/606079.

Electron microscopic analysis of neurosecretory granules in the neuroblastomas of paediatric patients

TAMARA KRAVIC-STEVOVIC[1], TAMARA MARTINOVIC[1], DARKO CIRIC[1], GORDANA SAMARDZIJA[2], SOFIJA JOVANOVIĆ[1], DJURICIC SLAVISA[2], DJOKIC DRAGOMIR[2],VUJIC DRAGANA[2,3], VLADIMIR BUMBASIREVIC[1]

[1] Institute of Histology and Embryology, Faculty of Medicine, University of Belgrade, Serbia; [2] Mother and Child Health Care Institute of Serbia "Dr Vukan Cupic", Belgrade, Serbia; [3] Mother and Child Health Care Institute of Serbia "Dr Vukan Cupic", Faculty of Medicine, University of Belgrade, Serbia

1. Introduction

Neuroblastoma represent a type of the most frequently diagnosed solid, extracranial tumors in paediatric patients [1]. A correlation between the aggressiveness of these tumors and their clinical prognosis has been discovered [2]. In cells of peripheral neuroblastic tumors, there are neurosecretory granules (NSG), same in nature as those observed in neuronal processes [3].

2. Aim

The aim of this study was to determine the presence of neurosecretory granules in neuroblastoma cells and to compare the number of neurosecretory granules found in cells of tumors with a favourable prognosis to the corresponding number in cells of tumors with an unfavourable one with the use of transmission electron microscopy (TEM).

3. Material and methods

Tumor samples were acquired through biopsies of peripheral neuroblastic tumor tissue from 10 newly diagnosed, previously untreated paediatric patients (ranging in age between 3 months and 15 years and 11 months, with an average age of 48.7 months at the time of diagnosis). Six of the patients were male, whereas the remaining four were female. The tumor samples were first frozen, then fixed in glutaraldehyde, and then processed for electron microscopy. Ultrastructural morphometry was performed on TEM ultra-thin sections in 60 cells per sample of tumor tissue. The structural hallmarks of the cells were observed and the number of NSGs in them counted. The analysis was done at a magnification that allowed maximum certainty whilst identifying the granules (28000x – 56000x).

4. Results

The neurosecretory granules were distinguished from the rest of the cytosol in photomicrographs as round structures with an electron dense center, surrounded with an electron lucent, peripheral halo (Figure 1). In numerous tumor cells, NSGs were found in close proximity to the nucleus. It was found that the cells of tumors with an unfavorable prognosis have more neurosecretory granules (141.2 ± 89.18) in their cytoplasm than the cells of tumors with a favorable one (37.2 ± 41.17) ($p < 0.05$) (Graph 1).

5. Conclusion

An increase in the number of neurosecretory granules in cells of tumors with an unfavorable prognosis, as established in this research, could partially shed light on the role these structures play in tumorigenesis.

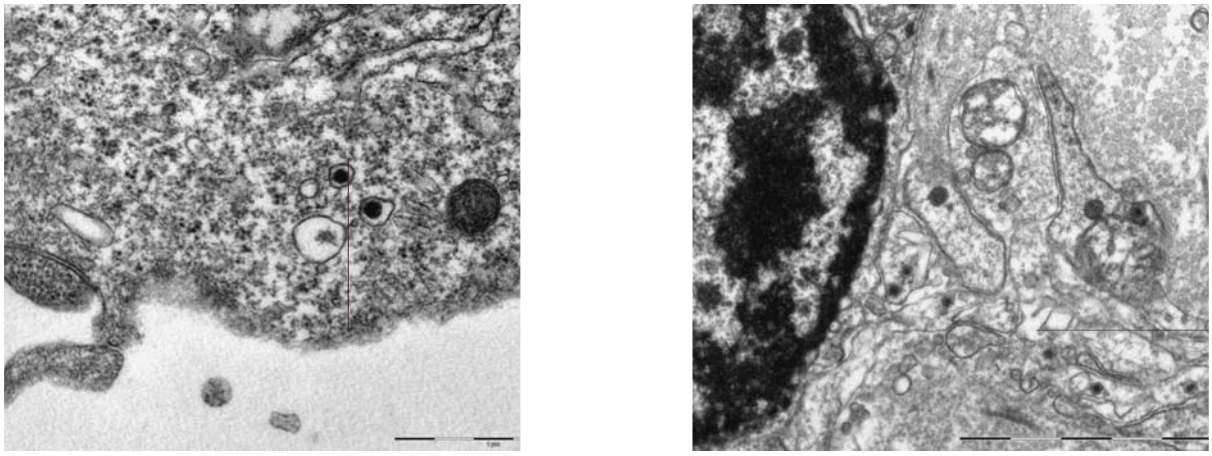

Figure 1. Electron photomicrograph of a favorable prognosis tumor cell (left, magnification 28000x) and unfavorable prognosis tumor cell (right, magnification 18000x). Red arrow showing neurosecretory granules.

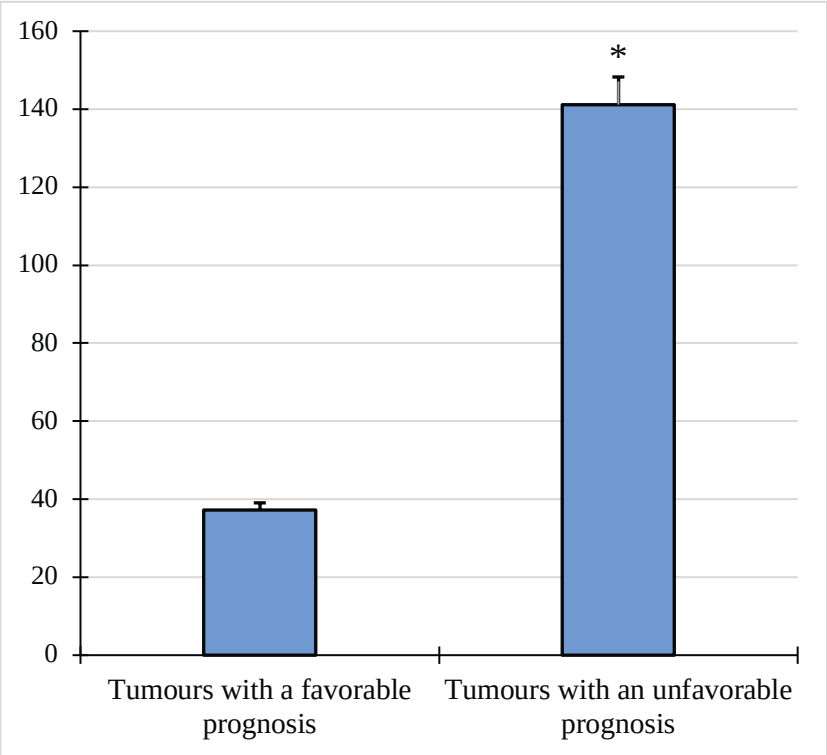

Graph 1. An average number of NSGs per tumor sample with a favorable versus corresponding average in sample with an unfavorable prognosis (asterisk shows statistical significance at $p < 0.05$).

References

[1] R Luksch, MR Castellani, P Collini et al. Crit Rev Oncol Hematol, 107 (2016) 163-81
[2] A Nakazawa, C Haga, M Ohira et al. Cancer Science, 106 (2015) 766-71
[3] S Romansky, D Crocker, K Shaw. Cancer, 2916 (1978) 2392–8

Developmental programming: Imact of prenatal exposure to dexamethasone on gonadotropic cells in female rat offspring

NATAŠA RISTIĆ, NATAŠA NESTOROVIĆ, MILICA MANOJLOVIĆ-STOJANOSKI, SVETLANA TRIFUNOVIĆ, BRANKA ŠOŠIĆ-JURJEVIĆ, BRANKO FILIPOVIĆ, VERICA MILOŠEVIĆ
Institute for Biological Research "Siniša Stanković", Belgrade, Serbia

Introduction The concept of developmental programming implies a linkage between adverse environmental signals during prenatal development and low birth weight as a marker, along with a greater incidence of pathophysiological conditions in postnatal life [1]. Overexposure to glucocorticoids during critical times in fetal development leads to major phenotypic outcomes associated with low birth weight, such as cardiovascular, metabolic and neuroendocrine disorders [2], [3]. The synthetic glucocorticoid dexamethasone (Dx) is often used in obstetrical practice to treat a wide variety of inflammatory conditions or when the risk of preterm delivery exists. Glucocorticoids are also used in numerous experimental protocols to induce developmental programming [2], [4], [5], [6]. Reproductive system is recognized as an important target for developmental programming. Fetal period is critical for pituitary development. Exposure to a compound that affects pituitary cell proliferation and differentiation, such Dx, may alter developmetal trajectory of pituitary gland. The aim of this study was to investigate the effects of prenatal exposure to Dx on gonadotropic cells during the fetal, neonatal, infantile and peripubertal period.

Details of experiment The gravid females were randomized into a control and an experimental group, each consisting of 10 animals. On day 16, 17 and 18 of pregnancy, experimental dams received 0.5 mg Dx s.c. /kg body weight. The control gravid females received the same volume of saline. Female offspring from control and experimental dams were sacrificed under ether narcosis on fetal day 19 and 21 and postnatally, on day 5 (neonatal period), day 16 (infantile period) and day 38 (peripubertal period). Randomization obviated any potential litter bias. The pituitary glands were excised and fixed in Bouin's solution for 48 h. After embedding in Histowax, each tissue block was serially sectioned at 3-µm thickness on a rotary microtome. Blood was collected from individual pups and sera were stored at –70 ° C until folliclestimulating hormone (FSH) and luteinizing hormone (LH) determination. Immunohistochemical, immunofluorescence (IFC), histological and stereological analysis were used in the study of gonadotrophic cells.

Results In 19-day old fetuses the pituitary gland already had definite histological organization. FSH and LH cells were strongly immunohistochemically stained and widespread throughout the pars distalis in small groups or as single cells. Histological characteristics of gonadotropic cells are preserved from fetal to peripubertal period of life. They were polygonal, oval or polyhedral in shape, with large, prominent often eccentrically located nuclei and a thin layer of surrounding cytoplasm. FSH and LH cells were in close contact with blood vessels. With maturation, from fetal to peripubertal period the number of gonadotrophic cells in the pituitary gland increased. Exposure to Dx during critical period in pituitary development decreased the number of gonadotrophic cells in fetuses. Since the number of gonadotrophic cells is mostly set during fetal life, reduction in number was longlasting and persists throughout neonatal, infant and peripubertal period (Fig. 1). Stereological analysis confirmed our histological observation (Fig. 2). Reduced serum concentrations of FSH and LH are likely due to the reduced number of gonadotrophic cells, as the

lack of a change in intensity of FSH and LH IFC signals suggests that the remaining gonadotropic cells were functional.

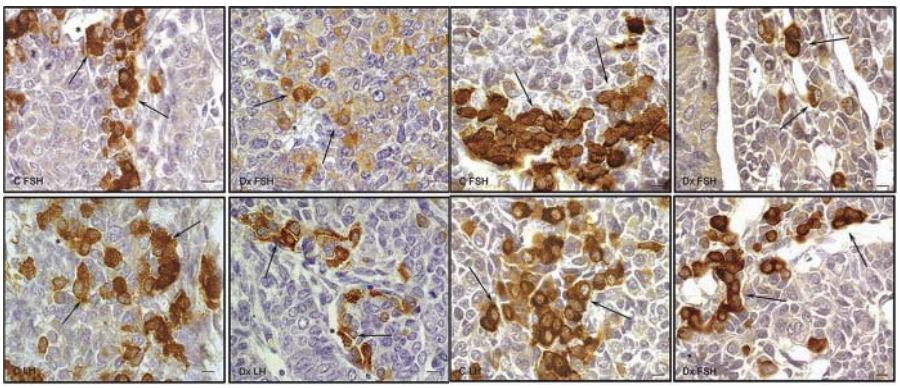

19. fetal day 21. fetal day

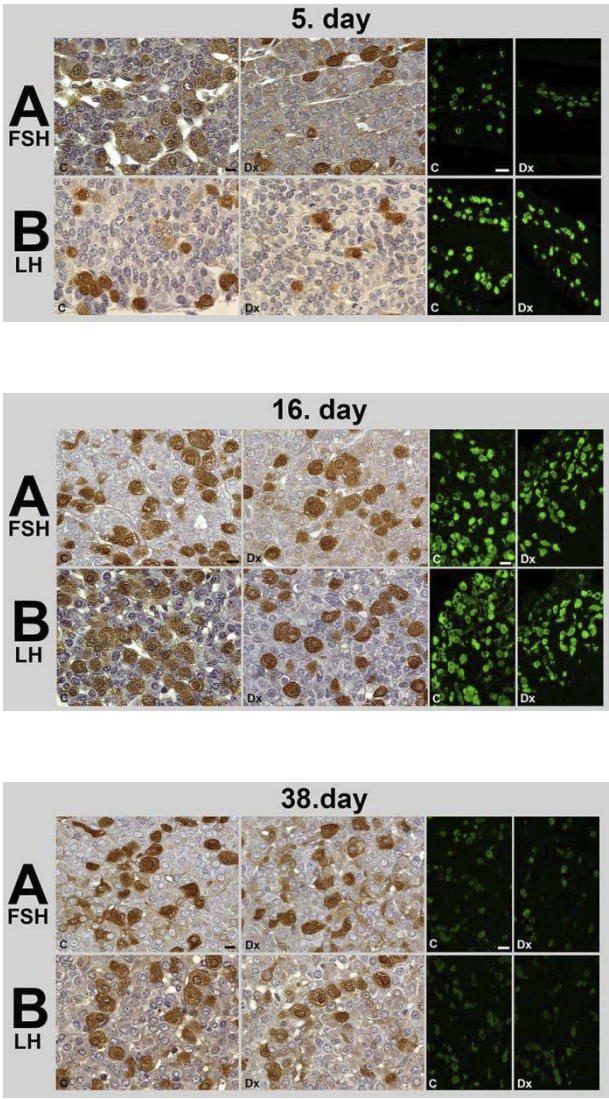

Figure 1. Gonadotropic cells in control and Dx exposed female offspring

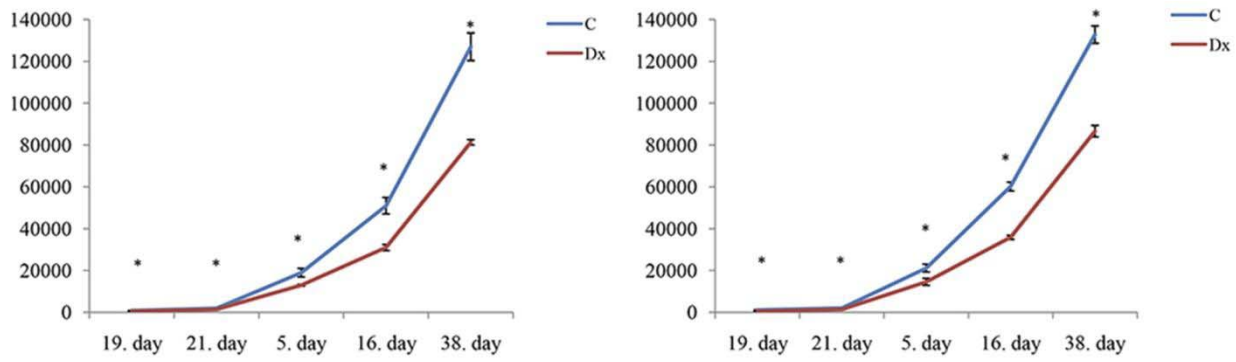

Figure 2.Total numbers of FSH and LH cells per pituitary gland in19- and 21-day old control and Dx exposed female fetuses and 5-16- and 38-day-old control and female offspring prenatally exposed to Dx. Results are given as means ± SD (n = 6)

References

[1] C. Rabadán-Diehl, P. Nathanielsz, J Dev Orig Health Dis, 4 (2013) 3–9

[2] D. O'Regan, C.J. Kenyon, J.R. Seckl, M.C. Holmes, J Endocrinol, 196 (2008) 343–352

[3] M. Manojlović-Stojanoski, N. Ristić, S. Singh, V. Milosević, J Med Biochem, 33 (2014) 1-10

[4] L. Ortiz, A., A. Quan, A. Weinberg, M. Baum, Kidney Int, 59 (2001) 1663–1669

[5] T.Iwasa, T. Matsuzaki, M. Murakami, R. Kinouchi, G. Gereltsetseg, S. Yamamoto, A. Kuwahara, T. Yasui, M. Irahara, Int J Dev Neurosci, 29 (2011) 183–188

[6] M. Poulain, N. Frydman, C. Duquenne, T. N'Tumba-Byn, A. Benachi, R. Habert, V. Rouiller-Fabre, G. Livera, J Clin Endocrinol Metab, 97 (2012) 1890–1897

Adrenal gland functioning in male and female offspring from Dx treated mothers

MILICA MANOJLOVIĆ-STOJANOSKI, NATAŠA NESTOROVIĆ, NATAŠA RISTIĆ, SVETLANA TRIFUNOVIĆ, BRANKO FILIPOVIĆ, BRANKA ŠOŠIĆ-JURJEVIĆ, VERICA MILOŠEVIĆ
Institute for Biological Research "Siniša Stanković"

1. Introduction

The organization and functioning of the hypothalamic-pituitary-adrenal (HPA) axis are highly conserved throughout mammalian phylogeny. There is a marked diurnal rhythm of HPA axis activity with peak levels proceeding the active part of the day in order to optimize energy mobilization and distribution. During the stress response, as the consequence of the HPA axis activation and increased adrenal glucocorticoid circulating level, energy usage is directed to promote survival [1].

The basic functioning as well as the stress response of the HPA axis show a clear sex-specific pattern. There are significant differences in the adrenocortical glucocorticoid release, caused by diverse real or anticipated situations that disrupt homeostasis, comparing males and females. The male or female gonadal hormones influencing hypothalamic neurons, mainly CRH synthetizing neurons, pituitary hormone producing cells, primarily ACTH cells, as well as adrenocortical steroidogenic cells, determined those differences [1]. The functioning of monoamine neurotransmitters that control HPA axis responses to acute and chronic stress in sex specific manner contributes to these differences [2].

Prenatal life experiences also have a significant impact on postnatal HPA axis functioning determining sexually dimorphic responses [3]. Exposures to excessive levels of maternal glucocorticoids signalize adverse environmental conditions for the developing fetus so the developmental trajectory must be adjusted to the expected postnatal surroundings. The application of synthetic glucocorticoids during gestation had similar effect on the developing fetus i.e. maturation of numerous tissues was promoted in parallel with growth retardation that occur causing permanent changes in the endocrine milieu [3].

The aim of this study was to determine eventual sex specific dexamethasone (Dx) programming effects of rat pituitary-adrenal (PA) axis examining offspring, after fetal glucocorticoid overexposure. Thus, the activity of the PA axis was considered in adult, 90 days old male and female offspring, from control and Dx treated mothers during pregnancy. To that end, stereological parameters of the adrenal gland, as final effector of the HPA axis, as well as ACTH circulating level, aldosterone and corticosteroid output from adrenal gland, were investigated.

2. Details of experiment

Thus gravid females were exposed to multiple doses of synthetic glucocorticoid dexamethasone (Dx) during 16-19 days of pregnancy (3x0.5mg/kg/b.m. Dx; 16th-18th gestational day). The activity of the PA axis was considered in 90 day old male and female rat offspring from control and Dx-treated dams. The adrenal glands from both groups were subject to histological and stereological analyses. In addition, concentrations of circulating hormones as ACTH, corticosterone and aldosterone were determined with chemiluminescence method and enzyme immunoassay, respectively.

3. Results

In males, the body mass was significantly increased, while adrenal gland weight and relative adrenal gland weight were significantly decreased in comparison to females. Dx exposure during pregnancy markedly decreased adrenal gland weight and relative adrenal gland weight in female offspring compared to the control group; in male offspring, the maternal Dx treatment did not provoke any changes to the examined parameters in relation to the control values (Table 1).

Table 1. Body mass, adrenal gland weight and relative adrenal gland weight from 3-month-old female and male offspring of control and Dx treated mothers.

	Body mass (g)		Absolute adrenal gland weight (g)		Relative adrenal gland weight (%)	
	Female	Male	Female	Male	Female	Male
C	198 ± 11	274 ± 15*	32.2 ± 2.1	27.8 ± 1.7*	16.2 ± 0.9	10.1 ± 0.8*
Dx	193 ± 8	277 ± 17*	26.3 ± 2.2[a]	25.1 ± 2.1	13.6 ± 1.0[a]	9.1 ± 1.2*

All values are provided as the mean ± SD; n=6. * $p<0.05$ *vs*. female; [a] $p<0.05$ *vs*. C.

The histological analysis and stereological measurement revealed that the volume of the male adrenal gland is markedly smaller in relation to the female volume ($p<0.05$) (Figure 1). Dx exposure during pregnancy significantly decreased ($p<0.05$) the volume of the female adrenal gland, while significant differences were not present in males (Graph 1).

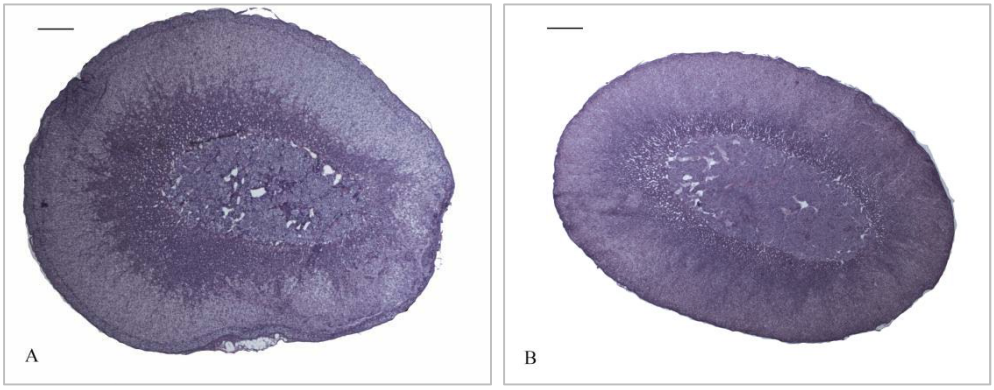

Figure 1. By comparing the central sections of the adrenal gland of the females (A) and males (B) differences in the size become clearly visible. Bar 400 µm.

Graph 1. Volumes of the male and female adrenal gland in offspring from control (C) and Dx-treated (Dx) dams.

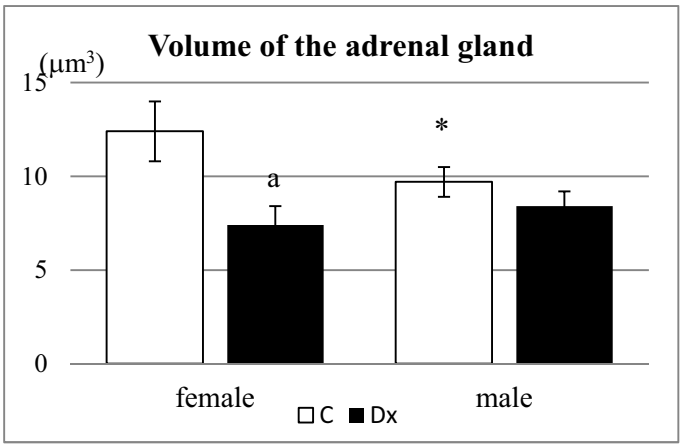

All values are provided as the mean ± SD; n=6. * $p<0.05$ *vs*. female; [a] $p<0.05$ *vs*. C.

In comparing female and male basal plasma ACTH concentration, significant differences were not established. Prenatal Dx exposure provoked marked elevation of the ACTH level in females in relation to control values, while there was no difference in male offspring. Corticosterone circulating concentration was significantly higher in females compared to males. Dexamethasone treatment of gravid females did not have a significant effect on the corticosterone concentration in both females and males compared to their respective control values. Comparing aldosterone concentration between female and male control rats significant decrease was determined in males. Dx exposure did not significantly change the aldosterone circulating level neither in females nor males (Table 2).

Table 2. Results of hormonal data in 3-month-old female and male offspring of control and Dx treated mothers.

	ACTH (pg/mL)		Corticosterone (ng/mL)		Aldosterone (ng/mL)	
	Female	Male	Female	Male	Female	Male
C	21 ± 4	25 ± 4	26 ± 4	15 ± 6 * ↓	0.109 ± 0.014	0.069 ± 0,009 *↓
Dx	31 ± 7 [a] ↑	28 ± 4	32 ± 4	23 ± 8	0.096 ± 0.007	0,075 ± 0,007

All values are provided as the mean ± SD; n=6. * $p<0.05$ *vs*. female; [a] $p<0.05$ *vs*. C.

3. Conclusions

Results of PA morphofunctional study revealed that under basal conditions, females have greater adrenal gland secretory ability due to increased adrenal weight, adrenal volume and circulating concentrations of adrenocortical hormones, corticosterone and aldosterone, in relation to males. Sex-specific programing effects after prenatal Dx exposure were pronounced in female offspring, where higher activity of the PA axis was observed after the hormonal study and adrenal gland stereological analysis; more precisely, in females, the increased ACTH forced adrenal gland synthetic activity, resulting in a corticosterone concentration as in control, reached by adrenal glands that have a reduced volume. Maternal Dx treatment did not change the hormonal output of the PA axis and adrenocortical volume in male offspring under basal conditions.

4. References

[1] N. Goel, J. L. Workman, T. T. Lee, L. Innala, V. Viau, Compr. Physiol., 4 (2014) 1121-1155

[2] R. Hiroi, D. L. Carbone, D. G. Zuloaga, H. A. Bimonte-Nelson, R. J. Handa, Neuroscience, 320 (2016) 43-56

[3] E. Poggi Davis, D. Pfaff, Psychoneuroendocrinology, 49 (2014) 11–25

The Effects of Experimentally-Induced Sepsis on Folliculogenesis in Rat Ovary

MÜGE TAŞDEMIR[1], TUĞBA EKIZ YILMAZ[1], MEHMET KAYA[2], NADIR ARICAN[3], BÜLENT AHISHALI[1]

[1] Istanbul University, Istanbul Faculty of Medicine, Department of Histology and Embriology, Istanbul, Turkey; [2] Istanbul University, Istanbul Faculty of Medicine, Department of Physiology, Istanbul, Turkey; [3] Istanbul University, Istanbul Faculty of Medicine, Department of Forensic Medicine, Istanbul, Turkey

Introduction: Sepsis is characterized by systemic inflammation which develops in response to infection (1). Various pro-and anti-inflammatory cytokines are documented to play multi-faceted roles in the regulation of ovarian folliculogenesis (2, 3, 4). This study was aimed to evaluate the effects of the sepsis conditions created with cecal ligation and perforation (CLP) method on the process of ovary folliculogenesis from morphological, ultrastructural and immunohistochemical aspects.

Materials and Methods: 28 day old immature Wistar Albino female rats were treated with pregnant mare serum gonadotrophin (PMSG; 15 IU, i.p) to develop the first generation of preovulatory follicles. Sepsis was induced by cecal ligation and puncture (CLP). Following in vivo 5-bromo-2-deoxyuridine (BrdU) labeling, animals were sacrificed and ovaries were embedded in paraffin and Epon. Sections were stained for BrdU, caspase-3 and p27 using immunohistochemistry and TUNEL labeling was performed. The alterations in immunoreactivities were analyzed by a semi-quantitative scoring system (HSCORE).

Results: In CLP operated animals, caspase-3 immunoreactivity was significantly increased in antral follicles compared to sham-operated animals. A slight increase was also noted in TUNEL labeling in the antral follicles of septic rats compared to controls. BrdU labeling in the ovarian follicles did not significantly differ between CLP and sham operated rats. In septic animals, p27 immunoreactivity increased significantly in the nuclei of oocytes and decreased in the cytoplasm of granulosa and theca cells in multilaminar primary follicles compared to sham operated rats. In electron microscopic evaluation, fragmentation was observed in the oocytes of early and advanced period follicles of the rats to which CLP operation was applied. Moreover, it was seen that, by being more significant in advanced period follicles, progressing to apoptosis

in granulosa cells increased and degenerations had emerged at the level of organelle in granulosa and theca interna cells.

Conclusion: In conclusion, experimentally-induced sepsis led to exacerbation of apoptotic process in ovarian follicles at advanced stages of development while no alteration was observed in cell proliferation. Our data suggest that although sepsis may not pose a potential threat on developing follicles at least in short term, a severe damage may occur during advanced stages of follicle development.

References

1. R.C. Bone, R.A. Balk, F.B. Cerra, R.P. Dellinger, A.M. Fein, W.A. Knaus, R.M. Schein, W.J Sibbald. Chest, 101(1992), 1644-1655.

2. M.M. Bevers, S.J. Dieleman, R. Van Den Hurk, F. Izadyar. Theriogenology, 47(1997), 13-22.

3. V. Barak, P. Yanai, A.J. Treves, I. Roisman, A. Simon, N. Laufer. Fertil Steril, 58(1992), 719-725.

4. A. Gallinelli, I. Ciaccio, L. Giannella,, M. Salvatori, T. Marsella, A. Volpe. Fertil Steril,; (79)2003, 1365-1372.

Ultrastructural features of mitochondria in lymphocytes of patients with Diabetes Mellitus type 2

TAMARA MARTINOVIC[1], DARKO CIRIC[1], TAMARA KRAVIC-STEVOVIC[1], ANDJELIJA STANKOVIC[1], K. LALIC[2], I. RASULIC[3] AND VLADIMIR BUMBASIREVIC[1]

[1] Institute of Histology and Embryology, Faculty of Medicine, University of Belgrade, Serbia; [2] Clinic for Endocrinology, Diabetes and Metabolic Disease, Clinical Center of Serbia, Faculty of Medicine, University of Belgrade, Serbia; [3] Clinic for Endocrinology, Diabetes and Metabolic Disease, Clinical Center of Serbia, Belgrade, Serbia

1. Introduction

Diabetes Mellitus type 2 (DM type 2) is a metabolic disorder caracterized with insulin resistance and hyperglycaemia.[1] Recent investigations indicate that there is an activation of the cells of immune system, like lymphocytes in chronic metabolic diseases such as DM type 2.[2] Alterations in mitochondria, that are main source of energy in cells, were noticed in activated lymphocytes and in diseases with disfunction of immune system, like DM type 2.[2]

2. Aim

The aim of this study was to determine the ultrastructural characteristics of mitochondria as well as the number and volume of mitochondria in lymphocytes of patients with DM type 2.

3. Material and methods

Mononuclear cells were isolated from peripheral blood of patients wih DM type 2 and healthy individuals, and processed for electron microscopic analysis. Cells were fixed in 2.5% glutaraldehyde, postfixed in osmium tetroxide, and embedded in Epoxy resins. Ultrathin sections were contrasted with lead citrate and uranyl acetate and examined on a transmission electron microscope. The number and volume of mitochondria in the cytoplasm of lymphocytes was determined with the use of “coherent point” grid. [3]

4. Results

Number of mitochondria was significantly higher in cells isolated from the blood of patients with DM type 2 (Graph 1). No difference was found in the fraction volume analysis of mitochondria between patients with DM type 2 and healthy individuals (Graph 2), indicating that in DM type 2 there is an increase in number of mitochondria which are less voluminous then in healthy persons. Electron microscopic analysis of mitochondria in lymphocytes of patients with DM type 2 revealed that they were frequently spherical and small (Figure 1).

5. Conclusion

Higher number of mitochondria with the same volume in patients with DM type 2 comparing to healthy persons indicates that in this disease there is most likely an increase in mitochondrial fission.

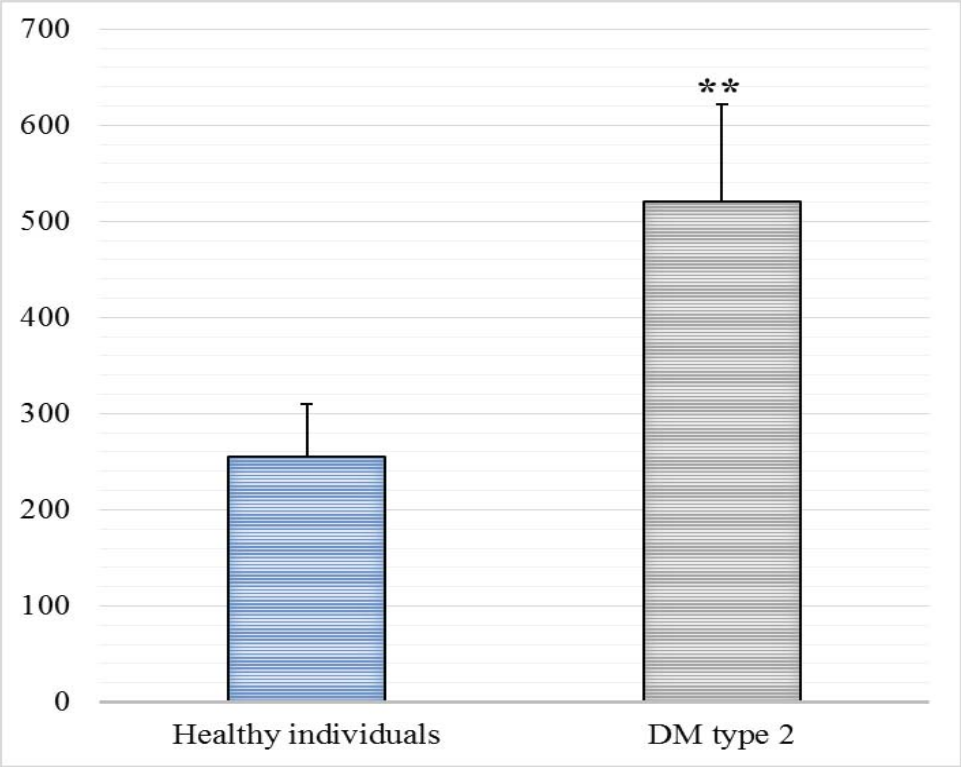

Graph 1. Average number of mitochondria in lymphocytes of DM type 2 patients and healthy individuals. (**p < 0.01)

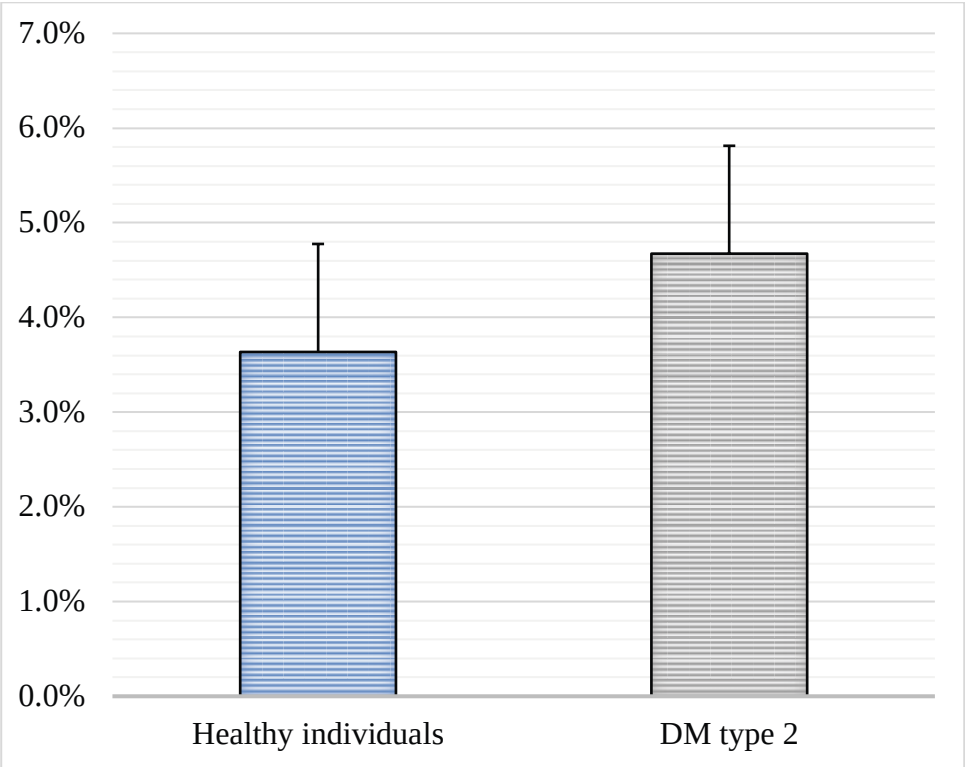

Graph 2. Fraction volume of mitochondria in patients with DM type 2 and healthy individuals.

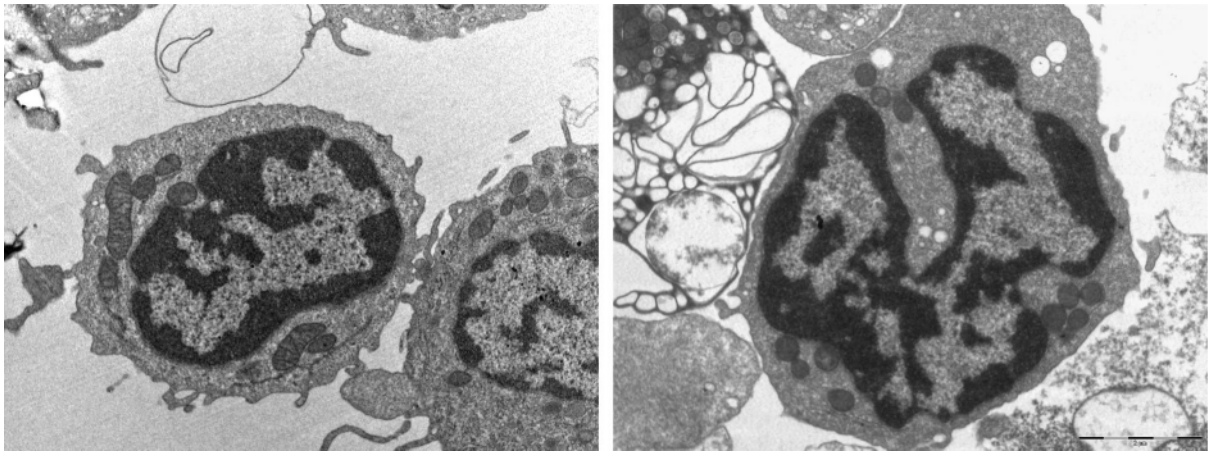

Figure 1. Electron microscopic appearance of mitochondria in lymphocytes of healty individuals (left picture) and patients with DM type 2 (right picture). (Magnification 8900x)

References

[1] American Diabetes Association. Diabetes Care, 37 (2014) S81-S90
[2] D Nicholas, E Proctor, FM Raval et al. PLoS One, 12 (2017) e0170975
[3] JM Lucocq, C Hacker. Autophagy, 9 (2013) 1443-8

The effects of anax imperator adipokinetic hormone on the expression of brain-derived neurotrophic factor in a rat glioma cell line

SIBEL DOĞAN[1], SIBEL KÖKTÜRK[1], OĞUZ MUTLU[2], FATMA KAYA DAĞISTANLI[3], ELIF GELENLI DOLANBAY[4], EMEL USTA[1], FERIDE ÖZDEMIR[1]

[1] Department of Histology and Embryology, Istanbul University, Istanbul Medical Faculty, Turkey; [2] Department of Medical Pharmacology, Kocaeli University, Kocaeli Medical Faculty, Turkey; [3] Department of Medical Biology, Istanbul University-Cerrahpasa, Cerrahpasa Medical Faculty, Istanbul, Turkey; [4] Department of Histology and Embryology, Istanbul Medeniyet University, Istanbul Medeniyet Medical Faculty, Turkey

Abstract

Objectives: Adipokinetic hormones (AKHs) are small stress peptides found in insects that regulate metabolic responses to stress (1). Insect anti-stress responses, including those induced by insecticides, are controlled by adipokinetic hormones. AKHs are synthesized by neurosecretory cells of the corpora cardiaca of insects. However, presence of AKHs had also been reported the cells within the brain, although their roles are not clear (2).

Astrocytes have been shown to play crucial roles in regulating both normal and disease states. Astrocyte dysfunction has been related to neuroautoimmune diseases, neoplasms and epilepsy (3-5). Brain-derived neurotrophic factor (BDNF) is one of the major neurotrophic factors produced by astrocytes to maintain the development and survival of neurons in the brain, and have recently been shown to modulate homeostasis of neuroinflammation. BDNF plays vitally important roles in neural development and plasticity in both health and disease. Glial cells are able to store and release BDNF (6) and it has been suggested that glial dysfunction may contribute to the patho-physiology of schizophrenia (7-9). The aim of this study was to investigate the effects of Anax imperator AKH (Ani-AKH) on the astrocyte-like model C6 rat glioma cell line, using BDNF immunohistochemistry stainings.

Methods:
The C6 rat glioma cell line was cultured in Dulbecco′s modified Eagle′s medium-F12 cell culture medium supplemented with 10% heat-inactivated fetal calf serum. Ani-AKH was applied to the cultured cells at the concentrations of 5, 10 and 50 µg/ml for 24 hours and evaluated the BDNF staining density.

Results: BDNF staining density was significantly increased in the Anax imperator AKH (Ani-AKH) 5, 10 and 50 µg/ml groups than the control group. BDNF staining density was higher in the 50 µg/ml Ani-AKH group than in the 5 and 10- µg/ml Ani-AKH groups.

Discussion: Our findings suggest that Ani-AKH has a potential increased the expression of BDNF on C6 rat glioma cell line. The further studies will be required working with additional cell lines, different doses and experimental design.

References

[1] S. Sajwan, R. Sidorov, T. Staskova, A. Zaloudikova, Y. Takasu, D. Kodrik, M. Zurovec, Insect biochemistry and molecular biology 61 (2015) 79-86.
[2] D. Kodrik, T. Staskova, V. Jedlickova, F. Weyda, R. Zavodska, J. Pflegerova, General and comparative endocrinology 210 (2015) 1-11.

[3] D.N. Louis, Annual review of pathology 1 (2006) 97-117.
[4] V. Brinkmann, British journal of pharmacology 158 (2009) 1173-1182.
[5] N.C. de Lanerolle, T.S. Lee, D.D. Spencer, Neurotherapeutics : the journal of the American Society for Experimental NeuroTherapeutics 7 (2010) 424-438.
[6] F. Angelucci, N. Croce, G. Spalletta, V. Dinallo, P. Gravina, P. Bossu, G. Federici, C. Caltagirone, S. Bernardini, Pharmacology 87 (2011) 5-10.
[7] H.G. Bernstein, J. Steiner, P.C. Guest, H. Dobrowolny, B. Bogerts, Schizophrenia research 161 (2015) 4-18.
[8] A.E. Steffek, R.E. McCullumsmith, V. Haroutunian, J.H. Meador-Woodruff, Schizophrenia research 103 (2008) 71-82.
[9] M. Jozwiak-Bebenista, M. Jasinska-Stroschein, E. Kowalczyk, Acta neurobiologiae experimentalis 77 (2017) 205-213.

nAChR α7 effects expression of synaptic translation control proteins CPEB3 and Ngdn in hippocampal organotypic slice culture

IREM L. ATASOY[1], SELMA YILMAZER[2], ERDINÇ DURSUN[1], DUYGU GEZEN-AK[1]
1 Istanbul University-Cerrahpaşa, Cerrahpaşa Faculty of Medicine, Department of Medical Biology; [2] Altınbaş Univesity, Faculty of Medicine, Department of Medical Biology

1. Introduction

Acetylcholine is a neurotransmitter, act as a significant modulator in synaptic plasticity, learning and memory (1-2). It is important to control local synaptic protein synthesis for synaptic plasticity (3).

2. Details of the experiment

In this study, hippocampal organotypic slice cultures were established. Specific nicotinic acetylcholine receptor alpha 7 (nAChR α7) antagonist methyllycaconitine (MLA) was applied to the organotypic slices. After 24th and 48th hours of MLA treatment periods both synaptic and total protein expression levels of cytoplasmic polyadenilation binding protein (CPEB) and neuroguidin (Ngdn) were determined by Western blotting. Localization of CPEB and Ngdn were determined by immunohistochemical method.

3. Results

Our Western blot analysis indicated that cholinergic activity through nAChR α7 receptor could have direct or indirect effects on synaptic plasticity by regulating protein expression levels of CPEB3 and Ngdn by a dose and time dependent manner of MLA treatment. After 24th and 48th hours of treatment, while CPEB3 and Ngdn total protein expression levels significantly increased in 10 nM MLA group ($p<0.05$), there was no differences between control and 20 nM MLA groups ($p>0.05$). While CPEB3 synaptic protein expression level was not significantly different between control and 10 nM MLA treatment groups both at 24th and 48th hours of treatment ($p>0.05$), there was significantly decreased at 24th hours of 20 nM MLA treatment and then increased at 48th hours of 20 nM MLA treatment group ($p<0.05$). Ngdn synaptic protein expression level was not significantly different MLA treatment groups after 24th and 48th hours of treatment when compared to control group ($p>0.05$). Our immunohistochemical results showed that CPEB3 and Ngdn immunoreactivity localized in the dentate gyrus after 48 hours of MLA treatment.

4. Conclusion

Consequently, our study indicated that the potential effects of cholinergic system through nAChR α7 may contribute to the maintenance of synaptic plasticity in the hippocampus since the receptor has regulatory effects on the protein expression levels of CPEB3 and Ngdn.

References

[1] Kaneko,N., Okano,H.,& Sawamoto,K.(2006). Role of the cholinergic system in regulating survival of newborn neurons in the adult mouse dentate gyrus and olfactory bulb. *Genes Cells, 11*(10), 1145-1159. doi:10.1111/j.1365-2443.2006.01010.x.

[2] McQuiston,A.R.(2014). Acetylcholine release and inhibitory interneuron activity in hippocampal CA1. *Front SynapticNeurosci*,*6*,20. doi:10.3389/fnsyn.2014.00020.

[3] Buffington, S. A., Huang, W., & Costa-Mattioli, M. (2014). Translational control in synaptic plasticity and cognitive dysfunction. *Annu Rev Neurosci*, *37*, 17-38. doi:10.1146/annurev-neuro-071013-014100.

Does the CO_2 that is used in horizontal incubators sufficiently clean? The effects of in-line filters in embryo development

OKTAY ARDA[1], EBRU ÖZTÜRK ÖKSÜZ[2], MURAT BAŞAR[2]
[1] Altınbaş University Medical Faculty, Histology & Embryology Department; [2] Anadolu Sağlık Merkezi Hospital, Gynecology Department, IVF Unit

1. Introduction: in an successful IVF laboratory one of the most important factor is the cleanness of the air in the laboratory. The presence of materials such as Volatile Organic Compounds (VOCs), microbes, and perfumes are extremely dangerous during in-vitro embryo development. Consequently systems such as HEPA filters and Coda Air Filtration System (CODA) are preeminently used to keep the air of the room clean.

Taking consideration of the critical air cleanness of the room so much, are we sure about the purity of the CO_2 that we are using in our applications of embryo cultures? If not, how are these impurities influence the embryo quality?

Our hypothesis is that, the gas filters of the horizontal incubators are inadequate to filter the harmful toxic molecules of the CO_2 for the embryo cultures. In case of adding extra filters to these incubators, will there be an increase in the embryo quality that can be the result of a decrease in unfolded proteins?

2. Materials and methods: We analyzed the purity of the CO_2. To figure out its effect on the quality of the embryos. First; we made two groups of <35 years old couples who had Intracytoplasmic sperm injection (ICSI). Among the embryos that showed 2PN of the same couple (siblings), half of them processed in horizontal incubators supplied with extra filters (IEF) and the other half processed in the ones that did not have any extra filters (INEF). As far as the filters are concerned, we use 3 different brands (CODA® XTRA INLINE® FILTERS – BLUE; ORIGIO® Gas Line Filter; REPROCARE GLF30 VOC Holder Filter) and we checked the quality of 3- and 5-days old embryos.
Second; 10 months old female BALB/C mice are stimulated with (n=10) FSH+hCG (5 IU, i.p.) and brought close together with mature male mice. We sacrificed the female mice that showed vaginal plate after 24 h and collected the embryos that showed one blastomere. Embryos are incubated in (IEF) and (INEF). We analyzed GRP78 levels by Western blot technique and referred to Student's t-test and ANOVA for statistics. $p<0,05$ value considered as significant.
3. Findings: There was; Ethyl methylketane, Tetrahydrofuran, Phenol, 2-heptenol and Formaldehyde (impurity percentages 0.000271, 0.001316, 0.001638, 0.000012, 0.001162) in the analyzed CO_2. These unusual impurities decreased in (IEF) ($p<0.05$). When we analyzed the 3 days old embryo qualities and blastocyte ratios in each 3 (IEF) there was a significant increase compared to (INEF) ($p<0.001$). There was no significant difference among the (IEF) groups ($p>0.05$).
We researched whether this increase in embryo quality and the blastocyte ratio related with Unfolded Protein Response (UPR) pathway by detecting the GRP78 protein levels. We found in INEF group (%61) GRP78 levels were higher than the IEF group (%37).
4. Conclusion: This research pointed out that the CO_2 used in IVF laboratories is not as clean as suggested. This favorableness can be compensated by attaching extra filters to the horizontal incubators. This reduced the cellular ER stress and increased the embryo quality.

Key words: CO_2 Impurities, Embryo Quality, ER Stress

Autophagy analysis in lymphocytes of patients with type 2 Diabetes Mellitus and hyperlipidemia

DARKO CIRIC[1], TAMARA MARTINOVIC[1],VLADIMIR BUMBASIREVIC[1], ALEKSA ZIVKOVIC[1], ANKICA JANKOVIC[1], K. LALIC[2], I. RASULIC[3] AND TAMARA KRAVIC-STEVOVIC[1]

[1] Institute of Histology and Embryology, Faculty of Medicine, University of Belgrade, Serbia; [2] Clinic for Endocrinology, Diabetes and Metabolic Disease, Clinical Center of Serbia, Faculty of Medicine, University of Belgrade, Serbia; [3] Clinic for Endocrinology, Diabetes and Metabolic Disease, Clinical Center of Serbia, Belgrade, Serbia

1. Introduction

Autophagy is a highly conserved process for degradation of the intracellular components, which is activated in numerous situations that can be features of both physiological and pathological conditions of the tissue and the organism [1]. Type 2 Diabetes Mellitus (T2DM) is global disorder linked to obesity and high levels of glucose in blood which appears as a consequence of the insulin resistance [2]. Beside hyperglycemia, one of the characteristics of this disease is also high levels of lipids in blood (hyperlipidemia) [3]. It was shown that there is correlation between autophagy and T2DM, some studies have shown increased [4] while others decreased level of autophagic processes [5].

2. Aim

The aim of this study was to determine the number of autophagic vesicles in the lymphocytes of patients with T2DM and hyperlipidemia and healthy individuals.

3. Material and methods

Mononuclear cells were isolated from peripheral blood obtained from patients with T2DM and hyperlipidemia and healthy individuals. After fixation in glutaraldehyde cells were postfixed in osmium tetroxide and uranyl acetate. Cells were dehydrated in alcohol and propylene oxide and later embedded in Epoxy resin. Embedded samples were then cut on ultramicrotome, contrasted with lead citrate and uranyl acetate and analyzed using transmission electron microscope. Quantification of number of the autofagic vesicles in lymphocytes was done during analysis on transmission electron microscope.

4. Results

Electron microscopic analysis of lymphocytes of both T2DM patients with hyperlipidemia and healthy individuals revealed the presence of autophagic vesicles in cytoplasm of these cells (Graph 1). Autophagic vesicles were seen as autolysosomes, autophagosomes and phagophores. Number of the autofagic vesicles in lymphocytes was higher in patients with T2DM and hyperlipidemia then in healthy individuals ($p < 0.05$) (Figure 1).

5. Conclusion

Presence of higher number of the autofagic vesicles in lymphocytes of patients with T2DM and hyperlipidemia compared to the healthy individuals indicates that the there is an alteration in the proces of autophagy in cells of these patients.

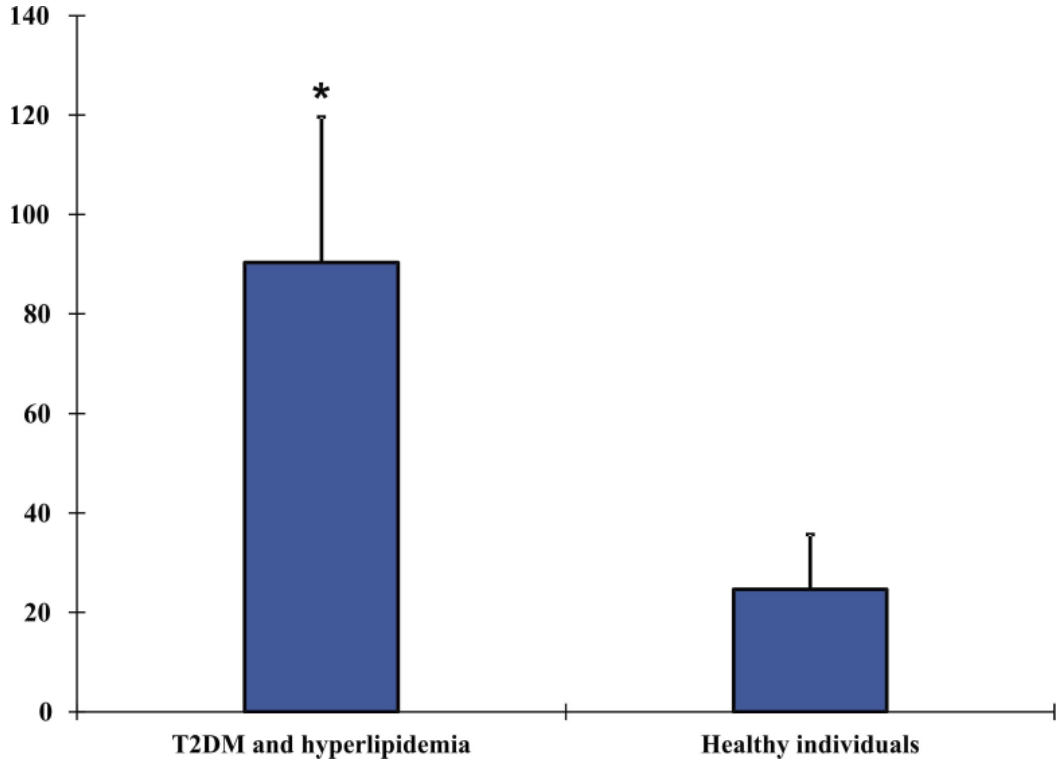

Graph 1. Average number of autophagic vesicles in lymphocytes of patients with T2DM and hyperlipidemia and healthy individuals (* $p < 0.05$)

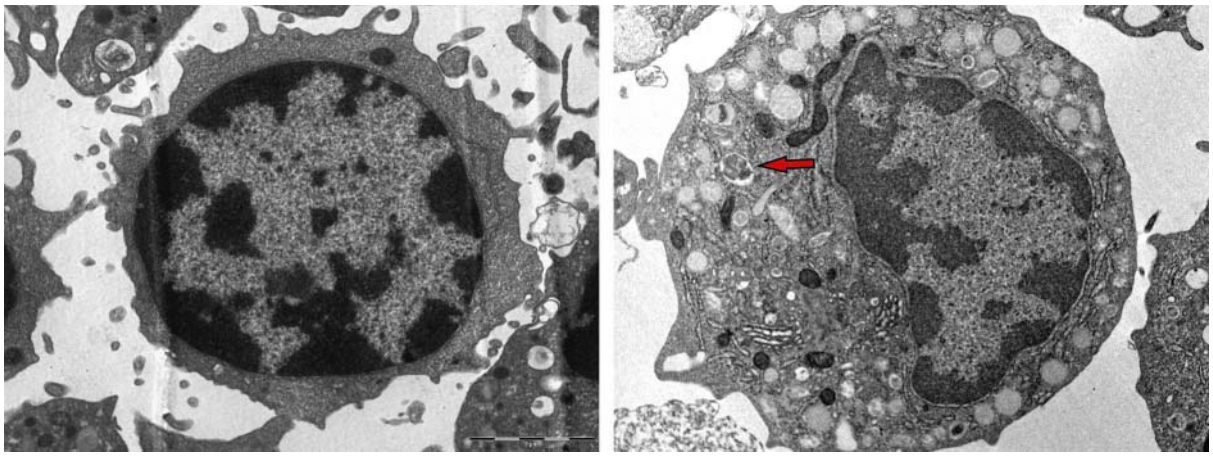

Figure 1. Ultrastructural apprearance of healthy lymphocyte (left picture) and lymphocyte of patients with T2DM and hyperlipidemia (right picture, red arrow showing autolysosome). Magnification x8900

References

[1] N Mizushima, M Komatsu. Cell, 147 (2011) 728–41
[2] AD American Diabetes Association. Diabetes Care, 41 (2018) S13–27
[3] A Pandey, S Chawla, P Guchhait. IUBMB Life, 67 (2015) 506–13
[4] S Rovira-Llopis, N Díaz-Morales, C Bañuls. Antioxid Redox Signal, 23 (2015) 1050-6
[5] S Alizadeh, H Mazloom, A Sadeghi, S Emamgholipour, A Golestani, F Noorbakhsh et al. J Physiol Biochem, 74 (2018) 369-379

A novel type of microglia-neuron interaction and the role of P2Y12 receptors

BALÁZS PÓSFAI[1,2], CSABA CSERÉP[1], REBEKA FEKETE[1,2], ANETT D. SCHWARCZ[1], KATINKA UJVÁRI[1], NIKOLETT LÉNÁRT[1], BARBARA ORSOLITS[1], ZSÓFIA I. LÁSZLÓ[3], ZSOLT LELE[3], ISTVÁN KATONA[3], ÁDÁM DÉNES1

[1] Momentum Laboratory of Neuroimmunology, Institute of Experimental Medicine, Hungarian Academy of Sciences, Budapest, Hungary; [2] János Szentágothai Doctoral School of Neurosciences, Semmelweis University; [3] Momentum Laboratory of Molecular Neurobiology, Institute of Experimental Medicine, Hungarian Academy of Sciences, Budapest, Hungary

Introduction

Microglia are the main immunocompetent cells of the nervous system and their role in brain development and maintenance of proper neuronal function is now widely recognized [1]. Microglia interact with most cell types via dynamic surveillance of the microenvironment by motile microglial processes [2]. Since changes in microglial activity are linked with major human diseases including stroke, epilepsy and neurodegeneration, microglia-neuron interactions have been attracting a great deal of interest recently. To date, the majority of studies have focused on the interactions between microglial processes and synapses [3]. However, there are several actions occurring at single-neuron level, which seem unlikely to be regulated merely by interactions between microglia and synaptic terminals [4]. We hypothesized that specific sites on neuronal somata may also exist, allowing the dynamic monitoring and assistance of neuronal function by microglia.

Methods

We used *in vivo* two-photon imaging of CAG-TdTomato-electroporated CX3CR1$^{GFP/+}$ mice, confocal laser-scanning-, STORM superresolution- and electron microscopy combined with electron tomography and advanced 3D-analysis to examine the communication interfaces between microglia and neurons in the mouse and the human brain. Chemogenetic neuronal activation was induced by injecting hm3Dq-DREADD into the somatosensory cortex of mice, followed by intraperitoneal CNO administration to study microglia-neuron interactions in response to increased neuronal activity. The role of P2Y12 receptors was investigated using a P2Y12R$^{-/-}$ strain, or by injecting the selective P2Y12 receptor inhibitor PSB-0739 into the cisterna magna of wild-type mice.

Results

Here we identify a novel site of communication between microglial processes and neuronal cell bodies, termed somatic junctions [5]. In anaesthetized mice we could observe that microglia frequently contact neuronal cell bodies and the lifetime of somatic junctions is significantly longer than microglial contacts established on neuronal dendrites (Fig. 1.).

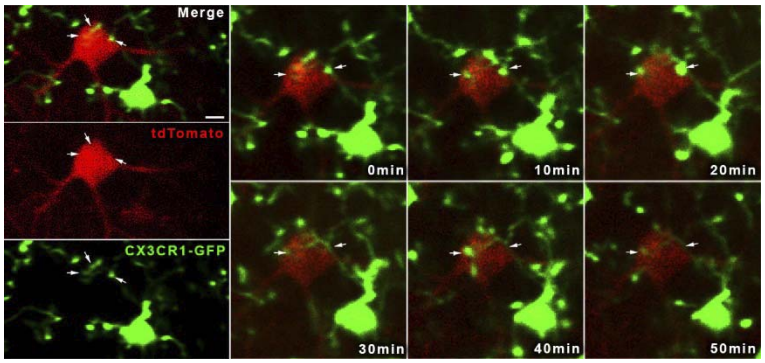

Figure 1. *In vivo* two-photon microscopy reveals the dynamics of microglia-neuron contacts.

We were able to confirm that a direct membrane-to-membrane contact exists at somatic junctions with electron microscopy both in mice and in post mortem human brain tissue. Extensive analysis of electron tomographic recordings showed a contact-dependent enrichment of P2Y12 receptors along microglial membranes, and a specific ultrastructure on the neuronal side of somatic junctions consisting of mitochondria, tubular as well as vesicular organelles (Fig. 2.).

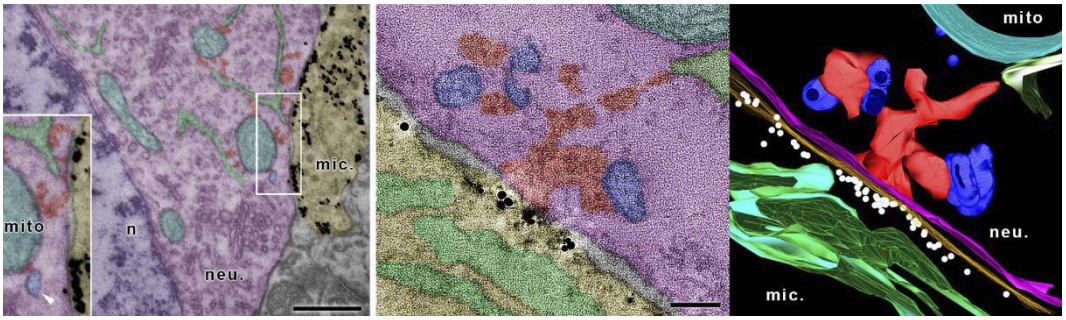

Figure 2. Transmission electron microscopy and electron tomography were used to analyze the ultrastructure.

Immunofluorescence revealed subcellular hallmarks of somatic junctions: mitochondria, vesicular nucleotid transporter (vNUT) containing vesicles and Kv2.1 clusters are present on the neuronal side, the latter perfectly opposite of microglial P2Y12 receptor clusters, as shown on superresolution images (Fig.3.).

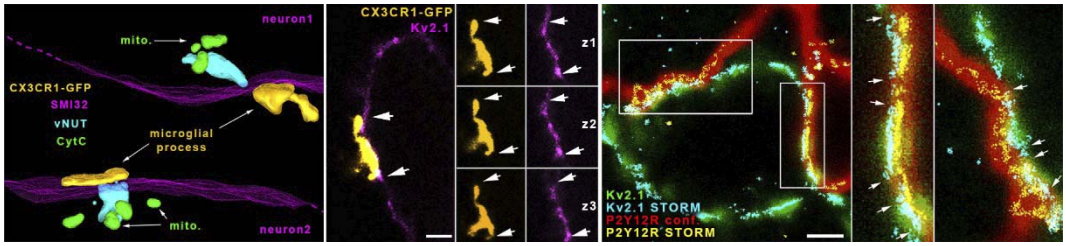

Figure 3. Confocal laser-scanning and superresolution images show somatic junctions.

The selective enrichment of P2Y12 receptors at somatic junctions suggests essential role for these receptors in the communication between microglia and neurons. Indeed, blockade of these receptors shortens the lifetime of somatic junctions, inhibits microglial response to neuronal hyperactivity and also affects the motility of surveilling microglial processes (Fig.4.)

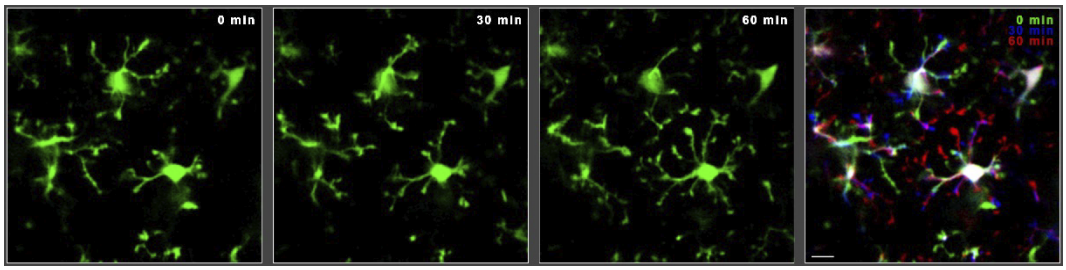

Figure 4. *In vivo* two-photon microscopic recordings reveal the dynamics of surveilling microglial processes under different circumstances.

Conclusions

In this study we show a novel site of communication between microglia and neurons and identify numerous elements of these junctions. Collectively, our results suggest that microglial processes recruited to these newly identified morpho-functional communication hotspots are in ideal position to readily monitor and dynamically influence neuronal functions via mitochondrion- and P2Y12R-dependent signalling pathways. Bidirectional communication between microglia and neurons via this interface is likely to be important in the healthy brain as well as in a number of neurological conditions, even as a possible future therapeutic target.

References

[1] K. Kierdorf and M. Prinz, *J. Clin. Invest*. 127 (2017), 3201-3209
[2] A. Nimmerjahn, F. Kirchhoff, F. Helmchen, *Science*. 30 (2005), 1314-1318
[3] Y. Wu, L. Dissing-Olesen, B. A. MacVicar, B. Stevens, *Trends Immunol*. 36 (2015), 605-613
[4] Z. Szepesi, O. Manouchehrian, s. Bachiller, T. Deierborg, *Front. Cell. Neurosci.* 12:323 (2018)
[5] C. Cserép, B. Pósfai, et al. *bioRxiv*. https://doi.org/10.1101/606079.

Histopathological Evaluation of Skin Dimple in Fibular Hemimelia

SALIH MARANGOZ[1], SALIME PELIN ERGÜVEN[2], BASAK ISILDAR[2], MEHMET KAYMAKOGLU[3] AND GUNEY YILMAZ[3]

1 Department of Orthopaedics and Traumatology, School of Medicine, Acibadem Mehmet Ali Aydinlar University, Istanbul, Turkey; [2] Department of Histology and Embryology, Cerrahpasa Medical Faculty, Istanbul University-Cerrahpasa, Istanbul, Turkey; [3] Department of Orthopaedics and Traumatology, Faculty of Medicine, Hacettepe University, Ankara, Turkey

1. Introduction

Fibular Hemimelia is a congenital long bone deficiency in which fibular bone is either absent or deficient. In such patients tibial bone has shortening and an anteromedial bowing, apex of which lies a skin dimple [1]. The depth of the skin dimple is not known to be related to the degree of the bowing or amount of shortening. The histological analysis of this pathological structure has not been investigated before.

2. Methods:

After the IRB approval, the patients with fibular hemimelia who are operated by superankle procedure to realign the ankle and the tibia were included. The osteotomy of the tibia was performed through an anterior approach, after excision of the skin dimple together with the periosteum underneath. The specimen was placed in formaldehyde solution and transferred to the Histology Department. For light microscopic evaluation, the skin tissues taken from patients were fixed in 10% neutral buffered formalin and embedded into the paraffin blocks after dehydration steps. Paraffin blocks were cut as 5 µ sections and stained with hematoxylin and eosin (H&E). The sections were analyzed and photographed by Olympus: BX61.

3. Results:

There were 11 specimens of 10 patients. All of them were classified as Paley type 3 equinovalgus type fibular hemimelia. One patient was bilateral fibular hemimelia. Histological examinations showed that 2 of the specimens had deep, 1 had middle, and 8 of them had less skin dimple. In all sections, the epidermis of the skin dimple areas was looking thin than the other sides of the epidermis areas. The numbers and the depth of the dermal papillae were less than the other sides of the epidermis areas. The stratum corneum at the dimple area was thin, the cells of the stratum spinosum were small and the squamous than the other side of the epidermises. Dermis at the skin dimple areas had no papillary dermis and the arrangement of the collagen fibers of the reticular dermis were dense and parallel to the skin dimple.

4. Conclusion:

This study analyzed the histology of the skin dimple in fibular hemimelia. There was no correlation between the amount of shortening or degree of deformity and the depth of the skin dimple.

References

[1] D. Paley, Tibial hemimelia: new classification and reconstructive options. *J Child Orthop*. 2016, 10(6):529-555.

Immunofluoroscent analysis of C6 glioma cell lines after paclitaxel treatment

ALEKSANDAR MIRČIĆ[1], MIHAJLO BOŠNJAK[2], VLADIMIR TRAJKOVIĆ[2] AND VLADIMIR BUMBAŠIREVIĆ[1]

[1] Institute of Histology and Embryology, Faculty of Medicine, University of Belgrade, Serbia, [2] Institute of Immunology, Faculty of Medicine, University of Belgrade, Serbia

1. Introduction

Apoptosis is a type of programmed cell death which is initiated by the activation of caspases cascade by intrinsic or extrinsic signals [1]. Microtubular poisons as agents for chemotheapie are widely used for treatment of malignances. Paclitaxel stabilizes microtubules and disrupt normal microtubular function and dynamics [2]. This process leads to arrest of cell division what result in mitotic blockade, multinucleated cells and cell death [3].

2. Material and methods

In this study we have analysed by immunofluoroscent staining the type of cell death in C6 glioma cell lines treated 24-72 hours by microtubular poison paclitaxel (2 μM). Cells were fixed and permeabilized for immunofluoroscent staining of microtubules. We used primary antibodies for α-tubulin and fluorescent stained secondary antibodies (Alexa 488) to examine paclitaxel influence on microtubules. Also, we used propidium iodide to show changes of nuclei and examined samples on confocal microscopy.

3. Results and discussion

In control samples analysis of C6 glioma cells on confocal microscopy showed normal morphological structures of cells with microtubules in cytoplasm and processes (stained green) and nuclei (stained red with propidium iodide) (Figure 1a). We also noticed cells in different stages of mitosis with microtubules of mitotic spindle and also cytoplasm microtubules of cells in interphase, specially around cytocenter (Figure 1b). Treatment with 24 hours of paclitaxel resulted in diminished cell growth, mitotic blockade and formation of characteristic bundles of microtubules in C6 glioma cells (Figure 2a). Prolonged incubation showed that in addition to mitotic blockade and cell death, paclitaxel induced appearance of multinucleated cells (red stained), but bundles of microtubules are still observed (green stained) (Figure 2b).

4. Conclusion

Our results showed that paclitaxel have a influence on C6 glioma cell lines and cells escape mitotic blockade what results in formation of multinucleated cells.

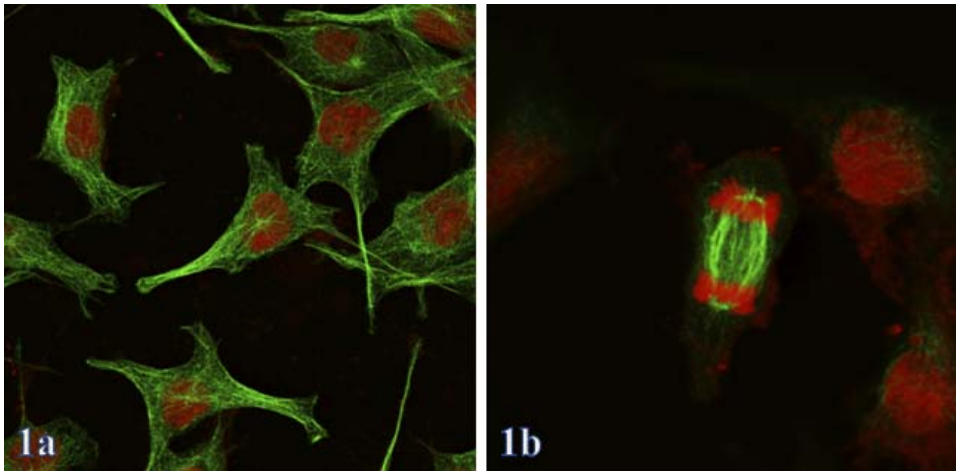

Fig.1 Immunofluoroscent staining of microtubules. a. control C6 glioma cells displayed well developed microtubular network; b. C6 glioma cells in stage of mitosis with microtubules of mitotic spindle

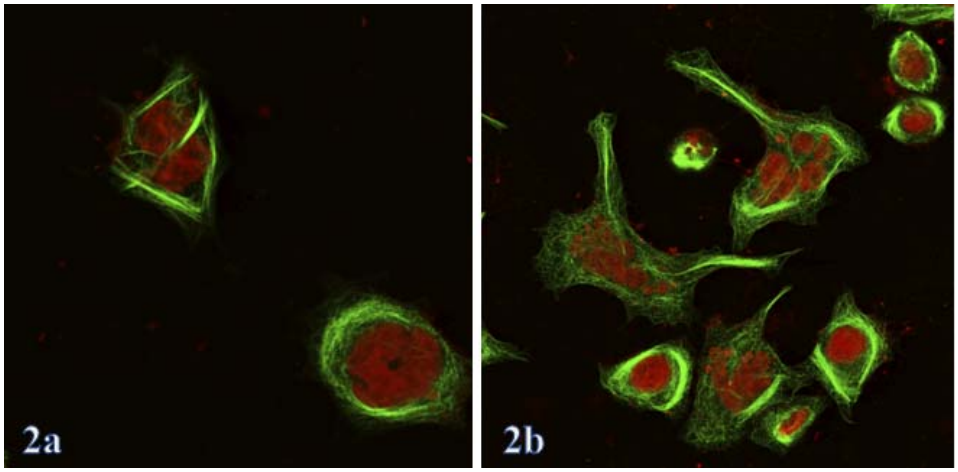

Fig. 2 Immunofluoroscent staining of microtubules. a. bundles of microtubules presented in C6 glioma cells after 24 h treatment by paclitaxel; b. appearance of multinucleated cells, but bundles of microtubules are still observed after prolonger incubation

5. References

[1] M. Gorka, WM Daniewski, B Gajkowska, E Lusakowska, MM Godlewski, T Motyl. Anti Canc Drugs, 16 (2005) 777-788
[2] A. Mircic, S. Mijatovic, D. Maksimovic-Ivanic, U. Vilimanovic, V. Bumbasirevic. 4th Serbian Congress of Microscopy, (2010) 137-138
[3] A. Mircic, U. Vilimanovic, G. Brajuskovic, V. Bumbasirevic. Acta Vet, 62 (2012) 17-26

Effects of Δ-9 tetrahydrocannabinol on the small intestine altered by high fructose diet

ALISA BAHAR BEYDOGAN[1], ISILDAR BASAK[2], ZEYNEP MINE COSKUN[3], ECE KOYUTURK[4], MERAL KOYUTURK[2] AND SEMA BOLKENT[1]

1 Department of Medical Biology, Cerrahpasa Medical Faculty, Istanbul University-Cerrahpasa, Istanbul, Turkey; [2] Department of Histology and Embryology, Cerrahpasa Medical Faculty, Istanbul University-Cerrahpasa, Istanbul, Turkey; [3] Department of Molecular Biology and Genetics, Faculty of Arts and Sciences, Demiroğlu Bilim University, Istanbul, Turkey; [4] Otto-von-Guericke University of Magdeburg, Faculty of Medicine, Magdeburg, Germany

Over the past few decades, epidemiological studies have demonstrated a strong correlation between high fructose diet (HFD) and obesity, type 2 diabetes, non-alcoholic fatty liver disease, and cardiovascular diseases (1). Overall, HFD is implicated in the pathogenesis of the metabolic syndrome, which is a result of interrelated abnormalities including obesity, dyslipidaemia, hyperglycaemia, and hypertension (2). Fructose is a natural monosaccharide, which is absorbed via facilitated Na^+ independent transport by glucose transporter glucose transporter GLUT5 across the brush border of small intestine into enterocytes and then transported by GLUT2 out of enterocytes into blood from the basolateral side (3). High fructose and its metabolites directly and/or indirectly cause oxidative stress, inflammation and autophagy, resulting in tissue and organ dysfunctions (4). High fructose intake and its association with dysfunctions of the intestinal system are not clearly known (5). Plant-derived cannabinoids and its synthetic analogs are used in the medically, Δ-9 tetrahydrocannabinol (THC) is mediated primarily by cannabinoid (CB) receptors. At least two types of them are demonstrated in mammalian tissues and are also represented in the gastrointestinal tract. These are CB1 and CB2 receptors and both are members of the G protein coupled receptors (6). Beneficial and modulatory effects of CB1 and CB2 receptors are suggested in intestinal inflammation (7). In this study, we aimed to research the potentially proctective effect of Δ9-THC on inflammatory and histological alterations of the small intestine induced by HFD with light and transmission electron microscopes.

Sprague-Dawley rats were allotted into the control, high fructose (HFD), THC, and HFD + THC groups (6 rats in each group). The control and HFD groups received tap water and 10% fructose in drinking water, respectively, for 12 weeks. The other groups were administered THC (1.5 mg/kg/day) for the last 4 weeks of the experiment. The jejunum segments were collected from the rats under anaesthesia. Light microscopic examination was performed on paraffin-embedded sections with Periodic Acid Schiff reaction & Haematoxylin (PAS&H). Immunohistochemical analysis of interleukin-6 (IL-6), c-Jun N-terminal kinase (JNK) and CB2 receptor antibodies were applied on paraffin sections by the streptavidin-biotin-peroxidase technique. In order to evaluate the transmission electron microscopy (TEM) examination, tissues were fixed with glutaraldehyde and were embedded in araldite after routine tissue processing.

In light microscopic examination, increased PAS positive mucus secretion was remarkable in the HFD and THC groups. Cellular junctions, which establish the intestinal barrier on lateral sides of enterocytes, have minimal changing in the HFD group. Number of mitochondria extremely elevated in the HFD+THC group. The quantity and intensity of immunoreactive cells for IL-6 and JNK increased significantly in the HFD group in comparison to the control group. The same correlation

was observed during the comparison between HFD and HFD+THC groups, indicating a convergence to data of the control group in the HFD+THC group. However, there was no significant difference in the number and intensity of CB2 immunoreactive cells in any group.

To conclude increased expression of IL-6 and JNK are marks of inflammation indicating the effect of HFD on the small intestine, which is seen to be reduced in the group treated by THC. Microscopic examinations also point out a regulator role of THC on enterocytes of the small intestine exposed to high fructose.

References

[1] Y. Pan, L.D. Kong. High fructose diet-induced metabolic syndrome: Pathophysiological mechanism and treatment by traditional Chinese medicine, Pharmacol Res, 130 (2018) 438-450
[2] Y. Rochlani, N.V. Pothineni, S. Kovelamudi, J.L. Mehta, Metabolic syndrome: pathophysiology, management, and modulation by natural compounds, Ther Adv Cardiovasc Dis, 11 (2017) 215-225
[3] R.P. Ferraris, J.Y. Choe, C.R. Patel, Intestinal absorption of fructose, Annu Rev Nutr, 21 (2018) 41-67
[4] D.M. Zhang, R.Q. Jiao, L.D. Kong, High dietary fructose: Direct or indirect dangerous factors disturbing tissue and organ functions, Nutrients, 29 (2017) E335
[5] C.A. Thaiss, M. Levy, I. Grosheva et al., Hyperglycemia drives intestinal barrier dysfunction and risk for enteric infection, Science, 23 (2018) 1376-1383
[6] R.G. Pertwee, Cannabinoids and the gastrointestinal tract, Gut, 48 (2001) 859-67
[7] K. Gyires, Z.S. Zadori, Role of cannabinoids in gastrointestinal mucosal defense and inflammation, current neuropharmacology, 14 (2016) 935-951

The Effects of Magnesium Sulfate on Cyclophosphamide Induced Ovarian Damage: Folliculogenesis

TUĞBA EKIZ YILMAZ[1], MÜGE TAŞDEMIR[1], MEHMET KAYA[2], NADIR ARICAN[3], BÜLENT AHISHALI[1]

[1] Istanbul University, Istanbul Faculty of Medicine, Department of Histology and Embriology, Istanbul, Turkey; [2] Istanbul University, Istanbul Faculty of Medicine, Department of Physiology, Istanbul, Turkey; [3] Istanbul University, Istanbul Faculty of Medicine, Department of Forensic Medicine, Istanbul, Turkey

Introduction: The adverse effects of alkylating chemotherapeutic agent cyclophosphamide (CYP) on folliculogenesis in ovary are well-known (1, 2, 3). There is a great clinical need to develop pharmacological strategies to prevent ovarian failure caused by chemotherapeutic agents. Magnesium has a variety of effects in organism owing to its catalytic function on the activation and inhibition of many enzymes with its regulatory function on cell proliferation, cell cycle and differentiation (4). This study aimed to evaluate the effects of magnesium sulfate ($MgSO_4$) on CYP induced ovarian damage.

Materials and Methods: 28 day old immature Wistar-Albino female rats were treated with pregnant mare serum gonadotrophin (PMSG; 15 IU, i.p) to develop the first generation of preovulatory follicles. All drug treatments to animals were applied i.p. 6 hours after PMSG injection. 1. Control group, only PMSG injection was applied. 2. CYP group was received a single dose of CYP (100 mg/kg). 3. $MgSO_4$ group was given $MgSO_4$ (initially 270 mg/kgx1 loading dose, then 27 mg/kgx12 maintenance dose as 30 min intervals for 6 hours (Kaya et al., 2004). 4. $MgSO_4$+CYP group was received $MgSO_4$ (initially 270 mg/kgx1 loading dose, then 27 mg/kgx12 maintenance doses as 30 min intervals for 6 hours). Additionally, 20 minutes after the loading dose of the $MgSO_4$, 100 mg/kg CYP was received. Following in vivo 5-bromo-2-deoxyuridine (BrdU) labeling, animals were sacrificed and ovaries were embedded in paraffin and Epon. The effects of $MgSO_4$ treatment on CYP induced gonadal damage were investigated morphologically, immunohistochemically (BrdU, cleaved-caspase 3, p27, TUNEL-labeling) and ultrastructurally on the follicular development process in the ovary.

Results: Decreased BrdU labeling, increased caspase 3 immunoreactivity and TUNEL labeling were observed in CYP treated rats. In these animals, while $MgSO_4$ did not alter BrdU labeling and caspase 3 immunoreactivity, it significantly reduced the increased TUNEL labeling.

Moreover, in CYP group p27 immunoreactivity significantly increased in the nuclei of granulosa and theca cells and these immunoreactivities are reduced after $MgSO_4$ treatment. Ultrastructurally, frequent apoptotic profiles were observed in granulosa and theca cells in early and advanced stage of follicles in CYP group and $MgSO_4$ treatment led to ultrastructural alleviation of apoptotic process.

Conclusion: In conclusion, our data suggest that $MgSO_4$ may represent an option of pharmacologic treatment for preserving fertility owing to its beneficial effects on chemotherapy-induced aggravation of follicular apoptotic process.

References

1. K. Ataya, E. Pydyn, J. Young, R. Struck, Sel Cancer Ther, 6(1990), 83-92.
2. M.A. Dooley, R. Nair, Nat Clin Pract Rheumatol, 4(2008), 250-257.
3. C.T. Lin, Y.H. Chen, D.Y. Chen, W.N. Huang, J.L. Lan, J Rheumatol, 21(2007), 53-58.
4. A. Hartwig, Mutat Res; 475(2001), 113-121.

LS5
High-resolution microscopy in life sciences

CHAIRPERSONS:

Jernej Jorgačevski, Marie Vancová

INVITED LECTURE

Super-resolution microscopy revealed unique organization of microtubules in tunneling membrane nanotubes

NATAŠA RESNIK[1], TIM PREZELJ[1], GIULIA MARIA RITA DE LUCA[2], ERIK MANDERS[2], ROMAN POLISHCHUK[3], PETER VERANIČ[1] AND MATEJA ERDANI KREFT[1]

[1] University of Ljubljana, Faculty of Medicine, Institute of Cell Biology, Ljubljana, Slovenia; [2] University of Amsterdam, Swammerdam Institute for Life Sciences, Amsterdam, The Netherlands; [3] Telethon Institute of Genetics and Medicine, Pozzuoli (NA), Italy

1. Introduction: Tunneling membrane nanotubes (TnTs) are intercellular connections with the role in cell-to-cell communication *in vitro* and *in vivo*. They serve as mediators for transfer of membrane and cytoplasmic molecules, implicated in spreading of diseases and maintenance of normal cell physiology. TnTs can extend up to several cell diameters and allow long-range contacts between cells, which requires stable and strong TnT structure to fulfil cell-to-cell bridging and transfer of molecules. The main mechanical supporters of the TnT structure are cytoskeletal elements. TnTs were primarily demonstrated as actin-based structures [1,2]. In this work, we were focused on other two indispensable cytoskeletal elements in TnT, namely on the co-occurrence and spatial organization of microtubules (MTs) and intermediate filaments (IFs).

2. Methods: We used double immunolabelling of MTs (α-tubulin) and IFs (cytokeratin 7) in normal and cancer urothelial cells and their TnTs. We analysed the samples with the wide-field fluorescence microscopy supplemented with deconvolution, confocal microscopy, and super-resolution, structured illumination microscopy (3D-SIM).

3. Results: Double immunolabelling revealed evident co-occurrence of MTs and IFs in urothelial cell TnTs. The proportion of TnTs that were double-labelled for MTs and IFs was 77% in TnTs of cancer urothelial cells and 90% in TnTs of normal urothelial cells. Close inspection with SIM revealed that MTs helically twist around IFs. Image analysis and 3D reconstructions showed that helical organization of MT could be found in 4% of normal and in 11% of cancer urothelial TnTs [3].

4. Discussion: The phenomenon of helical MT organisation in urothelial TnTs have been elucidated in greater detail due to advances in microscopy techniques. In addition, we demonstrated for the first time urothelial TnTs as MT- and IF-abundant structures. Our work paved the way to reveal cell-biological and physiological relevance for the helical MT organisation and MTs-IFs crosstalk.

References

[1] A. Rustom et al. Science, 303 (2004):1007–10
[2] P. Veranič et al., Biophys J 95 (2008): 4416–4425
[3] N. Resnik et al., Sci Rep, 8 (2018):17133

INVITED LECTURE

High-resolution detection and dynamics of poised human ribosomal genes

KLARA WEIPOLTSHAMMER, SYLVIA LAFFER, LUC SNYERS AND CHRISTIAN SCHÖFER
Dept. for Cell and Developmental Biology, Medical University of Vienna, Austria

Transcriptional activity of ribosomal genes depends on the metabolic demands of a cell. Only a fraction of the many ribosomal gene repeats is engaged in transcription. It is thought that part of the transcriptionally inactive genes are present in a particular chromatin state (poised state) that allows rapid recruitment of genes upon metabolic demands. Molecular studies previously identified a population of inactive rDNA genes carrying signatures of active (H3K4me3) and inactive (H3K9me3, H3K27me3) chromatin and it was shown that these genes engage in transcription upon increased metabolic demands [1]. While the presence of these poised genes was confirmed their distribution in the nucleus and their spatial dynamics during transcriptional modulation remained unknown. We addressed this question by combining immunofluorescence (H3K4me3 plus H3K27me3) and FISH (rDNA) approaches in cells of differing state of activity of ribosomal gene transcription. In Hela cells, we found loci positive for both chromatin marks and rDNA at the periphery of nucleoli. Inside nucleoli, rDNA signal never correlated with either of the two chromatin marks. In order to see if this difference is due to chromatin remodelling or histone depletion, we expressed the two canonical histone H3 variants (H3.1 and H3.2) in Hela cells and correlated these with rDNA. This approach confirmed presence of the histones at the nucleolar periphery while the nucleolar interior is largely free of histones. In conclusion, we found that poised genes predominantly localize to the nucleolar periphery where they reside amongst permanent inactive rDNA genes. We propose that both stably inactivated and poised genes are exposed to the silencing influence of the nucleolar periphery as part of the nucleolar-associated chromatin domain (NAD). Upon transcriptional recruitment, poised genes lose their signature of poised state along with their histone equipment and are then found in the interior of nucleoli.

References

[1] W. Xie et al. PNAS 2012; www.pnas.org/content/109/21/8161

Molecular interactions between Borrelia adhesins and extracellular matrix

MARTIN STRNAD[1,2], YOO JIN OH[3], MARIE VANCOVÁ[1,2], PETER HINTERDORFER[3] AND RYAN OM REGO[1]

[1] Biology Centre ASCR, v.v.i., Ceske Budejovice, Czech Republic; [2] Faculty of Science, University of South Bohemia, Ceske Budejovice, Czech Republic; [3] Institute of Biophysics, Johannes Kepler University Linz, Austria

Lyme disease (LD), also known as Lyme borreliosis, is the most prevalent vector-borne disease in the Northern hemisphere and, as such, one of the major public health concerns in Europe and North America. LD is caused by certain species of spirochetes of the *Borrelia burgdorferi* sensu lato complex. The adherence of Borrelia to cells or to the extracellular matrix (ECM) of tissues is a key step to promote colonization and further development of disease. Borrelia is known to produce a number of „sticky“ surface molecules (adhesins) that recognize diverse host ECM components and enable to interact with them.

Borrelia differ from most other motile bacteria in that the spirochete misses external appendages that are commonly required for bacterial motility. Nevertheless, Borrelia are able to reach speeds two orders of magnitude above the speed of the fastest cells in the body, and evade the clearance by the human immune system. Given the fact that the cellular morphology is exceptionally well-adapted to the motile nature of Borrelia, we aimed to study how the adhesins affect the motility of Borrelia during its infectious cycle.

In the preliminary studies, we designed a new in-vitro feeding setup mimicking the natural tick feeding on an infected host by using natural ECM analog. This system allows us to imitate the migration of Borrelia in a host at the time of spirochete acquisition by a tick and reliably assess and quantify the effects of adhesin expression on borrelial motility. Intriguingly, we observed that some of the studied borrelial adhesins (mainly DbpA/B) increase the motility of the bacteria and therefore acquisition of the spirochetes by ticks.

Using immuno-scanning electron microscopy, we determined the surface distribution of the surface adhesins and, using atomic force microscopy, we measured the specific binding interactions between borrelial adhesins and various ECM compoments. We characterized the dynamic, nano-mechanical molecular properties of borrelial surface proteins with ECM proteins, aiming to understand the underlying physical processes that govern the motility/adhesion of this malicous agent.

Invertebrate epithelia morphogenesis: integration of extracellular matrix, cytoskeleton and cell junctions imaging

POLONA MRAK, URBAN BOGATAJ, JASNA ŠTRUS AND NADA ŽNIDARŠIČ
Department of Biology, Biotechnical faculty, University of Ljubljana, Slovenia

1. Introduction

The integrity and mechanical properties of epithelia depend in a great deal on cytoskeleton organization, cell-cell adhesions and architecture of the surrounding extracellular matrix. These components connect cells and provide scaffolding for the whole tissue, and in addition actively participate in tissue dynamics accompanying physiological processes such as tissue morphogenesis and renewal [1, 2]. Interactions between these components during morphogenesis play an essential role in the establishment of epithelial polarity and specific morphological and functional characteristics of different epithelia.

The ectodermally derived epithelia in arthropods, including epidermis, hindgut and foregut, produce a chitinous apical matrix - cuticle, which is involved in diverse functions, *e.g.* body protection and support, animal locomotion and feeding. In crustaceans the cuticle is formed by differentiating epithelial cells during morphogenesis in embryonic and postembryonic stages [3, 4, 5, 6] and during cuticle replacement in molting adults [7]. Reorganization of cytoskeleton and junction complexes is an important aspect of epithelial morphogenesis, especially in the context of cell polarity. In polarized epithelial cells microtubules are generally oriented along the apico-basal axis. The subapical junction complex comprises adherens junction providing mechanical connections between cells, and occluding junction, in invertebrates present as septate junction [8].

Here we aim to elucidate formation and reorganization of cuticle matrix, cytoskeleton and junctional complexes in epidermis and hindgut of invertebrate *Porcellio scaber* (Crustacea: Isopoda) during development. The emphasis is given on the characterization of these tissue elements in the context of whole organism and its development. We have used complementary microscopic techniques of light microscopy, fluorescent labelling and ultrastructural analysis of the selected areas.

2. Details of experiments

Epidermis and hindgut epithelium were analysed in sequential developmental stages in comparison to adults in the invertebrate organism *Porcellio scaber*. The specific stages selected for the investigation range from mid-stage to late and prehatching embryos and from early to late postembryonic stages. Early postembryonic stages (marsupial mancae) develop in the marsupium, a female brood pouch and late postembryonic stages (postmarsupial mancae) are released from the marsupium and develop further in the external environment. The samples were prepared for fluorescence microscopy and for transmission electron microscopy.

Cuticle matrix of epidermis and hindgut was analysed by ultrastructural imaging, by chitin labelling with a chitin-binding protein (CBP) – fluorescein (FITC) conjugates and by labelling of *N*-acetyl-glucosamine containing molecules, including chitin, with a WGA lectin–gold conjugates. The samples were fixed in aldehydes and embedded in resin or in paraffin. After fixation, the samples of exoskeletal cuticle of adults were additionally decalcified using EDTA. Labelling with CBP–FITC was performed on semithin and on histological sections. Ultrathin sections of aldehyde-fixed specimens were labelled with WGA lectin–gold conjugates.

Next, the overview of microtubules arrangement was determined by immunofluorescence labelling on cryostat, paraffin and resin sections of aldehyde-fixed specimens. Primary mouse antibodies

against α-tubulin and secondary goat antibodies against mouse IgG conjugated with Alexa Fluor 488 were used. Sections were covered with mounting medium Fluoroshield with DAPI and imaged with a Zeiss AxioImager Z.1 light microscope. In addition, microtubules organization and the ultrastructure of cell junctions were inspected by transmission electron microscopy, and imaged with a Philips CM100 transmission electron microscope.

3. Results and discussion

The early stages of cuticle morphogenesis in *P. scaber* are similar in epidermis and hindgut and include formation of the precuticular matrices in mid-stage and late embryos (Fig. 1A). The first cuticle is formed in prehatching embryo and is replaced during postembryonic development. Thickening and structural elaboration of specific cuticular layers are accompanied by variation in organic matrix composition and calcification process in epidermis [5, 6]. As revealed by ultrastructure and WGA labelling the cuticle in epidermis and hindgut becomes in general similar to that in the adults in the period of early postembryonic development (Fig. 1B). The exoskeletal cuticle of adults displays spatially inhomogeneous organization of organic scaffold shown by ultrastructure, CBP-FITC labelling and WGA-gold labelling. In the transversally cut exoskeletal procuticle, comprising exo- and endocuticle, a clear chitin labelling was evident, showing localization pattern in horizontal lines of alternating intensity in the endocuticle (Fig. 1C). Interestingly, the pattern is similar to the pattern of helicoidally arranged chitin-protein fibers shown by ultrastructure and to the organic signal in Raman imaging shown by Hild et al. [9]. Ultrastructural appearance indicating helicoidal arrangement of chitin-protein fibers is evident also in the anterior hindgut procuticle of adults, while in the posterior hindgut the cuticle matrix appears more homogenous.

Within epidermis, microtubules are especially pronounced in tendon cells, specialized epidermal cells that mechanically connect muscles with exoskeleton. This structural framework of musculoskeletal linkage is clearly distinguished in the prehatching embryo and postembryonic stages, as evidenced by immunofluorescence labelling of α-tubulin and ultrastructure (Fig. 2). Microtubules are intensely labelled throughout the cytoplasm of tendon cell (Fig. 2B). Structural analysis shows the parallel arrays of microtubules extending from apical to basal surface of tendon cell (Fig. 2A), where they are positioned close to the junctions with cuticle (Fig. 2C) and to the myotendinous junctions, respectively.

Junctional complexes differentiation in epidermis and hindgut epithelium comprises first elaboration of adherens junctions and later septate junctions (Fig. 3A). Septate junctions are gradually formed, starting with the formation of individual sets of septa in late embryogenesis (Fig. 3A) and expanding considerably during postembryonic development. Septate junctions in the hindgut epithelium of adults are especially convoluted and numerous microtubules are evident in their close proximity (Fig. 3B).

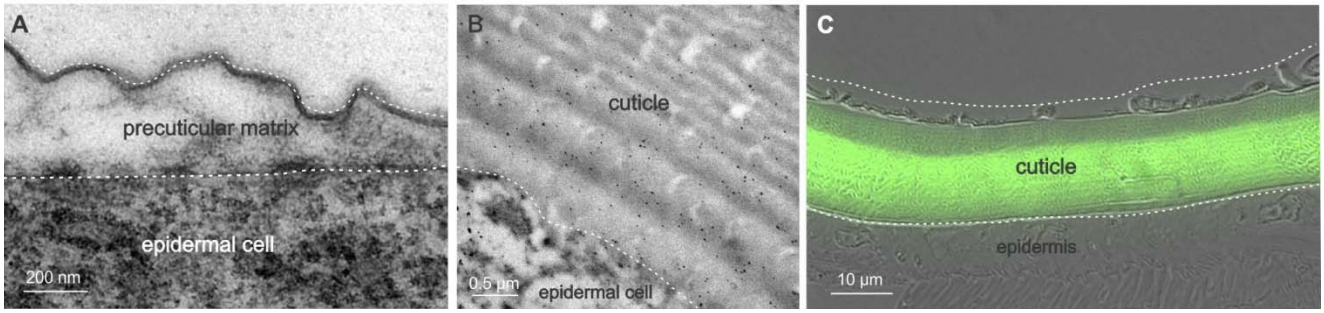

Figure 1. Cuticle matrix differentiation. A: Ultrastructure of epidermal precuticular matrix in late embryo. B: WGA-gold labelling of exoskeletal cuticle in postembryonic development. C: CBP-FITC labelling of exoskeletal cuticle of adult (merged image of fluorescence and differential interference contrast).

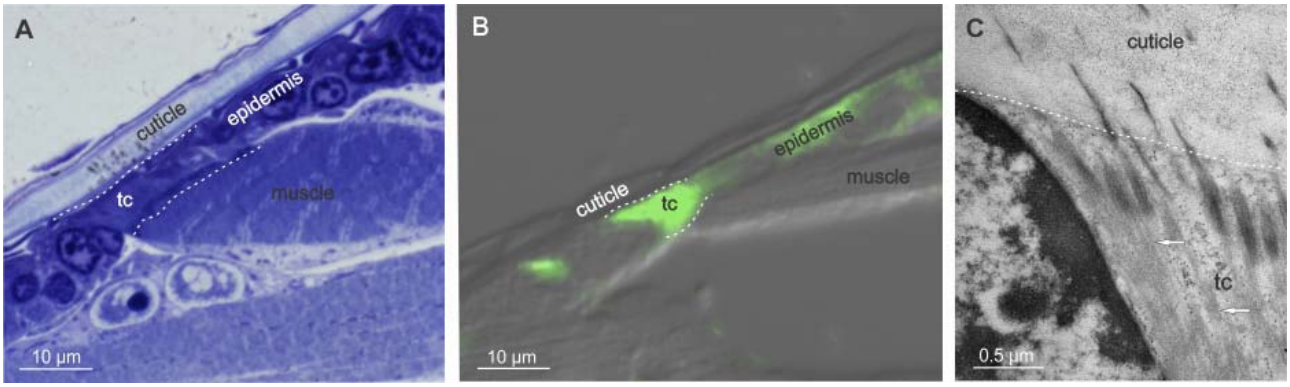

Figure 2. Organization of microtubules in tendon cells (tc). A: Semithin section of marsupial manca, showing the tendon cell that connects cuticle and muscle. B: Labelling of microtubules in the tendon cell of marsupial manca (image merged with DIC image). C: Ultrastructural imaging of apical connection of tendon cell with the cuticle, showing a high density of apico-basally oriented parallel arrays of microtubules (arrows) in postmarsupial manca.

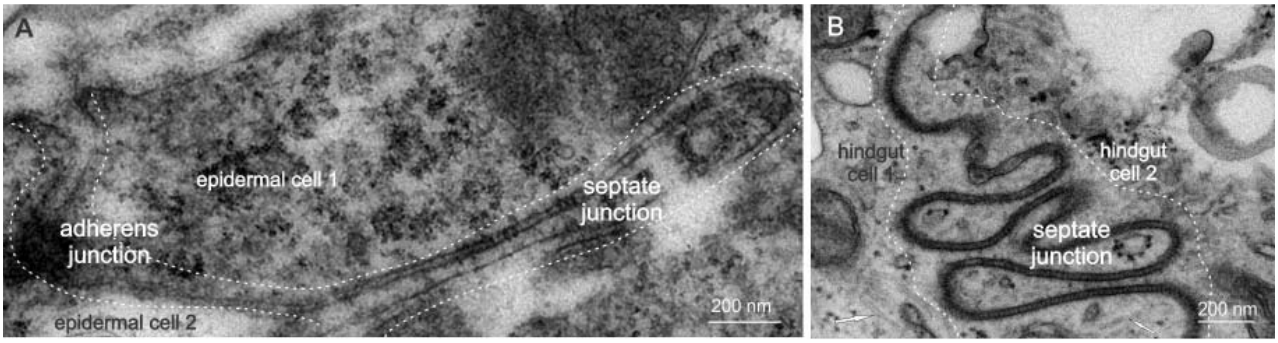

Figure 3. Cell junctions formation. A: In epidermis of late embryo adherens junction is evident subapically and septate junction septa are present below in the curved intercellular space. B: Septate junction in hindgut epithelium of adults is intensely convoluted and occupies a considerable portion of the lateral membranes. Microtubules (arrows) are concentrated in this cell area.

Imaging of extracellular matrix, cytoskeleton and junctional complexes at different scale levels in the same life stage provides a more complete insight in the epithelia scaffolding during morphogenesis. The major advances in cuticle and intercellular junction differentiation coincide with crucial events during animal development that are accompanied by the progress in animal motility and feeding, *i.e.* the transition from embryonic to postembryonic development. In this period muscoskeletal linkage is basically established via microtubules-rich tendon cells. Future research of epithelial morphogenesis is directed towards further studies of the interrelated modifications of cells and extracellular matrices during animal development to elucidate the differentiation at the tissue level.

References

[1] C.L. Simpson, D.M. Patel, K.J. Green, Nat Rev Mol Cell Biol, 12 (2011) 565–580
[2] M. Labouesse, Organogenesis, 8 (2012) 65–70
[3] P. S. Glas, L. A. Courtney, J. R. Rayburn, W. S. Fisher, Biological Bulletin, 192 (1997) 231–242
[4] J. Havemann, U. Müller, J. Berger, H. Schwarz, M. Gerberding, B. Moussian, Cell Tissue Res 332 (2008) 359–370
[5] P. Mrak, N. Žnidaršič, K. Žagar, M. Čeh, J. Štrus, Arthropod Struct Dev, 43 (2014) 423–439
[6] P. Mrak, U. Bogataj, J. Štrus, N. Žnidaršič, ZooKeys, 515 (2015) 93–109
[7] R. Dillaman, R. Roer, T. Shafer, S. Modla, In: L. Watling, M. Thiel, (Eds), vol. 1 (5), Oxford University Press, New York (2013) pp 140–166
[8] U. Tepass, V. Hartenstein, Dev Biol, 161 (1994) 563–596
[9] S. Hild, O. Marti, A. Ziegler, J Struct Biol, 163 (2008) 100–108

Three dimensional recontruction of the feeding apparutus of unfed nymph *Ixodes ricinus*

MARIE VANCOVÁ[1], TOMÁŠ BÍLÝ[2] AND JANA NEBESÁŘOVÁ[3]

[1] Laboratory of Electron Microscopy, Biology Centre CAS, České Budějovice, Czech Republic; [2] Faculty of Science, University of South Bohemia, České Budějovice, Czech Republic; [3] Faculty of Science, Charles University in Prague, Czech Republic

The tick utilize its mouthparts to penetrate the host skin and remain attached firmly in this place for about several days. The mouthpart comprise of a hypostome, armed ventrally with recurved denticles and dorsally acts as a channel for blood and saliva. Furthermore, retractable chelicerae armed with hook-like barbs [1]. Inside the mouthparts is located the food canal, that leads to the suction pump in the foregut, and the salivary canal connected with the salivary duct.

We used serial-section scanning electron microscopy and performed 3D reconstruction of these structures of an unfed nymph *I. ricinus.* Specifically, the whole reconstructed area was 156 µm x 136,5 µm and 455 µm in depth. The data were aligned and processed using both IMOD and AMIRA software. The nymphs were fixed in 2.5% glutaraldehyde, postfixed using 2% OsO4, 1% thiocarbohydrazide, 2% OsO4, *en bloc* stained in uranyl acetate, dehydrated in acetone and embedded into Hard Plus 812 resin. For reconstruction,500 nm serial thin sections were cut and stained in uranyl acetate, carbon coated and finally observed by scanning electron microscope JEOL 7401 F, at 4 kV, using the Autrata modified YAG BSE detector.

The 3D models enables us to visualized shapes and volumes of both the salivarium and pharynx and precise positions of associated muscles. Using the 3D model and based on previous observations, we animated each phase of the feeding process and tried to answer several unresolved questions about the exact mechanism of the blood feeding, eg. detailed function of pharyngeal valve, separation of blood and saliva; function of muscles attached to the salivarium and their possibility of open/close the salivarium, plausible explanation of movement of saliva within salivarium or massive outpouring of saliva.

Acknowledgement: This study was supported by the Technology Agency of the Czech Republic (TE01020118) and by the MEYS CR (LM2015062 Czech-BioImaging and Z.02.1.01/0.0/0.0/16_013/0001775).

References

[1] Richter D. et al 2013: How ticks get under your skin: insertion mechanics of the feeding apparatus of Ixodes ricinus ticks. Proc R Soc B 280: 20131758

West-Nile Virus and Mosquito-only Flavivirus are both infecting Human Neuroblastoma Cell Line cultivated on PET Membranes

MARKO KOLENC, MATEJA POLJŠAK-PRIJATELJ AND MIŠA KORVA
University of Ljubljana, Faculty of Medicine, Institute of Microbiology and Immunology, Ljubljana, Slovenia

1. Introduction

Flaviviruses are a large group of arthropod-borne viruses that can infect humans. West Nile virus (WNV) is mosquito transmitted flavivirus with worldwide distribution that can cause neurological disease and death. Genus *Flavivirus* includes also viruses which have been detected only in insects, without known vertebrate reservoir. The flaviviruses with close nucleic acid similarity associated exclusively with mosquitoes are named mosquito-only flaviviruses (MOFs) [1].

2. Materials and Methods

Human neuroblastoma cell line SK-N-SH (ATCC; HTB-11) were grown on translucent PET (polyethylene terephthalate) membranes in DMEM GlutaMAX supplemented with 10% fetal bovine serum at 37 °C in 5% CO_2. Cells were inoculated with WNV and MOF at MOI 1. At 72 h post infection, cells were fixed in modified Karnovsky fixative in 0.1M cacodylate buffer. Membranes were cut using razor blade into smaller pieces. Osmium tetroxide post fixation, washing, ethanol dehydration and epon embedding was done using automatic tissue processor (Leica EM TP). The ultrathin sections were contrasted with uranyl acetate and lead citrate using automatic contrasting system (Leica EM20) and examined by Jeol JEM-1400 Plus transmission electron microscope (TEM).

3. Results

After 72 h p.i. intensive cytopathic effect was observed in neuroblastoma cells infected with WNV, which resulted in only few cells still attached to PET membrane. In neuroblastoma cells infected with MOF no cytopathic effect was seen under light microscope. With TEM virus like particles were found in cells infected with WNV and in those infected with MOF. Both viruses were detected only in cellular processes, but not in vicinity of nucleus, in endoplasmic reticulum (ER) or Golgi apparatus (GA). In cells infected with WNV replication vesicles were found. But, in cells infected with MOF autophagosome like structures were observed. No budding through cell membranes and no extracellular flaviviruses were found (Figure 1).

4. Conclusion

Presence of replication vesicles and viral particles in cells infected with WNV shows that virus is successfully replicating in human neuroblastoma cells. Besides that, we have observed virus like particles also in cellular processes of cells infected with MOF, which suggests that MOFs can also infect human neuroblastoma cells. But successful replication inside these cells is yet to be determined. This is a preliminary study of flavivirus neurotropism.

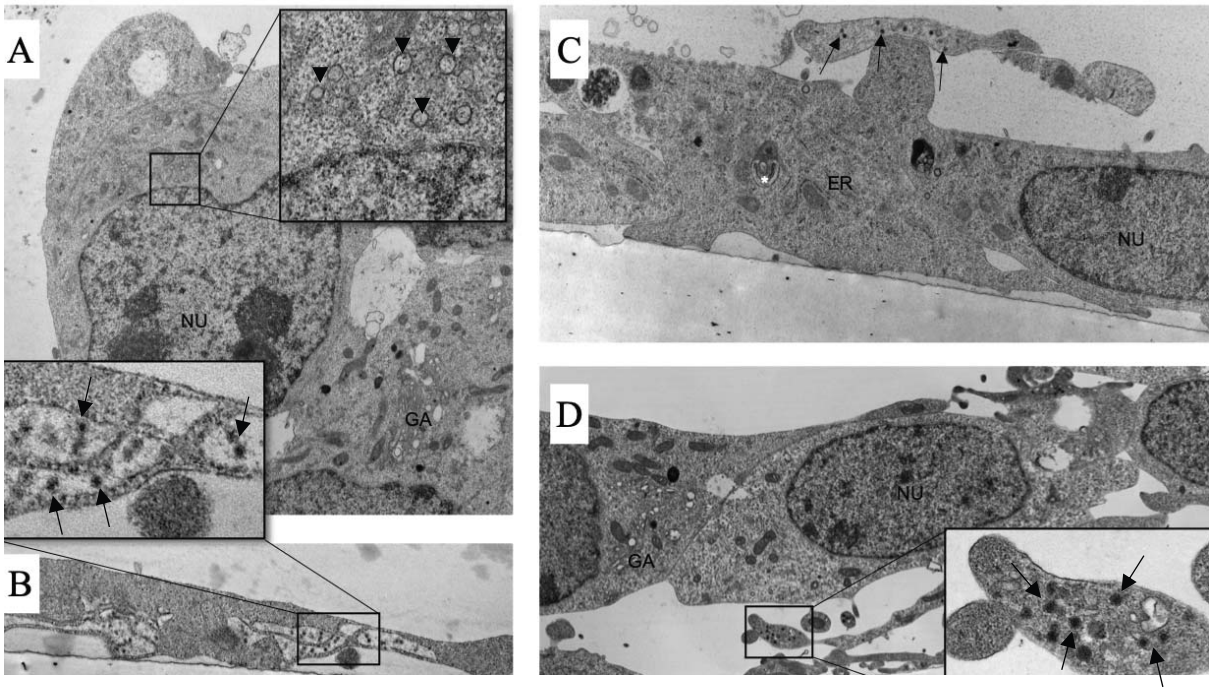

Figure 1. TEM micrographs of WNV (A, B) and MOF infected neuroblastoma cells (C, D). Arrowheads show replication vesicles in WNV infected cell (A). Arrows point to representative viral particles in cell processes of both WNV (B) and MOF (C, D) infected cells. *, autofagosome – like structure; GA, Golgi complex; ER, endoplasmatic reticulum; NU, nucleus.

Reference

[1] Calzolari M, Zé-Zé L, Růžek D, *et al.* Detection of mosquito-only flaviviruses in Europe. J Gen Virol 93 (2012) 1215–1225

LS6
Nanomaterials in biology and medicine

CHAIRPERSONS:

Serap Arbak, Stefania Meschini

INVITED LECTURE

Nanocarriers for neuromuscular diseases

MANUELA MALATESTA
Department of Neurosciences, Biomedicine and Movement Sciences, Anatomy and Histology Section, University of Verona, Italy

Myotonic dystrophy type 1 (DM1) and type 2 (DM2) are genetic disorders caused by a CTG repeat expansion in the 3' UTR region of the DMPK gene and a CCTG repeat in the first intron of the CNBP gene, respectively. Mutations in these two unrelated genes cause similar phenotypes characterized by a variety of pathological features especially concerning skeletal muscle functions (weakness, dystrophy/atrophy and myotonia), with disabling effects and possibly premature death. DMs fit into the category of dominant toxic RNA diseases; in fact, the most accepted pathogenic hypothesis for both DMs is an RNA gain-of-function due to expanded RNAs that accumulate in nuclear foci and sequester RNA-binding splicing regulators, thus causing a general splicing deregulation in multiple tissues [1, 2].

Currently, no therapy is available for DMs. To date, two main experimental therapies have been described to target expanded RNA repeats: antisense oligomer-induced degradation of toxic RNA (e.g. [3]), and inhibition of the pathogenic interaction of mutant RNAs with nuclear proteins by small compounds (such as pentamidine or actinomycin D) or antisense oligomers (e.g. [4, 5]). Although promising results have been obtained in experimental models *in vivo* and *in vitro*, at present all these molecules have scarce therapeutic applicability in humans because of their low bioavailability due to enzymatic degradation or high systemic toxicity.

Nanocarriers are able to protect encapsulated molecules from enzymatic degradation, and allow drug delivery and sustained release inside the cells [6]; they could therefore be suitable tools to improve the administration of therapeutic agents and decrease their adverse systemic side effects. These nanocarriers must obviously be biocompatible and biodegradable to play their therapeutic action without damaging patient's organism.

In this view, our research group has been working for long time to design a novel therapeutic strategy based on biocompatible nanoparticles (NPs) suitable for administering drugs or oligonucleotides able to counteract RNA toxicity in DMs, with special reference to skeletal muscle. We have developed different biocompatible nanocarriers (polymeric NPs, liposomes, mesoporous silica NPs, nanohydrogels, hyaluronic acid-based NPs) and we have analysed their interaction with muscle cells in *in vitro* systems. We elucidated the mechanisms of their uptake, distribution and degradation in cultured murine and human myoblasts and myotubes by fluorescence and transmission electron microscopy [7, 8]. As for myoblasts, all nanocarriers proved to be safe and efficiently internalised (Figure 1a), then undergoing degradation following physiological pathways (although with some peculiarities, depending on the nanocarrier type). On the other hand, myotubes showed a highest sensitivity to nanocarrier treatment, frequently undergoing structural alterations at long incubation times; moreover, their uptake capability was remarkably lower than in myoblasts for all nanocarriers tested (Figure 1b). These differences may probably be due to the fact that myoblasts are actively cycling cells whereas myotubes are terminally differentiated syncytia formed by myoblasts fusion; in addition, during the differentiation process the cell membrane undergoes important changes in protein and lipid composition, thus affecting the interactions with the nanoparticulates.

Among the different NPs tested, poly(lactide-co-glycolide) (PLGA) NPs and hyaluronic acid-based NPs were found to be especially suitable for both myoblasts and myotubes. Moreover, both PLGA and hyaluronic acid-based NPs efficiently load pentamidine, which is one of the promising therapeutic agents: preliminary results on cultured myoblasts from a DM1 patient demonstrated that pentamidine delivered by PLGA NPs reduced the pathological accumulation of nuclear foci while limiting drug cytotoxic effects.

Based on these encouraging results, PLGA NPs and hyaluronic acid-based NPs were submitted to further studies in order to investigate their distribution in the whole skeletal muscle. To this aim, explanted mouse soleus muscles were maintained in an innovative *in vitro* fluid dynamic system that demonstrated to significantly improve tissue preservation [9]. Fluorescent NPs were injected into the muscle, which was then incubated in the bioreactor. The muscle was finally cryofixed and cut with a cryostat. Observation at fluorescence microscopy demonstrated that many NPs remained confined in the connective tissue (Figure 1c), underlying the gap between single cell and whole organ as experimental systems to test nanocarriers. We are currently using explanted muscles to evaluate the efficacy of NP surface modifications aimed at improving targeting to the muscle fibres.

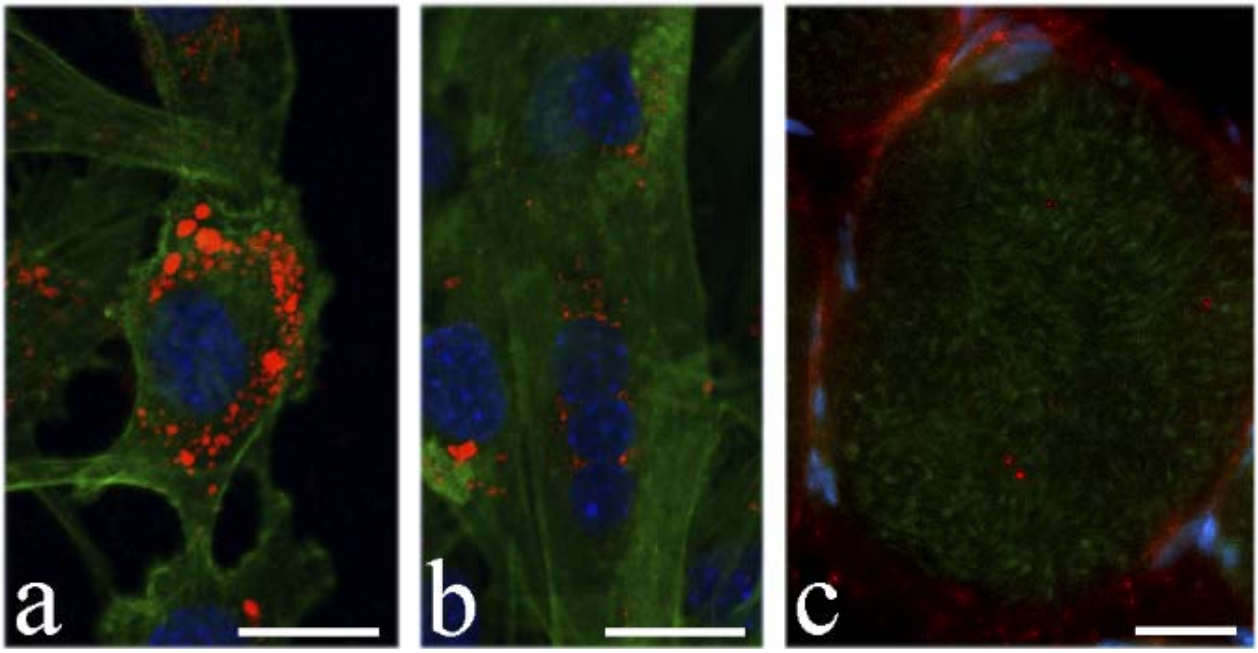

Figure 1. Confocal (a, b) and conventional (c) fluorescence microscopy. PLGA NPs (red) in mouse myoblasts (a), myotubes (b) and skeletal muscle tissue (c). Green: cytoplasm; Blue: nucleus. Bars: 25 µm.

References

[1] J. W. Miller, C. R. Urbinati, P. Teng-Umnuay, M. G. Stenberg, B. J. Byrne, C. A. Thornton, M. S. Swanson, EMBO J., 19 (2000) 4439–4448
[2] G. Meola, R. Cardani, Biochim. Biophys. Acta, 1852 (2015) 594–606
[3] T. M. Wheeler, A. J. Leger, S. K. Pandey, A. R. MacLeod, M. Nakamori, S. H. Cheng, B. M. Wentworth, C. F. Bennett, C. A. Thornton, Nature, 488 (2012) 111–115
[4] M. B. Warf, M. Nakamori, C. M. Matthys, C. A. Thornton, J. A. Berglund, Proc. Natl. Acad. Sci. USA, 106 (2009) 18551–18556
[5] C. H. Wong, Y. Fu, S. R. Ramisetty, A. M. Baranger, S. C. Zimmerman, Nucleic Acids Res., 39 (2011) 8881–8890
[6] D. Yohan, B. D. Chithrani, J. Biomed. Nanotechnol., 10 (2014) 2371–2392
[7] M. Costanzo, F. Vurro, B. Cisterna, F. Boschi, A. Marengo, E. Montanari, C. D. Meo, P. Matricardi, G. Berlier, B. Stella, S. Arpicco, M. Malatesta, Nanomedicine, 14 (2019) 301–316
[8] V. Guglielmi, F. Carton, G. Vattemi, S. Arpicco, B. Stella, G. Berlier, A. Marengo, F. Boschi, M. Malatesta, Int. J. Pharm., 560 (2019) 347–356
[9] F. Carton, L. Calderan, M. Malatesta, Eur. J. Histochem., 61 (2017) 2862

INVITED LECTURE

Calcium Phosphate Nanoparticles: Second Generation Non-Viral Vectors

FERAY BAKAN
Sabanci University Nanotechnology Research and Application Center (SUNUM), Istanbul, Turkey

Recently, targeted therapies are becoming more attractive since they do not harm healthy cells and have high selectivity. Gene therapy is a targeted therapy which can be used in the treatment of various acquired and inherited diseases. Inhabitation of a gene function, restoring or improving a gene, or gaining a new function can be achieved by gene therapy strategies. The most crucial step in this therapy is delivering the therapeutic material to the target. The carrier used for loading the therapeutic material is called “a vector”, while the vectors recently have been used for gene therapy are roughly sorted as viral vectors and non-viral vectors. As the use of nanoparticles has been a remarkable methodology in the solution of a variety of problems, they can be employed as non-viral delivery vehicles for oligonucleotides in molecular biology and medicine. Nano-sized calcium phosphates (CaPs) have been considered as promising carriers due to their excellent biocompatibility. In this study, the delivery of DNA, siRNA, and miRNA by using CaP nanocarriers were compiled in detail and the main parameters which can affect the carrier properties and thus the gene transfer efficiency were also discussed.

Keywords: Calcium phosphate nanoparticles, non-viral vector, hydroxyapatite, gene therapy, gene silencing.

Bacterial surface-layer proteins and their secrets

MARKUS EDER[1], ANDELA DORDIC[1], THEO SAGMEISTER[1], ELISABETH DAMISCH[1], DJENANA VEJZOVIC[1], LAVINIA GAMBELLI[2], WALTER KELLER[1], JANET VONCK[4], BERTRAM DAUM[2], A. PALVA[3] AND T. PAVKOV-KELLER[1]

[1] Institute of Molecular Biosciences, University of Graz, Austria; [2] Living Systems Institute, University of Exeter, United Kingdom; [3] Faculty of Veterinary Medicine, University of Helsinki, Finland; [4] Institute of Biophysics, Max-Planck Institute, Frankfurt, Germany

Surface layers (S-layers) are 2D crystalline arrays of proteins which cover the whole surface of many archaeal and bacterial cells. Since these proteins are in close contact with the environment they fulfil many essential tasks to the cell like bacterial adherence to other cells, protection against life-threatening conditions, maintenance of the cell shape and, auto- coaggregation. Interaction with the cell wall of the bacteria occurs by binding to secondary cell wall polymers like lipoteichoic acids in the case of lactobacilli. Only little is known about S-layers in consequence of a lack of structural knowledge [1]–[4].

In our work we focus on the structural characterization of the bacterial surface-layer proteins SbsC from *Geobacillus stearothermophilus* and SlpA from *Lactobacillus acidophilus*. Especially in Lactobacilli S-layers are of high biological and medical relevance because they are supposed to mediate their probiotic properties. S-layer proteins are the key players for understanding the role of lactobacilli for the microbiome of the gut. Lactobacilli S-Layers harbor outstanding therapeutic potential, especially for vaccines. It was shown that binding of the Lactobacillus vaccine vector, mediated by the S-layer protein, to the mucosal membrane of the host may be an advantage when a mucosal delivery route of the vaccine is considered [5]. In the case of SbsC it was reported that it is possible to functionalize this protein by inserting the sequence of the allergen Bet v 1 and could be therefore an ideal candidate for allergen specific immunotherapy [6].

To reach our goal to structuraly characterize these proteins we produced several soluble fragments as well as the full-length protein assembling into 2D-crystals. To find out more about the structure of self-assembled surface layers we are following an integrativ structural biology approach where we combined X-ray crystallography, mass spectrometry and electron microscopy. We elucidated the 3D atomic structures of several of these soluble fragments by X-ray crystallography. The structures of individual domains were then fitted into the 3D-Volume obtained by cryo-electron tomography sub-tomogram averaging of 2D-crystals.

The obtained results allow us to learn more about the self-assembly formation, cell wall binding and surface exposed areas available for the interactions with gut and dendritic cells.

Acknowledgments: This work has been supported by the Austrian Science Fund (FWF, project P29432).

References

[1] B. Kos, J. Šušković, S. Vuković, M. Sĭmpraga, J. Frece, and S. Matošić, “Adhesion and aggregation ability of probiotic strain Lactobacillus acidophilus M92,” *J. Appl. Microbiol.*, 2003.

[2] S. R. Konstantinov *et al.*, “S layer protein A of Lactobacillus acidophilus NCFM regulates immature dendritic cell and T cell functions,” *Proc. Natl. Acad. Sci.*, 2008.

[3] E. Smit and P. H. Pouwels, “One repeat of the cell wall binding domain is sufficient for anchoring the Lactobacillus acidophilus surface layer protein,” *J. Bacteriol.*, 2002.

[4] T. Pavkov-Keller, S. Howorka, and W. Keller, “The structure of bacterial S-layer proteins,” in *Progress in Molecular Biology and Translational Science*, 2011.

[5] U. Hynönen and A. Palva, "Lactobacillus surface layer proteins: Structure, function and applications," *Applied Microbiology and Biotechnology*. 2013.

[6] M. Gerstmayr *et al.*, "A Novel Approach to Specific Allergy Treatment: The Recombinant Allergen-S-Layer Fusion Protein rSbsC-Bet v 1 Matures Dendritic Cells That Prime Th0/Th1 and IL-10-Producing Regulatory T Cells," *J. Immunol.*, 2014.

Low energy STEM: new tool for visualization of nanoparticles conjugated with biomolecules

NEBESAROVA JANA[1,2], FRANK LUDĚK[3], PATAK ALEŠ[3], ĎURINOVÁ EVA[1,2], VANCOVA MARIE[1,2]

[1] Biology Centre of CAS, v.v.i., Institute of Parasitology, Ceske Budejovice, Czech Republic; [2] Faculty of Science, University of South Bohemia, Ceske Budejovice, Czech Republic; [3] Institute of Scientific Instruments CAS, v.v.i., Brno, Czech Republic

In this study, we used low energy STEM for visualization of nanoparticles conjugated to biomolecules which are standardly used as primary or secondary antibodies in immunolabeling procedures. Scanning transmission electron microscopy (STEM) represents the technique allowing the use of low energy primary electrons, in particular when implemented in a scanning electron microscope (SEM). The landing energy of electrons can be further drastically lowered by using the cathode lens with negatively biased sample [1]. In this configuration the resolving power is well preserved down to lowest landing energies. Insertion of the biased sample between two grounded detectors enables to detect all transmitted electrons (TE) in channels corresponding to the STEM detector rings (bright and dark field or even high-angle annular dark field) simultaneously with the backscattered electron signal (BSE).

We used the suspension of conjugated nanoparticles dripped on the copper grids covered with carbon supporting layers. Grids were treated by the glow discharge method to make them hydrophilic 2h prior to use. Part of the samples was negatively stained using 2% aqueous solution of uranyl acetate.

The microscopic examination was performed in the standard vacuum SEM Magellan 400L (FEI) equipped with a cathode lens and detectors of TE and BSE. We tested different values of the landing energy of electrons in the range from 1 to 30 keV, while we recorded simultaneously images in bright (BF) and dark (DF) field STEM and in backscattered electrons. Fig. 1 shows images of conjugated QDs recorded at 5 and 30/29 keV on stained/unstained specimens. It is clear that the decrease of the landing energy led to the image contrast grow, however only in the bright field STEM imaging. Let us note that the cathode lens field collimates a significant part of TE to the bright field detector. Nevertheless, the staining procedure was inevitable for the visualization of biomolecules bound to metal nanoparticles at higher electron energies. The combination of the image signals of transmitted and reflected electrons proved to be advantageous because it facilitates the interpretation of images.

References

[1] Frank L., Nebesarova J.,Vancova M., Patak A., Mullerova I.: Imaging of tissue sections with very slow electrons. Ultramicroscopy 148 (2015) 146-150

[2] We acknowledge financial support from the TE01020118 project of the Technology Agency of the Czech Republic (Competence Centre: Electron Microscopy) and the LM2015062 project of the Ministry of Education, Youth and Sports – National Infrastructure for Biological and medical Imaging, Czech-BioImaging.

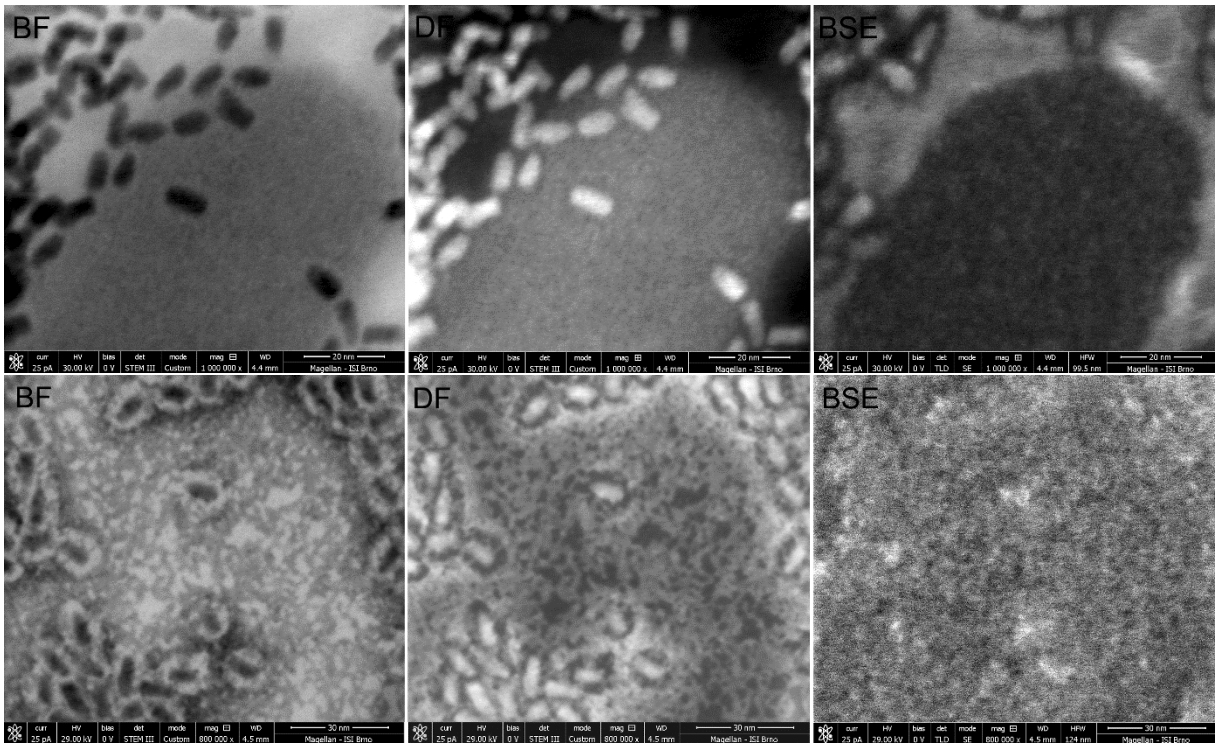

Fig.1. Comparison of Carboxyl Quantum Dot images (Qdot™ 605 ITK™) recorded on the unstained sample (the first row) and on the negatively stained sample (the second row) at 30/29 keV respectively, without any sample potential.

Autophagy and cell death role in the nanomaterials biodistribution and degradation

MARIA CONDELLO, EVELIN PELLEGRINI, GLORIA D'AVACK, STEFANIA MESCHINI
National Center for Drug Research and Evaluation, National Institute of Health, Rome, Italy

Nanomaterials exhibit unique properties that make them potentially usable in biomedical applications, as effective therapeutic and diagnostic tools. An increasing number materials as gold and silver nanoparticles (NPs), magnetic metal oxides, carbon nanotubes, quantum dots, natural and polymeric NPs have gained considerable attention to diagnose and treat diseases like cancer, cardiovascular diseases, microbial infection, neurodegenerative and autoimmune diseases [1]. Many researches on the nanomaterials and the biological system interaction have been started to prove their role in biomedicine and to exclude any toxic effects [2]. Several biological mechanisms, as cellular uptake, lipid peroxidation, mitochondrial dysfunction, oxidative stress, inflammation and genotoxicity are widely investigated. In addition to the known involvement of apoptosis, autophagy also could represent an interesting candidate as a potential contributor of nanomaterials toxicity. Autophagy is an evolutionarily conserved cellular process in which cellular components, including organelles and macromolecules, are delivered to the lysosomes for degradation. Autophagy has been shown to play a key role in different pathologies, such as cancer, neurodegenerative, inflammatory and pulmonary diseases [3]. Many nanoparticles, as metal oxide, graphene nanosheets or silver nanowires, can modify autophagic pathway, leading to blockade of autophagic flux and accumulation of autophagosomes, lysosomes and autolysosomes. Thus, accumulation of nanomaterials in the endo-lysosomal system might have widespread consequences, may be explained by a net inhibition of autophagic degradation capacity, such as induction of oxidative stress and inflammation. Detailed knowledge on how nanomaterials affect autophagy is important both for predicting toxic effects of nanomaterials in different cell types and organs, and also to harness the potential of nanomaterials in biomedicine, for instance in drug delivery.

Transmission electron microscopy (TEM) provides a significant contribution to the understanding of the NPs internalization mechanism, of the transport through the endo-lysosomal system and modification of the autophagic flow. As shown in figure 1, TEM observations showed that AuNPs are internalized by Balb 3T3 cells and they confined mainly in autophagosomes.

Understanding these mechanisms that may be considered risk factors for diseases such as cancer, chronic inflammatory diseases and neurodegeneration can be important to avoid potentially harmful consequences for human health.

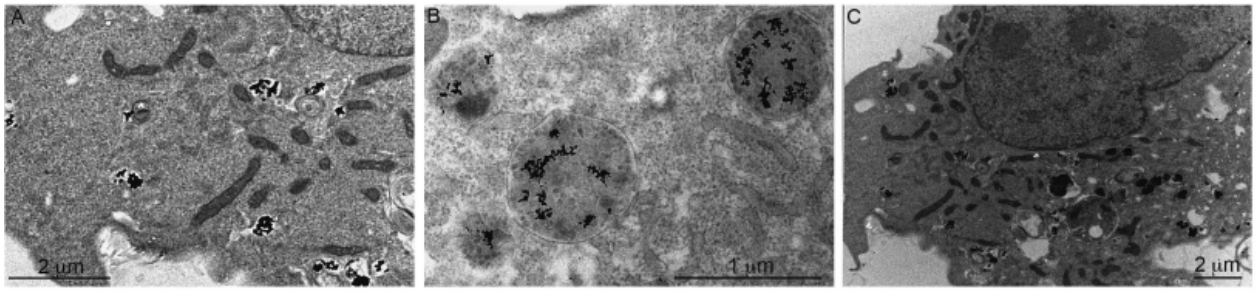

Figure 1. TEM images of Balb 3T3 cells exposed to 5 nm AuNPs (A); cells with hug vacuoles with AuNPs and digested materials (B); Balb 3T3 cells exposed to 15 nm AuNPs (C).

References

[1] M. Abd Elkodousa, Gharieb S. El-Sayyad, Ibrahim Y. Abdelrahman, Hanan S. El-Bastawisy, Abd Elrahman Mohamed, Farag M. Mosallam, Hebatallah A. Nasser, Mohamed Gobara, Ahmad Baraka, Mohamed A. Elsayed, Ahmed I. El-Batal, Colloids Surf B Biointerfaces, 180 (2019) 411-428.
[2] S. Pandey, A. Mishra. J Biochem Mol Toxicol, (2019) e22335.
[3] M. Condello, E. Pellegrini, M.Caraglia, S. Meschini, Int J Mol Sci, 20 (2019) E725.

Hyaluronic acid-based nanocomplexes as an innovative therapeutic tool to treat myotonic dystrophy

MATHIEU REPELLIN[1,2], FLAVIA CARTON[1,2], FEDERICO BOSCHI[3], ANDREA ALBANO[2], GIOVANNA LOLLO[2] AND MANUELA MALATESTA[1]

[1] Department of Neurosciences, Biomedicine and Movement Sciences, University of Verona, Italy;
[2] University of Lyon, Université Claude Bernard Lyon 1, CNRS, LAGEPP UMR 5007, Villeurbanne, France;
[3] Department of Computer Science, University of Verona, Italy

1. Introduction

Myotonic dystrophies (DMs) are the most common adult neuromuscular diseases of genetic origin that involve multiple organs and tissues, especially the skeletal muscles [1]. The molecular causes are linked to the pathological expansion of repeated nucleotide sequences in specific genes: these mutant sequences are transcribed into expanded RNAs that sequester splicing factors, with consequent alterations in the RNA and protein metabolism. Currently, no therapy is available for DMs, and treatments are only aimed at managing symptoms. Some molecules (*e.g.*, pentamidine or morpholino oligonucleotides) proved to be efficient in binding expanded RNA thus mitigating the pathological signs of DMs in experimental models. Actually, the therapeutic applications of these compounds is impaired by their low bioavailability or high systemic toxicity. Nanoparticles (NPs) could be an innovative solution to face these problems thanks to their ability to protect drugs from enzimatic degradation and to target specific cells or tissues. The aim of the present investigation was to assess the biocompatibility of novel hyaluronic acid (HA)-based NPs, and prove their ability of delivering pentamidine isothionate (PTM) to skeletal muscle cells *in vitro*.

2. Materials and Methods

HA-NPs and HA-NPs loaded with PTM (Loaded-NPs) were manufactured by ionic gelation technique (Carton et al., Submitted). Fluorescent HA-NPs (Fluo-NPs) were obtained by using HA labelled with fluorescein isothionate. The size and polydispersity index (PdI) were assessed by Dynamic Light Scattering. Murine C2C12 myoblasts were grown in Dulbecco's modified Eagle medium at 37°C in a 5% CO_2 humidified atmosphere. For cytotoxicity assays, cells were seeded in 96-multiwell plates while for fluorescence and transmission electron microscopy (TEM) they were planted onto glass coverslips in 24-multiwell plates. After 24h, cells were treated with the NPs. Untreated cells were used as absolute control. MTT viability assay was performed following the administration of blank HA-NPs, free PTM or Loaded-NPs at different concentrations for 2, 24 and 48 h. For fluorescence microscopy, the cells were incubated with Fluo-NPs for 2 and 24 h, fixed with 4% paraformaldehyde, and stained with Phalloidin-Atto 594; nuclei were counterstained with Hoechst 33342. For TEM, cells were fixed with 2.5% glutaraldehyde/2% paraformaldehyde, post-fixed with OsO_4 and potassium ferrocyanide, dehydrated and embedded in Epon resin.

3. Results and conclusions

NPs ranged 250 to 300 nm in size, with PdI <0.1, and PTM encapsulation efficency of 80%. Viability assays showed that blank HA-NPs induce an increase of cell death only at the highest concentration tested for long incubation times (48 h), thus demonstrating their good biocompatibility; actually, no cytological alterations were ever observed at TEM following administration of blank HA-NPs. As expected, free PMT induced concentration-dependent cell death; similar evidence was obtained after PMT administration *via* HA-NP, when cell mortality was sometimes even higher. Fluorescence microscopy (Figure 1) showed that Fluo-NPs are rapidly (<30min) and efficiently internalized by the cells in a time-dependent manner. TEM (Figure 2)

revealed that HA-NPs are internalized individually *via* endocytosis and localize throughout the cytoplasm, being never observed inside the cell nuclei. HA-NPs rapidly escape endosomes occuring free in the cytosol and, after 24 h, they may form large clusters (Figure 2b).

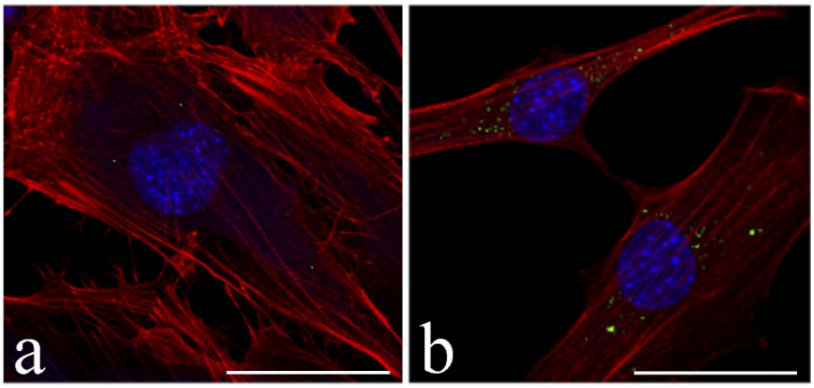

Figure 1. Confocal fluorescence micrographs of C2C12 cells treated with Fluo-NPs (green) for 30 min (a) and 24 h (b). Actin cytoskeleton in red (Phalloidin-Atto 594), nucleus in blue (Hoechst 33342). Bars: 50 µm.

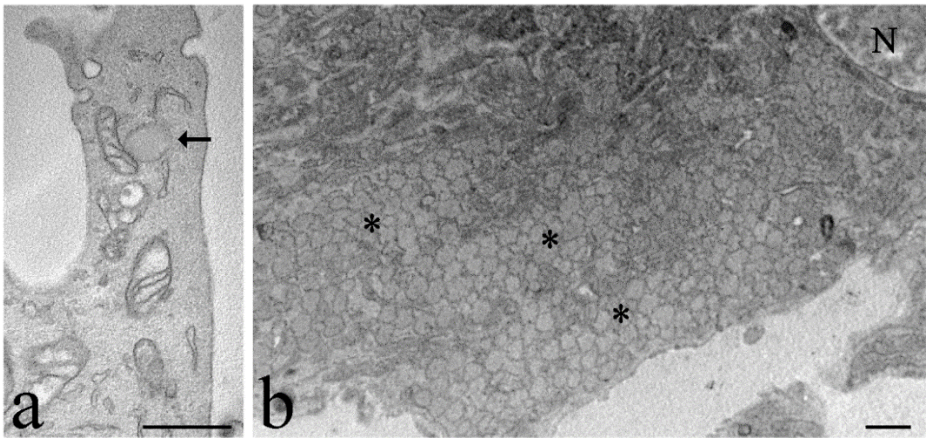

Figure 2. TEM micrographs of C2C12 cells treated with HA-NPs (arrow) for 2 h (a) and 24 h (b). Note the huge accumulation of NPs (asterisks) in the cytoplasm after 24 h. N: nucleus. Bars: 500 nm (a), 1 µm (b).

We may conclude that, due to the good encapsulation efficiency and the excellent capability to enter and accumulate inside C2C12 cells, Loaded-NPs cause a rapid and massive intracellular release of PMT which can account for the high cell mortality observed. We may hypothesize that HA-NPs loaded with very low PMT concentrations would be able to induce therapeutic effects on DM muscle cells with reduced cytotoxicity. Studies are presently in progress to verify this hypothesis.

4. Acknowledgments

M.R. is an INVITE PhD student of the Nanoscience and Advanced Technologies program, University of Verona. INVITE project received funding from EU Horizon 2020 GA No 754345.

References

[1] R. B. Siboni, M. J. Bodner, M. M. Khalifa, A. G. Docter, J. Y. Choi, M. Nakamori, M. M. Haley, J. Andrew Berglund, J Med Chem, 58 (2015) 5770-5780

Testing nanocarriers in vitro: are always cultured cells a reliable reference system?

MANUELA COSTANZO[1], FEDERICA VURRO[1], LAURA CALDERAN[1], FEDERICO BOSCHI[2], ILARIA ANDREANA[3], SILVIA ARPICCO[3], BARBARA STELLA[3] AND MANUELA MALATESTA[1]

[1] Department of Neurosciences, Biomedicine and Movement Sciences, University of Verona, Italy; [2] Deptartment of Computer Science, University of Verona, Italy; [3] Department of Drug Science and Technology, University of Turin, Torino, Italy

Myotonic dystrophy (DM) is an autosomal dominant disorder and represents the most common form of muscular dystrophy in the adults. DM is characterized by a variety of multisystemic features including myotonia, muscular dystrophy, dilated cardiomyopathy [1], and, at present, no therapies are available. In fact, small compounds that were successfully tested in experimental models *in vivo* and *in vitro* have scarce therapeutic applicability in humans because of their low bioavailability, due to enzymatic degradation or high systemic toxicity.

Nanocarriers have been attracting increasing interest because of their ability to protect the encapsulated molecules from enzymatic degradation and of their potential as drug-delivery systems for controlled and targeted drug release inside the cells [2]. To be used in therapy, nanocarriers must be biocompatible and biodegradable; therefore, their behaviour should be tested in a biological environment mimicking the functional and structural complexity of the living organism. Actually, conventional cell cultures are widely used to this purpose as they provide simple and controlled experimental conditions, though they barely reproduce the systemic milieu.

In this work, we investigated the interactions of some nanocarriers with skeletal muscle cells using two different experimental murine models *in vitro*: C2C12 cells and explanted soleus muscles.

C2C12 cells are immortalized murine myoblasts that spontaneously differentiate into myotubes after serum reduction, thus providing an *in vitro* model of both proliferating and terminally differentiated non-cycling muscle cells. Microscopy techniques were used to study the uptake and intracellular fate of liposomes (LPs) and Poly Lactic-co-Glycolic Acid nanoparticles (PLGA NPs). The nanocarriers were labelled with either fluorescein isothiocyanate (LPs) or Nile red (PLGA NPs) to make them detectable at confocal fluorescence microscopy (Figure 1a,b and 2a,b). Transmission electron microscopy was used to investigate the interaction of nanocarriers with organelles as well as the possible occurrence of cell damage. LPs enter the cells by a direct translocation through the plasmalemma, possibly due to the fusion with the cell membrane (Figure 1d); in the cytoplasm, LPs rapidly decompose and migrate through the cytosol toward lipid droplets. PLGA NPs are internalized by endocytosis and occur free in the cytosol for their capability to escape endosomes; however, they rapidly re-enter the lytic pathway *via* autophagy (Figure 2d). Both nanocarriers proved to be biocompatible to C2C12 cycling myoblast and non-cycling myotubes, even if their internalization in myotubes was lower than in myoblasts. Moreover, LPs were less efficiently internalized than PLGA NPs, in both myoblast and myotubes [3].

As a second step, we investigated the biodistribution of LPs and PLGA NPs in explanted mouse skeletal muscles maintained in a bioreactor, under fluid dynamic conditions [4]. Fluorescent nanocarriers were injected into the muscle and their biodistribution was observed in cryosections by confocal fluorescent microscopy. The results revealed that PLGA NPs were unable to enter muscle fibres, mostly accumulating in the perimysium and endomysium (Figure 2c). On the contrary, LPs showed higher capability to enter myofibres, although being partially entrapped in the connective tissue (Figure 1c). We are currently performing studies of nanocarrier functionalization to improve myofibre targeting in explanted muscle tissue.

The discrepancy between the results obtained in the two different *in vitro* models underlines the limitation of conventional cell cultures for testing the suitability of nanocarriers designed for biomedical use. In fact, it is worth considering that in organs/organisms various tissue surrounds the cells, above all the connective tissue that mediates cell interactions with the nanoparticulates.
Tests on cultured cells undoubtedly are very useful in the early research phase, to elucidate the uptake mechanisms, intracellular fate and degradation of NPs, but it should be more appropriate that the *in vitro* studies also include tissues and organs from biopsies or surgical material. In addition, this approach would potentially reduce the number of animals for the *in vivo* experimentation.

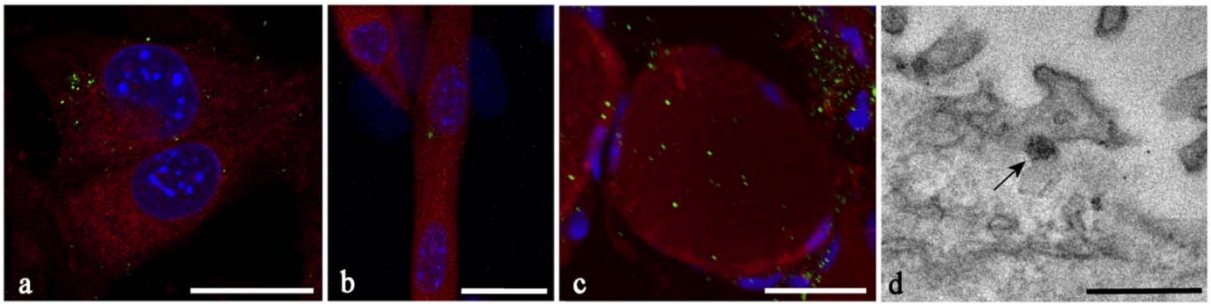

Figure 1. Confocal (a, b) and conventional (c) fluorescence microscopy. Liposomes (green) in mouse myoblasts (a), myotubes (b) and skeletal muscle tissue (c). Red: cytoplasm; Blue: nucleus. Bars: 25 µm. Transmission electron micrograph of C2C12 myoblast, aldehyde and osmium fixation, Epon embedding (d). A detail of a LP internalization (arrow). Bar: 250 nm.

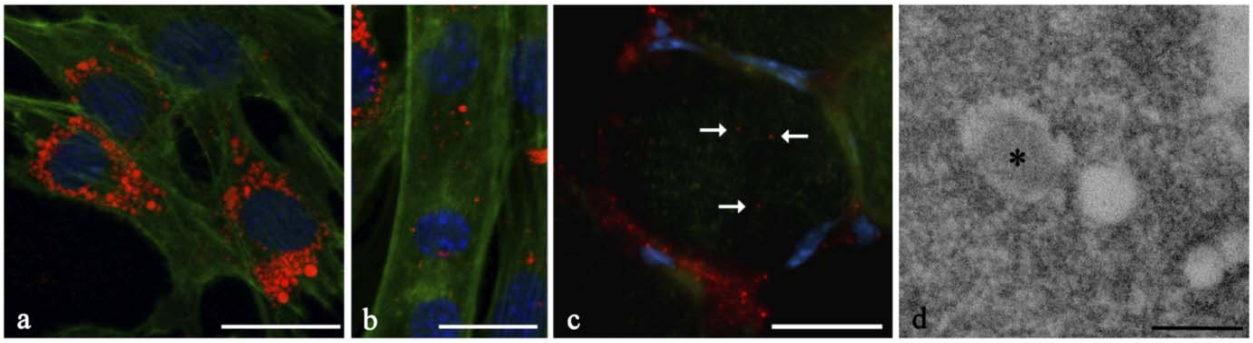

Figure 2. Confocal (a, b) and conventional (c) fluorescence microscopy. PLGA nanoparticles (red) in mouse myoblasts (a), myotubes (b) and skeletal muscle tissue (arrows in c). Green: cytoplasm; Blue: nucleus. Bars: 25 µm. Transmission electron micrograph of C2C12 myoblast, aldehyde and osmium fixation, Epon embedding (d). A PLGA NP (asterisk) enclosed in an endosome. Bar: 250 nm.

References

[1] P. S. Harper. “Myotonic Dystrophy” London: WB Saunders (2001)
[2] F. Dilnawaz, S. Acharya, S. K. Sahoo, Int. J. Pharm., 538 (2018) 263-278
[3] M. Costanzo, F. Vurro, B. Cisterna, F. Boschi, A. Marengo, E. Montanari, C. Di Meo, P. Matricardi, G. Berlier, B. Stella, S. Arpicco, M. Malatesta, Nanomedicine, 14 (2019) 301-316
[4] F. Carton, L. Calderan, M. Malatesta, Eur. J. Histochem., 61 (2017) 2862

Hyperthermic nanocarriers for biomedical applications

FEDERICA VURRO[1], SILVIA MANNUCCI[1], DAVIDE PROSPERI[2], MASSIMILIANO PERDUCA[3], CONCEPCIÓN JIMÉNEZ LÓPEZ[4], ALICE BUSATO[5], MARCO GEROSA[5], STEFANO TAMBALO[6], MARIA ROSARIA MARINOZZI[1], FEDERICO BOSCHI[5], MANUELA MALATESTA[1] AND LAURA CALDERAN[1]

[1] Dept. of Neurosciences, Biomedicine and Movement Sciences, University of Verona, Italy; [2] Dept of Biotechnology and Bioscience, University of Milano-Bicocca, Italy; [3] Dept of Biotechnology, University of Verona, Italy; [4] Dept. of Microbiology, University of Granada, Spain; [5] Dept. of Computer Science, University of Verona, Italy; [6] Center for Neuroscience and Cognitive Systems, @UniTn, Rovereto, Italy

In the last years, our group focused on magnetic nanoparticles (MNPs), which are able to induce hyperthermia, as potential biomedical tools. Magnetic hyperthermia is a term used to denote the generation of heat by MNPs in response to the application of an external alternating magnetic field. We applied hyperthermia *in vitro* with different aims, and the effects on cells were analyzed by applying viability test (MTT assay), and light and transmission electron microscopy (TEM) techniques.

We used superparamagnetic iron oxide NPs (SPIONs) to induce delipidation in 3T3 adipocytes and human adipose-derived adult stem cells. Immediately after hyperthermia, we observed a drastic lipid loss that persisted for at least 24 h in the absence of cell death, damage or dedifferentiation, as demonstrated by TEM (figure 1). These results open interesting perspectives for the application of hyperthermia to treat obesity [1].

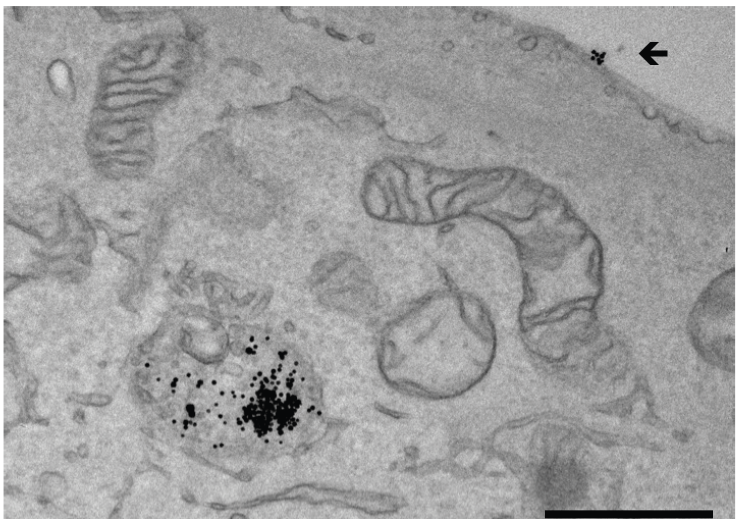

Figure 1. TEM micrograph of a 3T3 cell. SPIONs occur both at the cell surface (arrow) and inside vacuoles. Bar: 1 µm

We applied hyperthermic treatment also to cancer cells, known to be more sensitive to heat shock than healthy cells, in order to induce apoptosis [2]. A glioblastoma cell line (U87MG) was treated with either S1 NPs or biomimetic magnetic NPs (BMNPs). S1 are amphiphilic polymer, dodecyl grafted poly(isobutylene-alt-maleic anhydride) coated zinc-doped iron oxide (Fe_3O_4) NPs of 15 ± 2 nm size, and show a high thermal capacity. These NPs proved to be efficient in increasing both culture medium temperature and cell death rate as demonstrated by light microscopy analysis (figure 2). BMNPs, synthetized with the protein MamC from magnetotactic bacteria, may act as both drug carriers and hyperthermic agents, being promising tools for the treatment of many types of tumor [3].

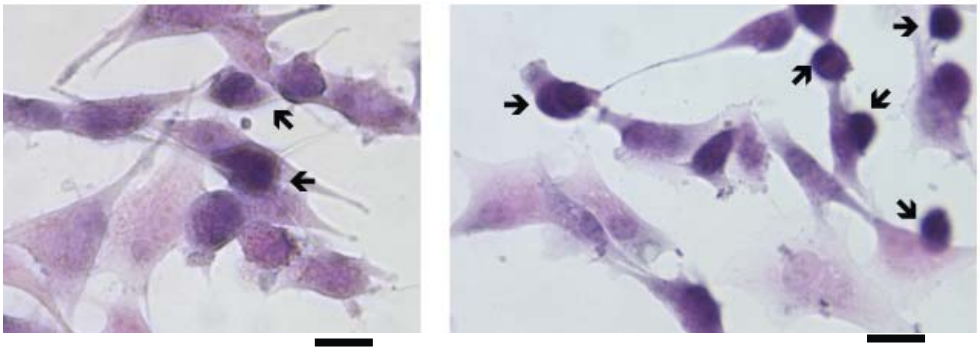

Figure 2. Light microscopy micrographs of U87MG cells incubated with S1 NPs (A, B). In B the cells were also submitted to hyperthermia. Note the high number of dead cells (arrows) in B in comparison to A. Bars: 50 µm.

BMNPs were also tested in a human hepatocyte carcinoma cell line (Hep-G2) after functionalization with a Choline Kinase inhibitor in order to obtain a nanocarrier potentially suitable for targeted chemotherapy. In fact, Choline Kinase is considered as a biomarker of tumor progression and carcinogenesis, and a target for cancer therapy [4]. Therefore, our nanocarriers would allow a local treatment of cancer thus avoiding/reducing possible systemic side effects. The internalization of BMNPs was evaluated using TEM (figure 3).

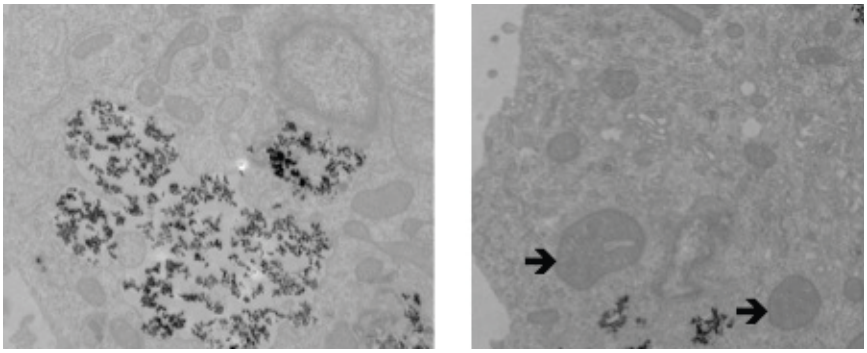

Figure 3 TEM micrograph of Hep-G2 cells treated with non-functionalized (A) and functionalized (B) BMNPs. Note the mitochondrial swelling (arrows) induced by functionalized BMNPs. Bars: 1 µm.

Taken together, our results prove the efficacy of MNPs in inducing hyperthermia in cultured cells. Although these basic data have been obtained in *in vitro* models, they suggest the suitability of these NPs as therapeutic tools and encourage further studies for their application in the biomedical field.

References

[1] M. R. Marinozzi, L. Pandolfi, M. Malatesta, M. Colombo, V. Collico, P. M. J. Lievens, S. Tambalo, C. Lasconi, F. Vurro, F. Boschi, S. Mannucci, A. Sbarbati, D. Prosperi, L. Calderan, Int. J. Biochem. Cell Biol., 93 (2017) 62–73
[2] B. Hildebrandt, P. Wust, O. Alhers, A. Dieing, G. Sreenivasa, T. Kerner, R. Felix, H. Riess, Crit. Rev. Oncol. Hematol., 43 (2002) 33–56
[3] G. García Rubia, A. Peigneux, Y. Jabalera, J. Puerma, F. Oltolina, K. Elert, D. Colangelo, J. Gómez Morales, M. Prat, C. Jiménez López, Langmuir, 34 (2018) 13713–13724
[4] K. Glunde, Z. M. Bhujwalla, S. M. Ronen, Nat. Rev. Cancer, (2011) 835–848

Alcian blue staining to study nanoparticle-cell interactions at transmission electron microscopy

FLAVIA CARTON[1,2], MATHIEU REPELLIN[1,2], GIOVANNA LOLLO[2] AND MANUELA MALATESTA[1]

[1] Department of Neurosciences, Biomedicine and Movement Sciences, Anatomy and Histology Section, University of Verona, Italy; [2] University of Lyon, Université Claude Bernard Lyon 1, CNRS, LAGEPP UMR 5007, Villeurbanne, France

1. Introduction

Transmission electron microscopy (TEM) is the technique of choice to investigate the distribution of nanoparticles (NPs) inside cells and tissues, providing essential information on their actual spatial relationships with biological structural components. In order to track NPs in the biological environment, they must be unequivocally visualised. This is easily obtained for NPs containing electron dense components such as metal ions, but it may be difficult for NPs made of organic components such as polymers or lipids: in fact, their moderate electron density makes them hardly detectable in the inter- and intracellular space. In previous studies, we solved this problem by labelling chitosan-based and phospholipidic NPs with fluorochromes, and subsequently applying the diaminobenzidine photo-oxidation technique. This method gives rise to a finely granular electron dense product thanks to the reactive oxygen species originating upon fluorochrome irradiation, thus allowing a very precise labelling of NPs at the ultrastructural level [1, 2]. However, in the absence of appropriate fluorochrome labelling or in the presence of a marked background, diaminobenzidine photo-oxidation cannot be applied. We recently faced this problem with hyaluronic acid-based (HA) NPs. As an alternative approach, we set up a novel application of a long-established histochemical technique suitable for revealing glycosaminoglycans, *i.e.*, the critical electrolyte concentration method of Alcian Blue (AB) staining [3].

2. Materials and Methods

NPs made of HA and polyarginine were obtained by ionic gelation technique (Carton et al., Submitted). NPs were characterized in term of size and polydispersity index (PdI) using Dynamic Light Scattering. C2C12 mouse myoblasts were grown in 75 cm^2 plastic flasks using Dulbecco's modified Eagle medium, at 37°C in a 5% CO_2 humidified atmosphere. When subconfluent, the cells were trypisinized and seeded onto slides in 24-multiwell plates; 24 h later, the cells were treated with NPs for 2 h and 24 h. Untreated cells were used as control. In order to visualise HA NPs at light microscopy, C2C12 cells were fixed with 4% paraformaldehyde, and the AB staining was performed under acid conditions [3]; the nuclei were counterstained with nuclear fast red that also makes the cytoplasm pale pink. Some HA NPs were submitted to the AB staining in suspension in culture medium. For TEM, we applied the protocol propopsed by Schofield and coworkers [4], who modified the original AB method intended for light microscopy to discriminate cartilage mucopolysaccharides at the ultrastructural level. Briefly, cells were fixed with 3% glutaraldehayde, stained with AB, post-fixed with OsO_4 and potassium ferrocyanide, dehydrated and embedded in Epon resin. Ultrathin sections were observed without lead staining with a Philips Morgagni TEM equipped with a MegaView II digital camera for image acquisition.

3. Results and Conclusions

HA NPs were about 300 nm in diameter, with a PdI of 0.04. After AB staining, HA NPs were visualized at light microscopy as blue dots both as free NPs in suspension (Figure 1a) and after their internalization in C2C12 cells (Figure 1b). At TEM, AB-stained NPs were easily detectable due to the presence of a granular electron dense product (Figure 2). No reaction product was found on any

cell structural components; moreover, in control cells no staining was observed. Thanks to the AB ultrastructural staining, we were able to describe the very early uptake steps as well as the intracellular fate of HA NPs in C2C12 cells. This result demonstrates that, in the nanomics era, the proper application of traditional histochemical techniques can be crucial to get direct evidence of the nanoparticle-cell interactions.

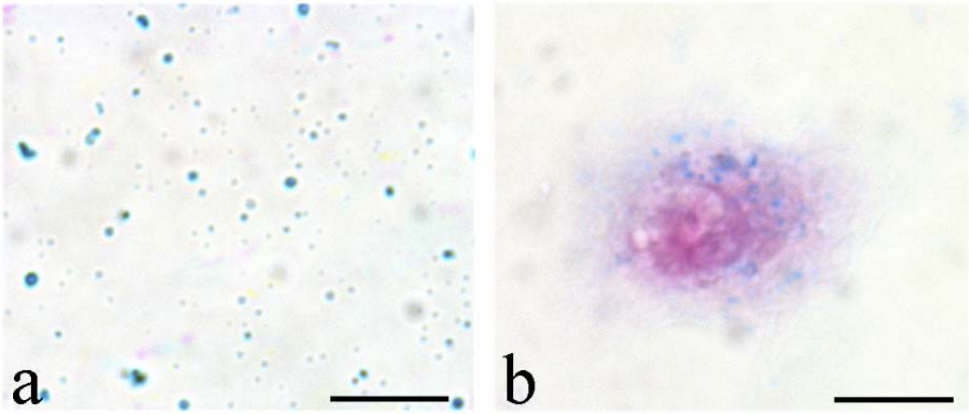

Figure 1. Light microscopy. AB-stained HA NPs suspended in medium (a) and inside a C2C12 myoblast (b). Bars: 20 µm.

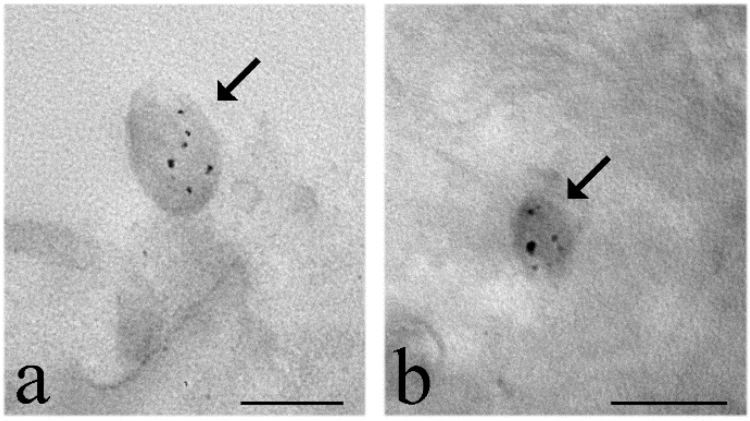

Figure 2. Transmission electron microscopy. AB-labelled HA NPs (arrows) occurring at the cell surface (a) and free in the cytosol (b). Bars: 200 nm.

4. Acknowledgments

M.R. is an INVITE PhD student of the Nanoscience and Advanced Technologies program, University of Verona. INVITE project received funding from EU Horizon 2020 GA No. 754345.

References

[1] M. Malatesta, M. Giagnacovo, M. Costanzo, B. Conti, I. Genta, R. Dorati, V. Galimberti, M. Biggiogera, C. Zancanaro, Eur. J. Histochem., 56 (2012) e20
[2] M. Costanzo, L. Scolaro, G. Berlier, A. Marengo, S. Grecchi, C. Zancanaro, M. Malatesta, S. Arpicco, Int. J. Pharm., 508 (2016) 83–91
[3] J. E. Scott, J. Dorling, Histochemie, 5 (1965) 221–233
[4] B. H. Schofield, B. R. Williams, S. B. Doty, Histochem. J., 7 (1975) 139–349

Microscopic evidence of the primary astrocytes' morphological differentiation and migration inside porous Poly-L-lactic acid 3D scaffolds

MARIA ANTONIETTA DI BELLA[1], FRANCESCO CARFÌ PAVIA[2], VALERIO BRUCATO[2], VALERIA BLANDA[2], FRANCESCA ZUMMO[3], ILENIA VITRANO[2], CARLO MARIA DI LIEGRO[3], GIULIO GHERSI[3], ITALIA DI LIEGRO[1] AND GABRIELLA SCHIERA[3]

[1] Department of Biomedicine, Neurosciences and Advanced Diagnostics, (BiND), University of Palermo, Italy; [2] Department of Engineering, University of Palermo, Italy; [3] Department of Biological Chemical and Pharmaceutical Sciences and Technologies (STEBICEF), University of Palermo, Italy

Tissue engineering is an emerging multidisciplinary field that aims at reproducing in vitro and/or in vivo tissues with morphological and functional features similar to the biological tissue of the human body [1]. In the attempt to construct suitable tissue models, a critical step is the setting of 3Dscaffolds that mimic the supportive structures of a natural extracellular matrix microenvironment into which cells are normally embedded. In this context, the generation of 3D cultures of brain cells is of particular interest. For instance, the poly L-lactic acid (PLLA) polymer is wildly used because of its biocompatible and biodegradable potential; the PLLA scaffold topography simulates the natural extracellular matrix (ECM) and can make it a good candidate for neural tissue engineering [2].

To achieve this goal, in this study, PLLA scaffold with characteristics of bioactivity was prepared via thermally-induced phase separation (TIPS) [3], and utilized as substrate for primary rat astrocytes 3D growth. To assess the cells spatial distribution and morphology within the scaffolds, the structures were characterized by scanning electron microscopy. For comparison, astrocytes were also cultured in the traditional 2D culture system that we have been using since 2003. Different scaffold morphologies and coatings such as collagen I and IV, and fibronectin were tested in order to evaluate their influence on astrocyte growth, morphology and EV production. To evaluate these effects on astrocyte morphology on the PLLA scaffolds, TEM preparation was also performed.

Cells were present in all regions of the scaffold, they were observed to adhere, grow and penetrating into the interior region of the scaffold, acquiring their typical morphology. In addition, they also secrete EVs as in vivo [4]. Their ability to produce EVs was demonstrated by both TEM and SEM analyses, which revealed intracellular MVBs and EVs compatible in size with exosomes.

The results revealed that the porous sheath of PLLA allowed cell migration inside the scaffold and that the one coated with collagen IV, served as very good matrices for astrocytes, suggesting that the chosen conditions could be a good starting point for the preparation of 3D brain cell coculture systems useful for clinical applications.

References

[1] R. Langer, JP. Vacanti. Science. 14 260 (1993): 920-926
[2] M. Soleimani, S. Nadri, I. Shabani. Int. J. Dev. Biol. 54 (2010) 1295-1300
[3] GA. Mannella, G. Conoscenti, F. Carfì Pavia, V. La Carrubba, V. Brucato. Mater Lett 160 (2015) 31-33
[4] G. Schiera, CM. Di Liegro, I. Di Liegro. Biomed Res Int (2015): 152926

Microstructure analysis of porous multilayered core/shell silica particles for immobilization of lipase

MILAN P. NIKOLIĆ[1], VLADIMIR V. SRDIĆ[2], SLOBODANKA S. NIKOLIĆ[1], KATARINA PAVLOVIĆ[3], ALEKSA MARIČIĆ[4]

[1] University of Kragujevac,, Faculty of Agronomy, Čačak, Serbia; [2] University of Novi Sad, Faculty of Technology, Novi Sad, Serbia; [3] University of Belgrade, Faculty of Biology, Belgrade, Serbia; [4] University of Kragujevac, Faculty of Technical Sciences Čačak, Serbia

1. Introduction

Lipases are enzymes which find increasing biotechnological applications because of their ability to catalyze regio- and enantioselective hydrolysis of many esters. In order to simplify separation of the enzymes from the reaction medium and enhance their stability under storage and operational conditions, enzymes can be used in an immobilized form [1]. The characteristics of the support, reactive groups and immobilization conditions have an enormous influence on the success of immobilization, so they must be carefully selected. Numerous materials with core/shell structure can be used for enzyme immobilisation. Although core/shell particles are typically spherical, they can be synthesized in various other forms such as nanotubes, nanowires, nanorods, nanorings and nanostars.

Multilayered core/shell silica is widely used support material for enzyme immobilization due to its high specific surface area and large porous volume, which enable high enzyme loading, prevent enzyme leakage and provide a protective barrier for the immobilized enzyme[2]. During fabrication of silica core/shell particles, silica core particles are usually synthesized by Stöber process, while the formation of mesoporous silica layers around silica cores is mainly based on the use of surfactants that are aggregated on the surface of the silica cores, after which the condensation of tetraethylortosilicate is carried out on the surface of modified cores. These materials should have an appropriate average pore size, uniform pore-size distribution, high total pore volume and high specific surface area [3]. In order to optimize structural development of these materials, in this study microstructure analysis of porous multilayered core/shell silica particles for immobilization of lipase has been performed.

2. Experimental procedure and discussion

Mesoporous silica particles for immobilization of lipase from *Candida rugosa* were prepared using precipitation and aggregation by hydrolysis and condensation of tetraethylortosilicate (TEOS). Fe_2O_3 nanoparticles were deposited on the surface of silica core particles in four successive stages. To allow electrostatic deposition of Fe_2O_3 nanoparticles on the previously deposited Fe_2O_3 layer, it was functionalized with silica nanoparticles generated by hydrolysis and condensation of TEOS at pH 7.

Microstructure analysis of multilayered core/shell structures has been performed by using transmission electron microscope (TEM, JEM-1400) and scanning electron microscope (JEOL JSM 6460 LV, Tokyo, Japan) coupled with energy dispersive spectrometer (EDS Oxford Instruments X-MaxN) (Figure 1). Prior to SEM imaging, the samples were sputtered with gold by using BALTEC SCD 005 sputter coater.

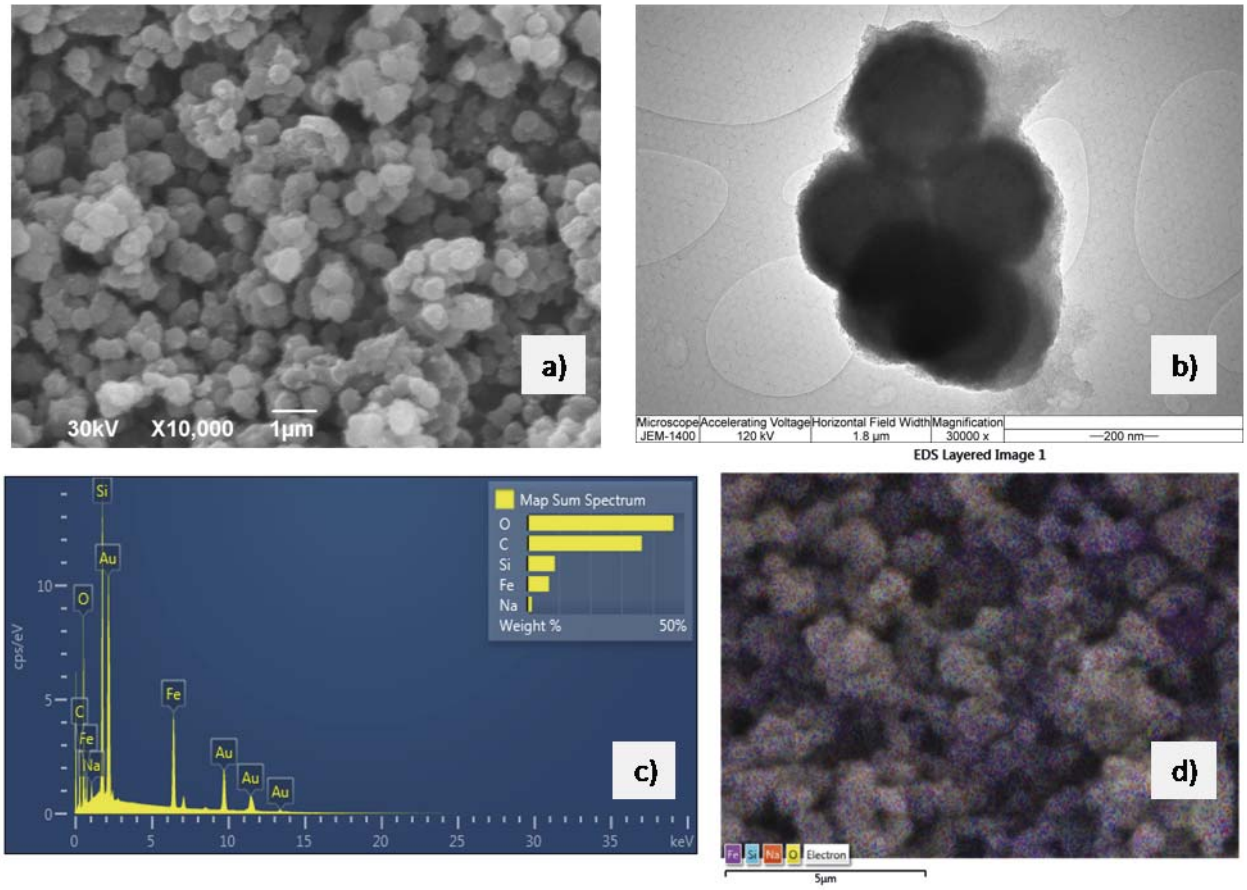

Fig. 1 Core/shell microstructure analysis: (a) SEM; (b) TEM; (c) EDS; (d) mapping of elements

Mesoporous silicates are attractive materials for use as supports for the immobilisation of enzymes, since their synthesis is relatively straight forward and produces materials with well defined and ordered pore structures, high surface areas and good mechanical and chemical stability. It has been found that silica core/shell particles are composed of microporous core and relatively uniform mesoporous shell. TEM micrographs also revealed that the silica particles used in this work have pores which are large enough so that lipase can penetrate and interact with surfaces inside the pores. This should result in a high adsorption capacity of the silica support. It should be emphasized that the successful immobilisation of an enzyme on a support requires that the structure of the enzyme should not be perturbed in a manner which significantly reduces the activity of the enzyme while diffusion of substrate/product to and from the active site should not be hindered. It should be noticed that accuracy of pore diameter determination by TEM can be limited by the number of pore observations. Therefore, nitrogen adsorption analysis should provide more accurate estimation of the pore diameter of the sample. Further microstructure analysis included chemical mapping of the surface of the Fe_2O_3 layer. The analysis revealed that the surface was functionalized with Si atoms. It has been noticed that external mesoporous silica layer on the previously obtained particles with silica core and four-layered Fe_2O_3 shell was formed by deposition of silica nanoparticles generated from the silicate solution. The thickness of the four-layered Fe_2O_3 shell and external silica shell was ~ 70 and 50 nm, respectively.

Although this study has established that the functionalization of the core-particles can improve the microstructure of the obtained materials, in order to further optimize properties of multilayered core/shell silica particles, future studies will concentrate more on improvement of the activity of the immobilized enzyme.

Acknowledgemets

This work is financially supported by the Ministry of Education, Science and Technological Development of Republic of Serbia under the Project III45021 and the Project OI 172057.

References

[1] R. DiCosimo, J. McAuliffe, A. J. Pouloseb, G. Bohlmannb Industrial use of immobilized enzymes Chem. Soc. Rev., 2013,42, 6437

[2] V. V. Srdić, B. Mojić, M. Nikolić, S. Ognjanović Recent progress on synthesis of ceramics core/shell nanostructures Processing and Application of Ceramics 7 [2] (2013) 45–62

[3] Y M. P. Nikolic, V. V. Srdic, M. G. Antov Immobilization of lipase into mesoporous silica particles by physical adsorption Biocatalysis and Biotransformation, 2009; 27(4): 254-262

LS7

Multidisciplinary approaches for medical and biological sciences

CHAIRPERSONS:

Elisabetta Falcieri, Melek Ozturk

INVITED LECTURE

Drug resistance in cancer and its overcoming

MARIA CONDELLO, EVELIN PELLEGRINI, STEFANIA MESCHINI
National Center for Drug Research and Evaluation, National Institute of Health,Rome, Italy

Cancer is one a main health problem, although chemotherapy, targeted therapy, radiation, immunotherapy and surgery are the main strategies for the treatment of disease, a major problem limiting their success is resistance to the drug treatments (1). When antineoplastic drugs are extruded from the cells, and their intracellular concentration drops below the cytotoxic threshold, multidrug resistance (MDR) phenotype arises. MDR may be intrinsic or innate, if the tumor cells are naturally resistant to the drug, or acquired if it arises after the pharmacological treatment.
MDR is due to several mechanisms including:
(a) The overexpression of ATP-binding cassette (ABC) transporters that pump out the chemotherapeutics (2);
(b) The mutation of oncogenes that become resistant to former treatments (3);
(c) The adaptation of cancer cells to the microenvironment (4);
(d) The presence of survived cancer stem cells (CSCs) that escape from conventional therapies (5);
(e) The activation of pro-survival mechanisms (6, 7).
(a) ABC transporters are 49 subfamilies of proteins classified from ABCA to ABCG that are in the cell membrane with different functions. A higher cell membrane expression of ABCB1 (P-glycoprotein, P-gp) or ABCG2 (breast cancer resistant protein, BCRP) or ABCC1 (multidrug resistance -associated protein 1, MRPR1) may lead to the resistance for the conventional chemotherapeutics, such as doxorubicin (Dox), paclitaxel, 5-fluorouracil (5-FU), colchicine etc.
(b) Cancer cells growing rapidly need more oxygen supply for signal transmission. Tissue hypoxia can occur for re-programming to cancer cell metabolism, so cancer cells adapt to less oxygen by up-regulating several key proteins, including hypoxia-inducible factor-1a (HIF-1a), HIF-2a.
Hypoxia can trigger MDR by decreasing the efficacy of anticancer drugs (24). Hypoxia may also promote the overexpression of ABCB1 and ABCG2 and inducing MDR.
(c) Cancer cells reorganize it to adapt to the change of the microenvironment. In the initial phase of the disease, the production of reactive oxygen species (ROS) can favour the onset of MDR. Moderate level of ROS can help to tumor development by promoting tumor cell proliferation and DNA mutations, while high ROS level may be lethal factor that finally induces cell death. A promising strategy to overcome MDR in cancer may be the targeting of oxidative stress.
(d) CSCs are a subset of cells in the niche of the tumor, composed of fibroblasts and endothelial, mesenchymal and immune cells. CSCs possess the potential of self-renewal, differentiation and tumorigenicity, are thought to be the major problem of cancer therapy failure. The elimination of CSCs represents one promising strategy to overcome MDR.
(e) Autophagy, a self-degradative system in which cells undergo degradation of intracellular components, is important for the cell energy balance in response to nutrient stress (36, 37). During chemotherapy, autophagy works as a prosurvival and resistance mechanism; therefore, the inhibition of autophagy can re-sensitize MDR cells and enhance the cytotoxicity of chemotherapeutic agents.
Studies have shown that some phases of the cell cycle exhibit resistance to chemotherapeutics, and the cancer cells that over-express cyclin dependent kinases (CDKs) and cyclins show resistance to conventional chemotherapeutics.
Various MDR reversal agents have been developed and some of them have entered into clinical trials, however, most of them failed due to severely adverse effects or because they suffered resistance in a short time.
Effective novel agents that surmount MDR remain an unmet clinical need.

References

[1] X. Wang, H. Zhang, X. Chen Cancer Drug Resist. 2 (2019) 141-60.
[2] W. Li, H. Zhang, Y.G. Assaraf, K. Zhao, X. Xu, J. Xie, et al. Drug Resist Updat. 27 (2016) 14 - 29.
[3] M. Xue, J. Cheng, J. Zhao, S. Zhang, J. Jian, Y. Qiao, et al. Int. J. Lab. Hematol. 41 (2019) 94 - 101.
[4] G. Yeldag, A. Rice, R. H. A. Del Cancers. 10:E471 (2018).
[5] M. Prieto-Vila, R.U Takahashi., W. Usuba, I. Kohama, T. Ochiya Int. J. Mol. Sci. 18: E2574 (2017).
[6] A.G. Smith, K.F. Macleod J. Pathol. 247 (2019) 708-718.
[7] M. Condello, E. Pellegrini, M. Caraglia. S. Meschini Int. J. Mol. Sci. 20 (3) (2019).

INVITED LECTURE

Centriolar satellites are required for the biogenesis and function of the centrosome/cilium complex

ELIF N. FIRAT-KARALAR
Department of Molecular Biology and Genetics, Koç University, Istanbul, Turkey

The centrosome/cilium complex is required for key functions ranging from cell division to cellular signaling and its deregulation causes various human diseases including cancer and ciliopathies. To elucidate disease mechanisms, it is essential to determine how centrosomes and cilia assemble and function in time and in space. To this end, we have focused on studying the vertebrate-specific components of the centrosome cilium complex, centriolar satellites, which are an array of membrane-less granules that localize around the centrosome/cilium complex. Although mutations affecting centriolar satellites were linked to ciliopathies, their precise functions, mechanisms and the functional significance of their typical clustering around the centrosomes remain poorly understood. To determine their cellular functions as discrete protein complexes, we generated satellite-less retinal pigmental and kidney epithelial cells and investigated the cellular and molecular consequence of satellite-loss. While satellites were essential for cilium assembly in retinal epithelial cells, satellite-less kidney epithelial cells still formed full-length cilia but at significantly lower levels, with changes in the centrosomal and cellular levels of key ciliogenesis factors. Using the kidney epithelial cells that ciliated, we identified the first satellite-specific functions at cilia, specifically in regulating ciliary content, Hedgehog signalling, and epithelial cell organization. Next, we investigated the functional significance of why satellites cluster around the centrosomes in most cell types. To this end, we employed a chemically inducible trafficking approach to restrict satellite localization at the cell periphery or the centrosome. Using these cells, we determined which proteins redistribute along with satellites and thereby are regulated by them. By studying the phenotypic consequences of satellite redistribution, we identified functions for centriolar satellites in cilium assembly and cell division. Together, our findings reveal that satellites regulate show that the satellites are required for efficient centrosome and cilium assembly and function and provide insight into disease mechanisms of ciliopathies.

Biomechanical fingerprint of disease: application of Atomic Force Microscopy to cell and tissue mechanics

GABRIELE CIASCA[1], MASSIMILIANO PAPI[1], CRISTINA ROSSI[2], FABIO DE-GIORGIO[3], ANGELO MINNELLA[4], ELEONORA MINELLI[1], MATTEO NARDINI[1], ALBERTO MAZZINI[1], MARCO DE SPIRITO[1]

[1] Institute of Physics, Catholic University of Sacred heart; Rome, Italy; [2] Institute of Biochemistry and Clinical Biochemistry, Catholic University; Rome, Italy; [3] Institute of Public Health, Catholic University of Sacred heart; Rome, Italy; [4] Institute of Public Health, Catholic University of Sacred heart; Rome, Italy

1.Introduction.

Mechanical forces play a key role in tissue growth and maintenance, deeply influencing human physiology. Similarly, in pathological conditions, cell and tissue mechanics undergo deep changes, which contribute to disease progression. Such alterations can be investigated using Atomic Force Microscopy (AFM), with the aim to search for novel mechanical biomarkers of pathologies. Here we present some AFM application to cell and tissue biomechanics in several human diseases, including brain and colorectal cancer, Alzheimer's Disease (AD) and ocular pathologies. AFM application to forensic science is also discussed.

2.Methods.

Cell and tissue elasticity were investigated through the acquisition of force-distance and creep-relaxation curves. The former were analyzed with the Sneddon model to retrieve Young's modulus and hysteresis. The latter were analyzed with the Standard Linear Solid model, in term of relaxation times and viscosity. Nanoscale mapping of the fitted parameters was performed, with the aim to generate functional images of the mechanical properties of the investigated samples. AFM data were compared with other imaging techniques including histology, confocal microscopy, US-Elastography, and computational techniques.

3.Results.

Our data show that AFM is able to detect and image mechanical alterations associated with the development of many pathologies. In detail:

i) we demonstrated that the biomechanical response of erythrocytes of AD patients is altered with respect to control subjects and correlates with the neurological examination;

ii) we unveiled the mechanical fingerprint of two frequently-occurring brain cancers (meningioma and glioblastoma), contributing to the development of novel AFM-based diagnostic methods to assess the tumor grade (figure 1).

iii) we studied the mechanical basis underlying subtle differences occurring into two ocular pathologies of surgical interest, Macular hole, and Pucker.

iv) we showed that AFM hysteresis has potential application in forensic science with particular regard to the estimation of the time-since-death as it allowed us to monitor the time behavior of rigor mortis

4.Conclusions.

Taken together, our results confirm that AFM has the potential to positively impact on the development of novel diagnostic and monitoring tools.

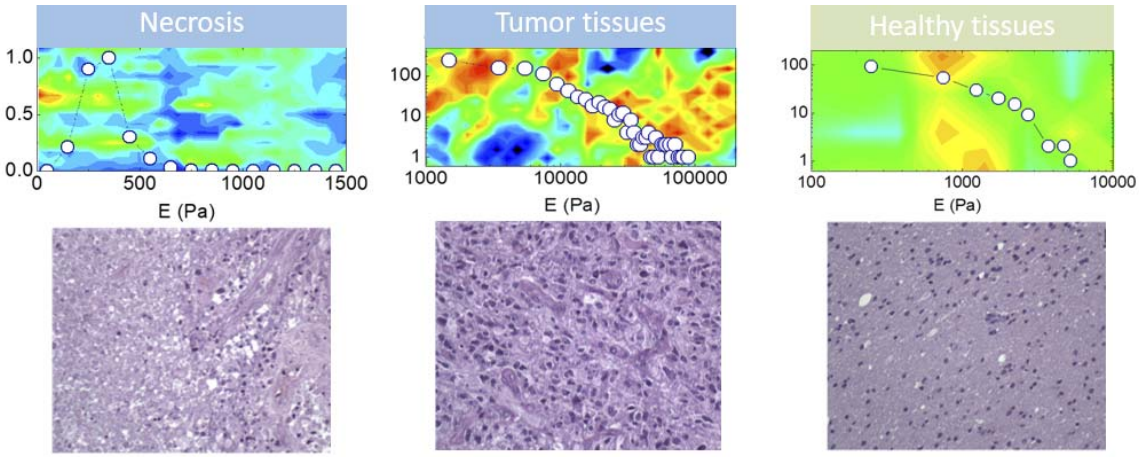

Figure 1. Mechanical fingerprint of brain cancer tissues. Young's modulus maps and frequency histogram of brain tissues obtained from patients diagnosed with Glioblastoma: Necrotic tissues (left), non-necrotic cancer tissues (center) and healthy tissues (right), together with histological sections.

References

[1] Ciasca, Gabriele, et al. Nanoscale 8.47 (2016): 19629-19643
[2] Ciasca, Gabriele, et al. Condensed Matter *4*.2 (2019), 58
[3] Minelli, Eleonora, et al. Appl. Phys. Lett. 111, 143701 (2017)
[4] Ciasca, Gabriele, et al. World J Gastroenterol. 2016 Aug 28; 22(32): 7203–7214.

Characterization of extracellular vesicles from in vitro and in vivo origins with electron microscopy

SAMO HUDOKLIN, NATAŠA RESNIK AND ROK ROMIH
Institute of Cell Biology, Faculty of Medicine, University of Ljubljana, Ljubljana, Slovenia

1. Introduction. Extracellular vesicles (EVs) are membrane-bound vesicles, which are secreted by eukaryotic cells (donor cells) into their surroundings, e.g. into growth media *in vitro* or into body liquids *in vivo* [1]. Since EVs contain biologically active molecules (proteins, lipids, nucleic acids) and can be transported to the distant tissues and influence there the physiology of the target cells, they are considered as a novel type of cell-to-cell communication [2]. Molecular composition of EVs resembles donor cell type and its physiological condition. That would make EVs very useful and convenient diagnostic markers for clinical use. As an example, EVs originating from tumour cells contain molecules characteristic for particular tumour type, i.e. carry tumour's molecular fingerprint [3]. Therefore, by analysis EVs from the patient blood or other body fluids, clinicians could diagnose potential presence of the tumour as well as its type. Moreover, biologically active molecules in tumour-originating EVs may have a role in progression of the disease; they can influence healthy target cells to start expressing tumour-characteristic genes (e.g. a cell with E-cadherin starts to produce N-cadherin), what makes target cells prone to tumour transformation and increases chances for survival of malignant cells [4, 5]. By elimination of such EVs, tumour progression could be supressed. Due to their potential as diagnostic markers and as targets to prevent tumourigenesis, EVs are currently in the centre of intensive biomedical research.

EVs are produced by investigations because of their putative diagnostic potential [7]. Aside from EVs isolated from body fluids *in vivo*, which present highly complex systems, many EVs studies are performed *in vitro*, which presents simpler systems that are easier to control.

After isolation of EVs from body fluids *in vivo* or from growth media *in vitro*, it is essential to make qualitative and quantitative analyses of the samples with biochemical and microscopy methods. It is crucial to check the purity of the sample for potential contaminations with cell debris and various components of body fluids or growth media. Next, one has to define the size of EVs in order to determine the type of EVs and molecular composition in order to define their origin and the role in cell communication. To achieve all these requirements, only biochemical analyses and light microscopy are not suficient. Since only electron microscopy has the resolution for direct visualization of EVs, we have checked and compared different transmission (TEM) and scanning (SEM) electron microscopy methods for ultrastructural and immunocytochemical analyses of EVs.

2. Methods. For characterization of EVs we used methods of TEM, i.e. negative staining, classical ultrathin sectioning and immunolabelling of cryo-ultrathin sections, and method of classical SEM. EVs were obtained from mammalian (urothelial cells, cells of Langerhans islets) and yeast cell cultures *in vitro*, and from human blood serum *in vivo*. Raw samples were first ultracentrifuged in sucrose gradient, currently widely used for separation of different types of EVs. To check the purity of EVs, we used negative staining or epon-embedded classical ultrathin sections. For negative staining samples were put on glow-discharged carbon-coated EM grid for 5 min, washed in de-ionized water, 1 min and stained with 1% uranyl acetate, 1 min. For Epon-embedding, samples were fixed with 2,5% glutaraldehyde in 0.1M cacodylate buffer, 2 h 45 min at +4˚C, post-fixed with 1% OsO_4 for 2h, dehydrated in series of ethanol (30, 50, 70, 90, 2×100%, 20 min each) and embedded in epon. After Epon polymerization, ultrathin section (thickness 60 nm) were cut with ultramicrotome UC6 (Leica), and stained with uranyl acetate and led citrate.

For detection of membrane proteins or cytosolic proteins in the lumen of EVs, we used immunolabelling of cryo-ultrathin sections. After centrifugation, pellets were fixed with 2% formaldehyde, 1 h at room T, embedded into 12% gelatine, cut into 1×1×1 mm cubes, cryoprotected by incubation in 2.3M sucrose 24h at +4˚C and stored in liquid nitrogen. Subsequently, samples were cut with cryo-ultramicrotome FCS (Leica) at -120˚C (thickness 70 nm) and processed for immnolabelling. Nonspecific labelling was blocked by 0.8% BSA, 0.1% fish gelatine and 5% fetal calf serum in PBS at room temperature for 30 min. Various mono- and polyclonal primary antibodies were incubated overnight at +4˚C, washed in PBS, and then incubated with secondary antibodies conjugated with colloidal gold, 1.5 h at room temperature. All TEM samples were examined with CM100 (Philips), running at 80kV.

For SEM, samples were fixed with 4% formaldehyde + 2% glutaraldehyde in 0.1M cacodylate buffer, 2 h 45 min at +4˚C, post-fixed with 1% OsO_4 for 2h, dehydrated in series of ethanol (30, 50, 70, 90, 2×x100%, 20 min each), and dried with HMDS. Samples were examined with Vega3 (Tescan) SEM, running at 20kV.

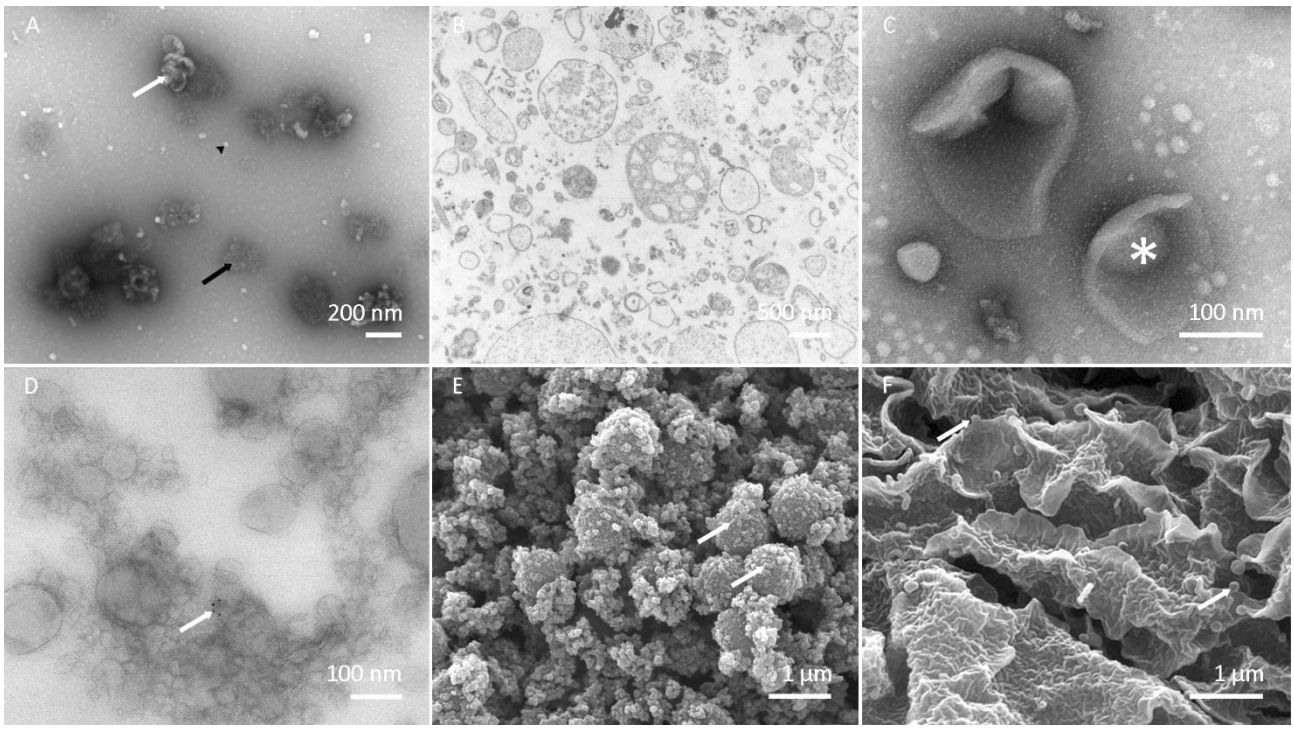

Figure 1. Extracellular vesicles (EVs) from *in vitro* and *in vivo* origins visualized with electron microscopy. A) EVs from human blood, negative staining. White arrow – EVs, black arrow – protein aggregates, arrowhead – lipoprotein particles. B) EVs from human embryonic kidney HEK293 cell line, Epon-embedded ultrathin section. C) EVs from yeast cell culture, negative staining. Asterisk – cup-shaped deformation of EV. D) EVs from human blood, immunolabelling of cryo-ultrathin section. Arrow – electron-dense gold particles marking position of membrane protein DGCR2. E) EVs from human blood on microbeads column, SEM. Arrows – position of EVs on 1 µm microbeads. F) EVs on supperficial cell of mouse urinary bladder epithelium *in vivo*. Arrows – budding of EVs from the plasma membrane.

3. Results. TEM analysis showed that EVs samples contained exosomes and frequently protein aggregates and lipoprotein particles (Fig.1A). Regardless of the isolation protocol being used the

diameter of EVs was ranging from 30 nm to several 100 nm (Fig.1B). EVs prepared with the method of negative staining were seen as cup-shaped spheres (Fig. 1C); cup-shaped deformation was more evident on larger EVs. Using cryo-methods, the expected spherical shape of EVs was better preserved (Fig. 1D). Immunolabelling of cryo-ultrathin sections by modified Tokuyasu method verified to be appropriate method to label cytosol proteins in the lumen of EVs (e.g. signal protein of immune response, MyD88) and EVs' membrane proteins (e.g. exosomal marker CD63) [8, 9]. Method of SEM enabled visualization of EVs being entrapped and purified by microbeads columns (Fig. 1E). SEM also enabled detection of EVs budding from plasma membranes of epithelial tissues *in vivo* (Fig. 1F).

4. Discussion and conclusions. For characterization of EVs it is crucial to complementary combine biochemical and electron microscopy methods. Our work shows that established protocols of selective EVs isolation have their weaknesses, in particular in the purity and heterogeneity of the samples. Without methods of electron microscopy, important conclusions on EVs could be misleadingly attributed to the wrong type- or mixture of different EVs. Additionally, classical and advanced methods of electron microscopy can be adapted to control the quality of EVs isolation steps and further characterize ultrastructure and molecular characteristics of EVs. We strongly agree with the recommendation of International society for EVs, that electron microscopy should be a method of choice when working with these clinically perspective vesicles [10].

References

[1] G. van Niel, G. D'Angelo, and G. Raposo, Nat Rev Mol Cell Biol, 19(4) (2018) 213-228
[2] P.D. Stahl, G. Raposo, Essays Biochem, 62(2) (2018) 119-124
[3] N. Kosaka, A. Kogure, T. Yamamoto, et al., Exp Mol Med, 51(3) (2019) 31
[4] L. Han, E.W. Lam, Y. Sun, Mol Cancer, 18(1) (2019) 59
[5] J. Clancy, C. D'Souza-Schorey, Cancer J, 24(2) (2018) 65-69
[6] M. Colombo, G. Raposo, C. Thery, Annu Rev Cell Dev Biol, 30 (2014) 255-89
[7] C. Campanella, C. Caruso Bavisotto, M. Logozzi, et al., Int J Mol Sci, 20(2) (2019)
[8] D. Lainscek, L. Kadunc, M.M. Keber, et al., ACS Synth Biol, 7(12) (2018) 2715-2725
[9] M. Mancek-Keber, D. Lainscek, M. Bencina, et al., Blood, 131(15) (2018) 1720-1729
[10] C. Thery, K.W. Witwer, E. Aikawa, et al., J Extracell Vesicles, 7(1) (2018) 1535750

Electron microscopy as a helpful tool for virus vaccine development against PRRSV2

SUSANNE RICHTER[1], TATJANA SATTLER[1,2], JASMIN FERTEY[3], BORIS HARTMANN[1], ADI STEINRIGL[1], VISKAM WIJEWARDANA[4], RICHARD KANGETHE[4], GIOVANNI CATTOLI[4], SEBASTIAN ULBERT[3], FRIEDRICH SCHMOLL[1]

[1] Inst. for Veterinary Disease Control Mödling, AGES, Mödling, Austria; [2] University of Leipzig, Clinic for Ruminants and Swine, Leipzig, Germany; [3] Fraunhofer Institute for Cell Therapy and Immunology, Leipzig, Germany; [4] International Atomic Energy Agency, Vienna, , Austria

1. Introduction

Porcine reproductive and respiratory syndrome (PRRS), a huge economic concern to the global pig industry, continues to be one of the most devastating diseases of swine throughout the world. The disease is caused by an enveloped RNA-virus, the PRRS virus (PRRSV), which is classified as Arterivirus, family Arteriviridae, order Nidovirales, genus Proarterivirus. The virus is macrophage-tropic in vivo, and replicates in MARC-145 cells, a PRRSV-permissive monkey kidney cell line in vitro. PRRSV causes widespread infections which until now are largely uncontrolled. Vaccination against PRRSV still remains unsatisfactory regarding efficacy and safety.

Inactivated vaccines offer some advantages compared to other types of vaccines (e.g. live-attenuated, vectored vaccines), including lack of ability to revert to a virulent state. Several methods exist for producing inactivated vaccines, e.g. a) virus inactivation with formaldehyde, a chemical that affects protein structures or b) the application of irradiation, which is said to have less effects on protein structures compared to formaldehyde, and instead alter nucleic acids in the virion. The effect of two different types of irradiation on virus structure of a highly pathogenic PRRSV2 (HP PRRSV2) field strain was examined by electron microscopy. In-vitro antigenicity and inactivation of the virus have also been proven.

2. Material and Methods

An HP PRRSV2 field strain, cultured in MARC 145 cells and concentrated by ultracentrifugation, was treated with low energy electron irradiation (LEEI) or ɣ-irradiation (with and without trehalose as stabilizer) at a dosage of 30kGry. Virus inactivation and virus antigenicity was tested before electron microscopic analysis of virus structure. Innocuity testing by three passages in cell culture demonstrated the successful inactivation of the virus. The viral load of both control and irradiated virus suspensions was determined by PCR. The in-vitro antigenicity was measured by an in-house ELISA by coating wells of a microtiter plate with live and the irradiated viruses, respectively and testing them with known antibody positive serum samples and known negative samples.

For electron microscopy the ultracentrifuged virus suspensions of PRRSV2 - a) a sample irradiated by LEEI, b) a sample irradiated by ɣ-irradiation as well as c) the control sample - were fixed in Karnovsky solution (2,5% FA & 2,5% GA). The preparation method of “negative staining” was performed to carry out quantitative and qualitative analysis of virus particles. For analyses, the grids were examined in a transmission electron microscope (Zeiss 906) operated at 80kV. Images were recorded at a resolution of 60 000x. Pictures from virus particles were selected using a systematic sample strategy in which 30 grid hexagons of each suspension sample were chosen randomly by lining up intact hexagons of the two grids from left downwards to right upwards. One square picture (689,2nm x 517,8nm) per grid hexagon was selected to be examined; in total

30 pictures per virus suspension samples were used for analysis. Analysis was performed with an automatic image analyses software (ITEM, Olympus). The mean diameter of undestroyed virus particles of each virus suspension was estimated for confirmation that intact virus particles were not damaged by irradiation. Virus particles on each sample picture were counted and classified in three groups: Group I intact, undestroyed virus particles with round morphology, intact lipid envelope; Group II deformed virus particles with intact lipid envelope; Group III partial ruptured virus particles with destroyed lipid envelope or particle remnants. The stereological counting rules were respected [1].

3. Results

After ultracentrifugation, the $TCID_{50}$ of the live HP PRRSV2 was 1E-6.75. A viral load of 6.6E+10 was measured. After irradiation, the viral load was 1.4E+10 and 1.1E+10 in ɣ-irradiated virus (+ trehalose) and 8.8E+9 in LEEI virus. In the ELISA, OD values in positive pig samples were above 1.5 and did not differ substantially between non-irradiated and irradiated virus wells. In negative serum samples, OD values stayed beneath 0.3.

By negative staining, purified, aldehyde-fixed intact virus particles of irradiated and non-irradiated virus suspensions appear as roughly spherical to somewhat oval particles with a mean diameter of about 54nm (Figure 2).

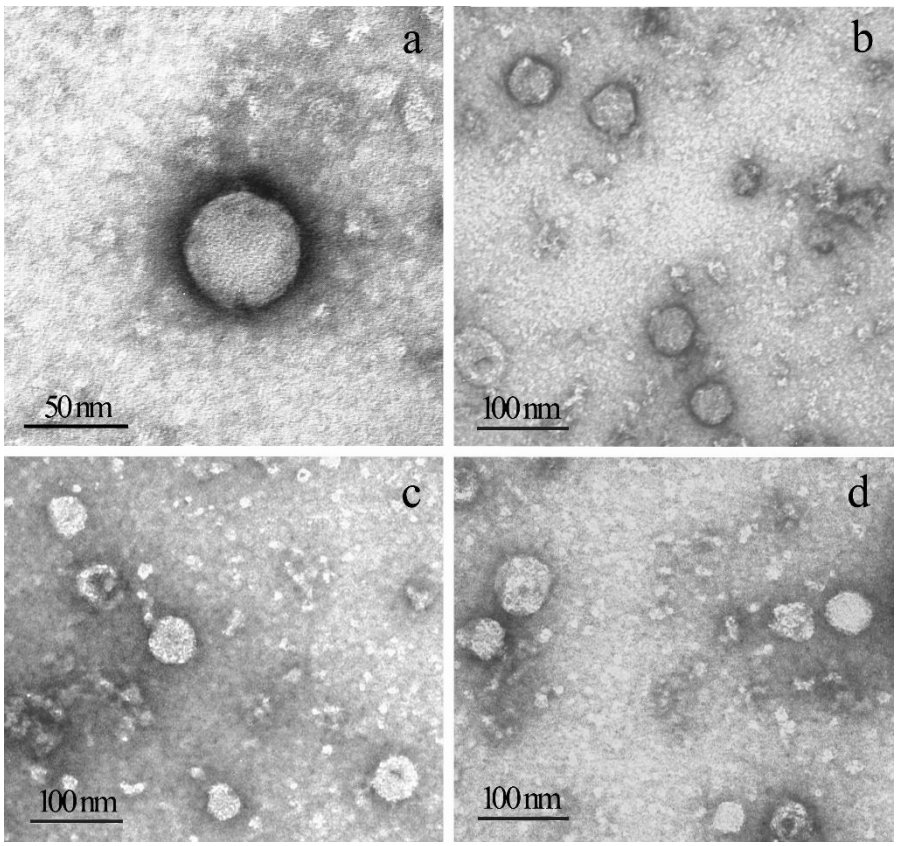

Figure 1. HP PRRSV2: a-b) intact virus – control group, c) virus - LEEI, d) virus – ϒ-irradiated

The mean diameter of intact virus particles of control and irradiated virus suspension samples concurs with the published data of negative stained PRRSV-particles [2]. The particles display a

mostly featureless surface, but sometimes a few protrusions can be observed (Figure 1). No internal structures are discernible in intact undestroyed particles because of the inability of the stain to penetrate through the lipid envelope. However, in partially ruptured, destroyed particles, the lipid bilayer and the core inside is discernible. The amount of ruptured virus particles or virus remnants is higher in irradiated PRRSV-samples; in the control sample there are twice as many intact particles (63%) as in the irradiated samples (38-29%); the amount of intact particles in the e-beam irradiate and ɣ-irradiated samples differs only slightly (Table 1). Intact virions of irradiated suspensions had a uniform viral envelope; neither damaged nor intact particles clumped together.

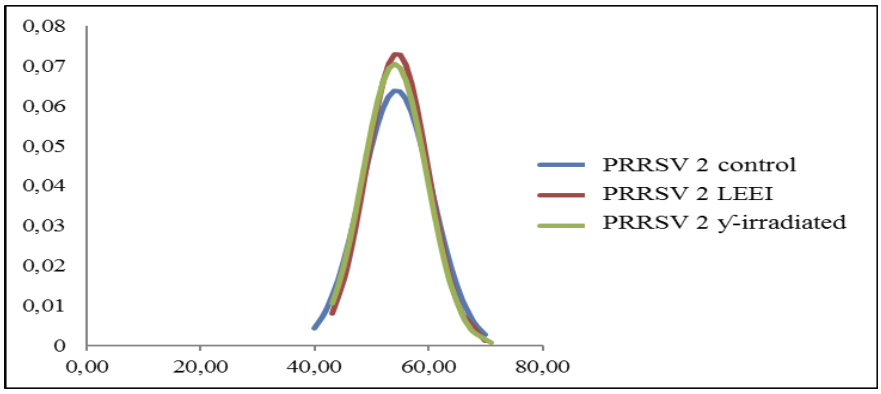

Figure 2. Nominal distribution of undestroyed particle diameters in irradiated and non-irradiated virus suspensions

Table 1. Group I virus particles: intact, undestroyed virus particles with round morphology, intact lipid envelope; Group II virus particles: deformed virus particles with intact lipid envelope; Group III virus particles: particle remnants or partial ruptured virus particles with destroyed lipid envelope

PRRSV2 sample	Virus particles counted	Group I particles	Group II particles	Group III particles
Non-irradiated (control)	915	63.5%	15.8%	20.7%
LEEI irradiated, 30 kGry	860	38.6%	19.1%	42.3%
ɣ-irradiated, 30kGry	1108	29.2%	18.5%	51.3%

4. Discussion and Conclusion

Radiation sterilisation has been used to develop a variety of vaccine types, because it can eradicate chemical contaminants and penetrate pathogens to destroy nucleic acids conserving most of the antigenic structures. In particular, the inactivation of virus with low energy electron irradiation (LEEI) for vaccine production is considered to be fast, safe and effective - with 80% conservation of antigens [3,4]. Both ɣ-irradiation as well as LEEI, were able to safely inactivate the tested HP PRRSV2 strain. The in-vitro antigenicity, the virus structure as well as the viral load of the irradiated viruses were comparable to the intact control virus. As shown by Feng et al. 2011 [5], the number of intact virus particles in irradiated virus suspensions was significantly reduced. Contrary to the study with vesicular stomatitis virus and murine norovirus, intact particles of irradiated virus suspensions retained their virus structure but not their RNA structure. In this study the inactivation of the PRRS virus resulted in no damage to the whole virus structure.

5. References:

[1] M. Oberholzer, Morphometrie in der klinischen Pathologie (1983), Springer Verlag, Berlin, ISBN-13:978-3-642-69102-7
[2] M.S. Spilman, C. Welbon, E. Nelson, T. Dokland, J Gen Virol 90 (2009) 527-535
[3] A.J. Hume, J. Ames, L.J. Rennick, W.P. Duprex, A. Marzi, J. Tonkiss, E. Mühlberger, Viruses 8 (2016) 204-2014, doi:10.3390/v8070204
[4] J. Fertey, L. Bayer, T. Grunwald, A. Pohl, J. Beckmann, G. Gotzmann, J.P. Casado, J. Schönfelder, F.-H. Rögner, C. Wetzel, M. Thoma, S.M. Bailer, E. Hiller, S. Rupp, S. Ulbert, Viruses 8 (2016) 319-330, doi:10.3390/v8110319
[5] K. Feng, E. Divers, Y. Ma, J. Li, Appl. Environ. Microbiol. 77 (2011) 3507-3517

Resveratrol recovers beta cell mass, islet morphology and apoptosis in fructose-fed streptozotocin induced rodent diabetes

FATMA KAYA DAGISTANLI[1], AYŞE SEDA AKDEMIR[1], MERVE ANAPALI[2], TURGUT ULUTIN[1], MELEK OZTURK[1]

[1] Istanbul University-Cerrahpasa, Cerrahpasa Faculty of Medicine, Medical Biology Department, İstanbul, Turkey; [2] Atatürk University, Faculty of Medicine, Medical Biology Department, Erzurum, Turkey

Diabetes Mellitus (DM) is a metabolic disease characterized by chronic hyperglycemia associated with impaired carbohydrate, lipid and protein metabolism. There are several experimental animal models in the investigation of diabetic complications and the development of a new treatment strategy. We used our modified version of a new model of Type 2 diabetes (T2DM) [1] induced by high fructose diet and low-dose streptozotocin (STZ) to rats. In our modified model, single dose of 40 mg / kg STZ injected after 10% fructose diet for 2 weeks, then continued the 10% fructose diet for 3 weeks. At the end of the 5th week, we started treatment. The aim of our model is search for the damages caused by fructose-rich diet continued after the development of diabetes and the possible recovery with treatment. Resveratrol is a natural, biologically active polyphenol with anti-diabetic and anti-inflammatory properties that maintain blood homeostasis and protects pancreatic β cells by reducing blood glucose levels [2]. In this study, we researched that effect of resveratrol treatment on pancreatic cell mass, islets organization and apoptosis in the fructose-fed STZ induced T2DM model.

In this study, 8-week-old male Sprague-Dawley rats were randomly subdivided into 4 groups of 7 animals in each group. The first group was diabetic group. Second group consisted of diabetic rats treated with 1 mg/kg/day resveratrol (i.p.) for 4 weeks. Third group consisted of nondiabetic rats treated with 1 mg/kg/day resveratrol for 4 weeks. The fourth group was control rats. At the end of 9 weeks rats were sacrificed and pancreas tissues were taken with ketamin/ksilazin anesthesia. Body weight and blood glucose levels of all rats were measured. The pancreatic tissue sections were immunostained with insulin, glucagon, somatostatin, and active caspase-3 antibodies. TUNEL assay was used for detection of apoptosis. All values were analyzed with statistical methods.

Blood glucose levels were significantly increased in untreated diabetic group compared with the other group. Blood glucose levels of resveratrol treated diabetic group were significantly lower than the diabetic group at the end of the experiment. When the islets in the diabetic group were compared with other groups, we found islets were small and number of the insulin positive cells were low ($p < 0.001$). In the resveratrol treated diabetic group, some islets were filled with beta cells, while some islets contained fewer beta cells as such in the diabetic group (Figure 1). Glucagon and somatostatin cells, which are cells placed in the islet periphery under normal conditions, spread towards the islet center in diabetic group (Figure 1), also somatostatin producing cells are found to be hypertrophic.

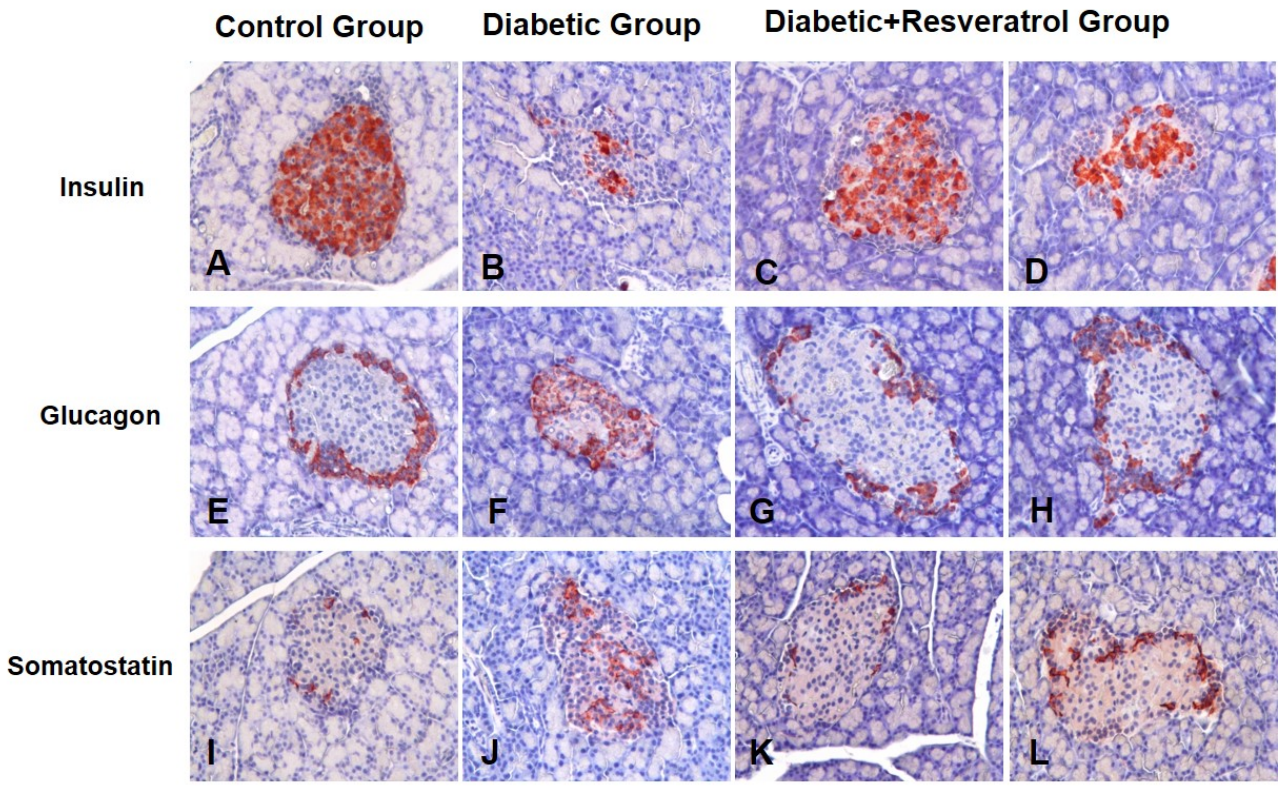

Figure 1: Immunolocalization of insulin, glucagon somatostatin in the pancreas of the control, diabetic and diabetic +resveratrol groups. Immunostaining: Streptavidin-biotin peroxidase method. Magnifications: 200x.

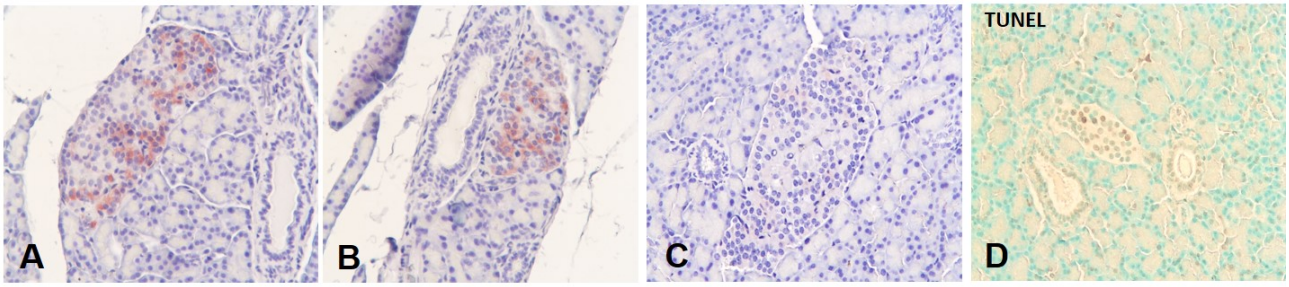

Figure 2: Immunolocalization of active caspase-3 and TUNEL in the pancreas for (A, B, D) Diabetic and (C) Diabetic+Resveratrol groups. Immunostaining: Streptavidin-biotin peroxidase (A, B, C) and TUNEL method. Magnifications: 200x.

In addition, both glucagon and somatostatin cell numbers were found to be increased in the diabetic group compared to other groups. In the islets, we found that the active caspase-3 positive and TUNEL-labeled apoptotic cells were also increased in the diabetic group (Figure 2). While there were only a few weak active caspase-3 positive cells in the islets of resveratrol treated diabetic group, no apoptic cells were detected. However, in the diabetic group, we found that there are a number of labelled apoptotic cells both in the exogenous tissue and islets.

As a result, this modified diabetes model and fructose diet after diabetes have caused beta cell loss and apoptosis of both endocrine and exocrine pancreatic cells. We suggest that resveratrol treatment improves glucose homeostasis, stimulates the increase of beta cell mass and inhibits apoptotic cell

death, and that it will bring a new perspective to treatment because of this positive effect in excessive degenerations caused by fructose in diabetics.

References

[1].R. D. Wilson, & M. S. Islam, Pharmacological Reports, 64 (2012) 129-139.

[2].T. Szkudelski, K. Szkudelska, Biochim Biophys Acta 1852 (2015) 1145–54.

Various microscopic techniques for tracing cancer urothelial cells in mouse bladder tumor model

ANDREJA ERMAN[a], GREGOR KAPUN[b], SARA NOVAK[c], MOJCA PAVLIN[d,e], GORAN DRAŽIĆ[b], DAMJANA DROBNE[c], PETER VERANIČ[a]

[a] Institute of Cell Biology, Faculty of Medicine, University of Ljubljana, Ljubljana, Slovenia; [b] National Institute of Chemistry, Ljubljana, Slovenia; [c] Department of Biology, Biotechnical faculty, University of Ljubljana, Slovenia; [d] Group for nano and biotechnological applications, Faculty of Electrical Engineering, University of Ljubljana, Ljubljana, Slovenia; [e] Institute of Biophysics, Faculty of Medicine, University of Ljubljana, Ljubljana, Slovenia

Mouse tumor models are widely used to elucidate mechanisms of tumor development and explore new therapeutic approaches for bladder cancer [1, 2]. We established an orthotopic mouse bladder tumor model to study early stages of implantation of cancerous urothelial MB49 cells *in vivo*, which have been overlooked until now. To explore initial interactions between cancerous and normal urothelial cells *in vivo*, the characteristics of both cell types should be recognized and a reliable method for discrimination of both cell types is required. Despite the frequent use of MB49 cells in establishing orthotopic bladder tumors, these cells have been poorly characterized at the molecular level until now [3].

Our main challenge was how to trace injected MB49 cells in the mouse urinary bladder and how to distinguish them from normal urothelial cells. We thus performed extensive molecular characterization of MB49 cells *in vitro* before experiments *in vivo*. To solve the problem of unequivocal discrimination of cancer cells from normal urothelial cells *in vivo*, we used various labeling and microscopic techniques (Figure 1). Furthermore, internalized cobalt ferrite ($CoFe_2O_4$) nanoparticles in cancer cells enabled us to find and identify them by different types of electron microscopy such as back-scattered electron microscopy (BS-SEM) and Focused Ion Beam Scanning Electron Microscopy (FIB-SEM) with energy-dispersive X-ray (EDX) detector to confirm the presence of Co and Fe in cancer cells.

With new approach by using endocytosed metal nanoparticles as a marker of cancer cells, we were able to trace them *in vivo*. We found that cancer cells attach to the urothelium or exposed basal lamina within just one hour of intravesical injection, whereas small tumors and localized hyperplastic urothelial regions develop already within two days. We also showed that cancer cells initially adhere to normal urothelial cells through filopodia and by focal contacts with exposed basal lamina.

Orthotopic mouse bladder model is as an appropriate model for the examination of the very first events of cancer cell attachment, which are the most crucial stages of tumor development. By combination of *in vitro* and *in vivo* studies, various types of electron microscopy and interdisciplinary approaches we obtained new data about the fate of injected cancer cells and poorly known early events of tumorigenesis in the urinary bladder.

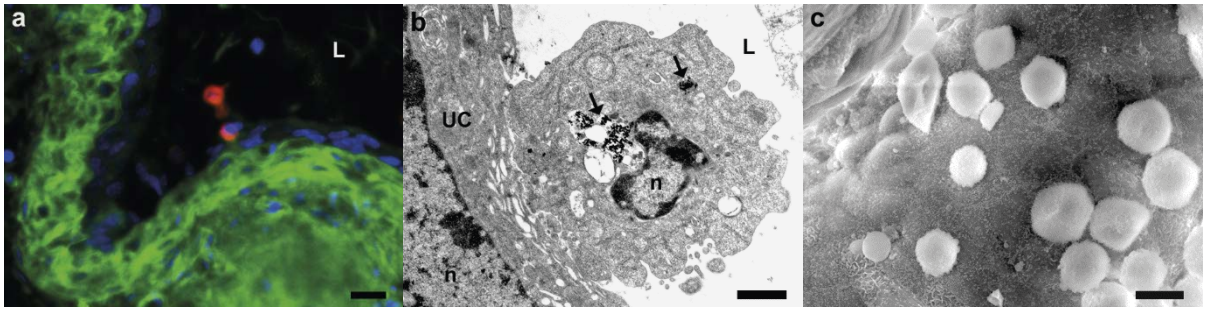

Figure 1. Adhered MB49 cells on the epithelium of the mouse urinary bladder within 2 days of intravesical injection. (a) Fluorescence micrograph of DiI-labeled and vimentin-positive cancer urothelial cells (orange fluorescence due to merged red fluorescence of DiI and green fluorescence of vimentin). Nuclei are stained with DAPI (blue fluorescence). (b) TEM micrograph of MB49 cell with endocytosed $CoFe_2O_4$ nanoparticles (arrows) in close contact with urothelial cell (UC). n-nucleus, L-lumen of the urinary bladder. (c) SEM micrograph of the region with numerous cells attached to the urothelium. Scale bars: 20 µm (a), 2 µm (b), 10 µm (c).

References

[1] N. Zhang, D. Li, J. Shao, X. Wang, Oncol Lett, 9 (2015) 1515-1519
[2] DS. Yu, C.F. Lee, S.Y. Chang, J Urol, 177 (2007) 738-742
[3] V.T. Fabris, C. Lodillinsky, M.B. Pampena, D. Belgorosky, C. Lanari, A.M. Eijan, Cancer Genet, 205 (2012) 168-176

Melatonin fails to protect cardiac mitochondria in Sirtuin 1 heterozygous mice placed on a high fat diet

ALESSANDRA STACCHIOTTI[1,2], RAQUEL GARCIA-GOMEZ[3], ANTONIO LAVAZZA[4], MARIA MONSALVE[3] AND RITA REZZANI[1,2]

[1] Department of Clinical and Experimental Sciences, Brescia University, Brescia, Italy; [2] Interdepartmental University Center of Research "Adaptation and Regeneration of Tissues and Organs (ARTO)", Brescia University, Italy; [3] Instituto de Investigaciones Biomedicas "Alberto Sols" (CSIC-UAM), Madrid, Spain; [4] Istituto Zooprofilattico Sperimentale, Brescia, Italy

Obesity is a worldwide epidemic status deeply associated to cardiovascular diseases [1]. Mitochondria provide most of the energy to terminally differentiated cardiomyocytes, so heart failure is considered a "bioenergetic affair" [2]. Silent information regulator 1 (SIRT1), the most studied isoform of NAD^+-dependent histone deacetylase enzymes, plays a crucial role to modulate energy metabolism in aging and diseases [3]. Melatonin, the nighttime pineal indole, is a strong anti-oxidant able to ameliorate mitochondrial shape and function in the heart of leptin-deficient genetically obese mice [4].
Male C57BL6/J mice (WT) and SIRT1 heterozygous (HET) mice were placed on a standard maintenance rodent diet (STD-8.4% kcal from lipids) or a high fat diet (HFD- 58.4% kcal from lard) for 16 weeks starting from 12 to 28 weeks of age, drinking or not melatonin (10 mg/kg). Light microscopy and transmission electron microscopy on cardiomyocytes and inter-myofibrillar and sub-sarcolemmal mitochondria have been carried out.

The present study aims to demonstrate (i) if oral melatonin in the diet improves adverse cardiac mitochondrial changes triggered by an obesogenic high-fat diet in mice and (ii) if reduced SIRT1 availability in heterozygous mice (HET) influences melatonin efficacy under the same dietary regimen.

No differences were observed in the heart of WT STD and HET STD mice drinking or nor melatonin. Conversely, in WT HFD mice heart, sustained lipid peroxidation and mitochondrial adaptation markers, like 4HNE, mitofusin 2 and HSP60 were significantly reduced by melatonin (**Figure 1 A)**. Interestingly, melatonin was ineffective in HET HFD heart that presented focal HSP60 positivity (**Figure 1B)**. Furthermore, to investigate whether the mechanism of action of melatonin might involve ER stress and autophagy in our model, we analyse the distribution of GRP78, the master ER chaperone, CHOP, a proapoptotic index regulated by energy status and p62/SQSTM1, a marker of impaired autophagy flux.

ER stress response and CHOP nuclear immunostaining have been observed in cardiomyocytes in WT HFD mice and was alleviated by melatonin (**Figure 1C**). Interestingly, CHOP signal persisted in HET HFD heart despite melatonin (**Figure 1D**). Remarkably, p62/SQSTM1 signal intense in cardiomyocytes in WT HFD mice, decreased in WT HFD mice drinking melatonin, but was barely expressed in HET mice.

All these data suggest that melatonin improves cardiac mitochondria in anabolic conditions triggered by high calorie lard-based diet in mice but only in presence of full availability of sirtuin 1. Nevertheless, further biochemical and molecular studies are needed to best clarify their strict interdependence, so opening new avenues to melatonin supplementation in clinical trials.

Thanks to FLAMMA S.p.A., Chignolo d'Isola, BG, Italy (http://www.flammagroup.com) for courteously providing melatonin (MelaPure™).

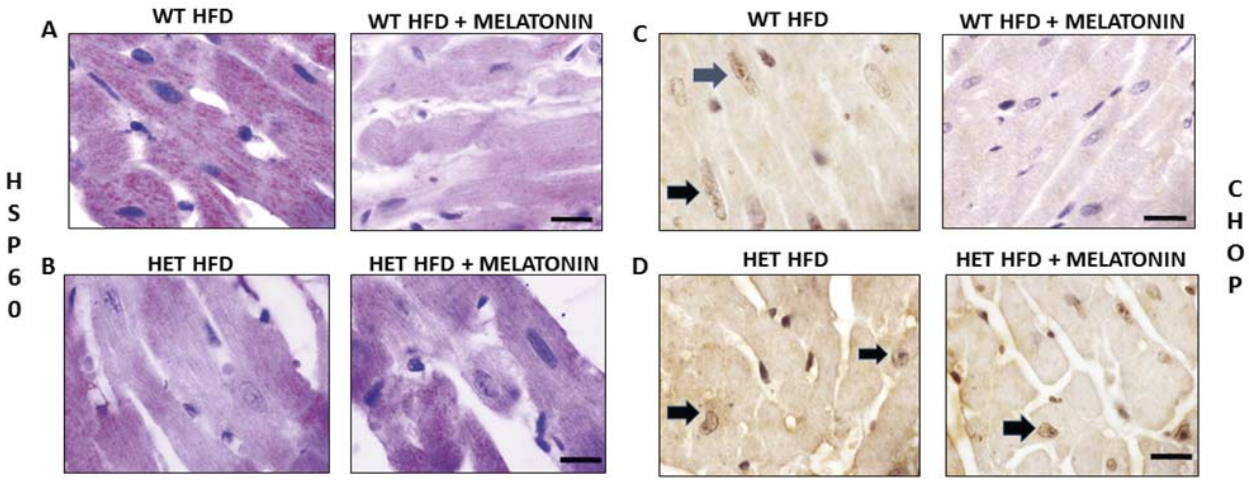

Figure 1. **HSP60** immunostaining developed by ABC-peroxidase in the heart. **A)** WT mice placed on HFD presented reduced brown signal by drinking melatonin and **B)** HET mice fed an obesogenic diet were unresponsive to oral melatonin for 16 weeks**. CHOP** immunostaining in obesogenic diet challenged mice heart. **C)** WT HFD mice showed nuclear positivity in cardiomyocytes that disappeared drinking melatonin and **D**) HET HFD mice showed brown nuclei in cardiomyocytes despite melatonin. Arrow-Nuclear positivity. Bar= 5µm.

References

[1] A.de Mello, A.Costa, J. Della Giustina Engel, G.Tezza Rezin, Life Sciences 192 (2018) 26-32
[2] F.Tahrir, D.Langford, S.Amini, T.Ahooyi, K.Khalili, J. Cell Physiol. 234 (2019) 8122-8133
[3] A.Kane, D.Sinclair, Circ.Res. 123 (2018) 868-885
[4] A.Stacchiotti, G.Favero, L. Giugno, I.Golic, A.Korac, R.Rezzani, Nutrients 9 (2017) 1323

The Effect Of Seeding In Programmed Slow Freezing Of Immature Testicular

GÜLNAZ KERVANCIOĞLU[1], ELIF KERVANCIOĞLU DEMIRCI[2] AND ŞULE ÇETINEL[3]

[1] Istanbul Aydın University, Faculty of Medicine, Department of Histology and Embryology; [2] İstanbul University, Istanbul Faculty of Medicine, Department of Histology and Embryology; [3] Marmara University, School of Medicine, Department of Histology and Embryology

Introduction: Fertility preservation in male children who will have cancer treatment is important in improving the quality of life after treatment. Cryopreservation is the only known option for long-term storage of these tissues. However, there is no standardized cryopreservation method yet for immature testicular tissue. In this study, the effect of seeding was investigated in the programmed slow freezing method to develop the most appropriate method for cryopreservation of testicular tissues. Thus, it was aimed to control the formation of ice crystals which can cause cell damage.

Materials and methods: Two groups were planned of the testicular tissues of 7 to 8-day-old male Wistar rats (n = 5) with and without seeding. Tissues were frozen with programmed slow freezing. High security straw was used as the carrier. Seeding was applied at the time of freezing with the help of a forceps cooled at -7°C. The freeze-thaw effects were quantitatively evaluated in light and transmission electron microscopy. Viability test was applied.

Results: The results were in the group with seeding and in the group without seeding: intratubular nucleus discrimination (%58.8+/-14.4), (%47.2+/-11.5); pyknotic nucleus ratio (%29.6+/-13.5), (%40.8+/-9.9); basal membrane decomposition (%13.0+/-9.1), (%14.6+/-13.0); tubuli without cytoplasmic degeneration (%10.4+/-8.0), (%5.2+/-4.3) and vitality rate (%46.8+/-15.3), (%30.2+/-7.7); respectively. There was no statistically significant difference between the groups but there was a tendency of decreasing in cell damage in the seeding group observed by light and by transmission electron microscopy (figures 1 and 2). The application of seeding can be preferred for freezing of immature testicular tissue with slow freezing because of the diminished ice crystal formation and therefore reduced cell damage.

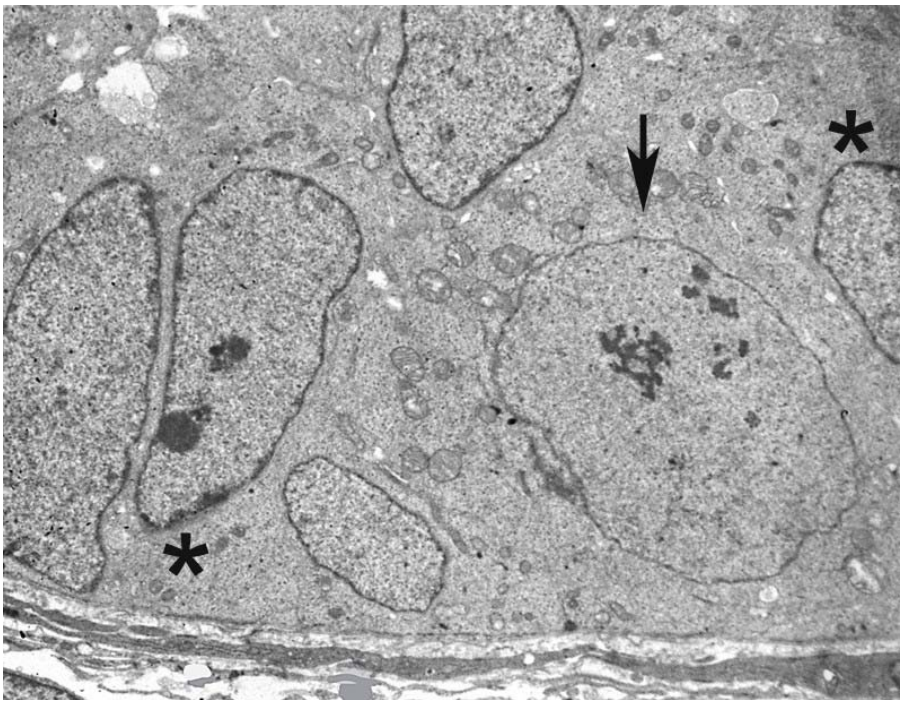

Figure 1. TEM micrograph of 8 days old control testicular tissue. Spermatogonium (arrow). Sertoli cells (asterisks) X5000 magnification.

Figure 2. TEM micrograph of testicular tissue with seeding. Spermatogonium (arrow), Sertoli sells (asterisks) X5000 magnification.

The effects of Trifolium pratense L. on the expression of leukemia inhibitory factor in the Ishikawa cell line

EMEL USTA[1], SIBEL DOĞAN[1], HAVVA ATAR[2], HATICE ÇÖLGEÇEN[2], GAMZE TANRIVERDI[3], FERIDE ÖZDEMIR[1], SIBEL KÖKTÜRK[1]

[1] Department of Histology and Embryology, Istanbul University, Istanbul Medical Faculty, Istanbul, Turkey; [2] Department of Biology, Zonguldak Karaelmas University, Faculty of Arts and Science, Zonguldak,Turkey; [3] Department of Histology and Embriology, Cerrahpasa Medical Faculty, Istanbul University-Cerrahpasa, Istanbul, Turkey

Abstract

Introduction and Aims: Leukemia inhibitory factor (LIF), a major cytokine regulating endometrial receptivity (1). The LIF plays an important role in reproduction by regulating immune response, decidualization, and implantation (2). In humans, maximal LIF secretion by the endometrium coincides with the window of implantation (3). The LIF expression deficiency has been shown to be involved in multiple implantations failures in patients with female infertility (4). Therefore, research has focused on developing novel candidates that stimulate embryo implantation rates by enhancing LIF expression, especially by using natural herbal medicines. To solve the problem of embryo implantation, it is crucial to enhance endometrial receptivity toward a properly developed embryo (5).

The isoflavones in Trifolium pratense L. has been reported to display estrogenic as well as cancer chemopreventive properties (6). Trifolium pratense contains the estrogenic isoflavones, daidzein, formononetin, biochanin A, and genistein (7). The Ishikawa endometrial cancer cell line widely used in reproductive biology research (8). We investigated Trifolium pratense L.-induced effects on the expression of LIF in human endometrial cell line (Ishikawa cells).

Methods: The regeneration of natural tetraploid Trifolium pratense L., originated from Erzurum-Turkey, is used in this study (9). The endometrial epithelial cell lines were cultured for 24 hours in a Dulbecco′s modified Eagle′s medium-F12 with 10% FBS cell culture medium containing Trifolium pratense L. extracts (Elçi red clover) (20, 30, 40 µM/ml).

Results: The LIF staining density was significantly increased by Trifolium pratense L. treatment in the Ishikawa cell line. In the Ishikawa cell line treatment the Trifolium pratense L. showed cell morphology including a large nucleus and vacuoles in the cytoplasm, indicating great metabolic activity.

Conclusions: We found that Trifolium pratense L. increases LIF level in cultured Ishikawa cell line. Thus, Trifolium pratense L. could include the regulation of LIF to be fundamental to endometrial receptivity during implantation. We will be also investigated whether Trifolium pratense L. is effects to leukemia inhibitory factor receptor (LIF-R). In view of the presented data and the reported studies design experimental research and clinical trials are required.

References

[1] E.Y. Kim, H.J. Choi, T.W. Chung, J.Y. Choi, H.S. Kim, Y.S. Jung, S.O. Lee, K.T. Ha, Journal of pharmacological sciences 131 (2016) 259-266.
[2] I. Yoo, S. Chae, J. Han, S. Lee, H.J. Kim, H. Ka, Asian-Australasian journal of animal sciences 32 (2019) 192-200.
[3] D.B. Chen, R. Hilsenrath, Z.M. Yang, S.P. Le, S.R. Kim, C.J. Chuong, A.N. Poindexter, 3rd, M.J. Harper, Human reproduction (Oxford, England) 10 (1995) 911-918.
[4] M. Wu, Y. Yin, M. Zhao, L. Hu, Q. Chen, Cytokine 62 (2013) 334-339.
[5] K. Diedrich, B.C. Fauser, P. Devroey, G. Griesinger, Human reproduction update 13 (2007) 365-377.
[6] N. Fokialakis, X. Alexi, N. Aligiannis, D. Siriani, A.K. Meligova, H. Pratsinis, S. Mitakou, M.N. Alexis, Bioorganic & medicinal chemistry 20 (2012) 2962-2970.
[7] J. Liu, J.E. Burdette, H. Xu, C. Gu, R.B. van Breemen, K.P. Bhat, N. Booth, A.I. Constantinou, J.M. Pezzuto, H.H. Fong, N.R. Farnsworth, J.L. Bolton, Journal of agricultural and food chemistry 49 (2001) 2472-2479.
[8] R.R. Gonzalez, B.R. Rueda, M.P. Ramos, R.D. Littell, S. Glasser, P.C. Leavis, Endocrinology 145 (2004) 3850-3857.
[9] H. Colgecen, M.C. Toker, Biological research 41 (2008) 25-31.

An innovative bioreactor for skin explants model

ENRICA CAPPELLOZZA, LAURA CALDERAN AND MANUELA MALATESTA
Department of Neurosciences, Biomedicine and Movement Sciences, University of Verona, Italy

1. Introduction

Skin is one of the major ways of communication between organism and environment and, as such, a possible route of administration for topical or transdermal drugs. Thanks to its organization in different layers, skin constitutes an excellent physical, immunological and sensory barrier, playing an important protective role against microbial attack, UV irradiation and chemicals of different types. It follows a crossing difficulty even for active compounds designed for therapeutic purpose. The currently available *in vitro* systems that try to mimic the cutaneous barrier are cell cultures, from conventional mono-layer cell cultures to more advanced three-dimensional co-cultures. They are widely accepted but certainly simplistic models compared to the real physiological structure and dynamic behavior of a living organism [1, 2]. The information gathered by tests on these *in vitro* models is therefore insufficient and *in vivo* experimentation still remains largely used, despite the 3Rs principles encourages a reduction and rationalization in the use of laboratory animals. The key challenge is therefore the development of an *in vitro* model able to be more predictive mimicking better the skin barrier, in order to fill the huge gap between *in vitro* and *in vivo* research. In this perspective, an innovative *in vitro* system for explanted skin testing has been developed by modifying a bioreactor for cell culture and has been evaluated for its ability to preserve skin samples in a fluid dynamic environment closer to the *in vivo* conditions.

2. Materials and methods

Skin samples explanted from the abdominal region of rats were immediately mounted in cell culture chambers of a bioreactor (IV-Tech S.r.l.), suitably modified to hold skin sample in tension to form an upper side (in contact with air) and a lower side (in contact with medium) (Figure 1). Culture medium, composed according to [3], was placed into a mixing chamber connected to a pump and to the lower chambers, joined in series, and a flow rate of 500 uL/min was applied. Skin samples were maintained under these conditions into the bioreactor, inside the cell incubator, for 3, 6, 12, and 24 hours. At the end of the incubation time, samples were processed to allow light and transmission electron microscopy. Sample sections for histological analysis were fixed with paraformaldehyde, embedded in paraffin wax, stained with Mayer's hematoxylin and eosin solution and observed with an Olympus BX51 microscope. Ultrathin sections of aldehyde-fixed, Epon embedded samples were stained with lead citrate and observed with a Philips Morgagni transmission electron microscope.

3. Results and discussion

At light microscopy no histological alterations were observed in the skin: the layers of the barrier are compact and sweat glands and hair bulbs appear well preserved up to 24 hours (Figure 2a). Ultrastructural observation confirmed the good preservation of cellular and extracellular components. The skin maintains its barrier features up to 24 hours, as demonstrated by the presence of numerous desmosomes between the plasma membranes of keratinocytes (Figure 2b). In the connective tissue collagen bundles are well organised (Figure 2c). These results prove that our fluid dynamic *in vitro* model can preserve skin samples for long time, getting closer to the physiological conditions compared to conventional cell cultures. Dynamic environment is fundamental not only for structural but also for functional preservation [4, 5]; in fact, it stimulates cell activity, ensuring intake of nutrients and removal of waste products along the entire thickness of the tissue. Another aspect to consider is the ethical value of this new *in vitro* system, that could contribute to the reduction in the use of experimental animals. In fact, from a single animal it is possible to obtain

various samples to test different drugs at different time-points. Furthermore, by mimicking better the physiological situation, our *in vitro* system is able to provide more predictive information essential for focused *in vivo* experimentation, thus resulting as an intermediate step between *in vitro* and *in vivo* research. Finally, our system can also be used on biopsies or surgical material from patients, reducing further, and maybe avoiding, tests on animals.

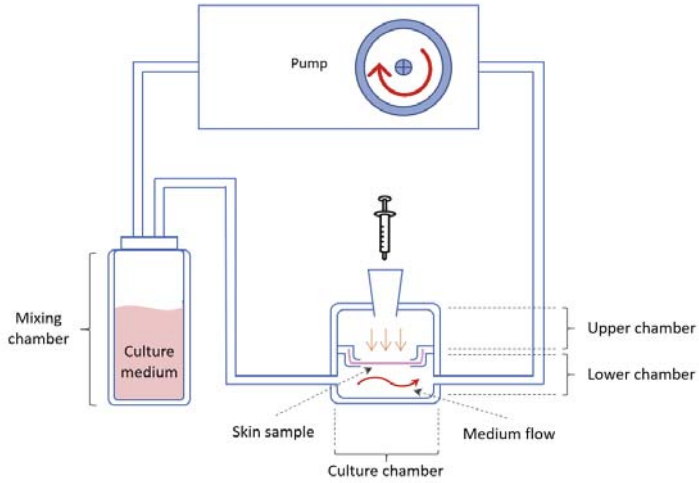

Figure 1. Explanatory scheme of the bioreactor.

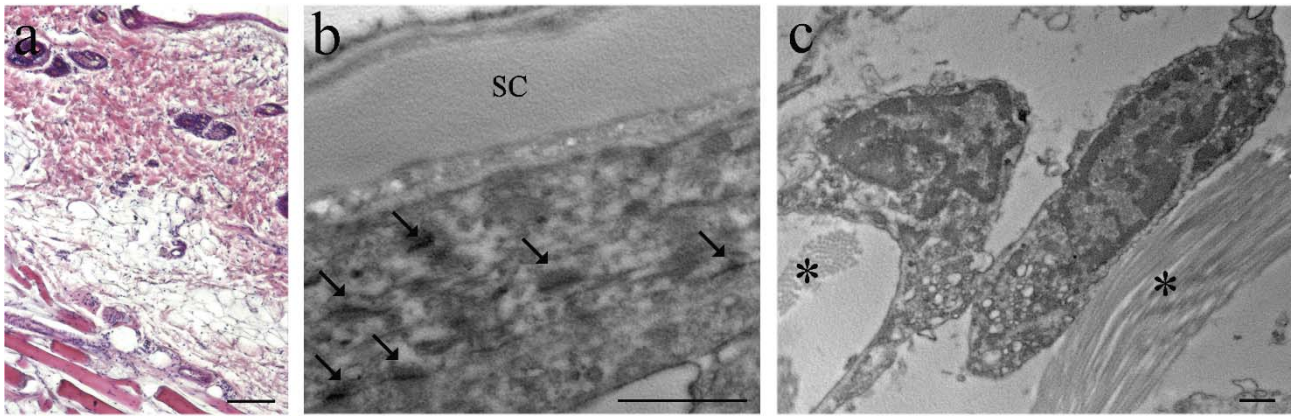

Figure 2. Skin samples after 24 hours in the bioreactor. Light microscopy of hematoxylin-eosin stained skin section (a). TEM micrographs of epidermis (b) and dermis (c). Note the numerous desmosomes (arrows) between plasma membranes of keratinocytes. SC, stratum corneum; asterisks, collagen bundles. Bars: 200 µm (a); 1 µm (b, c).

Acknowledgment
We thank IV-Tech S.r.l. for providing us with the modified holder for the bioreactor.

References

[1] V. Planz, C.-M. Lehr, M. Windebergs, J. Con. Rel., 242 (2016) 89–104
[2] J. Hansmann, F. Groeber, A. Kahlig, C. Kleinhans, H. Walles, Biotechnol J, 8 (2013) 298–307
[3] L. Steinstraesser, M. Srokin, A. D. Ntederbichler, M. Becerikli, J. Stupka, A. Daigeler, M. R. Kesting, I. Stricker, F. Jacobsen, M. Schulte, Arch. Dermatol. Res., 302 (2010) 357-365
[4] F. Carton, L. Calderan, M. Malatesta, Eur. J. Histochem., 61 (2017) 2862

Investigation in the Effects of Exercise on the Testicular Morphology, Cell Proliferation and Blood Testis Barrier in the High Fat Diet-Induced Obesity

MERVE ACIKEL ELMAS[1], OZLEM BINGOL OZAKPINAR[2], MELTEM KOLGAZI[3], GOKSEL SENER[4], SERAP ARBAK[1], FERIHA ERCAN[5]

[1,5] Acibadem Mehmet Ali Aydinlar University Department of Histology and Embryology; [2] Marmara University School of Pharmacy, Deptartment of Biochemistry; [3] Acibadem Mehmet Ali Aydinlar University Department of Physiology; [4] Marmara University School of Pharmacy, Deptartment of Pharmacology; [5] Marmara University Department of Histology and Embryology

1. **Background and Aim:** Obese male population has been increased up 3 times in the last thirty years. The latest studies show that the obesity has negative affects on male fertility not only sperm quality but also physical and molecular structural defects in testis germ cells. Because of high fat diet consumption spermatogenic cycle in seminiferous epithelium is damaged by disruption of blood testis barrier integrity and which would be cause abnormal sperm production. Exercise could be defined as a rapid increase in energy consumption. The studies showed that exercise has a positive effect on sperm morphology, motility and function. However, the effects on blood testis barrier integrity, which played an important role in spermatogenesis, were not investigated. The aim of this study was to investigate the effects of execise on spermatogenic cell proliferation, blood testis barrier, inflammatory and oxidative markers and hormone levels in testes of high fat diet (HFD) induced obese rats.

2. **Materials and Methods:** Sprague Dawley male rats were fed with standard (STD group; 6% calories as fat) or HFD (HFD group; 45% calories as fat) for 18 weeks. Half of these animals were trained swimming exercise (STD+EXC and HFD+EXC groups; 1 hour a day, 5 days a week) for the last 6 weeks (Fig 1). Testis samples were evaluated by histological and ultrastructural methods. Cell proliferation, apoptosis and blood testis barrier was examined by histochemical methods. Lipid and hormone levels in blood serum and oxidative stress markers in tissue were examined by biochemically. All data were analyzed by statistically.

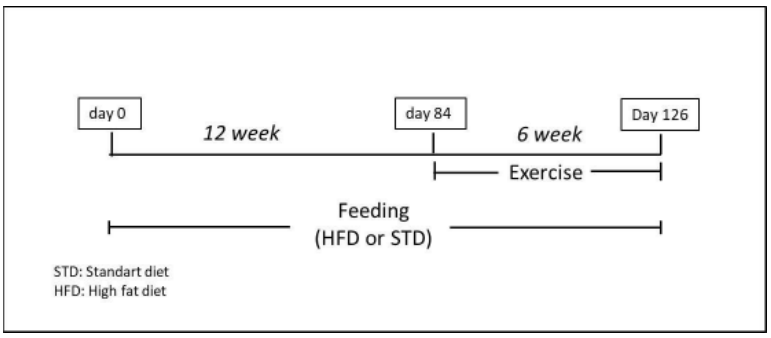

Figure 1. Experimental design

3. **Results:** Sertoli cells are affected by testosterone and FSH changes in HFD induced obesity. So Hypothalamus-pituitary-testis (HPT) axis could be unregulated and this situation which causes a change in signaling pathways that regulate the metabolism of Sertoli cells. A decrease in FSH and testosterone levels were observed in the HFD group while these hormone levels

were increased in HFD+EXC group. Damaged tubules and apoptotic cells were increased and dilated intercellular areas were seen in HFD group. The number of proliferative cells and Sertoli cell tight junction protein immunoreactivity (ir) of ZO-1, Occludin and gap junction protein ir of Cx 43 were decreased in the HFD group. In this group, serum total cholesterol and triglyceride level, tissue MDA level and MPO activity increased, GSH level and SOD activity were decreased. All these histological and biochemical findings were ameliorated in HFD+EXC group. It was observed that high fat diet caused degeneration of testis morphology, altered blood testis barrier integrity and increased oxidative damage.

4. **Conclusion:** It is thought that exercise prevented testicular damage by regulating hormonal balance and testicular functions, reducing inflammation, regulating oxidant/antioxidant and cell proliferation/apoptotic balance, and also preserving blood-testicular barrier integrity.

References

[1] Linden MA, Pincu Y, Martin SA, Woods JA, Baynard T (2014) Moderate exercise training provides modest protection against adipose tissue inflammatory gene expression in response to high-fat feeding. *Physiol Rep* 2

[2] MacDonald AA, Herbison GP, Showell M, Farquhar CM (2010) The impact of body mass index on semen parameters and reproductive hormones in human males: a systematic review with meta-analysis. *Hum Reprod Update* 16: 293-311

[3] Palmer NO, Bakos HW, Fullston T, Lane M (2012a) Impact of obesity on male fertility, sperm function and molecular composition. *Spermatogenesis* 2: 253-263

[4] Palmer NO, Bakos HW, Owens JA, Setchell BP, Lane M (2012b) Diet and exercise in an obese mouse fed a high-fat diet improve metabolic health and reverse perturbed sperm function. *Am J Physiol Endocrinol Metab* 302: E768-80

Prenatal dexamethasone treatment affects gonadotropic cells in adult male and female rats

NATAŠA NESTOROVIĆ, MILICA MANOJLOVIĆ-STOJANOSKI, NATAŠA RISTIĆ, SVETLANA TRIFUNOVIĆ, BRANKO FILIPOVIĆ, BRANKA ŠOŠIĆ-JURJEVIĆ, VERICA MILOŠEVIĆ
University of Belgrade, Institute for Biological Research "Siniša Stanković", Belgrade, Serbia

Developmental responses to environmental challenges during pregnancy may permanently alter fetal structure, physiology and/or metabolism. The responses to environmental challenges usually assist immediate fetal survival, but later in life these developmental changes are often shown to be disadvantageous. Link between adverse environmental signals during prenatal development and greater incidence of pathophysiological conditions in postnatal life, such as cardiovascular, metabolic and neuroendocrine disorders, is implied by concept of developmental programming. Adverse environmental conditions are usually signalled by increase of glucocorticoid levels, which results in fetal glucocorticoid overexpression. Hence, synthetic glucocorticoids such as dexamethasone (Dx), are used in numerous experimental protocols to induce developmental programming. Development of reproductive axis can also be affected by prenatal glucocorticoids, which may be associated with impaired reproductive function. Undisturbed functioning of pituitary gonadotropic cells that produce follicle-stimulating (FSH) and luteinizing hormone (LH), are essential for healthy reproduction. We have previously shown that prenatal Dx treatment evokes developmental programming of pitutary gonadotropic cells, which is apparent in neonatal, infantile and peripubertal females [1]. Wheather the changes of gonadotropic cells, caused by glucocorticoid overexposure in fetal period life, will persist till adulthood in female and male rats, is the aim of present study. To that end, relative intensity of fluorescence (RIF), as a measure of intracellular FSH and LH content, and the number of gonadotropic cells per mm^2 were determined.

Pregnant female Wistar rats subcutaneously received 0.5 mg Dx per kg/b.w. on 16th, 17th and 18th day of pregnancy. Control gravid females received the same volume of saline vehicle. Upon weaning, female and male offsprings were divided into four groups: control females (CF, n=6), control males (CM, n=6), and females (DxF, n=6) and males (DxM, n=6) prenatally exposed to Dx. Animals were sacrificed in adult period of life. Pituitary sections from dorsal, middle and ventral portion of *pars distalis*, were double immohistochemically stained using guinea pig anti-rat βFSH and rabbit anti-rat βLH primary antibodies. For visualization, Alexa-488 and -555 secondary antibodies were used, respectively. Images were obtained using a confocal laser scanning microscope (Leica TCS SP5 II Basic; Leica Microsystems CMS GmbH, Mannheim, Germany). An Ar-488 nm and HeNe-543 nm lasers were used for excitation of fluorescence. RIF in the cytoplasm of pituitary gonadotropic cells was evaluated according to previously described procedures [2]. Additionally, the number of gonadotropic cells *per* unit area was determined.

Gonadotropic cells in pituitaries of control animals were almost all bihomonal, i.e. both βFSH and βLH were present in most of the analysed cells. RIF of βFSH was not different between the sexes. However, in gonadotropic cells of CM rats, RIF of βLH was higher comparing to CF rats (Fig. 1a and 1b), by 32.9% ($p<0.05$). This is probably caused by the low content of LH in the female pituitaries during diestrus, when all females were sacrificed. After prenatal Dx exposure, the most prominent fluorescence was that of βLH, giving impression that only LH is present in gonadotropic cells. However, after quantification of the intensity of fluorescence signal, it was observed that βFSH intracellular content was dramatically decreased in both sexes, but still present (Fig. 1a). In DxF group, content of βFSH in gonadotropic cells was decreased by 69.7% ($p<0.05$) comparing to the control females. In males the same parameter was lowered by 58.4% ($p<0.05$) (Fig. 1a and 1b). Interestingly, the number of gonadotropic cells was changed only in females. Namely, comparing to corresponding controls, in pituitaries of females prenatally exposed to Dx, gonadotropic cells were decreased by 35.3% ($p<0.05$)(Fig. 1c).

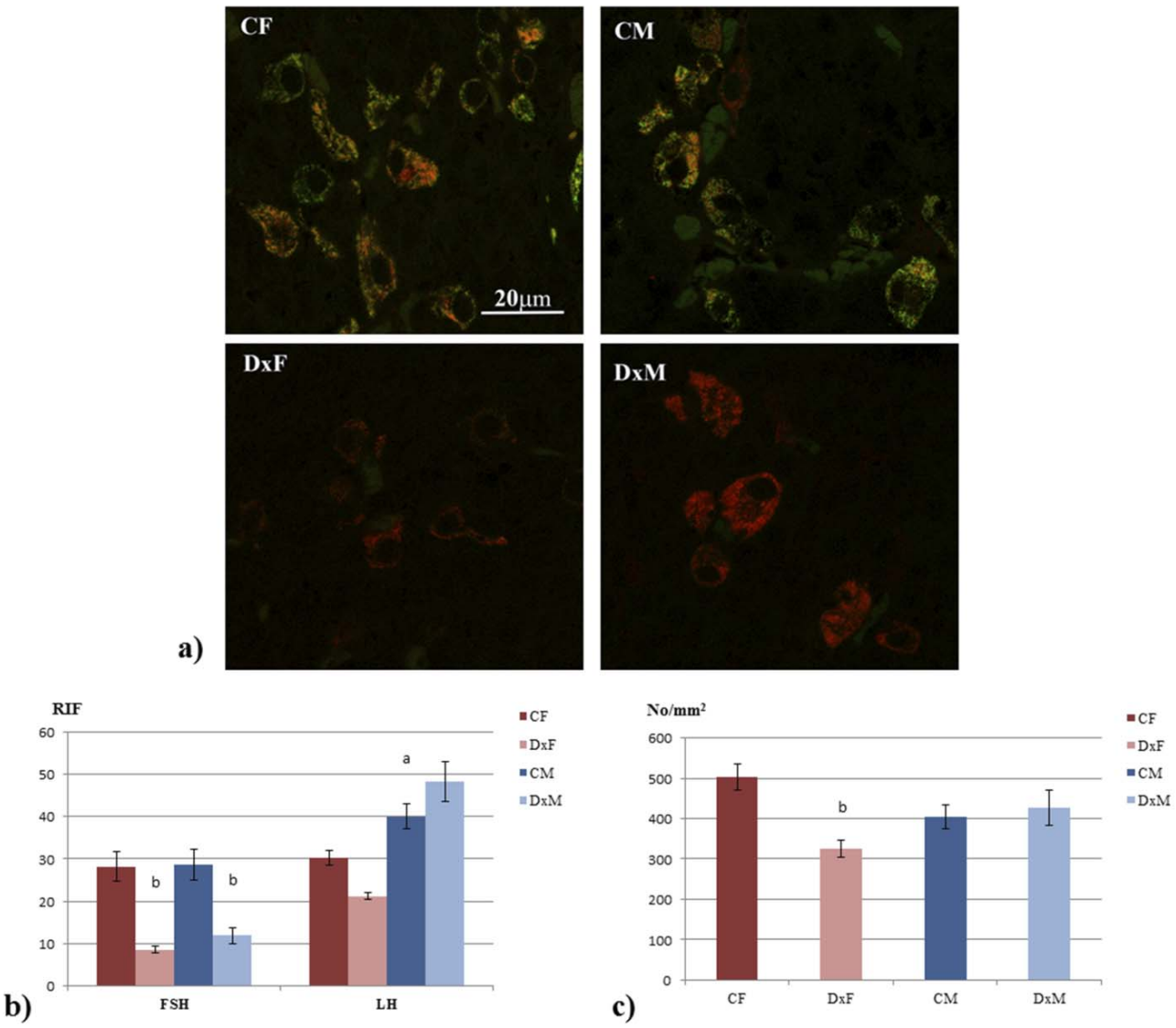

Figure 1. Immunofluorescence of pituitary gonadotropic cells. a) Representative micrographs of double immonostained gonadotropic cells; immunofluorescence for βFSH-green and βLH-red, bar-20µm; b) The relative intensity of fluorescence (RIF) of βFSH- and βLH- labeled cells; c) Number of gonadotropic cells per unit area (No/mm^2) in the pituitary *pars distalis* of control females (CF), control males (CM) and females (DxF) and males (DxM) prenatally exposed to Dx. All values are provided as the mean±SD; n=6. $^a p<0.05$ CM vs. CF, $^b p<0.05$ Dx vs. C.

On the basis of result presented, it can be concluded that prenatal dexamethasone exposure affects gonadotropic cells in females and males and that changes originated in fetal life persist till adulthood. The most prominent change observed is diminution of intracellular FSH content. Additionally, it appears that females are more affected, having in mind that the number of gonadotrops *per* unit area is decreased, while in males reduction in number did not occur.

References

[1] N. Ristić, W. Severs, N. Nestorović, I. Jarić, M. Manojlović-Stojanoski, S. Trifunović, L. Pendovski, V. Milosević, Cells Tissues Organs, 201 (2016) 148-158
[2] N. Nestorović, S. Trifunović, M. Manojlović-Stojanoski, I. Jarić, N. Ristić, B. Filipović, B. Šošić-Jurjević, V. Milošević, Anat Rec, 301 (2018) 1416-1425

Negative effects on endometrium of clomiphene citrate treatment can be prevented with resveratrol?

OLGU ENIS TOK[1,2], PINAR ÖZCAN[3] AND MUKADDES EŞREFOĞLU[4]

[1] Regenerative and Restorative Medicine Research Center, Istanbul Medipol University, Istanbul, Turkey; [2] Department of Histology and Embryology, International School of Medicine, Istanbul Medipol University, Istanbul, Turkey; [3] Department of Obstetrics and Gynecology, School of Medicine, Bezmialem Vakıf University, Istanbul, Turkey; [4] Department of Histology and Embryology, School of Medicine, Bezmialem Vakıf University, Istanbul, Turkey

1.Introduction

Clomiphene Citrate (CC) is a nonsteroidal estrogen receptor modulator that widely used in the treatment of infertility, especially polycystic ovary syndrome (PCOS) and unexplained infertility. Due to its anti-estrogenic effect on cervix, vagina and endometrial tissue, it can cause implantation failure and early pregnancy losses [1-3]. Structurally very similar to estrogen,CC binds to estrogen receptors in the hypothalamus and causes suppression of the hypothalamic gonadal axis via a negative feedback mechanism. Resveratrol is a natural polyphenol and phytoestrogen, found in grapes, red wine, peanuts, blueberry and several medicinal plants [4]. This agent may have antioxidant, anti-inflammatory and anti-apoptotic effects [5,6]. In this study, we aimed to reduce the adverse endometrial effects of CC in infertile women having a treatment with CC by taking advantage of these effects of resveratrol.

2. Material and Methods

Balb-C female mice were randomly divided into four groups (n = 6). Group Control, Group CC: CC injection (10 mg/kg), Group CC+LR: CC + low-dose resveratrol (5 mg/kg) and Group CC+HR: CC + high-dose resveratrol (50 mg/kg). Five days after drug administration, the mice were decapitated and uterine tissues were removed. For histological evaluations, sections of uterine tissue were stained with H&E for measuring thickness of endometrium and myometrium, TUNEL method for number of apoptotic cells, PCNA immunohistochemistry for number of proliferative cells and Glycodelin A (GdA) immunohistochemistry as a implantation marker for intensity of GdA positive cells. All data were evaluated statistically.

3. Results and Conclusion

Epithelial length and endometrial thickness were significantly increased in all groups compared with the control group. Although myometrial thickness increased in all groups compared with control group, no significant difference was observed. In the CC group, number of TUNEL positive cells were significantly increased in epithelial tissue and endometrium. Number of TUNEL positive cells were significantly decreased in CC + high-dose resveratrol group. Number of PCNA positive cells were significantly decreased in all groups compared with the control group. GdA staining intensity was significantly decreased in CC and CC + low dose resveratrol groups, whereas CC + high dose resveratrol group significantly increased (Figure 1, table 1).

Although CC has no adverse effect on endometrial thickness, it has an adverse effect on endometrium both increasing apoptotic cell number and decreasing proliferative cell number. However, it causes a significant decrease in expression of glycodelin A that demonstrates the success of implantation. As a conclusion, resveratrol is thought to increase the implantation success by reducing the negative effect of CC on the endometrium.

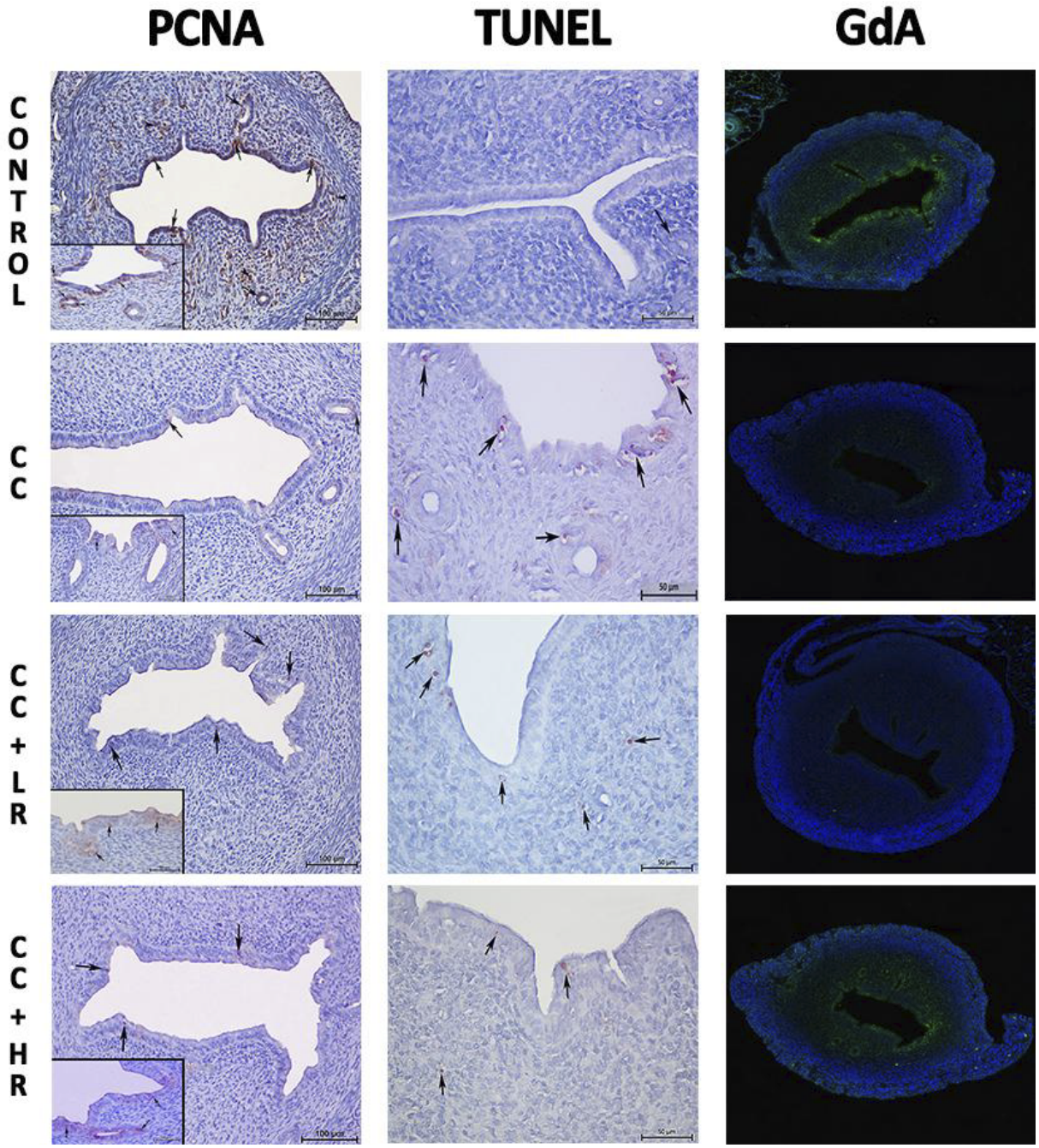

Figure 1: Analysis of uterine sections with stained TUNEL method, PCNA and GdA immunohistochemistry in all groups.

Table 1: The evaluation of length of endometrial epithelium, thickness of endometrium and myometrium, number of PCNA and TUNEL positive cells and intensity of GdA immunoreactivity in uterus.

	Control	CC	CC + LR	CC +HR
Length of Endometrial Epithelium (µm)	26,83±3,2	12,92±1,4****	28,23±2++++	30,24±2,4++++
Thickness of endometrium (µm)	211,3±23,7	157,1±30**	210,8±23,5++	252,4±17,3++++
Thickness of myometrium (µm)	111,4±11,4	85±10,6*	110,1±18,7+	113,3±14,3+
Number of PCNA Positive Cells	55±44	8,5±7,5**	8±7*	13,6±6*
Number of TUNEL Positive Cells	0,7±0,5	8,1±3***	4,2±3+	2,9±2,7++
Intensity of GdA Positive Cells	6785±2063	2908±552****	2659±417****	5411±1433++

All values are expressed as mean ± SD
*p < 0.05, **p < 0.01, ***p < 0.001, ****p < 0.0001, as compared with Control group.
+p < 0.05, ++p < 0.01, +++p < 0.001, ++++p < 0.0001, as compared with CC group.

4. References

[1] Baruah J, Roy K, Rahman S, Kumar S, Sharma J, Karmakar D. Endometrial effects of letrozole and clomiphene citrate in women with polycystic ovary syndrome using spiral artery Doppler. Arch Gynecol Obstet 2009; 279:311–4.

[2] Amita M, Takahashi T, Tsutsumi S, Ohta T, Takata K, Henmi N, Hara S, Igarashi H, Takahashi K, Kurachi H. Molecular mechanism of the inhibition of estradiol-induced endometrial epithelial cell proliferation by clomiphene citrate. Endocrinology 2010, 151:394–405.

[3] Bonhoff AJ, Naether OG, Johannisson E: Effects of clomiphene citrate stimulation on endometrial structure in infertile women. Hum Reprod 1996, 11:844–849.

[4] Ortega I, Duleba AJ. Ovarian actions of resveratrol. Ann. N.Y. Acad. Sci. 2015;(1348):86–96.

[5] Rege SD, Kumar S, Wilson DN, Tamura L, Geetha T, Mathews ST, et al. Resveratrol protects the brain of obese mice from oxidative damage. Oxidative Med Cell Longev. 2013;419092.

[6] Rauf A, Imran M, Suleria HAR, Ahmad B, Peters DG, Mubarak MS. A comprehensive review of the health perspectives of resveratrol. Food Funct. 2017; 10.1039/c7fo01300k.

Alteration in buccal mucosal cells due to the effect of smoking cigarette and periodontitis by assessing genetic and histopathologic damage

KÖROĞLU P[1], ALKAN B[2]

[1] Halic University, Faculty of Medicine, Department of Histology and Embryology, Istanbul, Turkey;
[2] Department of Periodontology, Faculty of Dentistry, Istanbul Medipol University, Istanbul, Turkey

Among the factors that cause changes in oral mucosa are bacterial, fungal, viral infections, physical, thermal factors, immune system changes, systemic diseases such as diabetes, neoplasms, radiotherapy, chemotherapy, some drugs and chemicals [1]. It is also known that chronic habits such as alcohol and smoking cause precancerous and cancerous lesions [2]. Cigarette that causes DNA damage and increases the risk of oral cancer is an important risk factor for oral diseases such as periodontal disease [3]. The aim of the study is to evaluate histological changes such as to the frequency of micronucleus, nuclear buds, binucleated, pycnotic and karyolytic cells in buccal swabs of the individuals that smoking cigarettes at different time/amounts and periodontitis. In this study, adult patients who had no systemic diseases who were admitted to Istanbul Medipol University Faculty of Dentistry, Department of Esenler Hospital were included. Our study was divided into five groups (n:10). Group 1. Non-smoker+healthy gingiva, group 2. Severe smoker+periodontitis, group 3. Non-smoker+ periodontitis, group 4. Heavy smoker+non-periodontitis, group 5. Mild smoker+non-periodontitis. Exfoliative cytology was performed with the aid of cytobrush to collect the material from either the lateral side of the tongue or mouth floor. After the cytological smears, the samples were immediately fixed with methanol fixative. For cytogenetic analysis, Feulgen reaction was applied to all oral smear samples. Quantitative determination of micronucleus index and analysis of cytogenetic damage were scored [4]. All tests were performed using SPSS and $p < 0.05$ was considered statistically significant. The highest histopathological damage score was observed in group 2. Overall, genetic damage frequency was significantly greater in grup 2 than other groups. In the literature, there is a large gap about the time and amount of cigarette consumption and histological damage. This study, filling this gap in the literature, evaluated the histological changes of smoking cigarette and periodontitis on oral smear samples. The results of our study showed that premalignant and malignant lesions were seen in oral smear obtained from individuals with heavy smoking and periodontitis. This study, thus, shows that smoking and periodontitis may cause alterations in the oral mucosal cells, their synergistic effect cause even more severe mutagenic changes at cellular levels, which may increase frequency of chromosomal damage.

References

[1] M. Rouabhia, Can J Infect Dis, 13 (2002) 47-51
[2] S. Gupta, R. Singh, O.P. Gupta, A.Tripathi, Natl J Maxillofac Surg, 5 (2014) 142-148
[3] C.F. Lima, E. Crastechini, N.C. Dos Santos, A.C. Prado Ribeiro, T.B. Brandão, F.C.F. Castro, J.S. Issa, J.D. Almeida. J Oral Pathol Med, 47 (2018) 293-298
[4] E.M. Cerqueira, C.L. Santoro, N.F. Donozo, B.A. Freitas, C.A. Pereira, R.G. Bevilacqua, G.M. Machado-Santelli. Acta Cytol, 42 (1998) 639-649

Morpho-functional effects of electronic cigarette in lung and trachea

SABRINA BURATTINI[1], SILVIA CIRILLO[2], FABIO VIVARELLI[2], VLADIMIRO CARDENIA[3], MARIA TERESA RODRIGUYEZ-ESTRADA[4,5], ELEONORA TURRINI[6], MORENO PAOLINI[2], ELISABETTA FALCIERI[1], CARMELA FIMOGNARI[6], DONATELLA CANISTRO[2]

[1] Department of Biomolecular Sciences, University of Urbino Carlo Bo, Campus Scientifico "E.Mattei", Urbino, Italy; [2] Department of Pharmacy and Biotechnology, Alma Mater Studiorum-University of Bologna, Italy; [3] Department of Agricultural, Forest and Food Sciences, University of Turin, Italy; [4] Department of Agricultural and Food Sciences, Alma Mater Studiorum-University of Bologna, Italy; [5] Interdepartmental Centre for Industrial Agrofood Research, Alma Mater Studiorum-University of Bologna, Cesena, Italy; [6] Department for Life Quality Studies, Alma Mater Studiorum-University of Bologna, Rimini, Italy

Electronic cigarette (e-cig) use has exponentially grown and has been introduced as a nicotine replacement therapy, obtaining increasing attention and popularity. However, several studies report that e-cig generates many hazardous chemical compounds (particularly carbonyl compounds, such as formaldehyde, acetaldehyde and acrolein) and free radicals, especially reactive oxygen species (ROS) (1,2).

Male Sprague Dawley rats were exsposed to e-cig aerosol composed of a 2.5 mL liquid tank in Pyrex glass and a rechargeable lithium battery (3.7 Volt EH IMR 18650; 2000 mAh), coupled with a dual coil atomizer (2 Ohm stainless steel resistance). Animals were submitted to 11 cycles/day for 5 consecutive days/week, and for 4 consecutive weeks.

Lung and tracheal morphological analyses were conducted by scanning (SEM) and transmission (TEM) electron microscopy (3). ROS levels and inflammatory process on the hematological parameter were investigated.

Observations by SEM and TEM showed a marked disorganization of alveolar and bronchial epithelium in 0.25 Ω group compared to 1.5 Ω ones. In 0.25 Ω trachea, apoptotic and necrotic cells were present (Figure 1). The pulmonary antioxidant and detoxifying impairment was demonstrated by the perturbation of the antioxidant and phase I and II enzymatic activities, probably related to the increased ROS levels ($p<0.01$) due to the enhanced activity of xanthine oxidase (XO) ($p<0.01$).

In this study, we demonstrate how several morphological and toxicological aspects, widely recognized as smoke-related injuries, can potentially occur in e-cig consumers who use low-voltage and resistance device coupled with nicotine-free liquid.

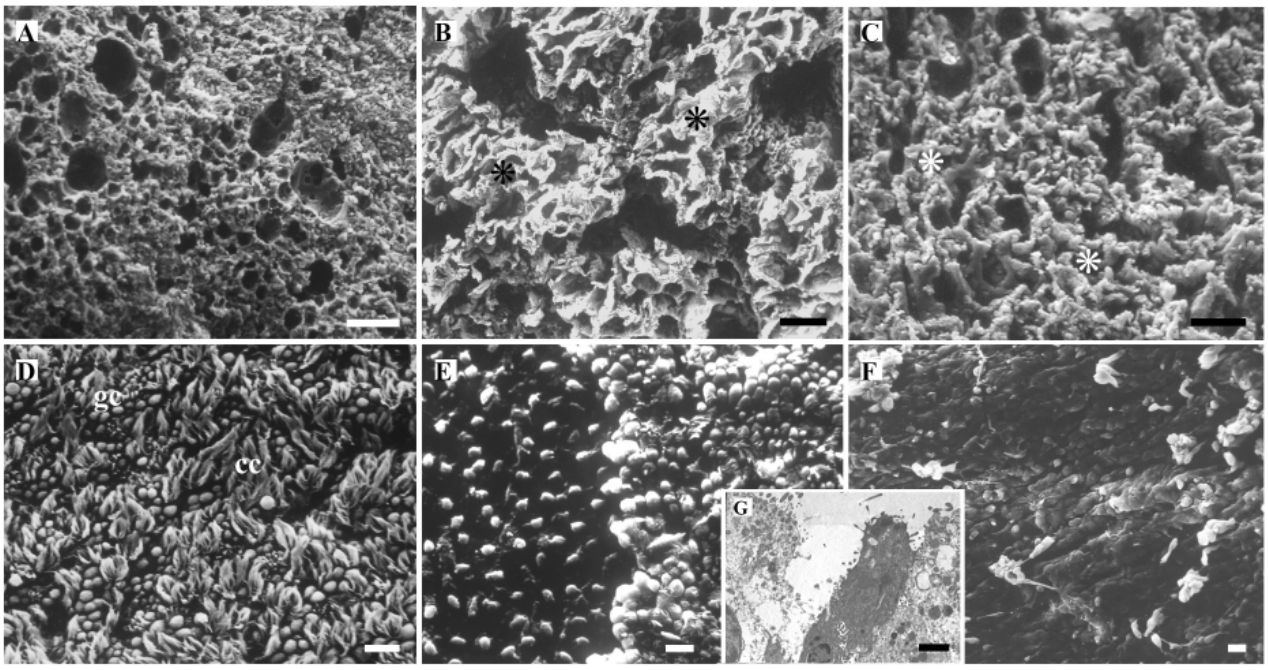

Figure 1. Morphologic alterations of lung tissue in rats exposed to the vapors generated by e-cig equipped with 1.5 Ω or 0.25 Ω coils at SEM (A-F) and TEM (G).
Control (A), 1.5 Ω (B), and 0.25 Ω (C) lung group are shown. * represents areas of alveoli collapse. Trachea control (D) in which both ciliated cells (cc) and globet cells (gc) are appreciable. In 1.5 Ω (E), and 0.25 Ω (F) trachea groups, large areas of tissue disruption are visible. Necrotic cells are evident in G. Bars: A,B,C = 50 µm; D,E,F = 10 µm; G = 2µm.

References

[1] C. A. Lerner, I. K. Sundar, H. Yao, J. Gerloff, D. J. Ossip, S. McIntosh, R. Robinson, I. Rahman, PLoS One 10 (2015) e0116732

[2] M.L. Goniewicz, J. Knysak, M. Gawron, L. Kosmider, A. Sobczak, J. Kurek, A. Prokopowicz, M. Jablonska-Czapla, C. Rosik-Dulewska, C. Havel, P. Jacob 3rd, N. Benowitz, Tob Control, 23 (2014) 133-139

[3] S. Burattini, M. Battistelli, S. Codenotti, E. Falcieri, A. Fanzani, S. Salucci, Acta Histochem, 118 (2016) 278-285.

Comparison of Basal Membrane Thickness of Granulosa Cells in PCOS

SULEYMAN EROL[1], SELIM ZIRH[1], GOKCE NUR ARI[2], CEMILE MERVE SEYMEN[2], GULNUR TAKE KAPLANOGLU[2] AND SEVDA MUFTUOGLU[1]

[1] Hacettepe University Faculty of Medicine, Department of Histology & Embryology, Ankara, Turkey;
[2] Gazi University Faculty of Medicine, Department of Histology & Embryology, Ankara, Turkey

1. Introduction

Polycystic ovarian disease (PCOS), the most common cause of the anovulatory infertility. It is characterized by abnormal gonadotropin synthesis affecting fertility and metabolism, finally arrest in ovarian follicle development. Folicle development comprises increase in granulosa cell layer, antrum formation and eventually expansion of follicle diameter. In PCOS; follicle development arrests and cystic follicles appear with decrease in granulosa cell layer & the appearance of polycystic formation (1). Various metabolic disorders; such as impaired steroid synthesis, insulin resistance and insulin metabolism disorders are the respondent factors for these ovarian changes.

The cellular differentiation is associated with the main architect of the microenvironment particularly extracellular matrix (ECM). The extracellular matrix provides physical and chemical support to the epithelial cells in organs. It has a fundamental role in pathological or physiological signal transduction and development. The basal membrane (BM) is a special form of ECM, which is a layer of basal compartment that cells located on and provides polarity to epithelial cells. The various properties of BM including thickness, rigidity, amount and biochemical content, can affect the behavior of the cell. All major BM components interact with growth factors and receptors in order to control and regulate the signaling molecules such as FGF, BMP, PDGF, VGEF, TGFß, EGF, HGF, IGF. Thus, they affect the function and differentiation potentiality of the epithelial cells.

In our study, the role of basement membrane thickness evaluated in PCOS pathogenesis. The various thickness of follicular basement membrane may suggest the quality of communication between the granulosa cells and follicular theca cells.

2. Materials And Methods

PCOS model was performed by using 1mg/kg Letrazole for 3 weeks to 6-8 weeks old Sprague-Dawley rats. LH/FSH measurements were done by ELISA for the determination of PCOS in serum samples of the all subjects.

The paraffin embedded ovaries, were sectioned after the routine procedure. Sections were stained with hematoxylin-eosin and PAS. Microscopic imaging and analysis were performed by Leica DM6B microscope and Leica DFC7000T camera. Follicle basement membrane thicknesses were measured between the granulosa cell and neighbouring theca cell by using FIJI (v2.35 for win10 64bit ImageJ version) software.

In the control and PCOS groups, randomly selected follicle basement membrane thickness were compared. At least 10 follicles were evaluated in each group. Measurements were made on 5 different regions of each follicle. Normality test was performed Shapiro-Wilk, according to independent sample t-test, P<0.05 was considered statistically significant.

3. Results

Ovaries exhibit many cystic follicles especially at the cortical regions in PCOS group. These cystic follicles composed of thinner luminal granulosa cell layer and increased antral space (Figure1). Many inflammatory cells were observed in interstitial regions between the follicles. The median of the total values were compared as control: 0.6245 ⌈m and PCOS: 1.177⌈m. The difference between control and PCOS groups was statistically significant (p<0.001) in Table 1.

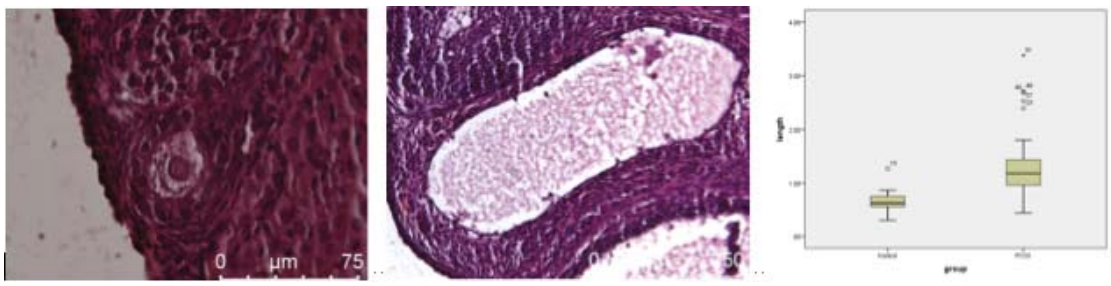

Figure 1: A: Control group, B: PCOS group, Graphic shows the difference between the thickness of the basement membranes

Table 1. Independent Samples T-Test

	W	p
Length (µm)	73.00	< .001

Note. Mann-Whitney U test.

4. Discussion

Basal membrane is an essential prerequisite for cells to form epithelial tissue and perform their functions. The properties of the BM, control the biological activities of cells such as development, growth, differentiation, proliferation and migration. It also regulates the cell behavior and physiology of them by controlling the concentration and transport of growth factors and cytokines (2).

Basal membrane related with its components; laminin, collagen type IV, perlecan and nidogen are state of interest in recent clinical studies. Nidogen has a important role in embryonic development as well as laminin that has high affinity and responsibility for the formation of basal membrane. They have a major contribution to anionic load in the basement membranes such as renal glomerular basement membrane (3).

The basal membrane is responsible for size and charge selectivity to the molecules and hormones that provide cross-talk between cell and ECM. The thickness of the basement membrane which is related with the amount of molecules laminin, nidogen, perlecan, collagen type III and IV, suggests its anionic property that enables FSH passaging to the granulosa cells.

In our study we examined the amount of basement membrane by measuring their thickness as well. We observed an increase within the thickness in the basement membrane which may cause alteration in effectivity of FSH and other cytokines. This inefficacy of the essential effect of the hormones and other cytokines on granulosa cells might suggest the impairment of the proliferation and follicular development upon their direct or indirect interactivity in PCOS.

References

[1] Goodarzi MO, et al. *Nat Rev Endocrinol*. 2011, doi:10.1038/nrendo.2010.217
[2] Kruegel J, et al. *Cell Mol Life Sci*. 2010 . doi:10.1007/s00018-010-0367-x
[3] Kunze A, et al. *Ophthalmic Res*. 2010; doi:10.1159/000247595

Immunogold labelling of vitamin D receptor and ultrastructural characterisation of metabolizing enzymes in lipid droplets in the rat liver

NATALIJA FILIPOVIĆ[1†], IVANA BOČINA[2†], IVANA RESTOVIĆ[3], NIVES KEVIĆ[2], MAXIMILIAN GROBE[1], GENIA KRETZSCHMAR[1], TOMISLAV MAŠEK[4], MARIJA VITLOV ULJEVIĆ[1], KATARINA VUKOJEVIĆ[1,5], MIRNA SARAGA-BABIĆ[5], ANA VUICA[1,6]

[1] Laboratory for Neurocardiology, Department of Anatomy, Histology and Embriology, University of Split, School of Medicine, Split, Croatia; [2] Department of Biology, University of Split, Faculty of Science, Split, Croatia; [3] Department of Teacher Education, University of Split, Faculty of Humanities and Social Sciences, Split, Croatia; [4] Department of Animal Nutrition and Dietetics, University of Zagreb, Faculty of Veterinary Medicine, Zagreb, Croatia; [5] Laboratory for Early Human Development, Department of Anatomy, Histology and Embriology, University of Split, School of Medicine, Split, Croatia; [6] Department of Nuclear Medicine, Clinical Hospital Centre Split, Split, Croatia

Vitamin D is a secosteroid with multiple actions throughout the body, usually obtained from diet, dietary supplements and exposure to sun lights. Its actions are mediated via its nuclear receptor, the vitamin D receptor (VDR). There are hard evidences that correlate vitamin D deficiency with liver lipid metabolism disturbances, but the mechanism of this action is still unknown. In our previous work, we localized the accumulation of VDR in membrane of the lipid droplets (LDs) in hepatocytes. In this study, we applied the transmission electron microscopy (TEM) by using a long-term (6 months) high sucrose intake rat model for research of the hepatic lipid accumulation. In addition to the VDR, vitamin D metabolizing enzymes 1α-hydroxylase and CYP 24 were found to be associated with the membrane of the LDs. A light-microscopy data revealed significant increase in expression of VDR and CYP 24 in liver of high-sucrose treated rats in comparison to controls. These results provide a new insight in the possible relation of vitamin D signalling system with LD morphology and function and with the lipid metabolism in general.

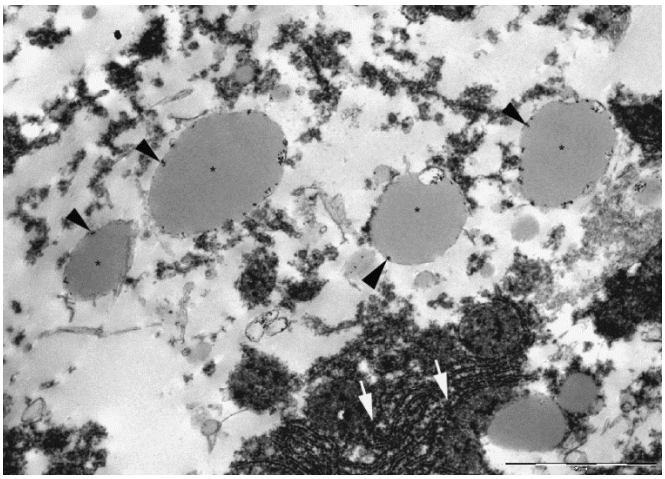

Figure 1. Immunogold labelling of VDR in lipid droplet membrane. Scale bar 3μm.

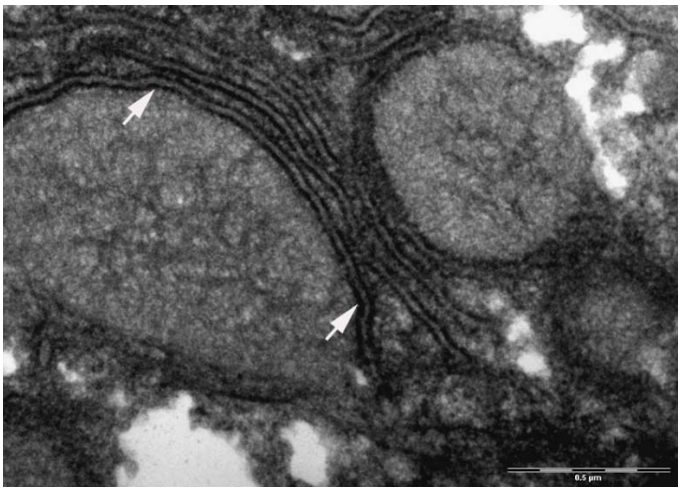

Figure 2. DAB (3,3 diamonobenzidine) staining of VDR in the rough endoplasmic reticulum of hepatocytes. Scale bar 1 µm.

References

[1] AS Greenberg, RA Coleman, FB Kraemer, JL Mcmanaman, MS Obin, V Puri, QW Yan, H Miyoshi, DG Mashek, J Clin Invest 121(2011) 2102-2110

[2] K Inouye, T Sakaki, Biotechnol Annu Rev 7 (2001) 179-194

[3] M Suzuki, Anat Sci Int 92 (2017) 50-54

[4] AR Thiam, M Beller, J Cell Sci 130 (2017) 315-324

Morphological evaluation of natural antioxidants protective effect in drug-induced C2C12 myotubes atrophy

DEBORA BURINI*, SABRINA BURATTINI, DAVIDE CURZI, GIOVANNI ZAPPIA, PIETRO GOBBI, ELISABETTA FALCIERI, SARA SALUCCI

Department of Biomolecular Sciences, University of Urbino Carlo Bo, Urbino, Italy

* PhD student in Life Sciences, Health and Biotechnology

Some skeletal muscle disorders are frequently correlated to excessive oxidative stress, which increases mitochondrial damage [1]. It may depend on prolonged anti-inflammatory drug treatment [2], whose effects could be limited by some natural antioxidants.

In this study, C2C12 myotubes were treated with a virgin oil flavonoid before a common glucocorticoid drug administration, which was used to mimic muscle atrophy *in vitro*. For the analysis we made use of inverted microscopy (IM), transmission electron microscopy (TEM), environmental scanning electron microscopy (ESEM) and confocal laser scanning microscopy (CLSM). A preserved myonuclei and mitochondria ultrastructure can be observed in control cells, which appear elongated and aligned (Figures 1A, 2A, 2B). On the contrary, glucocorticoid treatment induces a diffuse damage (Figures 1B, 2C, 2D), such as myotubes shrinkage, chromatin condensation, membrane blebs, altered or empty mitochondria and smaller fibers. Myotubes treated with antioxidant before drug administration, instead, show preserved mitochondria and fibers (Figures 1C, 2E, 2F), becoming comparable to the control ones. Taken together, these preliminary data evidence a probable role of this natural antioxidant in counteracting muscle atrophy, thus preventing or limiting muscle mass reduction and damage.

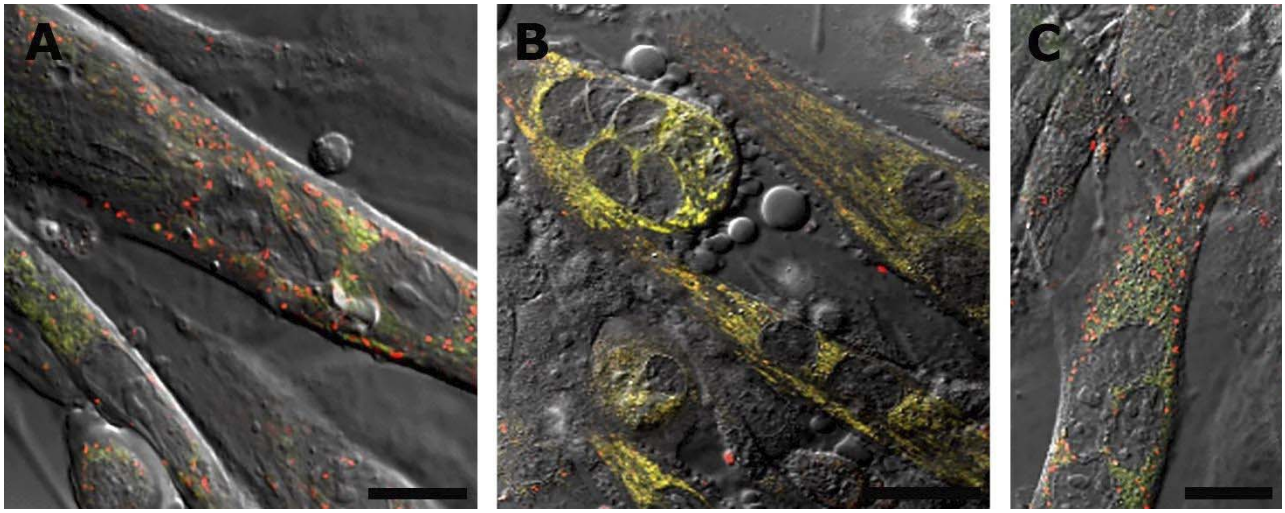

Figure 1. Control (A), glucocorticoid-treated (B) and previously antioxidant-treated (C) myotubes observed at CLSM. Bars: 10 µm.

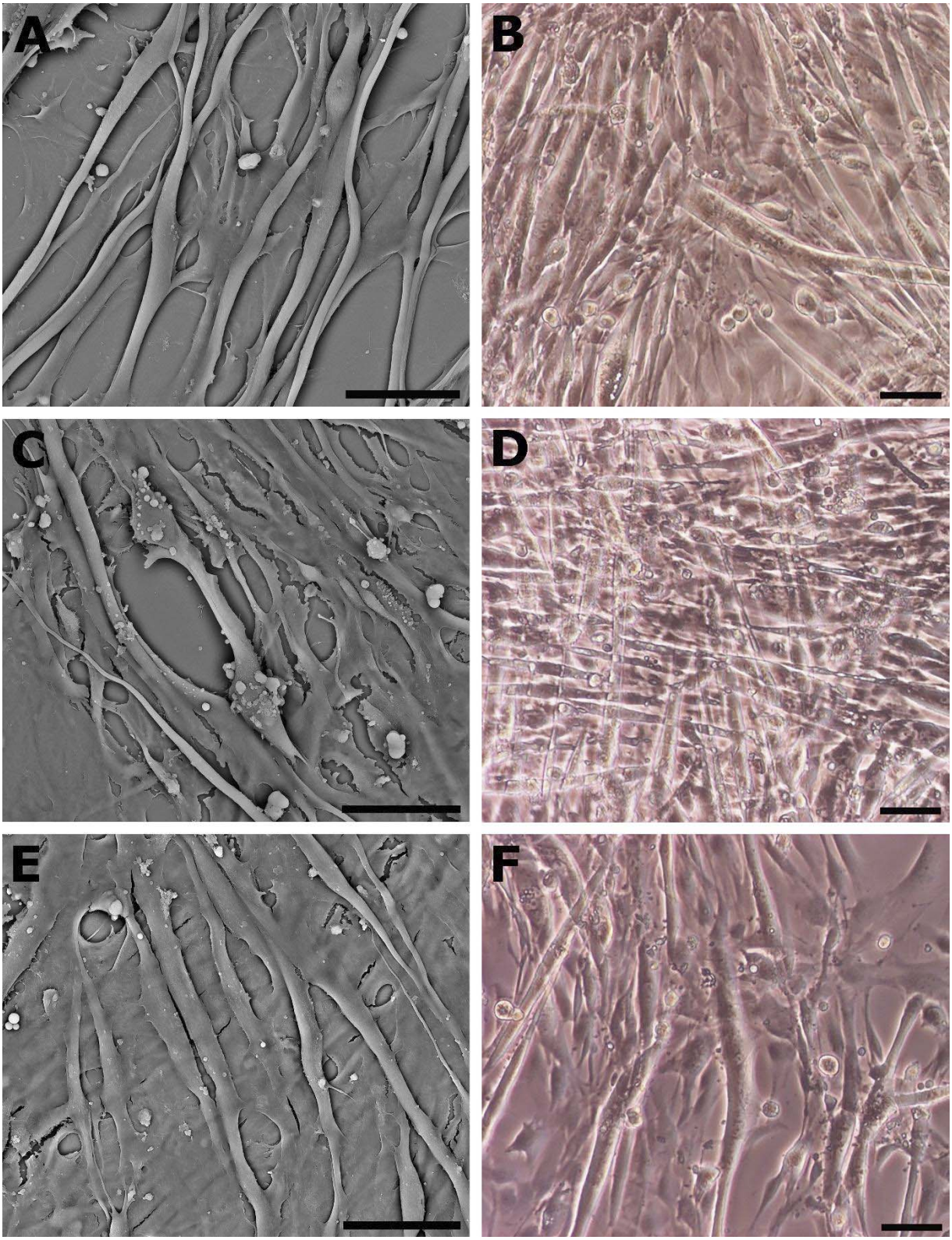

Figure 2. Control (A, B), glucocorticoid-treated (C, D) and previously antioxidant-treated (E, F) myotubes observed at ESEM (A, C, E) and IM (B, D, F). Bars: 50 µm for A, C, E; 20 µm for B, D, F.

References

[1] S. Salucci et al, Microsc Res Tech, 79 (2016) 532-540
[2] S. Salucci et al, Eur J Histochem, 61 (2017) 2784

Inhibition of cellular energy production in treatment of cancer inoculated to hamsters

DUŠICA J. POPOVIĆ[1], DUŠAN LALOŠEVIĆ[1], KOSTA J. POPOVIĆ[2], DEJAN MILJKOVIĆ[1], IVAN ČAPO[1] AND JOVAN K. POPOVIĆ3

[1] Department of Histology and Embryology, Faculty of Medicine, University of Novi Sad, Novi Sad, Republic of Serbia; [2] Department of Pharmacy, Faculty of Medicine, University of Novi Sad, Hajduk Veljkova 3, Novi Sad, Republic of Serbia; [3] Department of Pharmacology, Toxicology and Clinical Pharmacology, Faculty of Medicine, University of Novi Sad, Hajduk Veljkova 3, Novi Sad, Republic of Serbia

1. Introduction

We investigated the anticancer effect of an standard antihyperglycaemic drug metformin on *an in vivo* solid tumor model of fibrosarcoma in hamsters. Metformin reduces cellular energy production and inhibits growth of various cultured cancer cell lines [1-3].

2. Materials and methods

40 Syrian golden hamsters of both sexes (20 males and 20 females), weighing approximately 60 g, were randomly allocated to 3 experimental and 1 control groups (10 hamsters/group). 2 x 106 BHK-21/C13 cells in 1 ml were injected subcutaneously into the animals' back in all 4 groups. The first experimental group started peroral treatment with metformin 750 mg/kg daily via a gastric probe 7 days before tumor inoculation, the second 3 days before inoculation and the third immediately after inoculation. After 17 days, when the tumors were approximately 2-3 cm in the control group, all animals were sacrificed. The blood was collected for glucose and other analyses. The tumors were excised and weighed and their volume (by water displacement method) and diameters were measured. The tumor samples were histologically and immunohistologically assessed (Figure 1.) and the main organs toxicologically analyzed. Tumor volume was also determined using the formula $LxS^2/2$, where L was the longest and S the shortest diameter. Ki-67-positive cells in the tumor samples were quantified; images were taken and processed by software UTHSCSA Image Tools for Windows Version 3.00. Statistical significances of differences in tumor weight, volume, number of Ki-67-positive cells and other parameters were determined by the one way ANOVA.

3. Results

Metformin inhibited fibrosarcoma growth in seven-day pretreated hamsters without toxicity and without influence on blood analyses. The seven-day pretreatment was important for the statistically significant effect.

4. Conclusions

Inhibition of cellular energy production as an anti-tumor strategy might be an effective and safe therapeutic approach in novel nontoxic therapies and relapse prevention for human cancers.

Staining	Control	Metformin
iNOS	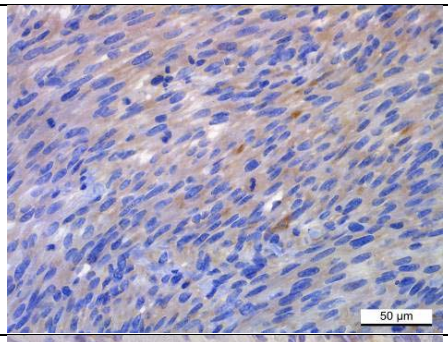	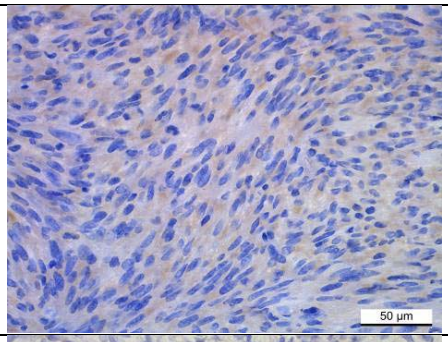
CD 34	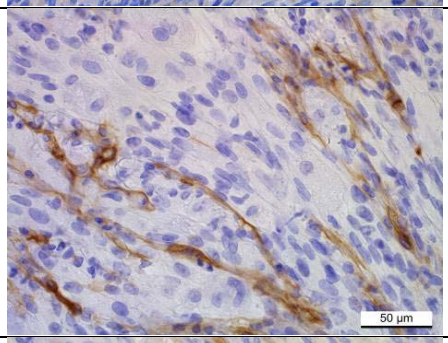	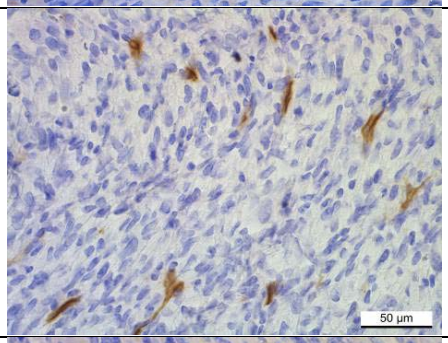
COX IV	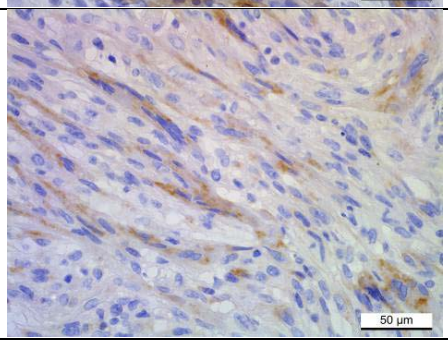	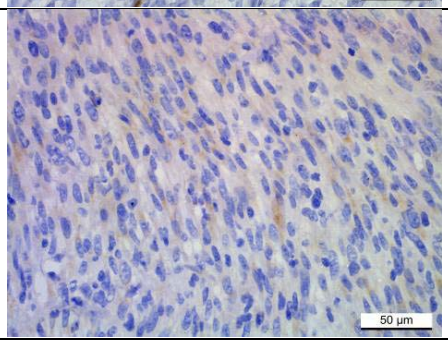

Figure 1. Immunohistochemical evaluation of tumor slices

References

[1] S. Y. Park, D. Kim, S. H. Kee, Oncol Lett, 17 (2019) 2695-2702
[2] F. Zi, H. Zi, Y. Li, J. He, Q. Shi, Z. Cai, Oncol Lett, 15 (2018) 683–690
[3] D. J. Popović, D. Lalošević, D. Miljković, K. J. Popović, I. Čapo, J. K. Popović, Eur Rev Med Pharmacol Sci, 21 (2017) 5499-5505

Nitroglycerin induces metformin anticancer effect on fibrosarcoma in hamsters

KOSTA J. POPOVIĆ[1], DUŠICA J. POPOVIĆ[2], DUŠAN LALOŠEVIĆ[2], DEJAN MILJKOVIĆ[2], IVAN ČAPO[2] AND JOVAN K. POPOVIĆ[3]

[1] Department of Pharmacy, Faculty of Medicine, University of Novi Sad, Hajduk Veljkova 3, Novi Sad, Republic of Serbia; [2] Department of Histology and Embryology, Faculty of Medicine, University of Novi Sad, Novi Sad, Republic of Serbia; [3] Department of Pharmacology, Toxicology and Clinical Pharmacology, Faculty of Medicine, University of Novi Sad, Hajduk Veljkova 3, Novi Sad, Republic of Serbia

1. Introduction

We investigated the effect of metformin and nitroglycerin on fibrosarcoma in hamsters. Nitroglycerin is converted to nitric oxide (NO) in the body, a small highly diffusible gas and ubiquitous bioactive signal molecule. NO has vasodilatator, antimicrobial, antimalarial (plasmodium infections) and tumorocide actions. It contributes to the pathogenesis and control of malarial megaloblastic anaemia, infectious diseases, autoimmune processes and chronic degenerative diseases. NO has a wide and complex role in the immune system [1-3].

2. Materials and methods

The 40 Syrian golden hamsters of approximately 100 g, both sexes, were randomly allocated in 3 experimental and 1 control groups of minimally 10 animals in each. 2 x 10^6 BHK-21/C13 cells in 1 ml were injected subcutaneously on the back of animals in 4 groups. The first experimental group started peroral treatment with metformin 500 mg/kg daily, second with nitroglycerin 50 mg/kg daily and third with combination of metformin 500 mg/kg and nitroglycerin 50 mg/kg daily, via gastric probe 3 days before tumor inoculation. After 18 days, when tumors were approximately 2-3 cm in control group, all animals were sacrificed, blood collected for glucose and other analyses, tumors excised, weighed, diameters measured, tumor samples pathohistologically (HE) and immunohistochemically (Ki-67, CD 31, COX IV, GLUT-1, i NOS) assessed (Figure 1.) and main organs toxicologically analyzed, including control animals receiving metformin and caffeine. Tumor volume was determined using the water displacement method and formula $L \times S^2 / 2$, L - the longest, S - the shortest diameter. Ki-67-positive cells in the tumor samples were quantified, images were taken and processed by software UTHSCSA Image Tools for Windows Version 3.00. Statistical significances were determined by the one way ANOVA.

3. Results

The combination of metformin and nitroglycerin inhibited fibrosarcoma growth in hamsters without toxicity.

4. Conclusions

Administration of metformin with nitroglycerin might be an effective and safe approach in novel nontoxic adjuvant anticancer treatment and relapse prevention antitumor therapy.

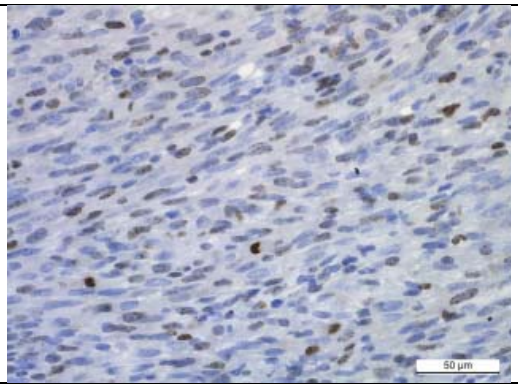

Ki-67 400x BHK TU+Met

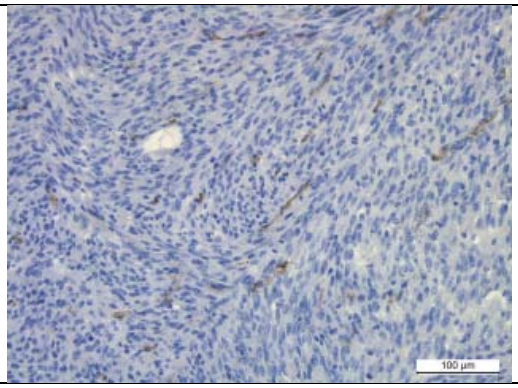

CD31 200x Tu

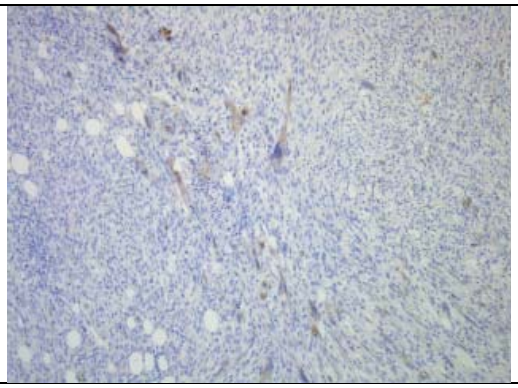

COX IV 100x TU

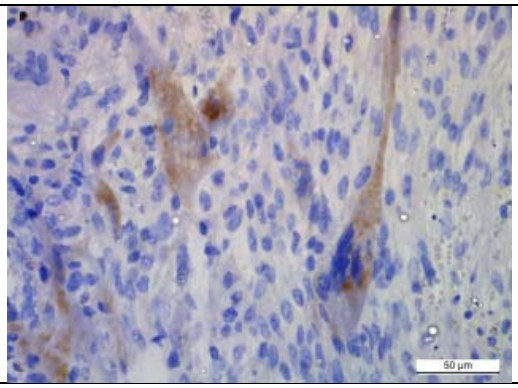

COX IV 400x TU

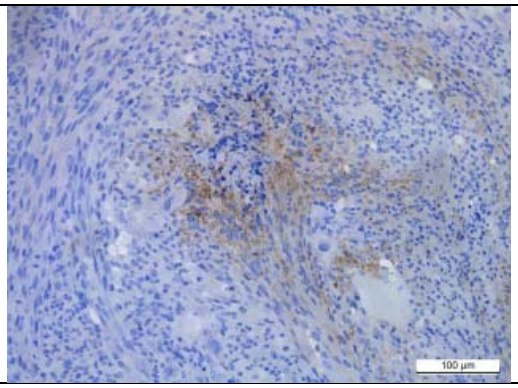

GLUT-1 200x TU

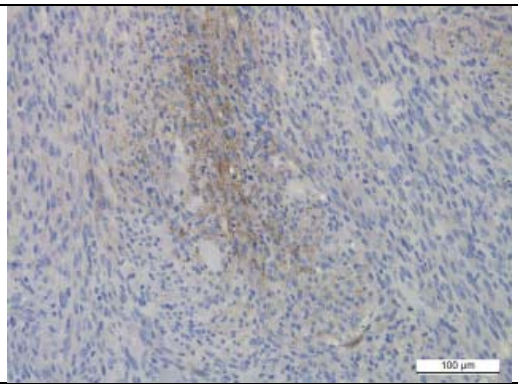

GLUT-1 200x TU+Met

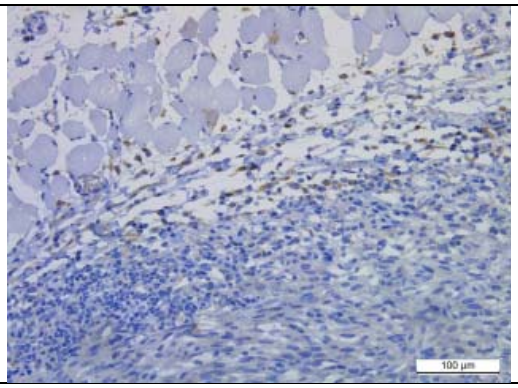

iNOS 200x TU+M

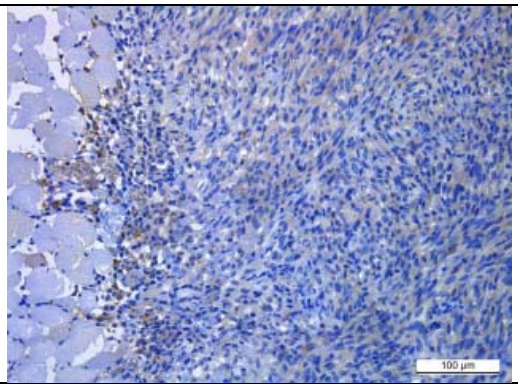

iNOS 200x TU+MET

Figure 1. Immunohistochemical methodology (TU - tumor, M – metformin + nitroglycerin, MET – metformin)

References

[1] K. De Sousa, M. S. Silva and L. T. Tavira, Afr J Biotechnol, 7 (2008) 796-799
[2] P. Pradhan, J Vector Borne Dis, 46 (2009) 100-108
[3] M. A. Erkurt, İ. Aydoğdu, N. Bayraktar, İ. Kuku, E. Kaya, Turk J Haematol, 26 (2009) 197-200.

Correlation of Light- and Transmission Electron Microscopy with NanoSIMS

REIPERT S[1], SCHINTLMEISTER A[2], LEGIN AA[3], VOLLAND J-M[4], CYRAN N[1], PEREDES G[5], GOLDAMMER H[1], ECKHARD M[1], WAGNER M[2], LICHTSCHEIDL I[1]

[1] Core Facility Cell Imaging and Ultrastructure Research, University of Vienna, Austria; [2] Large Instrument Facility for Adv. Isotope Research in the Life Sciences, University of Vienna; [3] Institute of Inorganic Chemistry, Faculty of Chemistry, University of Vienna, Austria; [4] Dept. of Limnology and Bio-Oceanography, University of Vienna, Austria; [5] Archaea Biology and Ecogenomics Division, University of Vienna, Austria

Both our Light-and Electron Microscopy Facility (CIUS) and the Large Instrument Facility for Advanced Isotope Research in the Life Sciences, with its centrepiece - the mass spectrometer NanoSIMS 50L (Cameca), are part of the „Vienna Life-Science Instruments“ (VLSI) initiative and an example of lively collaboration for the benefit of our users. Our work is focused on correlation of data obtained by laterally resolved isotope analysis with the underlying ultrastructure of cells and tissues revealed in the light- or electron microscope. By doing this we have to pay attention to sample preparation techniques that suit microscopy as well as NanoSIMS.

The requirements for NanoSIMS samples, in many aspects, are met by state-of-the-art TEM sample preparation. They both aim on rapid fixation of the living state and prevention of excessive wash-out of soluble components. This includes the isotopic labelling itself during sample dehydration by organic solvents, and embedding in epoxy resin. Studies of resin sections allow the semi-correlative exploration of the isotope distribution in the context of the cellular ultrastructure. For this, thin consecutive sections have to be mounted on TEM grids and on Sb-doped silicon wafers for NanoSIMS, respectively. The plane nature of the thin sections mounted on the wafers ensures that NanoSIMS analysis is undistorted by sample topography.

In practice, the diversity of research topics (reaching from intracellular localization of anti-cancer drugs [1,2] to symbiosis research [3] in animal and plant sciences), poses a challenge for TEM sample preparation; we meet it increasingly by inclusion of cryopreparation techniques such as plunge freezing, high-pressure freezing (HPF) and rapid low-temperature fixation and -dehydration in automated freeze substitution systems (AFSs). The latter we achieve by using patented agitation modules (Figure 1a) fitting in the cryochambers of AFS(1) and AFS2 (LEICA Microsystems) [4,5]. Freeze substitution (FS) under agitation in an AFS might be applied either to native or chemically fixed samples; both options take advantage of the fact that the wash-out of biological material is reduced at low temperatures if compared with processing at room temperature.

For samples collected in the field and infectious samples, cryofixation is not always an option. In such cases the aldehyde-fixed samples might still benefit from subsequent FS. The usefulness of such a cryo-hybrid approach for TEM/NanoSIMS was demonstrated by Volland et al. [3], who plunge-froze aldehyde-fixed ciliates *Zoothamnium niveum* harbouring bacterial endosymbionts and freeze-substituted them by using an agitation module for the AFS2 (LEICA Microsystems) (Figure 1a). Consecutive sections of the resin-embedded samples were used for correlating TEM studies with the localization of ^{13}C and ^{32}S isotopes by NanoSIMS. Consequently, thiotrophic symbiont bacteria were clearly identified as the site of ^{13}C incorporation (Figures 1b,c).

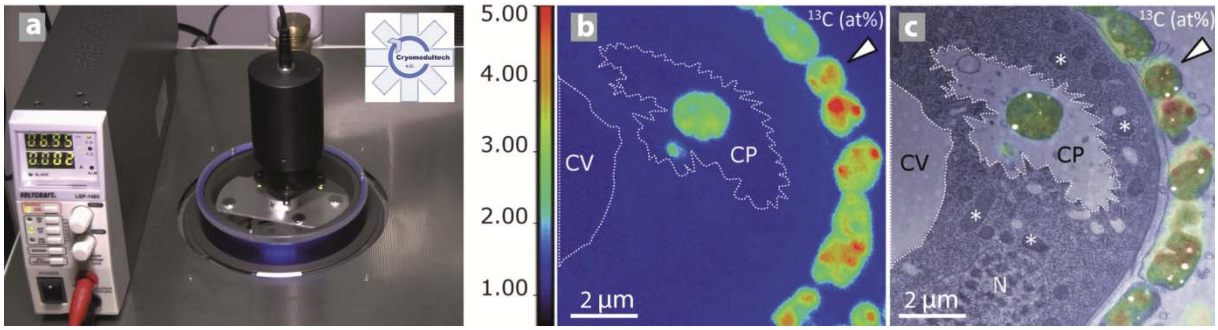

Figure 1. Freeze substitution under agitation – an effective way for semi-correlative TEM-and NanoSIMS studies. a) Patented agitation module for FS, manufactured by Cryomodultech, e. U. (holder: H. Goldammer) inserted in an AFS2 [5] b) ^{13}C localisation by NanoSIMS in a part of a microzooid of the ciliate *Zoothamnium niveum*. c) The ^{13}C signal correlates with the bacterial symbionts observed in the TEM image [3].

The authors acknowledge the Core Facility Cell Imaging and Ultrastructure Research (CIUS) and the Large Instrument Facility for Advanced Isotope Research in the Life Sciences, members of the „Vienna Life-Science Instruments“ (VLSI). (For more information: https://www.vlsi.at/).

References

[1] AA Legin et al, Chem. Sci 5 (2014), 3135–3143
[2] AA Legin et al, Chem Sci 7 (2016), 3052-3061
[3] J-M Volland et al, ISME J 12(2018), 714-727
[4] H Goldammer, S Reipert (2015) Patent No. AT515423; Ger. Utility Model DE 21 2015 000 100
[5] S Reipert et al, J Histochem Cytochem 66 (2018), 903-921

LS8

Emerging and miscellaneous topics in life sciences

CHAIRPERSONS:

Jana Nebesářová, Nela Puškaš

INVITED LECTURE

Quantitative Scanning-Free Confocal Fluorescence Microscopy for the Characterization of Fast Dynamic Processes in Live Cells

ALEKSANDAR J. KRMPOT[1,2], STANKO N. NIKOLIĆ[1,2], SHO OASA[1], DIMITRIOS K. PAPADOPOULOS[3], MARCO VITALI[4], MAKOTO OURA[5], SHINTARO MIKUNI[5], PER THYBERG[6], SIMONE TISA[7], MASATAKA KINJO[5], LENNART NILSSON[8], LARS TERENIUS[1], RUDOLF RIGLER[1,9,*], VLADANA VUKOJEVIĆ[1]

[1] Department of Clinical Neuroscience (CNS), Center for Molecular Medicine (CMM), Karolinska Institutet, Stockholm, Sweden; [2] Institute of Physics, University of Belgrade, Belgrade, Serbia; [3] MRC Human Genetics Unit, Institute of Genetics and Molecular Medicine, University of Edinburgh, Edinburgh, UK; [4] Sicoya GmbH, Berlin, Germany; [5] Laboratory of Molecular Cell Dynamics, Faculty of Advanced Life Science, Hokkaido University, Sapporo, Japan; [6] AlbaNova University Center, Royal Institute of Technology, Department of Applied Physics, Stockholm, Sweden; [7] Micro Photon Devices (MPD), Bolzano, Italy; [8] Department of Biosciences and Nutrition, Karolinska Institutet, Huddinge, Sweden; [9] Department of Medical Biochemistry and Biophysics (MBB), Karolinska Institutet, Stockholm, Sweden

Abstract

A time-resolved (21 µs/frame) confocal fluorescence microscopy imaging technique without scanning is developed for quantitative characterization of fast reaction-transport processes in solution and in live cells. The method is based on massively parallel Fluorescence Correlation Spectroscopy (FCS). To achieve simultaneous excitation of fluorescent molecules in multiple spots in the focal plane, a Diffractive Optical Element (DOE) is being used. Fluorescence from the DOE-generated 1024 illuminated spots is detected in a confocal arrangement by a matching matrix detector comprising 32×32 single-photon avalanche photodiodes (SPADs). Software for data acquisition and fast auto- and cross-correlation analysis by parallel signal processing using a Graphic Processing Unit (GPU) allows temporal autocorrelation across all pixels in the image frame in 4 s and cross-correlation between first and second order neighbour pixels in 45 s. We present here this quantitative, time-resolved imaging method with single-molecule sensitivity and demonstrate its usefulness for mapping in live cells location-specific differences in the concentration and translational diffusion of molecules.

Instrumental design

The instrumental design and the software for signal acquisition, processing and image rendering are described in detail in Krmpot *et al.* 2019 [1]. Key elements of the instrumental setup shown in Fig. 1 a), outline the working principle. Briefly, the light beam generated by the continuous wave (CW) 488 nm frequency-doubled diode laser is guided through a neutral density filter wheel (NDFW) for intensity regulation in discrete steps (OD 0.2-8.0). The laser beam is expanded using lenses L1 and L2 arranged in a Keplerian telescope configuration, and the beam path is deflected by two steering mirrors in periscope assembly (PA) in order to match the height and lateral position of the back port of the microscope. The expanded beam is focused by the plano-convex lens L3 through the diffractive optical element (DOE), designed to split the single laser beam into 32×32 beams, thus forming a 32×32 foci illumination matrix at the rear port image plane of the microscope. The relay optics (RO) of the rear port of the microscope, the longpass dichroic mirror (LPDM/EF; a high efficiency filter set (Filter Set 38 HE) for enhanced Green Fluorescent Protein (eGFP) consisting of an excitation bandpass filter EX BP 470/40 nm (central wavelength/bandwidth), longpass dichroic mirror with a cut-off wavelength of 495 nm, and an emission band pas filter EM BP 525/50) and the objective lens (OBJ; C-Apochromat 63×/1.2 W Corr objective), project the illumination matrix

from the rear port into the focal plane of the objective. After passing through the LPDM/EF, the spot-wise fluorescence matrix is imaged by the objective and the tube lenses onto an 18.0 megapixel digital single-lens reflex (DSLR) camera (Navigation camera; for quick sample localization) and then on a Single Photon Counting Camera that enables parallel single photon counting by means of a monolithic 32×32 array (SPAD camera). The photo sensitive area of the chip consists of 32×32 circular SPADs that are 20 µm in diameter. The shortest distance between adjacent diodes is 100 µm. Further details on the SPAD camera design and performance can be found in [2] and references therein. Since the aperture of every SPAD in the camera acts as a pinhole positioned in a conjugate focal plane with respect to the illumination matrix, confocal configuration is achieved for all 32×32 foci.

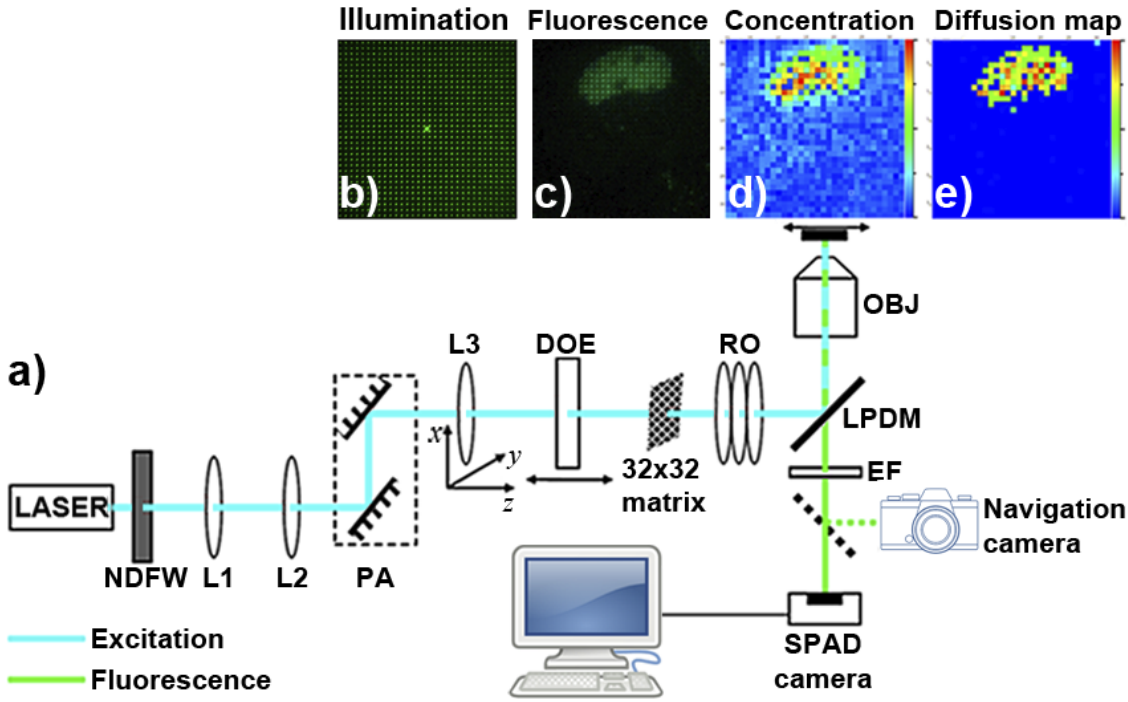

Figure 1. a) Schematic presentation of the optical arrangement. NDFW – Neutral Density Filter Wheel; L1-3 – Lenses; PA – Periscope Assembly; DOE – Diffractive Optical Element; RO – Relay Optics; LPDM – Longpass Dichroic Mirror; OBJ – Objective; EF – Emission Filter **b)** Image of the illumination matrix generated in the focal plane of the microscope objective. A thin layer formed by drying of a concentrated Rhodamine 6G (Rh6G) solution was used as a sample and the image was acquired by the 18.0 megapixel digital single-lens reflex (DSLR) camera. The 0th-order diffraction peak is readily visible when using the pixel-dense DSLR camera. **c)** Fluorescence image acquired using spot-wise illumination and the DSLR camera, showing in a live U-2 OS cell the nuclear localization of the period circadian protein homolog 2 genetically fused with the enhanced Green Fluorescent Protein (PER2-eGFP). **d)** PER2-eGFP concentration map. **e)** PER2-eGFP diffusion time map.

To visualize the illumination matrix, a uniform thin layer of dried Rhodamine 6G (Rh6G) was used. The image acquired using the pixel-dense DSLR camera shows that the sample is illuminated in a distinct spot-wise array of 32×32 well-separated points of similar intensity, except for the zero-order diffraction spot visible in the center (Fig. 1 b). The nuclear localization of the period circadian protein homolog 2 genetically fused with the enhanced Green Fluorescent Protein (PER2-eGFP) in live U-2 OS cells visualized using spot-wise illumination and the DSLR camera. Quantitative imaging of PER2-eGFP concentration (Fig. 1d) and diffusion time (Fig. 1 e) reveal local differences in PER2-eGFP association with other molecules implicated in the regulation of circadian clock.

Conclusion

The quantitative, time-resolved (here 21 µs/frame), scanning-free confocal fluorescence microscopy imaging approach presented here retains the capacity to perform optical sectioning and is empowered by the abolishment of scanning, thus allowing simultaneous data acquisition in all points in an image frame. It provides, with diffraction limited spatial resolution, quantitative information about location-specific differences in the concentration and mobility of molecules, which cannot be deduced otherwise [3]. The possibility to quantitatively, nondestructively, with the ultimate sensitivity and unprecedented temporal resolution characterize the fast cellular dynamics of molecules enables us to examine how biomolecules are integrated *via* chemical reactions and transport processes into dynamical self-regulated networks through which emergent properties, such as gene transcription and signal transduction arise at the higher level of organization and at longer spatio-temporal scales.

References

[1] A. J. Krmpot, S. N. Nikolić, S. Oasa, D. K. Papadopoulos, M. Vitali, M. Oura, S. Mikuni, P. Thyberg, S. Tisa, M. Kinjo, L. Nilsson, L. Terenius, R. Rigler, V. Vukojević, Anal. Chem. (2019) *in press*

[2] M. Vitali, D. Bronzi, A. J. Krmpot, S. N. Nikolić, F. J. Schmitt, C. Junghans, S. Tisa, T. Friedrich, V. Vukojević, L. Terenius, F. Zappa, R. Rigler, IEEE J Sel Top Quant 20 (2014) 344-353.

[3] A. K. Papadopoulos, A. J. Krmpot, S. N. Nikolić, R. Krautz, L. Terenius, P. Tomancak, R. Rigler, W. J. Gehring, V. Vukojević, Mechanisms of Development Mech. Dev. 138 (2015) 218-225.

INVITED LECTURE

Benefits and limitations of Scanning Electron Microscopy and Raman Spectroscopy in microbiological research

KAMILA HRUBANOVA[1], VLADISLAV KRZYZANEK[1], JANA NEBESAROVA[2], FILIP RUZICKA[3], ZDENEK PILAT1 AND OTA SAMEK[1]

[1] Institute of Scientific Instruments of the Czech Academy of Sciences, Brno, Czech Republic; [2] Biology Centre of the Czech Academy of Sciences, CZ-37005 Ceske Budejovice, Czech Republic 3Department of Microbiology, Faculty of Medicine, Masaryk University and St. Anne's Faculty Hospital, Brno, Czech Republic

Several microscopic organisms, including bacteria and yeasts investigated in this study (*Candida parapsilosis*, *Candida albicans* and *Staphylococcus epidermidis*), are able to adhere to surfaces or interfaces and to form organized communities – biofilms – embedded in the matrix of extracellular polymeric substances (EPS). In medicine, biofilm formation allows microorganisms to colonize the surface of implants, and also protects the microbial cells from attacks by the immune system and from the effects of antibiotics. Therefore, biofilms are considered to be an important virulence factor in these microorganisms [1]. Understanding the biofilm structure can contribute to understanding biofilm formation and the basic biochemical mechanisms underlying this process and thus it might aid in the development of more efficient treatment strategies for biofilm infections. Microbial biofilms and the matrix components are typically investigated and imaged by various microscopy techniques. The scanning electron microscopy (SEM) has the power to resolve the spatial distribution of individual biofilm-forming bacteria and yeast and their interaction in the biofilm. High magnification images are important for understanding the physiology of biofilms. However, conventional SEM is limited by the requirement of dehydration and drying of the samples during preparation, which can cause substantial changes in the microbial cell ultrastructure. The EPS in the biofilm, which contains approximately 95% of water, explored with SEM looks more like fibers than like a thick gelatinous matrix surrounding the cells. In the case of cryo-fixation, the biofilm is kept frozen to obtain high-resolution images closer to the native state of the sample. In this study we demonstrated that the most effective freezing with reduced ice crystal formation can be achieved by the high-pressure freezing (HPF) technique [2].

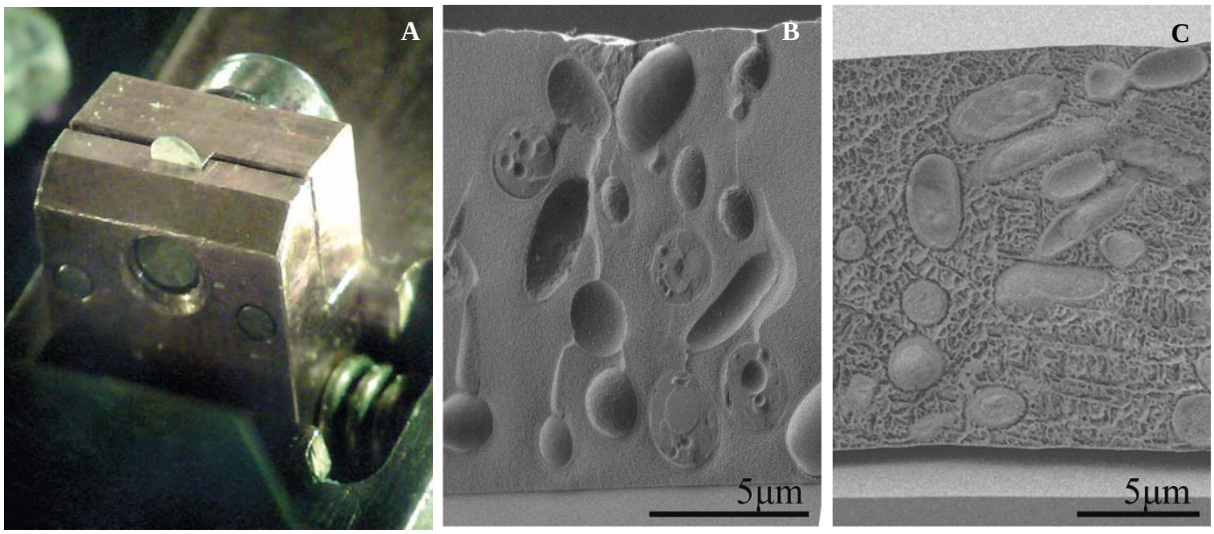

Figure 1. (A) A holder for perpendicular freeze-fracturing of the 1.4mm sapphire disc; (B) Freeze-fracture of *C. parapsilosis* grown on a sapphire disc and fixed by HPF and (C) *C. parapsilosis* grown on a glass substrate and fixed by plunging in nitrogen slush.

Main aim of this study was to employ high resolution SEM, which allowed one to visualize the biofilm structure, including the distribution of cells inside the extracellular matrix and the areas of surface adhesion (Figure 1). We compared various sample preparation protocols for SEM including cryogenic methods based on plunging the sample into various liquid cryogens, as well HPF. For imaging the biofilm interior, the freeze-fracture technique was applied. We showed that the different means of sample preparation have a fundamental influence on the observed biofilm structure. In addition, the SEM observations were complemented with Raman spectroscopic analysis, which allowed one to assess the time-dependent chemical composition changes of the biofilm *in vivo* [3]. We identified the individual spectral peaks of the biomolecules present in the biofilm and consequently, we employed principal component analysis (PCA) to follow the temporal development of the chemical composition of the selected samples (Figure 2) [2] (Table 1).

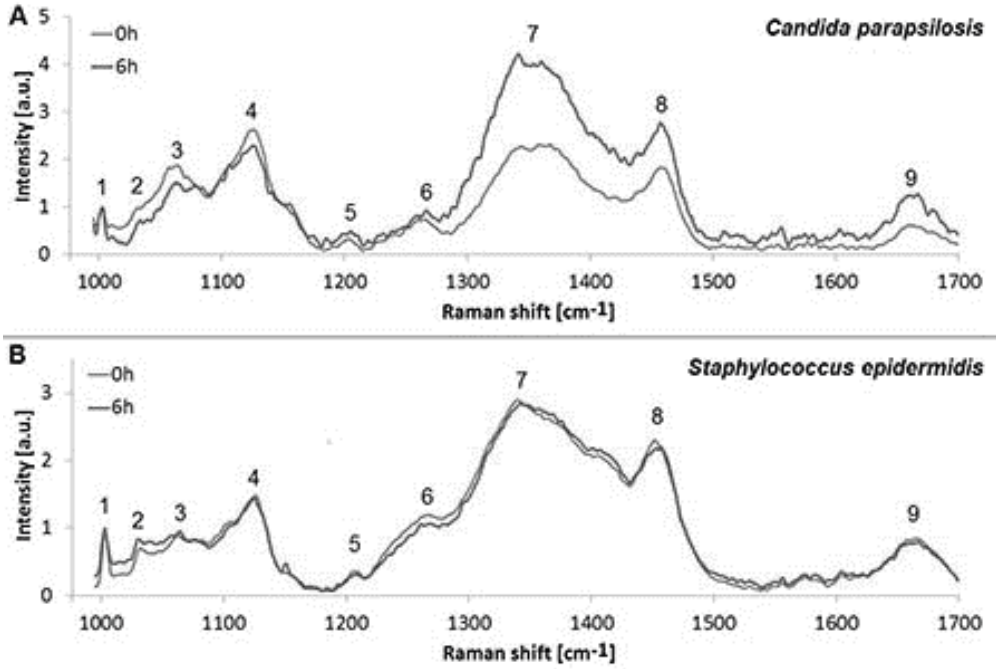

Figure 2. Raman spectra of biofilms: (A) *Candida parapsilosis*; (B) *Staphylococcus epidermidis*. Comparison of the freshly inoculated substrates containing no EPS with 6 hours old biofilm, showing the start of the EPS production. The Raman peaks associated with biomolecules are numbered, see Table 1 for the assignments. The spectra were averaged from 6 separate measurements.

Table 1 The assignments for Raman measurements.

Number	Wavenumber [cm^{-1}]	Peaks assignment
1	1002	Symmetric-ring breathing of Phe
2	1033	C-H in-plane stretch of Phe
3	1065	C-C stretch of lipids
4	1125	C-N stretch of proteins
5	1205	C-N stretch of proteins
6	1267	Proteins
7	1340-1360	Lipids, Amide III
8	1456	Proteins, Carbohydrates
9	1660	Amide I, Lipids

We showed that a combination of Raman spectroscopy with selected SEM techniques can provide a deeper insight into the chemistry and composition of biofilms. Such studies involving the influence of variations in the amount of extracellular material during the different stages of biofilm growth are currently under way in our laboratories, making use of a combination of SEM and Raman spectroscopy.

References

[1] K. Hrubanova, et al, Sensors 2018, 18, 4089.
[2] K. Hrubanova, et al, Micron 2018, 110, 28-35.
[3] O. Samek, et al, Sensors 2016, 16, 1808.

Acknowledgements

The research was supported by the Czech Science Foundation (project 17-15451S), the Technology Agency of the Czech Republic (project TN01000008) and the Ministry of Industry and Trade of the Czech Republic (project TRIO FV30271). The research infrastructure was funded by the Ministry of Education, Youth and Sports of the Czech Republic (LM2015062 Czech-BioImaging).

Line-FRAP: A Fast Technique to Differentiate between the Diffusion Rates of fast diffusing molecules from in vitro to *in vivo*

DR. DEBABRATA DEY[1], SHIR MARCIANO[1] AND PROF. GIDEON SCHREIBER[1]*
[1] Department of Biomolecular Sciences, Weizmann Institute of Science, Rehovot, Israel

FRAP or fluorescence recovery after photo bleaching is a widely used fluorescence microscopy technique for investigating diffusion of molecules inside the living cell. [1] Here, we have designed a quantitative ''Line-FRAP'' method, where scanning is done through a single line. Implementation of line-FRAP using two simultaneous scanners (SIM) and MAIN in a confocal microscope, has enhanced the rate to 1000 Hz from 40 Hz as observed earlier in the normal XY scanning FRAP mode. Introduction of the second scanner (SIM) reduces the dead time of the measurements and thus enhances the time resolution. [2] We have observed that small organic molecules that are mostly used as drugs or commercial dyes are in fact slow moving inside the living cell. We have measured the diffusion rates of Doxorubicin (as a model drug) and CCF2 (as a standard fluorogenic substrate molecule) *in vivo* and *in vitro* with different crowding conditions by line FRAP method. We have found out that these small molecules are actually moving much slower inside the living cell compared to *in vitro* possibly due to presence of various nonspecific interactions inside the complex environment of the cell. Sometimes transporter protein molecules like BSA or Myoglobin may help this hydrophobic small molecules to move faster when present together. Moreover, we have studied the diffusion rates of different proteins inside the complex environment of the living cell after microinjecting them inside. A direct comparison of the diffusion rates in eukaryotic and prokaryotic cells can reveal more about the evolutionary aspects of the proteins transports in the living system. Therefore, we believe that much faster line-FRAP can really overcome the limitations associated with the normal XY scanning FRAP mode and thus differentiate between the diffusion rates of the fast diffusing molecules in the complex environments including *in vivo*.

References

[1] K. Braeckmans, K. Remaut, R. E. Vandenbroucke, B. Lucas, S. C. De Smedt, J. Demester, Biophysical Journal, 92 (2007) 2172-2183

[2] A. Zotter, F. Bauerle, D. Dey, V. Kiss, G. Schreiber J. Biol. Chem, 38 292 (2017) 15838-15848

Quantifying organization of collagen fibers in the uninvolved human colon mucosa 10 cm and 20 cm away from the malignant tumor

SANJA DESPOTOVIĆ[1], NOVICA MILIĆEVIĆ[1], ŽIVANA MILIĆEVIĆ[1], ALEKSANDAR KRMPOT[2], MIHAILO RABASOVIĆ[2], ALEKSANDRA PAVLOVIĆ[3], VLADIMIR ŽIVANOVIĆ[3]

[1] Institute of Histology and embryology "Aleksandar Đ. Kostić", Faculty of Medicine, University of Belgrade; [2] Institute of Physics, Belgrade; [3] University Hospital Center "Dr Dragiša Mišović-Dedinje", Belgrade, Serbia

1. Introduction

Changes in morphology and organization of collagen fibers contribute to the formation of a microenvironment which facilitate tumor progression through the impact on migration and polarization of the cells [1]. Changes in morphology and organization of collagen fibers in cancer, itself, are the subject of numerous studies, while it is far less known about the changes in collagen fibers in the uninvolved mucosa away from cancer.

The main histochemical staining for detection of collagen fibers under light micrsocpy is Masson trichrome staining. Recently, second harmonic generation (SHG) imaging of collagen fibers using nonlinear laser scanning micrscopy emerged as a poweful tool enabeling imaging of collagen fibers in unstained and unfixed tissue [2].

Due to growing interest in role of collagen fibers in cancer progression, the number of methods for quantification of different parameters of collagen fibers is increasing. Currently available methods are based on the intensity derivates, intensity variation, Fourier transform, Hough transform, directional filters and fiber tracking algorithm [3].

The aim of our study was to analyse changes in morphology and organization of collagen fibers in the uninvolved colonic mucosa 10 cm and 20 cm away from the cancer, in comparison with healthy subjects, using Masson trichrome staining, SHG imaging and multiple complementary methods for quantification.

2. Matherials and Methods

Tissue samples

Tissue samples were obtained during colonoscopy at the Department of gastrointestinal endoscopy, University Hospital Center "Dr Dragiša Mišovic-Dedinje", Belgrade, Serbia, from patients suspected to suffer from colon cancer based on clinical symptoms. The samples of colon mucosa were taken 10 cm and 20 cm away in caudal direction from the suspected lesion. The samples of unaffected colon mucosa were obtained from 15 patients older than 60 years. Only tissue samples for which pathologist confirmed that the suspected lesion was colorectal adenocarcinoma, were included in the study. As a control, 20 samples of colon mucosa were collected in the same institution, from patients of corresponding age, who were indicated colonoscopy and were without any pathological finding or diagnosed only with uncomplicated haemorrhoids (*Haemorrhoides non specificatae sine complicationibus*). Patients with inflammatory bowel disease, infectious colitis or diverticular disease of colon were excluded from the study. Our study was approved by ethical committee.

Histochemical staining

The biopsies of the colon mucosa were fixed in 10% neutral buffered formalin, processed to paraplast and stained with Masson's trichrome staining for demonstration of collagen fibers.

Second harmonic generation imaging of colon tissue samples

An original lab frame nonlinear laser-scanning microscope (NLM) was used for identification of collagen fibers in label-free colon tissue samples [4]. For second harmonic generation (SHG) imaging of collagen fibers following experimental setup for NLM was used: The incoming infrared femtosecond pulses from the tunable mode-locked Ti:sapphire laser (Coherent, Mira 900) were

directed onto the sample by a dichroic mirror through the Zeiss EC Plan-Neofluar 40×/1.3 NA Oil objective. The laser wavelength was 840 nm. The SHG was selected by narrow bandpass filter at 420 nm (Thorlabs FB420-10, FWHM 10 nm). The average laser power on the sample was 30mW and the peak laser power was 2.5 kW.

Quantitative analysis of collagen fibers in colon lamina propria

To quantify representation and alignment of collagen fibers in colon lamina propria different approaches were used: Colour Picker Threshold Plugin within Icy software on Masson's trichrome staining images, computational method based on curvalet transform (CT-FIRE and CurveAlign software) on SHG images and method based on SHG polarization anisotropy [3].

Quantifying representation of collagen fibers

Masson's trichrome staining identified collagen fibers, which were green. A random selection of 15 fields per slide was assessed with Colour Picker Threshold Plugin Icy. For each slide, 10 positive and 10 negative colours were selected as recognition patterns of stained and unstained tissue elements. The presence of collagen fibers in colon lamina propria was expressed as the relative percentage of the area occupied by the collagen fibers divided by the area of the lamina propra selected with and imaging processor [5].

Computational Collagen Fiber Segmentation and Quantification

Using CT-FIRE, an open-source software package, we assessed individual collagen fibers and calculated important parameters as length, straightness, and width. CT-FIRE is developed to automatically extract and quantify individual collagen fibers from second harmonic generation images. CT-FIRE could calculate overall alignment of collagen fibers as well as individual length, straightness, and width. Fiber length and width are calculated as pixel values. Alignment represents the overall directionality of fibers within the image on a scale from 0–1, where 1 indicates all fibers are orientated at the same angle. Straightness is calculated by dividing the distance between each fiber end point by the distance along the path of the fiber and is also on a scale from 0–1, where 1 indicates a perfectly straight fiber. Besides analysing individual collagen fibers on whole SHG images, we choose 3 regions of interest per image, in the close vicinity to crypths, where the fiber remodeling happens first, and conduct analyses within them [3].

SHG polarization anisotropy

The anisotropy of SHG images can be used to quantify allignment of collagen molecules inside fibers. The anisotropy parameter was calculated by:

$\beta = (Ipar-Iorth)/(Ipar+2Iorth)$

where Ipar and Iorth represented SHG intensity detected when the analyzing polarizer is oriented parallel and perpendicular/orthogonal to the laser polarization. Values of β range from 0 to 1, where 0 represents completely random and 1 completely aligned collagene molecules organization. From each tissue sample 3 randomly chosen regions were measured [3].

Statistical analysis

The means and standard deviations were calcualted and the Student's t-test or ANOVA were used to indicate significant differences.

3. Results

On Masson trichrome staining and SHG images, collagen fibers in healthy colon lamina propria were orderly organized: the wavy bundles of collagen fibers extended around the crypts and in all directions throughout the lamina propra. At the distance of 10 cm and 20 cm away from the tumor, their proper arrangment is partially lost. Different patterns of collagen fibers are noticable: regions with parallel collagen fibers, thick collagen fibers, regions with edema of lamina propra where the prominent spaces between fibers could be seen and regions with collagen fibers organization resembling one in healthy subjects (Figure 1). Thus, the morphology and organization of collagen fibers are very heterogeneous, both between differenet groups and within each group between individual subjects.

We revealed that the representation of collagen fibers (%) in the lamina propria in the remote colon mucosa 10 and 20 cm away from the cancer was significantly lower (26.43±6.22 and 35.15±8.34, respectively) in comparison with the control, healthy individuals (48.05±8.92). Notably, the representation of collagen fibers was significantly lower in the lamina propria at the distance of 10 cm away from the tumor compared with that at the distance of 20 cm.

Using CT-FIRE and CurveAlign softwares, on whole SHG images, we showed that the width and lenght of collagen fibers are statistically higher 10 cm and 20 cm away from cancer (5±0.7, 5.32±0.58 and 55.12±2.73, 56.28±5.12), compared with healthy subjects (4.49±0.43 and 52.12±2.98). When we analyzed 3 regions of interest, in close proximity to crypts, per each photo, detected changes were even more obvious. Also, the collagen fibers 10 cm and 20 cm away from the cancer were significantly more orderly allign (0.47±0.19 and 0.59±0.19), compared with healthy lamina propra (0.36±0.20).

Anisotropy parameter β is significantly lower 10 cm and 20 cm away from the cancer (0.26±0.05, 0.34±0.09), compared with healthy lamina propria (0.39±0.09), indicating changes in organisation of collagen moleculer within fibers.

4. Conclusion

Using different, complementary approaches we detected changes in representation, morphology and organization of collagen fibers 10 cm and 20 cm away from colon cancer, compared with healthy subjects.

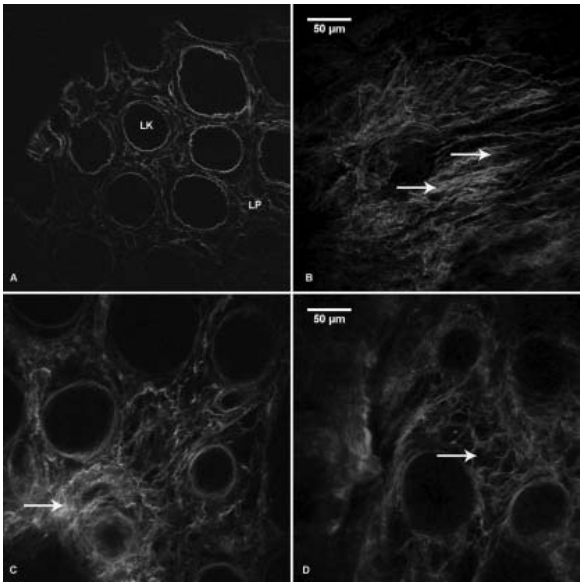

Figure 1. SHG images of collagen fibers in the colon lamina propria. A. Lamina propria of healthy subject; B.Lamina propria 20 cm away from cancer; arrows are showing regions with highly alligned collagen fibers; C. Lamina propria 10 cm away from cancer; arrow is showing region with dense collagen fibers; D. Lamina propria 10 cm away from cancer; arrow is showing enlarged spaces between collagen fibers;

References

[1] Vannucci L. Cancer Microenv 8 (2015) 159-166
[2] Rpuede D, Schaub E, Bellanger J. Sci Rep 7 (2017) 12197
[3] Rittie L. Methods in Mol Biol 1627 (2017) 429-450
[4] Rabasović MD, Pantelić DV, Jelenković BM. J Biomed Opt 20 (2015) 016010
[5] Despotović SZ, Milićević NM; Milošević DP. Tumour Biol 39 (2017)

Microscopy in dairy science: key hints for product understanding and technology improvement

PAOLO D'INCECCO[1], VERONICA ROSI[1] AND LUISA PELLEGRINO[1]
[1] Department of Food, Environmental and Nutritional Sciences, University of Milan, Italy

1. Introduction

The attention of both consumers and scientists to food quality has greatly grown in recent years as demonstrated by the increasing number of articles dedicated to this topic in scientific journals worldwide. To meet this interest, studies on food have widened the array of investigation approaches by combining microscopy evaluations to more traditional chemical or physical analyses. Two case studies are here presented explaining how microscopy was helpful in addressing quality issues that currently represent big challenges to manufacturers of dairy foods: the late blowing defect affecting extra-hard cheeses and the instability of UHT milk during the shelf life.

2. Case study 1

Italian cow's milk is mostly processed into traditional Protected Designation of Origin (PDO) cheeses, namely Grana Padano and Parmigiano-Reggiano. The consolidated cheese-making of these cheeses begins with the natural creaming of raw milk that stays at 8-20 °C for ~10 hours. During this step, fat globules rise toward the surface of milk together with bacteria cells, spores and somatic cells [1]. Thus, besides lowering its fat content, this process allows a profound cleaning of milk once the cream layer is removed [2]. The spores remaining in the milk, principally those of *Clostridium tyrobutyricum*, can germinate in cheese during the ripening, causing the so called late-blowing defect that is responsible for important economic losses. The defect is characterized by cracks and holes within the cheese loaf accompanied by an undesirable flavour. In fact, outgrowth of clostridia spores leads to butyric acid fermentation producing carbon dioxide and hydrogen [3]. Although the late blowing defect is a long-standing issue, it still represents a problem for these cheeses, because tools proposed so far to prevent it (addition of nitrate, milk bactofugation or microfiltration, etc.) are not allowed in PDO cheese manufacturing. Previous studies indicated milk immunoglobulins (Igs) to be one of the factors necessary for the removal of bacteria spore from milk by natural creaming but their specific role was not clarified [4]. We have therefore undertaken an ultrastructural study to investigate the behaviour of fat globules during raw milk creaming and the associated phenomena leading to the stable interactions between fat globules and bacteria or spores.

By CLSM of raw milk submitted to lab-scale natural creaming at selected temperatures we evidenced that fat globules (10^{14}/mL) go through interaction and coalescence phenomena as soon as the milk reaches a temperature of 8 °C or higher. These phenomena were attributed to the formation of triglyceride crystals likely impacting integrity of fat globule membrane. In contrast, interactions established between fat globules and spores were best investigated by transmission electron microscopy (TEM) with prior inclusion in resin. Lab-scale creaming trials were carried out using cast (microfiltered) milk added with a washed suspension of *Clostridium tyrobutyricum* spores and native Igs purified from cow's colostrum. Increasing amounts of added Igs significantly ($p < 0.05$) increased the number of interactions between fat globules and spores, demonstrating their specific role in anchoring spores to milk fat globule membrane. TEM observations of naturally separated cream showed that spores adhered to fat globules membrane by an electron-opaque material where presence of individual Igs classes (IgA, IgM, IgG) was identified by means of post immunogold labelling on ultrathin sections of resin-embedded cream (Fig. 1). IgA was the

prevailing Ig class. Our study supported the importance of keeping high levels of native Igs in milk to achieve an effective removal of cells and spores of Clostridia.

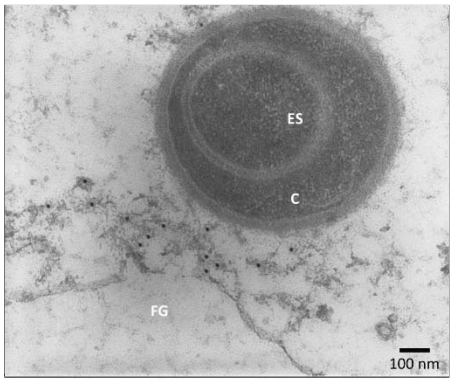

Figure 1. Transmission electron micrograph of an ultrathin section of raw milk cream separated by natural creaming. The electron-dense material present between the fat globule (FG) and the cell of *Clostridium tyrobutyricum* (C), containing its endospore (ES), was responsible for the interaction and was labelled by 20-nm gold-labelled IgA antibodies (black dots).

3. Case study 2

The second case study deals with the storage stability of UHT milk. This milk type is largely preferred by consumers in many countries because, in contrast to pasteurized milk, it can be stored at non-refrigerated condition for 3-4 months. At present, to successfully widen their market area and be competitive in very far regions, manufacturers should provide UHT milk that remains stable longer, likely up to 12 months. Fat separation and gelation represent the most characteristic signs of spoilage of UHT milk [5], both usually disregarded in the past because of the very low incidence in a short-term storage. Fat separation occurs when, although homogenized, fat globules rise to the top of the milk forming a cream layer in the package. Gelation instead involves the protein component and it is caused by residual activity of proteolytic enzymes on casein micelles causing their destabilization [6]. Although both phenomena are phenotypically well described in the literature, understanding both promoting conditions and initiating mechanisms were necessary to find out suitable strategies for prevention. An investigation at ultrastructure level seemed to be the best tool, although two independent studies were developed with respect to fat or protein instability since the subsequent technological interventions were expected to be different as well.

High-pressure double homogenization of UHT milk successfully prolonged the stability of fat globules up to 12 months of storage at 22 °C. Both CLSM and TEM analyses revealed that this new process not only decreased fat globule size, compared with the conventional single process, but also promoted interactions between fat globule membrane and protein micelles thus leading to formation of high-density aggregates (Fig. 2).

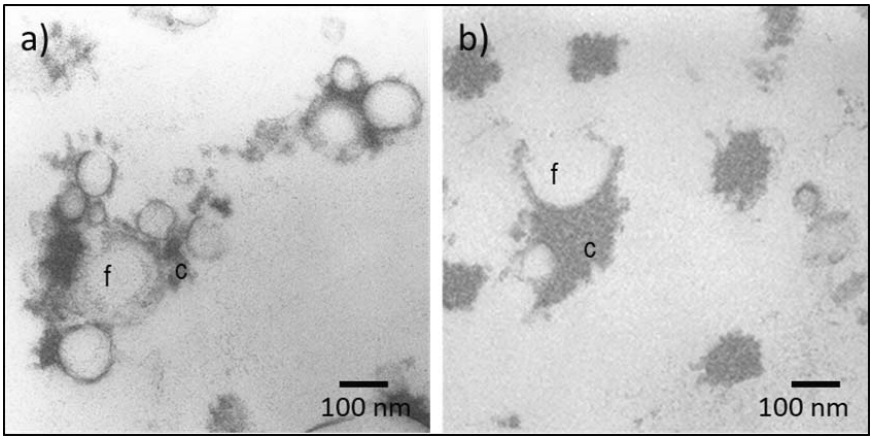

Figure 2. Transmission electron micrographs of ultrathin sections of UHT milk undergone to single homogenization (a), or double homogenization process (b). Aggregates of fat globules (f) and casein micelles (c) showed a lower proportion of fat globules respect to casein micelles in double homogenised sample.

Gelation of UHT milk was experimentally replicated by adding two proteolytic strains of *Pseudomonas* spp. to milk. Inoculated samples were stored at 25 or 40 °C up to 90 days. Changes in the microstructure of these samples were monitored by CLSM of milk stained by Fast green (protein) and Nile red (fat). In parallel to structural evaluation, proteolysis progress was monitored by capillary zone electrophoresis (CZE) and HPLC-MS. Caseinomacropeptides (CMPs), resulting from the specific activity of heat-resistant peptidases, were detected before gelation onset and accumulated during UHT milk storage. Thus, CMPs were proposed as marker for an early detection of UHT milk gelation. CLSM analysis showed to be an equally valid and faster approach for the early evaluation of UHT milk gelation since changes in protein microstructure of milk were observed while increasing the marker content of the milk (Fig. 3).

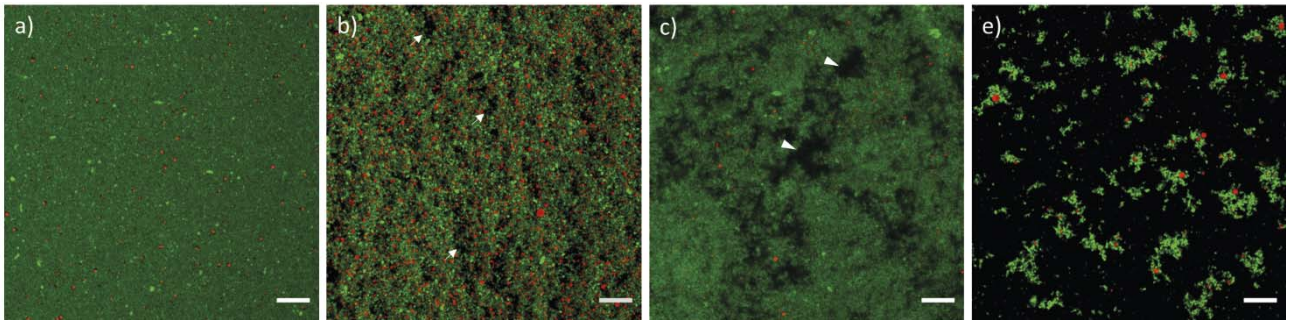

Figure 3. CLSM images of UHT milk with increasing level of protein destabilization up to complete gelation. Stable UHT milk (a) shows the typical microstructure with protein (green) occupying the whole milk volume; (b) early destabilization corresponding to initial protein networking and appearance of black areas of serum phase (arrows); (c) progress of protein destabilization with further release of serum (head arrows); (d) gelled milk. Bars are 10 µm in size.

4. Conclusion

The described case studies both refer to real issues of food spoilage sometimes causing consumer complaint and product recall with high economic loss. Furthermore, manufacturing wholesome and shelf-stable food has the side beneficial effect of limiting food waste. Microscopy proved to be of decisive importance for understanding the effects of process technologies on food matrix and their structural components. A multidisciplinary approach that combines chemical, biochemical,

microbiological and structural investigations is the successful strategy to have a complete characterization of complex samples like foods and to support the industry in their difficult task.

References

[1] Y. Ma, D. M. Barbano, J. Dairy Sci., 83 (2000) 1719–1727
[2] P. D'Incecco, F. Faoro, T. Silvetti, K. Schrader, L. Pellegrino, J. Dairy Sci., 98 (2015) 5164-5172
[3] M. Ávila, N. Gómez-Torres, D. Delgado, P. Gaya, S. Garde, Food Microbiol., 60 (2016)165-173
[4] S. R. Geer, D. M. Barbano, J. Dairy Sci., 97 (2014) 2027–2038
[5] S. G. Anema, Compr. Rev. Food Sci. Food Saf., 18 (2019) 140-166
[6] C. Zhang, E. Bijl, K. Hettinga, Food Chem., 263 (2018) 127-134

Vesicular traffic related proteins in superficial urothelial cells of urinary bladder cancer

DAŠA ZUPANČIČ, SAMO HUDOKLIN, ROK ROMIH
Institute of Cell Biology, Faculty of Medicine, University of Ljubljana, Slovenia

1. Introduction

Epithelial cells display an intrinsic polarity that is critical for their normal function and is disrupted during the cancer transformation. The targeting of membrane proteins to different membrane subdomains such as apical and basolateral surface of epithelial cells, is a fundamentally important cellular function and has been studied extensively. Nevertheless, there is little data about altered trafficking during cancer [1]. The highly differentiated superficial umbrella cells of the multi-layered urinary bladder urothelium provide an excellent model system for the study of apical targeting. This is because they synthesize a large amount of four major types of apically targeted integral membrane proteins named uroplakins [2]. Uroplakins form two-dimensional crystalline urothelial plaques that cover almost the entire urothelial apical surface of normal urothelium and contribute to blood-urine barrier [3]. During urothelial carcinogenesis, the expression of uroplakins is dysregulated [4], the structure of apical surface is altered and blood-urine barrier is disrupted [1, 5]. It is well known that in umbrella cells of normal urothelium, uroplakins are delivered to the apical plasma membrane via fusiform vesicles (FVs), which are transported along microtubules and actin filaments by the help of motor proteins. The mechanisms that regulate this pathway have only recently been elucidated [6]. It was shown that uroplakin delivering FVs contain Rab27b, which mediate apical transport via actin filaments [6]. Subsequently, apical fusion occurs via MAL-facilitated process [7]. Moreover, intermediate filaments keratin 20 (Krt20) trajectorial network, which lies approximately 200 nm below the apical plasma membrane of umbrella cells, has holes just the right sizes to allow FVs passage [8]. This Krt20 subapical network keeps a pool of primed and strategically located FVs waiting for fusion and probably plays a key role in regulating vesicular trafficking [6]. Here we studied the alterations of vesicular traffic machinery that may contribute to disrupted polarity of superficial urothelial cells in the animal model of N-butyl-N-(4-hydroxybutyl)nitrosamine (BBN)-induced urinary bladder cancer [9, 10, 11].

2. Material and methods

Twelve adult male Wistar rats were used in this study in accordance with European guidelines and Slovenian legislation. The experiments were approved by the Veterinary Administration of the Slovenian Ministry of Agriculture and Forestry (permit no. 34401-29/2007/3) in compliance with the Animal Health Protection Act and the Instructions for Granting Permits for Animal Experimentation for Scientific Purposes. Rats were divided into one experimental group of 8 and one control group of 4 rats by simple random sampling. All animals were housed in plastic cages at 23 ± 2°C and 50-60% relative humidity. Basal diet was available *ad libitum*. The BBN was obtained from Tokyo Chemical Industry Co., Ltd. (Tokyo, Japan) and diluted to 0.05% with tap water. This mixture was then given *ad libitum* to the experimental group for 10 weeks (BBN 10w). Control group (normal) of animals had tap water available *ad libitum*. The rats were euthanized by CO_2 inhalation. Urinary bladders were cut into pieces, designated for ultrastructural analyses (scanning electron microscopy, transmission electron microscopy) and for immunolabelling (immunofluorescence on semi-thin cryosections and immuno-gold labelling on ultra-thin cryosections). For scanning electron microscopy samples were fixed, critical point dried and

coated with gold. For transmission electron microscopy standard fixation and embedding in Epon was performed. Cryosections were prepared by modified Tokuyasu method and labelled with phalloidin conjugated to FITC or AF350 for labelling of actin filaments and with the following primary antibodies: anti-Krt20 (mouse monoclonal; Dako), anti-tubulin (rabbit polyclonal; Abcam), anti-uroplakins (rabbit polyclonal; a kind gift from Prof. T.-T. Sun, University of New York, USA), anti-MAL (mouse monoclonal; a kind gift from Prof. M.A. Alonso, University of Madrid, Spain), anti-Rab27b (rabbit polyclonal; SySy). The binding of primary antibodies was detected by appropriate secondary IgGs conjugated to either fluorescent label or to colloidal gold. To show co-localizations of various vesicular traffic related proteins, double and triple immunolabelling was performed.

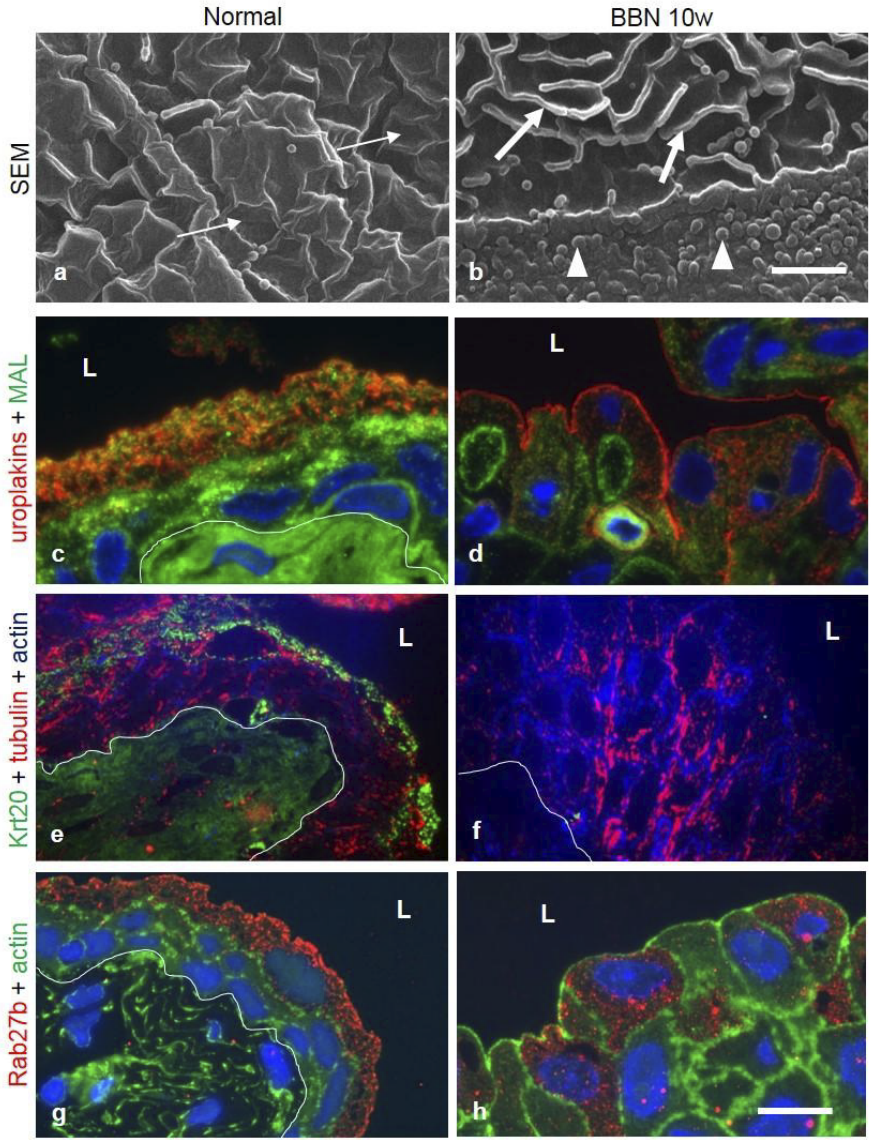

Figure 1. Superficial urothelial cells of control animals (normal) and animals treated with BBN for 10 weeks (BBN 10w). a, b - apical plasma membrane appearance as observed by scanning electron microscopy (urothelial plaques – thin arrows; microvilli – arrowheads, ropy ridges – thick arrows). c,d - Immunolabelling of uroplakins (red) and MAL (green). e, f – Immunolabelling of cytoskeletal proteins (Krt20 - green, tubulin - red and actin - blue). g, h – Immunolabelling of Rab27b (red) and actin (green). L – lumen of the urinary bladder. White line depicts basal lamina. Scale bars: a,b – 1 µm; c-h – 20 µm.

3. Results and discussion

In the normal urothelium the apical plasma membrane of umbrella cells contained urothelial plaques, separated by elevated interplaque regions, while in BBN 10w group the urothelial surface was covered by ropy ridges or microvilli (Fig.1a,b). Uroplakins were detected on the apical plasma membrane and on the FVs in the cytoplasm of umbrella cells (Fig.1c). After BBN treatment uroplakins were localised mainly in the apical plasma membrane of superficial cancer urothelial cells (Fig.1d). This results confirmed that normal polarity of superficial urothelial cells is altered in superficial cancer urothelial cells. Therefore, we analysed the distribution of cytoskeletal elements participating in uroplakins trafficking. Trajectorial organisation of Krt20 was present in subapical region of umbrella cells of normal urothelium, while no Krt 20 expression was detected in superficial cancer urothelial cells after BBN treatment (Fig.1e,f). Actin filaments were mostly absent from subapical region in umbrella cells, while they showed more pronounced presence in the subapical cytoplasm of superficial cells in BBN 10w group (Fig.1e-h). Tubulin forming microtubules were distributed throughout the cytoplasm of superficial cells reaching subapical trajectorial network of Krt20 in umbrella cells and reaching the subapical actin network in superficial cells of BBN 10w group (not shown). It seems that the major change in the organisation of the cytoskeleton during cancer transformation of superficial urothelial cells is loss of Krt20 and more pronounced actin filaments in subapical region, which might allow easier vesicular trafficking of uroplakins. Since Rab27b mediates apical transport of uroplakin delivering FVs, we further investigated the distribution of Rab27b in normal and cancer superficial urothelial cells. In normal cells Rab27b immunolabelling signal was strong in the cytoplasm with strongest labelling in the subapical regions (Fig.1g). Interestingly, two subpopulations of superficial cancer urothelial cells were observed after BBN treatment: i) cells with strong immunolabelling of Rab27b throughout their cytoplasm and ii) cells with weak or no labelling (Fig.1h). Since apical plasma membrane of superficial cells was uroplakin positive, we assume that in cells with weak or no Rab27b labelling uroplakin transport is facilitated via some other proteins. Similar as immunolabelling of Rab27b immunolabelling of MAL revealed two subpopulations of cancer urothelial cells: i) cells with strong MAL labelling and ii) cells with weak or no MAL labelling (Fig.1d). Double immunolabelling of MAL and uroplakins revealed that in the normal superficial urothelial cells they were co-localized (Fig.1c), while in the superficial cancer urothelial cells no co-localisation was observed (Fig.1d). We therefore suppose that MAL does not facilitate the fusion of uroplakin delivering vesicles with the plasma membrane in superficial cancer urothelial cells. To sum up, our study shows that the profound reorganization of vesicular traffic related proteins in superficial urothelial cells of urinary bladder cancer cause polarity disruption, changed apical plasma membrane structure and compromised barrier function.

References

[1] D. Zupancic, and R. Romih, Radiol Oncol, 47(4) (2013) 338-45
[2] X.R. Wu et al., J Biol Chem, 269(18) (1994) 13716-24
[3] C.C. Hu et al., Mol Biol Cell, 16(9) (2005) 3937-50
[4] H.Y. Huang et al., Hum Pathol, 38(11) (2007) 1703-13
[5] D. Zupancic et al., Virchows Arch, 458(5) (2011) 603-13
[6] B. Wankel et al., Mol Biol Cell, 27(10) (2016) 1621-34
[7] G. Zhou et al., Mol Biol Cell, 23(7) (2012) 1354-66
[8] P. Veranic and K. Jezernik, Cell Motil Cytoskeleton, **53**(4) (2002) 317-25
[9] I. Ariel et al., Mol Carcinog, 41(2) (2004) 69-76
[10] O.N. Gofrit et al., Urology, 68(1) (2006) 231-5
[11] K. Ogawa, , et al., Toxicol Pathol, 27(6) (1999) 645-51

Ultrastructure of traumatic resin duct formation in *Cupressus sempervirens* L. in response to the attack of the fungus *Seiridium cardinale* (Wag.) Sutton & Gibson

ALESSIO PAPINI[1,*], SALVATORE MORICCA[2], ROBERTO DANTI[3], CORRADO TANI[1], ISABELLA POSARELLI[2], SARA FALSINI[1], GIANNI DELLA ROCCA[3]

[1] Department of Biology University of Florence, Italy; [2] Department of Agrifood Production and Environmental Sciences, Plant Pathology and Entomology Division, University of Florence, Italy; [3] Institute for Sustainable Plant Protection, IPSP-CNR, Sesto Fiorentino, Italy

Cupressus sempervirens L. (cypress), belongs to family Pinaceae and represents an important tree for the typical tuscan and eastern-mediterranean landscape. In the last years this tree is frequently affected by fungal attack by the fungus *Seiridium cardinale* (Wag.) Sutton & Gibson, the cause of the so called cypress canker.

The main mechanism of defense of cypress from the pathogen is the post-infectional development of a well-structured necrophylactic periderm (NP) [1], the increase in polyphenol cells and the ex-novo formation of traumatic resin ducts.

This investigation deals with the microscopical analysis of the development of the traumatic resin ducts and the ultrastructure of the activity of the epithelial cells of the duct itself.

The samples were fixed in 1.25 % glutaraldehyde at 4°C in 0.1 M phosphate buffer (pH 6.8), then post-fixed in 1% OsO_4 in 0.1 M phosphate buffer (pH 6.8) for 1 hr. After ethanol series dehydration and a final propylene oxide step, the samples were embedded in Spurr's epoxy resin.The 80nm thick sections were stained with uranyl acetate and lead citrate. The observations were done with a Philips EM201 TEM.

The formation of the traumatic resin duct starts in the secondary phloem around a layer of sclerenchyma fibers (Fig. 1) as a result of degeneration (PCD) of sieve cells and the reprogramming of albuminous cells into epithelial cells that produce terpens that will enter into the duct to form the resin.

The epithelial cells show plastids specialized in the production of terpens. The plastids are surrounded by ER elements (Fig. 2) and fill themselves with a granular material that eventually will cross the plasmamembrane and enter into the resin duct.

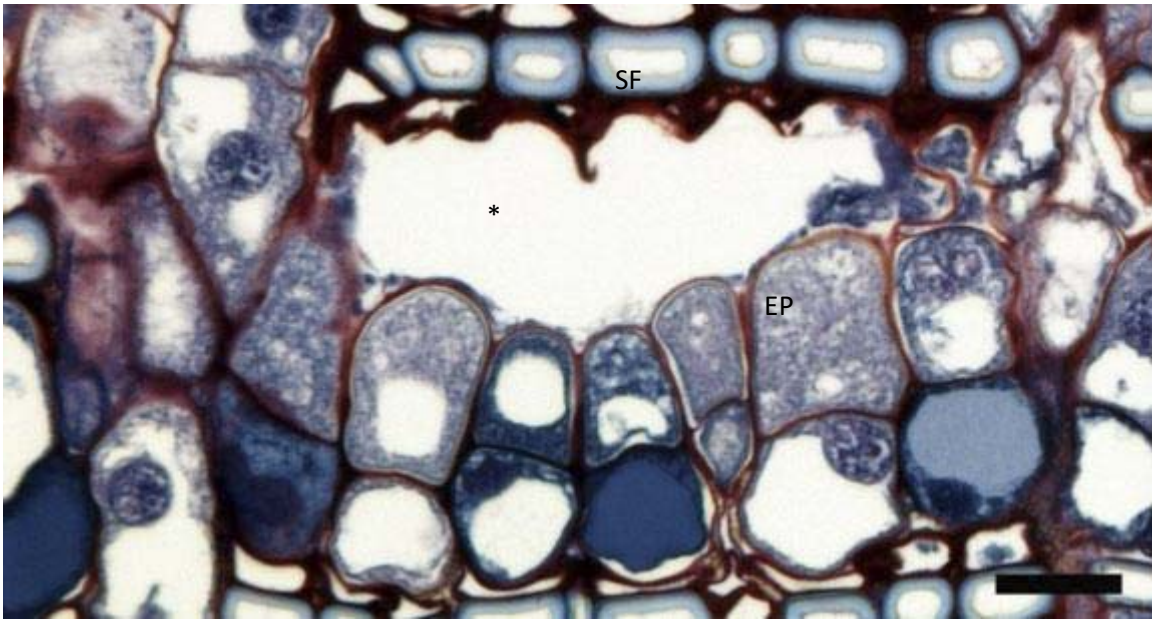

Figure 1. Traumatic resin duct. Light microscope. Toluidine blue staining. The lumen is indicated by an asterisk. EP = epithelial cell. SF = Sclerenchyma fiber. Bar = 25 µm. Bar = 1µm

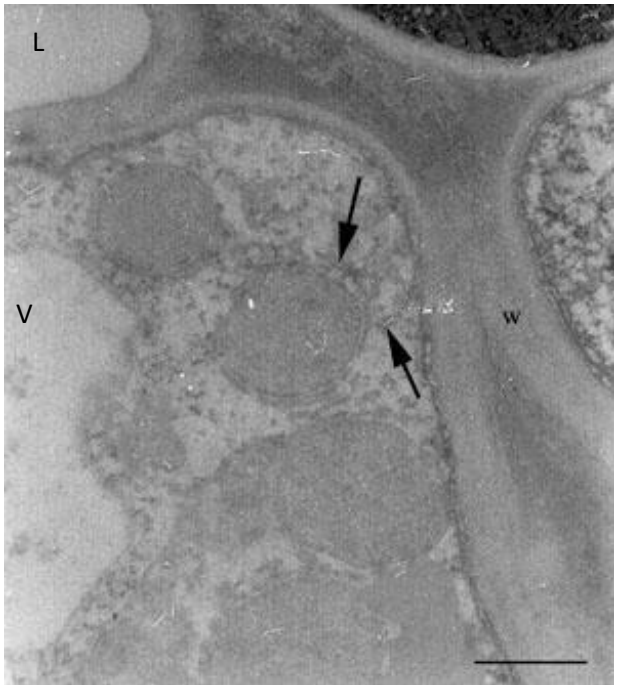

Figure 2. Traumatic resin duct. Transmission Electron Microscope. Detail of an epithelial cell. ER elements (arrows) are surrounding the plastids. W = cell wall; V = vacuole; L = lumen. Bar = 1µm.

References

[1] Danti R, Rotordam MG, Emiliani G, Giovannelli A, Papini A, Tani C, Barberini S, Della Rocca G (2018) Different clonal responses to cypress canker disease based on transcription of suberin-related genes and bark carbohydrates' content. Trees 32(6): 1707–1722

Effects of Monobenzyl Ether of Hydroquinone on 3T3 Mouse Fibroblast Viability and Ultrastructure

ASLI ERDOĞAN, HASAN SERDAR MUTLU, SIBEL DOĞAN AND TUĞBA KOTIL
İstanbul University, İstanbul Faculty of Medicine, Histology and Embryology Department, İstanbul, Türkiye

1. Introduction: Monobenzyl ether of hydroquinone (MBEH) is an FDA (Food and Drug Administration) approved topical agent with permanent effect which is used by vitiligo patients whose pigment loss scattered more than 50% of their skin with the aim to even skin tone by depigmenting melanocytes in unaffected areas (1, 2, 3). Different concentrations of MBEH application to melanocyte, keratinocyte and fibroblast cell cultures showed that keratinocytes are stronger but fibroblasts are sensitive like melanocytes to MBEH (3). Although there are many publications about effects of MBEH on melanocytes, studies related to its effect on fibroblasts remain limited. The aim of this study was to investigate potential effects of MBEH on 3T3 mouse fibroblast cell viability and ultrastructure.

2. Materials and Methods: 3T3 mouse fibroblast cell line was used in this study. Cells were incubated at 37°C and 5% CO_2 conditions in DMEM-F12 medium. Cells were treated with 250µM, 500 µM and 750 µM MBEH and vehicle (EtOH:DMSO) for 24 hours. Cells were counted with haemocytometer. Statistical analysis of the data was performed using the IBM SPSS 22 for Windows One-way ANOVA analysis using the Tukey test. For evaluation of apoptosis, cells were fixed with 70% ethanol and TUNEL assay was applied. For TEM analysis, cells were fixed with 2.5% gluteraldehyde. After routine tissue processing steps, thin sections were evaluated by Jem Jeol 1011 transmission electron microscope.

3. Results: When compared to the control group, a significant decrease was observed in the number of cells in the 250 µM, µ500 µM and 750 µM MBEH treated groups ($p<0.05$) (Figure 1). TUNEL positive cell rate was 2% in control group and 6% in vehicle group. In experimental groups, TUNEL positivity was increased in a dose dependent manner (7% in 250 µM MBEH treated group, 52% in 500 µM MBEH treated group and 67% in 750 µM MBEH treated group) (Figure 2). Under TEM, untreated cells exhibited active cells' characteristics with euchromatic genetic material, open nuclear pores, well developed rough endoplasmic reticulum (rER), abundant mitochondria and prominent Golgi apparatus. In 250 µM MBEH treated group, there was a slight dilation in perinuclear space. In some mitochondria, swelling and loss of cristae were observed. There were dilation in rER cisternae. Multilamellar bodies, abundant lysosomes and multivesicular bodies were seen. In 500 µM MBEH treated group, loss of cell volume was observed. Nucleus and cytoplasm were more electron dense than other groups and organelles were not prominent. There were abundant multivesicular bodies and autophagic vacuoles in cytoplasm. In 750 µM MBEH treated group, cells were completely degenerated (Figure 3).

4. Discussion: Results of this study suggest that melanocyte depigmenting agent MBEH may also negatively affect fibroblast cell number and ultrastructure and may trigger fibroblast cell death via different pathways.

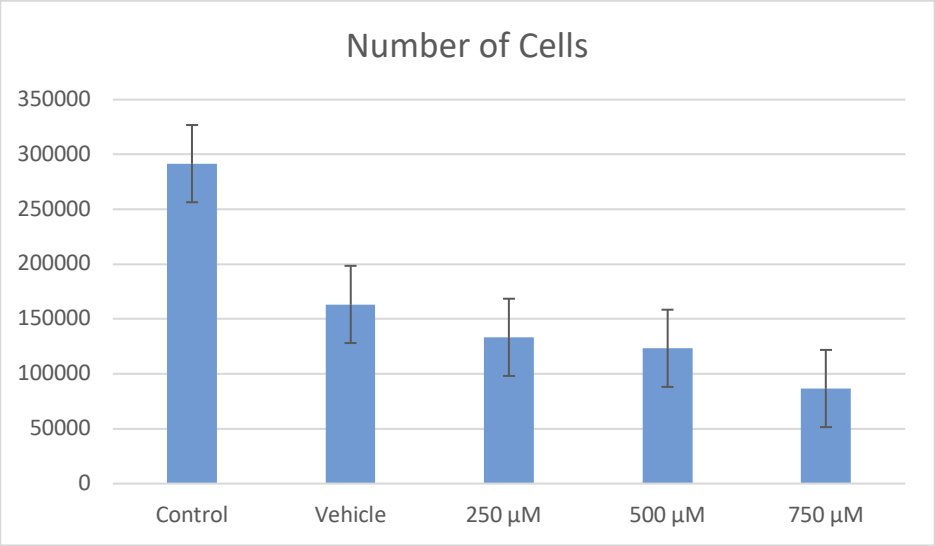

Figure 1: Cell number counts of control, vehicle and MBEH treated (250µM, 500 µM and 750 µM) groups

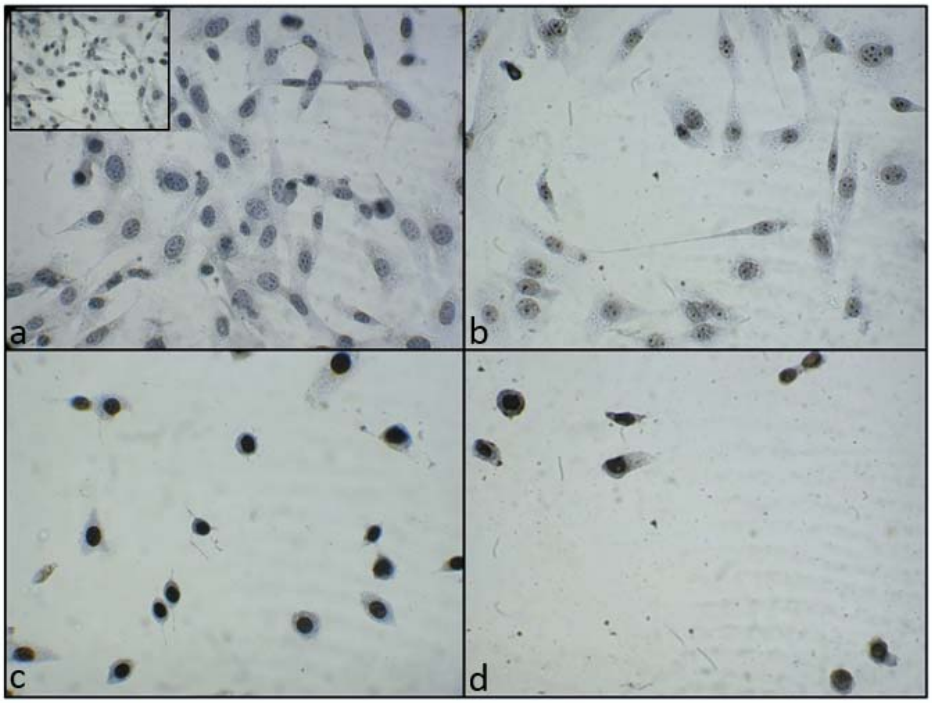

Figure 2: TUNEL staining of control (a), vehicle (a-inset), 250 µM MBEH treated (b), 500 µM MBEH treated (c), 750 µM MBEH treated (d) groups.

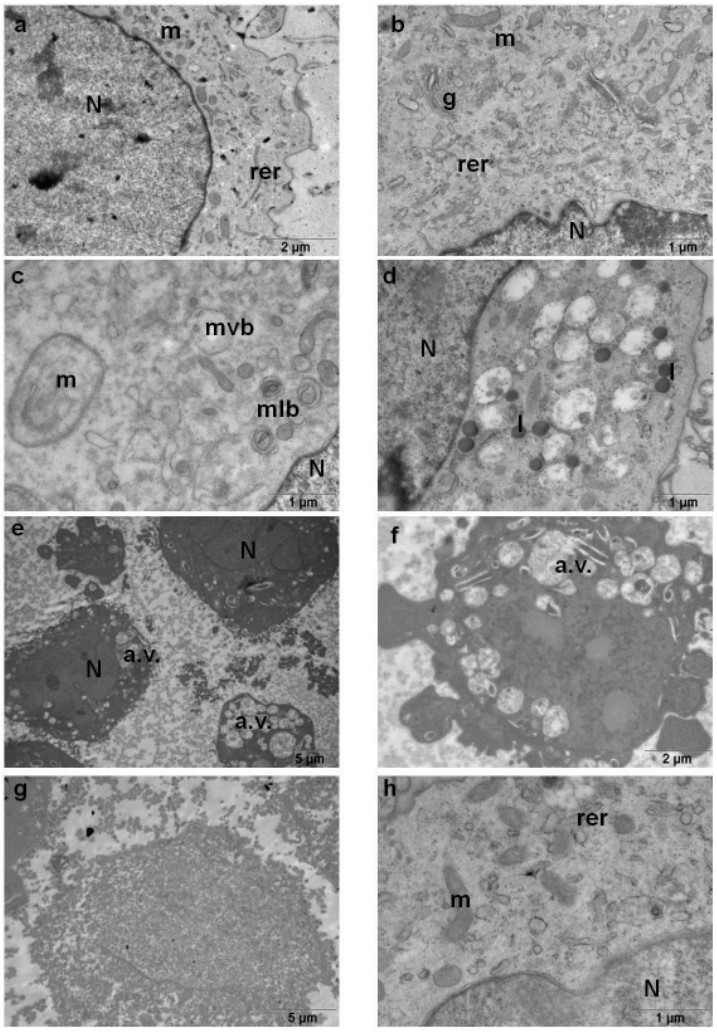

Figure 3: Control group (a,b): Intact morphology of cells were seen; 250 µM MBEH treated group (c,d): multilamellary and multivesicular bodies, swollen mitochondria and many lysosomes contact with mlv were seen; 500 µM MBEH treated group (e,f): many autophagic vocuoles were seen in cytoplasm of shrunken cells; 750 µM MBEH treated group (g): degenerated cells with ruptured plasma membrane and disrupted organelles; Vehicle group (h): intact morphology similar to control group were seen. N: nucleus, m: mitochondria, rer: roug endoplasmic reticulum, g: Golgi apparatus, mlb: multilamellary body, mvb: multivesicular body, l:lysosome, a.v: autophagic vocuole.

References:

[1] J. L. Bolognia, K. Lapia, S. Somma, Dermatologic Therapy, 14 (2001) 29-34.

[2] J. Bonchak, J. M. Eby, K. A.Willenborg, D. Chrobak, S. W. Henning, A. Krzywiec, S. L. Johnson, I. C. Le Poole, Archives of Biochemistry and Biophysics, 563 (2014) 71-78.

[3] V. Hariharan, J. Klarquist, M. Reust, A. Koshoffer, M. D. Mckee, R. E Boissy, I. C. Le Poole, Journal of Investigative Dermatology, 130 (2010) 211-220.

Soy extract-dependent modifications of the pituitary somatotrophs in rats: stereological, histological and functional study

SVETLANA TRIFUNOVIĆ[1], MILICA MANOJLOVIĆ-STOJANOSKI[1], NATAŠA NESTOROVIĆ[1], NATAŠA RISTIĆ[1], BRANKO FILIPOVIĆ[1], BRANKA ŠOŠIĆ-JURJEVIĆ[1] AND VERICA MILOŠEVIĆ[1]
University of Belgrade, Institute for Biological Research "Siniša Stanković", Department of Cytology, Belgrade, Serbia

Phytoestrogens are naturally occurring plant compounds, basically similar to mammalian oestrogens and their active metabolites. They can bind to the estrogen receptors (ER), and mimic the action of estrogens on target organs, thereby exerting many health benefits when used in some hormone-dependent diseases [1]. On the contrary, phytoestrogens are also considered as endocrine disruptors, substance capable to shift the function of the endocrine system [2]. The study reported here was designed to determine whether a phytoestrogen-containing soy extract could affect the morph-functional features of pituitary somatotrophs (GH cells) in rats.

To analyze the effect of soy extracts (soy-extract contained 40% of isoflavones: genistein ≥10%, daidzein ≥15%, genistin ≥3%, daidzin ≥5%, glicitin ≥1% and glicitein ≥0.5%) on morph-functional parameters of GH cell we used adult orchidectomized rats. The orchidectomized rats were subcutaneously injected: with soy extract (30 mg/kg w.w; S group) dissolved in a minimal volume of absolute ethanol in sterile olive oil, or with same volume of absolute ethanol in sterile olive oil (C group) for 3 weeks. Changes in the pituitary GH cells were evaluated using stereologicall system, controlled by newCAST stereological software package. Pituitary and adenohypophysis volume; and volume density of GH cells were estimated using Cavalieri's principle [3]. A fractionator/physical dissector design with two levels of sampling was used to estimate the total number of GH cells from all examined groups [4]. As the mean volume of a single GH cell is equivalent to the total volume occupied by GH cells divided by their number [5], the cell volume is calculated. Serum GH concentration was determined by Rat/Mouse Growth hormone ELISA test.

The GH cells in both experimental groups were frequently clustered together, but also appeared as single cells in the adenohypophysis. There were more GH imunoreactivity following soy extract treatment vs. control (Figure 1). The volume density of GH cells increased ($p \leq 0{,}05$) by 40% following soy extract treatment vs. control. The total number of GH cells in the S group decreased ($p \leq 0{,}05$) by 15%, while GH cells volume increased 1-fold, compared to the C group. Serum growth hormone concentrations were higher ($p \leq 0{,}05$) in the S group 2-fold when compared to the C group.

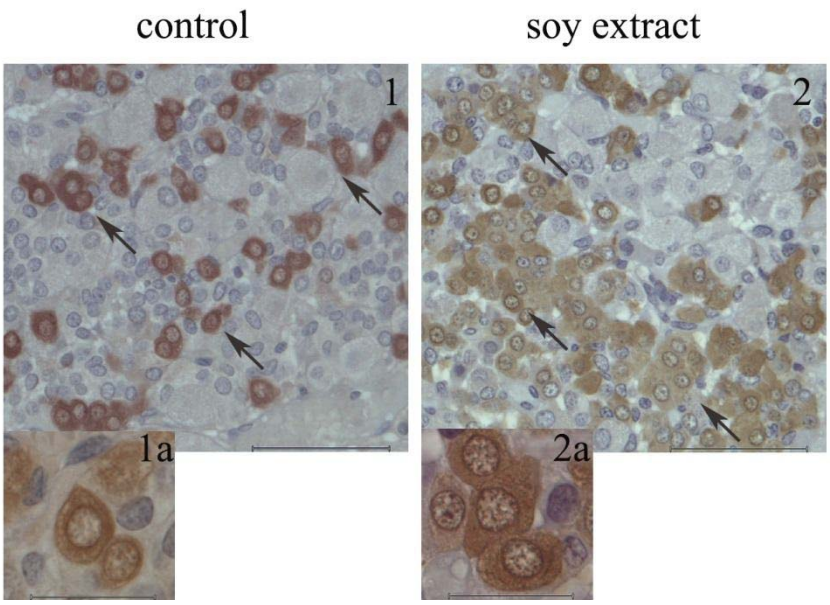

Figure 1. Immunoreactive GH cells in the pituitary in control (1, 1a) and soy extract (2, 2a) treated ratsscale bar 55 µm (1,2), insets scale bar 20 µm (1a, 1b)

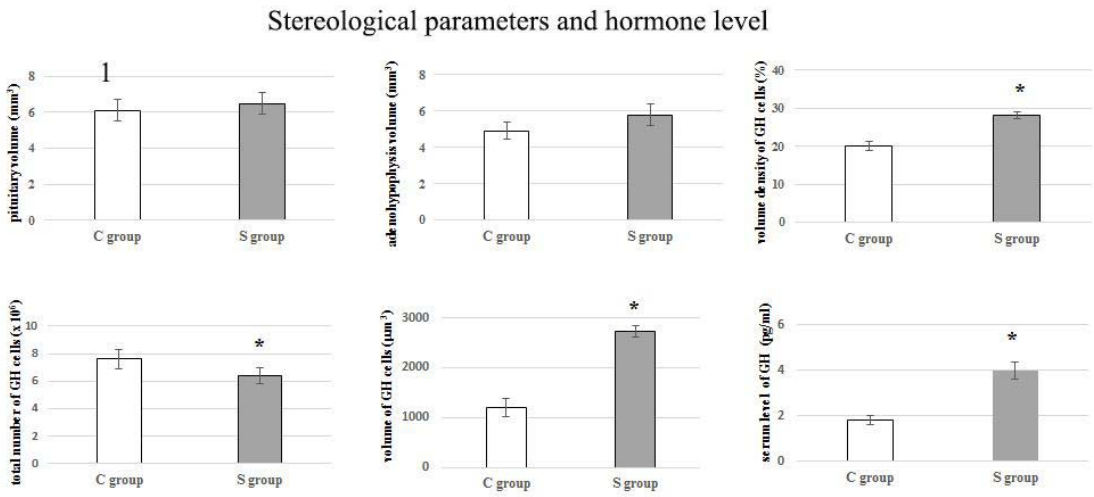

Figure 2. Stereological and hormonal parameters for pituitary GH cells in control (C) and soy extract treated rats: pituitary volume (1), adenohypophysis volume (2), volume density of GH cells (3), total number of GH cells (4), volume of GH cells (5) and serum level of GH (6). The values are means ± standard deviation, n = 6 animals per group * $p<0.05$ vs. C.

Following soy extract treatment, the increase of GH cell volume density was observed. Since, the pituitary as well as adenohypophysis volume were unchanged the enhancement was consequence of the altered percentage ratio of pituitary-producing cells affter soy extract treatment. Also, the observed increase may be result of phytoestrogen's indirect action *via* growth hormone releasing hormone (GHRH) and direct *via* ER, expressed in GH cells [6]. In contrast, the total number of GH cells decreased, probably as a result of the transdifferentiation of the plurihormonal cells [7]. Finally GH level were increased, so we could conclude that changes of stereological parameters following soy extract treatment provoked the increase of GH cells action.

Refrences:

[1] S. Lecomte, F. Demay, F. Ferrière, et al., Int J Mol. Sci., 18 (2017) 1381

[2] H. B. Patisaul, W. Jefferson, Front Neuroendocrino., 31 (2010) 400-419

[3] H. J. Gundersen, E.B. Jensen, J Microsc., 147 (1987) 229-263

[4] M. Manojlović-Stojanoski, N. Nestorović, N. Ristić, et al., Microsc. Res. Tech., 73 (2010) 1077-1085

[5] A. R. de Lima, J. R. Nyengaard, A. A Jorge, et al. Growth Horm. IGF Res., 17 (2007) 480-491

[6] G.V. Childs, Arch. Physiol. Biochem., 110 (2002) 42–49

[7] E. Seuntjens, A. Hauspie, H. Vankelecom, et al. J Neuroendocrinol., 14 (2002) 611-619

The Role of p-IRE1 in the Pathogenesis of Endometriosis: The Contrubition of Peritoneal Fluid

TUĞBA EKIZ YILMAZ[1], BAŞAK IŞILDAR[1], ALTAY GEZER[2], DUYGU KANKAYA[3], CEVRIYE CANSIZ ERSÖZ[3], ÜMIT KAYIŞLI[4], ELIF GÜZEL[1]

[1] Istanbul University-Cerrahpaşa, Cerrahpaşa Faculty of Medicine, Department of Histology and Embriology, Istanbul, Turkey; [2] Istanbul University-Cerrahpaşa, Cerrahpaşa Faculty of Medicine, Department of Obstetrics and Gynecology, Istanbul, Turkey; [3] Ankara University, Ankara Faculty of Medicine, Department of Medical Pathology, Ankara, Turkey; [4] University of South Florida Faculty of Medicine, Department of Obstetrics and Gynecology, Tampa, USA

Introduction: Endometriosis is the growth of endometrial glands and stroma outside the uterine cavity (1). Accumulation of unfolded proteins in the lumen of the endoplasmic reticulum (ER) cause ER stress and induce the unfolded protein response (UPR) (2). Peritoneal fluid (PF) is a cell and protein rich liquid and plays an important role in the pathogenesis of endometriosis (3). The aim of this study was to demonstrate the role of p-IRE1, one of the UPR signal protein, in the pathogenesis of endometriosis in vivo and the activation of p-IRE1 under the influence of PF in human endometrial stromal cells (ESCs) in vitro.

Materials and Methods: Normal, eutopic and ectopic endometrium tissues were divided into menstrual cycle phases (early and late proliferative, early and late secretory) and cyclic changes of p-IRE1 immunoreactivities were evaluated immunohistochemically in these tissues. On the other hand ESCs were treated with 10%-20% concentration of control PF (N-PF) and PF taken from patient with endometriosis (E-PF) for 10-30-60 min and 24-48 hr and p-IRE1 immunoreactivity were evaluated immunocytochemically in these cells. Both in vivo and in vitro p-IRE1 immunoreactivities were analyzed by H-Score method. The data were compared statistically and $p<0.05$ was considered to be significant.

Results: In normal endometrial glandular epithelium and stromal cells, p-IRE1 expression in late proliferative phase was lower compared to all other phases ($p<0.05$; $p<0.001$; $p<0.001$; respectively). p-IRE1 expression in late secretory phase was higher compared to early proliferative and early secretory phases ($p <0.05$). In eutopic endometrium, p-IRE1 expression in late proliferative phase was lower compared to late secretory phase in glandular epithelium

and stromal cells (p<0.05). In ectopic endometrial glandular epithelium, p-IRE1 expression in late proliferative phase was lower than to all other phases. (p<0.05; p<0.001; p<0.05, respectively). In ectopic endometrial stromal cells, p-IRE1 expression in late proliferative phase was lower compared to only late secretory phase (p<0,05).

When normal, eutopic and ectopic endometrium samples were compared; in early proliferative phase, p-IRE1expression was higher in both endometrial glandular epithelium and stromal cells of ectopic endometrium compared to the eutopic and normal endometrium (p<0,001, p<0,05; p<0,05 respectively). In late proliferative phase, there was no statistical difference between p-IRE1 expressions in normal, eutopic and ectopic endometrial glandular epithelium and stromal cells. In early secretory phase, while p-IRE1 expression was higher in ectopic endometrial glandular epithelium than eutopic endometrium (p<0,05), it was not statistically different in stromal cells. In late secretory phase, p-IRE1 expression was higher in eutopic endometrium than normal endometrium in glandular epithelium (p<0,05) and there was no statistical differences in stromal cells.

When the in vitro findings were evaluated, p-IRE1 expression in ESCs treated by low concentration of E-PF was not statistically different compared to ESCs treated by N-PF at 10-30-60 min. p-IRE1 expression was significantly increased in high concentration of E-PF treated ESCs at 10-30-60 min compared to N-PF (p<0,05). In addition, in E-PF treated ESCs, p-IRE1 expression decreased at 24 and 48 hr compared to 10, 30 and 60 min both in low concentration (p<0,05, p<0,001, respectively) and high concentration (p<0,001).

Conclusion: It was shown that p-IRE1 pathway activated in endometriotic tissue and p-IRE1 expression were increased as a result of high concentration exposure to E-PF in ESCs. Thus, this signal protein may be used as a potential biomarker both for the diagnosis of endometriosis and the development of therapeutic tools.

References

1. P. Vercellini, P. Vigano, E. Somigliana, L. Fedele, Nat Rev Endocrinol, 10(2014), 261-275.

2. Y. Wang, J.H. Wang, X.L. Zhang, X.L. Wang, L. Yang, Oncol Lett, 15(2018), 6087-6093.

3. M. Koutsilieris, L. Allaire-Michaud, M. Fortier, A. Lemay, 56(1991), 888-93.

Effects of knock-down of adhesive proteins on the ultrastructure of adhesive vesicles in the flatworm Minona ileanae

WILLI SALVENMOSER[1], ROBERT PJETA[1], TERESA HOFER[1], MICHAEL W. HESS[2] AND PETER LADURNER[1]

[1] Institute of Zoology and Center for Molecular Biosciences Innsbruck (CMBI), University of Innsbruck, Austria; [2] Division of Histology and Embryology, Medical University Innsbruck, Austria

Adhesive organs are common among free-living Platyhelminthes. They are used for temporary adhesion, i.e to attach to and release from the substrate. Frequently, they are concentrated at the tail, or tail plate of the animals. One single organ consists of three different cell types. One modified epithelial cell, called anchor cell, one adhesive gland cell and one releasing gland cell. Here we describe the adhesive system of *Minona ileanae*. The cell bodies of the gland cells are located within the tail and long gland cell necks proceed towards the tail plate, branch and lead into adhesive pads formed by the anchor cells. The adhesive vesicles of chemically fixed animals are ellipsoid and show a length of 456±72 nm and a width of 214±26 nm (n = 60). The releasing vesicles are spherical with a diameter of 99±8 nm (n = 75). Adhesive vesicles showed ring like substructures if cross sectioned and appeared as stripes if longitudinally cut, a morphological feature not found in other flatworms so far. Five adhesive proteins were identified with differential transcriptome analysis and subsequent in situ hybridisation screen. They were named Mile-ap 1-5 (*Minona ileanae* adhesive protein 1-5). Knockdown of these proteins with RNA interference (RNAi) revealed a less adhesive phenotype. RNAi of Mile-ap1showed spherical adhesive vesicles with a pronounced dark centre and an electron-lucent periphery. RNAi of Mile-ap2 showed an ellipsoid dense adhesive vesicle similar to the wildtype but no lucent periphery. In RNAi Mile-ap3 adhesive vesicles were missing the electron dense core. RNAi of Mile-ap3 and Mile-ap4 showed the same results. RNAi of Mile-ap5 led to a concentric zonation of the vesicle with a lack of electron dense material in the vesicle centre. Adhesive vesicles of a Luciferase RNAi negative controls did not show differences to the wildtype animals. Luciferase is a gene which is not present in flatworms and thus was taken as a negative control. RNAi of an intermediate filament (Mile-if1) showed collapsed adhesive organs and was used as a positive control. The investigation of the molecular mechanisms of bioadhesion in flatworms can lead into a development of non-toxic biomimetic glues with reversible properties.

This project was funded by the Austrian Science Fund (FWF) P 30347, the Tyrolean Science Fund and COST Actions TD0906 and CA15216.

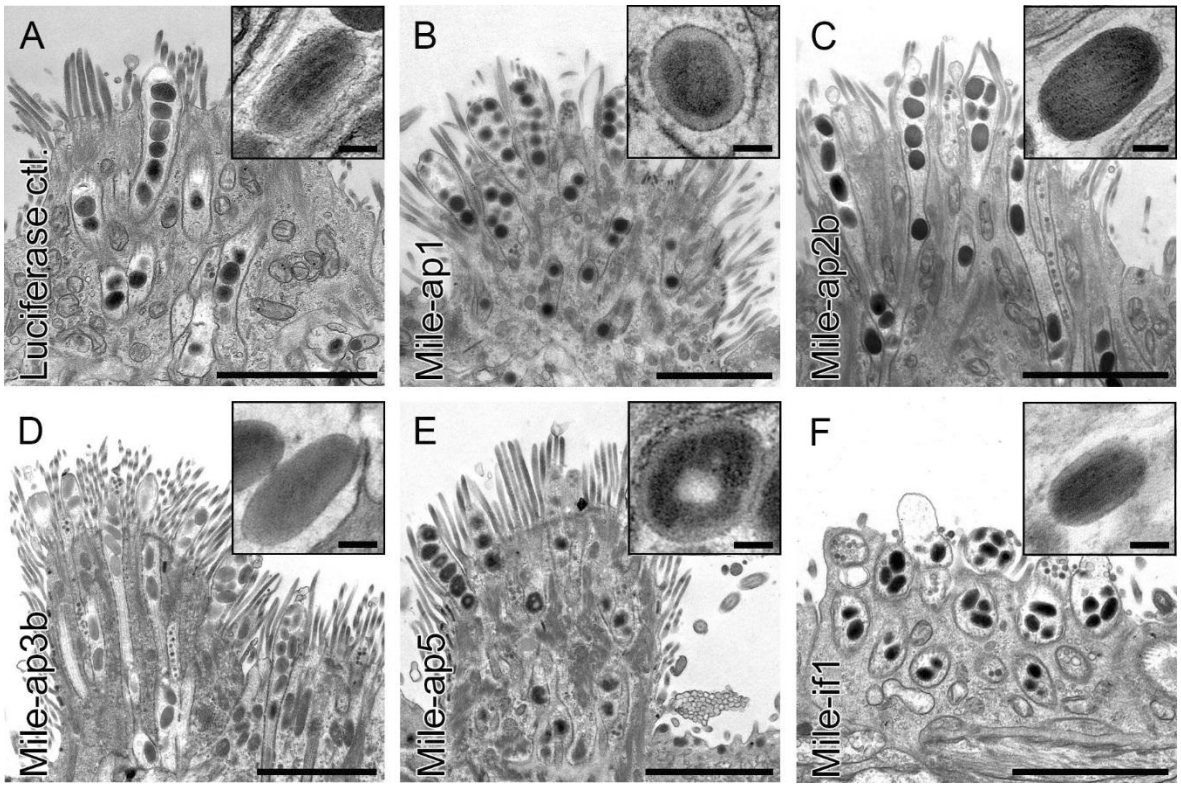

Fig.1: Results of RNAi knock down of different adhesion proteins in *Minona ileanae*.

(A) Luciferase control with normal adhesion vesicles. (B) RNAi of Mile-ap1 with spherical vesicles with prominent dark centre and bright periphery. (C) RNAi of Mile-ap2 with dark ellipsoid adhesion vesicles. Please note the absence of the bright periphery. (D) RNAi of Mile-ap3 with lacks the dense core. Mile-ap4 showed the same results as Mile-ap3. (E) RNAi of Mile-ap5 led to a concentric zonation of the vesicle with a lack of electron dense material in the vesicle centre. (F) RNAi of Mile-if1 positive control showed a collapsed adhesive organ but regular adhesive vesicles. Scale bars: (A-F) 2 µm; (Insets) 100 nm.

Electroporation: new strategy to improve the drug uptake and overcome the tumor resistance

MARIA CONDELLO, GLORIA D'AVACK AND STEFANIA MESCHINI
National Center for Drug Research and Evaluation, Istituto Superiore di Sanità, Roma, Italy

Electrochemoterapy (ECT) is an increasingly common and innovative therapeutic strategy to overcome the multidrug resistance (MDR) phenomenon of several neoplasms [1]. The anticancer treatment combines the administration of a chemotherapeutic agent with the application of electric pulses having appropriate waveforms to increase drug uptake [2]. The main goal of our project is to increase the effectiveness of the chemotherapy drugs used in human medicine by means of a non-toxic and well tolerated mechanical system. Its efficacy, as adjuvant therapy, has been already demonstrated in veterinary patients, in combination with several anticancer agents resulting in enhanced cytotoxicity [3]. Initial studies focused on the effects of doxorubicin (DOX) on MDR human colon adenocarcinoma cell line LoVo DX confirmed the chemosensitizing effect of the ECT by using trains of biphasic pulses. The in vitro experiments of the combinatorial treatment (DOX + ECT) gave the following results:

1) Enhancement of DOX accumulation in cell suspension after the electroporation evaluated by flow cytometry

2) Increase of the drug intranuclear localisation through observations made under confocal microscopy (Figure 1)

3) Evident morphological changes through the observation by scanning electron microscopy

4) Tumour destruction and replacement by scar tissue underlined by histopathological analysis.

To validate the action mechanism of the combined therapy, we tested two squamous carcinoma cell lines, tongue (CAL27) and pharynx (FaDu), using mitomycin C (MMC). We performed the cytotoxic test (MTT) measuring mitochondrial enzymatic activity, to analyse the cell viability of both lines after single electrochemotherapy, MMC and combined treatment (E + MMC). Our results showed a 20% reduction in cell viability after the combined E + MMC treatment. Samples treated with electroporation alone had the same cellular viability as the control. Further studies will be carried out to confirm the cytotoxic damage and assess the role of electrochemotherapy in the pharmacological resistance phenomenon.

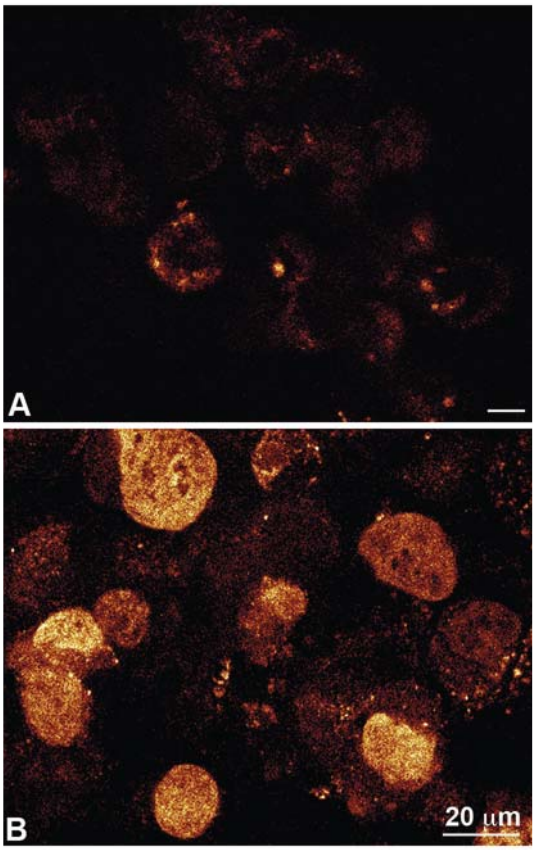

Figure 1. Laser scanning confocal microscopy (LSCM) images showing the intracellular localization of doxorubicin (DOX) in living LoVo DX cells after 3h of incubation. The nuclei of the cells treated with DOX (1 µg/ml) alone were negative while the cytoplasm showed a weak fluorescent signal (A). The cells exposed to the combined treatment (electroporation with DOX) displayed an increase of the intracellular drug uptake, preferentially in the nucleus (B).

References

[1] P. Pasquali, E. P. Spugnini, A. Baldi Dermatol Ther (Heidelb), 8 (2018) 143-146
[2] S. Meschini, M. Condello, P. Lista, B. Vincenzi, A. Baldi, G. Citro, G. Arancia, E. P. Spugnini Eur J Cancer, 48 (2012) 2236-43
[3] E. P. Spugnini, F. Menicagli, M. Pettorali, A. Baldi Open Vet., 7 (2017) 57-60

MATERIAL SCIENCES

MS1
Metals, alloys and intermetallics

CHAIRPERSONS:

Matjaž Godec, Željko Skoko

INVITED LECTURE

Analysis of inclusions in steels: a correlatve approach

BARBARA ŠETINA BATIČ, JAKA BURJA AND MATJAŽ GODEC
Institute of Metals and Technology, Ljubljana, Slovenia

Steels are still an important material in today's society. While the first metallurgists had only a limited number of tools to control their steelmaking process, and most of the discoveries were made by the trial and error method, nowadays the possibilities for a better insight into the process are made available with modern tools and techniques.

Today's steelmakers are striving to control non-metallic inclusions in the steel, in an ordeal to achieve a steel with high cleanliness. Even though non-metallic inclusions cannot be completely avoided, the trend is to make them smaller and as evenly as possible dispersed in the matrix phase. First studies of inclusions were made by utilizing an optical microscope, and a lot of work is still performed in this way. The presence of scanning electron microscopes, equipped with an EDS analyser, in many steelmaking plants have shown the benefits of additionaly determining the composition of the inclusions, which is not possible by optical microscope. Additionally, electron backscatter diffraction studies of the inclusions can give and additional insight into the formation and crystallographic type of the formed inclusions.

Microalloying of steels is an important way to control inclusion size, type and density in the final product. This contribution will present a complete study of microalloying, from preparation of the material to the characterization of microstructure and inclusion content, in various steel grades with different alloying elements.

Acknowledgment: The authors acknowledge funding from project ČMRLJ (Doseganje Čistosti in lastnosti z MikRo Legiranjem Jekel).

INVITED LECTURE

Single-step preparation of the mixed-metal oxides from the versatile oxalate precursors – characterization and properties

MARIJANA JURIĆ, LIDIJ ANDROŠ DUBRAJA, JASMINKA POPOVIĆ AND LIDIJA KANIŽAJ
Ruđer Bošković Institute, Zagreb, Croatia

Mixed-metal oxides are an important class of advanced materials due to their chemical stability, low cost, low toxicity, large scale of useful photophysical properties and wide range of technological applications. It is known that the microstructure of oxide materials can be tuned in part by changing the synthesis methods. Full control over particles dimensions and morphology is also prerequisite for the photocatalytic applications of oxide materials where large surface area promoting substrate adsorption at the surface and increasing the number of active sites, is considered to be an imperative. However, in general, synthesis approaches for obtaining highly crystalline materials utilize high temperature treatments, which often lead to the increase of particle size and consequently the decrease of the surface area. Thus, it is still challenging to attain both high crystallinity and high surface area in the same synthesis. Due to these limitations, in recent times, heteropolynuclear systems have been used as molecular precursors for the preparation of the mixed-metal oxides by their thermal decomposition. It has been observed that the use of a well-defined precursor can produce crystalline oxide materials under conditions that are significantly milder than those applied in traditional solid-state synthesis. Also, the single-source precursors provide better control over the stoichiometry of the metal ions in the final products as well as the homogeneity of the materials due to the mixing of the metals at the molecular level, and offer kinetically attractive low temperature decomposition. An effective *molecular precursor-to-material* conversion requires a reasonable choice of ligands. The nature of the ligand employed endows the precursor with a clean, low-temperature thermolysis leading to the phase-pure target material. Importantly, low cost of the ligand makes heterometallic precursor highly attractive to industrial applications. One of the suitable ligands for the synthesis of molecular precursors for oxides is the oxalate dianion, $C_2O_4^{2-}$, due to its easily decomposition on gaseous CO_2 and CO at low temperatures. Another advantage of this ligand is low cost. However, heterometallic complexes do not always contain the appropriate stoichiometry for the formation of the desired single phase oxide by thermal degradation in one step. Also, it is not easy to prepare coordination compound with three or more different metals (in an appropriate ratio), having also suitable coordinated ligand. So, sometimes multimetallic oxides could be prepared by mixing two or more agreeable precursors in appropriate ratio prior to thermal decomposition.

In our group we explore the ability of the heterometallic oxalate-based complexes to act as the single-source precursors for the formation of the mixed-metal oxides by heat treatment. We focused on the structural, optical, photocatalytic, and magnetic properties of the (nano)crystalline oxides prepared for the first time by facile *molecular precursor-to-material* route, investigated by electron microscopy, UV-vis diffuse reflectance spectroscopy and magnetization measurements, where long-term heating at high temperatures and repeated grinding procedures are successfully bypassed [1, 2].

References

[1] J. Popović, M.Jurić, D. Pajić, M. Vrankić, J.Zavašnik, J. Habjanič, Inorg. Chem. 56 (2017) 3983-3989
[2] L. Androš Dubraja, D. Pajić, M.a Vrankić, J. Dragović, M. Valant,M.Benčina, M. Jurić, J. Am. Ceram. Soc. (2019) DOI:10.1111/jace.16521

Microstructure and properties of Al-Fe-Mm-Mg-Si alloy prepared by powder metallurgy

ALENA MICHALCOVÁ, ANNA KNAISLOVÁ, ZDENĚK KAČENKA, JAN ZÁBRODSKÝ AND IVO MAREK

Department of Metals and Corrosion Engineering, Univeristy of Chemistry and Technology in Prague, Czech Republic

Aluminium alloys are widely used materials due to their strength to weight ratio. Industially produced alloys has already reached their performance limits. It means that it is not possible to increase their mechanical properties by further alloying. It is necessary to introduce nonconventional methods, e.g. powder metallurgy. Melt spinning can completly change phase composition of the alloy, introduce new phases and incerase solutibily of alloying elements in the Al matrix. The second step in milling of rapidly solidified ribbons followd by powder compaction. Spark plasma sintering is progresive compaction method with limited thermal influence to the material.

In this work, the Al-Fe-Mm-Mg-Si alloy was prepared by melt spinning and subsequently compacted by spark plasma sintering (SPS). Microstructure of bulk material was observed by optical microscope (Olympus PME 3), scanning electrone microscope (TESCAN VEGA 3 LMU) and transmission electron microscope (Jeol 2200 FS).

Acknoledgement
Authors thank for financial support by Czech Science Foundation, project No. GJ17-25618Y.
The authors acknowledge the assistance in TEM sample preparation provided by the Research Infrastructure NanoEnviCz, supported by the Ministry of Education, Youth, and Sports of the Czech Republic under Project No. LM2015073.

Characterization of nano-sized particles in 14%Cr oxide dispersion strengthened (ODS) steel using classical and frontier microscopy methods

YAEL TEMPLEMAN[1], SERGEY ROGOZHKIN[2,3], ARTEM KHOMICH[2], ALEKSANDER NIKITIN[2,3], MALKI PINKAS[4], LOUISA MESHI[1]

[1] Department of Materials Engineering, Ben Gurion University of the Negev, Israel; [2] Institute for Theoretical and Experimental Physics named by A.I. Alikhanov of National Research Centre «Kurchatov Institute», Moscow, Russia; [3] National Research Nuclear University «MEPhI», Moscow, Russia; [4] Nuclear Research Center-Negev, Beer-Sheva, Israel

Oxide dispersion strengthened (ODS) steels exhibit superior mechanical properties and irradiation resistance due to the nano-sized oxides, highly dispersed in metallic matrix [1, for example]. These properties change as a function of the structure, composition, size and density of the nano-sized oxides. Thus, characterization of these oxides is crucial. Despite the numerous reports on this subject, ambiguity remains. In the present study, characterization of the crystallographic structure of oxide particles existing in 14%Cr ODS steel was performed using classical and novel transmission electron microscopy (TEM) methods. 3D dispersion, density and composition of these oxides were evaluated by atom probe tomography (APT).

Nano-sized particles observed in the studied ODS steel varied greatly in size. It was possible to classify them into several populations. The largest particles in this steel were characterized using classical TEM methods as TiC (FCC) with a typical size of 100-150 nm. An example of such particle is shown in fig 1 (bottom right). This type of particles was the least frequent in the studied steel. Other large oxide particles with sizes of 50-150 nm belong to the second population, see fig 1 (bottom left). Energy Dispersive Spectroscopy (EDS) analysis preformed on these particles found that they are composed mainly of Y, Ti and O. The distribution of this type of particles was significantly higher than of TiC. In addition, dense distribution of nano-sized particles, varying from several to 20 nm, was observed in this steel. Due to their nanometric size, they were hard to detect on bright field (BF) TEM images. However, dark field (DF) images obtained from an extra (e.g. in addition to the Fe matrix`) reflections in the electron diffraction (ED) pattern enabled to observe them very clearly, see fig 1 (upper panel). These nano-particles were sometimes observed at the grain boundaries, and sometimes in the grains' interior, respectively. APT results allowed concluding that the nanosized oxides are composed of O, Fe, Ti, Cr and a negligible amount of Y.

Characterization of the relatively large oxide particles was performed using Electron Diffraction Tomography (EDT) method [2], since indexing of conventional ED patterns taken in the selected area (SAED) mode were ambiguous. For the EDT analysis, extraction replica TEM sample was prepared to eliminate the contribution of the matrix to the ED patterns and EDS measurements. Following manual data collection, the frames were merged using the EDT-process software which enables to reconstruct a 3D projection of the reciprocal space. Following a successful reconstruction, a list of d_{hkl} and intensities was extracted. The projections of the highest symmetry, i.e. [100], [010] and [001] are shown fig 1, bottom row. Their net symmetry was evaluated as 2*mm*. Thus, the crystal system was classified as orthorhombic and unit cell parameters were obtained. Analysis of the dataset intensities allowed deducing the following reflection conditions: h00 h=2n; 0k0 k=2n; 00l l=2n; hk0 h+k=2n; 0kl k+l=2n. These conditions belong to the P*n*_*n* extinction (diffraction) symbol, i.e. P*n*2*n* (34) or P*nmn* (58) space groups. According to the PDF4+ (2018)

database, the $YTiO_3$ with a distorted perovskite structure exists with close to the obtained here lattice parameters and P*nmn* space group. Thus, studied particles were attributed to this structure. In order to prove that the particles in the matrix had the same structure as those in the replica, ED patterns of the particles embedded in the matrix (e.g. original bulk TEM sample) were analyzed and successfully indexed in terms of the $YTiO_3$ structure. It should be noted that these patterns could not been indexed in terms of any other Y-Ti-O or Ti-O known structures. Moreover, the lattice parameters determined by EDT were somewhat different from the JCPDF card of the $YTiO_3$ structure. The new lattice parameters allowed immediate indexing of all patterns. In vast majority of the reports on ternary oxides in these steels other Y-Ti-O structures were noted, but the characterization was always ambiguous (e.g. one orientation ED and/or Fast Fourier Transform (FFT) of High resolution TEM). Here, the results were verified by two independent methods - zone axis ED patterns, taken from the bulk specimens and EDT data from the replica.

Smallest oxide particles were very difficult to characterize due to the fact that Fe matrix also contributed to the ED patterns and, furthermore, there exist distinct orientation relationship (OR) between the oxides and the matrix. Their crystallographic structure was determined here using the superimposed matrix/oxide ED patterns. ED patterns taken from [100] and [110] orientations of the matrix contained diffused scattering and some extra spots originated by these nanoparticles. In the [111] orientation, however, no additional spots had appeared. These Fe ED patterns were found to be identical to the reported in literature superimposed ED patters of Fe and its native oxide films [3, for example]. In order to verify that in our case these oxides are not native, the samples were cleaned using precision ion polishing system (PIPS) before each TEM session. We have successfully indexed these patterns in terms of Fe,Cr,Ti-O oxides with $MgAl_2O_4$-type spinel structure having Bain and Kurdjumov-Sachs ORs for the $[100]_{Fe}$ and $[110]_{Fe}$ orientations, respectively. Spinel structure is rarely reported in the literature regarding ODS steels. In fact, we have found only one article [4], which had reported existence of spinel $TiCr_2O_4$ in ODS. Our case is different, since measured by APT composition is not $TiCr_2O_4$ and our particles exhibit unique nano-size and uniform distribution. Correct and unambiguous characterization of nano-sized particles, attributing the strength to this ODS steel (which is potential candidate to be used as structural material in the IV generation nuclear reactors) – is a major breakthrough allowing full understanding of this steel`s properties.

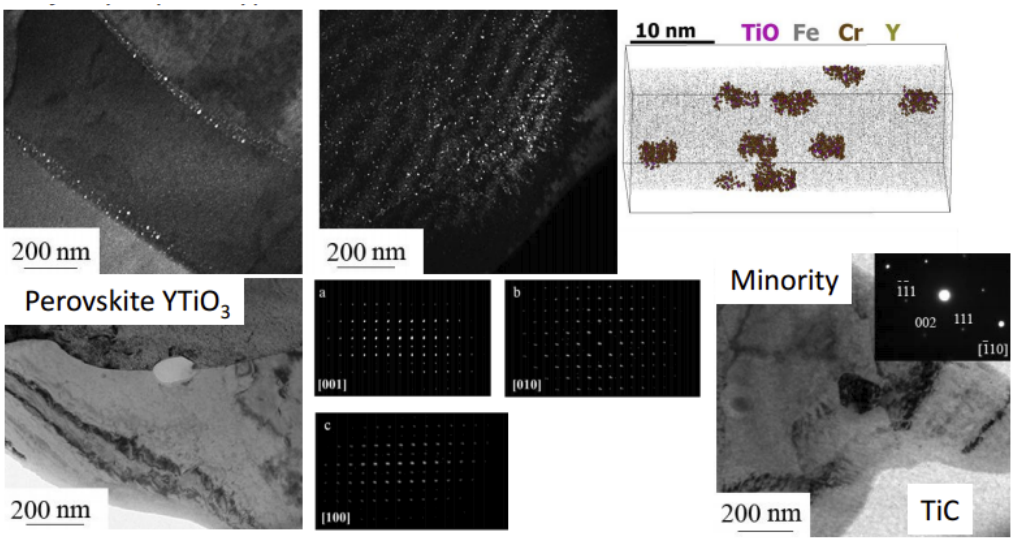

Figure 1: Upper panel: characterization of majority of particles. DF TEM images illustrate distribution of these particles in different grains. APT image shows their size and composition. Bottom panel: characterization of other particles as perovskite $YTiO_3$ (with three major orientations taken from EDT data) and TiC.

References:

[1] S. Ukai and M. Fujiwara, J. Nucl. Mater. **307–311**, 749 (2002).
[2] A. S. Eggeman, R. Krakow, and P. A. Midgley, Nat. Commun. **6**, 1 (2015).
[3] K. Kuroda, B.D. Cahan, T.E. Mitchell, J. Electrochem. Soc. **129** (1982) 2163.
[4] C. Lu, Z. Lu, R. Xie, C. Liu, and L. Wang, J. Nucl. Mater. **455**, 366 (2014).

Precipitation Behavior in an Intermetallic Fully Lamellar TiAl Alloy

MICHAEL BURTSCHER[1,3,*], MARTIN SCHLOFFER[2], DANIEL KIENER[3], HELMUT CLEMENS[1] AND SVEA MAYER[1]

[1] Department Materials Science, Chair of Physical Metallurgy and Metallic Materials, Montanuniversität Leoben, Austria; [2] MTU Aero Engines AG, Munich, Germany; [3] Department Materials Science, Chair of Materials Physics, Montanuniversität Leoben, Austria

Intermetallic TiAl alloys are applied as structural materials in aero engines and in the automotive sector for the production of turbine blades, valves and turbocharger wheels [1]. These alloys allow the substitution of Ni-base alloys in these applications due to their lower density of about 4.2 g/cm^3 [1,2]. Therefore, the moving mass of engine parts can be reduced drastically, which leads to faster acceleration at the start and lower fuel consumption during operational conditions [3]. Their advantage in the field of high temperature materials is attributed, moreover, to their high specific yield strength, resistivity against Ti-fire and excellent creep properties up to high temperatures. A promising alloy thereof is the TNM alloy with a nominal composition of Ti-43.5Al-4Nb-1Mo-0.1B (in at.%) [1,4]. As a result of the Al content, solidification via the single β phase field region takes place. This disordered high temperature β phase exhibits a body-centered cubic (bcc) crystal structure and is responsible for the good deformation behavior of the alloy [2,5]. During solidification, grain refinement due to the $\beta \rightarrow \beta + \alpha$ transformation as well as ordering reactions ($\alpha \rightarrow \alpha_2$, $\beta \rightarrow \beta_o$) and the precipitation of γ phase occur [6]. At room temperature (RT) the ordered hexagonal α_2-Ti_3Al, the ordered bcc β_o-TiAl and the ordered face-centered tetragonal distorted (c/a~1.02) γ-TiAl constitute the main phases [2,7].

In order to further improve the mechanical properties at high temperature, different alloying elements were evaluated. For example, C addition strongly influences the phase diagram of the Ti-Al system, raises the tensile strength and improves the creep properties [6,8,9]. Due to the modified phase diagram, special heat treatments to adjust a fully lamellar (FL) microstructure are possible [10,11]. This microstructure is favorable during creep and also resistant against cellular reactions in the aspect of long term high-temperature exposure. Furthermore, the addition of Si leads to the presence of ξ-Ti_5Si_3 silicides within the β_o and α_2 phase at RT [10,12]. These precipitations are capable to improve strength and long term stability of the microstructure.

In this work, the focus is on the appearance of different precipitations within a FL microstructure of a C and Si containing TNM alloy variant. Therefore, the alloy was heat treated within the single α phase field region and afterwards annealed to stabilize the formed α_2/γ-colonies. A backscatter electron (BSE) image of the FL microstructure is shown in Figure 1 a). Here, the α_2/γ-colonies exhibit a size of up to 100 µm and contain a small amount of globular γ phase at the colony boundaries [11,13]. Within the colonies bright and dark dots are marked by arrows, whereby, the dark dots represent holes within the sample originating from etched and removed precipitates and the white ones are retained ones.

To distinguish between the different kinds of precipitations, TEM investigations were conducted using a CM12 transmission electron microscope. Here, an acceleration voltage of 120 kV and an analytical holder from GATAN were used to take images in bright (BF) as well as in dark-field (DF) mode. To analyze single precipitates, an EDS system from EDAX applying a Si-detector was used. To achieve an acceptable accuracy, the spot size was decreased to <1 nm and focused in the center of the precipitate during the measurement. Therefore, different sized ζ-Ti_5Si_3 silicides could be identified within the α_2/γ colonies. Their morphology and chemical composition varies slightly

due to the forming mechanism. Silicides, exhibiting a quasi stoichiometric composition and a size of more than 1 µm were formed during the melting process. Smaller ones, with a maximum length of about 100 nm, precipitate during the cooling step after the heat treatment within the single α phase field region. The smallest silicides form during aging, where the alloy system converges to thermodynamic equilibrium. Hence, γ lamellae grow on the extent of α_2 lamellae, where Si is enriched and ζ -Ti_5Si_3 silicides precipitate. It is assumed that the precipitation of ζ -Ti_5Si_3 silicides retards the speed of the moving α_2/γ interfaces and, therefore, has a positive effect on the creep properties [10]. In Figure 1 b) a ζ -Ti_5Si_3 silicide is positioned near a vanishing α_2 lamella. Due to the appearing length and chemical composition, the silicide was formed during the cooling step after the heat treatment within the single α phase field region. Another effect, based on the system's aim to reach thermodynamic equilibrium, is the $\alpha_2 \rightarrow \alpha_2 + \beta_o$ transformation [8,10]. During the heat treatment a small amount of β_o platelets are stabilized within the α_2 lamellae by diffusional processes [10]. Additional DF-TEM images of selected diffraction spots were conducted to prove the existence of β_o phase within the α_2 lamellae. In Figure 2 a) a BF and the corresponding DF image (Figure 2 b) of such β_o phases are shown. A β_o diffraction spot was used to identify the β_o particles within the α_2 lamellae. Dark arrows highlight ζ-Ti_5Si_3 silicides allocated at a former α_2 lamella, which was identified by EDS.

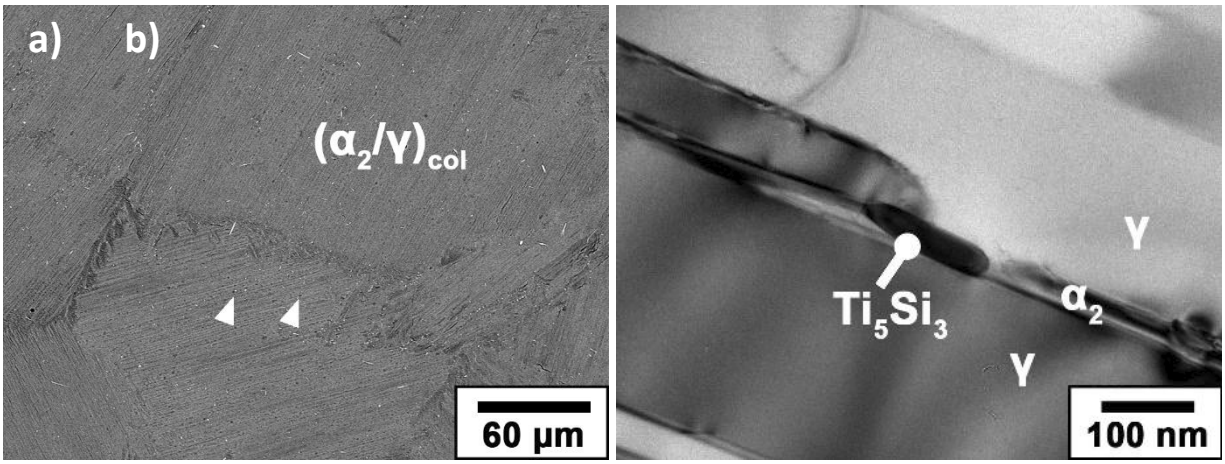

Figure 1. In a) an SEM image in BSE-mode of a FL microstructure of the investigated TiAl specimen is shown. Due to the heat treatment, precipitates (white arrows) are visible within the α_2/γ-colonies; b) depicts a BF-TEM image of α_2 and γ lamellae within an α_2/γ-colony. In the α_2 lamella a ζ -Ti_5Si_3 precipitate is highlighted. In the upper left, an ordinary dislocation is visible within a γ lamella.

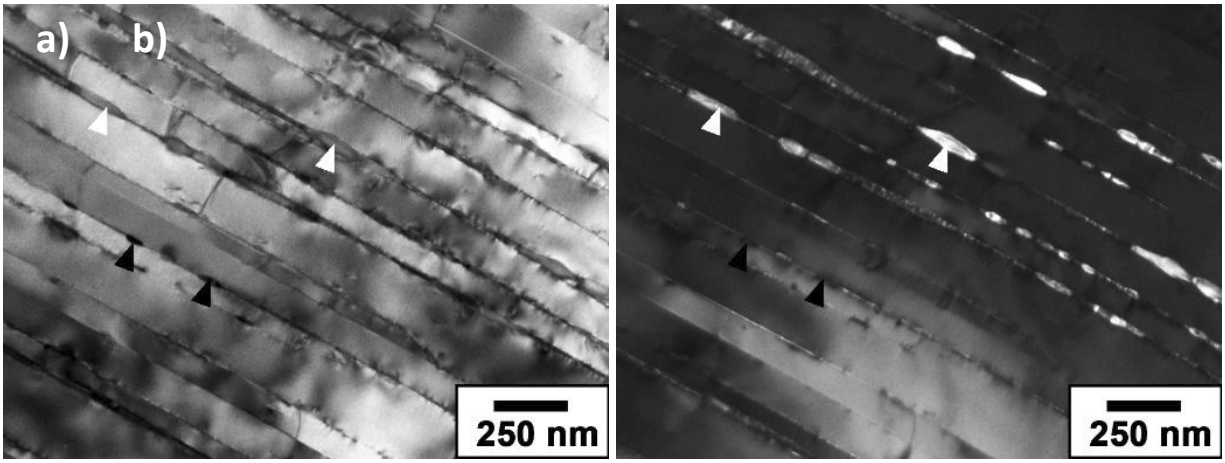

Figure 2. In a) the BF-TEM image of an α_2/γ-colony is shown. Here different plate-like precipitations can be seen within the α_2 lamellae. By the use of a β_o diffraction spot and recording a DF-TEM image b) these particles could be identified as ordered β_o-phase (white arrows).

In summary, in the framework of this study different electron microscopy techniques were used to identify precipitations within the FL microstructure of a C and Si containing TNM alloy variant. Hence, the presence of different composed ζ-Ti_5Si_3 silicides were determined. They were formed during production and different heat treatment steps. Furthermore, the precipitation of β_o phase due to saturation effects within the FL microstructure was proven by DF technique. In future, these precipitates might serve to further improve the high temperature strength and creep properties of the alloying system and this will extend the range of applications [6,8].

Acknowledgement:

*Presently supplied by the European Research Council under Grant number: 771146.

References:

[1] H. Clemens, S. Mayer, Adv. Eng. Mater., 15 (2013) 191–215.

[2] S. Mayer, P. Erdely, F.D. Fischer, D. Holec, M. Kastenhuber, T. Klein, H. Clemens, Adv. Eng. Mater., 19 (2017) 1600735.

[3] K. Gebauer, Intermetallics, 14 (2006) 355–360.

[4] H. Clemens, W. Wallgram, S. Kremmer, V. Güther, A. Otto, A. Bartels, Adv. Eng. Mater., 10 (2008) 707–713.

[5] F. Godor, R. Werner, J. Lindemann, H. Clemens, S. Mayer, Mater. Sci. Eng. A, 648 (2015) 208–216.

[6] E. Schwaighofer, B. Rashkova, H. Clemens, A. Stark, S. Mayer, Intermetallics, 46 (2014) 173–184.

[7] F. Appel, J.D.H Paul, M. Oehring, Gamma Titanium Aluminide Alloys: Science and Technology, Wiley-VCH, Weinheim, 2011.

[8] M. Kastenhuber, T. Klein, H. Clemens, S. Mayer, Intermetallics, 97 (2018) 27–33.

[9] R. Gerling, F.P. Schimansky, A. Stark, A. Bartels, H. Kestler, L. Cha, C. Scheu et al., Intermetallics, 16 (2008) 689–697.

[10] T. Klein, L. Usategui, B. Rashkova, M.L. Nó, J. San Juan, H. Clemens, S. Mayer, Acta Mater., 128 (2017) 440–450.

[11] M. Beschliesser, A. Chatterjee, A. Lorich, W. Knabl, H. Kestler, G. Dehm, H. Clemens, Mater. Sci. Eng. A, 329-331 (2002) 124–129.

[12] T. Klein, B. Rashkova, D. Holec, H. Clemens, S. Mayer, Acta Mater., 110 (2016) 236–245.

[13] F. Herrouin, D. Hu, P. Bowen, I.P. Jones, Acta Mater., 46 (1998) 4963–4972.

A microstructure development during intercritical annealing of ductile iron – the dual phase austempered ductile irons

PETAR JANJATOVIC[1], DRAGAN RAJNOVIC[1], OLIVERA ERIC CEKIC[2], SEBASTIAN BALOS[1], LEPOSAVA SIDJANIN[1]

[1] University of Novi Sad, Faculty of Technical Sciences, Department of Production Engineering, Novi Sad, Serbia; [2] University of Belgrade, Faculty of Mechanical Engineering, Innovation Centre, Belgrade, Serbia

1. Introduction

The development of the auto industry showed the continuous need for improving the strength of ductile irons. The preferable method is heat-treatment (austempering), in order to obtain ausferrite microstructures, and thus increase the mechanical properties. The ausferrite is a mixture of ausferritic ferrite and carbon enriched retained austenite [1], and the new material is known as the Austempered Ductile Iron (ADI). The ADI has a remarkable combination of high strength, toughness, and ductility, as well as good fatigue resistance and wear [2-5]. By further advancement of ADI materials, a Dual Phase Austempered Ductile Iron (DP-ADI) was created [6-8]. The dual phase microstructure is obtained by intercritical annealing (partial austenitization) in the (α+γ+graphite) region, whereby colonies of free (proeutectoid) ferrite are introduced into fully ausferrite microstructure. The final properties of DP-ADI depend on the volume amount of free ferrite (FF), which provides ductility and machinability, and the amount and morphology of ausferrite (AF), which grants strength and ductility [6]. Therefore, the DP-ADI has improved ductility and machinability, when compared to conventional ADI [6-8].
The aim of this study was to evaluate the influence of different intercritical austenitization temperatures on the volume amount of microconstituents (FF and AF) in the microstructure, and mechanical properties, i.e. hardness, as a measure of strength and ductility of the produced DP-ADI.

2. Experimental work

Unalloyed ductile irons with a chemical composition in wt.%: 3.53C; 2.53Si; 0.347Mn; 0.055Mg; 0.031P; 0.015S; were differently heat-treated, and 12 different DP-ADI specimens were obtained. Heat treatment consisted of austenitization within the intercritical interval at 6 temperatures from 880 to 780°C for 2 hours, and austempering at 400°C or 300°C for 1 hour. Standard metallographic preparation techniques (mechanical grinding and polishing, followed by etching in Nital) were applied prior to light microscopy (LM) examinations on a ‘‘Leitz-Orthoplan’’ microscope. The relationship between the amount (% in volume) of free ferrite (FF), ausferrite (AF), and graphite (Gr) in DP-ADI microstructures was quantified by JMicroVision software. The reported values are the average of at least five fields of view on each sample. The Vickers hardness HV10 (ISO 6507) was determined with a test load of 98.07 N (10 kg) and a dwell time of 15 s.

3. Results

Figures 1 and 2 illustrate the microstructures obtained for all samples, while the hardness values are given in Figure 3. The different austenitization temperatures allowed the attainment of microstructures composed of different percentages of ausferrite (AF) and free ferrite (FF) in both sample groups. At higher austenitization temperatures, there is a higher percentage of AF, which is decreased as the austenitization temperature decreases. At the same time, the amount of FF increases with the lowering of the austenitization temperature. The change is not linear, as can be seen from diagram in Figure 3.

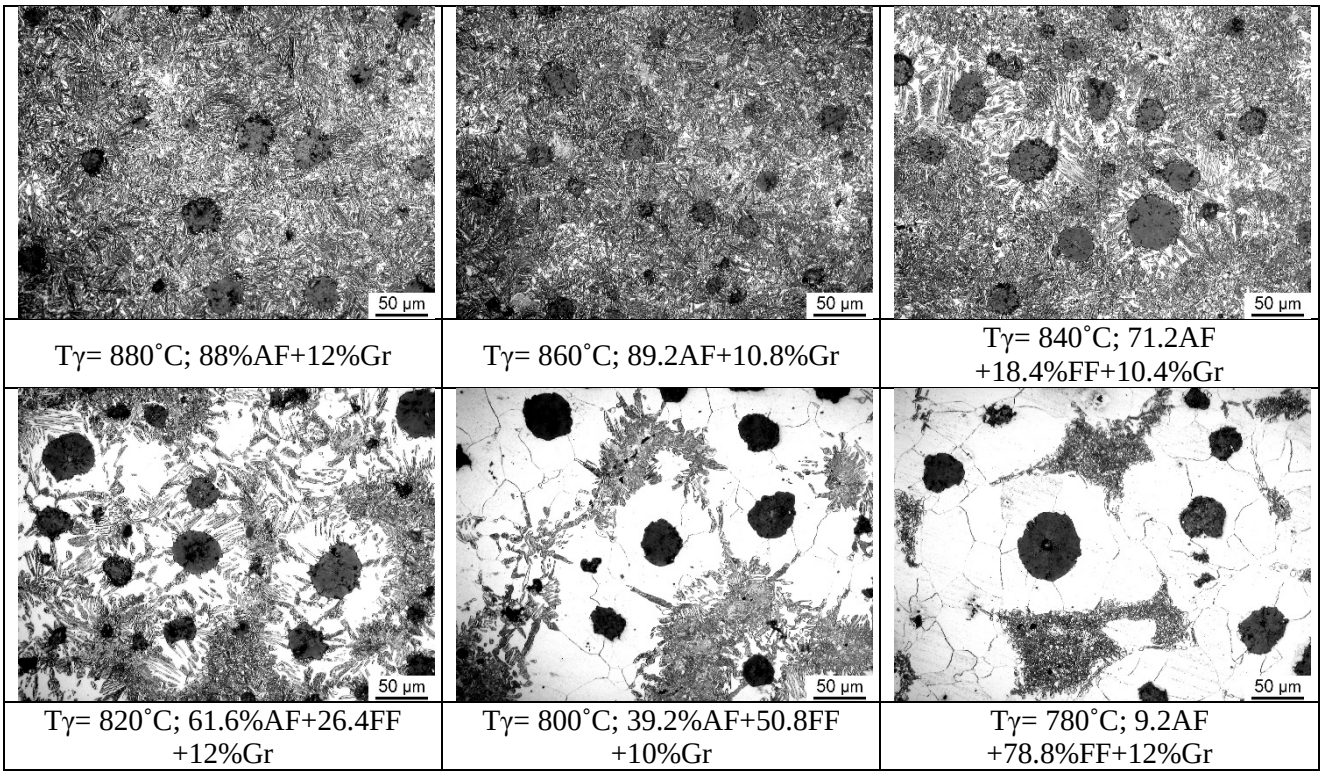

Tγ= 880˚C; 88%AF+12%Gr	Tγ= 860˚C; 89.2AF+10.8%Gr	Tγ= 840˚C; 71.2AF +18.4%FF+10.4%Gr
Tγ= 820˚C; 61.6%AF+26.4FF +12%Gr	Tγ= 800˚C; 39.2%AF+50.8FF +10%Gr	Tγ= 780˚C; 9.2AF +78.8%FF+12%Gr

Figure 1. Microstructure for samples austenitized at different austenitization temperatures Tγ; austempering temperature is 400˚C/1h.

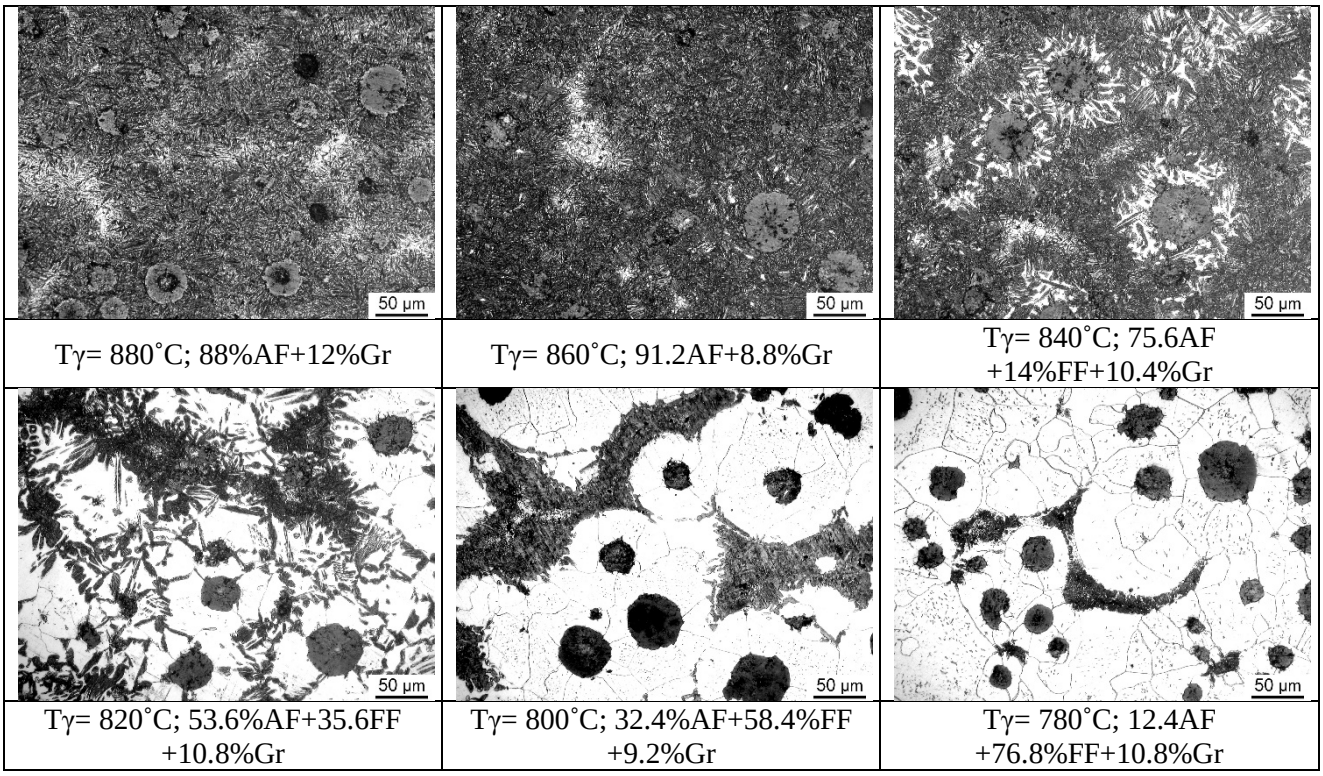

Tγ= 880˚C; 88%AF+12%Gr	Tγ= 860˚C; 91.2AF+8.8%Gr	Tγ= 840˚C; 75.6AF +14%FF+10.4%Gr
Tγ= 820˚C; 53.6%AF+35.6FF +10.8%Gr	Tγ= 800˚C; 32.4%AF+58.4%FF +9.2%Gr	Tγ= 780˚C; 12.4AF +76.8%FF+10.8%Gr

Figure 2. Microstructure for samples austenitized at different austenitization temperatures Tγ; austempering temperature is 300˚C/1h.

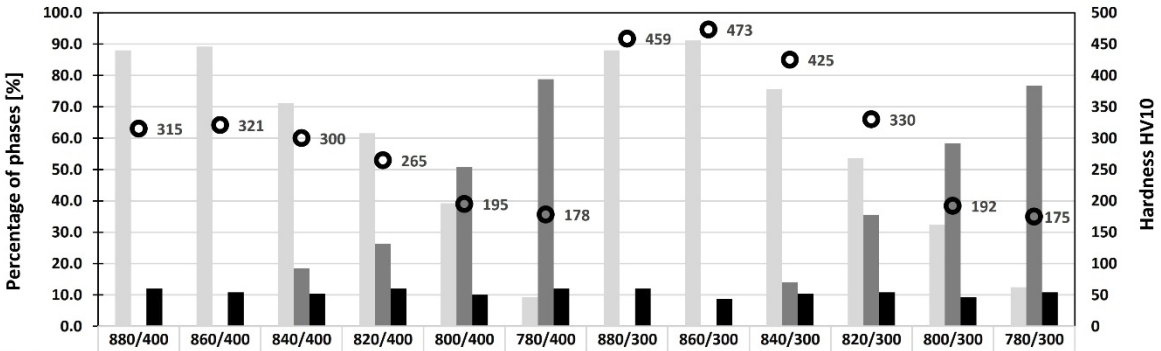

	880/400	860/400	840/400	820/400	800/400	780/400	880/300	860/300	840/300	820/300	800/300	780/300
Ausferrite [%]	88.0	89.2	71.2	61.6	39.2	9.2	88.0	91.2	75.6	53.6	32.4	12.4
Free ferrite [%]	-	-	18.4	26.4	50.8	78.8	-	-	14.0	35.6	58.4	76.8
Graphite [%]	12.0	10.8	10.4	12.0	10.0	12.0	12.0	8.8	10.4	10.8	9.2	10.8
Hardness HV10	315	321	300	265	195	178	459	473	425	330	192	175

Figure 3. Effect of microconstituents percentages on the hardness values of Dual Phase Austempered Ductile Iron

Moreover, when the amount of FF is less than ~50%, the samples that were heat treated at a lower austempering temperature (300°C) have a higher level of hardness than samples heat treated at 400°C. In this case, different morphology of AF primarily influences the hardness. The acicular appearance of AF at 300°C yields higher hardness values, while more plate like morphology of AF at 400°C gives lower hardness values. When the amount of the soft phases (FF and Gr) is more than ~65%, the morphology of AF does not have any more primarily influence, and both groups of samples have similar, low hardness values.

3. Concluding remark

Finally, it could be concluded that amount of microconstituents, and their morphology have a profound influence on the mechanical properties of DP-ADI materials. It is shown that DP-ADI could provide a wide range of mechanical properties as a function of the relative proportion of free ferrite and ausferrite constituents.

Acknowledgment
The authors gratefully acknowledge research funding from the Ministry of Education, Science and Technological Development of The Republic of Serbia under grant number TR34015.

References

[1] L. Sidjanin, R.E. Smallman, J.M. Young, Acta Metallurgica Materialia, 42/9 (1994) 3149-3156
[2] O. Eric, D. Rajnovic, S. Zec, L. Sidjanin, T. Jovanovic, Materials Characterization 57 (2006) 211-217
[3] L. Sidjanin, D. Rajnovic, O. Eric, R.E. Smallman, Materials Science and Technology, 26/5 (2010) 567-571
[4] R.A Harding, Kovove Materials, 45 (2007) 1–16
[5] O. Eric, D. Rajnovic, L. Sidjanin, S. Zec, T. Jovanovic, J of the Serbian Chemical Society, 70/7 (2005) 1015-1022
[6] A. Basso, J. Sikora, Int. J of Metal casting, 6/1 (2012) 7-14
[7] V. Kilicli, M. Erdogan, Materials Science and Technology, 22/8 (2006) 919-928
[8] A. Basso, M. Caldera, J. Massone, ISIJ International, 55/5 (2015) 1106–1113

Effects of alloying elements on the microstructure of Ti-Al-Si alloys

ANNA KNAISLOVÁ, VENDULA ŠIMŮNKOVÁ, PAVEL NOVÁK AND FILIP PRŮŠA
Department of Metals and Corrosion Engineering, University of Chemistry and Technology, Prague, Czech Republic

Ti-Al-Si intermetallic alloys are very promising materials with high oxidation resistance, creep resistance and low density for applications where low density and structural stability at high temperatures are essential - in automotive, aviation and space applications. These materials are considered as substitutes of widely used heat resistant steels and nickel superalloys, which have excellent mechanical properties and structural stability at high temperatures, but very high density [1, 2]. A big problem is the brittleness of silicides, so they need to be very fine or fibrous so that the fracture toughness of the material will be increased [3]. The principle of improving low ductility at room temperature, strength and toughness at high temperatures is to control the microstructure by microalloying [4] or thermo-mechanical processing [5] or by chemical composition [6, 7]. It is necessary to design a material, which has the composition as close as possible to the eutectic - that the eutectic phases are very fine.

Ti-Al-Si alloys can be prepared by conventional casting techniques. The use of these methods causes serious obstacles because of high melting points of intermediary phases, exothermic reactions during their formation and high reactivity of the melt with the melting crucibles [8, 9]. Sharp-edged coarse silicides of Ti_5Si_3 phases are formed by melting metallurgy of Ti-Al-Si alloys. Coarse oriented sharp-edged silicides have a negative effect on mechanical properties because they decrease the fracture toughness of the resulting material [9]. Powder metallurgy is a promising method for preparation intermetallic alloys based on Ti-Al-Si system, it allows to produce components of very complicated shapes without the additional machining. Powder metallurgy enables to combine the elements with different melting points, different solubility or different density [10, 11]. The possibility to prepare these alloys with fine grains and more homogeneous structure is mechanical alloying - a very energy-intensive process but effective in obtaining sufficiently fine grains [1]. Mechanical alloying produces powders with nanometer-scale grain size and homogeneous dispersion of individual phases. The achieving of the compact sample with nearly-full density from powder can be by Spark Plasma Sintering method (SPS). The main advantage of SPS is a short time of sintering and the use of lower sintering temperatures compared with conventional sintering methods (e.g. hot isostatic pressing). A pulsed high electric current is forming spark discharges between powder particles, and they generate plasma. Spark discharges remove the oxide films and impurities on the particle surface. Joule heating also contributes to the densifications of powders [12-14].

In this work, the microstructure of Ti-Al-Si intermetallic alloys prepared by mechanical alloying and Spark Plasma Sintering will be described. The TiAl15Si15 (wt. %) alloy with the most homogeneous structure was chosen from previous research at UCT Prague. The effect of alloying elements (cobalt, chromium, iron, molybdenum, niobium and nickel) on the microstructure of TiAl15Si15 alloy will be studied. The result of Ti-Al-Si-X (X = Co, Cr, Fe, Mo, Nb, Ni) alloys will be compared with the same alloy prepared without alloying elements.

References

[1] Z.Q. Guan, T. Pfullmann, M. Oehring, R. Bormann, J. Alloy. Compd., 252 (1997) 245-251

[2] A. Knaislová, P. Novák, M. Cabibbo, F. Průša, C. Paoletti, L. Jaworska, D. Vojtěch, J. Alloy. Compd., 752 (2018) 317-326

[3] S. Romankov, W. Sha, S.D. Kaloshkin, K. Kaevitser, Surf. Coat. Technol., 201 (2006) 3235-3245

[4] C.T. Liu, Mater. Chem. Phys., 42 (1995) 77-86

[5] Y.-W. Kim, JOM, 41 (1989) 24-30

[6] J.M. Larsen, S.M. Russ, J.W. Jones, Metall. Mater. Trans. A, 26 (1995) 3211-3223

[7] S.L. Kampe, P. Sadler, L. Christodoulou, D.E. Larsen, Metall. Mater. Trans. A, 25 (1994) 2181-2197

[8] A. Knaislová, V. Šimůnková, P. Novák, F. Průša, S. Cygan, L. Jaworska, Manufacturing Technology, 17 (2017) 483-488

[9] P. Novák, D. Vojtěch, J. Šerák, J. Kubásek, F. Průša, V. Knotek, A. Michalcová, M. Novák, Chem. Listy, 103 (2009) 1022-1026

[10] S.A. Tsukerman, INTRODUCTION, in: Powder Metallurgy, Pergamon, 1965, pp. vii-xi.

[11] A. Knaislová, P. Novák, K. Nová, Manufacturing Technology, 16 (2016) 946-949

[12] Z.-H. Zhang, Z.-F. Liu, J.-F. Lu, X.-B. Shen, F.-C. Wang, Y.-D. Wang, Scr. Mater., 81 (2014) 56-59

[13] S.-X. Song, Z. Wang, G.-P. Shi, Ceram. Int., 39 (2013) 1393-1396

[14] D.S. Perera, M. Tokita, S. Moricca, J. Eur. Ceram. Soc., 18 (1998) 401-404

In Situ TEM Fracture Experiments on Ultrafine Grain Chromium at RT: Dislcoations Processes and Toughnening Mechanisms

INAS ISSA[1], ANTON HOHENWARTER[1], REINHARD FRITZ[1,2], DANIEL KIENER[1]
[1] Department Materials Science, Chair of Materials Physics, Montanuniversität Leoben, Austria; [2] now at Voestalpine Tubulars GmbH & Co KG, Austria

Achieving high fracture toughness and maintaining high strength at the same time are main goals in materials science. In this work, scale-bridging fracture experiments on ultrafine-grained chromium (UFG, Cr) are performed at different length scales, starting from the macroscale (conventionl thre point bending tests) over the microscale (in situ SEM) down to the nanoscale (in situ TEM).

This UFG Cr structure is produced with one highlighted severe plastic deformation method, namely high pressure torsion (HPT). Wedge-shaped samples were prepared by conventional wire cutting, gentle grinding, and subsequent electrochemical etching to remove any deformation layer. Fabrication of miniaturized bending beams along this sample is conducted using a focused ion beam (FIB). A single notch cantilever bending test geometry is chosen for SEM and TEM specimens. The bending beams are clamped from one side to reflect the most common fracture experiment geometry used at small scales. Annealing treatments in the TEM are performed prior to in situ TEM tests. This process allows to eliminate defects and pre-existing dislcoations introduced during HPT or FIB preparation. Very sharp notches, arround 2 nm tip radius maximum, are introduced in the TEM by converging the electron beam at high magnification and scanning the area to be notched for few minutes.

A quantitative assessment of the fracture toughness yields values of ~3 $MPa.m^{1/2}$, at the three different tested scales, within the frame of linear elastic fracture mechanics. In situ TEM tests reveal explicitly the occurrence of dislocation emission processes involved in energy dissipation and crack tip blunting serving as toughening mechanisms before intercrystalline fracture in UFG bcc metals.
Diffraction patterns of the grains arround the notchs collected prior to tests, see Figure 1(a) , revealed their crystallographic orientations. This allows the characterisation of emitted dislocations from the notch and grain boundaries arround the noth. The dislcoations characters and their Burgers vector explain the specific direction of the notch opening, as shown in Figure 1(b-f).

Two groups of specimens are tested: one with notches along grain boundaries (see Figure1 (a)) and another with notches within a single grain (see Figure2 (a)). Specimens notched along a grain boundary show further dislocation emission and ductility prior to crack propagation. However, the specimens notched within a single grain exhibit fewer dislcoation emission events from the notch, followed by a fracture along the neareast grain boundary (see Figure 2(b). Quantifying the bending stress measured at fracture, as shown in Figure 2(c), shows that the stress needed to allow a crack to propagate along GBs is higher than that required to emit dislocations from them, as represented in the scheme of Figure 2(d). This underlines that dislocation emission occurs before intercrystalline brittle fracture. Thanks to these in situ TEM tests, one can conclude that a promising strategy to promote ductility and induce additional toughness in UFG bcc materials is by strengthening GBs [1].

Increasing grain boundaries cohesion (or strength) is possible by locally adding adhesion improving impurities such as Carbon or Boron to the grain boundary sites. The amount of local segregation and thus modification in GBs cohesion will also depend on the atomistic grain boundary configuration in front of the notch and the grain-boundary character. Progress towards this intentional GB modification to imcrease toughness will finally be addressed.

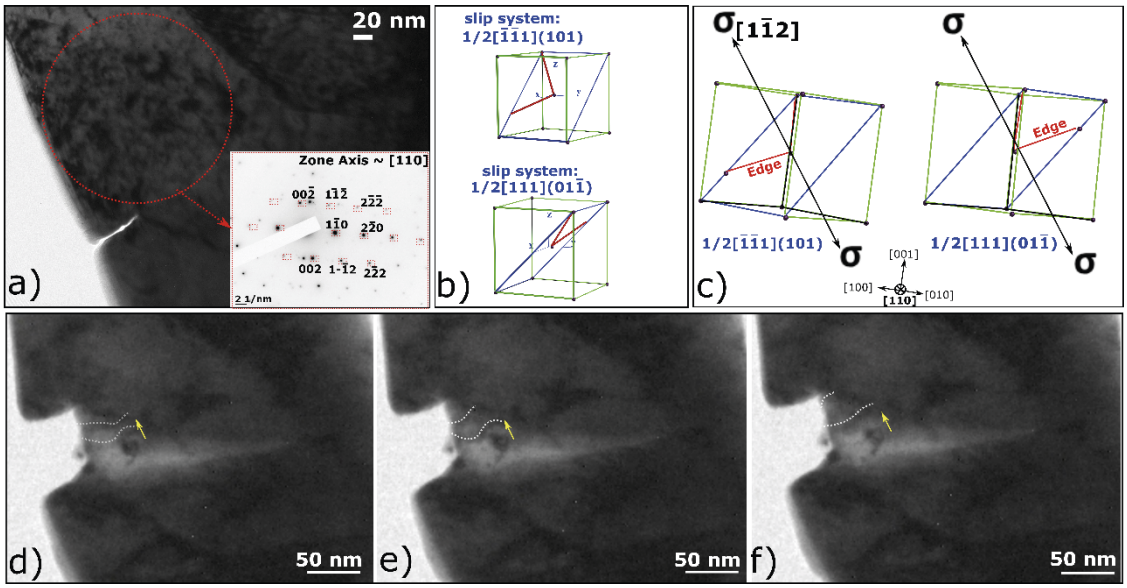

Figure 1: a) TEM image of a notched specimen with the notch along a GB. Inset: SAD pattern of the selected grain. b) Schematic representation of the two possible slip systems likely to be activated in the corresponding configuration of the crystal in the specific grain near the notch. c) Same slip systems viewed along the zone axis [110], in correspondence to the TEM images. d-f) Consecutive TEM images extracted from the in situ TEM test with dislocation emission and glide along the direction presented by the arrow.

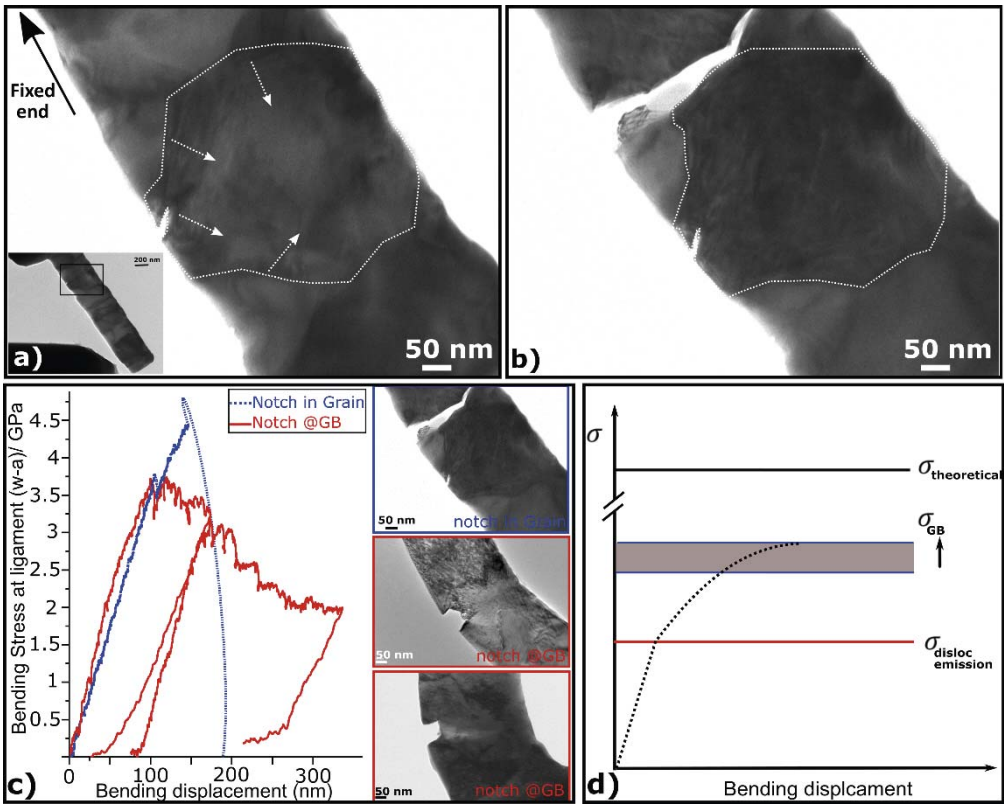

Figure 2: (a) TEM image of a notched cantilever with the notch situated within a grain, at an early stage of dislocations emission. (b) TEM image showing the fracture occurring along a GB. (c) Nominal uniaxial bending stress at ligament of a specimen notched along the GB (red curve) with two cycles of loading–unloading and other notched in a grain (blue dotted curve), as a function of the bending displacement. Inset: TEM images after tests of (from top to down) the specimen with the notch situated in the grain and below the two specimens notched along GBs. The bottom TEM image corresponds to the red curve. (d) Schematic detailing the stress required to allow a crack to propagate along a GB being higher than that required to nucleate dislocations. However, both are well below the theoretical shear strength of Cr.

References:

[1] Issa, I., Hohenwarter, A., Fritz, R., & Kiener, D. (n.d.). Fracture properties of ultrafine grain chromium correlated to single dislocation processes at room temperature. Journal of Materials Research, 1-14. doi:10.1557/jmr.2019.140

Acknowledgement
Inas Issa and Daniel Kiener acknowledge funding by the European Research Council under Grant number 771146 (TOUGHIT)

Distribution of dislocations on the Lüders band front during cold deformation in steel

M. MATVIJA[1], S. REŠKOVIĆ[2], T. BRLIĆ[2]
[1] Technical University of Košice, Faculty of Materials, Metallurgy and Recycling, Košice, Slovakia;
[2] University of Zagreb, Faculty of Metallurgy, Sisak, Croatia

The appearance of inhomogenous deformations, i.e. Lüders bands today is considered as significant problem in forming of different types of metals during cold deformation [1]. This is a significant problem because final products where surface roughness remains can be obatined and can affect the final product quality.

Therefore, very intensive research of the mechanism of formation and propagation of the Lüders bands in different metal materials is carried out [2]. Niobium microalloyed steels are one of the steels that show the appearance of inhomogeneous deformations during cold deformation and because of that, intensive research is carried out on these steels [3].

The steel behavior during cold deformation can be monitored very well using methods thermography [4] and digital image correlation [5]. Thermography allows to follow temperature changes, i.e. stress changes during the Lüders bands propagation while the digital image correlation allows to measure the strain amounts at any time during cold deformation in the deformation zone.

Today, the results of steel behavior during cold deformation are often associated with the microstructure of steel [6]. Some authors are used metallography to observe how the microstructure influences the appearance of the Lüders bands [7] and found that heterogeneous microstructures can affect the occurrence or reduction of yield point elongation. Singh et al are used scanning electron microscopy [8] for detection of different types of precipitates present in steel during the Lüders band formation. Recently, transmission electron microscopy has also been used to gain the clearest role of dislocation and precipitates at the start of plastic material flow, primarily in the mechanism of propagation of the Lüders bands.

However, determination of the influence of dislocations and precipitates present in the microstructure of steel has not been investigated.

The aim of this paper is to determine the distribution of dislocations and precipitates on the Lüders band front during propagation of the Lüders band through the deformation zone.

The chemical composition of niobium microalloyed steel is shown in Table 1.

Table 1. Chemical composition of niobium microalloyed steel (wt%)

Element	C	Mn	Si	P	S	Al	Nb	N	Fe
Microalloyed steel	0.12	0.78	0.18	0.011	0.018	0.020	0.048	0.008	Bal.

In this research thermography and digital image correlation are used simultaneously with static tensile testing. Thermography is used for determine temperature changes, i.e. stress distribution and digital image correlation for strain distribution during the Lüders bands propagation on the Lüders band front. Testing area researched with transmission electron microscope is marked with black rectangle on the Lüders band front, Figure 1.

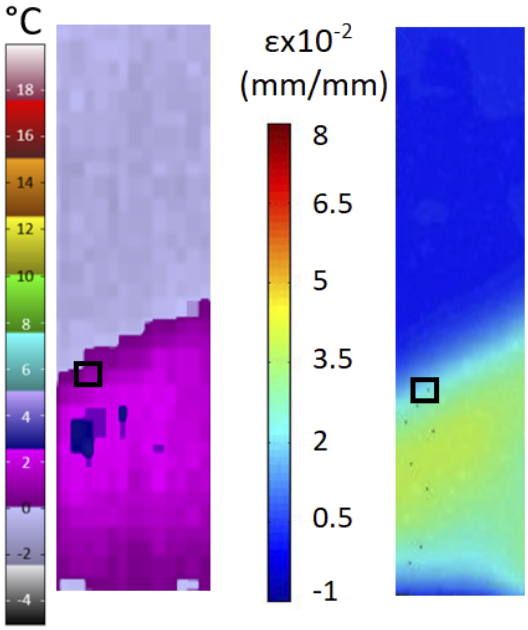

Figure 1. Studied Lüders band front marked with a black rectangle on: a) thermography and b) digital image correlation (DIC)

Distribution of dislocations on the Lüders band front determined with transmission electron microscope is shown in Figure 2.

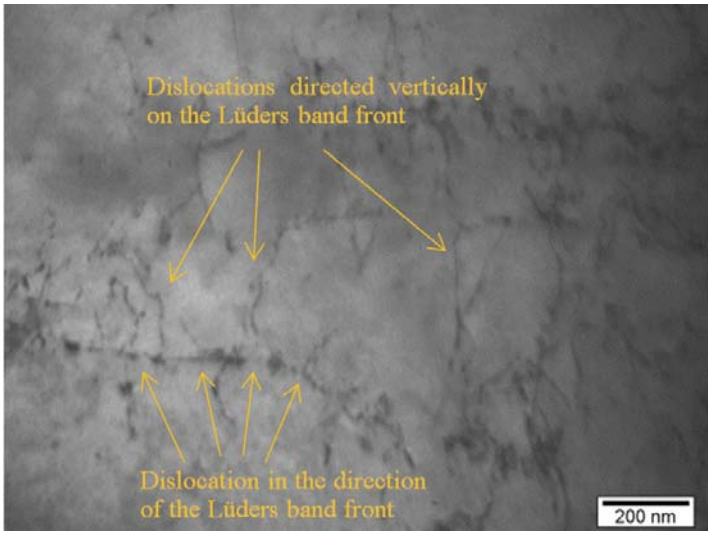

Figure 2. Direction of dislocations on the Lüders band front at magnification 85 000x

Dislocations on the Lüders fronts are partially directed in the direction of the Lüders band front and partially of the dislocations is directed vertically on the Lüders band front. Dislocations directed vertically on the Lüders band front have tendency to go in the direction along the Lüders band front as the propagation of the Lüders band proceeds.

Interaction between dislocations and small precipitates is noted at the Lüders band front.

Further detailed research on particular areas of the Lüders bands will show dislocations distribution and precipitates distribution in various areas of the Lüders band.

Acknowledgement
This work has been fully supported by Croatian Science Foundation (IP-2016-06-1270).

References

[1] J.F. Hallai, S. Kyriakides, Int J Solids Struct, 48 (2011) 3275-3284
[2] N. Srinivasan, R. Narayanaswamy, B. Venkatraman, J Mater Eng Perform, 22 (2013) 3085-3092
[3] T. Brlić, S. Rešković, I. Jandrlić, I Met Mater Int, (2019) https://doi.org/10.1007/s12540-019-00336-w
[4] J. Petit, D. Wagner, N. Ranc, G. Montay, M. François, Comparison of different techniques for the monitoring of the Lüders bands development, Proceedings book of the 13th International Congress on Fracture 2013, IFC-13, Beijing, (2013) 3797-3809
[5] T. Brlić, D. Debruyne, P. Lava, S. Rešković, I. Jandrlić, Identıfıcatıon of Lüders bands using digital image correlation, Holistic Approach Environ, 9 (2019) 8-11
[6] D.H. Johnson, M.R. Edwards, P. Chard-Tuckey, Microstructural effects on the magnitude of Luders strains in a low alloy steel, Mat Sci Eng A 625 (2015), 36-45.
[7] T. Zhou, H. Zurob, P. Zhang, K. Kuuskman, S.H. Cho, D. Burella, Control of edge breaks during cold mill processing of commercial and drawing quality low-carbon steels, Ironmak Steelmak, (2018)
[8] G. Singh, T. Nanda, S.J. Miadad, N.C. Gorain, T. Venugopalan, B.R. Kumar, Arch Civ Mech, Eng. 19 (2019) 469–483

Evaluation of fracture toughness and recrystallization behaviour of ultrafine grained tungsten wires

VLADICA NIKOLIĆ[1], MANUEL PFEIFENBERGER[1], ANTON HOHENWARTER[2] AND REINHARD PIPPAN[1]

[1] Erich Schmid Institute of Materials Science, Austrian Academy of Sciences, Leoben, Austria;
[2] Department of Materials Science, Chair of Materials Physics, University of Leoben, Austria

Tungsten (W) and tungsten-based materials are recognised as leading candidates for divertor and plasma facing components (PFC) of future nuclear fusion devices [1]. The unique suitability of these materials for the very challenging fusion reactor application is due to their excellent high temperature properties. However, a significant drawback for the structural application of tungsten is its poor fracture toughness and low ductility at room temperature (RT), coupled with a high ductile-to-brittle transition temperature (DBTT) [2]. These properties cause serious restrictions on both, its performance in demanding applications, as well as its workability. Therefore, progress and success of using tungsten for structural components are strongly dependent on the introduction of toughening mechanisms, making tungsten in such a way a more fracture resistant material.

Among several ductilization strategies, one of the promising options is the development of W-fibre reinforced W-composite materials (Wf/W) [3]. This composite structure is obtained by embedding commercially available drawn tungsten wires in a tungsten matrix, which is produced either by powder metallurgy or by a chemical deposition process. The advantage of W_f/W is its pseudo ductile behaviour and thereby increased toughness as a consequence of extrinsic toughening mechanisms such as crack bridging by intact fibres, fibre pull-out, crack deflection and ductile deformation of fibres [4]. In such a way, the brittleness of W can be mitigated, making W_f/W composites a feasible PFC alternative. The drawn tungsten wires used as reinforcements are the key components which determine the structural integrity of the W_f/W composite. This sets the requirement of exceptional properties and brings an interest in studying them. Fracture properties of the wires at moderate temperatures and a complete understanding of the underlying micromechanisms controlling the fracture process is of fundamental importance for the composite development.

This contribution is oriented towards the investigation of the fracture behaviour of heavily deformed 150µm pure and K-doped W wires with the main focus on the effect of heat treatments and their microstructrual stability upon annealing. A scanning electron microscope equipped with an electron backscattered diffraction detector was used to perform detailed analyses of the evolution of different aspects of the microstructure (nature of grain boundaries, grain shape and size, texture). Vacuum annealing in the temperature range from 900-1600°C enables the investigation of the microstructural stability of the two materials and arising annealing phenomena - recovery, recrystallization and grain growth. The results demonstrate that pure tungsten wires fully recrystallize in the temperature range between 1300-1500°C accompanied with tremendous coarsening and a complete loss of the initial fibrous, elongated grain structure (Figure 1). In contrast to this, potassium doped wires show superior high temperature properties, where the performed heat treatments cause less pronounced microstructural changes, consequently suppressing recrystallization and grain growth to temperatures well above the highest one investigated.

Room temperature fracture experiments of the wires were conducted with the emphasis on the evolution of the fracture micromechanisms in respect to annealing treatments. Single-edge-notched specimens were used, with the crack growth direction perpendicular to the drawing axis of the wire. The occurrence of either a brittle or a ductile response in the as-received state of both materials is a strong indication that the DBTT is around RT. Pure, annealed tungsten wires experience a tremendous drop in fracture toughness of about 70% after the heat treatments, followed by a prominent transition

of the failure mode. The observed embrittlement by annealing can be related to the loss of the fibrous, elongated microstructure. In contrast to this, the results of the annealed, doped wires demonstrate that the microstructural stability and preservation of the initial, beneficial grain structure is directly reflected in the crack resistance of the material. Predominately ductile behaviour, with characteristic knife-edge necking, is seen even after annealing at 1600°C (Figure 2). In addition, in order to investigate the anisotropy of the fracture properties and evaluate the crack growth resistance along the elongated microstructure, in-situ experiments were conducted with the crack propagation direction parallel to the principal drawing direction. Femtosecond laser processing was used to fabricate micro single leg bending specimens. The obtained fracture toughness values are significantly lower in comparison to the other orientation. The fracture initiation toughness and R-curve behaviour are mainly controlled by the morphology of the fracture surface and roughness of the evolving crack paths.

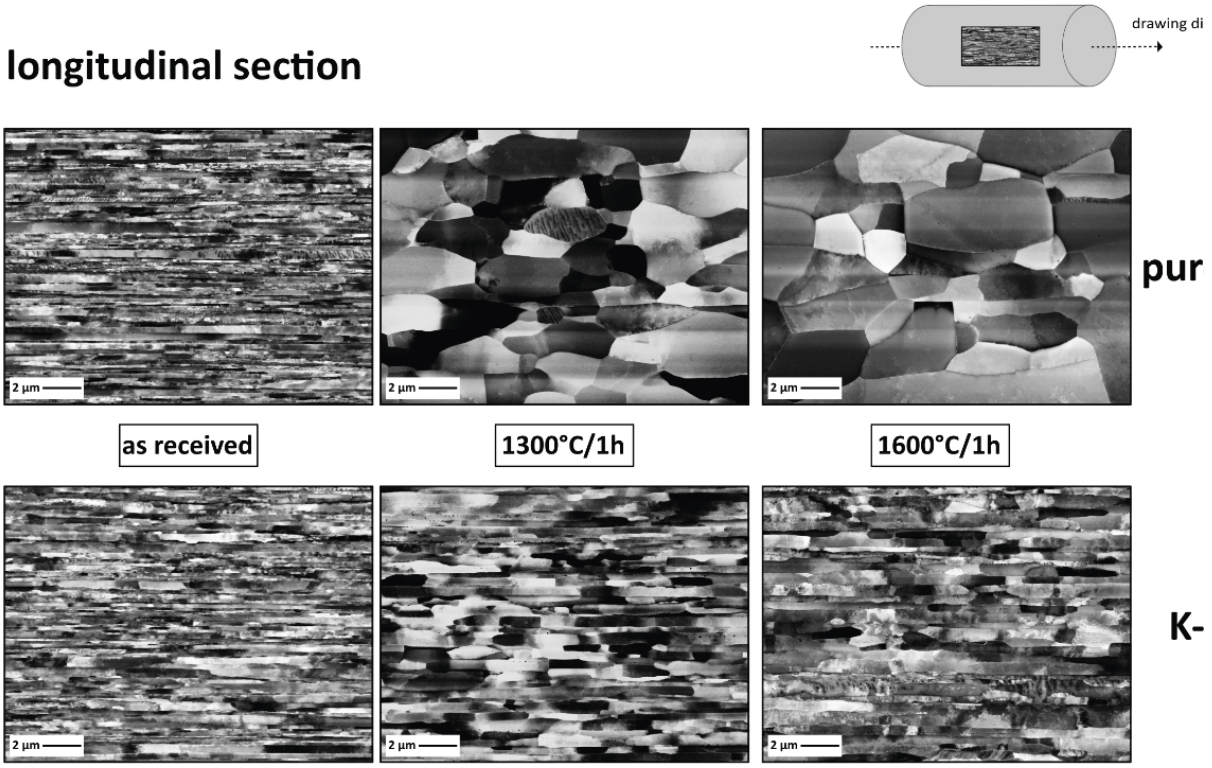

ed
tungsten wires in the as-received and annealed states (1300 °C and 1600 °C). The images are taken in the center of longitudinal sections. The schematic drawing shows the principle direction of deformation, as well as the position of the typical scanning area with respect to the drawing direction.

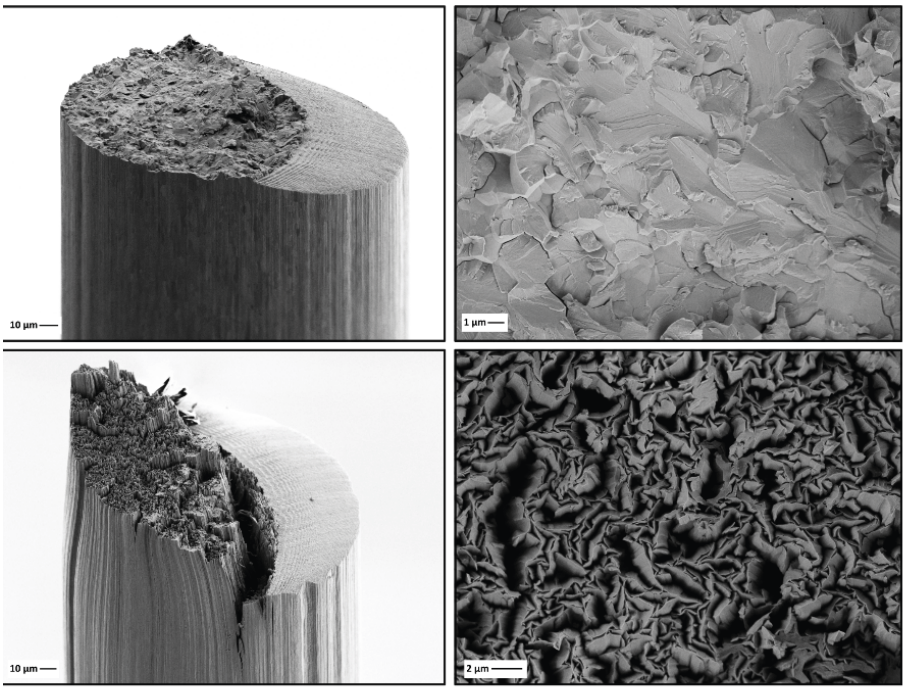

Figure 2. Fractographs of tungsten wires annealed at 1300°C for 1h. A comparison is made between a pure W wire having mixed, brittle failure mode that consists of both, cleavage and intergranular fracture and a K-doped W wire having predominately a typical ductile, knife-edge necking dominated fracture behaviour.

References

[1] M. Rieth et al., J. Nucl. Mater., vol. 432, no. 1-3 (2013) 482-500.
[2] E. Lassner and W.D. Schubert, Tungsten – Properties, Chemistry, Technology of the Element, Alloys and Chemical Compounds, New York: Kluwer Academic / Plenum Publishers (1999).
[3] R. Neu et al., Nucl. Mater. Energy, vol. 9 (2017) 1308-1313.
[4] J. Riesch et al., Phys. Scr., vol. T159, no. 14031 (2014) 1-7.

Homogeneity in superconducting Nb_3Sn wires: exploring the routes towards high-performance bending magnets for the CERN Future Circular Collider

ALICE MOROS[1], MATTIA ORTINO[2], STEFAN LÖFFLER[1], MAXIM ALEKSEEV[3], ANASTASIA TSAPLEVA[3], PAVEL LUKYANOV[3], ILDAR M. ABDYUKHANOV[3], VICTOR PANTSYRNY[3], BERNARDO BORDINI[4], AMALIA BALLARINO[4], SIMON C. HOPKINS[4], MICHAEL STÖGER-POLLACH[1], JOHANNES BERNARDI[1], MICHAEL EISTERER[2]

[1] TU Wien, USTEM, Wiedner, Vienna, Austria; [2] TU Wien, Atominstitut, Vienna, Austria; [3] A. A. Bochvar High-Technology Research Institute on Inorganic Materials, Moscow, Russia; [4] CERN, Espl. des Particules 1, Meyrin, Switzerland

There are numerous open questions regarding the origin of the universe and the European Organization for Nuclear Research (CERN) keeps on looking for new routes to find the answers: to that end, a conceptual design for a proposed next-generation high-energy hadron-hadron collider (CERN Future Circular Collider, FCC-hh) was published. The new machine would be located in a 100 km circumference ring close to Geneva (Switzerland) and its target centre-of-mass energy is 100 TeV, assuming a nominal magnetic dipole field of 16 T, produced by superconducting coils at an operating temperature of 4.2 K. The best candidate for such magnets is Nb_3Sn, a low temperature superconductor (critical temperature T_c up to 18.3 K) which is in principle able to reach the related requirements for the construction of such a particle accelerator: a critical current density J_c of 1.5 kA/mm^2 at 16 T and 4.2 K.

As the chemical composition has a great influence on the performance of Nb_3Sn, energy dispersive X-ray (EDX) spectroscopy was employed with both scanning electron microscopy (SEM) and transmission electron microscopy (TEM) to analyze the elemental distributions over the cross-sections of prototype internal tin Nb3Sn wires manufactured with different designs and heat treatments. Figure 1 shows pictures produced by back-scattered electrons representing two different investigated wires.

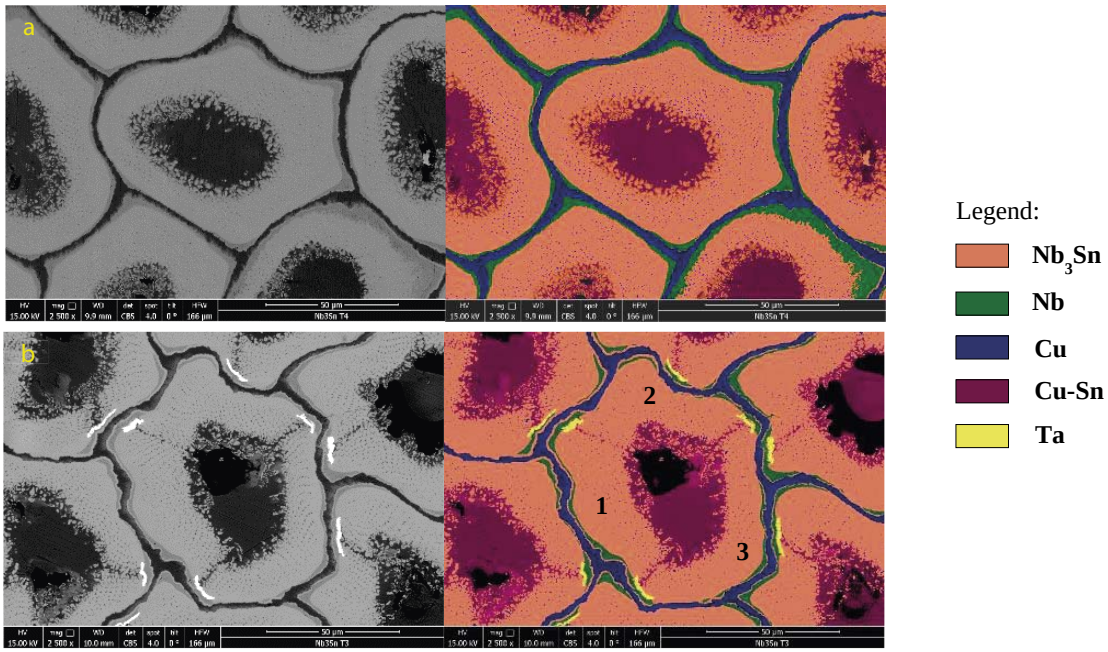

Figure 1. Examples of wire sub-elements with different designs. The pictures represent a Nb_3Sn wire with (a) “standard” sub-elements and (b) sub-elements showing “clusters” (labeled 1,2,3). The different colours indicate regions with different elements or phases.

In particular, EDX line scans were performed along the radial direction in wire sub-elements, from the Nb barrier in the peripheral region to the Cu-Sn core (as shown in Figure 2). During the analysis the main focus was set on Sn concentration and its homogeneous distribution, which has a great impact on the wires superconducting properties.

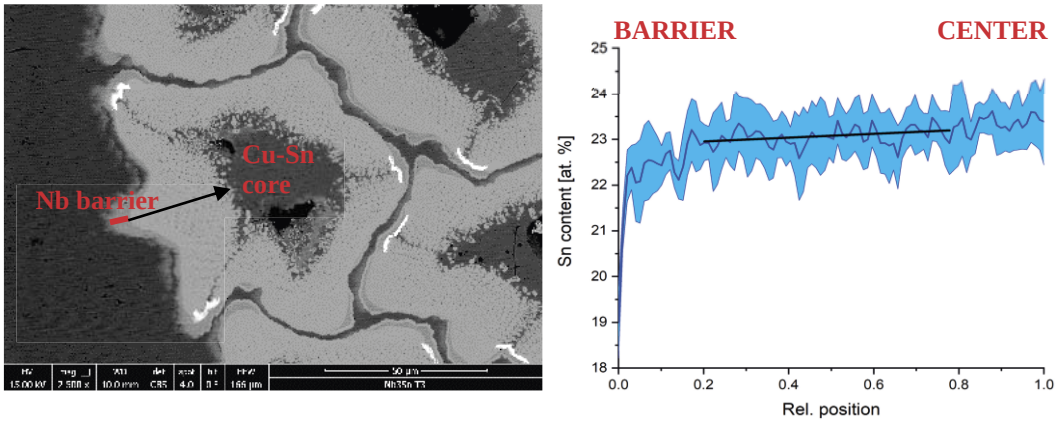

Figure 2. Left: example of the path used for EDX line scans of sub-elements in the radial direction from the Nb barrier to the Cu-Sn core. Right: Sn concentation along the measured path with a line fit showing a small but relevant gradient.

The connections between the elemental distribution analyses and the wires magnetic and superconducting properties measured by SQUID magnetometry and scanning Hall probe microscopy will be discussed as well.
This study will help to better understand which directions should be followed in the manufacturing process in order to obtain wires with improved microstructural and superconducting attributes.

This work is part of the Marie Skłodowska-Curie Action EASITrain (European Advanced Superconductivity Innovation and Training), funded by the European Union's H2020 Framework Programme under grant agreement no. 764879. The development of wires by the Bochvar Institute (addenda KE2968 and KE4037) and their characterisation at TU Wien (addendum KE3194) was supported by CERN in the context of the FCC Study.

Electron microscopy analysis of flash-annealed CuZr based bulk metallic glass

CHRISTOFFER MÜLLER[1], CHRISTIAN EBNER[2], CHRISTOPH GAMMER[1], KONRAD KOSIBA[3], BENJAMIN ESCHER[3], SIMON PAULY[3], JÜRGEN ECKERT[1] AND CHRISTIAN RENTENBERGER[2]

[1] Erich Schmid Institute of Materials Science, Austrian Academy of Science, Leoben, Austria; [2] Physics of Nanostructured Materials, Faculty of Physics, University of Vienna, Vienna, Austria; [3] Institute for Complex Materials, IFW Dresden, Dresden, Germany

1. Introduction

Bulk metallic glasses (BMGs) are amorphous materials showing attractive physical and mechanical properties like high yield strength and a high elastic limit due to their unique atomic structures. Despite the lack of a long-range order, still topological and chemical short-range and medium-range order are expected to occur. Although being amongst the strongest engineering materials known, they exhibit a disappointingly low plastic deformability.

2. Objectives

To circumvent this limited ductility the concept of heterogeneous microstructure e.g. by the formation of composites has recently been used [1]. One way to achieve such a structure is thermal treatment of the BMG. Here we present the analysis of flash-annealed CuZr based BMGs.

3. Materials and Methods

During the flash-annealing process the atomic structure of $Cu_{44}Zr_{44}Al_8Hf_2Co_2$ BMGs is modified by rapid heating to different target temperatures above glass transition temperature (712 K) and the subsequent cooling in a water bath. The samples were heated to 817 K, 898 K and 916 K with a mean rate of 67 K/s and studied in a Zeiss Supra 55VP scanning electron microscope (SEM) at 20 kV as well as a Philips CM200 transmission electron microscope (TEM) operating at 200 kV using tilted dark-field (DF) fluctuation electron microscopy (FEM).

4. Results

Using back-scattered electrons the SEM observation of the sample heated to 916 K reveals both an amorphous and a crystalline part each taking up about half of the sample with spherical crystallites of different size in between (Figure 1a). Figure 1b illustrates a TEM image of a FIB lamella taken from one of the crystallites embedded in the amorphous structure. The corresponding diffraction pattern (DP) contains superlattice reflections indicating the presence of the B2 ordered structure. This is interesting as in crystalline CuZr based materials, devitrified from the amorphous structure, $Cu_{10}Zr_7$ and $CuZr_2$ structures are expected to occur.

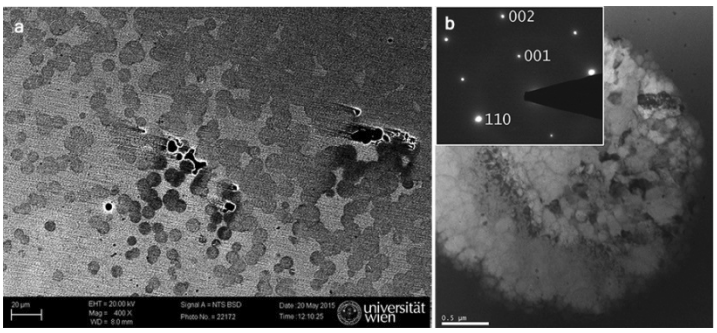

Figure 1. (a) SEM image of the transition area from fully amorphous to fully crystalline structure in the sample heated to 916 K showing micrometer-sized crystallites. (b) TEM bright-field image and DP of a spherical crystallite embedded in the amorphous matrix revealing defective B2 ordered crystal structure.

In order to analyse and compare the structures of the fully amorphous samples flash-annealed to 817 K and 898 K as well as the amorphous part of the sample heated to 916 K, variable resolution DF FEM was applied. Figure 2a shows a DP with integrated intensity using the software PASAD [2] indicating the amorphous structure. Figure 2b illustrates a tilted DF image taken with a given scattering vector k showing intensity variations in the form of speckles due to local structural correlations.

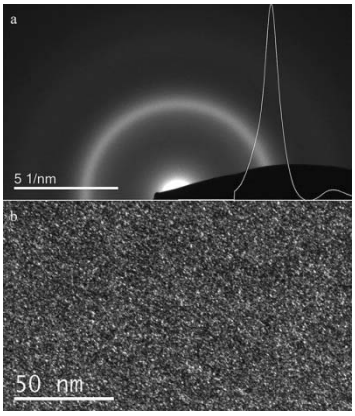

Figure 2. (a) Characteristic DP and (b) tilted DF image of the amorphous structure.

Fluctuations of DF image intensity reveal structural ordering at the medium range. Acquiring a series of DF images at different vectors k and azimuthal angles φ provides the mean intensity and normalized variance as a function of k. The normalized variance is defined as

$$V(k) = (\langle I(k,r)^2\rangle / \langle I(k,r)\rangle^2) - 1$$

with I being the image intensity and <> meaning averaging over sample position r. Figure 3 illustrates the mean intensity and normalized variance curves of the differently treated samples, calculated from 320 images each, using an aperture size of 10 µm. It is interesting to compare the profile of the normalized variance to the 4 most intense peaks in the X-ray diffractogram of B2 structured CuZr, as they show remarkable similarities.

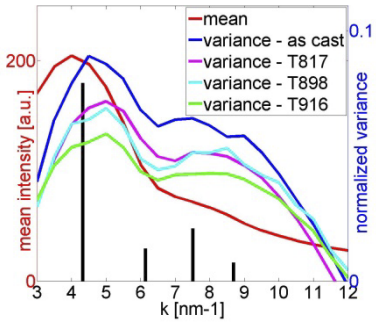

Figure 3. Mean intensity and normalized variance curve of the different samples as a function of the scattering vector k used for the tilted dark-field images.

By changing the aperture size and thus varying the spatial resolution the correlation length, a length scale for medium-range order, can be derived from the pair persistence model [3]. Figure 4 compares the correlation lengths of the flash annealed amorphous samples to the as-cast state showing a continuous increase in medium-range order with increasing target temperatures.

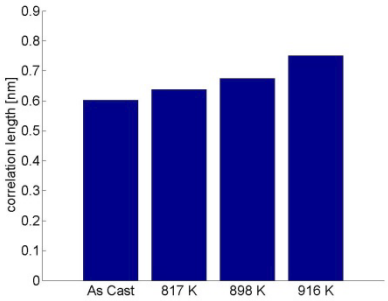

Figure 4. Calculated correlation length in the amorphous phases of the as cast and flash-annealed samples.

5. Conclusion

Based on our results, flash-annealing of CuZr based BMGs facilitates the modification of the amorphous phase and the formation of crystalline spheres with B2 ordered structure. The modification of the amorphous structure could be monitored by tilted dark-field fluctuation electron microscopy. The profile of the normalized variance as a function of the scattering vector indicates structural similarity of the amorphous phase to B2 structured atomic clusters since the profile resembles the X-Ray diffractogram of the B2 structure when the most intense peaks are considered. The correlation length, here as a measure for B2 like medium-range order, which can be derived from the pair persistence model, is consistent with typical correlation lengths for amorphous CuZr reported in literature and increases continuously with the target temperature for flash-annealing.

6. Acknowledgement

Financial support of the Austrian Science Fund (FWF): [I1309] and the provision of the Zeiss Supra 55 VP SEM by the Faculty Centre for Nanostructure Research at the University of Vienna are acknowledged.

References

[1] J. Eckert, J. Das, S. Pauly, C. Duhamel, Journal of Materials Research 22, 285 (2007).
[2] C. Gammer, C. Mangler, C. Rentenberger, H. P. Karnthaler, Scr Mater 63, 312 (2010).
[3] J.M. Gibson, M.M.J. Treacy, P.M. Voyles, Ultramicroscopy 83, 169 (2000).

Interaction of picosecond Nd:YAG laser irradiation with Ti-13Nb-13Zr alloy surface in air and argon atmosphere

SLAĐANA LAKETIĆ[1], MARKO RAKIN[2], MILOŠ MOMČILOVIĆ[1], JOVAN CIGANOVIĆ[1], ĐORĐE VELJOVIĆ[2], IVANA CVIJOVIĆ-ALAGIĆ[1]

[1] Institute of Nuclear Sciences „Vinča", University of Belgrade, Serbia; [2] Faculty of Technology and Metallurgy, University of Belgrade, Serbia

1. Introduction

Titanium and titanium alloys are most commonly used as hard tissue implants. In order to avoid implant failure due to defective osseointegration, laser surface modification is used to improve implant biocompatibility and osseointegration. The aim of the presented study was to investigate the influence of the laser irradiation parameters on the titanium-based alloy surface morphology and damage characteristics which directly influence the implant alloy biointegration properties.

2. Experimental details

The Ti-13Nb-13Zr (mass%) alloy, produced in the Institute of Nuclear Sciences „Vinča" [1], was subjected to the laser surface modification treatment. Before irradiation, Ti-13Nb-13Zr alloy surface was prepared by the standard metallographic procedure (grinding, polishing and cleaning). Laser irradiation was carried out using Nd:YAG laser operating at 1064 nm wavelength and pulse duration of 150 ps in air and argon atmosphere under laser output energy of 5 and 30 mJ and irradiation time of 5 and 100 s. The laser was operated with a repetition rate of 10 Hz. Field emission - scanning electron microscopy (FE-SEM) and profilometry were used to analyze the surface morphology and surface damage characteristics after laser irradiation.

3. Results and discussion

During laser irradiation, laser energy was partly reflected and partly absorbed by implant material surface [2]. Absorbed laser irradiation caused various macroscopic and microscopic changes in the surface morphology. Morphological changes of the target surface for a pulse energy of 5 and 30 mJ after irradiation in the air for 5 s are presented in Figure 1. Short-term alloy irradiation with lower laser pulse energy resulted in the appearance of the superficial craters (Figures 1a and 1b). Increased laser pulse energy caused melting of the target material and formation of the hydrodynamic effects in the form of wave-like structures (Figure 1c). Presence of the microcracks in the damaged area is more pronounced when the alloy surface was irradiated with higher laser energy. Increase in the irradiation time and energy led to the formation of deeper surface craters (Figure 1d).

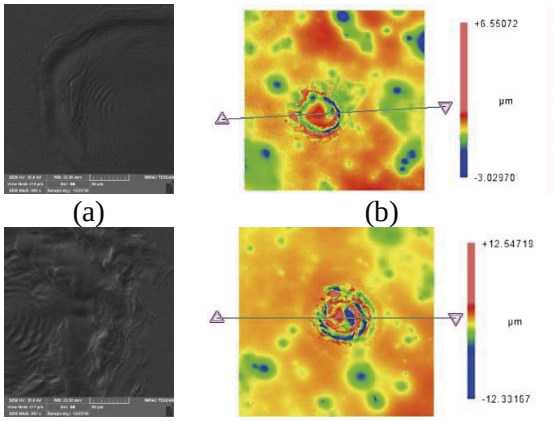

(a) (b)

(c) (d)

Figure 1. (a),(c) FE-SEM micrographs and (b),(d) 2D profilometric analysis showing the surface damage of the Ti-13Nb-13Zr alloy target during the irradiation time of 5 s in air under laser pulse energy of (a),(b) 5 mJ and (c),(d) 30 mJ

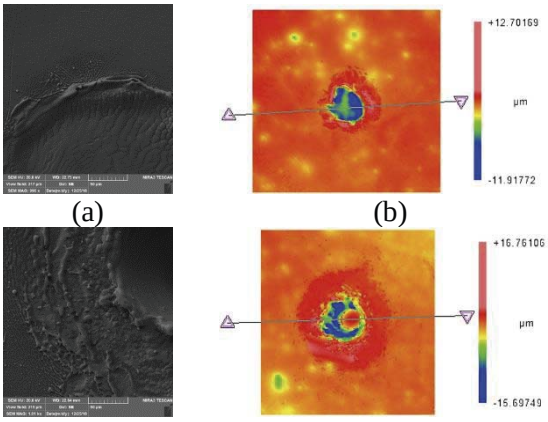

(a) (b)

(c) (d)

Figure 2. (a),(c) FE-SEM micrographs and (b),(d) 2D profilometric analysis showing the surface damage of the Ti-13Nb-13Zr alloy target during the irradiation time of 100 s in air under laser pulse energy of (a),(b) 5 mJ and (c),(d) 30 mJ

After increasing the irradiation time, the formation of more pronounced craters with microcracks and hydrodynamic effects in the form of solidified droplets can be observed (Figures 2a and 2c). Prolonged irradiation in the air also resulted in an increase of the crater depth (Figure 2b). Impact of the high laser energy and long-term irradiation can be seen in Figure 2c where clearly visible crater with rapidly melted and solidified surrounding area is presented. Increase of the irradiation time and laser pulse energy led to the formation of deeper craters on the alloy surface (Figure 2d).

Laser surface irradiation in argon also resulted in the formation of microcracks, craters and hydrodynamic effects in the form of solidified droplets and wave-like structures (Figures 3 and 4). Comparing the surface modifications achieved during the laser irradiation in air and argon atmosphere under the same irradiation conditions, it was found that the higher damage degree along the target depth was achieved in the argon atmosphere.

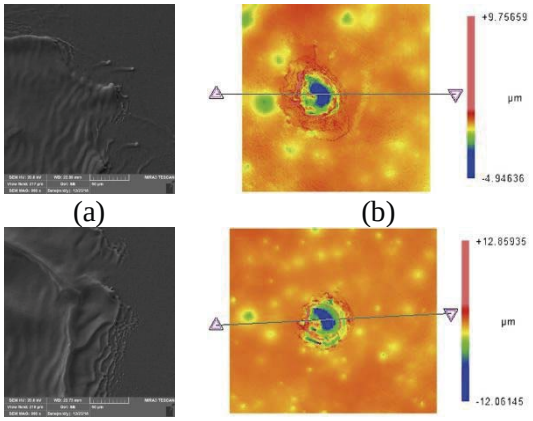

(a) (b)

(c) (d)

Figure 3. (a),(c) FE-SEM micrographs and (b),(d) 2D profilometric analysis showing the surface damage of the Ti-13Nb-13Zr alloy target during the irradiation time of 5 s in argon under laser pulse energy of (a),(b) 5 mJ and (c),(d) 30 mJ

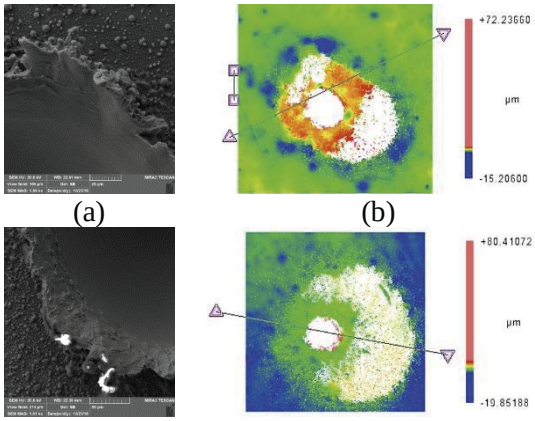

(a) (b)

(c) (d)

Figure 4. (a),(c) FE-SEM micrographs and (b),(d) 2D profilometric analysis showing the surface damage of the Ti-13Nb-13Zr alloy target during the irradiation time of 100 s in argon under laser pulse energy of (a),(b) 5 mJ and (c),(d) 30 mJ

4. Conclusion

Laser irradiation parameters significantly affect the morphology of the modified titanium alloy surface. The interaction of laser irradiation with Ti-13Nb-13Zr alloy led to the formation of surface craters and microcracks accompanied by hydrodynamic effects in the form of wave-like structures and solidified droplets. Laser irradiation in argon atmosphere resulted in the formation of the deeper craters with more pronounced hydrodynamic effects.

Acknowledgments
This work was financially supported by the Ministry of Education, Science and Technological Development of the Republic of Serbia through Projects No. ON174004 and ON172019.

References

[1] I. Cvijović-Alagić, Doctoral Thesis (in Serbian), Faculty of Technology and Metallurgy, University of Belgrade, Belgrade, Serbia (2013)
[2] M. Trtica, B. Gaković, D. Batani, T. Desai, P. Panjan, B. Radak, Applied Surface Science, 253 (2006) 2551-2556

Microstructure and fracture analysis of T6 treated hypereutectic Al-13.5Si alloy for IC engine components

DARKO VUKSANOVIC[1], VANJA ASANOVIC[1], ZORICA CVIJOVIC[2], JELENA SCEPANOVIC[1] AND DRAGAN RADONJIC[1]

[1] University of Montenegro, Faculty of Metallurgy and Technology, Podgorica, Montenegro; [2] University of Belgrade, Faculty of Technology and Metallurgy, Belgrade, Serbia

1. Introduction

Aluminum-silicon alloys have been applied significantly in the automotive, transportation, and several other industries due to their good strength, lightweight, castability, corrosion resistance, and excellent thermal conductivity [1-3]. Silicon as a major alloying element is added to aluminum alloys to improve their castability and fluidity as well as reduce shrinkage during solidification [4]. The mechanical properties of aluminum-silicon alloys depend on the morphology of eutectic silicon and intermetallic phases [5]. Magnesium, nickel, copper, and zinc having strengthening effects are added to aluminum-silicon alloys in order to improve their mechanical, physical, and service characteristics [4]. On the other hand, iron is a common impurity in aluminum and its alloys [4, 6]. Depending on chemical composition and production procedures various intermetallic phases such as Al_2Cu, Mg_2Si, Al_2CuMg [7], and Al(Fe,M)Si, where M denotes manganese, vanadium, chromium, molybdenum or copper could be expected in the microstructure of aluminum-silicon alloys [8]. Besides, the addition of magnesium may lead to precipitation of insoluble $Al_5Cu_2Mg_8Si_6$ phase with a low melting point [5]. Strength improvement of aluminum-silicon alloys at elevated temperatures is mainly caused by the precipitation of intermetallic Al_3Ni phase [6]. Since the solubility of iron in liquid aluminum and its alloys is high but very little in the solid, it forms different intermetallic phases with other elements such as α-Al_8Fe_2Si, β-Al_5FeSi, π-$Al_8FeMg_3Si_6$, and α-$Al_{15}(Fe,Mn)_3Si_2$ [6, 9]. The present work was undertaken to study the influence of T6 treatment on microstructure, mechanical properties, and tensile fracture of hypereutectic Al-13.5Si alloy. Our previous investigation has revealed that as-cast samples of Al-13.5Si alloy have exhibited properties which are in line with commercially available materials for manufacturing of internal combustion engine parts [10].

2. Experimental procedure

The hypereutectic Al-13.5Si alloy with the composition shown in Table 1. was made by melting AlSi10Mg master alloy, Al-based pre-alloys (Al-33%Cu, Al-60%Mn and Al-75%Fe) as well as technically pure silicon, nickel, and molybdenum in an electric resistance furnace. The Al-10% Sr master alloy was added to the melt for modification of eutectic silicon. Details of the casting and poring procedures have already been published [10]. In order to provide a better combination of tensile strength and elongation compared to cast condition [11], the T6 treatment was performed. The solution treatment carried out at 520 $^oC \pm 5\ ^oC$ for 6 hours was followed by quenching in water (at 70^oC). The subsequent artificial aging treatment was performed at 205 $^oC \pm 5\ ^oC$ for 7 hours while specimens were finally cooled in ambient air. The tensile strength and relative elongation of the T6 treated specimens were determined at room temperature using the machine 1195 Instron, whereas the hardness was determined as Brinell hardness HB 5/250/30 by testing machine produced by Karl Frank Gmbh, type 38532. An optical microscope and scanning electron microscope JEOL JSM-6460 LV examined the microstructures of T6 treated samples. The characterization of fracture morphology of the samples after tensile testing was carried out with JEOL JSM-6460 LV in secondary electron mode.

Table 1. Chemical composition of Al-13.5Si alloy (wt%).

Si	Cu	Mg	Ni	Co	Fe	Mo	Mn	Sr	Al
13.50	1.47	1.30	0.36	0.35	0.33	0.20	0.07	0.048	Bal.

3. Results and discussion

The microstructure of as-cast samples consists of the fine dendrites of α-Al phase, 31.11 vol.% of disperse eutectic silicon, about 10 vol.% of intermetallic phases based on iron, manganese, copper, nickel, cobalt, silicon and magnesium, as well as a small amount of a brittle β-Al_5FeSi(Mn) phase [10]. Considering that hypereutectic Al-13.5Si multicomponent alloy has hypoeutectic morphology, it is evident that the addition of strontium has caused the decreasing of Al-Si eutectic temperature and shift of the eutectic composition away from 12 % of silicon [10]. Besides α-Al phase, the rounded eutectic silicon (24.72 vol.%) and several intermetallic phases (6.67 vol.%) were revealed in T6 treated specimens. About 0.16 vol.% of β-Al_5FeSi(Mn) phase were found, especially in the central part of T6 treated specimens (Fig. 1 a-c). The fine and rounded particles of Al_3Ni phase in the quantity of 5.02 vol.% (Fig. 1.d), traces of Al_3(Fe,Mn,Cu,Co,Ni) and only 0.09 vol.% of α-Al_{15}(Fe,Mn,Cu)$_3Si_2$ with a Chinese script morphology were recognized in T6 treated samples (Fig. 1.c). Insoluble $Al_5Cu_2Mg_8Si_6$ phase was observed in the quantity of 1.4 vol.%, while only traces of $M_{g2}Si$ phase are found after T6 treatment. Other phases based on copper and magnesium were mostly dissolved.

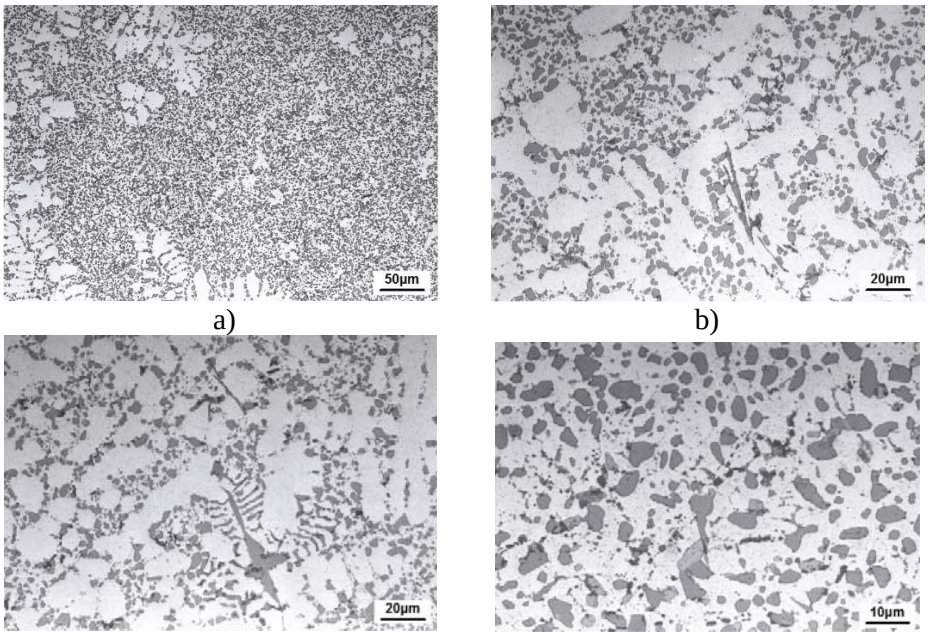

a) b) c) d)

Figure 1. The microstructure of T6 treated Al-13.5Si alloy.

The values of the mechanical properties of as-cast alloy are explained in our previous work [10]. Compared to cast samples, T6 treated specimens have exhibited a better tensile strength and elongation, but the lower hardness (Table 2.). A wide dispersion of eutectic silicon particles after T6 treatment may cause a decrease in hardness [12]. Although the tensile strength of T6 treated samples of Al-13.5Si alloy are comparable with results obtained for hypoeutectic Al-Si alloys [12, 13], the elongation could be better. Furthermore, a slight increase in the tensile strength due to T6 treatment suggests a further investigation of solution treatment parameters for achieving the best combination of mechanical properties of Al-13.5Si alloy.

Table 2. Mechanical properties of as-cast [10] and T6 treated samples of Al-13.5Si alloy.

Specimen	R_m [MPa]	Hardness [HB]	Elongation [%]
As-cast	254.8	1.4	138.0
T6 treated	269.7	2.1	102.0

Fracture analysis of samples after T6 treatment has revealed a plane surface indicating a brittle fracture (Fig. 2.a). Higher magnification has discovered the predominantly intercrystalline fracture

with features of ductile failure (Fig. 2.b-f). Rounded eutectic silicon and low quantity of intermetallic phases contribute to the ductile fracture nature. Nevertheless, β-Al_5FeSi(Mn) and small intermetallic particles with smooth surfaces have caused a brittle fracture.

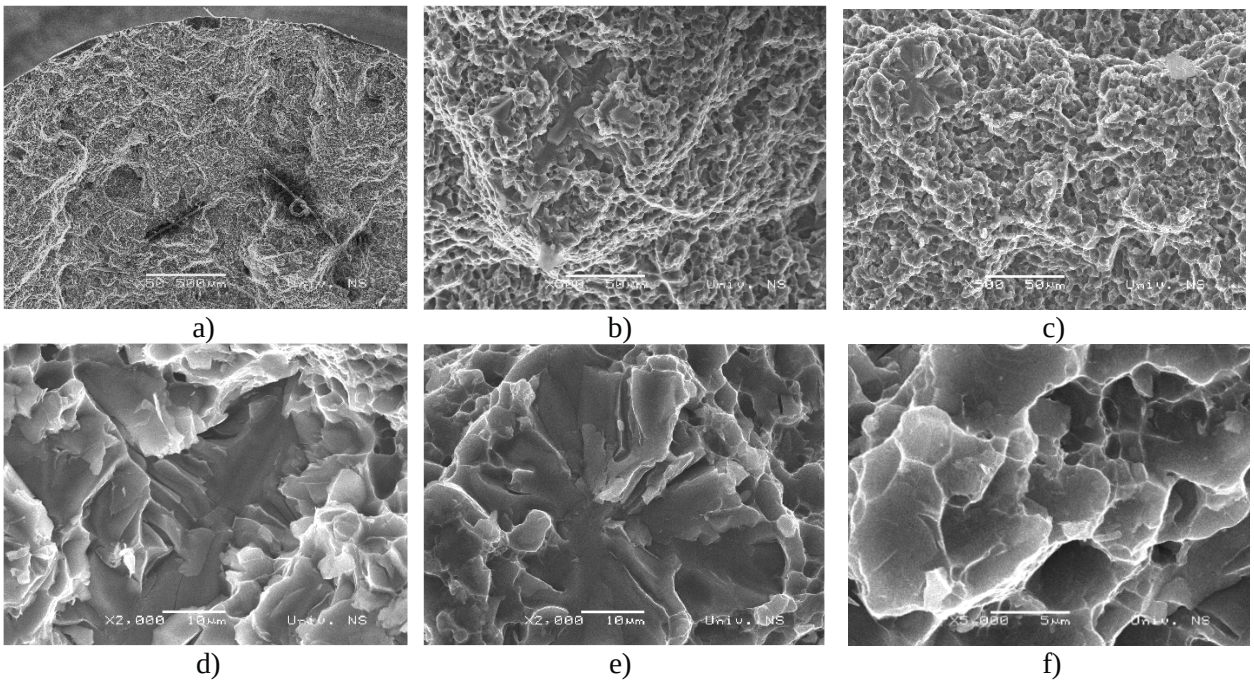

Figure 2. Fracture surface morphologies of T6 treated specimes of Al-13.5Si alloy.

4. Conclusions

The microstructure of T6 treated Al-13.5Si alloy consists of α-Al phase, the rounded eutectic silicon (24.72 vol.%) and several intermetallic phases (6.67 vol.%). T6 treated specimens have exhibited a better tensile strength and elongation, but the lower hardness compared to as-cast samples. Although the mechanical properties are in line with other available hypoeutectic alloys, the next study will be focused on solution treatment parameters for achieving the best combination of strength and ductility.

The predominantly intercrystalline fracture with features of ductile failure was observed. While rounded eutectic silicon and low quantity of intermetallic phases contribute to the ductile fracture nature, β-Al_5FeSi(Mn) phase and small intermetallic particles with smooth surfaces have caused a brittle fracture.

References

[1] G. K. Sigworth, Int. J. Metalcast., 2 (2) (2008) 19-40
[2] L. Liu, A. M. A. Mohamed, A. M. Samuel et al., Metall. Trans. A, 40A (10) (2009) 2457-2469
[3] M. Javidani, D. Larouche, Int. Mater. Rev., 59 (3) (2014) 132-158
[4] F. C. Robles-Hernandez, J. M. H. Ramírez, R. Mackay, Al-Si Alloys: Automotive, Aeronautical, and Aerospace Applications, Springer, Cham, Switzerland, 2017
[5] Y. Han, A. M. Samuel, H. W. Doty, S. Valtierra, F. H. Samuel, Mater. Des., 58 (2014) 426-438
[6] J. A. Taylor, Procedia Mater. Sci., 1 (2012) 19-33
[7] R. Konecná, G. Nikoletto, L. Kunz, M. Svoboda, A. Baca, Procedia Eng., 74 (2014) 43-46
[8] G. Mrówka-Nowotnik, Arch. Mater. Sci. Eng., 38 (2) (2009) 69-77
[9] C. Triveño Rios, R. Caram, C. Bolfarini et al., Acta Microscopica, 12 (1) (2003) 77-81
[10] J. Scepanovic, V. Asanovic, S. Herenda et al., Int. J. Metalcast., 13 (2019) 700-714
[11] F. J. Tavitas-Medrano, J. E. Gruzleski et al., Mater. Sci. Enh., A, 480 (2008) 356-364
[12] M. Ishak, A. Amir, A. Hadi, ICMER2013, Pahang, Malaysia, 2013
[13] M. F. Ibrahim, E. M. Elgallad, S. Valtierra et al., Materials, 9 (2):8 (2016) 1-17

Crack development at in-situ tensile testing

MARTIN BYSTRIANSKÝ[1], LUDMILA KUČEROVÁ[2] AND JAN HAJŠMAN[3]

[1] Regional Technological Institute, University of West Bohemia in Pilsen, Czech Republic; [2] Regional Technological Institute, University of West Bohemia in Pilsen, Czech Republic; [3] Regional Technological Institute, University of West Bohemia in Pilsen, Czech Republic

Using in-situ tensile stage placed in SEM provides good insight to observation of microstructure deformation. Deformation can be visible both in SE or EBSD mode. Various steel (e.g. TRIP steel, maraging steel prepared by additive manufacturing, tool steel) specimen were used for tensile testing. Experiments cover whole area of stress-strain curve and are performed until complete break of the specimen. The progress of sample deformation and the development of the crack is strongly affected by the quality of the material. Also any eventual presence of a defect in the structure (such as inclusions, pores, microcracks, unmelted metal powder particle, AM laser trace residuum) can cause changes not only in microstucture deformation process but can lead to changes in results of tensile testing. Different shape of the stress-strain curve was observed comparing defect and defect-free sample of the same steel.

These areas of inhomogeneity may also act as crack initiators or, if in large number or suitable distance, determine the direction of the crack propagation. However, it was found (Fig. 1a,b) that such defect (inclusion in a low alloyed bainitic steel) act as a point where tensile stress was released, propagation of the crack stopped and new branch of the crack started to propagate in an opposite direction to the original crack.

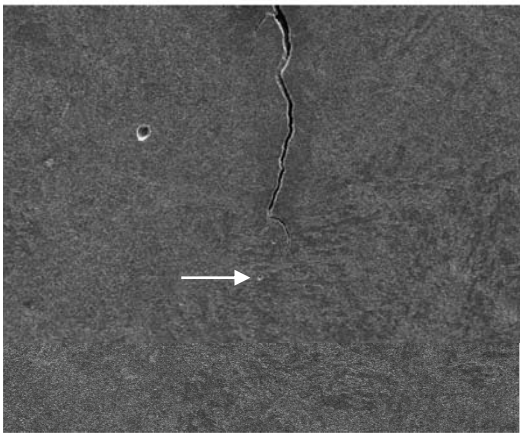

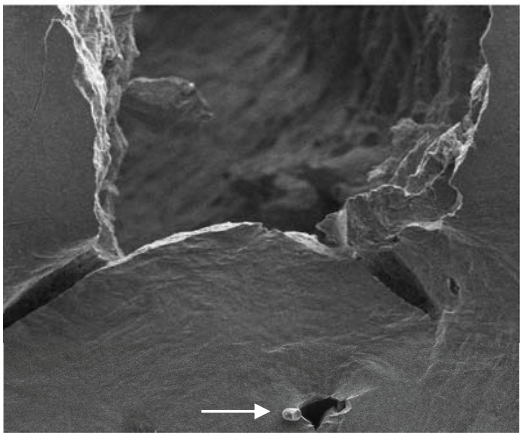

But mostly, inclusions are of course the weak points of the material and irreversible break or separation from the matrix occurs while the material is still in the elastic deformation (Fig. 2,3). The structure deformation takes place afterward.

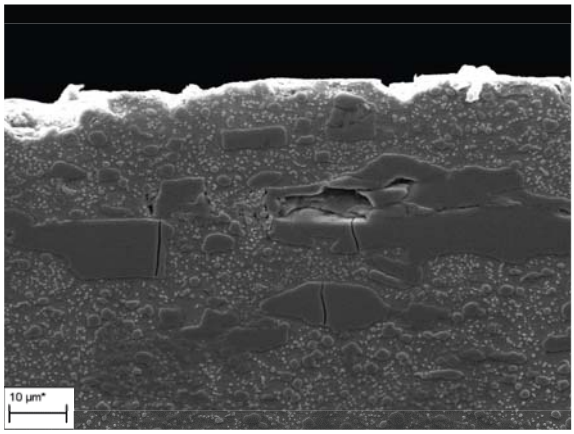

Figure 2 Cracking of chromium carbides in tool steel.

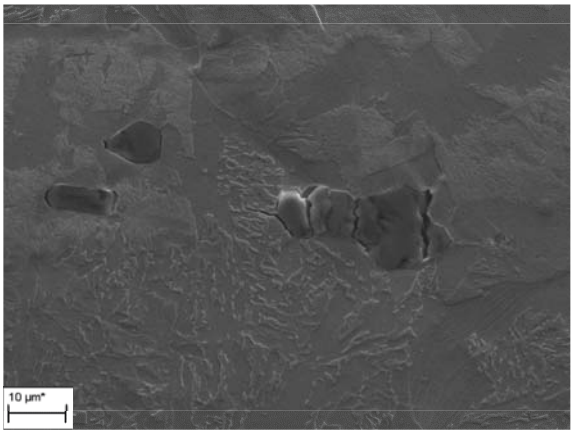

Figure 3 Interface decohesion of Al particle in a TRIP steel matrix.

Acknowledgement

This contribution has been prepared under project LO1502 'Development of the Regional Technological Institute' under the auspices of the National Sustainability Programme I of the Ministry of Education of the Czech Republic aimed at supporting research, experimental development and innovation.

Effect of particle size TiO_2 Flux in A-TIG welding

MIROSLAV DRAMICANIN[1], SEBASTIAN BALOS[1], PETAR JANJATOVIC[1], DRAGAN RAJNOVIC[1], SAVKA ADAMOVIC[1]

[1] University of Novi Sad, Faculty of Technical Sciences, Novi Sad, Serbia

In this paper, the influence of submicron and nanoparticle sized TiO_2 particles in Activated TIG (A-TIG) welding was studied. Penetration depths and microstructures after welding were the bases for creating the material flow model, to prove the main mechanism of increasing penetration in A-TIG welding compared to TIG welding.

Tungsten Inert Gas (TIG) welding is a well-known welding process which can produce high-quality welds on various materials, including different stainless steels and numerous non-ferrous. However, it has a low deposition rate and also low penetration which results in relatively low productivity, that is, the application is limited to thin sections [1, 2]. To solve this problem, the flux for increasing the penetration depth was developed and this welding process was called Activated TIG (A-TIG). In this welding process, flux is sprayed or applied with a brush over the cleaned and prepared surface to be welded. Fluxes were fabricated by mixing, usually metallic oxide powders with solvents, most frequently acetone and ethanol [3, 4].

Six different flux mixtures were prepared using 20 nm nanoparticle TiO_2 (N) and 0.3 µm submicron particle TiO_2 (M), containing 5 wt. % of particles in acetone. After that, welding - remelting was done on a stainless steel plate (AISI 304) having the dimensions of 50x50x10 mm. One pass was without flux as a control sample (0). The coating was applied to a base material about 20 mm wide with a 10 mm brush. Welding - remelting was done with 2.4 mm tungsten - 2% thorium electrode with a conical shape angle 90° with 0.5 mm frustum at the tip. Arc length was 2 mm, welding speed was 100 mm/min, the protective gas argon flow rate was 12 l/min, while welding current was 200 A. After welding, the plates are cut in half at the crossbar to the metal seam, then standardly metallographic prepared, and finally etch by aqua regia. Macro and microstructure examination were done on a Leitz Orthoplan light microscope which was used for weld dimension measurements, also.

Macro images of welds obtained without and with flux, with indicated depths, widths, and depth to width ratios and weld surfaces are shown in Figure 1. Penetration depths of specimens welded with flux are higher than in the control specimen. Also, the flux containing submicron particles had a lower penetration depth than the flux containing nanoparticles. The highest penetration was with a mixture of micro and nano particles (3M2N). Figure 2 shows the weld metal of the selected samples, where the usual dendritic structure for metal can be observed. Microstructure near fusion line under the surface is shown in Figure 2, while microstructure near fusion line under weld metal is shown in Figure 3. It can be seen that in specimen welded without flux (0-F) austenite grain coarsening has been noticed near the surface, while in specimen 3M2N-F and 5N-F it was in the bottom, under the weld metal. The growing of austenite grains occurs due to high temperature in the certain area, caused by the direction of melt flow, as shown in the material flow model, Figure 5 [5]. This type of changing material flow using activated flux called reversed Marangoni effect and has a significant impact on increased penetration.

Acknowledgments

The authors gratefully acknowledge research funding by the project entitled “Development and Application of Advanced Characterization of Materials and Welds in Production Engineering” on the Department of Production Engineering, Faculty of Technical Sciences Novi Sad, Serbia.

References

[1] K.-H. Tseng, P. Lin, Materials, 7 (2014) 4755-4772
[2] S. Nayee, V. Badheka, 16 (2014) 137-143
[3] H-Y. Huang, Metall Mater Trans A, 41 (2010) 2829-2835
[4] R. Vidyarthy, D. Dwivedi, J Manuf Process, 22 (2016) 211-228
[5] S. Balos, M. Dramicanin, P. Janjatovic, I. Zabunov, D. Klobcar, M. Busic, M. L. Grilli, Metals, 9 (2019) 567-578.

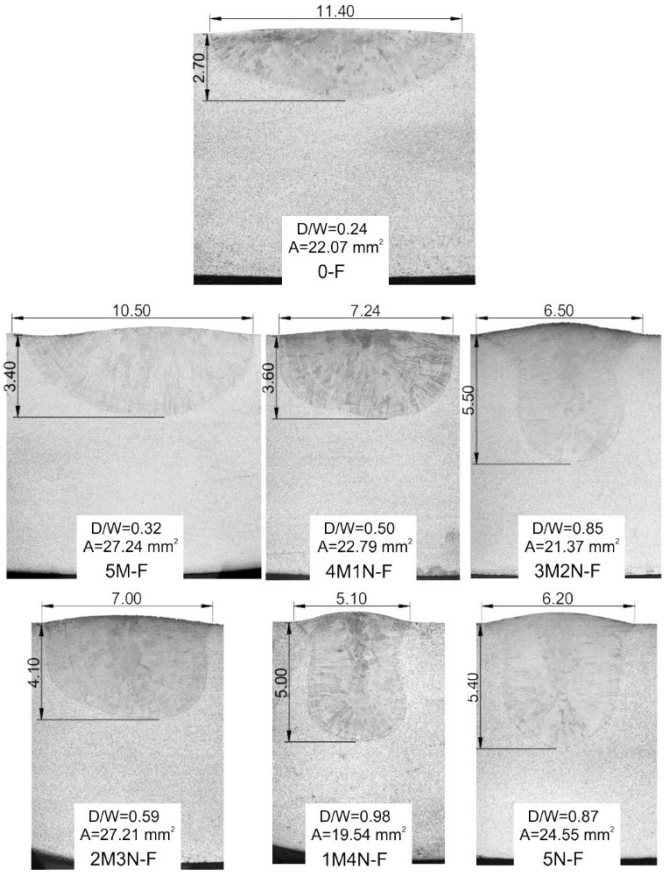

Figure 1. Macro images of specimens welded without and with flux, with indicated depths, widths, depth to width ratios and weld surfaces

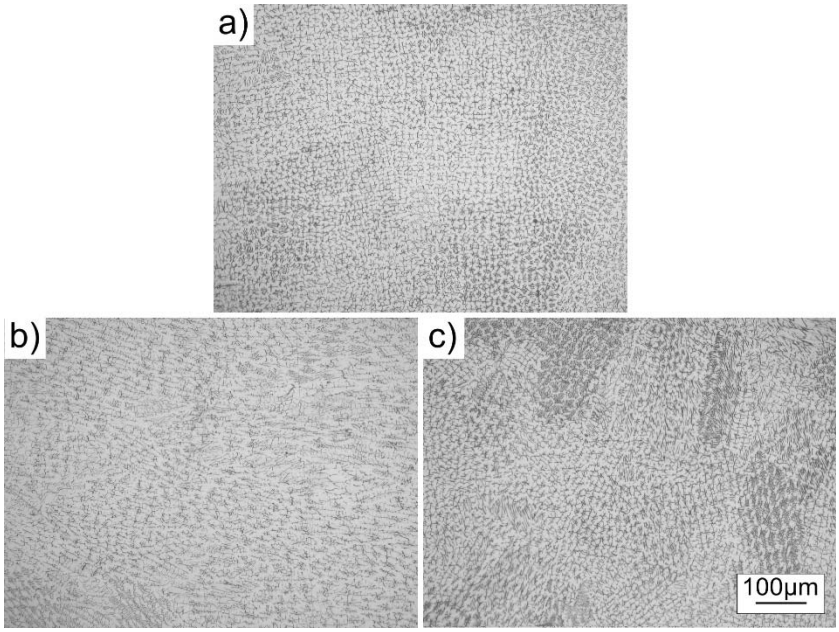

Figure 2. Weld metal microstructure: a) specimen 0-F; b) specimen 3M2N-F; c) specimen 5N-F

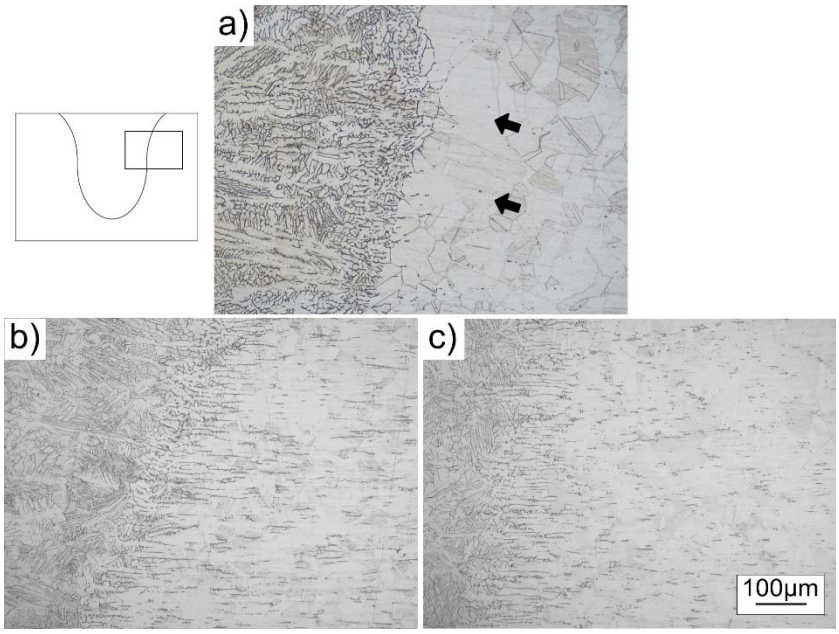

Figure 3. Microstructures near fusion line under the surface: a) specimen 0-F; b) specimen 3M2N-F; c) specimen 5N-F

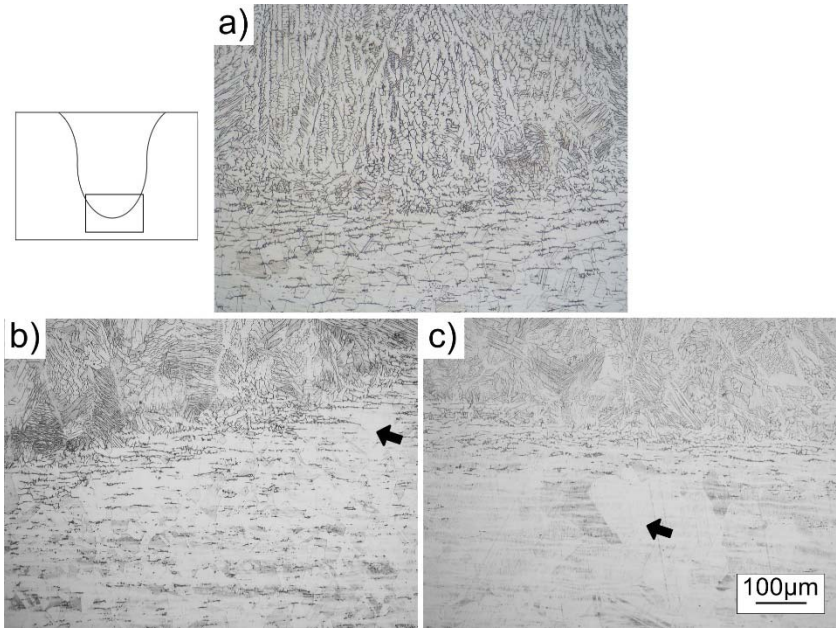

Figure 4. Microstructure near fusion line at the bottom of the weld: a) specimen 0-F; b) specimen 3M2N-F; c) specimen 5M-F

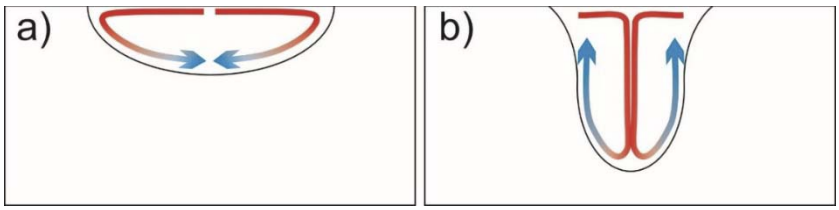

Figure 5. TIG and A-TIG metal flows: a) without the flux; b) with the flux

Properties of the FeAl20Si20-MoX (X=5, 10, 15, 20 wt.%) alloy prepared by mechanical alloying and compacted via SPS

FILIP PRŮŠA[1], ANDREA ŠKOLÁKOVÁ[1] AND JIŘÍ LIETAVEC[3]

[1] University of Chemistry and Technology, Prague, Department of Metals and Corrosion Engineering, Prague, Czech Republic

The Fe-Al-Si-based alloys belong to a recently developed group of materials which might replace the nickel-based superalloys, heat-resistant steels or cobalt alloys. Their main advantage is the combination of relatively low density with excellent mechanical properties and corrosion resistance while maintaining low production costs. However, the production of these alloys using conventional casting metallurgy is often highly problematic. Thus, the powder metallurgy processes, represented by mechanical alloying, are high of interest for the preparation of these alloys. The process itself allows preparing the intended alloys with ultrafine-grained or even nanocrystalline microstructure while simultaneously increasing their mechanical properties via intensive plastic deformation.

The FeAl20Si20-MoX (X=5, 10, 15, 20 wt.%) alloys were prepared by a combination of mechanical alloying and spark plasma sintering. The compact samples were investigated for microstructure, and the mechanical properties, including the Vickers hardness. Besides, the compressive stress-strain test done at laboratory temperature either on the as-compacted samples and the samples annealed up to 100 h at 800 °C were done. The compressive tests were also done on the compact samples at a temperature of 800 °C. Samples were also investigated for thermal stability by measuring the Vickers hardness change as well for the high-temperature oxidation resistance.

All of the prepared samples showed ultrafine-grained microstructure with grains dimensions around or below 200 nm. The present phases were mainly identified as FeSi, Fe_3Si and $MoSi_2$. It was found that the increasing content of Mo improves the hardness and the ultimate compressive strengths of prepared alloys reaching its maxima for the FeAl20Si20Mo20 alloy. All of the tested alloys also showed excellent oxidation resistance due to the formation of a protective layer of Al_2O_3.

Acknowledgement

This research was carried out in the frame of the project 17-07559S, financed by Czech Science Foundation.

The effect of Ni and Mo addition on microstructure and properties of Fe-Al-Si alloys

ANDREA ŠKOLÁKOVÁ[1], OLGA PROSHCHENKO[1] AND FILIP PRŮŠA[1]
[1] University of Chemistry and Technology, Prague, Department of Metals and Corrosion Engineering, Prague, Czech Republic

The Fe-Al-Si alloys belong to advanced materials for high-temperature applications in the automotive industry. These alloys excel in ultra-high hardness, strength, oxidation resistance, excellent strength at elevated temperatures and resistance against high-temperature reactions with gases, promising magnetic properties and many others. Moreover, these alloys could be an alternative to the materials containing, for example, Cr which belongs to the critical raw elements in the past. Possible production routes of Fe-Al-Si alloys concern casting technology which is considerably inconvenient (cost, impurities, high melting point, inhomogeneity) or powder metallurgy processes.
The Fe-Al-Si-X-Y (X, Y = Mo, Ni) alloys were prepared by a combination of mechanical alloying and compaction via spark plasma sintering. Chemical composition of studied alloys corresponded to FeAl20Si20Ni5Mo15, FeAl20Si20Ni10Mo10, FeAl20Si20Ni15Mo5 (wt.%). The microstructure, thermal stability, oxidation resistance and mechanical properties were observed and compared with FeAl20Si20 alloy. Based on the results, it could be concluded that the addition of Ni and Mo has a positive effect on the overall mechanical properties. The hardness and compressive strength of obtained alloys were higher than in the case of FeAl20Si20 alloy due to the presence of mainly $MoSi_2$ phase. Furthermore, the Fe_3Si phase was supersaturated by aluminium. On the other hand, alloys were very brittle and exhibited worser thermal stability compared the the reference FeAl20Si20 alloy.

Acknowledgement
This research was carried out in the frame of the project 17-07559S, financed by Czech Science Foundation.

Friction Stir Spot Welding of Multiple Ultrathin Sheets of aluminium-magnesium alloy

DANKA LABUS ZLATANOVIC[1], SEBASTIAN BALOS[1], JEAN PIERRE BERGMANN[2], MICHAEL GRÄTZEL[2], DRAGAN RAJNOVIC[1], TOBIAS KÖHLER[2] AND LEPOSAVA SIDJANIN[1]

[1] Department of Production Engineering, Faculty of Technical Science, University of Novi Sad, Serbia;
[2] Department of Production Technology, Ilmenau University of Technology, Ilmenau, Germany

1. Introduction

Nowadays, the use of light alloys in automotive and aerospace industries is increased, due to the higher demand for weight reduction. Substitution of copper by aluminium is widely persuaded in order to save weight and material costs, for battery components and wire connectors. The decreasing in the energy requirements of the manufacturing processes is also desirable, as well as the stability of material cost on the market. Therefore, the development of joining technologies of aluminium and its alloys, with acceptable weld characteristics and minimal energy consumption is demanded [1–3].

Friction stir welding (FSW) is the technique which was developed at The Welding Institute (TWI), UK in 1991 [3–8]. It offers various advantages such as small or no distortion, high mechanical properties, low energy consumption, no consumable material or shielding gas are needed, it offers convenient microstructure and is especially well suited to the welding of aluminium alloys [7]. The basic concept is relatively simple. A rotating tool with a special designed pin and shoulder penetrates the upper side of the sheet in the overlapping area until a certain plunge depth is reached. The process lasts until the sheets are joined. Then the rotational tool retracts, and a keyhole is formed. The keyhole affects surface quality and mechanical properties of the joints, especially on thin aluminium sheets. In this paper, the convex pin-less tool is used to overcome this disadvantage.
The aim of this study is to evaluate influence of rotational speed on the microstructure of four-layer lap-joint from ultrathin aluminium-magnesium sheets during friction stir spot welding (FSSW).

2. Experimental work

Specimens used for FSSW were cut from thin sheets of rolled commercial aluminium alloy 5754 to dimensions of 44 × 90 × 0.3 mm. Experiments were carried out on force controlled EJOWELD C50R FSSW machine with maximal rotational speed 9000 RPM, with maximum force 8 kN and maximum time 5 s. The convex pin-less tool made from H13 (X40CrMoV51) hot-work tool steel was originally designed and used for experiments. The force and plunge depth were 2.2 kN and 0.25 mm, respectively, while the rotational speed was varied (1750, 2750 and 3750 RPM). After the FSSW, the standard metallographic preparation (grinding and polishing) followed with electrolytical etching with Barkers regent was performed. The cross-section morphology of the joints was analysed by light microscope Zeiss AxioScope.A, for etched samples and Zeiss Axio Vert.A1 MAT, for polished samples with crossed polarised light and sensitive tint. Further characterisation of samples was carried out using the Field Emission Scanning Electron Microscope (FE-SEM) Hitachi S-4800.

3. Results

The top view and cross-section morphology (polished and etched) of the samples welded with 2.2 kN force, 0.25 mm plunge depth and rotational speeds 1750, 2750 and 3750 RPM are shown in Figure 2.

In all samples top surfaces have two different zones. The smooth zone marked with a red arrow is the zone that corresponds to the welding area, while the rough zone marked with a white arrow is a zone where presence of edge chipping is observed. The upper sheet has no flashes and from Figure 1(a,b) it is clear that no welding defects such as porosity, wormhole, partially bonded area or hook defects in the cross section were observed. However, in the sample in Figure 1(c) the last two sheets are only partially bonded.

The difference in grain size in base material and in samples with different rotational speeds taken from areas in white squares marked in Figure 1 are shown in Figure 2. The grain size intensively decreases with decreasing of rotational speed.

In Figure 3, the difference between the well bonded (Fig 1(c) – white square) and partially bonded area (Fig 1(c) – red square) can be observed. In figure 3(a), a fully bonded region did not show any obvious boundary at the interfacing surfaces, whereas in some other regions, as shown in figure 3(b), there were some partially bonded regions characterised by intermittent welded areas and intermittently present interfacial boundaries were noticed especially pronounced at higher rotation speeds.

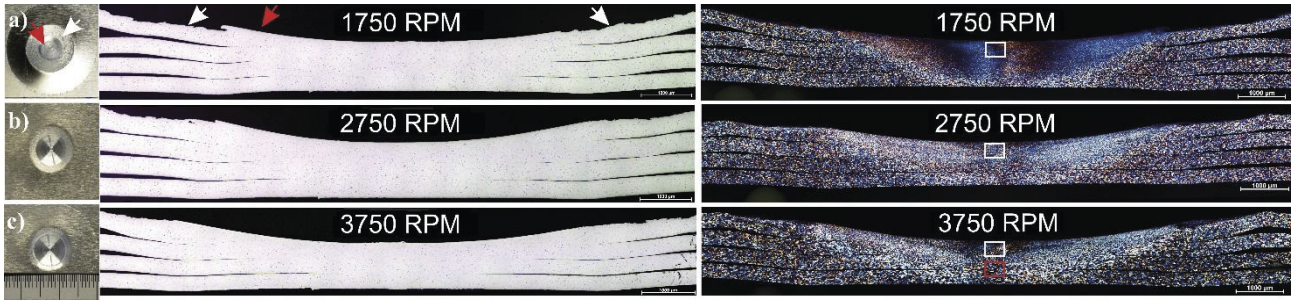

Figure 1. Macrographs and cross-section view of the welded joints at different RPM

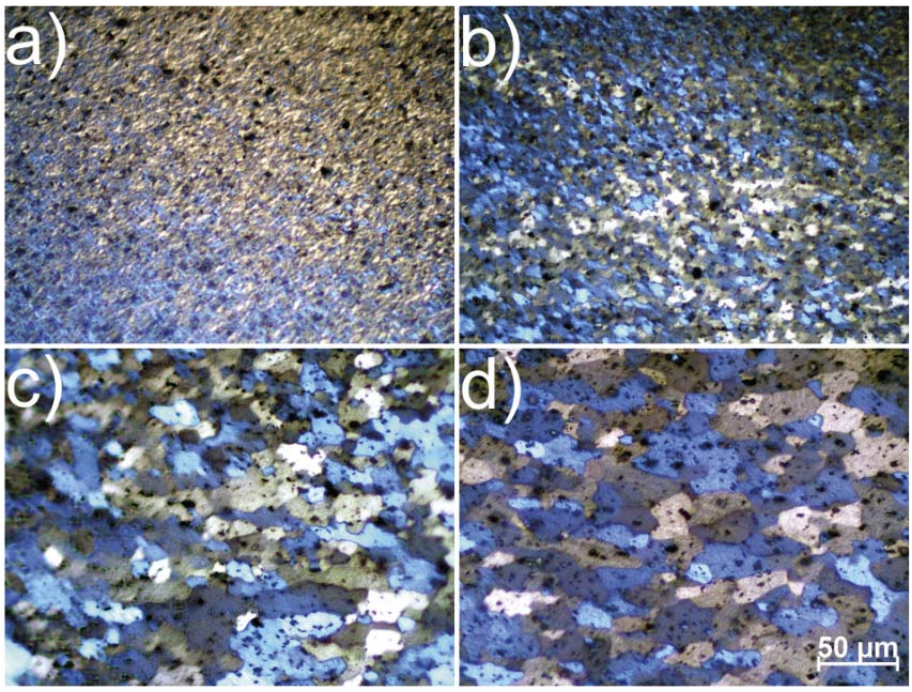

Figure 2. Cross-section light microscopy images (white squares in Figure 2 showing grain microstructure of: a) 1750 RPM; b) 2750 RPM; c) with 3750 RPM; d) base material

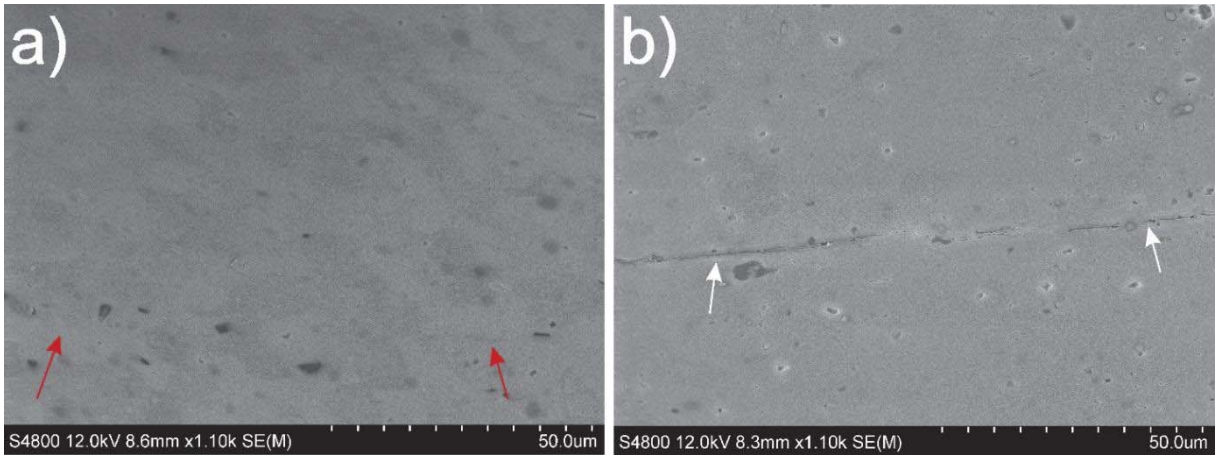

Figure 3. SEM images of welded sheets joined at a rotational speed of 3750 RPM showing (a) interface between first and second sheet and (b) second and third sheet interface sheets highlighting fully bonded and partially bonded regions

4. Concluding remarks

By designing pin-less convex shaped tool, the paper reports achieving successful defect-less joining of four overlapped aluminium-magnesium sheets. Presented results show that rotational speed is responsible for the alteration of the microstructure. Significant drop of grain size with drop of rotational speed can be observed, while samples welded with higher rotational speed have grain size approximately to the base material. With higher rotational speed there is a higher possibility of defects to occur (as partially bonded area).

Acknowledgment

The authors gratefully acknowledge research funding by the project entitled "Advanced technologies and interdisciplinarity in production engineering" on the Department of Production Engineering, Faculty of Technical Sciences Novi Sad, Serbia. Also, authors are grateful to the DAAD program for the scientific support.

References

[1] A. Regensburg, F. Petzoldt, T. Benss, J.P. Bergmann, Weld. World. 63 (2018) 117–125.
[2] D. Bakavos, Y. Chen, L. Babout, P. Prangnell, Metall. Mater. Trans. A Phys. Metall. Mater. 42 (2011) 1266-1282.
[3] O.O. Ojo, Emel Taban, Erdinc Kaluc, Mater. Test. 57 (2015) 595–627.
[4] R.S. Mishra, Z.Y. Ma, Mater. Sci. Eng. R. 50 (2005) 1–78.
[5] J.M. Piccini, H.G. Svoboda, T, J. Manuf. Process. 26 (2017) 142–154.
[6] S. Babu, V.S. Sankar, G.D. Janaki Ram, P. V. Venkitakrishnan, G. Madhusudhan Reddy, K. Prasad Rao, J. Mater. Eng. Perform. 22 (2013) 71–84.
[7] X.W. Yang, T. Fu, W.Y. Li, Adv. Mater. Sci. Eng. (2014) 1-11.
[8] A. Gerlich, P. Su, M. Yamamoto, T.H. North, J. Mater. Sci. 42 (2007) 5589–5601.

Microstructure and phase constitution of near-Co2FeSi Heusler alloy

JIŘÍ BURŠÍK AND YVONNA JIRÁSKOVÁ
CEITEC IPM, Institute of Physics of Materials of the Czech Academy of Sciences, Brno, Czech Republic

Heusler alloys are characterized by formula X_2YZ, where X and Y are transition metals (e.g. Fe, Co, Mn) and Z is an element from group III, IV, or V. They form a broad and heterogeneous class of alloys, many of them still attracting remarkable attention regarding their physical properties and subsequent applications [1]. The Co-based Heusler compounds are of particular interest being good ferromagnetic materials, showing comparatively high Curie temperatures and having relatively low degrees of atomic disordering. They are used e.g. for magnetic data storage applications and as ferromagnetic materials in spintronic devices.

Here we focus on a Co_2FeSi Heusler alloy prepared by arc melting. The nominal composition was close to the stoichiometric one, hence the microstructure was formed primarily by equiaxed coarse grains of Co_2FeSi phase (Fm-3m cubic crystal lattice with a = 0.5658 nm [2]). The details of sample preparation, basic microstructure characterization and a thorough measurement of magnetic properties can be found in [3]. An interesting feature of forming a continuous layer of another phase along grain boundaries (GBs) was observed and it is studied here in detail. EDX maps reveal an increase of Co and Si at the expense of Fe in an interfacial (IF) layer about 2–3 µm thick (Fig. 1). Searching the ICSD [2] offers two candidate phases consistent with the results of quantitative EDX analyses, namely $(Co,Fe)_2Si$ and $Co_3(Fe,Si)_2$.

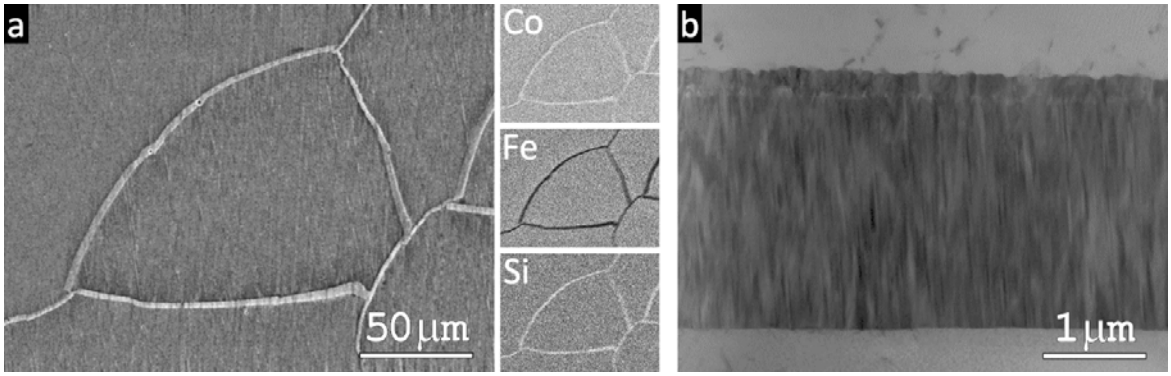

Figure 1. A SEM micrograph of grains with a continuous layer of IF phase along boundaries documented also on EDX maps (a), and a TEM image showing the twinned IF layer (b).

A focussed ion beam was used to prepare several thin lamellae from the GB region and study details of IF phase structure by means of electron diffraction and HRTEM imaging using a Philips CM12 STEM and a Thermo Scientific Titan Themis 60-300 cubed microscopes. The work was supported by the Ministry of Education, Youth and Sports of the Czech Republic under the project CEITEC 2020 (LQ1601) and used facilities of the CEITEC Nano research infrastructure.

[1] C. Felser and A. Hirohata, Editors, Heusler Alloys - Properties, Growth, Applications, Springer Series in Materials Science, Vol. 222, Springer International Publishing, Switzerland (2016)
[2] Inorganic Crystal Structure Database, http://www2.fiz-karlsruhe.de/icsd_home.html, NIST/FIZ, version 1.9.8, 2016-2
[3] A. Titov, O. Životský, A. Hendrych, D. Janičkovič, J. Buršík, Y. Jirásková, Acta Phys. Pol. A 131 (2017) 654–656

MS2

Nanoscale, nanostructured, and carbon based materials

CHAIRPERSONS:

Andreja Gajović, Sanja Milošević Govedarović

INVITED LECTURE

Low-energy electron microscopy of 2D graphene-hexagonal boron nitride heterostructures

MARIN PETROVIĆ[1,2]
[1] Faculty of Physics and CENIDE, University of Duisburg-Essen, Duisburg, Germany;
[2] Institute of Physics, Zagreb, Croatia

Low-energy electron microscopy (LEEM) is a surface-sensitive experimental technique which provides many possibilities for the investigation of morphology, crystallography, and electronic structure of interfaces, thin films and 2D materials. In this talk, LEEM study of the atomically-thin lateral heterostructures of hexagonal boron nitride (hBN) and graphene on Ir(111) will be presented. The heterostructures have been synthesized by sequential chemical vapor deposition (CVD) in ultra-high vacuum [1]. Firstly, well-defined hBN islands were grown by CVD from borazine, and real-time LEEM imaging of the synthesis enabled identification of substrate steps as decisive factor governing the shape of hBN islands. In the next stage, graphene was grown by CVD from ethylene and has formed exclusively at the edges of the preexisting hBN islands, thus constituting 2D lateral heterostructures (see Figure 1). However, in addition to the graphene and hBN regions, the heterostructures contain alloyed material composed of B, C and N atoms arranged in a 2D hexagonal lattice. It was found that the alloying originates from intermixing of the precursor fragments that are involved in the sequential CVD synthesis, and that the alloy characteristics can be modified by controlling the parameters of the synthesis.

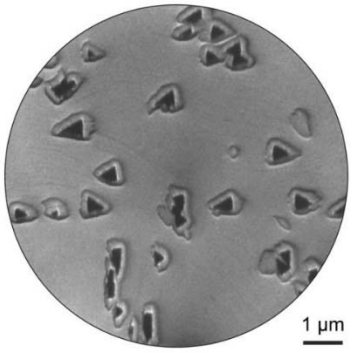

Figure 1. LEEM image of hBN-graphene heterostructures on Ir(111) synthesized by sequential CVD process. HBN cores (dark contrast) are surrounded by B-C-N alloy and graphene.

In addition, a new method for in situ fabrication of graphene and B-C-N microstructures is introduced, which relies on the decomposition of hBN on Ir(111) at elevated temperatures [1,2]. This method enables fabrication of atomically thin conducting and semiconducting micro-elements, which could be utilized in future for the construction of more complex (opto)electronic devices based on 2D materials.

References

[1] M. Petrović, M. Horn-von Hoegen, and F.-J. Meyer zu Heringdorf, Appl. Surf. Sci., 455 (2018) 1086
[2] M. Petrović, U. Hagemann, M. Horn-von Hoegen, and F.-J. Meyer zu Heringdorf, Appl. Surf. Sci., 420 (2017) 504

INVITED LECTURE

Dynamic acoustic modulation of quantum light emission from GaN/InGaN nanowire quantum dots

SNEŽANA LAZIĆ[1], ŽARKO GAČEVIĆ[2] AND ENRIQUE CALLEJA[2]

[1] Departamento de Física de Materiales, Instituto 'Nicolás Cabrera' and Instituto de Física de Materia Condensada (IFIMAC), Universidad Autónoma de Madrid, Spain; [2] ISOM-DIE, Universidad Politécnica de Madrid, Spain

Single-photon sources are key elements for applications in quantum photonics. Among various non-classical light sources available, quantum dots (QDs) outdo with their integrability into existing semiconductor-based on-chip solutions. Future quantum communication and information processing, however, requires controllable quantum light sources that can be operated on-demand and with the possibility of in situ control of the photon emission wavelength and its polarization state. Here, we report on the first proof-of-principle demonstration of the dynamic real-time control using radio frequency surface acoustic waves (SAWs) of the optical emission from QDs embedded in epitaxially grown core-shell GaN/InGaN nanowire (NW) heterostructures [1]. The SAWs are excited on the surface of a piezoelectric $LiNbO_3$ crystal equipped with an acoustic delay line onto which the NWs were mechanically transferred [2,3]. Luminescent QD-like exciton localization centers, induced by indium content fluctuations within the InGaN nanoshell, are identified using spatially, polarization- and time-resolved stroboscopic micro-photoluminescence (μ-PL) spectroscopy. They exhibit narrow and highly linearly polarized emission lines in the μ-PL spectra and a pronounced antibunching signature of single-photon emission in the photon correlation experiments [2,3]. Depending on their location within the InGaN nanoshell, nonpolar (*m*-), semipolar (*r*-) or polar (*c*-facet) QDs are discerned, thereby making these NWs the first single nanostructures able to host non-classical light emitters with both high- as well as low-polarity crystallographic orientations [1]. Owing to their shorter radiative lifetimes resulting from weak built-in electric field values along the growth axis, the III-nitride QDs grown on alternative low-polarity crystallographic planes are greatly advantageous for future high-speed quantum information technologies. When such NWs are perturbed by the propagating SAW, the embedded QDs are periodically strained and their excitonic transitions are modulated by the acousto-mechanical coupling, giving rise to a spectral fine-tuning within a ~2 meV bandwidth at the acoustic frequency of ~330 MHz [2,3]. This outcome is further combined with spectral detection filtering for temporal control of the emitted photons [2]. In this way, both spectral tunability and on-demand emission of single photons is achieved simultaneously. Moreover, the acousto-electric effect inflicts changes in the QD charge population [3] and its optical polarization. Reduction (up to 30%) in the initially high linear polarization degree is observed. This is an important advance since, to date, the photon polarization state of III-nitride QDs has been either probabilistic or pre-determined by electronic properties of the system. Altogether, this study opens the door to the use of sound for scalable integration of III-nitride-based quantum emitters in nanophotonic and quantum information technologies. The advantage of the acousto-optoelectric over other control schemes is that it allows in-situ manipulation of the optical emission properties over a wide frequency range (up to GHz frequencies).

References

[1] Ž. Gačević et al., ACS Photon. **4** (2017) 657.
[2] S. Lazić et al., Semicond. Sci. Technol. **32** (2017) 084002.
[3] S. Lazić et al., J. Phys. D: Appl. Phys. **51** (2018) 104001.

Formation and Microstructure Regulation of Ultra-Strong Nanocrystalline Tungsten Nanofoams by Reverse Phase Dissolution

MINGYUE ZHAO[1], INAS ISSA[1], MANUEL J. PFEIFENBERGER[2], MICHAEL WURMSHUBER[1] AND DANIEL KIENER[1]

[1] Department Materials Science, Montanuniversität Leoben, Austria; [2] Erich Schmid Institute of Materials Science, Austrian Academy of Science, Leoben, Austria

Nanoporous metals possess a number of positive attributes such as light weight, large surface area and energy absorption capability, making them a good candidate as future radiation shielding materials [1]. Tungsten (W) seems to be ideally suited as the base material for such a foam, as it is commonly used in nuclear facilities, medical diagnosis systems and a number of other circumstances in order to protect personnel and sensitive equipment from radiation [2]. Therefore, it is of great value and interest to tailor such novel nanoporous tungsten, in order to combine the beneficial properties of tungsten with the positive attributes of nanoporous foams.

In this work, nanoporous tungsten foams with 35 % porosity were created on a bulk scale through a unique route involving severe plastic deformation of a coarse-grained tungsten-copper (W-Cu) composite, followed by the selective dissolution of the nobler copper phase [3]. The mechanical properties, which are an important consideration in many thermal shielding applications, were investigated by employing depth-sensing nanoindentation. To characterize the microstructural evolution during reverse phase dissolution and analyse the way the etching solutions affect the resulting nanoporous structures, a series of electron and ion microscopy techniques were employed: (i) A field emission transmission electron microscope (TEM) was used for acquiring bright field (BF), high-resolution (HR) and scanning (S) TEM images as well as selected area electron diffraction (SAED) patterns (Fig. 1). From SAED patterns (Fig. 1d and 1h), the phase constitution and crystalline nature (single crystalline or polycrystalline) were determined. BF-TEM (Fig. 1b, 1c, 1d and 1g) and HR-TEM analyses were utilized to document the microstructure on a nanometer scale. From HR-TEM images and the corresponding Fast Fourier Transform (FFT) patterns, lattice features of the nanomaterial structure within the area of interest are clearly seen, thus further discerning the crystalline nature and obtaining information on lattice defects. EDX mapping in STEM using a high-angle annular dark field (HAADF) mode was used to acquire the compositional information at the nanoscale, especially at the interfaces; (ii) A dual beam FIB/SEM workstation, containing an integrated femtosecond laser [4], was used to produce large scale cross-section specimens (see Fig. 2) for observing depth-depended evolution of porosity by scanning electron microscopy (SEM);

The results show that in the used etching solution Cu can be efficiently removed while the less noble W stays unattacked. Moreover, the W grain structure of the nanocrystalline W-Cu precursor is well retained during the etching process (Fig. 1), indicating that the used solution has little influence on the surface diffusion of W atoms. Nevertheless, owing to the creation of mobile W atoms at the interfaces after the removal of Cu atoms, surface diffusion over a short range occurs to form low-defective W grain boundaries. As a result, strong-bonded and interconnected W ligaments consisting of one to three W nanocrystals (Fig. 1) are formed in the tailored porous structure. Using nanoindentation we demonstrate that, due to the nanoscale microstructure, the created nanoporous tungsten possesses outstanding strength, making it an attractive material for applications in radiation shielding fields.

This work for the first time provides an innovative and adaptive approach to create nanoporous tungsten on a bulk scale. The developed reverse phase dissolution method is generally applicable and can be transferred to other attractive active metals in the future. The detailed characterization of microstructure evolution for tungsten nanofoams and their promising mechanical results will serve as foundation for forthcoming related scientific studies and engineering applications.

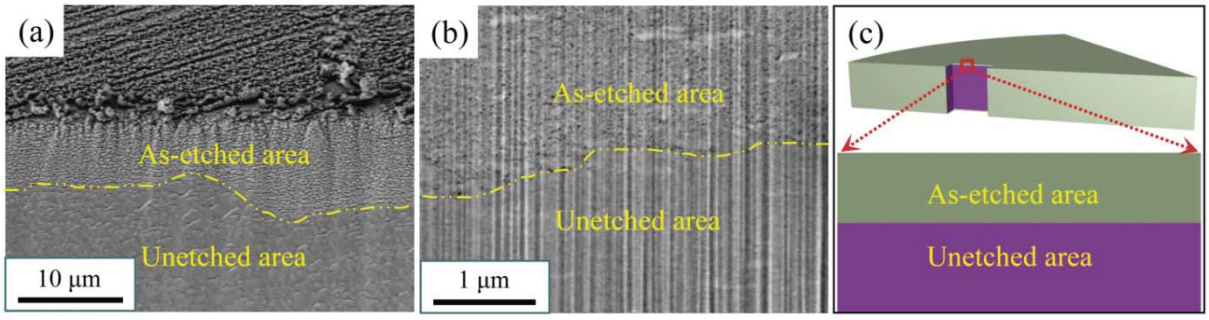

Figure 1. Cross-sections of nanocrystalline W-Cu precursor after etching. (a): Femtosecond laser processed cross-section. (b): FIB reworked cross-section. The etching front is marked by a yellow dashed line. (c): Schematic drawing showing the location of the observed cross-section in the specimen. Details see [3].

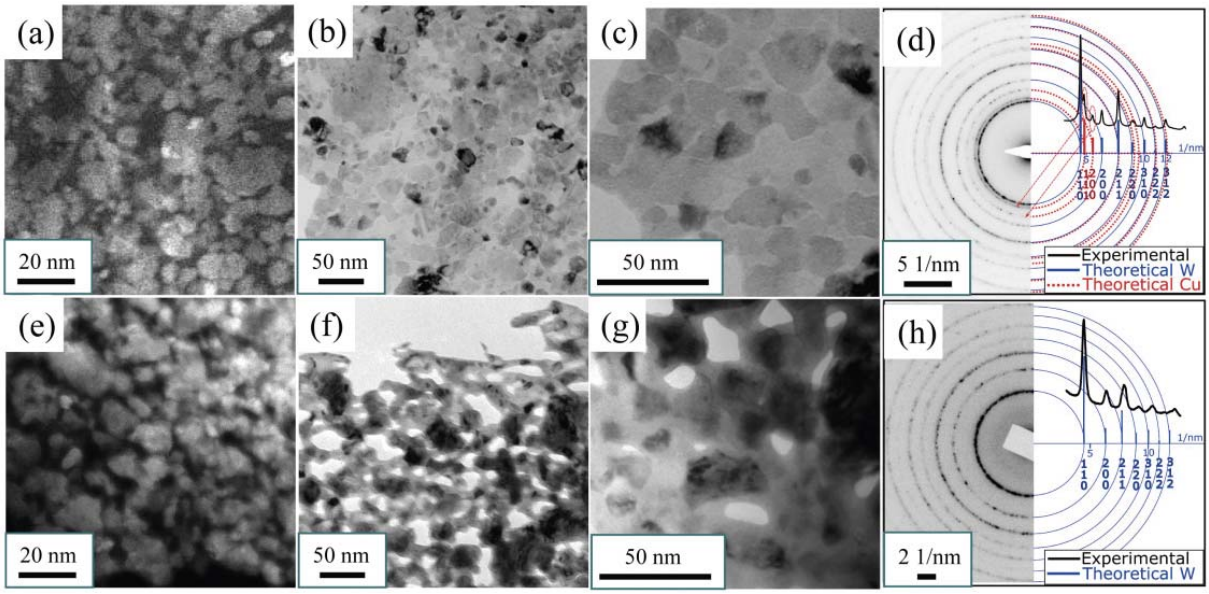

Figure 2. Nanocrystalline W-Cu precursor (a-d) and nanoporous W (e-h). (a) and (e): STEM-HAADF images, (b) and (f): BF-TEM images, (c) and (g): higher magnified BF-TEM images, (d) and (h): SAED patterns. Note the dark contrast phases in (a) and (e) are Cu and pores, respectively. Details see [3].

References

[1] S. Xu. M. Bourham, A. Rabiei. Mater. Des. 31 (2010) 2140-2146.

[2] S. Kobayashi, N. Hosoda, R. Takashima. Nucl. Instrum. Methods A 390 (1997) 426–430.

[3] M. Zhao, I. Issa, M.J. Pfeifenberger, M. Wurmshuber, D. Kiener. Acta Mater. (2019) under review.

[4] M.J. Pfeifenberger, M. Mangang, S. Wurster, J. Reiser, A. Hohenwarter, W. Pfleging, D. Kiener, R. Pippan. Mater. Des. 121 (2017) 109-118.

Microstructural Characterization of Zinc Tin Oxide (Zn_2SnO_4) Particles Synthesized Via Hydrothermal Synthesis to be Used in Sputter Target

UMUT SAVACI[1], CEM ACIKSARI[1,2] AND EMEL OZEL[1], ENDER SUVACI[1], SERVET TURAN[1]
[1] Dep of Mat Sci & Eng, Eskisehir Technical University, Eskisehir/Turkey;
[2] TUPRAS R&D Center, Kocaeli/Turkey

Metal oxide based materials are widely used in numerous electronic applications such as data storage, digital screens, solar panels, transparent thin film transistors and transparent conductive electrodes due to their exceptional physical, chemical, electrical and optical properties. In the high quality display technology, amorphous indium galium zinc oxide (IGZO), which is an amorphous oxide semiconductor (AOS), has been commercially used in thin film transistors due to its high electrical conductivity, electron mobility and optical transparency since 2012. However, due to limited reserves and expensive raw materials of In and Ga elements, researches have been focussed on an alternative AOS materials to IGZO. According to the literature; the possible systems are binary, ternary and quaternary compositions of ZnO, SnO_2 and CdO. Due to the toxic nature of CdO, zinc tin oxide (ZTO-Zn_2SnO_4) ternary system becomes one of the best cadidate. ZTO is an n-type semiconductor having; high electron mobility and electrical conductivity, relatively lower production costs and environmental stability. Transparent thin film transistors and conductive oxides are generally produced by using RF and DC sputtering of target material onto glass or plastic substrate. For the oxide TFT production with sputtering method, ceramic targets having high density and small grain size are preferred to obtain uniform and homogeneous thin films. Sputtering targets are produced with sintering of corresponding powder particles, therefore in order to control the microstructural requirements of ceramic targets, particle characteristics such as purity, homogeneity, size and morphology needs to be controlled during powder synthesis. In literature there are various different synthesis methods are used for inorganic powder synthesis however, in this study hydrothermal synthesis methods are used for the production of ZTO particles. Solid state synthesis is one of the commerically avaliable powder synthesis method. This technique is relatively cheap and easy to process compared to other chemical synthesis techniques. In solid state reaction, basically, two or more oxide powders are mixed within a liquid media and then dried prior to heat treatment at higher temperatures, 1000°C i.e. However, this method has several disadvantages. Firstly, aforementioned particle characteristics can not be controlled during heat treatment process. Secondly during mixing of raw materials, impurity phases, that can affect the chemical and electrical properties, can be incorporated into the mixture from ground mixing balls. Third one is requirement of extra milling process to obtain powder with smaller particle size. Hydrothermal synthesis is a popular and alternative method for the powder synthesis and can overcome disadvantages of solid state synthesis. Hydrothermal process can be defined as dissolution and recrystallization by chemical reactions of starting raw materials which dissolved in liquid media, with an application of pressure and relatively lower temperature, 200°C i.e. With this method, homogeneous inorganic powders are synthesized with high purity with controlled particle size and morphology by changing the process parameters such as precursor solution pH, cation concentration and ratio, process temperature, time and pressure. Particle sizes and

morphologies have significant effects on sintering parameters and process, therefore particle characteristics needs to be characterized to obtain dense ceramic sputtering targets at low temperatures. In this study, ZTO powders synthesized via hydrothermal method are characterized with both imaging and spectroscopic techniques by using (scanning) transmission electron microscopy in order to understand the effects of process parameters, such as solution pH after precipitation, cation concentration (Zn^{2+}/Sn^{4+}) ratio, sythesis temperature and time on the particle size, morphology as well as phase and chemical purity of the produced materials. Additionally, X-ray diffraction and scanning electron microscopy methods are also utilized for supporting information. These analyses clearly showed that the solution pH of mixed precursors before loading hydrothermal vessels affect the phase purity of Zn_2SnO_4 particles. When the solution pH increased from 6 to 10, excess SnO_x phase with different particle size and morphology precipitated because of the different solubility rate of Zn^{2+} and Sn^{4+} in the solution. The amount of SnO_x phase being covered Zn_2SnO_4 crystals with cubic morphology and seperately precipitated SnO_x increased with altering solution pH. When the hydrothermal synthesis temperature increased from 160 to 240°C, cubic Zn_2SnO_4 particles began to grow ranging from 20 to 50 nm. Zn_2SnO_4 nano sized particles (<100nm) having narrow particle size distribution were succesfully synthesis via hydrothermal method at 220°C for 24 h for utilising as a ceramic oxide sputter target to make thin film transistors in electronic devices.

Scattering-Type Scanning Near-field Optical Microscopy and Spectroscopy for Nanoscale Chemical Analysis

ADRIAN CERNESCU, SERGIU AMARIE AND JAN VÁVRA
Neaspec GmbH, Eglfinger Weg2, Haar

Scattering-type Scanning Near-field Optical Microscopy (s-SNOM) is an optical microscopy and spectroscopy approach based on scanning probe technology, bypassing the ubiquitous diffraction limit of light to achieve a spatial resolution below 20 nanometers. s-SNOM employs the strong confinement of light at the apex of a sharp metallic AFM tip to create a nanoscale optical hot-spot. Analyzing the scattered light from the tip enables the extraction of the optical properties absorption, reflectivity) of the sample directly below the tip and yields nanoscale resolved images and nanoscale spectroscopy (hyperspectral nano-FTIR) information simultaneous to topography. This presentation we will introduce the basic principle of near-field microscopy and hyperspectral nano-FTIR for imaging and spectroscopy with 10 nanometer spatial resolution. In addition we will summarize the latest achievements in the field of near-field microscopy and spectroscopy on polymers, biomaterials and 2D materials and will focus on applications in chemical analysis and material identification at the nanoscale.

References

[1] F. Huth, et al., Nano Lett. 12, 3973 (2012).
[2] C. Westermeier et al., Nat Commun. 5, 4101 (2014).
[3] I. Amenabar, et al., Nature Commun. 8, 14402 (2017).

The structure analysis methods for synthetized diamonds consolidation and fractals characterization

SANDRA VELJKOVIC[1], VOJISLAV V. MITIC[1,2], GORAN LAZOVIC[3], VESNA PAUNOVIC[1], MARKUS MOHR[4], HANS FECHT[4]

[1] University of Nis, Faculty of Electronic Engineering, Nis, Serbia; [2] Institute of Technical Sciences of SASA, Belgrade, Serbia; [3] University of Belgrade, Faculty of Mechanical Engineering, Belgrade, Serbia; [4] Institute of Functional Nanosystems FNS, Ulm University

Synthetized diamonds have application in many areas, especially for electronic devices and components or mechanisms in watches, and medicine where they can be used for surgery knifes. Considering that for small grains is commonly known that atomic structure of grain size has strong impact on structural characteristics of synthetized diamonds, research of fractal nature of microstructure of diamond films can have very important role in optimization of properties of these films. Regarding these processes, it was applied several characterization methods like SEM, EDS. These data were prepared and used as a source for fractal analysis application. Fractal theory can help in explanation of systems in which, at first sight, roles chaos. For that reason, fractal analysis can be applied on surface topology of synthesized diamonds and during the process of characterization of grains morphology. Thin films of diamonds, which are examined, are formed in chemical vapor deposition or CVD process. Aldo in some implementations is desirable to reduce the grain size, it can bring to the reducing the hardness of ultra-nanocrystalline or UNCD thin films. Because of that, it is very important to find the optimum between smooth surfaces from one side and hardness from the other side in order to create contact which is resistant to wear. Diameter of grain and their fractal geometry are very important microstructural characteristics. which have strong influence on all physical and chemical characteristics. In this paper, the goal is development of more accurate models which describe transportation and mechanical properties of polycrystalline diamonds.

Key words: fractals, synthetized diamonds, characterization, microstructures

Reduced graphene oxide-chitosan flexible nanocomposite for efficient bacteria capture and photothermal ablation

MILICA BUDIMIR[1,2], ALEXANDRE BARRAS[2], DUSKA KLEUT[1], RABAH BOUKHERROUB[2] AND BILJANA TODOROVIC MARKOVIC[1]

[1] "Vinca" Institute of Nuclear Sciences, Vinca, Belgrade, Serbia; [2] Univ. Lille, CNRS, Centrale Lille, ISEN, Univ. Valenciennes, Lille, France

Bacterial infection-associated diseases are nowadays one of the major public health concerns. In the present study, we will demonstrate a simple and efficient method for bacteria capture and elimination through photothermal ablation. The developed material consists of a flexible Kapton substrate, coated with reduced graphene oxide-chitosan (rGO-CS) thin films. Reduced graphene oxide has strong absorption in the near-infrared (NIR) region, while chitosan has the ability to bind bacteria through electrostatic interactions. The K/rGO-CS device proved to capture and efficiently eradicate both planktonic Gram-positive *Staphylococcus aureus (S. aureus)* and Gram-negative *Escherichia coli (E. coli)* bacteria after 10 min of NIR (980 nm) irradiation.

Reduction of graphene oxide and graphene quantum dots using nascent hydrogen: investigation of morphological and structural changes

SVETLANA JOVANOVIC[1], OLAF C. HAENSSLER[2], MILICA BUDIMIR[1], DUŠKA KLEUT[1], JOVANA PREKODRAVAC[1] AND BILJANA TODOROVIC MARKOVIC[1]

[1] Vinca Institute of Nuclear Sciences, , Belgrade, Serbia; [2] Division of Microrobotics and Control Engineering, University of Oldenburg, Germany

In order to modify both chemical and electrical properties of graphene-based nanomaterials, we conducted the chemical modification of graphene oxide (GO) and graphene quantum dots (GQDs). The reaction of the reduction with nascent hydrogen was conducted on both materials. The structure and morphology of produced chemically reduced GO and GQDs were analyzed. While the chemical composition of both GQD and GO changed significantly, GO showed also significant changes in morphology as opposite to GQDs where were morphological changes were not observed.

MS3

Thin films, coatings, surfaces and interfaces

CHAIRPERSONS:

Aleksandar Miletić, Regina Ciancio

INVITED LECTURE

Atomic Resolution Imaging of Epitaxial Strain Driven Phenomena In Complex Oxides

CÉSAR MAGÉN

[1] Instituto de Ciencia de Materiales de Aragón, Univ. de Zaragoza-CSIC, Zaragoza, Spain; [2] Laboratorio de Microscopías Avanzadas (LMA), Instituto de Nanociencia de Aragón (INA) and Departmento de Física de la Materia Condensada, Universidad de Zaragoza, Spain

Progress in Nanoscience relies on the accurate control of matter down to atomic level, so nanomaterials can be synthesized with atomic precision with the aim of custom-tailoring their physical properties. A paradigmatic example are complex oxides thin films, which present a wealth of exotic physical phenomena, exhibited upon subtle modifications of the crystal structure or composition. A key parameter to tune the physical properties of single crystal thin films is the epitaxial strain induced by the substrate. The adaptation of the material's crystal to the substrate lattice imposed by epitaxy induces a distortion of film's structure, sometimes also of the stoichiometry, which has proven to trigger unprecedented novel physical phenomena in oxide thin films [1].

The correlation between the strain-driven macroscopic properties (ferromagnetism, multiferroicity, metallicity, superconductivity) with the microscopic mechanism underneath requires a detailed analysis of the atomic structure of nanomaterials, based on the accurate determination the atomic positions (or interatomic distances), the chemical composition and the electronic state with atomic resolution. For his purpose, aberration-corrected STEM is a revolutionary nanocharacterization technique: the smart combination of STEM imaging (in Z-contrast or Annular Bright Field) and EELS spectroscopy enables to determine the chemistry, crystal and electronic structure of new materials locally, with atomic resolution, and often in a quantitative way by the smart combination of imaging and spectroscopy [2].

This lecture will review the possibilities of atomic resolution STEM in this field, complemented by other TEM techniques, focusing on the family of manganite oxide thin films, to which epitaxial strain confers unexpected properties and functionalities: a highly anisotropic epitaxial strain in orthorhombically distorted multiferroic terbium manganite thin films ($TbMnO_3$) causes a atomic rearrangement at the domain walls of these films that induces ferromagnetism at low temperature [3]; epitaxial strain causes the segregation of a magnetically dead layer ferromagnetic colossal magnetorresistance manganites [4]; finally, the interplay between epitaxial strain and chemical doping induces polar order in antiferromagnetic $Ba_xSr_{1-x}MnO_3$ thin films [5-7].

References

[1] D. Schlom, L. Chen, C. Fennie, V. Gopalan, D. Muller et al., MRS Bulletin, 39 (2014) 118-130.
[2] Scanning Transmission Electron Microscopy, ed. S. J. Pennycook and P. D. Nellist (Springer New York, 2011).
[3] S Farokhipoor, C Magen, S Venkatesan, J Íñiguez et al., Nature 515 (2014), 373.
[4] L. Marín, L.A. Rodriguez, C. Magén, E. Snoeck, R. Arras et al., Nano Letters 15 (2015) 492.
[5] R. Guzmán, L. Maurel, E. Langenberg, A. R. Lupini, et al, Nano Letters 16 (2016), p. 2221.
[6] E. Langenberg, L. Maurel, N. Marcano, R. Guzmán, et al. Adv. Mater. Inter. 4 (2017) 1601040.
[7] L. Maurel, N. Marcano, E. Langenberg, R. Guzmán, et al., APL Materials 7, 041117 (2019).

INVITED LECTURE

An investigation on the effects of thickness on growth, structure and properties of RF magnetron sputtered ITO coatings

ANDRIUS SUBACIUS[1], ETIENNE BOUSSER[1,2], BILL BALOUKAS[2], STEVE HINDER[3], MARK BAKER[3], DUC-THE NGO[1], CLAUS REBHOLZ[1,4] AND ALLAN MATTHEWS[1]

[1] School of Materials, University of Manchester, ICAM-Pariser Building, Manchester, UK; [2] Department of Engineering Physics, Polytechnique Montreal, Montreal, Canada; [3] Department of Mechanical Engineering Sciences, University of Surrey, Guildford, UK; [4] Department of Mechanical and Manufacturing Engineering, University of Cyprus, Nicosia, Cyprus

Indium tin oxide (ITO) is one of the most widely used transparent conducting oxides due to its electrical conductivity and optical transparency, and it can be used for many applications, such as LEDs, flat-panel displays, smart windows and architectural windows. As typical for transparent conducting films, there is a trade-off between conductivity and transparency.

In this work, the effect of film thickness on the evolution of growth, microstructure and electrical and optical properties was studied. ITO coatings with different thickness values (200, 800 and 3000 nm) were deposited onto unheated soda lime glass substrates by r.f. sputtering from a ceramic (In_2O_3:SnO_2, 90:10 wt.%) target. X-ray diffraction (XRD), transmission Kikuchi diffraction (TKD) and transmission electron microscopy (TEM) analysis revealed an increase in crystallinity with growing ITO film thickness. While the 200 nm thin film appeared amorphous in XRD measurements, the 800 and 3000 nm coatings were found to be crystalline. The 3000 nm thick film displayed preferred orientations in the (440) and (400) directions. In the case of the 200 nm film, TKD results showed local crystallinity with 50-200 nm grains imbedded in an amorphous or possibly nanocrystalline matrix. The luminous transmittance in the visible range was found to decrease with increasing film thickness from 81.7 % for the 200 nm film down to 70 % for the 800 nm one and 44.6% for the 3000 nm film. On the other hand, electrical resistivity values only slightly decreased with increasing film thickness from 6.15×10^{-4} Ω·cm to 5.36×10^{-4} Ω·cm and 5.23×10^{-4} Ω·cm for 200 nm, 800 nm and 3000 nm films, respectively.

Impact of Oxygen Vacancies on Electronic Properties of Anatase Thin Films

DANIEL KNEZ[1], GORAN DRAŽIĆ[2], SANDEEP KUMAR CHALUVADI[1], PASQUALE ORGIANI[1] AND REGINA CIANCIO[1]

[1] Istituto Officina dei Materiali-CNR, Area Science Park, S.S.14, Km 163.5, Trieste, Italy; [2] Laboratory for Materials Chemistry, National Institute of Chemistry, Ljubljana, Slovenia

TiO_2 in the anatase crystallographic structure finds wide applications in optoelectronics and photoelectrochemistry due to its optical transparency, catalytic activity and electrochemical stability. The presence of Ti^{3+} localized states, triggered by intrinsic defects, dopands or photoexcitation, extends the light absorption into the visible range [1,2]. Although it is likely that such electronic states originate from structural changes within the TiO_2 films, the exact mechanisms are not yet understood.

Here we investigate the relation between structure and electronic properties of anatase thin films grown by Pulsed Laser Deposition on $LaAlO_3$ (001) substrates. To this end we apply different transmission electron microscopy (TEM) techniques. Phase contrast in bright field (BF) TEM (Figure 1a) reveals the presence of [103] ordered arrays of defects in the film which are related to the formation of Ti_nO_{n-1} superstructures originating from the occurrence of oxygen vacancies within the film [3]. This is confirmed by selected area electron diffraction (SAED) showing the presence of extra spots superimposed to the characteristic anatase [010] SAED (see arrowed spots in the inset of Figure 1a). The defect arrays are visible also in scanning TEM (STEM) annular BF (ABF) and, due to the low vacancy concentration (5 - 12 %), are barely visible in high-angle annular dark-field (HAADF) (Figure 1b). Columnwise integration of the HAADF signal, however, allowed to identify slight intensity variations within the dumbells which can be related to local rearrangements of the Ti cations induced by the oxygen vacancies.

We support our results with multislice simulations based on structures obtained from atomistic calculations, electron loss near edge structure (ELNES) studies and correlative spectroscopic techniques available at the APE beamline at Elettra synchrotron.

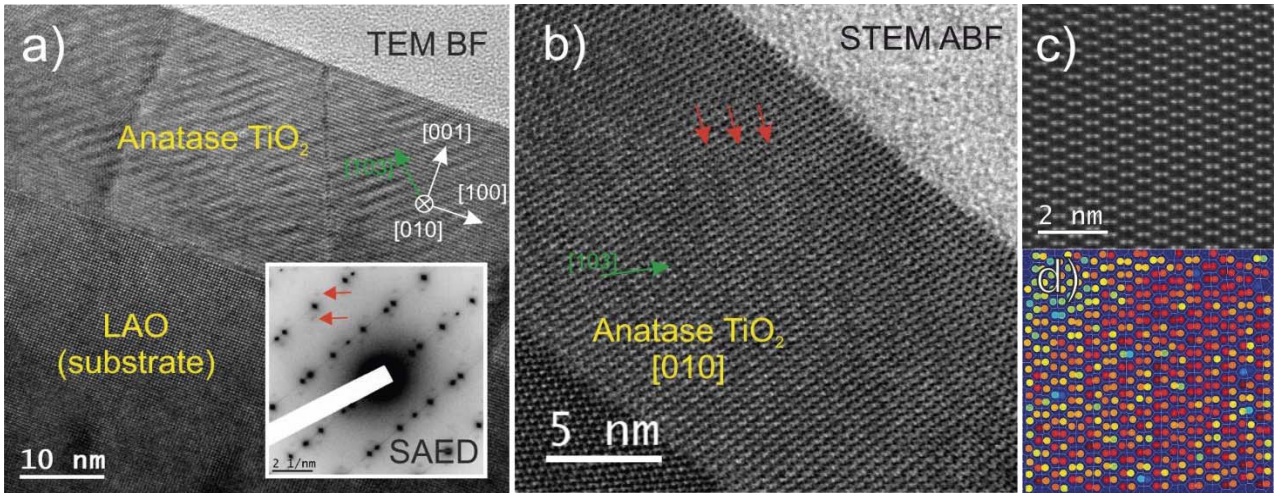

Figure 1. a) TEM BF micrograph of the anatase film in [010] zone axis, inset shows corresponding SAED pattern. Satellite spots caused by the superstructure are indicated by red arrows. b) STEM ABF image showing slight contrast variations in [103] direction. c) Intensity variations, especially between two dumbell sites can be seen after column-wise intensity integration of the HAADF signal.

References

[1] F. Zuo, L. Wang, T. Wu, et al., Journal of the American Chemical Society 132 (2010) 11856
[2] B. Gobaut, P. Orgiani, A. Sambri et al., ACS Applied Materials & Interfaces 9 (2017) 23099
[3] R. Ciancio, E. Carlino, G. Rossi et al., Phys. Rev. B 86 (2012) 651

Orientation dependence of metastable-AlN stability in gradient CrN/AlN multilayers revealed by HRTEM

ZHUO CHEN[1], DAVID HOLEC[2], MATTHIAS BARTOSIK[3], PAUL H. MAYRHOFER[3], ZAOLI ZHANG[1,4]

[1] Erich Schmid Institute of Materials Science, Austrian Academy of Sciences, Leoben, Austria; [2] Department of Materials Science, Montanuniversität Leoben, Leoben, Austria; [3] Institute of Materials Science and Technology, TU Wien, Vienna, Austria; [4] Institute of Material Physics, Montanuniversität Leoben, Austria

Metastable rock-salt AlN (*c*-AlN) can be epitaxially stabilized and grown in CrN/AlN multilayers when its thickness is thin enough, i.e. 1.0~3.0 nm. When its thickens exceeds above this critical value, thermodynamically stable wurtzite-AlN structure (*w*-AlN) grows [1, 2]. However, relationships between the c-AlN phase stability and the crystallographic growth orientation as well as the interface structure has hardly been addressed to date. To explore this, in this work, a bilayer-period-gradient (21 repeated blocks, each consisting of 10 bilayers with AlN layer-thicknesses ranging from 1.0 to 10.0 nm, ~2.0-µm-thick in total), reactively magnetron sputtered CrN/AlN multilayer was characterized in detail with a spherical aberration-corrected high-resolution transmission electron microscopy (HRTEM) and associated techniques (i.e. Geometrical phase analysis etc..), as well as dark-field transmission electron microscopy (TEM) that provides a large scale representation of the texture evolution and the phase composition of thin film. A JEM JEOL 2100F microscope with an image-side corrector was used for this study.

HRTEM observations and statistical analysis (Figs.1) reveal that the *c*-AlN/*c*-CrN grains with the <111> growth-orientation exhibit a smaller critical layer thickness for c-AlN, while with the <100> and <110> growth-orientations this critical thickness is larger. The *c*-AlN can be found even in the 5th AlN layer with a measured thickness of 4.1 nm (Fig.1(a) [100] orientation) and 4.0 nm (Fig. 1(b) [110] orientation). HRTEM results show several different *w*-AlN/*c*-CrN interface structures with different growth orientation relationship (Figs.2), e.g. $(111)_{c\text{-CrN}}\|(0002)_{w\text{-AlN}}$, $(002)_{c\text{-CrN}}\|(0002)_{w\text{-AlN}}$ and $(002)_{c\text{-CrN}}\|(10\bar{1}1)_{w\text{-AlN}}$. Combined with HRTEM interface structures observation and DFT calculations suggest that the larger critical thickness of AlN layers in <100> and <110> orientation is allowed by the lower surface energy and higher cubic/wurtzite interfacial energy. Thus, the experimental observations about orientation dependence of metastable *c*-AlN stability can be rationalized by a combined effect of the growth plane surface energy, strain energy anisotropy and the change of c-CrN/*w*-AlN interface structures [3].

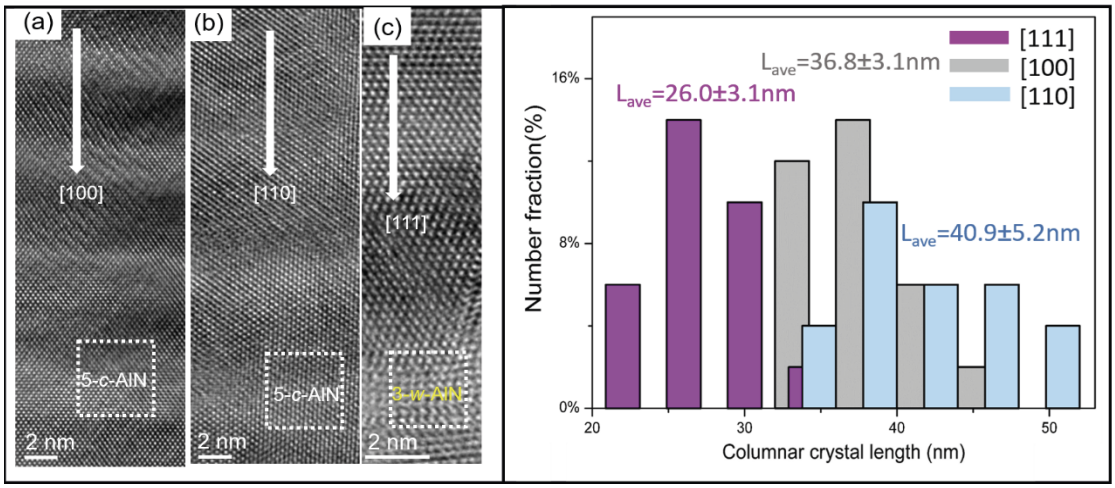

Figure 1 (a)-(c) HRTEM images of one portion of several columnar grains, (a) [100], (b) [110] and (c) [111] growth-orientation. (d) Histogram distributions of columnar grain lengths in different orientations acquired by HRTEM images.

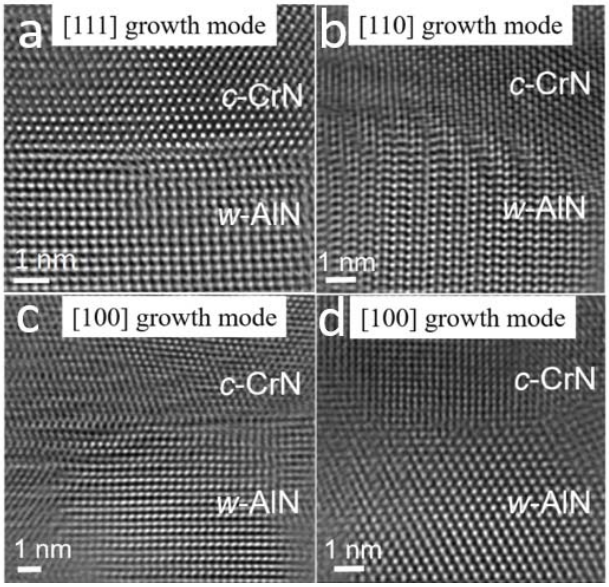

Figure 2 (a)-(d) Typical HRTEM images of the *w*-AlN/*c*-CrN interface with different growth orientations.

References

[1] A. Madan, I.W. Kim, S.C. Cheng, P. Yashar, V.P. Dravid, S.A. Barnett, Physical Review Letters 78(9) (1997) 1743-1746.
[2] D. Chen, X.L. Ma, Y.M. Wang, Acta Materialia 53(19) (2005) 5223-5227.
[3] Z. Chen, D. Holec, M. Bartosik, P.H. Mayrhofer, Z. Zhang, Acta Materialia 168 (2019) 190-202.

Si nanocrystal growth in a-Si:H thin films and multilayers at various conditions and surrounding materials by TEM and XRD study

ROSTISLAV MEDLÍN, PAVOL ŠUTTA, PAVEL CALTA
University of West Bohemia, New Technologies-Research Centre, Plzeň, Czech Republic

In recent years, hydrogenated nanocrystalline silicon (nc-Si) has attracted much attention for the applications in fields such as data storages or optoelectronics (Si-based light emitters and next generation all-Si based solar cells). The study of growing nc-Si at various conditions can get information on behavior of materials because the size of the crystals and their volume fraction affect the properties of films and their specific orientation may appear useful for some particular device applications.

In this work we performed a detailed comparative study of the structural, TEM and XRD properties of Si nanocrystas (sometimes called Quantum Dots) formed in annealed amorphous hydrogenized Si (a-Si:H) and a-Si:H/SiN_x and a-Si:H/SiO_2 multilayers thin films. Samples consisting of up to hundred alternating sublayers of silicon and silicon nitride or silicon oxide as dielectric barrier sublayers have been grown by means of PECVD with a substrate temperature of 250°C using silane, nitrogen and nitrous oxide as precursor gases and post-annealed between 600-1100°C.

TEM, TEM ED and XRD characterization of material structures and it‘s changes during in-situ heating is discussed together with influences of different surroundings by SiN_x and SiO_2 materials. The size of the formed Si-QDs depend on the annealing temperature as well as the sublayer thickness. Columnar growth and evolution of wavy interface morphology was observed together with effect of surrounding materials on multilayer structures.

References

[1] A.V. Shah, H. Schade, M. Vanecek, J. Meier, E. Vallat-Sauvain, N. Wyrsch, U. Kroll, C. Droz, J. Bailat, Thin-film silicon solar cell technology, Progress in Photovoltaics: Research and Applications 12, 113-142 (2004).
[2] M.A. Green, Third Generation Photovoltaics: Advanced Solar Energy Conversion, Berlin, Germany: Springer, Chapter 5 (2006).

Phase Distribution and Orientation Analysis with EBSD for Different Concentrations in Electroless Ni-B Coatings

ERDEM KILIÇASLAN[1,2], MEHMET UYSAL[1] AND HATEM AKBULUT[1]

[1] Sakarya University, Faculty of Engineering, Department of Metallurgy and Materials Engineering, Sakarya, Turkey; [2] Sakarya University Research, Development and Application Center (SARGEM), Esentepe Campus, Sakarya, Turkey

Electroless plating is an autocatalytic process used in many industrial applications such as automotive aerospace, arms, food, petroleum, petrochemical, chemical, plastics injection, optics to improve the surface properties of different substrates without the application of an external current [1-3]. Electroless Ni–B depositions are achieved by the reduction of boron including reducing agents such as dimethylamine borane or $NaBH_4$ and their surface morphology and wear and hardness properties depend on concentration of boron in the plating bath[2-4].

In this study, electroless Ni-B alloy coatings were deposited from plating bath containing different $NaBH_4$ concentrations on mild steel substrates with dimensions of 10×10×2 mm. Electroless bath exhibited, sodium borohydride as a reducing agent and nickel chloride as a source of nickel. In the relevant literature, there are limited studies on structure-property relationship of deposited nickel-boron coatings with different $NaBH_4$ concentrations, especially on EBSD (Electron backscattered diffraction) analysis of nickel-boron depositions. In this study, electroless nickel-boron depositions with different $NaBH_4$ concentrations were investigated via SEM equipped with EBSD technology to show relationship with structure and property changes of electroless Ni-B coatings. First of all, produced electroless Ni-B coatings with different $NaBH_4$ concentrations were prepared with suitable sample preparations. Due to, importance of orientation of electroless Ni-B coatings, full automated mechanical sample preparation system is the most convenient method within different steps of preparation than other sample preparation methods (etc. electrolytic polishing). Surface of the substrates was polished with SiC paper up to 1200, then cleaned by an alkaline solution. Etching was then carried out in 50 % hydrochloric acid for 30 s to achieve good adhesion between substrate and coating. Finally, the samples were then transferred immediately to the electroless deposition bath. Acording to EBSD orientation and phase analyses results of electroless Ni-B coatings, results compared for all concentrations with XRD phase results, respectively. Accordingly, EBSD based grain size distribution and grain boundary rotation angle analyses completed for all concentrations and analyses results are correlated with hardness tests results. The chemical composition of the electroless Ni–B alloy deposition were studied at 1 g/L, 1,5 g/L, 2 g/L and 2,5 g/L of sodium borohydride, designated as S1, S2, S3 and S4, respectively, is given in Table 1.

Table 1. Deposition parameters of electroless Ni-B alloy coating

Operating Temperature and Coating Parameters	S_1	S_2	S_3	S_4
$NiCl_2$ $6H_2O$ g/L	20 g/L	20 g/L	20 g/L	20 g/L
$NaBH_4$ g/L	1 g/L	1,5 g/L	2 g/L	2,5 g/L
NaOH g/L	90 g/L	90 g/L	90 g/L	90 g/L
$PbNO_3$ g/L	0,016 g/L	0,016 g/L	0,016 g/L	0,016 g/L
Ethylenediamine ml/L	90 g/L	90 g/L	90 g/L	90 g/L
pH	13	13	13	13
Time (min)	60	60	60	60
Temperature (ºC)	90	90	90	90

Fig. 1a shows the SEM images of surface morphology of electroless Ni–B alloy coating relating to S1 in its as-plated condition. As seen in Fig1a, electroless Ni-B alloy coatings are seen to exhibit a cauliflower surface morphology which is typically exhibited by electroless coatings. The elemental composition of the Ni-B alloy deposited by electroless coating obtained dissolution and ICP analysis, is 94.8wt.% nickel, 5.2 wt.% boron Fig. 1b shows cross section of the Ni–B alloy coating indicating that its columnar morphology because of the growth mechanism of the coating. Moreover, electroless Ni-B (S1) alloy coating appeared to be crack-free, quite dense with no porosity and without defects such as cracks, pores. The X-ray diffraction pattern of electroless Ni–B alloy coating, deposited at 1 g/l of sodium borohydride after heat treatment at 400 °C for 2 h is displayed in Fig. 1c. As seen in Fig1c, after heat treatment, Ni–B coating transformed into crystalline Ni (FCC), Ni_3B (orthorhombic) and Ni_2B (tetragonal) of peaks at 51.5◦ (2 0 0), 45.6◦ (0 3 1) and 49.83◦ (1 1 2), respectively.

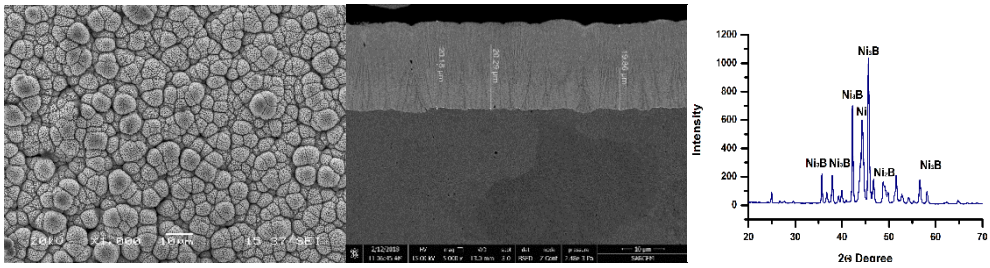

Fig 1. a) The surface morphology of the as-plated Ni–B coating b) The cross section of the as-plated Ni–B c) X-ray diffraction pattern of heat treated Ni–B coating

Fig 2 shows phase distrubition of electroless Ni-B alloy containing 1.0 g/l $NaBH_4$. In the phase distribution, red-colored regions show Ni_3B phase distrubition which is 63% of the total fraction, the green-colored regions, the Ni2B phase and 31.6% of the total fraction. Finally, the nickel is shown as white-colored and nickel distrubition is of 5.1% of all fraction.

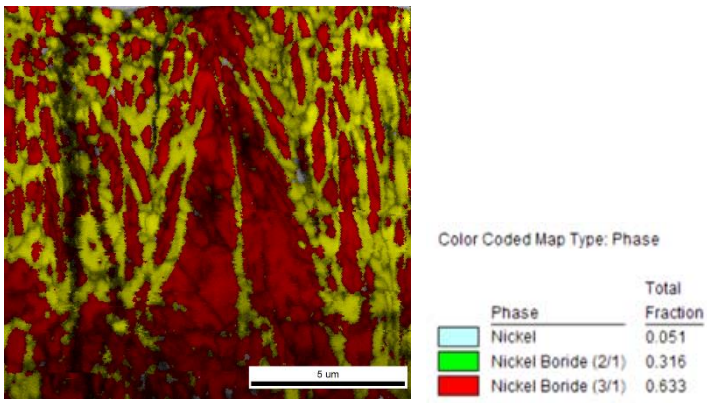

Fig 2. 1 g/l $NaBH_4$ concentration; Phase distribution of heat treated electroless Ni-B coating

References

[1] S. Pal, V. Jayaram, Materialia 4, (2018) 47-64
[2] K. Krishnaveni, T.S.N. Sankara Narayanan, S.K. Seshadri Surf Coat Tech 190, (2005), 115-121
[3] V. Niksefat, M. Ghorbani J. Alloys Compd 633, (2015), 127-136
[4] B. Oraon, G. Majumdar, B. Ghosh Mater Des 29, (2008), 1412-1418

Quantitative low-voltage WDS electron-probe microanalysis of PMN-PT thin films prepared by pulsed-laser deposition

ZORAN SAMARDŽIJA[1], URŠKA GABOR[2], MATJAŽ SPREITZER[2]
[1] Department for Nanostructured Materials, [2] Advanced Materials Department
Jožef Stefan Institute, Ljubljana, Slovenia

The $67Pb(Mg_{1/3}Nb_{2/3})O_3$–$33PbTiO_3$ (PMN-PT) thin films with thickness between 0.5 µm and 0.7 µm were prepared by pulsed-laser deposition (PLD) directly on single-crystal $SrTiO_3$ substrates. The compositional complexity of the PMN-PT, the set-up of PLD parameters and target choice have to be carefully considered to minimize the variations of film's chemical composition from ideal perovskite ABO_3 stoichiometry. For the growth of epitaxial PMN-PT thin films the PLD target should contain an excess of PbO which compensates for the Pb-loss upon film's growth. A reliable, accurate compositional analysis of the PMN-PT thin films is therefore very important to control, tune and select correct film's processing conditions.

In this study the chemical composition of PMN-PT thin films was analysed and determined by quantitative electron-probe microanalysis (EPMA) using wavelength-dispersive X-ray spectroscopy (WDS). Analyses were performed in a FEGSEM JEOL JSM-7600F equipped with Oxford Instruments INCA Wave system. Here a special attention was given to the optimization of low-voltage (LV) EPMA-WDS approach for the measurements of X-ray spectral lines Pb-Mα, Nb-Lα, Ti-Kα and Mg-Kα. Using the Monte–Carlo simulations we found that at electron–beam energy of 8 keV maximum depth of X–ray generation was ≤ 0.30 µm for all elements. Consequently it was verified that all selected X-rays were emitted only from the PMN-PT thin films without the influence of the $SrTiO_3$ substrate. Also sufficient overvoltage ratio at accelerating voltage of 8 kV was ensured for efficient excitation of all analytical spectral lines.

The intensities of Pb-Mα, Ti-Kα and Nb-Lα X-rays were measured using a PET crystal with sealed Xe-filled proportional counter while the Mg-Kα was measured on a TAP crystal with gas-flow (P10) proportional counter. The WDS settings were carefully and precisely optimized by means of correct detector bias, accurate peak and background positions and correct pulse-height analysis parameters. Focused 8-kV point-beam measurements on the PMN-PT thin film samples were carried out under electron dose of 3.5 µC per point, which ensured that sufficient number of X-ray counts were acquired to keep the standard counting error below ± 2 % relative for each element. Consequently high analytical precision and accuracy were achieved. The standards used for quantification of Pb, Ti, Nb and Mg were pure stoichiometric oxides PbO, $SrTiO_3$, Nb_2O_5 and MgO, whereas the oxygen content was calculated from the stoichiometry to nominal cation valences. In addition, a piece of 67PMN-33PT bulk single crystal was used as a reference material to test the reliability and accuracy of quantitative low-voltage WDS analysis.

Five contemporary PhiRoZ-Φ(ρz) quantitative matrix-correction algorithms were used to calculate elemental concentrations from measured *k*-ratios and [1, 2]. The best Φ(ρz) algorithm was then chosen as the one which gave the best results for the bulk PMN-PT reference material, as presented in Table 1. Within the range of experimental uncertainty the obtained elemental concentrations showed excellent agreement with nominal 67-33 composition. An additional criterion used to evaluate analytical results was the value of atomic Mg/Nb ratio which is nominally equal to 0.50 in stoichiometric 67PMN-33PT [3]. Exactly this value was obtained when using Φ(ρz)-ALS algorithm and is only slightly lower, i.e. 0.49, using the algorithm Φ(ρz)-XPHI.

Table 1. Comparison of LV-WDS quantitative results for 67PMN-33PT reference material obtained with five Φ(ρz) matrix-correction algorithms: ALS, XPHI, XPP, PROZA and PAP.

	Atomic %					Mg/Nb	Formula coefficients				
	Pb	Mg	Nb	Ti	O*	ratio	Pb	Mg	Nb	Ti	O
nominal	*20.00*	*4.46*	*8.94*	*6.60*	*60.00*	*0.50*	*1.00*	*0.22*	*0.45*	*0.33*	*3.00*
ALS	19.95	4.54	9.03	6.47	60.01	0.50	1.00	0.23	0.45	0.32	3.00
XPHI	20.04	4.36	8.96	6.61	60.03	0.49	1.00	0.22	0.45	0.33	3.00
XPP	20.36	4.22	8.97	6.49	59.97	0.47	1.02	0.21	0.45	0.32	3.00
PROZA	20.41	4.25	8.95	6.45	59.94	0.47	1.02	0.21	0.45	0.32	3.00
PAP	20.40	4.25	8.95	6.46	59.95	0.47	1.02	0.21	0.45	0.32	3.00

Consequently the ALS and XPHI algorithms were recognized as the most appropriate giving superior, high confidence quantitative results for investigated PMN-PT thin films with their compositions given in Table 2.

Table 2. Results of quantitative LV-WDS analyses of the chemical compositions of three PMN-PT thin films obtained with favourite Φ(ρz) quantitative algorithms ALS and XPHI.

		Atomic %					Mg/Nb	Formula coefficients				
sample	Φ(ρz)	Pb	Mg	Nb	Ti	O*	ratio	Pb	Mg	Nb	Ti	O
PMN-PT	ALS	21.84	3.16	8.95	6.22	59.83	0.35	1.10	0.16	0.45	0.31	3.00
TF #1	XPHI	21.83	3.03	8.89	6.39	59.90	0.34	1.09	0.15	0.45	0.32	3.00
PMN-PT	ALS	20.78	4.05	8.77	6.55	59.85	0.46	1.04	0.20	0.44	0.33	3.00
TF #2	XPHI	20.76	3.89	8.72	6.72	59.90	0.45	1.04	0.19	0.44	0.34	3.00
PMN-PT	ALS	21.29	3.68	8.76	6.46	59.80	0.42	1.07	0.18	0.44	0.32	3.00
TF #3	XPHI	21.27	3.54	8.71	6.62	59.84	0.41	1.07	0.18	0.44	0.33	3.00

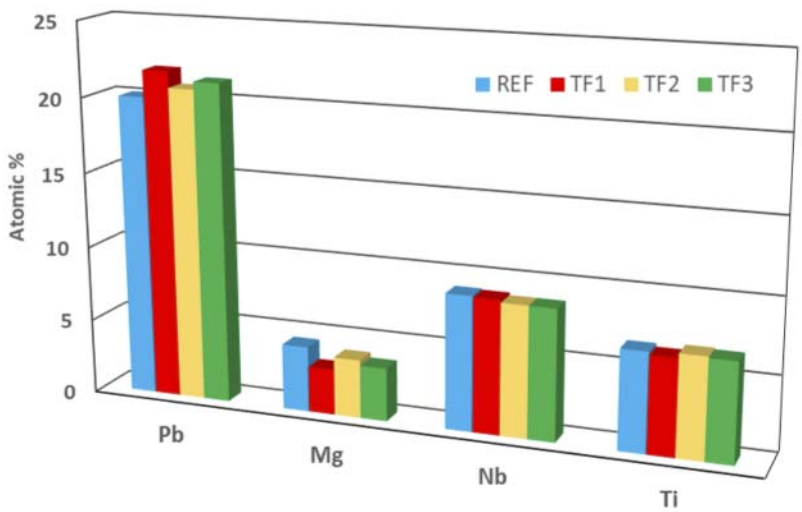

Figure 1. Comparison of overall results of quantitative WDS analyses for reference 67PMN-33PT material (REF) and three PMN-PT thin films (TF1, TF2, TF3). Slight excess of Pb and deficiency of Mg from nominal perovskite stoichiometry were found in thin films whereas the Nb and Ti concentrations remain consistent with nominal composition.

We have showed that by applying different Φ(ρz) matrix-correction algorithms we have got certain discrepancies between the quantitative results. This indicates that the choice of Φ(ρz)-based physical models which were used for the atomic number (Z), absorption (A) and fluorescence (F) corrections as well as the definition of Φ(0) and the choice of mass-absorption coefficients (MAC) play a significant role in the efforts to achieve accurate quantitative electron-probe microanalysis.

The surplus of Pb and a slight deficit of Mg from ideal perovskite stoichiometry in thin films were observed, as shown in Figure 1. This Pb excess is compensated by the formation of out-of-phase boundaries whereas the Mg deficit preserves macroscopic electro-neutrality [4]. Our achieved results confirm that an optimized low-voltage WDS is a reliable and accurate method for quantitative compositional analysis of the PMN-PT thin films.

This study also illustrate that the EPMA-WDS analysis has to be carefully optimized for each particular material by means of the use of best analytical conditions, optimal X-ray spectroscopic measurements and most appropriate quantitative matrix-correction algorithms.

References

[1] J. T. Armstrong et al, Microscopy and Microanalysis, 19 (Suppl 2) (2013) 812-813
[2] C. Merlet, Mikrochimica Acta, 114/115 (1994) 363-376
[3] Z. Samardžija, Microscopy and Microanalysis, 21 (2015) 1138-1144
[4] U. Gabor et al, Journal of the European Ceramic Society, 38 (2018) 4453-4462

Study of thin plasma-polymer film growth under dusty plasma conditions

VILMA BURSIKOVA[1], VOJTĚCH HOMOLA[1], ŠTĚPÁNKA BITTNEROVÁ[1], ROMAN PŘIBYL[1], PETR TOMŠEJ[1], MONIKA STUPAVSKÁ[1], ANNA CHARVATOVA CAMPBELL[2], PETR KLAPETEK[2], JIŘÍ BURŠÍK[3] AND VRATISLAV PERINA[4]

[1] Institute of Physical Electronics, Faculty of Science, Masaryk University, Brno, Czech Republic; [2] Czech Metrology Institute, Brno, Czech Republic; [3] Institute of Physics of Materials, Academy of Sciences of the Czech Republic, Brno, Czech Republic; [4] Institute of Nuclear Physics, Academy of Sciences of the Czech Republic, Rez near Prague, Czech Republic

During the past decades nanocomposite polymer coatings have attracted increasing attention because of their unique optical, mechanical, magnetic and optoelectronic properties arising from the combination of organic matrix and inorganic nanoparticles. Combinations of the attractive functionalities of both components at the nanolevel acquired from organic polymers and inorganic nanoparticles, are expected to exhibit synergistically improved material properties. Among the numerous nanocomposite preparation methods, the deposition under dusty plasma condition is one of the most attractive tools, which could be successfully applied in many industrial and technological applications, ranging from microelectronic industry to aerospace industry and biomedical applications [1-6]. In the present work plasma-polymer nanocomposite thin films were prepared under dusty plasma conditions. Due to their nanocomposite structure, the films showed very interesting mechanical properties, for example high elastic recovery resulting in behaviour similar to superelasticity. Variation of the deposition conditions enabled to vary the surface composition and structure of the deposited films. The surface structure of the films influenced their surface free energy in a wide range so it was possible to prepare films with hydrophilic as well as hydrophobic properties.

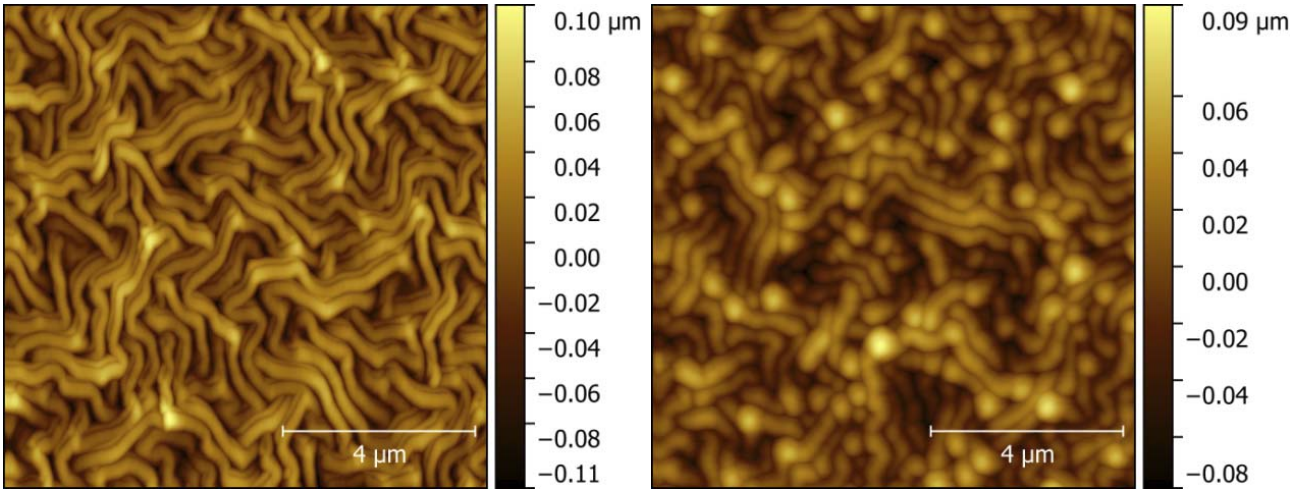

Figure 1. Surface structure of the plasma polymer organosilicon films prepared using PECVD method. The applied power was 25W, the flow rate of hexamethyldisiloxane was 2 sccm, the flow rate of the oxygen was 5sccm, the deposition pressure was 37Pa. The films differed in the deposition time. The deposition time of the film on the left was 0.75 minutes and the deposition time of the film on the right was 7 minutes.

The mechanical properties of the films were studied using nanoindentation technique and the surface structure was studied using atomic force microscopy, scanning confocal microscoppy and scanning electron microscopy. The atomic composition and chemical structure of the films was studied using combined RBS/ERDA (Rutheford Backscatter spectroscopy/Elastic Recoil Detection Analysis), XPS (X-ray Photoelectron Spectroscopy) and FTIR (Fourier Transform Infrared) spectroscopy.

Acknowledgement
The present work was supported by Czech Science Foundation under project GACR 19-15240S and by Ministry of Education, Youth and Sports of the Czech Republic under project NPU (LO1411).

References
[1] L. Boufendi and A. Bouchoule, Plasma Sources Sci. Technol., 3/3(1994)262
[2] M. Cavarroc et al., J. Appl. Phys., 99 (2006) 064301
[3] A. Bapat et al., J. Phys. D: Appl. Phys. 40 (2007) 2247
[4] P. R i Cabarrocas et al., J. Phys. D: Appl. Phys. 40 (2007) 2258
[5] M. Cavarroc et al., IEEE Transactions on Plasma Science, 36/4 (2008) 1016
[6]V. Bursikova et al., Journal of Physics and Chemistry of Solids 68(5-6) (2007) 701

Functionalized magnetite nanoparticles for drug loading, release, and delivery of poorly soluble active biomolecules

LUCIJA MANDIĆ, ANJA SADŽAK, SUZANA ŠEGOTA
Division of Physical Chemistry, Ruđer Bošković Institute, Zagreb

Nanotechnology provides smart materials for drug delivery, prognosis, and treatment for diseases. The drug applications of nanoparticles as drug carries allows improved localizations of the therapeutics on the target site. Metal or metal oxide nanoparticles such as superparamagnetic iron oxides nanoparticles are most commonly used as drug carries. These nanoparticles are nontoxic, biodegradable and biocompatible. Magnetite nanoparticles emerge as the ones having effectively controlled particle size and surface chemistry, enhanced permeation, flexibility, solubility and release of therapeutically active agents to attain the target and specific activity at a predetermined rate and time. The intention was to use the flavonoid loaded clusters of magnetite nanoparticles as vectors that can be directed using a magnetic field gradient towards a certain location. Loading of poorly soluble, hydrophobic flavonoid onto mesoporous clusters comprised of coated PEG magnetite nanoparticles and their release under the influence of permanent and/or alternating magnetic field was investigated. [ref. 1]. A structural and morphological characterizations of magnetite nanoparticles have been performed by means scanning electron microscopy (SEM) and X-ray diffraction (XRPD). This research aimed to circumvent the problems of flavonoid stability and low solubility by their incorporation in the mesoporous nanoparticles, which should result in an alternative therapeutic approach for neurodegenerative diseases such as Alzheimer disease. The results of our experimental investigation confirmed that the mesoporous magnetite nanoparticles present a universal, stable and excellent drug carries particularly able to load and release with higher efficiency flavonoids of different physicochemical and/or structural properties.

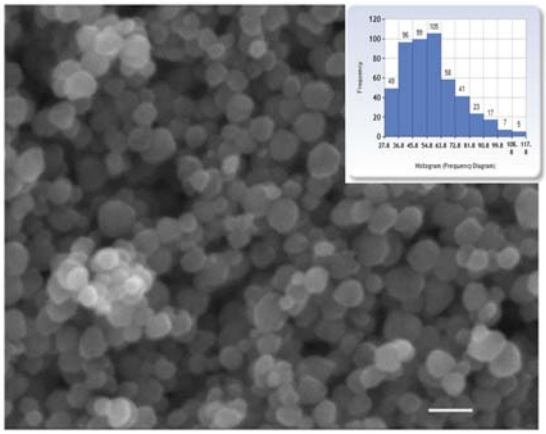

Figure 1. SEM image and histogram of diameters of magnetite nanoparticles

References

[1] S. Rajesh Kumar, S. Priyatharshni, V. N. Babu, D. Mangalaraj, C. Viswanathan, S. Kannan, N. Ponpandian, Journal of Colloid and Interface Science, 436 (2014), 234–242

Plasma electrolytic oxidation of Zn alloy in aluminate electrolyte

SERGEY KARPUSHENKOV[1], HANNA MALTANAVA[2], ALIAKSANDR MIKHAILAU[3], SERGEY POZNYAK[2], LARISA KARPUSHENKAVA[1], KIRYL YASAKAU[3], STEVAN STOJADINOVIĆ[4], RASTKO VASILIĆ[4]

[1] Belarusian State University, Faculty of Chemistry, Minsk, Belarus; [2] Research Institute for Physical Chemical Problems of the Belarusian State University, Minsk, Belarus; [3] Department of Materials and Ceramic Engineering, CICECO - Aveiro institute of materials, University of Aveiro, Aveiro, Portugal; [4] University of Belgrade, Faculty of Physics, Belgrade, Serbia

The method of plasma-electrolytic oxidation (PEO) is one of the most promising ways to obtain functional coatings on metals and alloys in aqueous solutions. The PEO method is based on the process of the emergence of migratory point sparks and arc discharges on the metal surface under the action of high voltage in electrolyte [1]. PEO anodizing has several advantages such as the use of ecological-friendly electrolytes, the obtaining of thick coatings without expensive equipment and no special surface preparation prior to plasma application. Although numerous papers were devoted to PEO process on the different metals, there is a lack of information concerning the PEO coatings on zinc. Herein, we studied the PEO process on zinc anodes in an alkaline solution of sodium aluminate.

The deposition of coatings on zinc in the mode of microplasma anodizing was carried out using a DC pulsing power source in a cylindrical glass cell equipped with a magnetic stirrer. PEO synthesis was performed in the voltage range from 250 V to 350 V during 1-5 min. Zinc plates (99.9%) were used as a working electrode (anode) and stainless steel plate as a counter electrode (cathode). The aqueous solution containing 8.2 g/L $NaAlO_2$ and 2 g/L KOH was used as an electrolyte. The morphology and phase composition of PEO coatings were investigated by scanning electron microscopy (SEM) and X-ray diffraction analysis (XRD).

PEO process on Zn in an alkaline aluminate solution starts at a voltage of ~250 V which is illustrated by a drop of the current density and appearance of a large number of small micro-discharges with white color ("soft sparking" mode). Sparks are characteristic of the PEO process and play a crucial role in the formation of the coatings. At 300 V the micro-discharges become more intense and their color changes from white to yellow ("spark" mode). When a voltage of 350 V is reached, the sparks become significantly larger while their color alters to orange. With time, orange sparks evolve to micro-arcs that start to destroy the coating. Since the PEO coatings prepared at 250 and 300 V are uniform and have good adhesion to the Zn substrate, this voltage range was selected for further studies of the coating growth on Zn. XRD analysis demonstrated that the PEO coatings obtained at 250 and 300 V contain ZnO (wurtzite) and $ZnAl_2O_4$ (spinel) phases. In addition, some unidentified phases are also present and can be attributed to mixed oxides. The EDX analysis showed that the prepared coatings include almost all elements (Zn, O, and Al) contained in the electrolyte and substrate. This fact indicates that the electrolyte components undergo destruction in microplasma channels occurring on the electrode surface during anodization and further the elements are included in the growing coating. SEM inspection showed that the prepared samples have the fused surface with randomly distributed microcraters. The size of the microcraters grows with increasing the voltage and anodization time.

References

[1] S. Stojadinović, R. Vasilić, M. Perić, RSC Advances 4 (2014) 25759–25789.

Optimisation of $BaTiO_3$ thin films prepared by magnetron sputtering for sensor and solar cell use

MARIO BOHAČ, KRUNOSLAV JURAIĆ, IVANA PANŽIĆ, ANDREJA GAJOVIĆ
Ruđer Bošković Institute, Zagreb, Croatia

Perovskites are mineral materials which contain titanium, oxygen and at least one additional metal such as: Sr, Ba, Ca. Because of their good ferroelectric and piezoelectric properties, perovskites have found their use in electronics (capacitors, microphones, devices for digital data storage). Barium titanate ($BaTiO_3$) is a ceramic perovskite oxide that besides having ferroelectric has good optical properties. That alone makes it an interesting material for photovoltaics. Recently $BaTiO_3$ was used in thin film form (pure or as a composit material with TiO_2) as a electrode in dye sensitized solar cells (DSSC). It was also shown that an addition of a $BaTiO_3$ thin film can improve overall performance in gas sensors based on CuO.

$BaTiO_3$ can be prepared by chemical (hydrolysis, hydrothermal synthesis, sol-gel method) and physical methods (such as laser ablation, spray pyrolysis and magnetron sputtering). Magnetron sputtering is a widely used method for thin film preparation. The method is based on the process in which plasma is created and positively charged ions from the plasma are accelerated by an electrical field and strike the negative electrode with sufficient force to eject atoms from the target. Atoms ejected from the target are then depositioned on the substrate placed in proximity to the target, producing a thin film. Choosing different target materials there can be prepared various thin films, comprised of metals, oxydes, semiconductors or ceramics.

In this paper, using RF magnetron sputtering, there were produced $BaTiO_3$ thin films. Deposition parameters were optimised for producing thin films with the most favorable optical and electrical properties, keeping in mind the application for photovoltaic cells and sensors.

Structural propertis of the obtained $BaTiO_3$ thin films (examined by Raman spectroscopy, GIXRD and Scanning Electron Microscopy) were correlated to optical properties (examinde by UV-VIS spectroscopy).

Oxidative stress in model membranes: protection via flavonoid embedded nanoparticles

ANJA SADŽAK, LUCIJA MANDIĆ, SUZANA ŠEGOTA
Division of Physical Chemistry, Ruđer Bošković Institute, Zagreb, Croatia

Flavonoids, polyphenolic biomolecules with antioxidative activity, have recently emerged as potential novel therapeutics for neurodegenerative diseases [ref 1]. In addition to the fact that the mechanisms of their antioxidant effects have not yet been fully elucidated, their applicability is rendered by poor water solubility and chemical instability under physiological conditions encountered during pharmaceutical product consumption. Flavonoid incorporation in nanoparticles (NPs) as carriers has been proposed as a possible solution to surpass these obstacles. The aim of the research is to overcome the problem of poor water solubility and chemical instability of flavonoids by delivering them loaded in biodegradable mesoporous NPs to model membranes and neurons whereby their protective effects should be enhanced.

Mesoporous NPs were selected to increase the flavonoid loading and entrapment efficiency, as compared to so far used organic or inorganic NPs, and to enable protection of flavonoids in physiological conditions.

The model membranes made of an unsaturated lipid (DOPC) with and without embedded flavonoids were investigated with the respect to flavonoid influence on the membrane structure, elasticity, and its functionality, especially regarding lipid order. Model lipid membranes were studied before and after lipid peroxidation (LP), which was induced by the addition of H_2O_2 and Fe^{2+}. By combining AFM imaging and ATR FTIR spectroscopy, the new approach was established to gain insight into flavonoid protective mechanism towards the oxidative stress, as well as the altered nanomechanics and structural reorganization of the membrane after inducing peroxidation.

Results from the studies proposed within research will pave the way towards the development of innovative and improved therapies for oxidative stress-associated neurological disorders. In addition, the knowledge obtained within this research could be extended to designing effective delivery systems for the incorporation, protection, and release of other unstable bioactive molecules with an aim to improve human health or to increase the shelf life of pharmaceutical or food products.

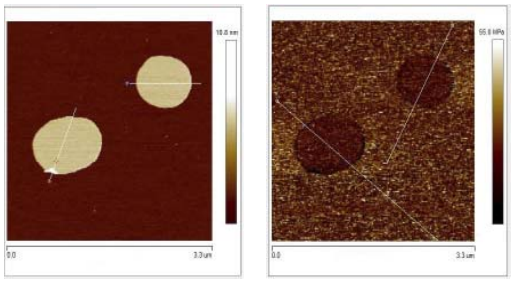

Figure 1. AFM images of DOPC liposomes.

[1] A. Federico et al., Neurol. Sci., 322 (2012) 2542

Demystifying the composition and thickness of long-lasting commercially available tool coatings by the use of microscopy

SARA HAWI AND SAURAV GOEL
School of Aerospace, Transport and Manufacturing, Cranfield University, Cranfield, UK

1. Introduction

Demand on high accuracy products for aerospace, biomedical, automotive and robotics applications is the driving factor for the development of high-performance cutting technologies such as micromilling. As the tool size (diameter) shrinks, the stresses start to become higher. For instance, tools used in micro milling are of diameters less than 1 mm and operate at very high spindle speeds ranging from 10,000 RPM to about 50,000 RPM with a contact ball bearing spindle. The microtools used in micromilling experience high stresses and high temperatures at the contact interface, changing chip thickness and abrupt changes in shear force. All of these conditions have a big impact on tool life thus the application of hard, wear resistant and self-lubricating coatings for microcutting tools has been investigated heavily in order to prolong tool life and ensure the quality and surface finish of manufactured parts. Cemented tungsten carbide (W-C:Co) microtools are widespread in machining applications. Tungsten carbide (WC) is a hard metal composite material exhibiting excellent wear resistance due to its unique properties and high specific hardness. Functional multilayered tool coatings designed to target a range of complex problems encountered while milling have gained an increased research and industrial interest. Studies have been conducted towards the improvement of their properties by a directed selection of mechanical and crystal-chemical characteristics of their individual layers and their sequencing [1]. In addition to the governing properties of each functional layer, multilayered coatings are more wear resistant than single layered coatings because each interface between the layers acts as a barrier to thermal wave propagation as well as to the crack propagation thus delaying wear progression [2]. Hence, the choice of tool coating which is strongly influenced by the interaction with the workpiece material and machining parameters (feed, speed, depth of cut) is very important to ensure good machined surface quality as well as longevity of the tool. This is where the characterisation of tool coatings gains its importance when dealing with undisclosed commercial details. There are numerous articles published in the literature reporting ways using focussed ion beam cross-sectioning or nanoindentation based destructive techniques to find out mechanical properties of the coatings [3]. However, no method was observed that categorically gives a good enough estimate of the composition and thickness of the commercially unknown tool coating details. Driven from this need, the aim of this work was merely to use simple shop-floor based method for quick estimation of the thickness of the coating as well as to be able to know the chemical composition of the tool coating.

2. Experimental Details

Uncoated Tungsten Carbide (WC) endmills were procured from Louis Bellet via Rainford Precision who is an approved tool supplier for use on Kern Micromilling machines. PVD (physical vapor deposition) coated Tungsten Carbide endmills, with two types of coatings; a UT (UTCOAT) coating and an HM (HardMAX) coating were purchased from Union Tools via Rainford Precision. All tools had a nominal diameter of 200 µm. Figure 1 shows the Kern Evo micromilling machine tool where these microtools are used for precision milling operations.

As a first step to characterising the coatings, the coated tools were ultrasonically cleaned in acetone prior to the EDS analysis in a scanning electron microscope (SEM).
As for the sample preparation, the microtools were mounted in resin, ground and polished to reveal their cross-sectional areas. A thin layer of gold (i.e.10 nm) was sputtered on the resin mounted samples. This provides a conduction path which allows the imaging of these samples at high voltages, thus high resolution (small effective beam diameter).

3. Results and Discussion

The micromilling tools were screened in order to evaluate their quality and sharpness (see figure 2). Some of the uncoated tools that were procured fresh were observed not to be sharp enough as they had severely eroded cutting edges. An elemental analysis of the uncoated tool showed 83.63 wt% of tungsten, 7.89 wt.% of cobalt and 8.48 wt % of carbon in the micromilling tool.

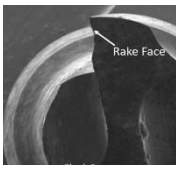

ure 2: Severely eroded uncoated tool cuttin

The results for the HM coat reas the results for UT coatings are shown in figure 4. The presence of vanadium seen in these results may be attributed to the fact that the titanium target used in the deposition process (PVD) was not a pure titanium as vanadium is a very common alloying element for titanium. The manufacturer revealed the hardness of the coatings to be 3000 to 3500 Vickers for the UT coating and about 3500 to 4000 Vickers for the HM coating. Surveying the wealth of literature revealed Table 1 showing reported hardness of popular tool coating materials.

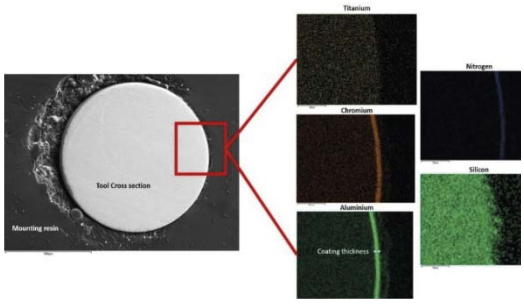

Figure 3: Cross-sectional imaging and EDS mapping of HM coated tool (TiAlN based)

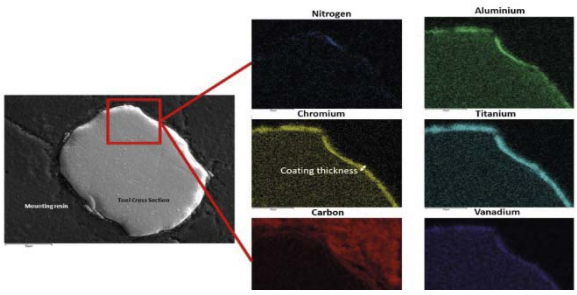

Figure 4: Cross-sectional imaging and EDS mapping of UT coated tool (TiCN based)

C eing
th o be

TiCN/TiAlCrN based while its measured thickness was around 4 μm and (ii) the HM coating appears to be TiAlN/CrSiN based and that the thickness of coating was around 6 μm. Further work is underway in the Centre of Doctoral Training in Ultra-Precision Engineering at Cranfield University in use of these coated tools for evaluation of their life while machining Ti-6Al-4V alloys used commonly in biomedical and aerospace applications.

Table 1: Hardness of different coating systems found in literature

Coating	Hardness (Vickers)	Reference
TiAlN	2850	[4]
TiAlN/TiSiN	3500	[4]
TiAlN/CrAlN	3800	[4]
TiAlCrN	3500	[5]
TiCN	2500-2800	[6]
Ti/TiCN/TiAlCrN	3900	[7]
TiAlN/CrSiN	3300-3600	[8]

4. Conclusions

This work is a preliminary attempt to obtain a quick shop floor idea on the composition and thickness of a tool coating using commonly employed microscopy tools like SEM. The EDS analysis in the SEM coupled with hardness values correlation reported in the literature revealed that the two commercially coated tools based on the two undisclosed coating types (herein referred as UT coating and HM coating) were based on TiCN/TiAlCrN (UT coating) with a thickness of about 4 μm while the other coating was TiAlN/CrSiN coating (HM coating) having thickness of about 6 μm.

Acknowledgements:

The work was carried out in the Centre for Doctoral Training in Ultra-Precision at Cranfield University which is supported by the RCUK via Grants No.: EP/K503241/1 and EP/L016567/1. Part of this work used other supports like the RCUK (Grant No. EP/S013652/1 and EP/S036180/1), Cost Actions (CA15102 and CA18125) from H2020 and Royal Academy of Engineering (Grant No. IAPP18-19\295). We also thank Rainford Precision and Vice-Chancellor Fellowship from Cranfield University to support Sara's PhD research.

References

[1] V. P. Tabakov, A. S. Vereschaka, and A. A. Vereschaka, *Mech. Ind.*, **2017**, 18(7), 706.
[2] A. Rizzo, L. Mirenghi, M. Massaro, U. Galietti, L. Capodieci, R. Terzi, L. Tapfer, and D. Valerini, *Surf. Coat. Tech.,* **2013**, 235, 475–483.
[3] Bouzakis KD., Michailidis N., Skordaris G., Bouzakis E., Biermann D., and M'Saoubi R.. CIRP Annals - *Manu Tech*. CIRP; **2012**; 61(2): 703–723.
[4] W. Darmawan, H. Usuki, I. S. Rahayu, C. Gottlober, and R. Marchal, *Forest Prod. J.*, **2013**, 60(7), 615–621.
[5] L. Ning, S. C. Veldhuis, and K. Yamamoto, *Int. J. Mach. Tool Manu.*, **2008**, 48(6), 656– 665.
[6] M. Wang and S. Miyake, intech. open, **2018**, 77–100.
[7] A. A. Vereschaka, S. N. Grigoriev, N. N. Sitnikov, G. V. Oganyan, and A. Batako, , surf. Coat. Tech., **2017**, 332, 198–213.
[8] C.-m. Kao, J.-w. Lee, H.-w. Chen, Y.-c. Chan, J.-g. Duh, and S.-p. Chen, *Surf. Coat. Tech.*, **2010**, 205(5), 1438–1443.

MS4

Ceramics, composites, cultural heritage materials, rocks and minerals

CHAIRPERSONS:

Aleksander Rečnik, Snežana Vučetić

INVITED LECTURE

The microstructure and texture of spinel reaction layers around corundum: effects of reaction interface orientation

GERLINDE HABLER[1], ROMAN SCHUSTER[1], CHEN LI[1,2], LISA BALDWIN[1], PETR JEŘÁBEK[3] AND RAINER ABART[1]

[1] University of Vienna, Dept. of Lithospheric Research, Vienna, Austria; [2] University Antwerpen, EMAT, Antwerpen, Belgium; [3] Charles University Prague, Faculty of Science, Praha, Czech Republic

1. Introduction

In previous studies the mechanisms underlying the kinetics of spinel ($MgAl_2O_4$) reaction layer growth have been investigated experimentally using single-crystal corundum (Al_2O_3) and periclase (MgO) as reactant phases. Different temperatures, uniaxial load conditions and run durations were applied [1-5]. It was found that the spinel grain boundary characteristics are sensitive to deviatoric stress and that the grain boundary character influences the reaction kinetics during the advanced reaction stages where the reaction rate is primarily controlled by diffusion across the growing layer. In addition, remarkable differences in the dislocation structures of the two reaction interfaces bounding the spinel layer towards corundum and periclase, respectively, were identified, and interface processes were shown to influence reaction kinetics especially during early growth stages [3-5].
Whereas in experiment only one particular reaction interface orientation with planar geometry was applied, a natural spinel layer that had formed by reaction of a centimeter-sized corundum xenocrystal with the hosting basalt melt allowed to investigate the influence of reaction interface orientation on the internal microstructure and texture of the spinel layer. The c. 150 micrometer thick concentric spinel reaction layer formed along different crystal facets of the corundum precursor. Owing to the magmatic environment, layer growth occurred under hydrostatic stress. Several spinel layer segments associated with different reaction interface orientations were investigated regarding the internal microstructure and the crystallographic texture. Comparison of the observations from the rock sample with those from the experimental samples revealed similarities and remarkable differences between different spinel layer segments and between natural and synthetic spinel layers. Therefrom we infer the primary controls on microstructure and texture evolution during layer growth.

2. Analytical methods

We used a multi-methodological analytical approach to characterize spinel reaction layer segments associated with reaction interfaces showing particular orientations with respect to the corundum lattice. At millimeter scale the spinel layer segments appear straight, and associated with particular facets of corundum. The 3D geometry of the natural spinel layer was determined by micro-computed tomography (micro-CT) using a SkyScan/Bruker 1173 instrument at the Department of Palaeontology, University of Vienna (Austria). Micrometer-scale characterization employed various electron beam microanalytical methods using an FEI Quanta3D field-emission scanning electron microscope with integrated focused ion beam (FIB-FEG-SEM), and a Cameca SXFive field emission electron microprobe (FE-EPMA) at the Department of Lithospheric Research, University of Vienna (Austria). EPMA analyses yielded the major and minor element chemical composition, and compositional variations across the spinel layer and along the reactive interface between corundum and spinel. Furthermore, secondary electron (SE)-, back scattered electron (BSE)- and foreward scattered electron (FSE)-imaging was applied to characterize the micrometer scale internal microstructure of spinel, and the bounding reaction interfaces. Electron back scatter diffraction (EBSD) data were collected with an EDAX Digiview 4 EBSD camera and OIM 7.3 software and

yielded crystal orientation maps (COMs) of selected reaction layer segments. The EBSD datasets were evaluated for the nature and quality of the crystallographic orientation relationships between reactant and product phases, and for the geometry, density and preferred orientation of general grain and twin boundaries of spinel. EBSD COMs from both the natural and experimental samples represented the basis for identifying reaction interface segments for dedicated focused ion beam (FIB) preparation of orientation- and site specific specimens for aberration corrected scanning transmission electron microscopy (STEM) [6]. STEM analysis was performed using a NION UltraSTEM fifth-order aberration corrected STEM at the Faculty of Physics, University of Vienna (Austria).

3. Results

In all studied samples, the spinel reaction layers have a polycrystalline appearance in orientation contrast FSE-images, which –in the absence of externally applied deviatoric stress- is due to the presence of low angle grain boundaries, spinel twin boundaries, and particular high angle grain boundaries showing only small deviations from spinel twin misorientations. These boundaries separate homogeneously oriented spinel domains. Only in some experiments, where moderate uniaxial load was applied perpendicular to the reaction interface, a significant fraction of general high angle boundaries formed.

In all samples the initial reaction interface between corundum and the second reactant phase, basaltic melt in the natural sample and single crystal periclase in the experimental samples, is reflected by a very fine-grained zone within the spinel layer. The initial growth stage is associated with progressively increasing spinel grain size due to selective growth, which is less pronounced at more advanced stages.

For most spinel layer segments that grew under hydrostatic stress conditions, more than 90 volume% of the spinel with growth direction towards corundum is constituted by grains with less than 15° misorientation relative to the usual specific topotaxy with corundum, as defined by one Spl<111> // Crn[0001] and three of the Spl<101> // Crn<10-10>. Two spinel twin orientations – twin individuals mutually rotated 60° about the Spl⟨111⟩ // Crn[0001]– comply with this specific crystallographic orientation relationship. Also, large parts of the experimentally grown reaction layers that grew towards periclase show topotaxy with the specific cube-to-cube orientation relationship. Despite of this strong crystallographic preferred orientation of spinel, remarkable orientation deviations from perfect topotactic match with corundum or periclase, respectively, were observed. Contrasting with the experimental samples, the quality of topotactic match between spinel and corundum in the rock sample does not improve during progressive layer growth. Instead, systematic deviations from perfect topotaxy are characteristic for certain portions of the concentric spinel layer. In the natural sample, the density of spinel grain boundaries within a certain boundary misorientation range, and the characteristics of the orientation distribution of general grain boundaries depend on the orientation of the reaction interface relative to the corundum lattice. Three types of layer segments are distinguished based on their spinel boundary trace orientation distribution in the 2D section. The mode indicates one of the following preferred orientations: i) parallel to the trace of the corundum basal plane and perpendicular to the trace of the reaction interface, when the reaction interface corresponds to a prismatic corundum facet, ii) intermediate between normal to the trace of the reaction interface and the trace of the corundum basal plane, or iii) perpendicular to the trace of the reaction interface independent of the corundum lattice. The grain boundary orientation distribution curve is symmetric in case iii) or asymmetric otherwise. Only in two exceptional cases there is no clear maximum developed.

The Σ3 spinel twin boundaries of most segments of the concentric layer in basalt are straight and strictly parallel to the Spl(111) plane that is (sub)parallel to the Crn basal plane. Contrastingly, the experimentally grown reaction layers show highly curved, serrated Σ3 boundaries at the micrometer

scale, which is consistent with the unique naturally grown layer segment that has a reaction interface orientation parallel to the corundum basal plane. For experimental samples, STEM analyses at atomic scale resolution have shown that the spinel boundaries with twin misorientation consist of alternating nanometer scale segments of straight spinel twin boundaries strictly parallel to Spl (111) and stepped/curved Σ3 boundaries. Also, the corundum/spinel interface was found to propagate by the glide of partial dislocations with Burgers vector parallel to the Crn (0001) and Spl (111) planes, which are also parallel to the reaction interface [3]. From comparing data from the studied rock and experimental samples we suppose that spinel boundaries with twin misorientation preferably take an orientation strictly parallel to Spl (111) whenever the reaction interface is inclined with respect to the corundum basal plane. Only when the reaction interface is orientated parallel to Crn (0001), the formation of true spinel twin boundaries is impeded, and Σ3 boundaries with highly irregular boundary geometry form.
Contrasting to the reaction interface orientation, the presence and frequency of Ti-oxide nano-inclusions in corundum in the basaltic rock does not seem to influence the nature of the spinel layer microstructure and texture. These inclusions are either dissolved or recrystallize during the corundum to spinel transformation.

4. Conclusions

Various criteria for characterizing the nature of a concentric spinel reaction layer that had formed by diffusive phase transformation of a corundum single crystal yield complementary but consistent information on how the variation of the reaction interface orientation effects the 2D microstructure and the crystallographic texture of the spinel layer. The orientation of the reaction interface with respect to the corundum lattice clearly affects the preferred orientation of general grain boundaries, the area density of particular boundary types, and the geometry of Σ3 boundaries. The observed polycrystalline appearance of the natural spinel layer is caused by deviations from perfect topotactic match between spinel and corundum. Spinel mean orientations from different oppositely positioned segments along the concentric layer show systematic, oppositely directed rotation out of perfect topotactic match. As the quality in topotactic match does not improve with progressive layer growth, the spinel orientation variations supposedly are inherent to the reaction process.
Correlating data from analytical methods that operate at different spatial scales yielded different information content. Especially the grain and phase boundary geometries in 2D sections show different characteristics when observed at millimeter, micrometer and nanometer scale. Supposedly, different processes govern the structural evolution at different scales.

References

[1] P. Jeřábek, R. Abart, E. Rybacki, G. Habler, Am. J. Sci., 314 (2014) 940-965
[2] L. M. Keller, L. C. Götze, E. Rybacki, G. Dresen, R. Abart, Am. Mineral., 95 (2010) 1399-1407
[3] C. Li, G. Habler, T. Griffiths, A. Rečnik, P. Jeřábek, L. C. Götze, C. Mangler, T. J. Pennycook, J. Meyer, R. Abart, Acta Cryst. A, 74 (2018) 466-480
[4] C. Li, T. Griffiths, T. J. Pennycook, C. Mangler, P. Jeřábek, J. Meyer, G. Habler, R. Abart, Philosophical Magazine, 96 (2016) 2488-2503
[5] R. Abart, J. Svoboda, P. Jerabek, E. Povoden-Karadeniz, G. Habler, Am. J. Sci., 316 (2016) 309-328
[6] C. Li, G. Habler, L. C. Baldwin, R. Abart, Ultramicroscopy, 184 (2018) 310-317

Precession Electron Diffraction: Application to Various Ceramic Composites

UMUT SAVACI AND SERVET TURAN
Dep of Mat Sci & Eng, Eskisehir Technical University, Eskisehir/Turkey

Materials tetrahedron is a conceptual tetrahedron and it has been used to guide research and development studies in materials science and engineering. In this tetrahedron each corner is filled with the key elements of materials science: structure, property, process and performance. These elements and relationships between them are used to understand and design new materials. Performance is the most important aspect of the final product and it is determined by the structure of material. Therefore it is very important to understand the relation between structure and property to develop new materials. Properties of the materials are controlled with various microstructural features such as distribution of phases, grain boundary angles, crystal orientations and texture. For example, mechanical and electrical properties may change depending on the characteristic grain boundary angles between grains [1]. Material properties can be also modified with processing routes, such as pressureless or pressure assisted sintering that result in different material's properties due to the texture formation as a result of the applied pressure. Microstructural texture formation into preferred orientation may result in enhanced properties such as toughness, electrical/thermal conductivity and piezoelectricity. Because of these reasons, understanding the relationship between structure and property becomes a key factor for material's research and development.

In order to understand this relationship, various methods are used to characterize microstructural features. Electron back scatter diffraction (EBSD) technique with scanning electron microscopy is widely used to obtain local orientation relationships within a given microstructure; however, this method has limited resolution down to 50-100 nm [2]. In order to characterize local misorientations and phases smaller than 100 nm, transmission electron microscopy (TEM) based methods need to be used. The precession electron diffraction (PED) technique is the only automated TEM method used for orientation imaging microscopy (OIM) down to 1 nm resolution. The aim of this study is application of PED method to obtain phase and orientation maps of different ceramic composites and characterize any possible orientation relations between matrix and in-situ formed phases as well as phase identifications. For these purposes; SiAlON-hBN, SiC-hBN, B_4C-TiB_2 ceramic composites produced with pressure-assisted hot pressing and spark plasma sintering methods were studied. Further, orientation relation between $Pb(Mg_{1/3}Nb_{2/3})O_3$-$PbTiO_3$ matrix and $BaTiO_3$ seed particles within textured piezoelectric composite produced with templated grain growth methodology was also studied with PED method in TEM. Characterization of the samples were carried out using JEOL JEM2100F field emission transmission electron microscope equipped with STEM high-angle annular dark-field (HAADF) detector, and JEOL JED2300T energy dispersive X-ray spectrometer with GATAN GIF Tridiem electron energy loss spectrometer. Phase and orientation maps were collected by scanning of nano sized probe, having 0.7° precession angle, over the user specified region of interest. The obtained results as well as challenges and advantages of this method during its application to ceramic composites will be given and discussed in this presentation.

References

[1] S.H. Shim, K. Nihara, K.H. Auh, K.B. Shim, Journal of Microscopy, 205 (2002) 238-244
[2] M. Abbasi, D. I. Kim, H.U. Guim, et al, ACS Nano, 9 (2015) 10991-11002

TEM/MD investigation into the dynamics of SHI induced track formation in insulators

JACQUES O'CONNELL[1], RUSLAN RYMZHANOV[2], NIKITA MEDVEDEV[3], VLADIMIR SKURATOV[2] AND ALEXANDER VOLKOV[2]

[1] CHRTEM, NMU, University Way, Port Elizabeth, South Africa; [2] FLNR, JINR, Dubna, Russia; [3] Institute of Physics, Czech Academy of Sciences, Prague, Czech Republic

1. Introduction

A swift heavy ion (SHI, E >1 MeV/amu) loses the largest part of its energy (>95%, 5–50 keV/nm along the ion trajectory) through excitation of the electronic subsystem of the target material [1,2]. Subsequent relaxation of the excited volume occurs at ulrashort spatial (nanometers) and temporal (femto- to pico-second) scales and cannot be described in the framework of usual macroscopic models [3,4] and is impossible to follow experimentally. As a result, unusual kinetics often produce unusual structure and phase transformations which constitute a latent ion track: structure modified material with a diameter of ~1–10 nm and a length of ~10–100 μm along the trajectory of the projectile. The identification of mechanisms governing these kinetics forms a fundamental field of interest in SHI track effects. SHI penetration trough different insulators have shown quite different manifestations of structure transformations [1]: amorphous tracks (e.g. $Y_3Fe_5O_{12}$, α-quartz), defected crystalline tracks (e.g. Mg_2AlO_4, Al_2O_3, ZrO_2, TiO_2) or production of isolated point defects and color centers (e.g. MgO, alkali halides). This motivates research aimed at the understanding of mechanisms of track (and surface hillock) formation in these materials. As with most multiscale physics problems, track formation cannot be traced accurately within a single model posing formidable challenges for the theoretical description and understanding of the underlying physical mechanisms. In order to determine which of the above-mentioned process is the main governing mechanism of track formation, we have chosen three dielectric materials (Al_2O_3, MgO and $Y_3A_{l5}O_{12}$) with different lattice structures but comparable energy deposited into the lattice. It has been shown that SHI irradiation of these targets leads to quite different damage structures, despite the fact that the initial damaged regions have similar sizes and structures.

2. Experimental

We compared the responses of single crystalline α-Al_2O_3, MgO and $Y_3Al_5O_{12}$ (YAG) specimens to irradiation with 167 MeV Xe ions at 300 K. The irradiations were performed at fluences ranging from 10^{10} to 10^{12} cm^{-2} at the IC-100 cyclotron at FLNR JINR (Dubna, Russia). In order to avoid track overlap, the average ion flux was limited to ~10^9 $cm^{-2}s^{-1}$. Ion beam homogeneity better than 5% at the surface of the irradiated specimen was achieved using beam scanning in horizontal and vertical directions. High resolution transmission electron microscopy (HRTEM) studies were carried out at the Centre for HRTEM at Nelson Mandela University (Port Elizabeth, South Africa). TEM lamellae were extracted using an FEI Helios Nanolab 650 FIB. Samples were imaged using a JEOL ARM-200F TEM operating at 200 kV.

3. Theoretical

A hybrid approach used in this work consists of two models: Monte Carlo simulation (MC code TREKIS [5, 6] of the electron kinetics, and Molecular Dynamics (MD) model of atomic dynamics. TREKIS describes the temporal evolution of excited electrons generated by a SHI as well as the interaction of primary and secondary electrons with the target lattice in an ion track. The resulting distribution of energy transferred to the ionic subsystem of the target is inserted into classical MD

code LAMMPS [19] which is used to simulate lattice energy relaxation and further structure transformations in the vicinity of the ion trajectory. No a-posteriori fitting parameters are used in the model.

4. Results

Despite comparable energy deposition into the lattice (especially for radii >1 nm), the passage of 167 MeV Xe produced notably different damaged structures in the investigated oxides. Figure 1 shows the simulation results for track formation in MgO, Al_2O_3 and YAG with experimental TEM insets for Al_2O_3 and YAG (MgO showed no experimentally observable track which is consistent with simulation results of scattered point defects only). Good agreement was found between simulation and experiment for both bulk track structure as well as surface hillocks. TEM image simulation of the MD simulation cell produced images consistent with experiment. These results suggest that the employed inteatomic potentials as well as initial energy distribution due to SHI passage reasonably accurately reproduce the relaxed structures observable by TEM. Based on this observation, it is reasonable to considder the relaxation kinetics within the MD simulation as representative of the actual system.

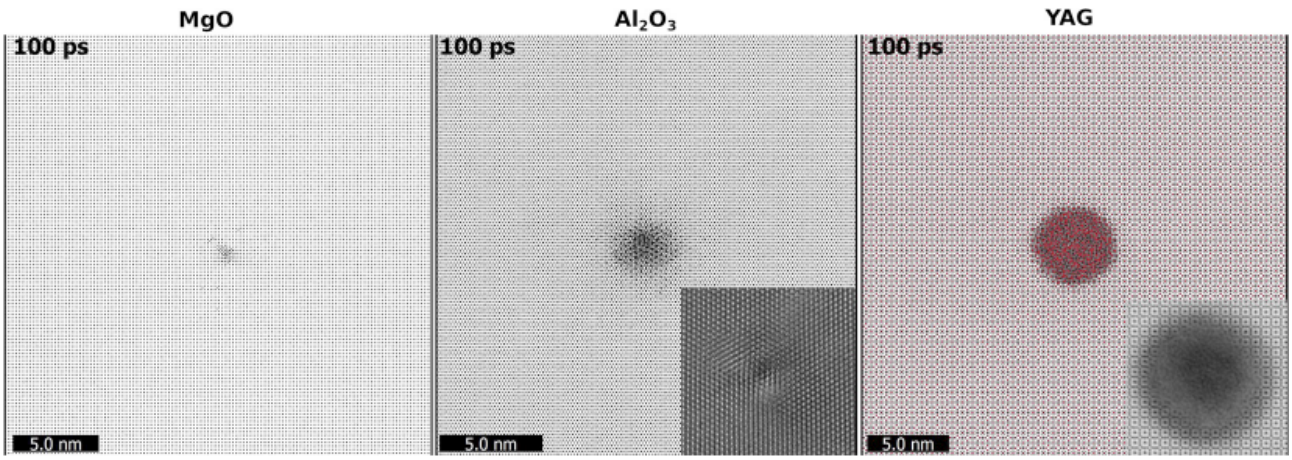

Figure 1. Snapshots of modeled 167 MeV Xe tracks in three materials at 100 fs after ion passage with the experimental latent tracks as insets. The scales of MD images and TEM insets are the same.

It was found that initial excitation of the target produced a dissordered volume in all materials. The major contributing factor leading to differences in the final relaxed state seems to be the ability of the material to recrystalize within the short cooling period as well as the viscosity of the molten state.

References

[1] F.F. Komarov, Physics-Uspekhi 46, 1253–1282 (2003).
[2] F. Aumayr, S. Facsko, A.S. El-Said, C. Trautmann, M. Schleberger, J. Physics. Condens. Matter 23, 393001 (2011).
[3] M. Toulemonde, C. Dufour, A. Meftah, E. Paumier, Nucl. Inst. Meth. B. 166–167, 903–912 (2000).
[4] D.M. Duffy, S.L. Daraszewicz, J. Mulroue, Nucl. Inst. Meth. B. 277, 21–27 (2012).
[5] N.A. Medvedev, R.A. Rymzhanov, A.E. Volkov, J. Phys. D. Appl. Phys. 48, 355303 (2015).
[6] R.A. Rymzhanov, N.A. Medvedev, A.E. Volkov, Nucl. Inst. Meth. B 388, 41–52 (2016).
[7] S. Plimpton, J. Comput. Phys. 117, 1–19 (1995).

INVITED LECTURE

The synergy of polarized transmitted light microscopy and scanning electron microscopy in mineralogical-petrological investigations of cultural heritage objects

KRISTINA ŠARIĆ, VESNA MATOVIĆ AND SUZANA ERIĆ
University of Belgrade - Faculty of Mining and Geology, Belgrade, Serbia

Two complementary techniques – polarized transmitted light microscopy (PTLM) and scanning electron microscopy coupled with energy- or wave-length dispersive spectrometry (SEM-EDS/WDS) are among the basic methods in mineralogical-petrological investigations of geological material (minerals and rocks) and various artificial items (ceramics, mortar, pigments). The PTLM characterizes the studied material by analyzing the rays of transmitted polarized light taking into consideration that different substances transmit polarized light in different way. On the other hand, the SEM-EDS/WDS method provides both morphological and chemical analyses of samples by scanning their surface based on bombing with an electron beam a sample with electrons and analyzing the response which depends on the energy emitted from the studied sample.

Plenty of objects of tangible cultural heritage, both movable (various archaeological artifacts, sculptures) and immovable (various architectural and civil engineering objects), are made of stone. Therefore, in most up to date multidisciplinary investigations of cultural heritage objects, a mineralogical-petrological study represents one of the main steps. The mineralogical-petrological characteristics provide constraints on many important issues, such as: a) determination of primary features of the material used for objects (mineral composition, fabric, porosity etc), b) the origin of stone (solid stone, clays, sand) used as raw material in the production of stone tools, ceramics, sculptures, as well as buildings, c) specification of different processes that might have occurred during the interaction between cultural heritage objects and the environment, d) behavior of stone material against the substances used for its protection from decay, e) estimating the compatibility between the original stone material and potential material used for reparation and/or protection, f) providing recommendations for monument protection, restoration etc (Figure 1). In the following text we illustrate four examples of the application of PTLM and SEM-EDS methods in studying Serbian cultural heritage objects: from Prehistoric tools to medieval monuments.

In investigating abrasive and polished stone tools from the Eneolithic site of Masinske Njive (Šumadija, Serbia) the main task was to define the provenance of used raw material in order to help the archaeologists to define the area of everyday activities of tribes and to derive conclusions on possible communications among communities, economics (trade), way of life etc. As Šarić et al. [1] reported, the PTLM revealed the presence of hydrothermally altered volcaniclastics, coherent quartzlatites with sieved plagioclases and one metamorphic rock - sericite-muscovite-quartz schist, but it was not sufficient to establish the provenance of this raw material. However, SEM-EDS analyses provided evidence that in the studied quartzlatites processes of phlogopitization of biotites had occurred. Such mineralogical and textural features are typical for Cenozoic volcanic complexes of Serbia, such as Rudnik, Rogozna or Kopaonik [2], [3], [4], among others. Although none of the Cenozoic complexes could be excluded as a potential source of the raw material, the authors regarded Rudnik as the most suitable candidate, because this area is closest to Masinske Njive. The provenance of a single sample of sericite-muscovite-quartz schist is not possible to determine until more data are available.

An example of the application of PTLM and SEM-EDS technique (in combination with X-ray powder diffraction - XRPD) in studying ancient ceramics is the analyses of 63 samples of ceramic shards (cooking and table ware) and three samples of pristine clay regarded as possible raw material from the Serbian Medieval monastery Studenica (UNESCO world heritage site). The study was

performed by Šarić et al. [5] who concluded that: a) the mode of matrix crystallinity (PTLM), the morphology of fracture surfaces of the shards (SEM) and chemical reactions between the clasts and the matrix (SEM-EDS) indicate different temperatures of firing: samples displaying an anisotropic matrix, rough fracture surfaces and lacking reactions between the clasts and the matrix were fired at lower temperatures (600-700 oC), whereas those having an isotropic matrix, smooth fracture surfaces and exhibiting reactions between the quartz clasts and the matrix indicate firing temperatures of minimum 800-900 oC; b) the characterization of clasts (PTLM + SEM-EDS), and matrix and the clay compositions (SEM-EDS + XRPD) imply that most shards originated from local production, whereas four wares could have been imported from Peloponnese; c) illitic type of possible raw material was also determined (SEM-EDS + XRPD).

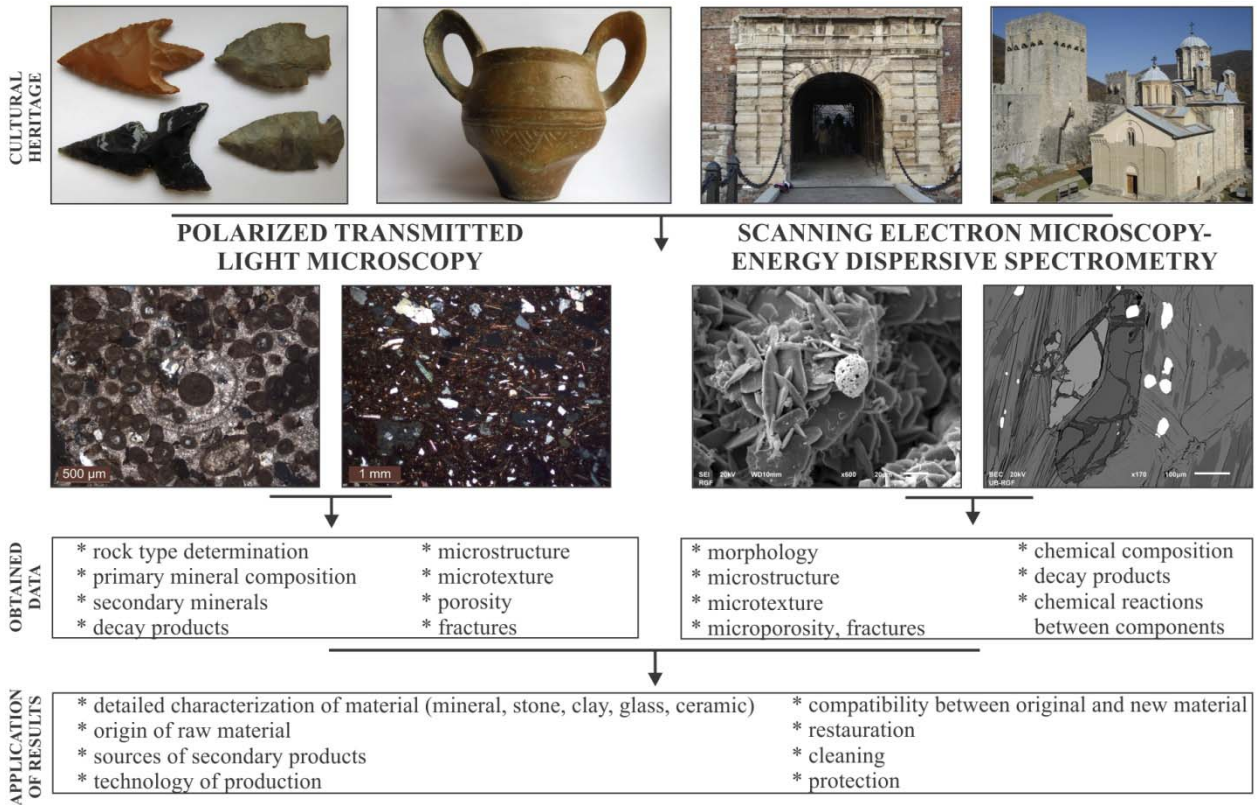

Figure 1. Application of PTLM and SEM-EDS/WDS methods in mineralogical-petrological investigations of cultural heritage objects.

Two complex studies done for the Manasija Monastery from the XV century [6] and the Gradac Monastery from the XIII century [7] involve: a) determining the composition, fabric and microstructures of primary stone material, b) the characterization of secondary crusts and products of efflorescence formed over the stone, and c) the identification of processes which may have caused the formation of the crusts and stone degradation. The PTLM investigations show that primary blocks of the stone in the walls of the Manasija complex are represented by two varieties of limestone and sandstone, whereas the church of Gradac was built of tufa. Various types of aggressive salts, identified by SEM-EDS on the surfaces of the primary stone material, are: Na-sulfates and carbonates (thenardite, mirabilite thermonatrite, trona – mostly in Manasija), Ca- and Mg sulfates (gypsum, epsomite, hexahydrate – mostly in Gradac) and other complex salts (eugsterite, darapskite, aphthitalite, blodeite, syngenite – developed on both objects). The formation of the salts is explained as follows: Na- and Na-Ca salts from the walls of Manasija generated from cement mortar used for repairs. The lithological type and chemical composition of the substrate had

also an influence on the development of these salts, because Ca partly derived from different types of limestone. On the other hand, it is found that the efflorescence marked by Mg-phases (epsomite and hexahydrate) on the tufa walls of Gradac originated from several sources: the original lime mortar which contains Mg-rich aggregates, the lime cement mortar used for repairing, the dolostone of the rubber core, and Mg-rich rocks of the monastery basement. The acquired data underline the complexity of research of the cultural heritage objects, emphasizing the importance of recognition of both natural factors and damages caused by inadequate material for reparation.

The last example (walls and gates of the Belgrade's fortress) is dedicated to the problem of the recovery of stone monuments and the replacement of damaged stone blocks or their parts by new material – natural and the same if possible. The PTLM indicates that the majority of the blocks of the walls and gates of the Belgrade's fortress are made of Middle Miocene limestones from the vicinity of Belgrade. However, all known quarries from this area have been abandoned since more than 100 years. The PTML reveals petrological (structural characteristics, mineral composition, type of porosity) and geochronological (determination of the Badenian Lower Sarmatian fauna) similarities of the original stone and the stone from quarries at the Fruška Gora Mts, especially from the open pit Mutalj. This led to successful substitution of the damaged stone blocks (Matović, unpubl).

According to the given examples it could be concluded that the application of PTLM and SEM-EDS/WDS methods in unraveling mineralogical-petrological characteristics has a significant role in the investigation of cultural heritage in all stages of examination: from the characterization of primary material to the determination of secondary products and the estimation of potential material used for restoration etc.

Acknowledgements
This study was done within the project no. 176016 of the Serbian Ministry of Education, Science and Technological Development.

References
[1] K. Šarić, S. Erić, V. Cvetković, J. Šarić, D. Antonović, J SAS, 33 (2017) 283-307
[2] S. Borojević Šoštarić, V. Cvetković, F. Neubauer, L.A. Palinkaš, M. Bernroider, J. Genser, Lithos, 148 (2012) 176-195
[3] V. Cvetković, K. Šarić, Z. Pécskay, A. Gerdes, Geol Croat, 69:1 (2016) 89-99
[4] A. Mladenović, B. Trivić, V. Cvetković, Tectonophysics, 646 (2015) 36-49
[5] K. Šarić, V. Bikić, S. Erić, Microsc Microanal, 24 (2018) 744-761
[6] V. Matović, S. Erić, D. Srećković-Batoćanin, Ph. Colomban, A. Kremenović, Environ Earth Sci, 72:6 (2014) 1939-1951
[7] S. Erić, V. Matović, A. Kremenović, Ph. Colomban, D. Srećković-Batoćanin, M. Nešković, A. Jelikić, Constr Build Mater, 98 (2015) 25-34

Use of Optical Microscopy, SEM and EDS Analysis for Investigation of Historical Paint Layers

SNEŽANA VUČETIĆ[1], OLIVERA BRDARIĆ[2], JOHN MILAN VAN DER BERGH[1], BOJAN MILJEVIĆ[1] AND JONJAUA RANOGAJEC[1]

[1] University of Novi Sad, Faculty of Technology, Novi Sad, Serbia; [2] Provincial Institute for Protection of Cultural Monuments, Petrovaradin, Serbia

Scanning Electron Microscopy with Energy Dispersive Spectroscopy (SEM-EDS) and Optical Microscopy with Polarised Light (OM) are often irreplaceable techniques for the analysis of complex works of art. The stratigraphic investigation provides important information about the structure, morphology, painting technique and composition of layers, which is crucial for making decisions about future conservation approaches and techniques. This paper presents investigation of samples from fresco painting from the Serbian Orthodox Church of the Nativity of the Blessed Virgin Mary in Sremska Kamenica, Serbia, a baroque building built in 1758.
The analysis presented combined use of OM, SEM and EDS analysis on one of the samples from the Orthodox Church fresco painting. The OM was employed for detecting paint layers, while the immersion oil technique improved the numerical aperture (resolution) of the optical system. In total, 5 layers were identified (Fig. 1).

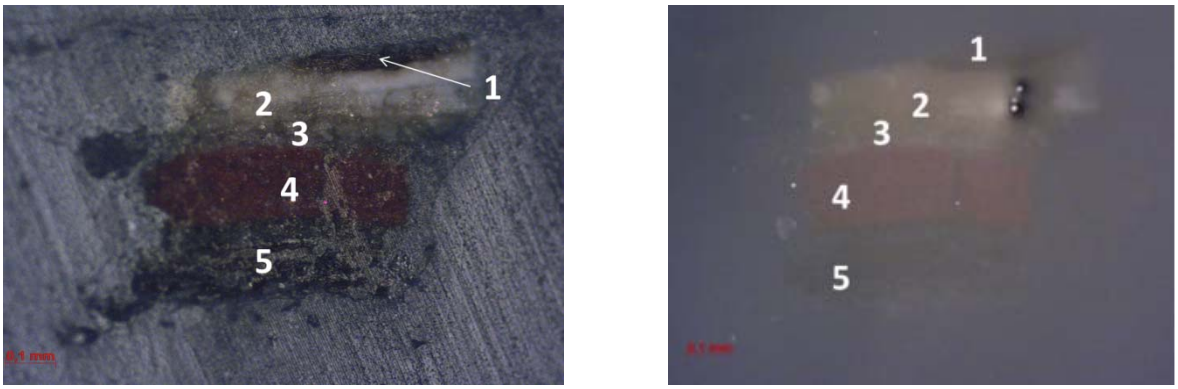

a) b)

Figure 1. Serbian Orthodox Church fresco painting sample: a) Optical Microscopy image without immersing oil, x100; b) Optical Microscopy image with immersing oil, x100

The thickness of each layer was identified using SEM - BEI (Backscattered Electron Image) analysis, while the chemical composition was detected based on EDS (Table 1.), which was later coupled with the results of FTIR and XRF analyses. The main identified historical paint layers are the top layer – no. 1 (Ultramarine based) and layer no. 4 (Vermilion based). They form a so-called "double sample", with the paint layers separated from each other by a well-defined "new" ground layer (layers no. 2 and 3). The OM and SEM images of the sample showed the heterogeneity and fragility of the layer no. 3 (Spectra 2, 3 and 5 in Fig. 2b) which should be taken into account in future conservation works.

The presented results confirmed that the combination of different microscopy and spectroscopy techniques are crucial for deeper understanding of painting composition which is more often than not a lot more complex than the eye sees. The obtained microscopy and spectroscopy results were further enlarged with FTIR and XRF investigation and together they provide invaluable inputs for future conservation of fresco paintings, based on modern principles of collaboration between science and conservators.

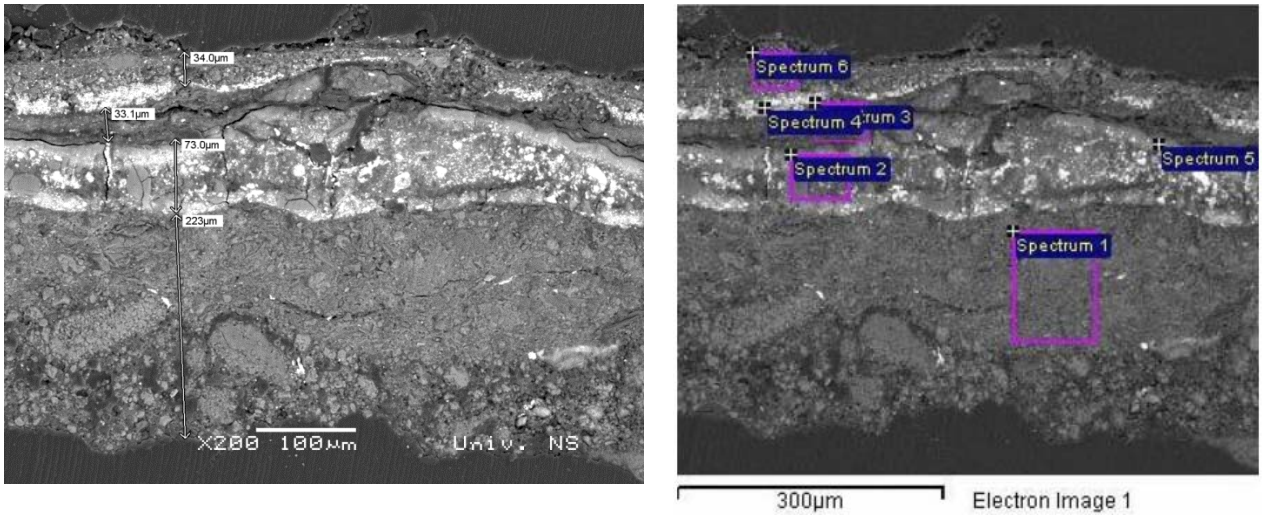

a) b)

Figure 2. Serbian Orthodox Church fresco painting sample: a) SEM - BEI image, x200, with marked thickness of each paint layer; b) SEM image, x200 with marked positions of EDS analyses

Element	Spectrum 6	Spectrum 4	Spectrum 2	Spectrum 3	Spectrum 5	Spectrum 1
	mas. %					
C	57,51	45,56	58,38	73,31	49,92	46,79
O	16,75	12,33	13,45	10,28	16,24	23,14
Na	1,68	-	0,36	-	-	-
Mg	0,34	-	0,32	0,35	-	0,45
Al	2,04	-	3,15	0,43	2,93	5,53
Si	2,99	-	0,92	0,99	0,73	12,71
S	1,67	-	-	-	-	-
Cl	0,64	-	1,78	0,80	0,43	-
K	1,18	0,54	0,47	0,35	0,35	0,95
Ca	3,85	2,68	2,50	5,52	2,88	2,65
Ti	2,14	-	-	-	-	0,53
Fe	5,43	3,39	2,06	0,64	3,51	6,40
Pb	3,77	35,50	16,61	7,33	23,01	0,85
Total	100,00	100,00	100,00	100,00	100,00	100,00
Corresponds with the layer identified by OM	1 - Blue	2 - White	3 - Grey-yellowish			4 - Red

Table 1. Results of EDS analyses in correlation with painted layers identified by OM and SEM

Acknowledgment

Financial support from the Ministry of Education, Science and Technological Development of the Republic of Serbia (Project no. III45008) is gratefully acknowledged.

References

[1] Winter J, West FitzHugh E. Pigments based on Carbon, Chapter in Berrie B.H. (Ed.): *Artists' Pigments, A Handbook of Their History and Characteristics*, Volume 4 (2007)
[2] Kraigher-Hozo M. *Metode slikanja i materijali.* KULT-B, Sarajevo (2006)
[3] Spring M. New insights into the materials of fifteenth- and sixteenth-century Netherlandish paintings in the National Gallery, London. *Heritage Science*, 5 (2017)
[4] Eastaugh N, Walsh V, Chaplin T, Siddall R: *Pigment Compendium: A Dictionary and Optical Microscopy of Historical Pigments.* Elsevier, USA (2008)

Scanning (SEM) and Transmission Electron Microscopy (TEM) in Cultural Heritage

SABRINA BURATTINI, ELISABETTA FALCIERI AND LAURA BARATIN
Department of Biomolecular Sciences, University of Urbino Carlo Bo, Campus Scientifico „E.Mattei", Urbino, Italy; Department of Pure and Applied Sciences (DiSPeA), Università degli Studi di Urbino "Carlo Bo", Urbino, Italy

Over the years, microscopy has become an integral part of programs for the preservation of Cultural Heritage, because it provides information on specimen ultrastructural morphology and degradation phenomena.
SEM study, through the rapidity of sample preparation, the high resolution, and 3D-analysis, gives us information on the nature and surface properties, on the modifications induced both by technological treatments and accidental causes as well as by the action of chemical, physical, mechanical or natural agents.
In the case of wooden and textile finds of historical-artistic interest, SEM can be used for conservation interventions, such as the identification of sample nature through the study of surface and of their alterations. Furthermore, it is possible to carry out the characterization of the degradation state, the evaluation of the conservative intervention and the study of the restored substrate in order to verify the state of conservation (1). On the other hand, TEM observation, after an appropriate sample preparation and thanks to the high resolving power, allows the ultrastructural analysis of the internal structures of cells and / or tissues, correlated to the qualitative investigation of sample structure conservation status.
Moreover, it represents a particularly useful tool in identifying the biotic agents of degradation, allowing to understand / reconstruct the history of the artifacts and helping to set a correct restoration
project.

References

[1] M. C. Timar, L. Gurau, M. Porojan, E. Beldean, Europ J Sc Theol, 9 (2013), 243–252

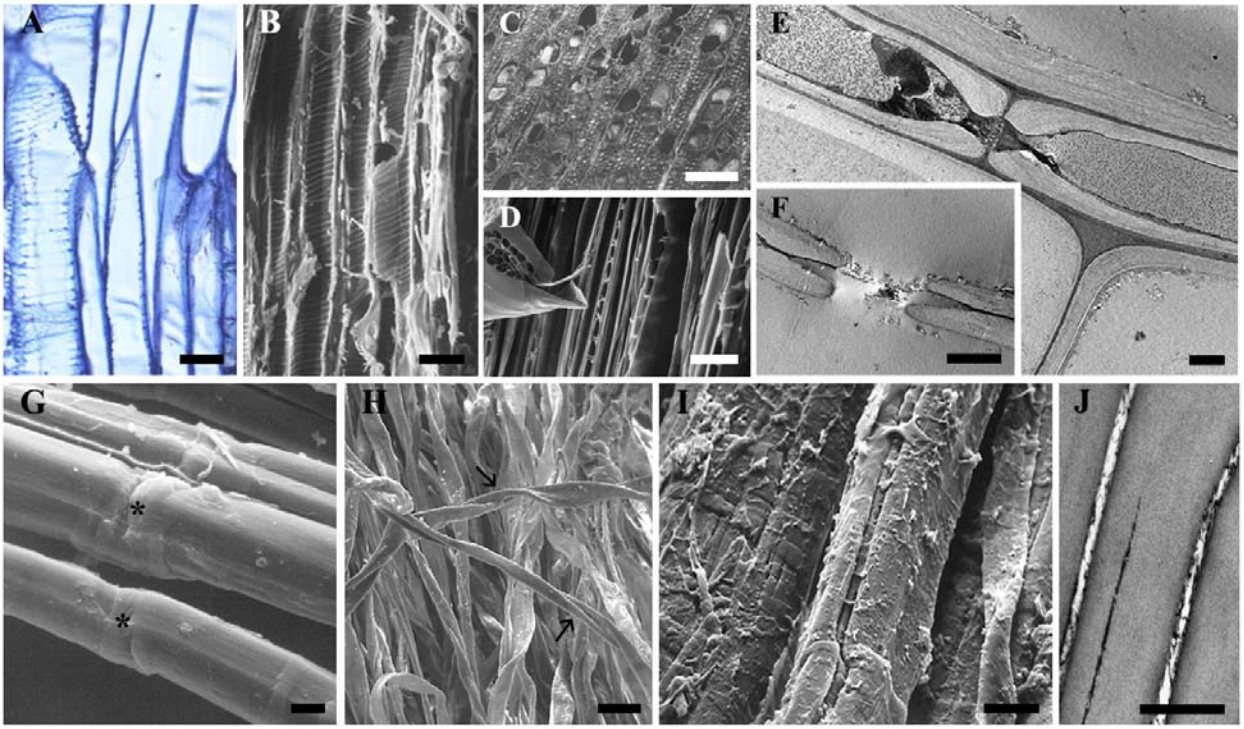

Figure 1. Light microscopy (A), SEM (B-D, G-I) and TEM (E, F, J) of wood (A-F) and yarns (G-J). Fibers and vessels in tangential section are visible (A, B). C, wood in cross section. Tyloses formation are present. Ray cells, plasmodesmata structures and bordered pits are shown in C-F, respectively. Linen (G; *, knots) and cotton (H; →, twisted ribbon) fibers are displayed. In I, contaminated hemp fiber are present. J, cotton fibers in longitudinal section. Bars: A,B,E,I = 0.5 µm; C = 20µm; D,H = 10 µm; F = 0,2µm; G=1µm; J=0.1µm.

The nanoscale origin of chatoyancy in chrysoberyl from Pratinhas, Brazil

SANDRA DREV[1], ALEKSANDER REČNIK[2], MATJAŽ MAZAJ,[3] AND NINA DANEU[4]

[1] Center for Electron Microscopy and Microanalysis, Jožef Stefan Institute, Ljubljana, Slovenia; [2] Department for Nanostructured Materials, Jožef Stefan Institute, Ljubljana, Slovenia; [3] Laboratory for Inorganic Chemistry, National Institute of Chemistry, Ljubljana, Slovenia; [4] Advanced Materials Department, Jožef Stefan Institute, Ljubljana, Slovenia

Chrysoberyl ($BeAl_2O_4$) from Rio das Pratinhas near Arataca in the Bahia state of Brazil displays the optical effect of chatoyancy (Figure 1), commonly ascribed to oriented inclusions of other minerals, such as rutile. To identify the origin of this effect we studied the chrysoberyl crystals using powder x-ray diffraction and electron microscopy and spectroscopy methods. The chrysoberyl structure was first determined by Bragg and Brown (1926). It crystallizes in an olivine-type structure, a hexagonal close-packed (*hcp*) analogue of cubic (*ccp*) spinel ($MgAl_2O_4$) structure. It has a slightly distorted *hcp* O-sublattice with Al^{3+} and Be^{2+} ions partially occupying octahedral and tetrahedral interstices. The structure has been often revisited and reports do not differ that much in cell parameters as they do in the orthorhombic unit cell settings leading to space groups variants: Pnma, Pbnm, Pmnb, *etc*. Our choice is based in accordance to the spinel archetype structures. *hcp* planes of the O-sublattice were oriented normal to the crystallographic *c*-axis so that (001) planes of chrysoberyl correspond to (111) planes of spinel, with the *a*-axis aligned parallel to the $(1\bar{1}0)$ axis of spinel, allowing direct comparison between the spinel, taaffeite and chrysoberyl [1]. Experimental diffraction pattern was best matched with the crystal structure of chrysoberyl at the atmospheric pressure (Hazen 1987; JCPDS 01-078-0956), with minor reflections belonging to rutile (Figure 2). The chrysoberyl structure was refined by Rietveld analysis (Topas-Academic V4) in the orthorhombic Pmnb (62) space group, using starting structural model from Hazen [2]. In the final stage, nanocrystalline rutile was included as a minor secondary phase. The refinement of rutile included in chrysoberyl was less reliable due to broad and weak reflections of rutile, which can be attributed to relatively low concentration of rutile, its small crystal size, and possible structural anisotropy. Quantitative analysis including refined chrysoberyl and rutile structures resulted in 98.0(9) mol% of chrysoberyl and 2.0(9) mol% of nanocrystalline rutile with an average particle size of ~50 nm. Refined unit-cell parameters of chrysoberyl crystals from Pratinhas are: a = 5.4825(1), b = 9.4163(2), c = 4.4308(1) Å (space group *Pmnb*, *no*.62), whereas those of rutile converged to a = 4.7331(4), c = 2.880(2) Å (space group $P4_2/mnm$, *no*.136). The Rietveld refinement was stopped with R_{wp} of 7.8 %.

The samples were further studied in [001] orientation by transmission electron microscopy (TEM). Figure 3 shows a thin crystal foil of chrysoberyl with numerous precipitates in oriented fashion, suggesting that some exsolution process took place after the formation of chrysoberyl crystals. They are oriented in two specific orientations with respect to chrysoberyl lattice, occasionally coinciding to form obtuse L-shaped or acute V-shaped pairs, enclosing 98.7° or 81.3°. These angles correspond to {120} planes of chrysoberyl lattice, suggesting that the precipitates exsolved along these specific planes. No additional reflections could be seen in selected area electron diffraction patterns due to relatively low concentration of precipitates and their small size, even when using the smallest selected area apertures. Energy dispersive x-ray spectroscopy (EDS) showed that the precipitates are Ti-rich. They are only few nanometers thick, and up to 50 nm long on average. To determine the orientation of *a* and *c*-axes, distances along the three pseudo-hexagonal directions of the rutile lattice were measured over several tens of lattice planes to ensure higher accuracy (Figure 4). The resulting interplanar distances were d_{101} = 2.456 and d_{001} = 2.875 Å, and the lattice parameters of rutile were calculated: a = 4.725 and c = 2.875 Å [3]. The result surprisingly matches the lattice parameters determined by Rietveld refinement and implies large deformations of rutile imposed by the host chrysoberyl lattice after precipitation. This was explained that during phase separation

process the morphology of precipitates is dictated by the lowest energy interfaces between the two structures, where the longest dimensions of precipitates commonly correspond to the best matching directions that exist between the two phases. Orientation relationship determined from HRTEM images of chrysoberyl-rutile interfaces such as shown in Figure 4 is: $[001]_{Ch}\{120\}_{Ch}||[010]_{R}\{103\}_{R}$. Precipitation of rutile probably occurred on cooling of Ti^{4+}-rich chrysoberyl solid solution when supersaturation conditions were reached and separation process took place. Determined orientation relationship has interesting implications for determination of rutile exsolution temperature, helping to disclose the dynamics of geochemical processes during crystallization of chrysoberyl.

Acknowledgements: This work is a part of the Ph.D. thesis of S. Drev financed by the Slovenian Research Agency. The TEM work was performed at the Centre of Electron Microscopy at JSI.

Figure 1: Uncut chrysoberyl crystal from Pratinhas, Brazil and cabochon showing chatoyancy effect due to nanosized rutile precipitates.

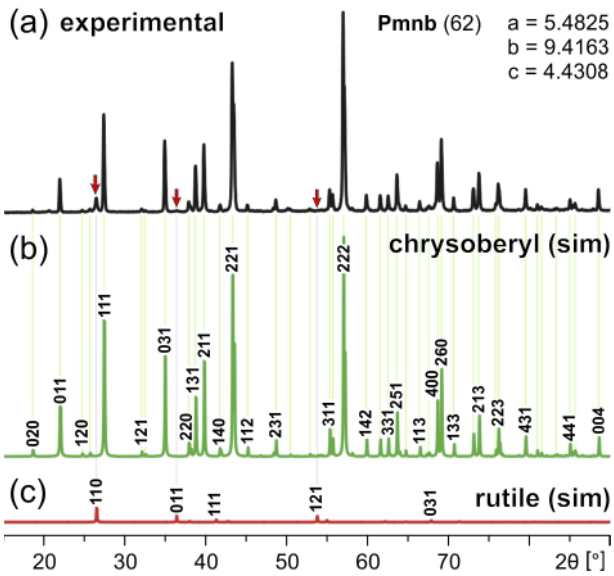

Figure 2: X-ray diffraction analysis of chrysoberyl crystal from Pratinhas. (a) Experimental pattern with red arrows indicating positions of rutile reflections. (b) Simulated pattern of chrysoberyl after Rietveld analysis. (c) Simulated pattern of rutile.

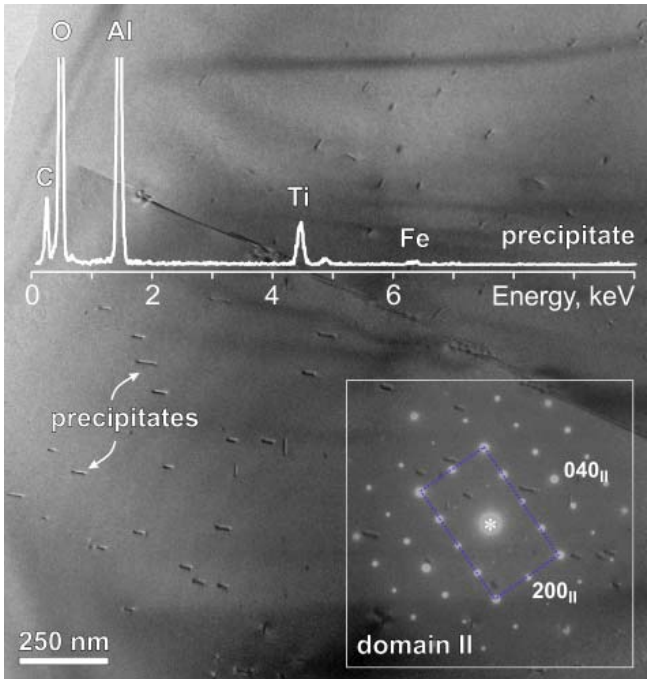

Figure 3: TEM and electron diffraction study of chrysoberyl from Pratinhas. EDS analysis from the precipitate shows enrichment with Ti.

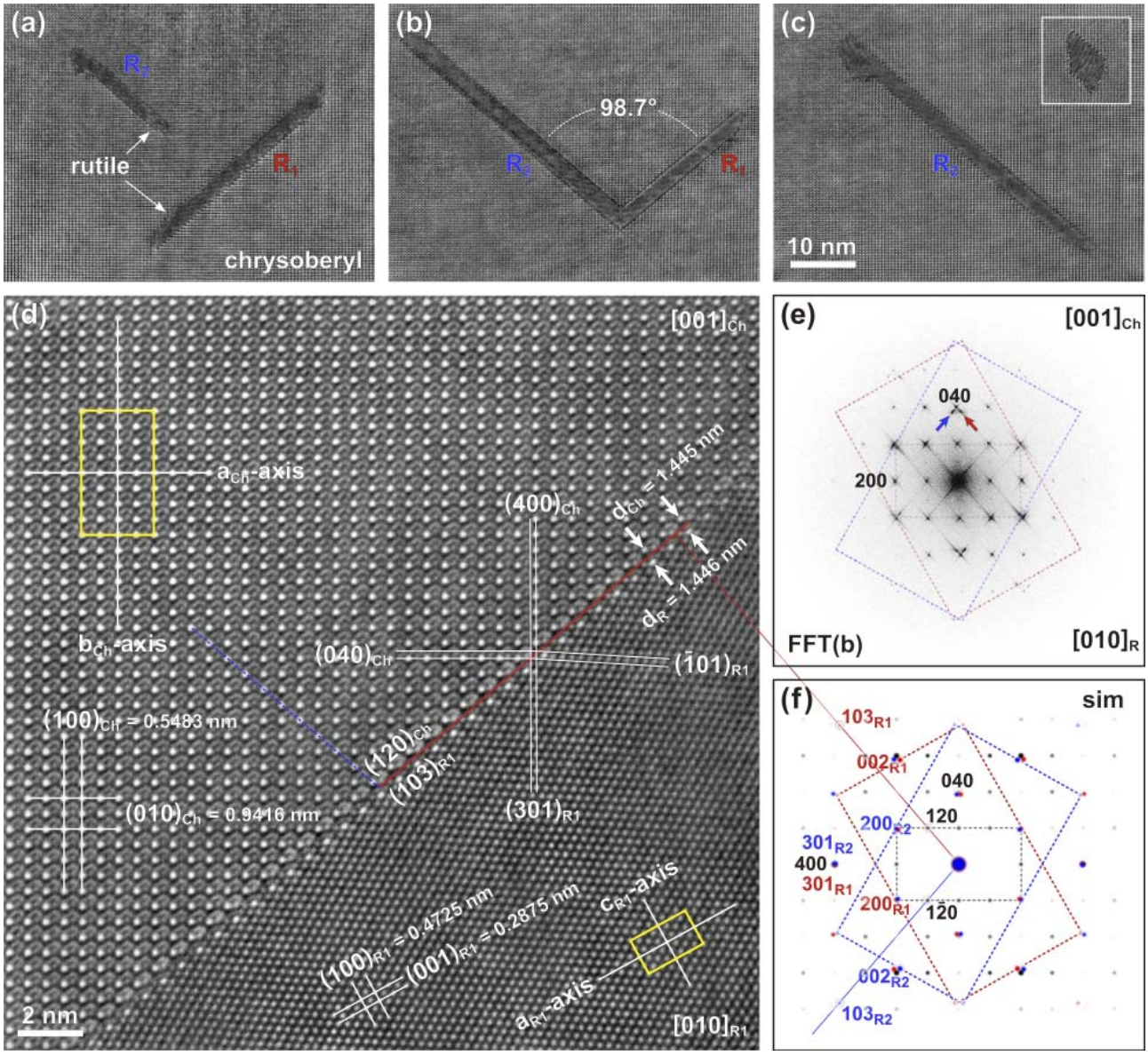

Figure 4. TEM study of rutile precipitates in chrysoberyl from Pratinhas. (a) Two orientations are observed (R1 and R2). (**b**) L-shaped cluster composed of two impinging rutile precipitates enclosing an angle of 98.7°. (**c**) Isolated rutile precipitate. In addition, small xenomorphic grains of faulted rutile are present (*see* the inset). The magnification in all three images is identical. (d) Structural analysis of chrysoberyl-rutile (Ch|R1) interface. Real space 4×4 unit-cells are outlined in yellow. (e) Fast Fourier transform (FFT) of the HRTEM image from (b) displaying additional reflections from rutile R1 and R2 precipitates (indicated by arrows). (f) Reconstructed EDP of chrysoberyl and rutile precipitates calculated with lattice parameters of deformed rutile from the HRTEM analysis (d), with $(120)_{Ch} \parallel (103)_{R1}$ and $(1\bar{2}0)_{Ch} \parallel (103)_{R2}$. Reciprocal 2×2 unit-cells are outlined (chrysoberyl = *grey*, R1 = *red*, R2 = *blue*). Ref. Drev *et al* (2015).

References

[1] S. Drev, A. Rečnik, N. Daneu, CrystEngComm, 15 (2013) 2640-2647.
[2] R.M. Hazen, Physics and Chemistry of Minerals, 14 (1987) 13–20.
[3] S. Drev, M. Komelj, M. Mazaj, N. Daneu, A. Rečnik, Am Mineral., 100 (2015) 861-871.

Microstructural Characterizations of $K_{0.5}Bi_{0.5}TiO_3$-$BaTiO_3$-$Na_{0.5}Bi_{0.5}TiO_3$ Textured Lead-Free Piezoelectric Ceramics

UMUT SAVACI[1], CEREN AŞKIN[1], H. ŞULE TETIK[1], İSMAIL ŞAHIN[1], GÜROL ÖZARSLAN[1], A. MURAT AVCI[2], SERVET TURAN[1] AND ENDER SUVACI[1,2]

[1] Eskisehir Technical University, Department of Materials Science and Engineering, Eskisehir/Turkey;
[2] ENTEKNO Corp. Eskisehir/Turkey

Piezoelectric ceramics, which convert mechanical energy into electrical energy or vice versa, have been used in various applications such as transducers, actuators and piezo generators. Lead based piezoelectric ceramics have been widely used due to their excellent performance; however, due to the toxic nature of the lead element, researches have focussed on finding alternative lead-free piezoelectric ceramics, having high piezoelectric performance. Lead-free sodium bismuth titanate (NBT) ceramic composition is an important alternative to lead based ceramics due to its high piezoelectric performance. Properties of piezoelectric ceramics can be improved with different approaches like compositional modifications and microstructure engineering. In the first method, the performance of NBT ceramics can be improved by addition of potassium bismuth titanate (KBT) and barium titanate (BT) modifiers and these modifiers also increase the phase transformation temperature of NBT. The second method is tailoring of the microstructure with texturing due to anisotropic nature of piezoelectric properties. Texturing of the microstructure can be done with various methods. Among those methods, templated grain growth (TGG) method is the most widely used one. In TGG method, anisotropically shaped templates are used for producing ceramics with oriented grains via a proper heat treatment process. During heat treatment, densification and grain orientation occur due to Ostwald ripening. In this study, textured NBT-KBT-BT ceramics were produced by using BT, KBT and BiT template particles and microstructural characterizations of produced samples were carried out by x-ray diffraction (XRD), scanning electron and transmission electron microscopes (SEM and TEM) to evaluate effects of time, temperature and template type on the texture formation. Orientation relations between matrix and template particles were characterized by using novel precession electron diffraction in TEM. In this presentation, the results of these analyses will be discussed in detail.

EBSD and STEM analysis of cyclic twins in SnO_2 ceramics doped with CoO and Nb_2O_5

NINA DANEU[1], JOSÉ ALBERTO PADRÓN NAVARTA[2], FABRICE BAROU[2], GORAN DRAŽIĆ[3], SARA TOMINC[4], ALEKSANDER REČNIK[4]

[1] Advanced Materials, Jožef Stefan Institute, Ljubljana, Slovenia; [2] Géosciences Montpellier, Université de Montpellier and CNRS, Montpellier, France; [3] Materials Chemistry, National Institute of Chemistry, Ljubljana, Slovenia; [4] Nanostructured Materials, Jožef Stefan Institute, Ljubljana, Slovenia

SnO_2 ceramics sintered with small additions of CoO and Nb_2O_5 exhibit excellent current-voltage nonlinearity and low leakage current, a combination of properties advantageous for varistor applications [1]. During sintering of the ceramics, three types of SnO_2 grains develop: normal (untwinned) grains, simple contact twins on {101} planes and multiple cyclic twins with more than three domains extending from a common central point. The fraction of twinned grains increases with the addition of Nb_2O_5. Single and cyclic twins are regularly observed in rutile-type structures like TiO_2 and SnO_2 and their formation is usually related to topotaxial recrystallization or epitaxial growth on a structurally related precursor [2]. In rutile-type structures, cyclic twins may have two different configurations with coplanar or alternating ('up' and 'down') tetragonal axes as observed in rutile (TiO_2) sixlings and eightlings [3]. In this work we focused on the crystallography of cyclic twins in (Co,Nb)-doped SnO_2 ceramics using electron back-scatter diffraction (EBSD), while further scanning transmission electron microscopy (STEM) in combination with energy dispersive X-ray spectroscopy (EDXS) was used to understand the mechanism of their formation.

The ceramic samples were prepared by homogenization of SnO_2 powder with the addition of 1 mol% CoO and 1 mol% Nb_2O_5, pressing into pellets and sintering at 1430°C for 5 hours in air atmosphere. For EBSD observations, the microstructures were prepared by polishing the cross-sections down to 0.25 µm with diamond paste and subsequent annealing (thermal etching) at 1250°C for 15 min. The heat-treatment of the surface resulted in removal (recrystallization) of the amorphous surface layer yielding EBSD patterns with excellent quality (high contrast Kikuchi patterns and therefore high indexing rate). The EBSD analyses were performed using dedicated instrument CamScan X500FE Crystal Probe at Géoscience Montpellier with inclined column optimized for EBSD and field-emission electron gun allowing high-resolution spatial analyses. The EBSD patterns were recorded at 20 kV accelerating voltage and working distance 20 mm. The patterns were indexed automatically using AZtechHKL® software package from Oxford Instruments. Grains misorientation boundaries were determined using MTEX open source code [4,5]. The models of cyclic twins were reconstructed by transforming EBSD data of each domain into vectors for Crystal Maker® Software Ltd, Oxford, UK. Data for different domains forming a cyclic twin were inserted into a molecule-type file enabling visualization of relative orientation of crystal domains not related by symmetry operations. Schematic morphologies (crystal shapes) of the cyclic twins were drawn in Vesta [6]. Samples for transmission electron microscopy (TEM) were prepared using the conventional thinning, dimpling and ion-milling approach. The atomic-scale analyses were performed using aberration corrected scanning TEM (STEM) Jeol ARM 200CF at National Institute of Chemistry in Ljubljana equipped with Jeol Centurio EDXS system with 100 mm^2 SDD detector for chemical analysis at the nanoscale.

Figure 1a is a band contrast map of the doped SnO_2 ceramics. It shows typical dense microstructure with grains having average size of around 10 microns. The Euler colored orientation map (Fig. 1b) reveals random grain orientation. Identification of grains misorientation boundaries was used to distinguish between random grain boundaries and domains in {101} twin orientation with ~68° angle

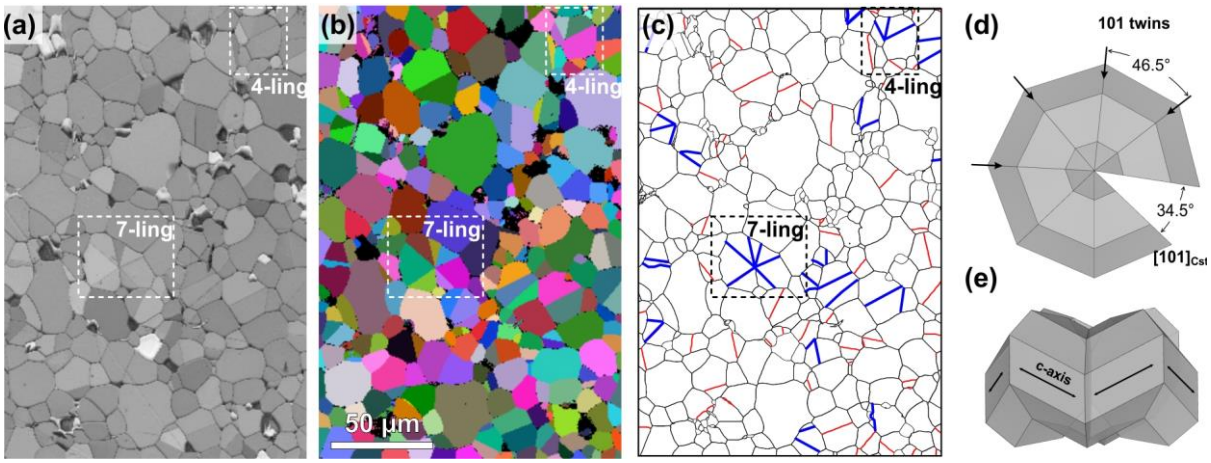

Figure 1. (a) Band contrast and (b) Euler color map of the (Co,Nb) doped SnO_2 ceramics microstructure. (c) Grain boundaries (thin black contours) with simple contact (red) and cyclic (blue) {101} twin boundaries. (d) Schematic model of the sevenling marked in the maps a-c oriented along the common twin axis and (e) in side-view, where alternating orientation of the twin domains' *c*-axes is clearly observed.

between ⟨100⟩ axes of the twin domains (Fig. 1c). The presence of {301} twins was not detected. The analysis of twinned grains has shown that besides simple contact twins, cyclic twins with 3-7 domains occur regularly (Fig. 1c). In general, cyclic twins in rutile-type structures occur in two different morphologies, with coplanar or alternating tetragonal *c*-axes of the domains in twinned orientation [3]. The number of domains in coplanar rutile twins is limited to 6 (with one imperfectly developed domain), therefore the observation of twins with seven domains was the first implication that the morphology of cyclic twins in (Co,Nb)-doped SnO_2 ceramics is different. Absolute orientation of the domains forming a cyclic twin with seven domains (7-ling or sevenling) indicated in figures 1a-c was determined based on the EBSD data and the result has confirmed that the cyclic twins have the morphology with alternating *c*-axes. Figure 1d is a schematic model of a sevenling oriented along the common twin axis. In this orientation, all seven cyclic SnO_2 domains are oriented along ⟨111⟩ zone axis and the {101} twin boundaries are in edge-on orientation. A similar type of cyclic twins occur in rutile (TiO_2) crystals from Magnet Cove (Arkansas, USA), where perfect eightlings with $\bar{8}2m$ morphological symmetry [3] are observed in contrast to cyclic twins with maximum seven domains as observed in our case. This is due to the difference in the angle between the (101) and $(01\bar{1})$ planes of 46.48° and 45.02°in SnO_2 (cassiterite) and TiO_2 (rutile), respectively. The small difference of ~1.5°is enough that the remaining angular gap of 34.5° doesn't allow for the development of the eight twin domain (eightlings) in the case of cassiterite.

Cyclic twins with alternating *c*-axes develop regularly in SnO_2 ceramics co-doped with CoO and Nb_2O_5, indicating that their formation is not accidental. We have shown previously that the formation of twins in rutile is related either to oriented recrystallization or epitaxial growth on a structurally related precursor, usually with the corundum-type structure. Oriented (topotaxial) recrystallization of ilmenite ($FeTiO_3$) according to the $\langle 101\rangle_{Rt}\ \{010\}_{Rt} \parallel \langle 210\rangle_{Ilm}\ \{001\}_{Ilm}$ orientation relaitonship leads to development of rutiles with coplanar *c*-axes in twinned [2] or pseudo-twinned orientation [7]. Formation mechanism of cyclic twins with alternating c-axes therefore have different origin. In order to understand the formation mechanism of cyclic twins in cassiterite, we analyzed the samples down to the atomic scale using HAADF-STEM and EDS. Although cyclic twins are not that rare in the microstrucutres, grains in suitable ⟨111⟩ orientation and with visible nucleation core are rarely found in thin parts of the TEM samples.

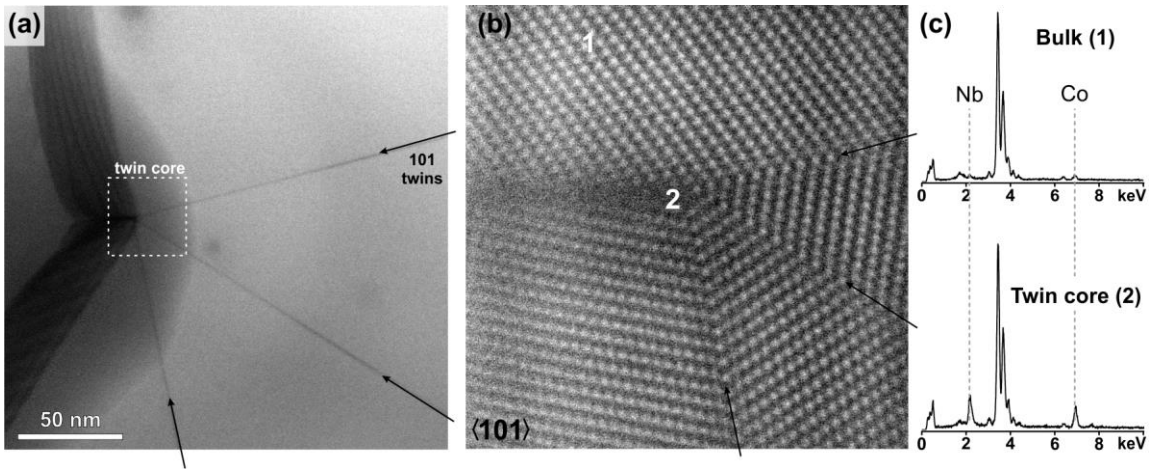

Figure 2. (a) Low-magnification HAADF-STEM image of a cyclic fourling. (b) Atomic-scale HAADF-STEM image around the twin core. All twin domains are oriented along the ⟨111⟩ zone axis, the {101} twin boundaries are edge-on and originate from the twin core. (c) EDS spectra taken from the SnO_2 grain and the area around the twin core (nucleation point) showing enrichment with Co and Nb in the center of the twin.

An example of a twin with four developed domains (4-ling or fourling) is shown in Figure 2. It can be observed that the twin core is located near the edge of the grain and that all four twin boundaries extend from a common nucleation point indicating the formation in the beginning of the grain growth with nucleation on a common nucleaiton core. In this cross-section (Fig. 2b), the nucleus appears as nano-sized amorphous core. EDXS spot analyses taken in the bulk SnO_2 and in the core show significant enrichment with Co and Nb in the core area, which exceeds concnetrations at the normal grain boundaries [1]. This implies that the cyclic twins in SnO_2 nucleated on a strucutrally related Co-Nb-rich phase in the beginning of grain growth.

Acknowledgement
The authors gratefully acknowledge financial support by the Slovenian Research Agency under the Project No. J1-9711.

References
[1] S. Tominc, A. Rečnik, Z. Samardžija, G. Dražić, M. Podlogar, S. Bernik and N. Daneu, Ceram. Int., 44 (2018) 1603-1613.
[2] A. Rečnik A, N. Stanković and N. Daneu, Contrib. Mineral. Petrol. 169(2) (2015) 19/1-22.
[3] Th. Hahn and H. Klapper, International Tables for Crystallography (2006). Vol. D, 393–448.
[4] R. Hielscher and H. Schaeben, J. Appl. Cryst. (2008) 41, 1024-1037.
[5] D. Mainprice, F. Bachmann, R. Hielscher, H. Schaeben, H., in D.R. Faulkner, J. Meckenburgh, E. Mariani (eds) Geological Society, London, Special Publications (2014) 409.
[6] K. Momma and F. Izumi, J. Appl. Crystallogr., 44 (2011) 1272-1276.
[7] N. Stanković, A. Rečnbik, N. Daneu, J. Mater.Sci. 51 (2016) 958-968.

Optimization of Carbon Nanotube Content of Asphalt Nano composites with Regard to Resistance to Permanent Deformation

EMMANUEL GADZAMA HAMATU
Disotos Global Services Limited, Port Harcourt, Nigeria

This paper presents the results of the development of asphalt Nano composites containing carbon nanotubes (CNTs) with high resistance to permanent deformation, aiming to increase the performance of asphalt surfaces in relation to the rutting problem. Asphalt Nano composites were prepared with the addition of different proportions of CNTs (1%, 2% and 3%) in relation to the weight of asphalt binder. The base binder used was a conventional binder (50-70 penetration) classified as PG 58-22. The optimum percentage of CNT addition in the asphalt binder (base) was determined through the evaluation of the rheological and empirical characteristics of the Nano composites produced. In order to evaluate the contribution and the effects of the Nano composite (optimized) in relation to the rutting, the conventional and Nano modified asphalt mixtures were tested in a French traffic simulator (Orniéreur). The results obtained demonstrate the efficient contribution of the asphalt Nano composite containing CNTs to the resistance to permanent deformation of the asphalt mixture.

ONE of the structural defects most commonly encountered in asphalt pavements is permanent deformation. This can be defined as a depression in the wheel track with the possible occurrence of an elevation along the edges of this depression. Permanent deformation mainly originates from the instability of the asphalt concrete due to the excessive fluency of the mixture, aggravated by high temperatures, heavy traffic and the relief conditions [1]. In this context, this phenomenon is one of the main problems in developing countries with a tropical climate, where an increase in the volume and aggressiveness of the traffic has been recorded and also better quality asphalt pavements and coatings are required [2]. This defect leads to the formation of an uneven pavement surface, increasing the irregularity, the discomfort to road users and in some cases a loss of drivability. On rainy days the accumulation of water in the wheel tracks can cause accidents due to the phenomenon of aquaplaning, which occurs when vehicles lose the tire/pavement adherence required to maintain In this study, the following materials were used: conventional asphalt binder (asphalt matrix) and CNTs (reinforcing load) for the preparation of asphalt Nano composites, and aggregate minerals and hydrated lime for the production of the asphalt mixtures. The base asphalt binder used in the study is classified according to the penetration as being within a range of 50-70 tenths of a millimeter and as PG 58-22 according to the Super pave classification. The CNTs are comprised of multiple layers and have the characteristics shown in Table I, where the micrographic details of this nanomaterial can be observed.

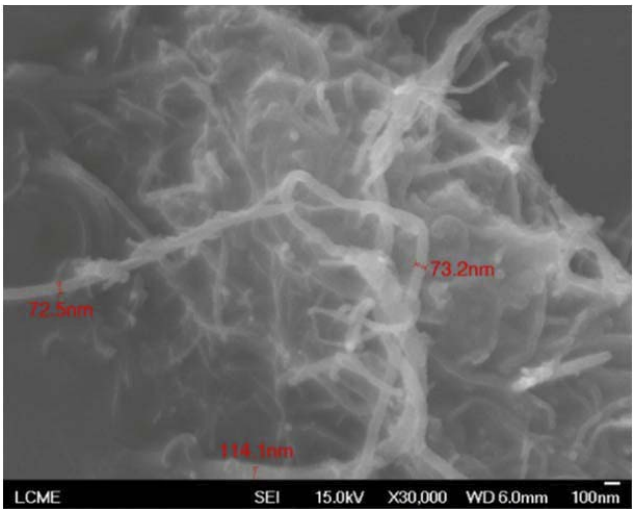

Fig. 1 Micrograph of a CNT: magnification 30,000 times

Table 1. Characteristics of CNTS

Properties	Results
External diameter	50-80 nm
Internal diameter	5-15 nm
Length	10-20 µm
Density	2.1 g/cm^3
Specific surface area	60-80 m^2/g
Carbon*	97.37%
Nickel*	1.86%
Iron*	0.55%
Chlorine*	0.20%
Sulfur*	0.02%

*Results obtained in the analysis by energy dispersive X-ray fluorescence (Shimadzu EDX-700).

References

[1] Ali B. Modèle numérique pour comportement mécanique des chausses: application à l'analyse de l'orniérage. These. Laboratoire de Mécanique de Lille. Ecole Polytechnique Universitaire de Lille. 2015.

[2] Akindele Samuel M. Precautions when interpreting rutting results from the LCPC traffic simulator. 2º Afriasphalt & Afrobitume Congress Lagos, 2016.

MS5
Polymers, biomaterials, and soft materials

CHAIRPERSONS:

Cristiano Albonetti, Suzana Šegota

INVITED LECTURE

Nanomechanics of biomaterials: vesicles and biopolymers

FRANCESCO VALLE
Consiglio Nazionale delle Ricerche – ISMN – Bologna Italy; Consorzio Interuniversitario per lo Sviluppo dei Sistemi a Grande Interfase (CSGI)

Scanning probe microscopy has historically allowed, besides the high resolution imaging, a nanoscale mapping of physical-chemical properties previously inaccessible. Atomic Force Microscopy in particular has opened the way to an accurate characterization of the samples in terms of their local mechanical properties. Herein I intend to show how this kind of measurements can provide precious information in the field of biomaterials. Biological processes are in fact known to be highly controlled by the local mechanical properties such as the stiffness. Among the examples that I am going to report:

1) Extracellular vesicles (EVs), nano-sized lipid vesicles produced and released by cells involved in intercellular communication. They serve as cargoes for lipids, carbohydrates, proteins and several nucleic acids. Quantitatively assessing their physicochemical properties is still an open issue. In particular EV nanomechanical characteristics are considered to influence biological function while their measurement remains elusive. Herein our latest results regarding the nanomechanical characterization of individual EVs via atomic force microscopy (AFM)-based force spectroscopy (AFM-FS) will be presented and their significance and perspectives discussed. The results concerning the still poorly understood mechanical properties of EVs are providing important information regarding their membrane composition through a nanomechanical classification with respect to other synthetic lipid vesicles.

2) Cellulose fibres: the most common biopolymer and the main components of paper sheets. In particular the nanomechanical characterization has been used to monitor the degradation of this biopolymer as a consequence of aging in the perspective of developing a novel diagnostic tool for paper samples in the cultural heritage domain.

INVITED LECTURE

Mechanical properties on cellular and molecular level, AFM study

JAN PRIBYL
CEITEC MU, NanoBio Core Facility, Masaryk university, Brno, Czech Republic

Atomic Force Microscope (AFM) is not only a highly sensitive microscope, however, can be also employed as a mechanical nano-transducer, e.g. in either cell-based sensing of drug effects or in study of effects of growth factor on cells. Among the number of methods applied to measure mechanical properties of cells and tissues, AFM-based nano-indentation provides a way to reliably determine the stiffness of living cells

In comparison to the other devices for micro and/or nano-indentation, the AFM microscope can be applied to characterize mechanical properties (stiffness) of living cells and tissues. Moreover, AFM operates under nearly physiological conditions- i.e. in a liquid medium under elevated temperature. In so called force-mapping mode, cell is indented at many sites and its complete elastic response is recorded which enables to reconstruct the stiffness map. Combination of the stiffness mapping with confocal (fluorescence) microscopy can give us better understanding to the cellular processes, when the cytoskeleton remodelling is related to the mechanical properties of the cell. Use of AFM spectroscopy in biomechanical studies of drug response of cardiomyocytes and post-cryopreservation regeneration of fibroblast cells will be presented as an example of practical application of nanoindentation mapping of living cells. Moreover, structural and mechanical changes in hyaluronic acid molecules after its interaction with myeloperoxidase will illustrate the capability of the method to recognize such changes even on a molecular level.

This research has been financially supported by the Ministry of Education, Youth and Sports of the Czech Republic under the project CEITEC 2020 (LQ1601) and the CIISB research infrastructure project LM2015043 supported the AFM measurements at the Core Facility Nanobiotechnology.

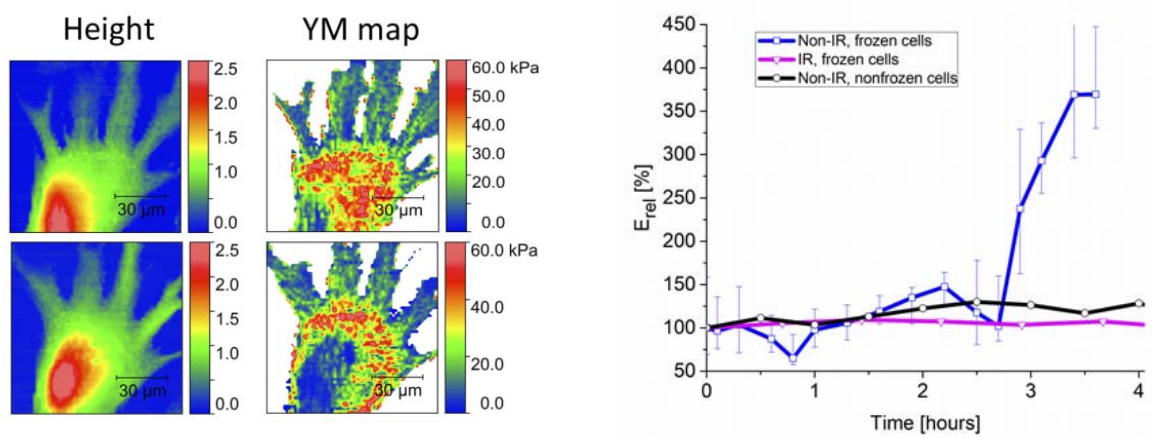

References

NARDONE, Giorgia, Jorge Oliver-De La CRUZ, et al.," YAP regulates cell mechanics by controlling focal adhesion assembly". Nature Communications 8: ncomms15321, 2017.

M. Pesl, J. Pribyl et al., "Atomic force microscopy combined with human pluripotent stem cell derived cardiomyocytes for biomechanical sensing". Biosensors and Bioelectronics 85:751, 2016.

Direct visualizaton of lipid-polymer structures by cryo-TEM

ALEKSANDER FORYŚ[1], MARIA CHOUNTOULESI[2], NATASSA PIPPA[2], STERGIOS PISPAS[3], COSTAS DEMETZOS[2], BARBARA TRZEBICKA[1]

[1] Centre of Polymer and Carbon Materials, Polish Academy of Sciences, Zabrze, Poland; [2] Department of Pharmacy, National and Kapodistrian University of Athens, Panepistimioupolis Zografou, Athens, Greece; [3] Theroetical an Physical Chemistry Institute, National Hellenic Research Foundation, Athens, Greece

Self-assembled, stabilized by polymers lipid based structures, as cubosomes, hexosomes or chimeric liposomes have increased research interest because of their potential to become biocompatible carriers in drug delivery systems and attractive platforms for drug solubilization. The most popular structures, reported in recent years as carriers, are glyceryl monooleate (GMO) and phytantriol (PHYT) stabilized by PEO_{99}-PPO_{67}-PEO_{99} triblock copolymer (P407) [1,2].

Table 1. Examples of cubosomes as drug delivery platforms.

Lipids	Polymer	Therapeutic agent
Glyceryl monooleate	P407	Cinnarizine
Glyceryl monooleate	P407	Clonidine
Glyceryl monooleate	P407	Cyclosporin A
Phytantriol	P407	Sulforhodamine B
Phytantriol	PEG-100 Stearate	Docetaxel

In this work the interactions of lipids (e.g. GMO, DPPC, PHYT) and polymers (e.g. P407, PDMAEMA-b-PLMA, PEO-b-PCL) (Fig. 1) were studied.

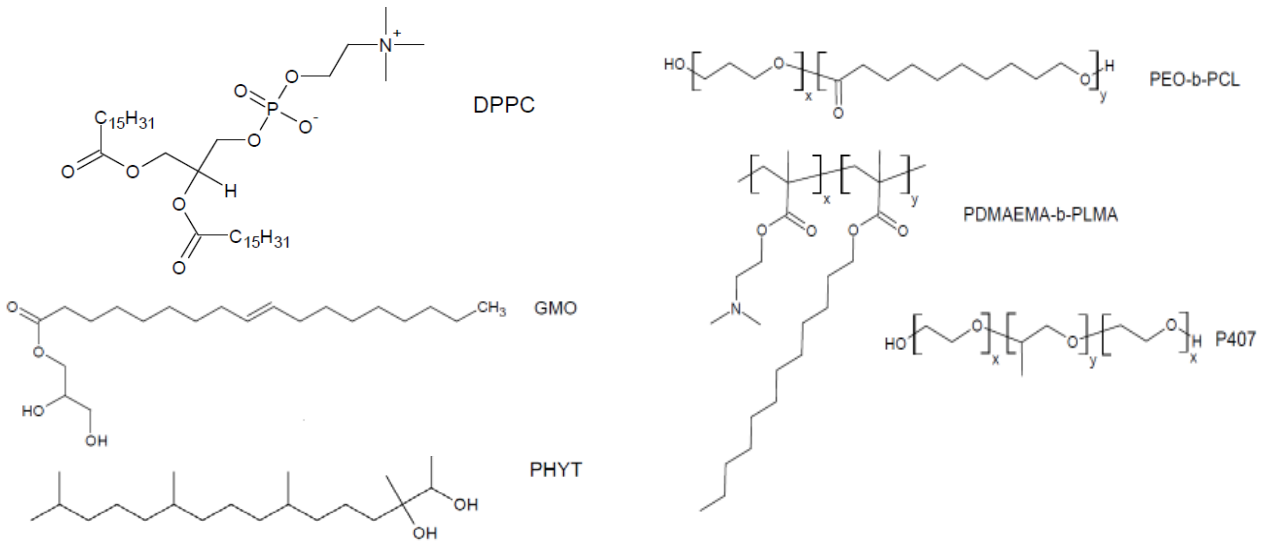

Figure 1. Chemical structures of used lipids and polymers.

The structures of hexosomes and cubosomes, prepared by Bottom Up Method and Top Down Method [3], are shown in Fig. 2a and 2b respectively. For chimeric liposomes (Fig. 2c) the thin film hydration method was used [4]. The method of preparation, nature and amount of lipid and block copolymer used to form lipid-polymer structures, dectates the morphology of the resulting objects. Some of the particles observed by cryo-TEM had an hierarchically ordered internal structure, as shown in Fig. 2a, which has been confirmed also by FFT patterns.

There is a gamut of complementary techniques for characterization of the particles (DLS, XRD, SAXS, m-DSC) but only cryo-TEM allows for direct morphological visualization at near native state. The comprehensive characterization is possible by a combination of the aforementioned techniques, for example using Dynamic Light Scaterring as is demonstrated for chimeric liposomes in Fig.3.

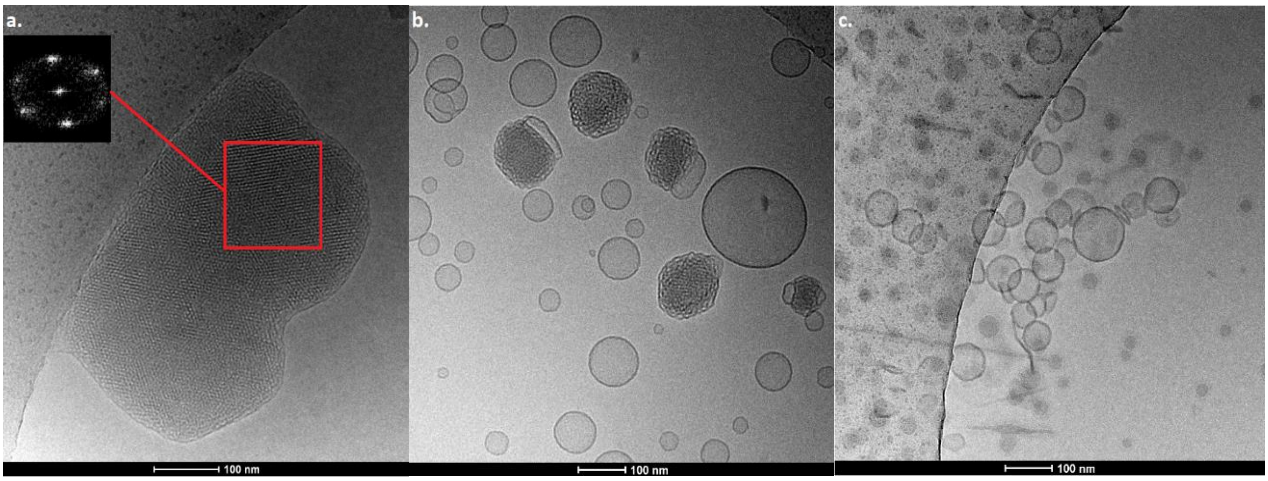

Figure 2. Cryo-TEM images of PHYT:P407 9:1 hexosomes (a), GMO:P407 4:1 cubosomes (b) and DPPC:PEO-b-PCL 9:1 chimeric liposomes (c).

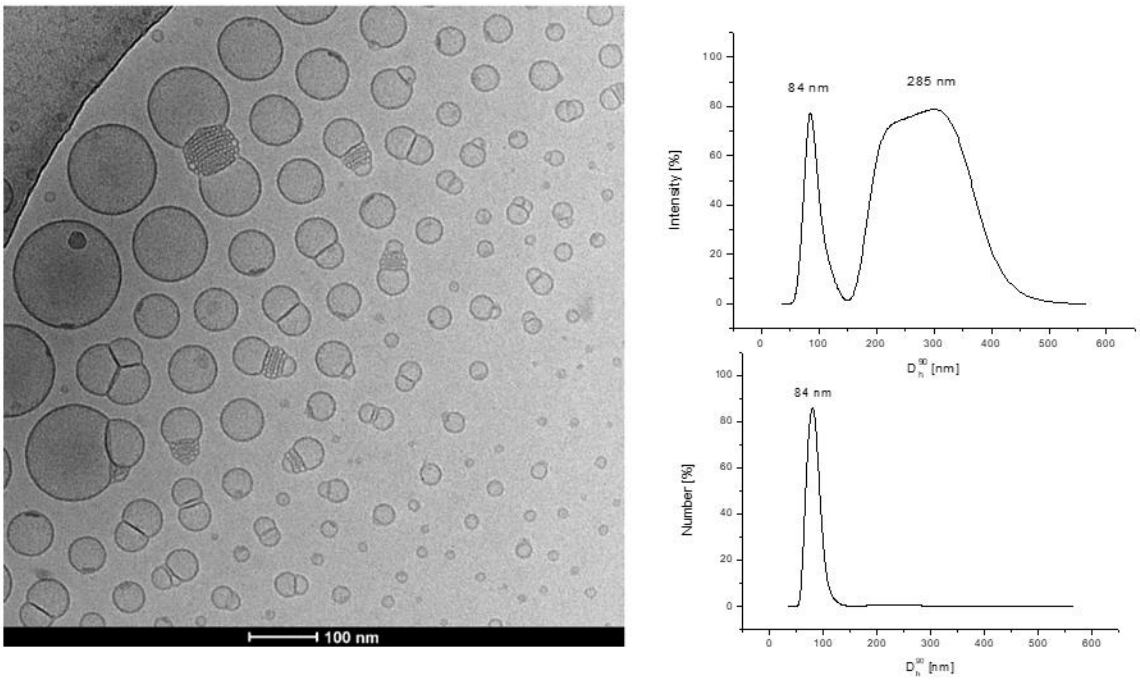

Figure 3. Cryo-TEM image and size distributions from DLS of the GMO-PDMAEMA-b-PLMA 9:1 systems.

References

[1] Z. Karami, M. Hamidi, Cubosomes: remarkable drug delivery potential, Drug Discovery Today, 2016, 21, 789-801

[2] I. Azmi, A. Yaqhmur, S. Moghimi, Cubosomes and hexosomes as versatile platforms for drug delivery, Therapeutic Delivery, 2015, 6, 1347-1364

[3] M. Chountoulesi, N. Pippa, S. Pispas, E. D. Chrysina, A. Forys, B. Trzebicka, C. Demetzos, Cubic lyotropic liquid crystals as drug delivery carriers: Physicochemical and morphological studies, International Journal of Pharmaceutics, 2018, 550, 57-70
[4] N. Pippa, D. Perinelli, S. Pispas, G. Bonacucina, C. Demetzos, A. Forys, B. Trzebicka, Studying the colloidal behavior of chimeric liposomes by cryo-TEM, microdifferential scanning calorimetry and high-resolution ultrasound spectroscopy, Colloids and Surfaces A, 2018, 555, 539-547

Polymerization shrinkage-stress-related dental cusp deformation assessed by digital holography

EVGENIJE NOVTA[1], TIJANA LAINOVIĆ[1], DUŠAN GRUJIĆ[2], DEJAN PANTELIĆ[2], LARISA BLAŽIĆ[1,3]

[1] University of Novi Sad, Faculty of Medicine, School of Dentistry, Novi Sad, Serbia; [2] University of Belgrade, Institute of Physics Belgrade, Serbia; [3] Dentistry Clinic of Vojvodina, Novi Sad, Serbia

Polymerization shrinkage stress of resin-based dental composites (RBC) is influenced by numerous factors, some of them related to cavity configuration [1,2]. Due to its capability of measuring submicron deformations noninvasively, digital holography (DH) is a highly recommended method for studying dental biomechanics [3,4]. Deformation is presented as a series of interference lines (fringes) superposed on the computed image. Period, shape and orientation of fringes give information about specimen's deflection.

The aim of this study was to examine the influence of two cavity types filled with the same RBC on internal stress and cuspal deflection by using DH.

The research was conducted at the Institute of Physics Belgrade, using a custom-made holographic set-up with a laser adjusted at 532 nm wavelength (Figure 1.). Specimens of molars with second class cavities, which were all cut along the vestibule-oral plane in order to reveal internal tissue deformation, were tested. The teeth were mounted in an aluminum cylinder and permanently fixed with dental gypsum, while the entire tooth crown remained visible and accessible for holographic measurement (Figure 2.). Cavities were filled with RBC and light cured with standard mode for 40 seconds. Cusp deflection was directly monitored using real-time holographic interferometry during 6 minutes from the beginning of photoactivation. In one group (G1) a piece of cover glass was attached to their proximal surface, simulating a matrix used in clinical conditions, while still retaining the visibility of internal tissue. The other group (G2) was observed without a cover glass, as a reference.

Figure 1. DH set-up

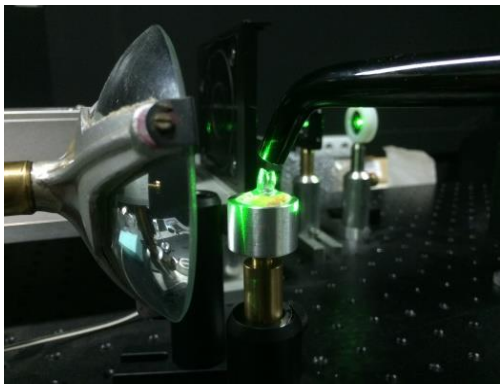

Figure 2. Mounted tooth specimen

Our results showed statistically significant differences between the two groups, with an average deformation per cusp of 5.4 µm in G1 and 2.4 µm in G2 (Figures 3-6).

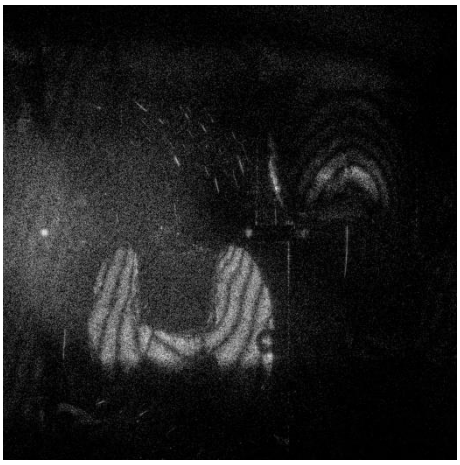

Figure 3. DH image of a tooth examined with a cover glass (G1) at the end of photoactivation

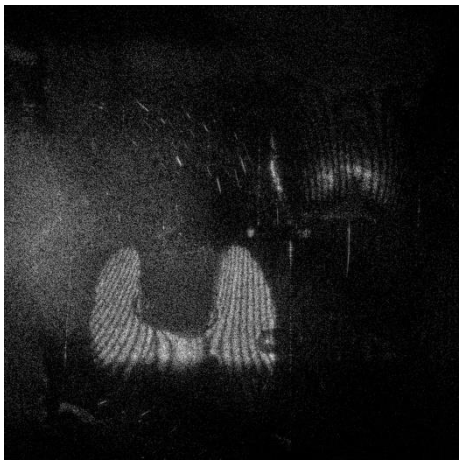

Figure 4. DH image of a tooth examined with a cover glass (G1) at the end of observation period

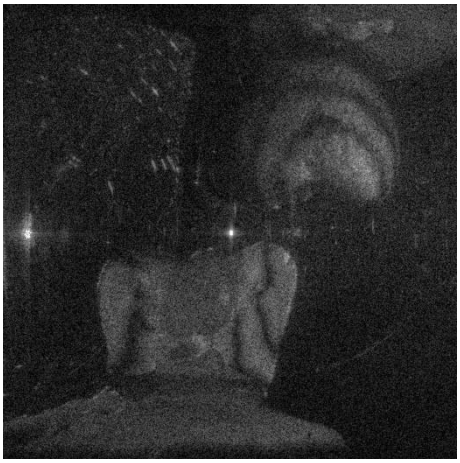

Figure 5. DH image of a tooth examined without a cover glass (G2) at the end of photoactivation

Figure 6. DH image of a tooth examined without a cover glass (G2) at the end of observation period

The cover glass has changed the cavity configuration significantly, presented as excessive cuspal deformation. Within the limitations of this study, we proved that using a matrix in clinical practice reduces the number of available free surfaces necessary for the relief of internal stresses.

References

[1] S.H. Han, et al. Internal adaptation of resin composites at two configurations: influence of polymerization shrinkage and stress. Dental Materials 32.9 (2016): 1085-1094.
[2] A.S.L. Fok, A.A. Wondwosen. The two sides of the C-factor. Dental Materials 34.4 (2018): 649-656.
[3] D.V. Pantelić, D.Ž. Grujić, D.M. Vasiljević. Single-beam, dual-view digital holographic interferometry for biomechanical strain measurements of biological objects. Journal of biomedical optics 19.12 (2014): 127005.
[4] H.Xia, et al. Mechanical behavior of CAD/CAM occlusal ceramic reconstruction assessed by digital color holography. Dental Materials 34.8 (2018): 1222-1234.

Formation of calcium phosphates on TiO_2 nanotubes in the presence of albumine: insight in formation of multifunctional nanocomposites

INA ERCEG, ATIĐA SELMANI AND MAJA DUTOUR SIKIRIĆ
Laboratory for Biocolloids and Surface Chemistry, Ruđer Bošković Institute, Zagreb, Croatia

Among largest health issues in modern society increased frequency of hard tissue chronical diseases takes special place [1]. These diseases could be a consequence of physical trauma, birth defects, other diseases (cancer), etc. In response to this problem, World health organization has appointed years 2000-2010 a Bone and Joint Decade [2]. Often the only treatment of such diseases is implantation with the aim to regenerate damaged or diseased tissue. However, only in the USA, approximately 10% of implants fail prematurely [3]. In addition, due to the continuous population ageing, many patients are outliving their implants [4]. These problems clearly urge the need to develop new, innovative implant materials. The solution of such problems is sought in development of multifunctional materials, which in addition to replacing missing tissue or enabling its regeneration, as well as having improved mechanical properties, will act as local drug delivery system [4-6]. New hard tissue regeneration biomaterials emerging in recent years are composite materials based on calcium phosphates (CaPs) and different inorganic nanomaterials as they offer possible ways of preparing multifunctional materials because inorganic nanomaterials embedded within CaP can increase their mechanical strength [7] and can be used as drug delivery systems, like TiO_2 nanotubes (TiNTs). Nowadays it is possible to produce arrays of TiNTs with precisely controlled diameter, length, wall thickness and phase [8]. *In vitro* cells response to nanotubular surface is better compared to not treated surfaces and can be modulated by changing the diameter of TiNTs [9]. TiNTs also offer a possibility to covalently immobilize bioactive molecules, and in that way act as drug delivery system [10]. Modifying TiNTs arrays with CaP can be achieved by different techniques, biomimetic, electrochemical and magnetron sputtering being mostly used [11]. However, to the best of our knowledge TiNTs are not used as fiber reinforcements of CaP ceramics and cements.

In this research we have investigated the impact of TiO_2 nanotubes (TiNT) on properties of formed CaP solid phase at conditions closed to physiological in the presence of bovine serum albumine (BSA). BSA is the most abudant protein in human plasma and is one of first macromolecules that will interact with synthesised nanocomposites in human body. It is one of three soluble proteins which are immediately adsorbed on the surface of the implant, influencing its *in vivo* performance [12]. However, its role in mineralization of titanium implants is still controversial [13].

All experiment systems were preformed in a thermostated double-walled glass vessel with a 50 mL capacity at 25 °C. Precipitation systems were not additionaly stirred. Control precipitation system (CS) was prepared by fast mixing of equal volumes (20 mL) of equimolar $CaCl_2$ and Na_2HPO_4 reactant solutions (c = 4 mmol dm^{-3}), so-called anionic and cationic solution. The pH of anionic solution was adjusted to 7.4 with HCl. Precipitation systems containing TiNT and/or BSA were prepared by adding TiNT suspension or BSA solution to the anionic reactant solution. Before mixing the reactant solutions the pH was readjusted when necessary. The progress of reaction was followed by measuring the pH of the precipitation systems. Based on pH curves induction time (t_{ind}), the time passed from initiation of precipitation process untill the begining of amorphous CaP (ACP) transforms into more stable crystalline phase was calculated. Prepared precipitates were filtered after 60 minutes of reaction time. The influence of TiNT and BSA on structure and morphology of precipitated CaP phase was investigated by Fourier – Transform Infrared spectroscopy (FTIR), Raman spectroscopy, Poxwder Diffaction (XRD), Scanning Electron microscopy (SEM), Transmission Electron Microscopy (TEM).

Representative pH vs time curves are shown in Fig. 1. Curves obtained in all investigated systems showed typical sigmoidal shape reflecting three stages of the precipitation process: i) initial slight pH decrease associated with the formation of ACP, during which the changes in pH and calcium concentrations are small or absent, ii) an abrupt decrease in pH associated with the secondary precipitation of crystalline phase upon ACP, iii) final slight pH change associated with solution-mediated growth and phase transformation [14,15]. Induction times were obtained from intersection of the tangents drawn on the second and third section of pH *vs.* time curve (Table 1.). In the presence of TiNTs a significant reduction of induction time was observed, indicating promotion of ACP transformation, which was not concentration dependent in the investigate concentration region. Contrary to TiNTs, in the presence of BSA transformation is inhibited and the influence is concentration dependent. In the precipitatuion systems containing both TiNTs and BSA the transformation was faster at higher TiNTs concentrations.

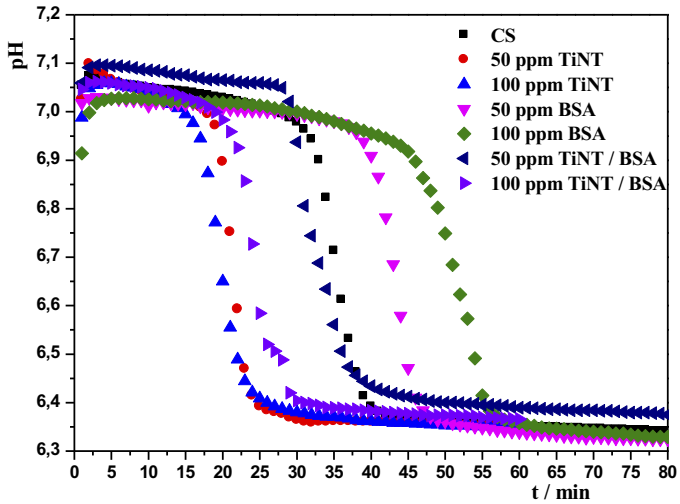

Figure 1.Representative pH vs. time curves of investigated precipitation systems. pH_{init} = 7.4, θ / °C = (25 ±0.1).

Table 1. Average induction times (t_{ind}) obtained from pH vs. time (t) curves (Fig. 1) from 5 measurements with standard deviations (SD). pH_{init} = 7.4, θ / °C = (25 ±0.1).

	(t_{ind} ± SD) / min		
γ / mg L^{-1}	**TiNT**	**BSA**	**TiNT / BSA**
0		29.4 ± 3.2	
50	17.4 ± 0.9	39.7 ± 1.0	28.2 ± 1.1
100	17.9 ± 1.9	45.1 ± 0.9	20.3 ± 1.5

PXRD patterns and FTIR spectra showed that presence of either TiNTs or BSA, or both of them does not influence the composition of the formed precipitate. In all systems calcium deficient hydroxyapatite (CaDHA, $Ca_{10-x}(HPO_4)_x(PO_4)_{6-x}(OH)_{2-x}$, $0 < x < 2$) was formed. CaDHA is considered to be a promising material for manufacturing biomaterials for hard tissue regeneration as biological apatite, the main inorganic part of animal hard tissues, is in fact ion-substituted CaDHA [16]. Althought TiNTs do not influence the morphology, SEM investigation have shown that CaDHA grows on TiNT surface in linear layout (Fig. 2).

The obtained results point to a biomimetic preparation route of multifunctional CaP based biomaterials.

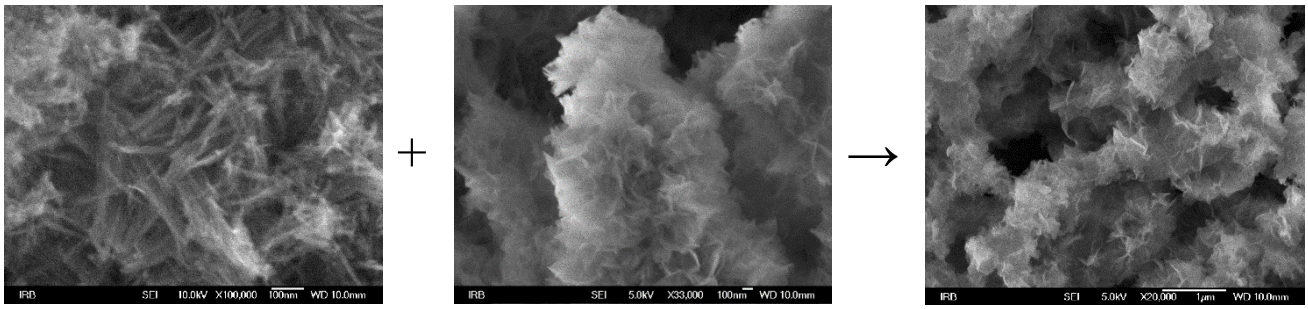

a) b) c)

Figure 2. SEM images of a) TiNT, b) CS and c) nanocomposites CaP/TiNT obtained after 60 minutes of reaction time.

References

[1] Moroni, A. Nandakumar, F. B. De Groot, C. A. van Blitterswijk and P. Habibovic, J. Tissue Eng. Regen. Med. 9 (2015) 745–759.
[2] J. Cambron and T. King, The Bone and Joint Decade: 2000 to 2010, J. Manipulative Physiol. Ther. 29 (2006) 91–92.
[3] S. Kurtz, F. Mowat, K. Ong, N. Chan, E. Lau and M. Halpern, JBJS 87 (2005) 1487–1497.
[4] J. Raphel, M. Holodniy, S. B. Goodman and S. C. Heilshorn, Biomaterials 84 (2016) 301–314.
[5] E. J. Tobin, Adv. Drug Deliv. Rev. 112 (2017) 88–100.
[6] S. Bose and S. Tarafder, Acta Biomater. 8 (2012) 1401–1421.
[7] C. Canal and M. P. Ginebra, J. Mech. Behav. Biomed. Mater. 4 (2011) 1658–1671
[8] P. Roy, S. Berger and P. Schmuki, Angew. Chem. Int. Ed. 50 (2011) 2904–2939.
[9] E. Beltrán-Partida, B. Valdéz-Salas, A. Moreno-Ulloa, A. Escamilla, M. A. Curiel, R. Rosales-Ibáñez, F. Villarreal, D. M. Bastidas, J. M. Bastidas, J. Nanobiotechnology 15 (2017) 10-15.
[10] M. Lai, K. Cai, L. Zhao, X. Chen, Y. Hou, Z. Yang, Biomacromolecules 12 (2011) 1097–1105.
[11] R. V. Chernozem, M. A. Surmeneva, B. Krause, T. Baumbach, V. P. Ignatov, A. I. Tyurin, K. Loza, M. Epple, R. A. Surmenev, Appl. Surf. Sci. 426 (2017) 229–237.
[12] A. P. Serro, A. C. Fernandes, B. Saramago, J. Lima, M. A. Barbosa, Biomaterials 18 (1997) 963–968.
[13] P. Marques, A. P. Serro, B. J. Saramago, A. C. Fernandes, M. C. F. Magalhaes and R. N. Correia, Biomaterials 24 (2003) 451–460.
[14] A. Selmani; I. Coha; K. Magdić,B. Čolović, V. Jokanović, S. Šegota, S. Gajović, A. Gajović, D. Jurašin, M. D. Sikirić, CrystEngComm 2015, 17, 8529–8548.
[15] Bar-Yosef Ofir, P.; Govrin-Lippman, R.; Garti, N.; Füredi-Milhofer, H., Cryst. Growth Des. 2004, 4, 177–183.
[16] S.V. Dorozhkin, Calcium Orthophosphate-Based Bioceramics and Biocomposites, 1st ed., 2016, Wiley-VCH Verlag GmbH & Co. KGaA, Weinheim, Germany

Acknowledgment

This work has been financially supported by the Croatian Science Foundation under project IP-2018-01-1493.

Porous ceramic scaffolds with bioactive compounds for bone tissue engineering

VERA LUKASOVA[1,2], MICHALA RAMPICHOVA[2], JANA DORAZILOVA[3], PREMYSL STASTNY[3], RADEK SEDLACEK[4], MARTIN TRUNEC[3], MILAN KRTICKA[5], LUCY VOJTOVA[3]

[1] University Centre for Energy Efficient Buildings of Czech Technical University in Prague, Bustehrad, Czech Republic; [2] Institute of Experimental Medicine of the Czech Academy of Sciences, Prague, Czech Republic; [3] CEITEC - Central European Institute of Technology, Brno, Czech Republic; [4] Czech Technical University in Prague, Czech Republic; [5] The University Hospital Brno, Brno, Czech Republic

Critical size defects in bones do not heal spontaneously; therefore the use of temporal filling material is advantageous in order to provide migrating cells a scaffold for their adhesion and proliferation. During bone healing, the scaffold is gradually replaced by the extracellular matrix produced by adhered cells. Subsequently, the extracellular matrix is mineralized and fully functional bone tissue is formed. The ceramic scaffolds can be manufactured in high porosity with interconnected pores; these features are important for cell migration into the whole volume of the scaffold. Hydroxyapatite (HA) and tricalcium phosphate (TCP) are suitable materials for bone tissue engineering since they serve as a source of calcium and phosphate which are compounds connected with the mineralization process. HA/TCP ceramic scaffolds are biocompatible materials that support adhesion and proliferation. These scaffolds could be further enriched by bioactive compounds with the aim to promote osteogenesis.

In this study, human mesenchymal stem cells (hMSCs) were seeded on six types of ceramic scaffolds. In general, all ceramic scaffolds consisted of HA and TCP in the ratio of 1:3. This porous ceramic scaffold was further enriched with polyphosphate (PolyPS) (scaffold 2); biopolymers + PolyPS (scaffold 3); polydopamin (PDA) (scaffold 4); PolyPS + PDA (scaffold 5); or with biopolymers + PolyPS + PDA (scaffold 6), in order to induce osteogenic differentiation of the cultured cells. A plain ceramic scaffold was used as a control group (scaffold 1).

hMSCs were seeded on the surface of the ceramic scaffolds and cultivated in the growth media enriched with osteogenic supplements (dexamethasone, ascorbate-2-phosphate and β-glycerol phosphate). During the four-week experimental period, cell metabolic activity was examined using MTS assay. Cell proliferation was evaluated using Quant-iT™ dsDNA Assay Kit, adhesion and the proliferation of hMSCs was further evaluated by confocal microscopy. The induction of osteogenic differentiation was verified by q-PCR and by indirect immunohistochemical staining of osteocalcin.

From the data obtained we observed a gradual proliferation of hMSCs on scaffolds 1-3 and 5. The cells seeded on scaffold 6 showed a lower proliferation rate during the first three weeks of incubation; however on day 28 the results were comparable with scaffolds 1-3 and 5. Scaffold 4 did not promote proliferation for the whole incubation period. The metabolic activity showed a similar trend to the proliferation assay. The q-PCR analysis detected expression of RunX2, an early transcription factor connected with the induction of osteogenic differentiation and collagen type I, an extracellular matrix protein, on all of the tested scaffolds. However, the indirect immunohistochemical staining of osteocalcin revealed the highest concentration of this extracellular matrix protein on scaffolds 2, 3 and 5.

In conclusion, scaffolds 1-3 and 5 supported hMSCs adhesion, proliferation and metabolic activity. Therefore, the addition of PolyPS, biopolymers + PolyPS or biopolymers + PolyPS + PDA had no detrimental effect on cell behavior, compared to the control scaffold which only

consisted of HA/TCP. Furthermore, these scaffolds promoted osteogenic differentiation of cultured hMSCs; shown on scaffolds 2, 3 and 5 where we detected the highest amount of osteocalcin. On the other hand, the sole addition of PDA was evidently cytotoxic for the cells. The addition of PolyPS to the scaffolds with PDA, led to retardation in proliferation and cell metabolic activity which was possibly due to poor cell adhesion, however the results from the assays were comparable with the control scaffold in the last days of the experiment. Moreover, the addition of PolyPS + biopolymers (scaffold 5), to scaffold with PDA, resulted in good metabolic activity, proliferation and even the induction of osteogenic differentiation.

Acknowledgement: This study has been supported by the Internal Grant Agency of the Ministry of Health of the Czech Republic (MZ-VES project no. 17-31276A) and the Czech Science Foundation, grant number 18-09306S.

Polyesteramide Nanofibrous Scaffolds for Bone Tissue Engineering

KAROLINA VOCETKOVA[1,2], RADEK DIVIN[1,2,3], VERA SOVKOVA[1,2,3], VERONIKA BLAHNOVA[1,2,3], VERA LUKASOVA[1,2], EVZEN AMLER[2,3], KAROLINA REHAKOVA[4], JIRI BROZEK[4], EVA FILOVA[1]

[1] Institute of Experimental Medicine of the Czech Academy of Sciences, Prague, Czech Republic; [2] University Center for Energy Efficient Buildings, Czech Technical University in Prague, Bustehrad, Czech Republic; [3] 2nd Faculty of Medicine, Charles University, Prague, Czech Republic; [4] Department of Polyemrs, University of Chemistry and Technology Prague, Prague, Czech Republic

With the ageing population and our current lifestyle choices, bone disorders represent a major healthcare issue worlwide. Bone tissue engineering has developed to promote the self-healing capacity of bone tissue. Bone tissue engineering aims to provide an alternative to bone grafting, reducing the risk of disease transmission and overcoming the supply limitation. To do so, it employs suitable biomaterial with cells and bioactive molecules. Such biomaterials may be fabricated using electrospinning technique. The unique characteristics of the resulting nanofibrous layers include nanotopograhy mimicking the structure of natural extracellular matrix and large surface-to-volume ratio facilitating functionalization of the nanofibers with bioactive molucules. Poly(ε-caprolactone) (PCLO) is an FDA-approved biodegradable polymer used in clinical practice. However, its degradation rate is rather slow. Therefore, using copolymeration of ε-caprolactone and ε-caprolactam a polyesteramide poly[(ε-caprolactam)-*stat*-(ε-caprolactone)] may be introduced. The copolymer composition may influence its degradation rate and thus the application of the nanofibrous scaffolds.

The aim of the study was to fabricate nanofibrous scaffolds composed of the above-mentioned copolymer with different ratio of the ε-caprolactam and ε-caprolactone units. The prepared nanofibrous scaffolds were tested using human mesenchymal stem cells to evaluate their osteogenic potential.

The nanofibrous scaffolds were fabricated using electrospinning. Then, the scaffolds were seeded with human mesenchymal stem cells (hMSCs). The scaffolds were characterized using scanning electron microscopy. The metabolic activity (MTS test), proliferation and osteogenic differentiation of the hMSCs was evaluated. Furthermore, the cells were visualized using confocal microscopy.

According to the obtained data, the copolymer nanofibrous scaffolds showed superior properties to the PCLO control samples in terms of metabolic activity, cell proliferation and activity of alkaline phosphatase (early osteogenic marker).

The work was supported by the Grant Agency of Charles University (grants No. 512216 and 448218) and the Ministry of Education, Youth and Sport within the National Sustainability Program (grants No. NPU LO1508 and NPU LO1309) and University of Chemistry and Technology Prague.

Collagen type I scaffold coated with nature inspired polymer

VERONIKA BLAHNOVÁ[1,2], KATARÍNA KACVINSKÁ[3], LUCY VOJTOVÁ[3], EVA FILOVÁ[1,2]

[1] Second Faculty of Medicine, Charles University, Prague; [2] Institute of Experimental Medicine of the Czech Academy of Sciences, Prague; [3] CEITEC, University of Technology, Brno – Královo Pole

Polydopamine (PDA), final oxidation product of dopamine, is a catecholamine known mainly as a neurotransmitter. It is a simple organic molecule capable of polymerization and subsequent adhesion to any material. In nature it is synthesized by invertebrate *Mytilus edulis* and used for mussel adhesion to the surface. Due to its exceptional features, dopamine can be used in tissue engineering as a linker of various bioactive substances. But in the first place, it is necessary to properly investigate PDA biocompatibility in both *in vitro* and *in vivo* conditions. Also it has to be verified whether PDA linking influences biological activity of molecules attached. For that purpose we used bFGF, growth factor known for its positive effects on proliferation.

In our work we used collagen type I scaffolds with addition of chitosan, oxidized cellulose and basic fibroblast growth factor. Each scaffold was seeded with 70000 of mouse 3T3 fibroblasts. The cells were cultivated in DMEM, 10% FBS and 1% penicilin/streptomycin for 14 days. The culture medium was changed each fourth day for fresh. The level of cellular metabolism was evaluated by MTS test on the day 1, 3, 7 and 14. On the same days we measuerd the total amount of dsDNA. Adhesion of the cells was visualized using DiOC and propidium iodide fluorescent staining. Nuclei of living and dead cells were visualized using Live/Dead fluorescent staining with BCECF and propidium iodide, respectively.

Metabolic activity showed significantly higher levels on scaffolds with PDA addition. However, in this particular study scaffolds without polydopamine were shown to be cytotoxic. On the other hand on scaffolds with PDA we observed continual cell proliferation during the whole experiment which confirms cytocompatibility of all materials used. Besides, we have shown significant positive effect of oxidized cellulose on the number of adhered cells. We did not observe any positive effect of bFGF neither linked nor only adhered on the surface of our scaffolds.

The aim of our experiment was to evaluate polydopamin cytocompatibility *in vitro*. Based on our results we assume polydopamine not to be cytotoxic in the concentration used and therefore to be suitable for using as a linker in tissue engineering applications.

Acknowledgement: This work was supported by the Grant Agency of Charles University grant no. 448218,. the Ministry of Education, Youth, and Sports of the Czech Republic, Research Program NPU I:LO1508 and I:LO1309 and project CEITEC 2020 (LQ1601).

Examining Hydrogel Structure Using Freezing Methods, Cryo SEM Imaging and Image Analysis

KATERINA ADAMKOVA[1], KAMILA HRUBANOVA[1], MONIKA TRUDICOVA[2], PETR SEDLACEK[2] AND VLADISLAV KRZYZANEK[1]

[1] Institute of Scientific Instruments of the CAS, v. v. i., Brno, Czech Republic; [2] Brno University of Technology, FCH, Brno, Czech Republic

Gels are omnipresent porous permeable substances with mechanical properies interconnecting liquids and solids in a very unique manner. The solid part creates elastic hydrophilic polymer chains connected via so called crosslinks in 3D network which entrapps the liquid part (water, air, oil) inside due to the surface tension effect. This means that at some specific conditions, gels can have properties of liquids (viscosity), contrarily, under different conditions, they can act as solids (elastic response). The density of the network varies to a large extent. Within this paper, gels incorporating water, so called hydrogels, are dealt with. Hydrogels were chosen mainly because they are a constituent of living organisms, in recent years there has been an increasing interest in them and they can be applied in a considerably high number of fields – the possibilities begin with medicine and pharmacy (contact lenses, wound healing dressings, artificial replacement tissues and drug delivery systems), continue with cosmetics, and close with food industry and agriculture.

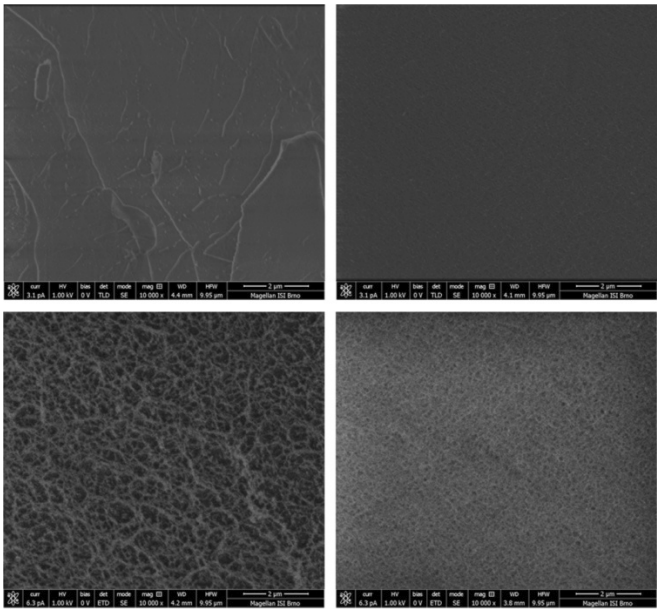

Figure 1. Agarose hydrogel concentrations 0.5 % (left column) and 4.0 % (right column) a), b) prior to the freeze-etching, c), d) after the first sublimation step (temperature briefly risen to -100 °C and returned to -120 °C), e), f) after the third sublimation step (temperature risen to -100 °C and returned to -120 °C after 15 minutes).

Our intent was to examine and describe the agarose hydrogel ultrastructure and to assess the distribution and size of its pores in dependence on its concentration. Agarose is a hydrophilic polysaccharide with gelling properties in solution that can be obtained by extraction from marine red algae. The agarose used within this experiment was Sigma Aldrich type II, medium EEO; CAS number 9012 36 6.

The agarose powder was dissolved in deionized water; subsequently the mixture was stirred and heated for several minutes. There were four concentrations of this hydrogel prepared – 0.5 %,

1.0 %, 2.0 % and 4.0 %. The hydrogel was applied between two special carriers and frozen using the high pressure freezing method (HPF), which proved the most successful within preliminary testing. Subsequently, the frozen samples were processed in the cryo-vacuum chamber (ACE600, Leica Microsystems) – they underwent freeze-fracturing (scratching or breaking the surface using a special knife at high vacuum and low temperature) – transferred into the cryo-SEM (Magellan 400L, FEI) via the cryo shuttle system (VCT100, Leica Microsystems) and imaged at the temperature of -120 °C without any coating. The cryo-SEM method was selected for being particularly useful in studying hydrated samples, since the their native structure remains preserved thanks to its frozen state. Three steps of freeze-etching succeeded. Images were taken before the freeze-etching and after each step respectively. The resulting images were compared and evaluated. As we can see in Figure 1, the pore sizes decreased proportionally with increasing agarose hydrogel concentration, in other words, the higher was the concentration the smaller were the pores.

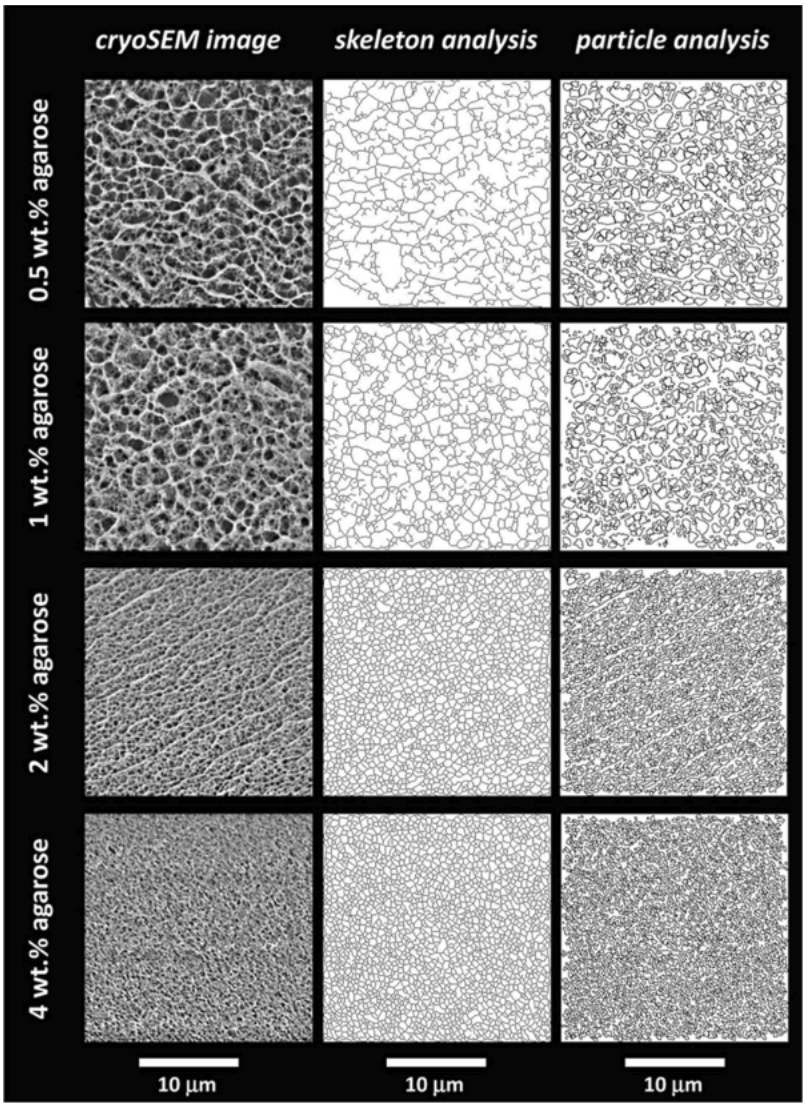

Figure 2. Image processing of the cryo SEM images of various agarose gels. Sections of the micrographs which were subjected to further processing and analysis (left). Mask representation of the same sections processed for the Skeleton analysis (middle) and Particle analysis (right) in ImageJ.

Obtained images can also be further processed in order to gain some quantitative structural parameters. The images were analyzed using two approaches of the image processing that are

implemented in ImageJ software: Particle analysis and Skeleton analysis, results of whoch can be seen in Figure 2.

Moreover, the pore sizes were assessed using the indirect estimation by means of turbidimetry method based on light scattering in the colloidal solutions. Figure 3 shows results obtained using the turbidimetry method compared to the results from the analysis of cryo-SEM images. As can be seen, the absolute values determined by turbidimetry are significantly lower (although of the same order of magnitude) than the linear parameters resulting from the cryo-SEM image analysis. Nevertheless, the decreasing trend of the pore sizes with the agarose concentration is comparable with the concentration dependence of the cryo-SEM results. Our experimental results can contribute to the widening of knowledge about the influence of hydrogel composition on its structure.

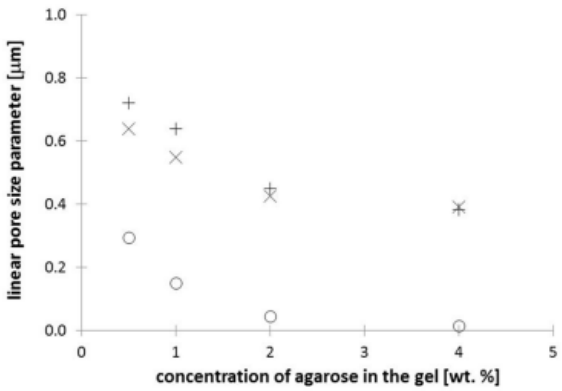

Figure 3. Linear parameters representing the average pore size of the agarose gels determined by Skeleton analysis of cryoSEM images (×), Particle analysis of cryoSEM images (+) and by turbidimetry (o), respectively.

Our most recent experiment was to add polystyrene sulfonate, alternatively alginate to the agarose hydrogel – they affect properties such as diffusion, but at the same time we do not want them to change the structure. So far achieved results seem to be promising for further examination.

References

[1] J. Kopecek, Hydrogel biomaterials: A Smart future, Biomaterials 28 (2007) 5185-5192
[2] M. Pekar, Hydrogels with micellar hydrophobic (nano)domains, Frontiers in Materials, 1 (2015) 35
[3] K. Hrubanova et al., The innovation of cryo-SEM freeze-fracturing methodology demonstrated on high pressure frozen biofilm, Micron 110 (2018) 28–35
[4] J. E. Heuser, The origins and evolution of freeze-etch electron microscopy, Journal of Electron Microscopy (2011) S3-S29
[5] N. J. Severs and D. M. Shotton, Rapid freezing of biological specimens for freeze fracture and deep etching. in *Cell Biology: A Laboratory Handbook* (ed. J.E. Celis et al, 3rd edition, Academic Press, New York, 2006) 249-255
[6] P. Aymard et al., Influence of thermal history on the structural and mechanical properties of agarose gels, Biopolymers 59 (2001) 131-144

Acknowledgements

The research was supported by the Czech Science Foundation (project 17-15451S), the Ministry of Industry and Trade of the Czech Republic (project TRIO FV30271); the infrastructure by the Czech Academy of Sciences (project RVO:68081731).

Nanoscale characterization in a multiphasic polymeric system - morphology@mechanical property@chemical composition complementary studies.

MARCO CASINELLI
Basell Polyolefine Italia, LyondellBasell company G.Natta Research Center, Ferrara, Italy

Polyolefins are polymeric materials widely used in many applicative fields due to their versatility in properties and application. By using different rubber content and semicristalline contribution we can obtain a multiphasic system that drives to differences in term of phisycal and mechanical behaviour. This goal was achieved through a polymer structure in wich a dispersed phase, generally costituted by an elastomeric ethylene-propylene copolymer (EPM), was regulary distributed inside the semicristalline polypropilene (PP) homopolymer matrix. In this study we have evaluated a thermoplastic polyolefinic elastomer (TPO) with high EPM content around 50%, mixed with PP and high density polyethylene (HDPE). Polymer morphology results in a cocontinuous and interpenetrated structure of amorphous and semicristalline olefinic copolymers [1]. The multiphasic system was investigated with three different complementary techniques: TEM, AFM PeakForce QNM, nanoIR. This correlative evaluation allowed to extract informations regarding morphology , nanomechanical and chemical composition of the dispersed phases in a region of interest (ROI).

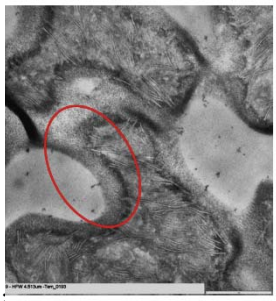

Figure 1. TEM

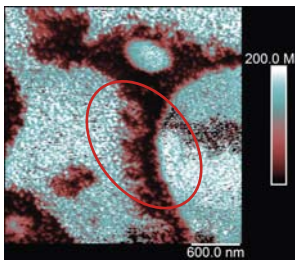

Figure 2. AFM QNM

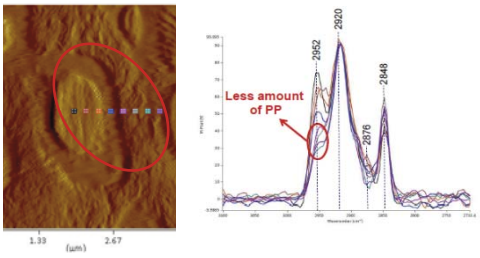

Figure 3. nanoIR

References

[1] G. Collina, A. Pelliconi, P. Sgarzi, F. Sartori, G. Baruzzi, Polymer Bulletin, 39 (1997) 241–247

Transmission-Electron-Microscopy Characterization of Nanodebris Particles from the Wear of a Biocompatible Ceramic-On-Ceramic Artificial Hip Part

DARJA FEIZPOUR[1], MONIKA JENKO[1], BORUT POMPE[2], BOŠTJAN KOCJANČIČ[2], MATJAŽ GODEC[1] AND DRAGO DOLINAR[2]

[1] Institute of Metals and Technology, Ljubljana, Slovenia; [2] Department for Orthopedic Surgery, University Medical Center Ljubljana, Slovenia

The ability to replace weakened, diseased or traumatized natural human joints with artificial prostheses to prevent disability and ease pain is one of the main breakthroughs in the research of total joint arthroplasty, which started with the first total joint replacement in 1891. Total hip arthroplasty (THA) is considered as one of the most successful orthopedic interventions. Several materials have been used in the history of THA: ivory, glass, stainless steel, alloys (Co-Cr-Mo, Ti-Al-Nb, Ti-Al-V), polymers (ultra-high-molecular-weight polyethylene, highly crosslinked polyethylene) and ceramics (Al_2O_3 with additives of Zr-, Sr- and/or Y-oxides). The ideal bearing surface has a low coefficient of friction, a small volume of wear-particle formation, a low tissue reaction with wear particles, a high resistance to third-body wear and enough deformation of articular surfaces to permit adequate fluid-film lubrication during the stance phase without increasing the wear. Ceramic-on-ceramic (COC) bearings, based in alumina or zirconia ceramic, have several advantages compared to other materials used in THA: inert substance, high density, hydrophilicity, smooth polished surface, high hardness, resistance to scratches, low friction, few debris particles and lower linear wear rate. The disadvantages of COC bearings are high price, a precise and expert surgical insertion technique to prevent early damage, chipping and complete fractures, noise on movement (squeaking), and osteolysis. Compared to a CoCr/Polyethylene bearing with a wear rate of 200 microns/year, ceramic Alumina/Alumina bearings have a wear rate of less than 1 micron/year.

In this case study the debris particles obtained from the tissue around a patient's damaged COC bearing were characterized in detail using transmission electron microscopy (TEM) and scanning TEM (STEM) combined with light microscopy (optical microscopy and optical profilometry) and scanning electron microscopy (SEM), X-ray fluorescence spectrometry (XRF) and X-ray powder diffraction (XRD). Artificial hip parts were constructed of COC bearings (femoral head and acetabular inner cup), a Ti-Al-V acetabular metal outer cup, and a corundum grit-blasted Ti-Al-V femoral stem. The aim of the study was to determine what kind of wear-debris particles were present in the tissue, what was their composition and possible crystal structure.

The debris particles were obtained by dissolving the tissue sample in 95–97% sulfuric acid, washing the remains with distilled water, filtering them, and finally cleaning them with ethanol and leaving them to dry, and as such were used for the different, above-mentioned investigation techniques. Extracted debris particles were further prepared for the TEM with the drop-casting technique on a lacy formvar/carbon-coated Cu grid and analyzed at 200 kV. The particles were mainly agglomerated, which was clearly visible from the STEM elemental mapping, and were between a few µm to around 10 nm in size (Figure 1). Their shape varied from rods, rectangular and rounded. The larger particles usually had sharp edges, and the smallest particles in the nm range were usually a rounded shape. Some particles were amorphous and some crystalline.

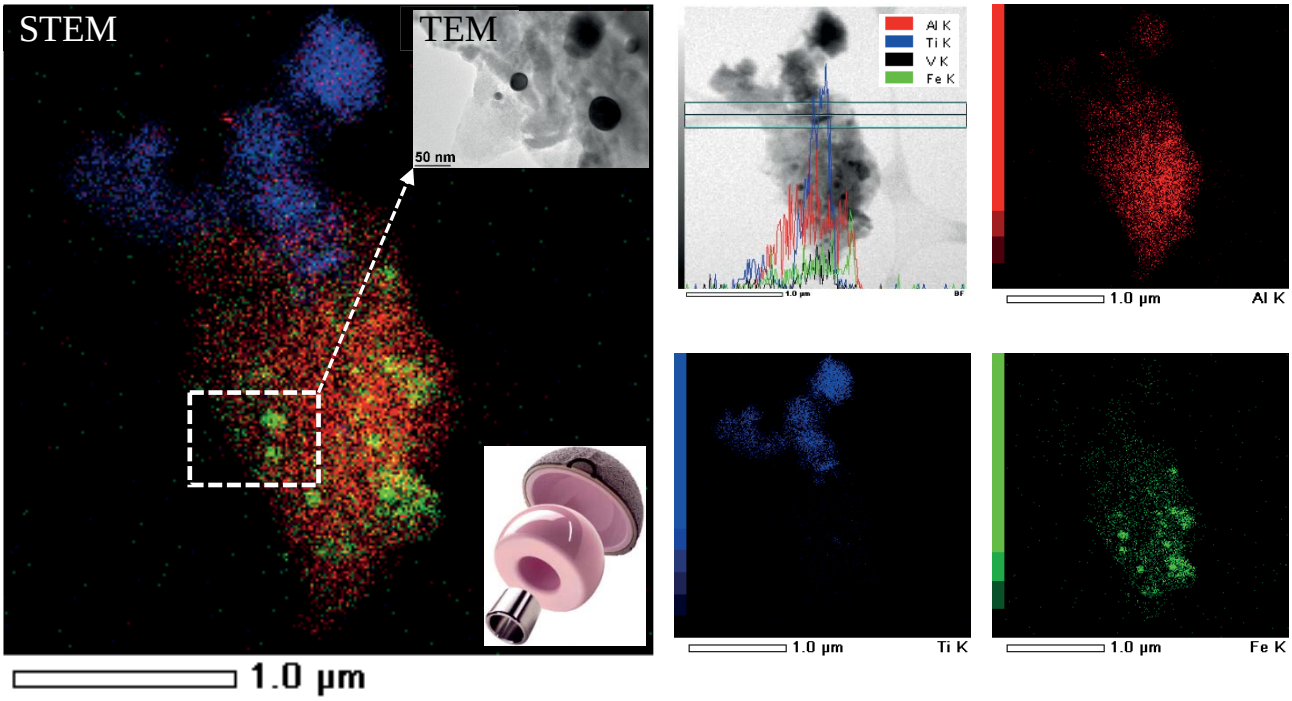

Figure 1. STEM EDS mapping with an inset TEM image in the overlay STEM map and STEM image with a line profile of one example of the debris particles obtained from the tissue around the damaged COC artificial hip part. The bottom-left inset image in the overlay STEM map shows parts of the COC bearing.

Polyesteramide nanofibers for skin tissue engineering

VĚRA SOVKOVÁ[1,2,3], KAROLÍNA VOCETKOVÁ[1,2], RADEK DIVÍN[2,3], KAROLÍNA ŘEHÁKOVÁ[4], JIŘÍ BROŽEK[4], EVA FILOVÁ[1], EVŽEN AMLER[2,3]

[1] Institute of Experimental medicine CAS, Prague Czech Republic; [2] University Centre for Energy Efficient Buildings of Technical University in Prague, Buštěhrad, Czech Republic; [3] Second Faculty of Medicine, Charles University in Prague, Czech Republic; [4] University of Chemistry and Technology, Prague, Czech Republic

Tissue engineering is a multidisciplinary area based on repairing damaged tissues.The aim is to create a scaffold that simply mimics the natural microenviroment of an existing tissue and serves as a physical support for cell adhesion and growth. Cells then contribute to the degradation of the scaffolds and instead produce an extracellular matrix in which they further proliferate and cooperate. In tissue engineering, poly (-ε-caprolactone) (PCLO), a biocompatible and biodegradable polymer approved by the American FDA for clinical use, is used in preference to prepare nanofibrous scaffolds. Its disadvantage is the relatively long degradation. Polyesteramide (PEA) - poly [(ε-caprolactam) -stat- (ε-caprolactone)] was prepared by copolymerization of ε-caprolactone (CLO) with ε-caprolactam (CLA). The composition of the copolymer influences the speed of degradation and therefore, the use of nanofibrous layers.

The aim of this study was to prepare nanofibrous scaffolds from copolymers containing different ratios of ε-caprolactone and ε-caprolactam units. The prepared nanofibrous scaffolds were tested *in vitro* using dermal cells.

Nanofiber layers were prepared by electrospinning from two types of PEA dissolved in a mixture of acetic acid and formic acid (molar ratio of CLO: CLA 80:20 and CLO: CLA 70:30). The polymers were spun from a mixture of formic acid and acetic acid. As a control, fibers containing only ε-caprolactone units were used. The prepared layers were characterized by scanning electron microscopy. Sterile scaffolds were seeded with keratinocytes and fibroblasts and their metabolic activity and proliferation were determined on days 1, 7, 10, and 14 of the experiment. The morphology of adherent cells was visualized by confocal microscopy.

Characterization of the scaffolds by SEM showed a morphology typical of nanofibers. The control fibers contained a larger number of spherical defects. *In vitro* testing of the prepared scaffolds showed that all prepared layers are biocompatible and noncytotoxic. On a PEA sample (CLO: CLA 80:20), a statistically significant higher metabolic activity and keratinocyte proliferation was detected throughout the experiment, compared to the PEA (CLO: CLA 70:30) and the PCLO control samples. Furthermore a statistically significant higher metabolic activity of fibroblasts was detected on all copolymers, compared to the control; there were no statistically significant differences between the PEA CLO: CLA samples. The confocal microscopy was consistent with other methods used.

It was confirmed that the prepared nanofibrous scaffolds are biocomatible and noncytotoxic. Keratinocytes preferred copolymer which contained 80% CLO units and 20% CLA units. In the case of fibroblasts, there was no difference between the copolymer samples, but both promoted better fibroblast viability than the control sample.

This study has been supported by the Research Program NPU I:LO1508, Prague Competitiveness CZ.2.16/3.1.00/21528, Internal Grant Agency of the Ministry of Health of the Czech Republic No 17-32285A.

MS6

Semiconductors, devices, and magnetic materials

CHAIRPERSONS:

János Lábár, Roberto Balboni

INVITED LECTURE

Confinement effects in semiconducting nanostructures revealed with STEM-EELS

GIOVANNI BERTONI[1], ROSARIA BRESCIA[2], QUENTIN RAMASSE[3], CLIVE DOWNING[4], VALERIA NICOLOSI[4], LUCA DE TRIZIO[2], JAVAD SHAMSI[2], STEFANO TOSO[2], DMITRY BARANOV[2] AND LIBERATO MANNA[2]

[1] CNR - Istituto Nanoscienze, Modena, Italy; [2] Istituto Italiano di Tecnologia, Genova, Italy; [3] SuperSTEM, SciTech Daresbury Science and Innovation Campus, Daresbury, UK; [4] Trinity College Dublin, Ireland

1. Introduction. The combination of high spatial resolution and high energy resolution achievable with last generation transmission electron microscopes allows investigating confinement effects in nanostructures. Well-known examples are the localized plasmon resonance in metallic nanoparticles (Ag, Au, …). However, interesting effects can be revealed in semiconductors. In this contribution, we present two examples of semiconducting nanostructures obtained by chemical synthesis: copper phosphide hexagonal nanoplates ($Cu_{3-x}P$), and thin cesium lead bromide perovskite (PV) nanosheets ($CsPbBr_3$). These systems have absorption or photoluminescence in the infrared (IR) in copper phosphide or the visible/near-UV for the PV.

In the case of copper phosphide, localized surface plasmons resonances (LSPR) may be generated due to the presence of holes in the $Cu_{3-x}P$ structure arising from Cu vacancies, as found in other Cu semiconductors [1]. Recently, we have found a broad peak in the absorption spectrum at around 1500 nm for this system, which should indeed correspond to a plasmon excitation [2].

In the case of lead halide bromide $CsPbBr_3$, electronic confinement in the *z*-direction due to the small thickness results in the widening of the optical band-gap and blue-shift of the photoluminescence maximum [3].

2. Details of experiments. Electron energy loss spectra (EELS) were acquired in STEM mode on a Nion UltraSTEM (Daresbury, UK) operated at 60 kV and equipped with a probe corrector and a monochromator (Wien filter), resulting in a spatial resolution <100 pm and an energy resolution (FWHM of the Zero-Loss peak) of 20 meV. Dual eels acquisition assures the almost simultaneous acquisition of the 0 energy reference in the spectra to minimize the energy drift between the spectra at each pixel. The spectra were aligned in energy according to the position of the zero-loss peak and background subtracted or smoothed if needed. HAADF images were acquired at 60 kV (Daresbury, UK) or 200 kV (Dublin, Ireland).

3. Results.

3.1 $Cu_{3-x}P$ hexagonal nanoplates. Figure 1a shows the HAADF image from a single hexagonal crystal. The structure matches very well with ICSD #15056 with trigonal symmetry (Figure 1b). The Cu columns are surrounded by mixed P and Cu columns. The shift of the Cu atoms orthogonal to the *z*-direction gives the elongated spots in the image.

Most interesting, the energy loss spectra shows a broad peak below 1 eV, which matches the peak at 1500 nm found in optical absorption. The SI obtained across the edge of a 50 nm hexagon reveal two modes: one localized at the edge of the crystal at 0.6 eV and one localized at the center of the crystal at 0.8 eV (Figure 1c). These can be predicted within a simple Drude model with a bulk hole carrier concentration $n_h \sim 2*10^{21}$ cm^{-3}.

3.2 $CsPbBr_3$ PV nanosheets. The high-resolution image from a [001] projection of a defect-free $CsPbBr_3$ nanoplatelet is presented Figure 2a. The columns corresponding to Pb, Cs, and Br atoms are easily recognizable. The Br octahedra around Pb are tilted due to the Ian-Teller distortion as expected in the orthorhombic structure (ICSD #97851).

The band-gap position was inferred from the maximum in the first derivative of the EEL spectrum, after smoothing was applied to reduce fluctuations due to noise, following a similar procedure as in ref. [4]. The results as a function of thickness are presented in Figure 2b. The thickness of the nanoplatelets was measured from the t/λ ratio obtained with lower dispersion. The experimentally measured band-gap points were fitted with a power function according to the equation of confinement of a particle of mass *m** in a crystal by impenetrable barriers in the *z*-direction. Extrapolation to lower thickness values (Figure 2c) gives a good prediction of the values found in the literature [5].

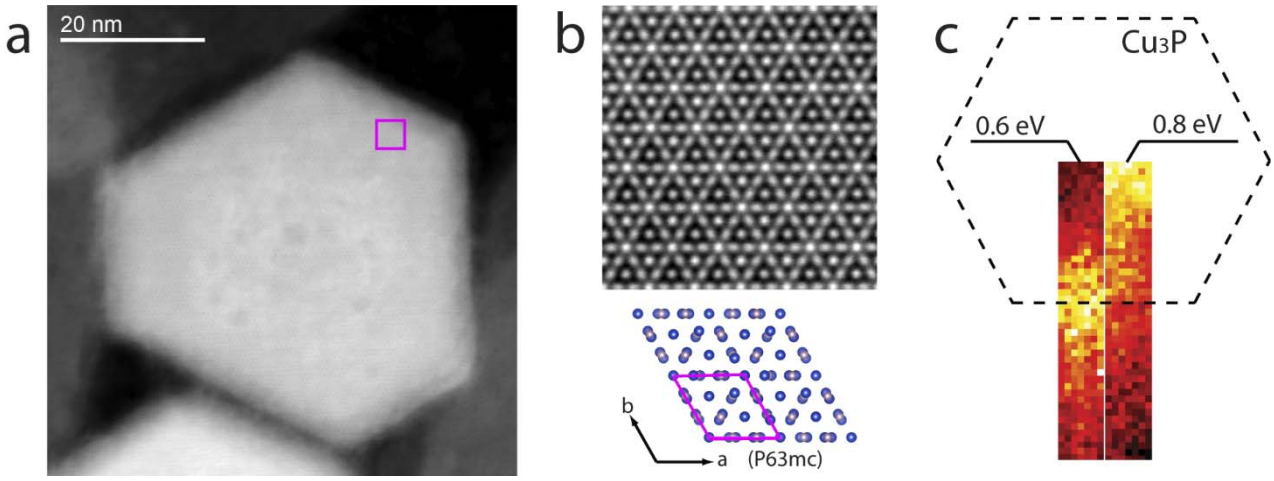

Figure 1. (a) HAADF image of a hexagonal $Cu_{3-x}P$ nanoplate. (b) Detail of the structure, that matches well with P63mc symmetry. (c) Extracted intensities from the EEL spectrum images taken across an edge of the nanoplate. Two LSPR modes are evident: one at the edge at 0.6 eV and one localized at the center of the nanoplate at 0.8 eV.

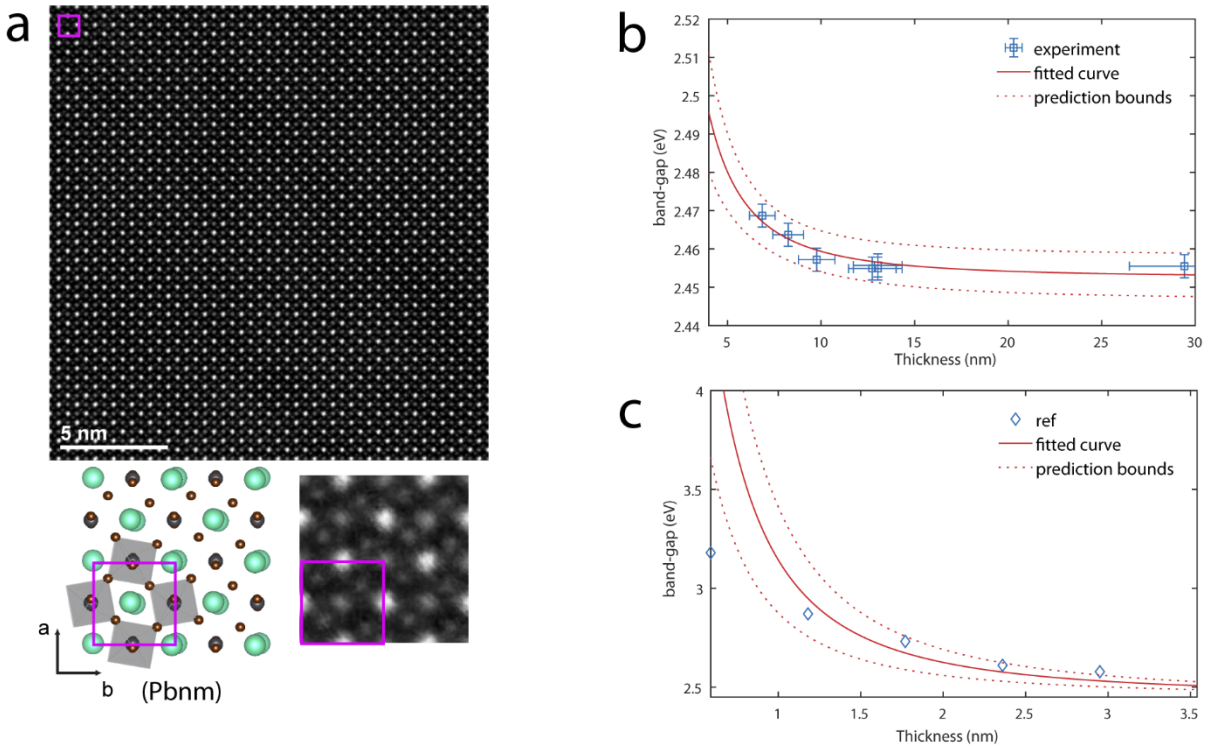

Figure 2. (a) HAADF image of a $CsPbBr_3$ nanosheet with orthorhombic structure (Pbnm). (b) Band-gap fitting from the EEL spectra in the thickness region of weak confinement. (c) Extrapolation of the fit at ultra-low thickness and comparison with data from the literature.

5. Conclusion. Scanning spectroscopic images (STEM-EELS) permits to measure the effect of electronic confinement also on individual semiconduction crystals, *e.g.* to visualize LSPR on $Cu_{3-x}P$ or to measure the band-gap widening in thin $CsPbBr_3$, with the advantage to avoid the effect of size average arising by collecting the signal from multiple crystals as in conventional spectroscopies (such as light absorption).

The authors thank the financial support from the European Union Seventh Framework Programme under grant agreement No. 614897 (ERC Consolidator Grant "TRANS-NANO"). G.B. thank the support from the European Union Horizon 2020 Research and Innovation Program under grant agreement No. 766970 Q-SORT (H2020-FETOPEN-1-2016-2017).

References

[1] J. M. Luther, P. K. Jain, T. Ewers, A. P. Alivisatos, Nature Materials, 10 (2011), 361–366
[2] L. De Trizio, R. Gaspari, G. Bertoni, I. Kriegel, L. Moretti, F. Scotognella, L. Maserati, Yang Zhang, G. C. Messina, M. Prato, S. Marras, A. Cavalli, and L. Manna, Chemistry of Materials, 27 (2015), 1120-1128
[3] J. Shamsi, Z. Dang, P. Bianchini, C. Canale, F. Di Stasio, R. Brescia, M. Prato, L. Manna, JACS, 138 (2016) 7240-7243
[4] J. Lin, L. Gomez, C. de Weerd, Y. Fujiwara, T. Gregorkiewicz, K. Suenaga, Nano Lett., 16 (2016) 7198–7202
[5] Y. Bekenstein, B. A. Koscher, S. W. Eaton, P. Yang, A. P. Alivisatos, JACS, 137 (2015), 16008-16011

Analysis of extended defects in high dose proton bombarded GaAs using Cs-corrected STEM

JOHANNES NEETHLING, JACO OLIVIER AND ARNO JANSE VAN VUUREN
Centre for HRTEM, Nelson Mandela University, Port Elizabeth, South Africa

1. Introduction

Proton bombardment of GaAs using doses in the range 10^{14} - 10^{15} H^+ cm^{-2}, has been used to create high-resistivity regions in GaAs device technologies [1]. The remnant damage after annealing at about 500 °C consists mainly of dislocation loops which appear to have only a minor effect on the electrical properties of the implanted layer [1]. Although the first author of this paper (JN) has investigated radiation damage and the formation and growth of dislocation loops in n-type GaAs since the 1980s [2,3,4], the earlier transmission electron microscopy (TEM) studies of radiation damage in proton bombarded GaAs [2,3,4] were carried out long before probe-Cs-corrected high angle annular dark field (HAADF) scanning transmission electron microscopy (STEM) imaging became available and hence it was challenging to distinguish between interstitial dislocation loops and hydrogen platelets. Since HRTEM image characteristics are influenced by the foil thickness and defocus value, the interpretation of HRTEM images of lattice defects is problematic. Cs-corrected STEM with the HAADF imaging mode is a powerful technique for the determination of structural and chemical information at atomic resolution since the image characteristics do not depend on foil thickness and defocus value. In earlier papers, the first author (JN) and co-workers concluded that the loop-like defects on {110} planes in 300 keV proton bombarded (10^{15} to 10^{16} H^+ cm^{-2}) n-type Si-doped GaAs annealed in the range 500 °C to 900 °C were hydrogen filled vacancy loops (called hydrogen platelets) [2,3,4] which, due to the gas pressure inside the loops, would appear to be of interstitial nature [3]. However, in a recent paper we compared earlier TEM results of dislocation loops generated in n-type GaAs by 1 MeV electron and fast neutron irradiation with recent Cs-corrected HAADF STEM images of {110} and {111} dislocation loops in neutron irradiated and annealed n-type GaAs [5]. The new data enabled us to reinterpret the older defect models [2,3,4] in proton bombarded n-type GaAs, *i.e.* the {110} loops in proton bombarded and annealed GaAs are now considered to be interstitial dislocation loops while hydrogen platelets form on {111} planes in high-dose proton bombarded GaAs (5×10^{16} – 10^{17} H^+ cm^{-2}) [5]. Cs-corrected HAADF STEM imaging of {110} and {111} dislocation loops in neutron irradiated and annealed (600°C for 20 minutes) n-type GaAs revealed that the plane of the {110} loop consists of two layers of GaAs atoms, which is consistent with the model for a {110} pure-edge interstitial dislocation loop in GaAs. The plane of the {111} interstitial loop consists of one layer of GaAs atoms while the stacking sequence across the loop is consistent with that of an extrinsic stacking fault [5]. In this paper, probe-Cs-corrected HAADF STEM is used to image loop-like defects on {111} planes in high-dose proton bombarded (10^{17} H^+ cm^{-2}) n-type GaAs. The defects in the bombarded samples before and after annealing (500 °C) are also compared.

2. Experimental

The n-type Si doped (10^{18} carriers cm^{-3}) GaAs samples were bombarded with 300 keV protons at 7° off the [001] to total doses in the range 10^{15} to 10^{17} H^+ cm^{-2}. Post-implantation annealing was carried out in a tube furnace under flowing argon. HRSTEM specimens were prepared by using a Helios Nanolab 650 focused ion beam (FIB) SEM. HAADF STEM imaging was carried out using a double Cs-corrected JEOL ARM 200F operated at 200 kV.

3. Results

Fig. 1 (a) and (b) show cross-sectional bright field TEM micrographs of the defect structure in n-type GaAs bombarded with 300 keV protons to a dose of 10^{17} cm^{-2}. The <001> direction of

implantation is indicated by H^+. Loop-like defects on {111} planes at a depth of about 2.7 μm from the surface, are indicated by L and E. Loop E in (a) is viewed edge-on while loop L lies on an inclined {111} plane and show inside and outside contrast in (a) and (b) respectively. Fig. 1 (c) is a typical HAADF STEM lattice image of the loop-like defect E in (a). This type of {111} loop-like defect present at the peak of the H^+ projected range in the 300 keV proton bombarded GaAs was found to consist of a single {111} GaAs layer (indicated by the arrow in (c)) with adjacent areas of lower crystal density (dark regions) which are suggested to be small hydrogen bubbles formed by H_2 molecules trapped at tetrahedral sites [6] adjacent to the {111} plane of the interstitial loop.

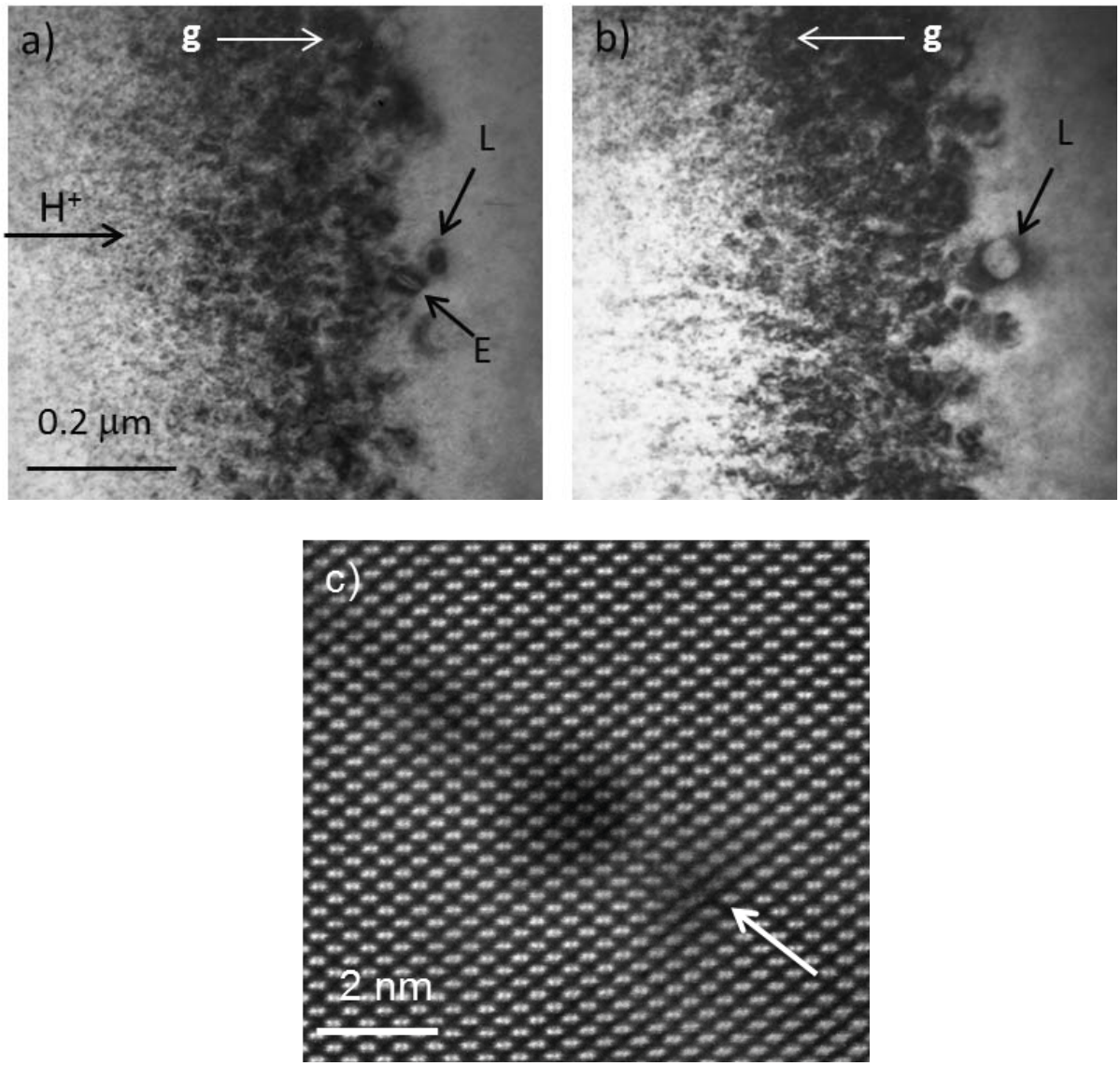

Figure 1. (a,b) Cross-sectional bright field TEM micrographs of the defect structure in n-type GaAs bombarded with 300 keV protons to a dose of 10^{17} cm^{-2}. The <001> direction of implantation is indicated by H^+. Loop-like defects on {111} planes at a depth of about 2.7 μm from the surface, are indicated by L and E. Loop E in (a) is viewed edge-on and loop L lying on an inclined {111} plane show inside and outside contrast in (a) and (b) respectively. The **g** vectors are **g** = $00\bar{4}$ in (a) and **g** = 004 in (b) with **s** positive. (c) Typical HAADF STEM lattice image of the loop-like defect E in (a). The single {111} GaAs layer of the interstitial loop forming the core of the hydrogen platelet is indicated by the arrow in (c). The electron beam direction is <110>.

Fig. 2 (a) shows a HAADF STEM image of bubbles (voids) in n-type GaAs bombarded with protons to a dose of 10^{17} cm^{-2} and annealed at 500 °C for 15 min. Void formation is most likely assisted by the presence of hydrogen. The hydrogen platelet defects observed in the unannealed samples (Fig. 1) were absent after annealing at 500 °C. Fig. 2 (b) is a HAADF STEM lattice image of a typical planar defect present in the middle (R) of the bubble (void) distribution shown in (a). This defect consists of a nano size stacking fault on a {111} plane with a modified layer created by a 180 ° rotation of the tetrahedral unit as indicated by the arrow in (b).

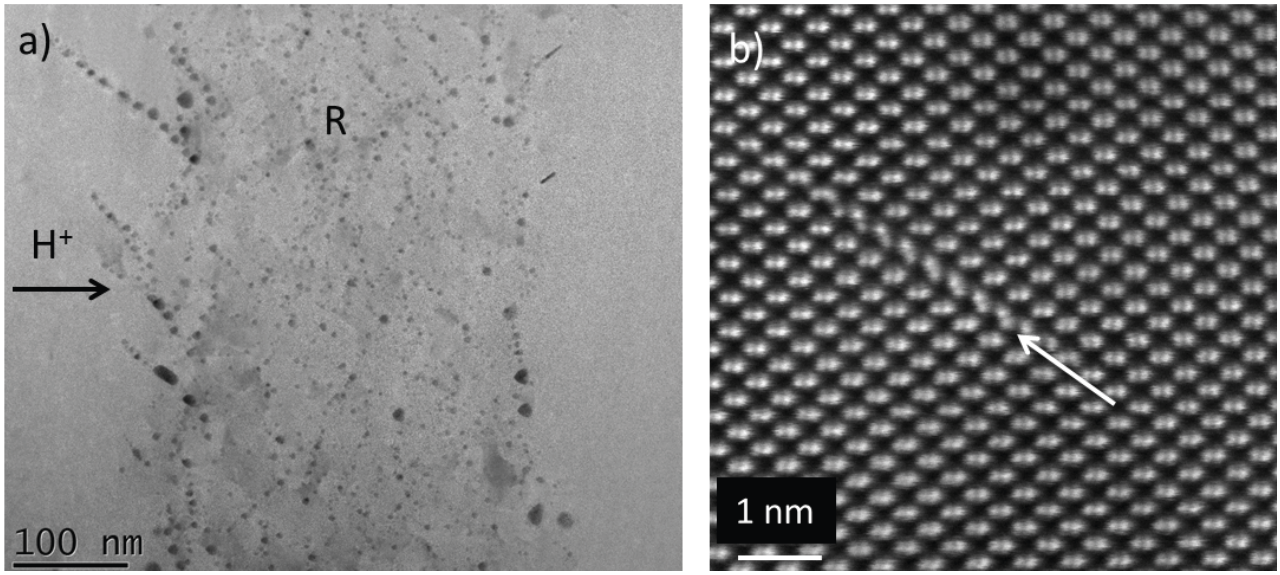

Figure 2. (a) HAADF STEM image of bubbles (voids) in n-type GaAs bombarded with 300 keV protons to a dose of 10^{17} cm^{-2} and annealed at 500 °C for 15 min. The <001> direction of implantation is indicated by H^+. (b) HAADF STEM lattice image of a typical planar defect present in the middle of the bubble (void) distribution. The defect consists of a nano size stacking fault on {111} plane with a modified layer created by a 180 ° rotation of the tetrahedral unit. The electron beam direction is <110>.

4. Conclusions

GaAs interstitials seem to agglomerate in a number of different configurations: interstitial edge dislocation loops on {110}planes, extrinsic Frank loops on {111} planes [5] and a type of hydrogen platelet proposed to be an interstitial loop on a {111} plane with hydrogen molecules in small bubbles adjacent to the {111} loop plane. No vacancy loops have been observed in irradiated and annealed n-type GaAs by the authors of this paper [2 -5]; evidence for vacancy condensation was only produced by the presence of three-dimensional bubbles (voids) in proton bombarded GaAs.

References

[1] S.J. Pearton, Mater. Sci. Rep. 4 (1990) 313-367
[2] J.H. Neethling, H.C.Snyman, J. Appl. Phys. 60 (1986) 941- 945
[3] J.H.Neethling, H.C. Snyman, C.A.B. Ball, J. Appl. Phys. 63 (1988) 704-711
[4] J.H Neethling, Physica B, 170 (1991) 285-291
[5] J.H. Neethling, A. Janse van Vuuren, E.J. Olivier, P.A. van Aken, Acta Physica Polonica A (2019, in press).
[6] L. Pavesi, P. Giannozzi, Phys. Rev. B 46 (1992) 4621 – 4629

Segregation of Ca Towards the Compressive Strain Interface of an Epitaxial Grown Bismuth Ferrite Thin Film

U. HASELMANN[1], G. HABERFEHLNER[2], D. KNEZ[3], M. N. POPOV[4], L. ROMANER[4], A. GHASEMI AND Z. L. ZHANG[1,5]

[1] Erich Schmid Institute of Materials Science, Austrian Academy of Sciences, Leoben, Austria; [2] Institute of Electron Microscopy and Nanoanalysis, Graz University of Technology, Graz, Austria; [3] Graz Centre for Electron Microscopy, Graz, Austria; [4] Materials Center Leoben Forschung GmbH, Leobe, Austria; [5] Institute of Material Physics, Montanuniversität Leoben, Austria

1. Introduction and Motivation

The perovskite Bismuth Ferrite ($BiFeO_3$) is one of the few single phase multiferroic materials with coupling of its ferroelectric and antiferromagnetic moments far above room temeperature with a Néel temperature of 370°C and a Curie temperature of 830°C and has therefore attracted much scientific interest [1][2]. The antiferromagnetic domains were electerically controled [2] and therefore have great potential for various applications such as new types of memory devices with superior speed and storage density [3], spin valves, spintronic devices,and sensors[4].

Doping of $BiFeO_3$ with various elements has been done with the intention to purposely design new properties or improve existing ones like to raise a ferromagnetic behaviour in $BiFeO_3$ instead of the antiferromagnetic one[5]. However, segregation and diffusion processes of the dopants severly dammage the functionality of devices using this effects. While there are many studies about the segregation towards surfaces, thanks to a variety of surface sensitive but also surface limited analysis methods, segregation processes towards non-surface interfaces are barely studied [6][7].

2. Experiments and Results

A Ca and Mn co-doped $BiFeO_3$ (BFO) film was grown by pulsed laser deposition (PLD) on a (100) $SrTiO_3$ (STO) substrate with a substrate temperature of 700°C. For comparision a film containing only Mn was grown on the same substrate. For transmission electron microscopy (TEM) studies cross-sections have been prepared by mechanical grinding and polishing and subsequent ion milling. Scanning transmission electron microscopy (STEM) has been performed and high-angle annular dark field (HAADF), electron energy loss spectroscopy (EELS) and energy dispersive X-ray (EDX) at atomic resolution were simultaneously acuired to analyze the structural and chemical film composition. The HAADF image in Fig. 1a shows the epitaxial film-substrate interface. The EELS atomic resolution elemental map from this area in Fig. 1b shows that the Ca, which is displayed in red, is not uniformly distributed within the film but agglomerated at the interface of the film and the substrate (Fe and Ti are displayed in green and blue, respectively). Since it is known from X-ray photon spectroscopy (XPS) that the Ca concentration in the target during the deposition was uniform, the Ca segregation must have happened in the thin film during and shortly after the deposition, while the whole system was still at high temperatures.

High-resolution transmission electron microscopy (HRTEM) of the interfaces of the film with the Ca agglomeration at the interface (Fig. 1c) and without Ca doping (Fig. 1d) were done and the strain states of the films were analyzed. The in-plane strain (ε_{xx}, blue curve) in both films is as expected around 0%, since both films are grown epitaxially. For the out-of-plane strain (ε_{yy}, pink curve) of the films, a positive strain value is expected. However, while the out-of-plane strain increases immediately at the interface for the film without Ca doping (Fig. 1d), the increase of the out-of-plane strain for film with the Ca agglomeration at the interface (Fig. 1c) is delayed within the green area and sets in afterwards.

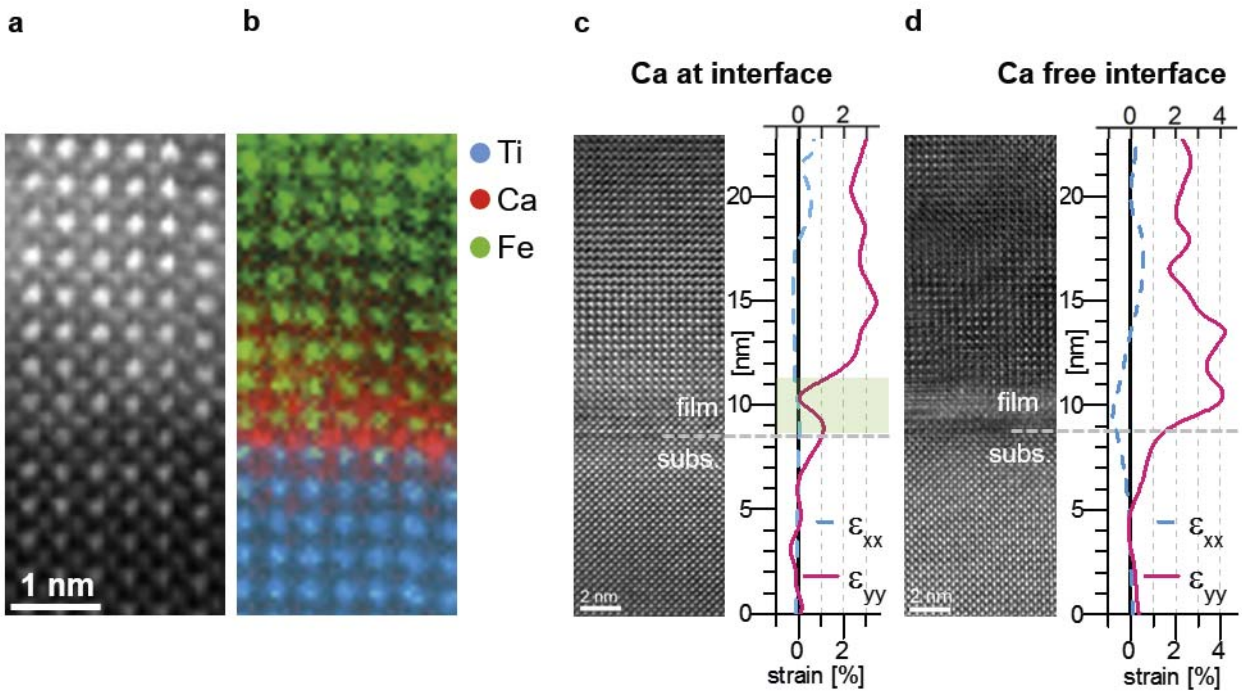

Fig. 1 a, HAADF image of a substrate-film interface **b,** PCA filtered elemental map for Ti, Ca and Fe gained from the EELS data show Ca agglomeration at the interface. HRTEM images and in-plane (ε_{xx}) and out-of-plane (e_{yy}) for **c,** a film with Ca agglomeration at the interface and **d,** a film without Ca.

Analyzing the intensity of the HAADF image in Fig. 2a (the intensity map in Fig. 2b) shows that the A-site intensities of the film are reduced until the 5th to 6th layer due to the Ca content in this layers. In this area also the out-of-plane strain is reduced as can be seen in Fig. 2c (marked by the green rectangle). This means that the strain reduction at the interface and the Ca content are directly connected.

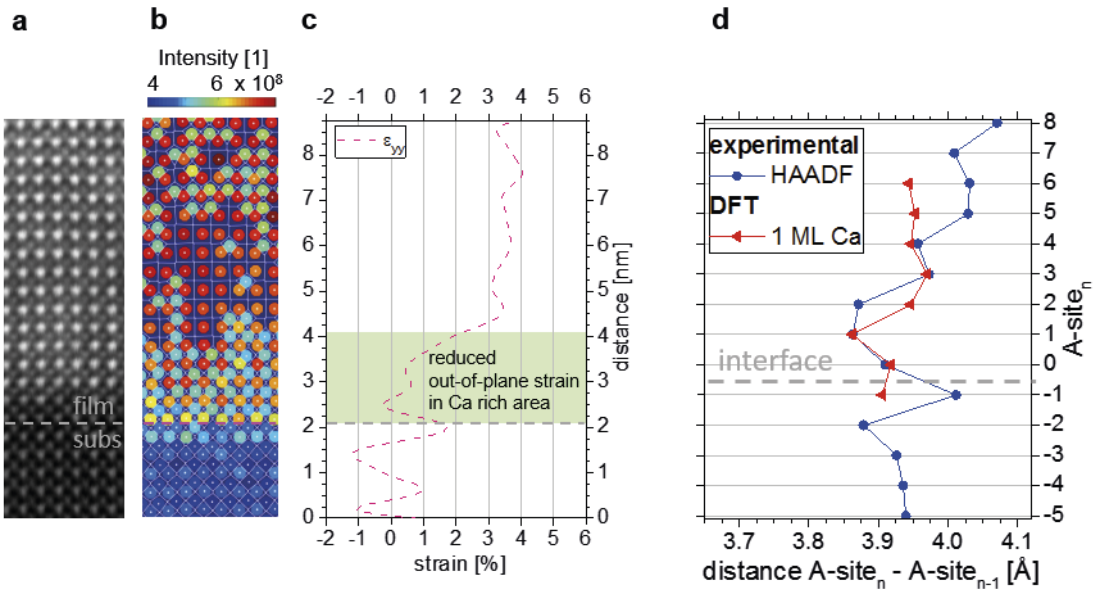

Fig. 2 a, HAADF image of film with Ca agglomeration at the interface. **b,** Intensity map of the HAADF image **c,** Out-of-plane strain (e_{yy}) in the area of the HAADF image. **d,** Lattice spacing from the HAADF image compared with the values from the DFT simulations with 1 ML of Ca at the interface.

Furthermore, the DFT calculations were conducted and confirmed that Ca agglomeration at the interface is energetically more favourable. Additionally the distances between two adjectent A-sites received from the DFT calculations were compared with those received from the HAADF images. As can be seen in Fig. 2d, the calculated distances from the DFT calculations for 1ML of Ca directly at the interface displayed by the red curve fit very well with the distances from the HAADF image displayed by the blue curve.

3. Conclusion

The experiments showed that under a compressive strain from the substrate, the Ca dopant of a Bismuth ferrite thin film can segregate to the film-substrate interface. This leads to a strain reduction at the interface and DFT calculations showed that it is energetically more favorable. For device applications making use of the, with the dopants, purposely designed properties, such as ferromagnetic behavior for Bismuth ferrite, dopants segregation lead to device failure. The results presented here contribute to a better understanding of the processes behind dopant segregation and may pave the way for a better controllability of these unwanted effects.

Acknowledgments: The financial support by the Austrian Science Fund (FWF): No. P29148-N36 is kindly acknowledged. We want to express our gratitude to the group of Prof. Yunbin He from the Hubei University in the PRC for providing the samples, Gabrielle Felber for help with the sample preparation and Prof. Christian Mitterer and Dipl.-Ing. Martin Rausch for their contribution in the discussion of the deposition kinetics and their help with the SRIM simulations. Additionally we would like to say a big thank you to Dr. Markus Kubicek and Dr. Markus Katzer for the fruitful discussions.

References

[1] G. Catalan, J. F. Scott, *Adv. Mater.*, 21 (2009) 2463–2485
[2] T. Zhao, A. Scholl, F. Zavaliche, *et al.*, *Nat. Mater.*, 5 (2006) 823–829
[3] J. F. Scott, *Nat. Mater.*, 6 (2007) 256-257
[4] A. Manzoor, A. M. Afzal, M. Umair, A. Ali, M. Rizwan, M. Z. Yaqoob, *J. Magn. Magn. Mater.*, 393 (2015) 269–272
[5] V. A. Khomchenko, J. A. Paixão, *Mater. Lett.*, 183 (2016) 69–72
[6] Y. Li, J. W. Han,† Y. Chen, Z. Cai, B. Yildiz *et al.*, *Chem. Soc. Rev.*, 46 (2017) 6345–6378
[7] U. Haselmann *et al.*, journal article in preparation

Direct atomic identification of cation migration induced gradual cubic-to-hexagonal phase transition in $Ge_2Sb_2Te_5$

YONGHUI ZHENG[1], YONG WANG[1], TIANJIAO XIN[1], YAN CHENG[1,2], RONG HUANG[2], PAN LIU[3], MIN LUO[4], ZAOLI ZHANG[5], SHILONG LV[1], ZHITANG SONG[1], SONGLIN FENG[1]

[1] State Key Laboratory of Functional Materials for Informatics, Shanghai Institute of Microsystem and Information Technology, Chinese Academy of Sciences, Shanghai, China; [2] Key Laboratory of Polar Materials and Devices (MOE), Department of Optoelectronics, East China Normal University, Shanghai, China; [3] State Key Laboratory of Metal Matrix Composites, School of Materials Science and Engineering, Shanghai Jiao Tong University, Shanghai, China; [4] Department of Physics, Shanghai Second Polytechnic University, Shanghai, China; [5] Erich Schmid Institute of Materials Science, Austrian Academy of Science, Leoben, Austria

Significant advancement in the semiconductor technology has led to the use of phase change memory (PCRAM) in commercial product to perfect the storage system. As the most important key material of PCRAM, $Ge_2Sb_2Te_5$ (GST) alloy, is proved to have long cyclability, high density and nanosecond switching speed characteristics[1, 2]. Induced by thermal annealing, amorphous (a-) GST material will crystallize into a metastable face-centered-cubic (f-) structure ($Fm\bar{3}m$, a=6.02 Å) at ~150 °C with a cationic Ge/Sb/vac f-sublattice and an anionic Te f-sublattice. If f-phase material was overheated, for example, 320~350 °C, it will transform into stable hexagonal (h-) phase (a=4.20 Å, c=16.96 Å), which is not favorable during the PCRAM application. Directly resolved the local atomic arrangement of $Ge_2Sb_2Te_5$ alloy during intermediate steps is an effective method to understand its transition mechanism from face-centered-cubic to hexagonal phases.

In this study, we provide insights into the atomic arrangement variation during face-centered-cubic to hexagonal transition process in $Ge_2Sb_2Te_5$ alloy by using advanced atomic resolution energy dispersive X-ray spectroscopy[3,4]. Induced by thermal annealing, randomly distributed Ge and Sb atoms would migrate to the specific (111) layer in different behaviors, and Sb atoms migrate earlier than Ge atoms during the phase transition process, gradually forming intermediate structures similar to h-lattice. With the migration completed, the obtained stable h-structure has a partially ordered stacking sequence described as below: -Te-Sb_x/Ge_y-Te-Ge_x/Sb_y-Te-Ge_x/Sb_y-Te-Sb_x/Ge_y-Te- (x>y), which is directly related to the migration process. The current visual fragments suggest a gradual transition mechanism, acting as a solid experiment basis for understanding the microscopic properties in GST alloy and pave the way of further application of phase change memory.

References

[1] Salinga, M. & Wuttig, M. Phase-change memories on a diet. ***Science*** 332 (2011) 543-544.

[2] Wong, H.-S. P. & Salahuddin, S. Memory leads the way to better computing. ***Nat. Nanotechnol.*** 10 (2015) 191-194.

[3] Y. Zheng, Y. Cheng, R. Huang *et al.* Surface energy driven cubic-to-hexagonal grain growth of $Ge_2Sb_2Te_5$ thin film. ***Sci. Rep.*** **7** (2017) 5915.

[4] Y. Zheng, Y. Wang, T. Xin *et al.* Direct atomic identification of cation migration induced gradual cubic-to-hexagonal phase transition in $Ge_2Sb_2Te_5$. ***Commun. Chem.*** **2** (2019) 13.

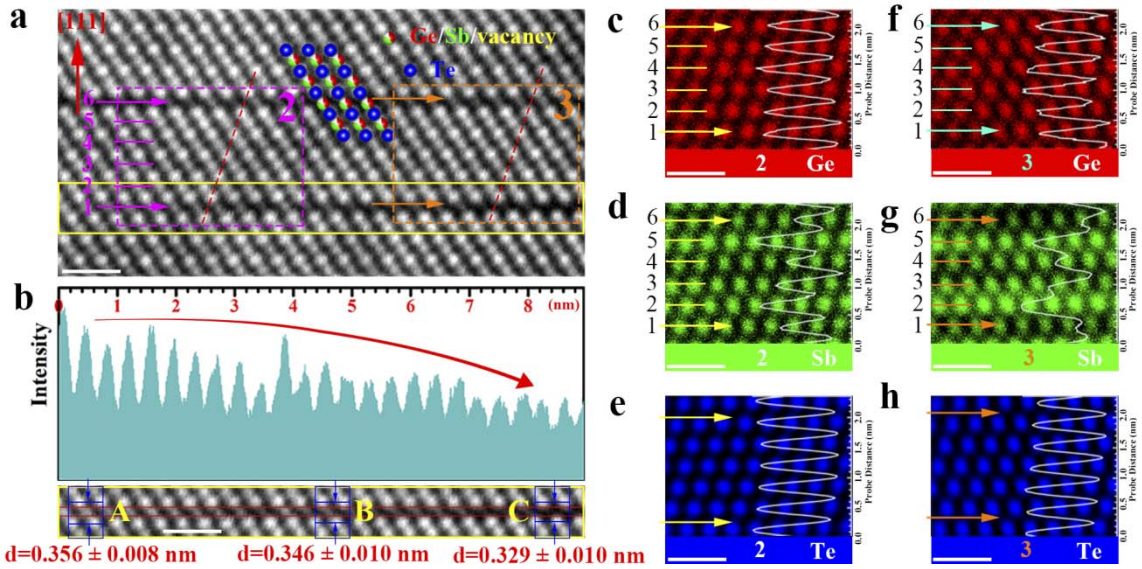

Figure 1. Atomic resolution elemental map of i-phase GST at initial stage. (a) The HAADF image of i-phase GST alloy projected along [1$\bar{1}$0] orientation, the dashed white line along anionic atoms shows f-phase stacking feature. The atomic model is shown in the center area, and line 1 to 6 denotes the cationic layer, respectively. **(b)** HAADF image extracted from the yellow rectangle in (a), and the intensity profile is calculated from the dark columns exhibiting a decreasing intensity trend. **(c-e)** and **(f-h)** are the atomic mapping resolutions of Ge, Sb and Te atoms taken from area 2 and 3, respectively. Scale bar, (a-h) 1 nm.

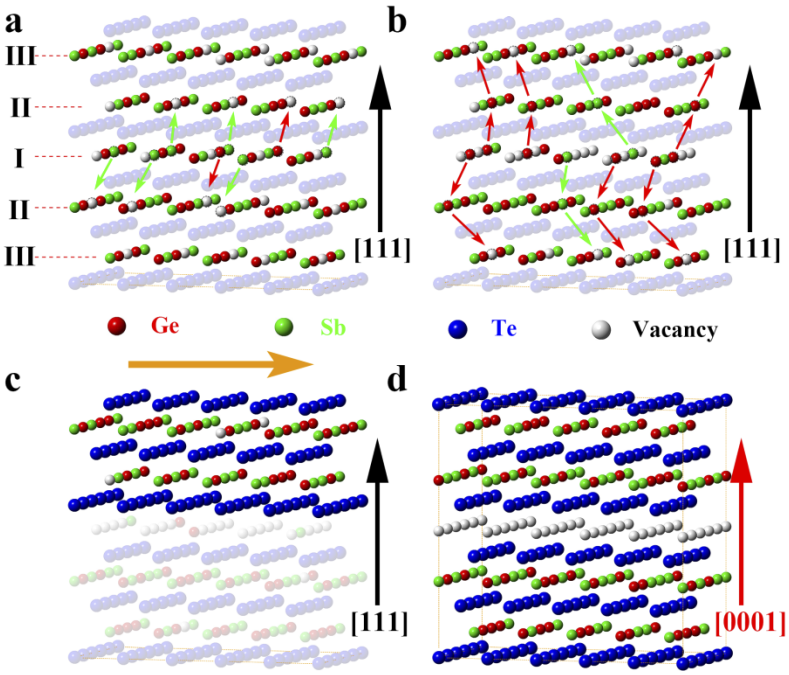

Figure 2. A schematic scenario of the f-to-h phase transition. (a) The initial f-phase projected along [111] direction, in which cationic sites are randomly occupied by Ge, Sb and vacancy. **(b)** The atomic configuration of i-phase after the migration process described in (a). **(c)** The atomic configuration of a deeper migration extent i-phase after the majority of Ge and Sb atoms in layer I have migrated, h-lattice like atom arrangement makes the stacking block easily to slip to transition into h-phase. **(d)** The atomic configuration for the stable h-phase projected along [0001] direction, where Ge element prefers the inner cationic layers and Sb element likes the outer cationic layers in the blocks.

Role of Dy diffusion in sintered Nd-Fe-B hard magnets

KRISTINA ŽAGAR SODERŽNIK[1], ANDRÁS KOVÁCS[2], MARTIAL DUCHAMP[3], ANDRAŽ KOCJAN[4], RAFAL E. DUNIN-BORKOWSKI[2], JOACHIM MAYER[2,4], SPOMENKA KOBE[1]

[1] Jožef Stefan Institute, Ljubljana, Slovenia; [2] Ernst Ruska-Centre for Microscopy and Spectroscopy with Electrons (ER-C) and Peter Grünberg Institute 5 (PGI-5), Forschungszentrum Jülich, Germany; [3] Nanyang Technological University, Singapore; [4] Institut of Materials and Technology, Ljubljana, Slovenia; [4] RWTH Aachen, Germany

High coercivity Nd-Fe-B permanent magnets play an important role in rapidly-growing renewable energy sector (electric vehicles or wind turbines). To retain the coercivity at high operating temperature, heavy-rare-earth elements (HRE), such as Dy and Tb, are added using grain-boundary diffusion (GBD) process. The addition of HRE results in a significant improvement of the coercivity due to the increase of the intrinsic resistance to demagnetization.

In the present study, we report on the correlation between magnetic properties and the distribution of the DyF_3 in the melt-spun $Nd_2Fe_{14}B$ ribbons that were coated with 2 wt.% Dy, spark-plasma sintered (SPS) and annealed at 600°C for 30 h [1]. During SPS and annealing process Dy diffused along grain boundaries (GB) into the outer parts of Nd-Fe-B grains, thus forming core-shell grains with Dy-rich shell and Nd-Fe-B core. The magnetometry measurements showed that the addition of Dy increased the coercivity in heat-treated samples by 25 %. For the structural and compositional studies, we used a Cs-corrected scanning transmission electron microscope (FEI Titan 80-200) equipped with SuperX electron dispersive X-ray (EDX) spectrometer and electron energy-loss (EEL) spectrometer (Gatan Enfinium ER model 977).

The analyses were carried out in the so-called wheel side region of the annealed sample where the size of the Dy-treated Nd-Fe-B grains varies between 50-100 nm. The EDX maps confirmed the core-shell-like structure. However, the reliability of the EDX analysis is compromised by overlapping of the Fe-K, Dy-L and Co-K lines. Therefore, to separate the contribution of these elements and provide more reliable compositional maps, EEL spectra of the same grains were recorded. Direct integration of the power law background-subtracted spectra does not allow to fully separate the different contributions as the Fe-L edge overlaps with the F-K edge tail overestimating the Fe contribution. An overlap of the Nd-M_3 and Dy- $M_{4,5}$ edges is also present at higher energies and prevent an accurate determination of the Dy concentration. To unwrap the spectra the vertex component algorithm (VCA) was applied and thus we were able to determine the local repartition of the present elements and extract Fe-$L_{2,3}$/Co $L_{2,3}$, Nd-$M_{4,5}$, Dy-$M_{4,5}$, F-K and O-K maps. The results confirmed the Dy,Nd-Fe phase formation at the shell around the pure Nd-Fe-B core grains. Further studies will focus on quantitative analysis of the as SPS sample which will at the end pave the way to observe the diffusion of DyF_3 as a function of heat-treatment process and correlate it with the magnetic properties of the magnet.

References:

[1] K. Žagar, A. Kocjan, S. Kobe, JMMM, 403 (2016) 90-96

Analytical electron microscopy of Half-Heusler thermoelectric alloys

JIŘÍ BURŠÍK[1], GERDA ROGL2 AND PETER ROGL[2]
[1] Institute of Physics of Materials of the Czech Academy of Sciences, Brno, Czech Republic; [2] Institute of Materials Chemistry, University of Vienna, Wien, Austria

Novel material concepts and nanotechnology have recently resulted in a great increase of the conversion efficiency of thermoelectric (TE) materials [1]. Among the broad range of materials, half-Heusler (HH) compounds continuously attract high attention due to their promising TE properties and thermal stability at service temperatures [2]. In general, good thermoelectrics have a high Seebeck coefficient, a high electrical conductivity, and a low thermal conductivity at the same time. HH compounds have elemental formula XYZ and consist of three interlaced face-centered cubic sub-lattices. A great advantage is the possibility to dope each of the three sublattices individually in order to optimize the thermoelectric properties. Besides doping, another means of improving TE properties is decreasing thermal conductivity by nanostructuring [3].

In this work, we characterize the microstructure of p-type $Ti_{0.15}Nb_{0.85}FeSb$ HH TE samples in various stages of preparation: (i) after the initial ball milling and hot pressing (BM+HP), (ii) after additional high pressure torsion (HPT) and (iii) after additional annealing. Fracture surfaces of the processed samples were studied in a Tescan LYRA 3XMU SEM×FIB scanning electron microscope (SEM). Thin cross sectional lamellae were prepared by FIB (focused ion beam) in SEM. A Philips CM12 STEM transmission electron microscope (TEM) operating at 120kV, a JEOL JEM 2100F high resolution TEM operating at 200kV with an X-Max80 Oxford Instruments energy dispersive X-ray (EDX) analytical system and a Thermo Scientific Titan Themis 60-300 cubed image corrected high resolution TEM were then used to study the microstructure (Fig. 1).

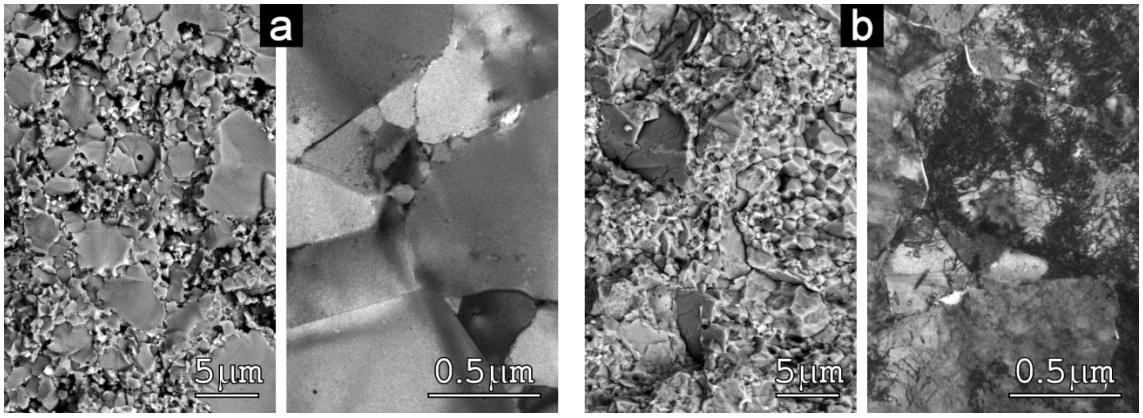

Figure 1. SEM micrograph of fracture surface (image of backscattered electrons) and TEM micrograph of sample after BM+HP (a) and after BM+HP+HPT (b).

The work was supported by the project 17-12844S of the Czech Science Foundation and we took advantage of the facilities of the CEITEC Nano research infrastructure in Brno, Czech Republic.

[1] G. Schierning, R. Chavez, R. Schmechel, B. Balke, G. Rogl, P. Rogl, Transl. Mater. Res. 2 (2015) 025001
[2] A. Tavassoli, F. Failamani, A. Grytsiv, G. Rogl, P. Heinrich, H. Müller, E. Bauer, M. Zehetbauer, P. Rogl, Acta Materialia 135 (2017) 263–276
[3] P. Pichanusakorn, P. Bandaru, Mater. Sci. Eng. R 67 (2010) 19–63

MS7

Materials for energy harvesting, production, storage, and catalysis

CHAIRPERSONS:

János Lábár, Roberto Balboni

INVITED LECTURE

Investigation on the effect of hydrogen on dislocation patterns in high-strength steels using electron channelling contrast imaging in the scanning electron microscope

STEFAN ZAEFFERER, DAYONG AN, YUCHEN SHAN
Max-Planck-Institut für Eisenforschung, Düsseldorf, Germany

The move towards a sustainable energy supply requires the use of hydrogen for energy storage. Hydrogen, however, enters into most metals and leads to their embrittlement, particularly for high strength steels and superalloys. The interaction mechanisms of hydrogen with metals and alloys are, thus, of high research and technological interest. Nevertheless, a number of issues prevent from direct investigation of the mechanisms of embrittlement. First, hydrogen is practically invisible to most high-resolution observation techniques and can, therefore, only be observed indirectly. As a consequence, it is usually not clear whether and how hydrogen interacts with dislocations, grain boundaries or other defects in a microstructure. Second, hydrogen is highly mobile in microstructures and may, therefore, quickly leave a material during an observation campaign.

The electron channelling contrast imaging (ECCI) technique applied in SEM may contribute to solve some of these problems, as it allows direct observation and quantification of lattice defects (dislocations, stacking faults, grain boundaries, elastic strain regions) close to the surface of *bulk* samples. The bulk nature of the sample allows keeping much larger hydrogen quantities in the material than TEM thin foils and it enables performance of (quasi) in-situ deformation experiments.

For our research we observed and quantified the behaviour of dislocations and grain boundaries in high Mn-TWIP steels (22 mass-% Mn, 0.6 mass-% C) with and without hydrogen charging under monotonic and cyclic loading.

For the monotonic loading we performed nanoindentation into the same bulk crystals before and after hydrogen charging. It was found that the dislocation structures developed quite differently with and without charging. The fact that the indents are observed on bulk samples makes it possible to observe many indents, obtained from different grains and at different locations, as shown in Figure 1(a). From the dislocation fields it was possible to extract dislocation data with high statistical significance. Figure 1(b) displays the ECC image of the dislocation field formed around a nano-indent in the non-charged sample. In a subsequent step the sample was lightly polished to remove the indents but conserving the grains; it was then electrolytically charged with hydrogen and the same grains indented and observed again. One indent is shown in Figure 2(c). Here, dislocations with extended stacking faults reach much further out than in the uncharged sample, indicating a reduction in stacking fault energy by hydrogen and an increase of dislocation density as proposed by the hydrogen enhanced local plasticity (HELP) mechanism (68).

For cyclic loading we observed the dislocation patterns formed in low-cycle shear fatigue after 50 to 200 cycles. In the non-hydrogen-charged sample complex patterns form, consisting of dislocation walls with high dislocation densities and dislocation channels with almost no dislocations. In the hydrogen-charged sample a high amount of stacking faults and, out of these, ε-martensite plates are formed. The ε-martensite plates reduce the rate of dislocation pattern formation and lead to the very early formation of cracks at those locations where they intersect grain boundaries. We suppose that the stacking faults that move back-and-forth during cyclic loading lead to a transport of hydrogen to the grain boundary and, thus, to a local reduction of decohesion forces ("hydrogen enhanced decohesion", HEDE). A typical ECC image for this situation is shown in figure 2.

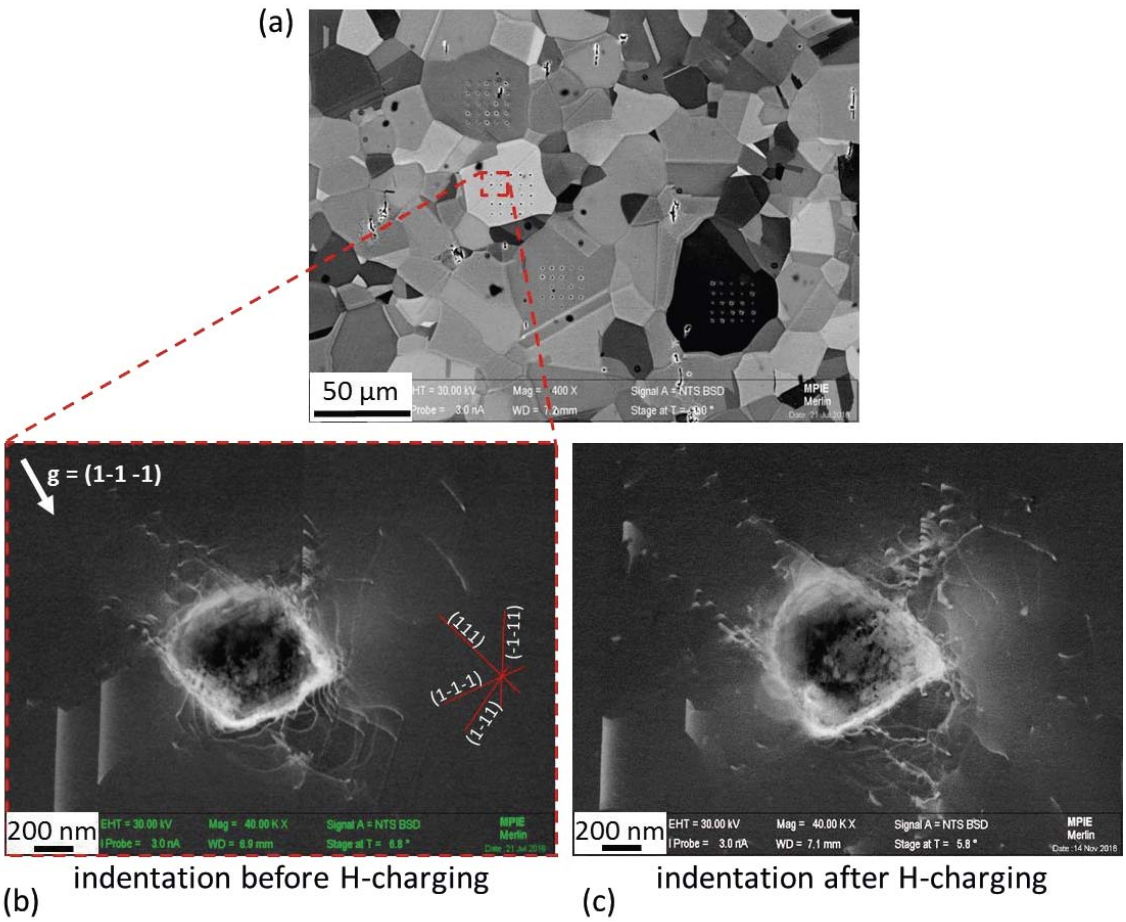

Figure 1. ECC images of nano indents into a high-Mn TWIP steel before and after H-charging. (a) Overview on the indented area, observed before H-charging. (b) One example of an indent into one grain in (a), showing the dislocation field. (c) Indent into the same grain and observed under the same conditions as that in (b) but after H-charging. (modified from Gianola, Britton, Zaefferer, MRS Bulletin, 2019)

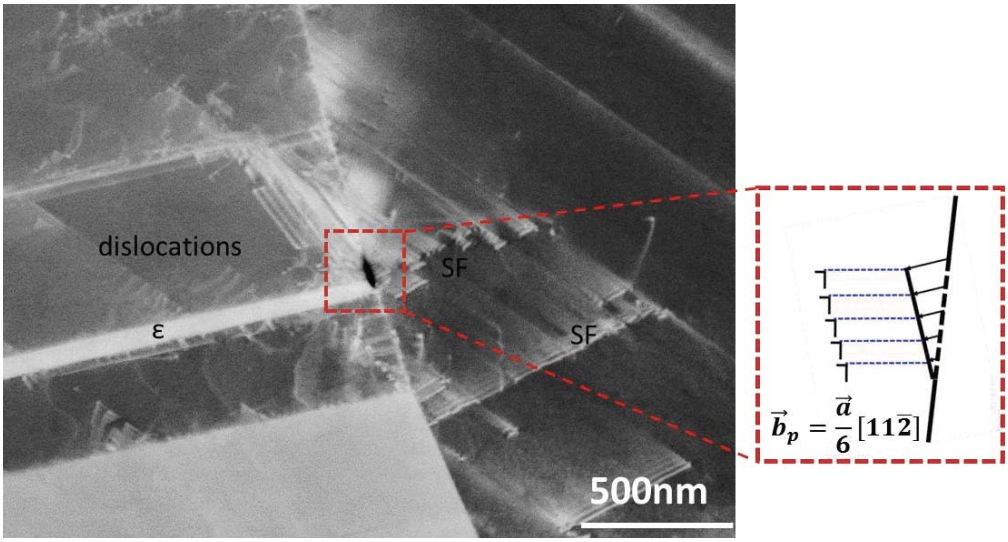

Figure 2: ECC image of the microstructure of a H-charged TWIP steel after 5 cycles of shear deformation. ε-martensite plates are forming and impinging on an existing boundary. A boundary crack forms and opens fully brittle, which is visible by the fact that the opening angle corresponds exactly to the shear created by the ε-martensite plate which itself is created by collection of Shockley partials on every second (111) plane. (modified from An & Zaefferer, manuscript submitted to Acta Materialia)

INVITED LECTURE

Electrochemical approaches to design materials for potential sensing and energy related applications

LIDIJA D. RAFAILOVIĆ[1], CHRISTOPH GAMMER[2], TOMISLAV TRIŠOVIĆ[3], CHRISTIAN RENTENBERGER[4], ALEKSANDAR Z. JOVANOVIĆ[5], IGOR A. PAŠTI[5], H. PETER KARNTHALER[4]

[1] CEST, Centre of Electrochemical Surface Technology, Wr. Neustadt, Austria; [2] Erich Schmid Institute of Materials Science, Leoben, Austria; [3] Institute of Technical Sciences of the Serbian Academy of Sciences and Arts, Belgrade, Serbia; [4] University of Vienna, Faculty of Physics, Physics of Nanostructured Materials, Vienna, Austria; [5] University of Belgrade, Faculty of Physical Chemistry, Belgrade, Serbia

It is the aim of our work to carry out fundamental studies on designing and synthesizing high surface area functionalized foam and ordered structures for their potential sensing and energy related applications. We combine electrochemical synthesis with structural studies on different length scales including transmission electron microscopy. Templates are directly grown by electrodeposition, either by hydrogen bubble formation or by utilizing of ordered structures formed by anodic electrochemical oxidation [1-3]. Recently we also demonstrate the synthesis of highly defected Al coatings by electrodeposition [4].

We employed an advanced approach to obtain open foam deposits of Ni and Ni alloys, by using electrodeposition at high current densities which promote hydrogen evolution and bubble templating (cf. fig.1 and fig.2) [1]. In the next step, the high surface area of such materials was functionalized by Pd utilizing a galvanic displacement reaction. Electrochemical testing of the obtained open foam deposits shows promising catalytic activity for hydrogen evolution in alkaline environments, as well as methanol and ethanol oxidation. In the case of fabrication of nanodendritic Ag, simultaneously grown with porous anodic aluminium oxide (cf. fig.3), we accomplished well anchored dendritic Ag nanostructures [2] of long-term stability [3].

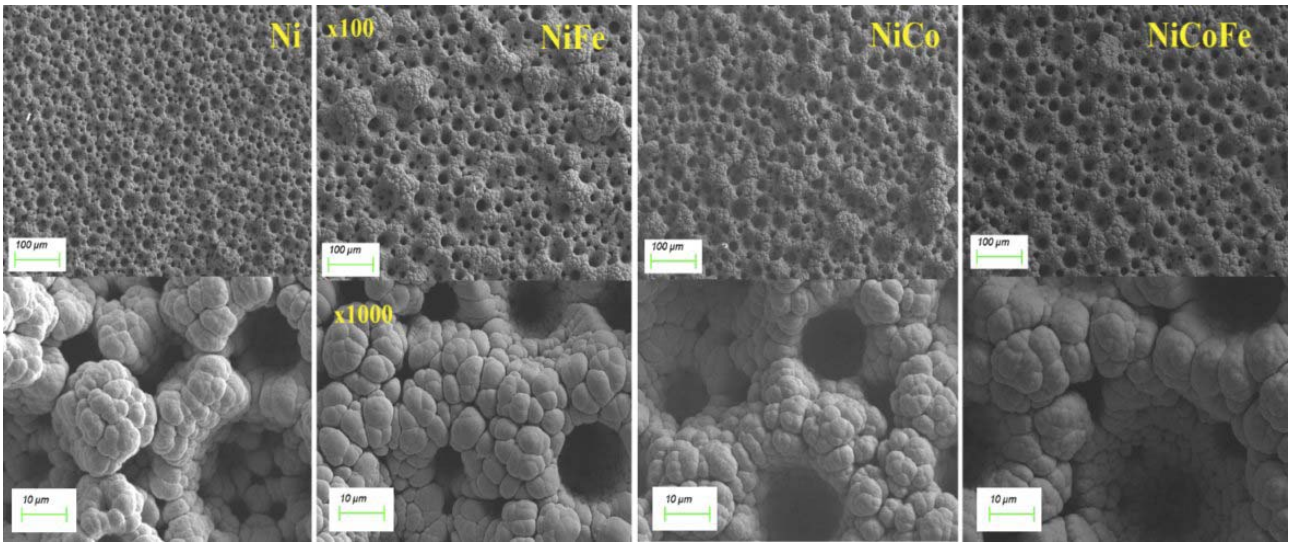

Figure 1. SEM images of high surface area foams of Ni and Ni alloys showing an open porous 'cauliflower-like' morphology, obtained by dynamic hydrogen template bubble deposition. The catalytic activity of NiCoFe foam is strongly enhanced for both, catholic reduction of oxygen and anodic evolution of oxygen showing a good reversibility. Therefore, this new material is promising as bifunctional catalyst in electrochemical energy conversion and storage devices [1].

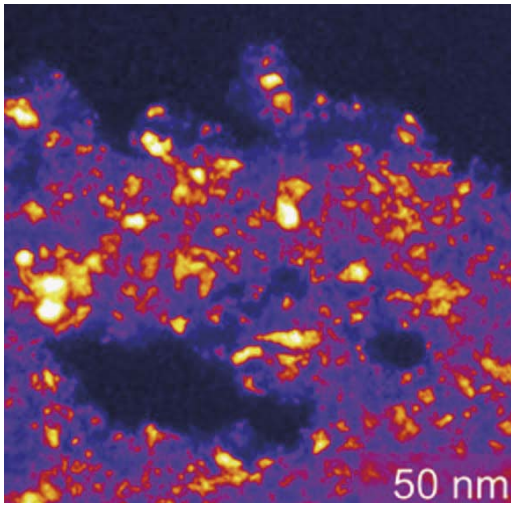

Figure 2. Open dendritic NiCoFe foam obtained by electrodeposition. TEM dark field image of the highly branched dendritic structure with crystallites smaller than 10 nm [1].

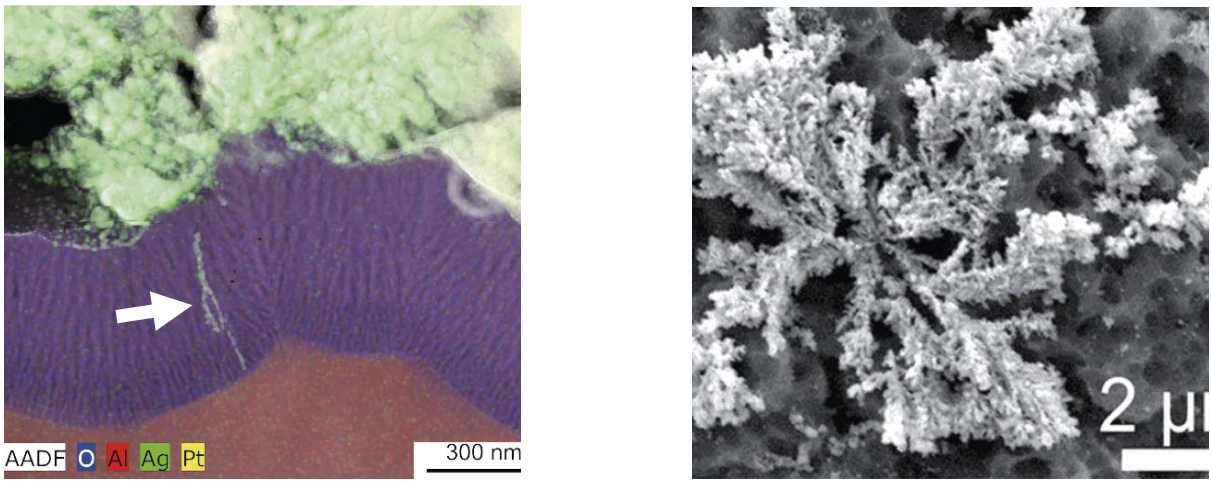

Figure 3. Aluminium oxide functionalized by Ag dendrites deposited at the anode during simultaneous electrochemical oxidation of Al. Ag is known for its high catalytic effectiveness in electrochemical oxygen reduction. (a) STEM image artificially coloured according to the results of EDX analysis including the elements O, Al, Ag and Pt. A striking feature is the channel (marked) in the Al_2O_3 layer showing it contains Ag and indicating it acts as root of the Ag dendrite above [2]. (b) SEM image of Ag dendrite revealing its fine branched structure and several Ag nanoparticles distributed on the porous Al_2O_3 surface [3].

References

[1] L. D. Rafailović, C. Gammer, C. Rentenberger, T. Trišović, C. Kleber, H. P. Karnthaler, Nano Energy, 2 (2012) 523

[2] L.D. Rafailović, C. Gammer, C. Rentenberger, T. Trišovic, C. Kleber, H.P. Karnthaler, Advanced Materials, 27 (2015) 6438

[3] L.D. Rafailović, C. Gammer, J. Srajer, T. Trisovic, J. Rahel, H.P. Karnthaler, RSC Advances, 6 (2016) 33348

[4] L.D. Rafailović, C. Gammer, C. Ebner, C. Rentenberger, A. Z. Jovanović, I. A. Pašti, N. V. Skorodumova and H.P. Karnthaler, Science Advances, (2019) accepted

TEM characterization of some sensitive materials based on MgH_2 and nanoporous carbons

PAVEL MARKOV[1], DIANA NIHTIANOVA[1,2], BOYKO TSYNTSARSKI[3] AND ELI GRIGOROVA[1]

[1] Institute of General and Inorganic Chemistry, Bulgarian Academy of Sciences, Sofia, Bulgaria; [2] Institute of Mineralogy and Crystallography, Bulgarian Academy of Sciences, Sofia, Bulgaria; [3] Institute of Organic Chemistry, Bulgarian Academy of Sciences, Sofia, Bulgaria

1. Introduction

Hydrogen storage materials development is one important scientific topic related with more extensive application of hydrogen as energy carrier. Transmission electron microscopy (TEM) characterization of these materials is somehow challenging because of their sensitivity to oxidation and the high energy of the electron beam exposure in TEM, which could cause negative impact. Some ways that minimize the radiation damage of the samples are using more intense electron sources with more sensitive electron detectors, digital control of the beam in STEMs (Scanning TEM), using low noise, charge-coupled device (CCD) cameras and specimen cooling (cryo-microscopy) or combination of some of them [1]. The nanoporous carbons prepared by hydro-pyrolysis from two different biomass precursors cherry stones and crushed walnut shell and also a ball milled mixture under argon with composition 80 wt % MgH_2 - 15 wt% Ni- 5 wt % nanoporous carbon from crushed walnut shells are analyzed by TEM. The additional and profound information about structural details at unit cell level, presence of some phases with very low concentration and morphology could be received by TEM characterization of these materials [2-6]. In some of these studies of MgH_2 based materials cryogenic holder is used in order to increase the stability time of the hydride under electron beam exposure [3]. According A. Surrey et al. the MgH_2 sensitivity to the electron beam is high and a high-resolution TEM study (HRTEM) of unprotected nanostructured MgH_2 with large electron doses is not feasible [4]. The results obtained by TEM give a more comprehensive description of the microstructures and aid in the development of improved materials for hydrogen storage.

2. Details of experiment

The nanoporous carbons from two different biomass precursors (cherry stones and crushed walnut shell) are subjected to hydro-pyrolysis at 700^0C for 60 min, with a heating rate of 5^0C/min, in a stainless-steel vertical reactor, placed in a tube furnace. Resulting samples are denoted as CSC (cherry stones carbon) and CWC (crushed walnut shell carbon) further in the text, and they have BET surface area of 800 m^2/g and 750 m^2/g, respectively. The sample 80 wt % MgH_2 - 15 wt% Ni-5 wt % CWC is ball milled in a planetary mill for 60 min., under argon and with rotation speed of 200 rpm. After that a volumetric Sievert type apparatus is used for hydrogen sorption measurements. Structure, phase and surface composition of obtained materials are examined by TEM (TEM HR STEM JEOL JEM 2100 with GATAN Orius 832 SC1000 CCD Camera) at accelerating voltage of 200 kV. The preparation procedure of the specimens is consisted of dispersing them in ethanol by ultrasonic treatment for 6 min. The suspensions are dripped on standard holey carbon/Cu grids. The samples are exposed briefly to air during transfer to the TEM holder.

3. Results and Discussion

A part of handling and preparation of studied materials are made under protective argon atmosphere and glove box. By HRTEM is obtained information that the both nanoporous carbons contain mainly graphitic structure, but also some phases like oxides, carbonates and hydroxides of calcium and magnesium from the biomass precursors (Fig.1). The interplanar distances of the lattice fringes of about of 0.701 nm and 0.216 nm correspond to (002) and (100) planes of the graphite phase in the both nanoporous carbons.

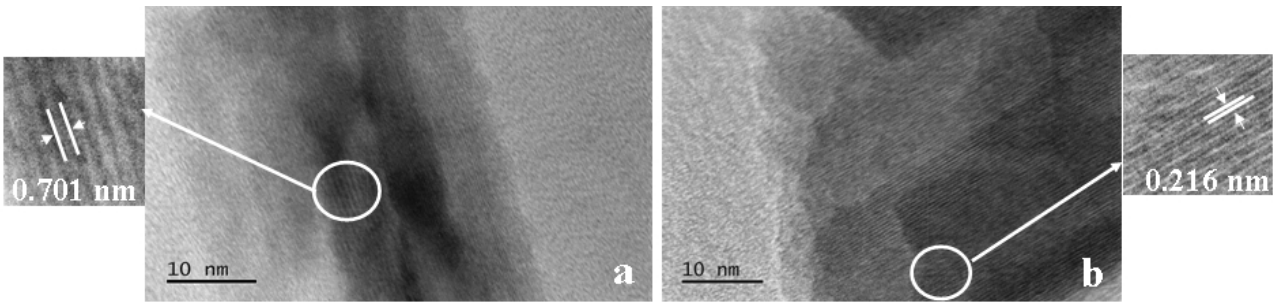

Figure 1. Experimental HRTEM pictures and Fourier filtered images of nanoporous carbons from: a) from cherry stones and b) crushed walnut shell.

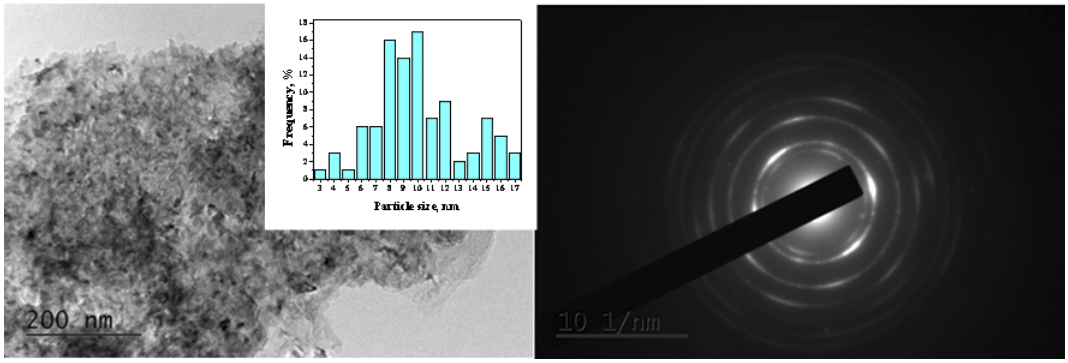

Figure 2. Bright field micrograph, particles size distribution and polycrystalline SAED pattern of the 80 wt % MgH_2 - 15 wt% Ni- 5 wt % nanoporous carbon from crushed walnut shells after hydriding.

The SAED- TEM observation revealed that the sample based on MgH_2 after hydriding at temperature of 300 ^{0} C and a pressure of 1 MPa consists of MgH_2, but also orthorhombic Mg_2NiH_4 and the same ternary hydride with different types of monoclinic structure e.g. C2/c, Cc and C2/m is formed. The rings of polycrystalline SAED pattern in Fig. 2 are with d-spacings as follow: 1- 0.247 nm, 2- 0.214 nm, 3- 0.151 nm, 4- 0.124 nm, 5- 0.108 nm, 6- 0.097 nm, 7- 0.089 nm and 8- 0.072 nm. The particles size distribution with help of the image processing program Image J represented in Fig.2 for 80 wt % MgH_2 - 15 wt% Ni- 5 wt % nanoporous carbon from crushed walnut shells shows an average particles diameter size of 9 nm. The particles size values are between few nm to less than 20 nm. For this sample also Experimental HRTEM pictures and Fourier filtered images are obtained (not shown) and they reveal additionally to the monoclinic types and orthorhombic Mg_2NiH_4 phase also a presence of MgH_2 and Mg.

4. Conclusions

The TEM characterization of these sensitive materials particularly HRTEM and SAED is obtained by low beam current values. HRTEM of the both nanoporous carbons is showed that they consist of areas with graphitic structure and contain some impurities of carbonates and oxides of calcium and magnesium which are related with the biomass precursors. The nanoporous carbon derived from walnut crash shells is used as additive to MgH_2 based material for hydrogen storage with composition 80 wt % MgH_2 - 15 wt% Ni- 5 wt % CWC. TEM characterization of this sample revealed co-existence of a few monoclinic and also orthorhombic types of Mg_2NiH_4 phase. This material is a fine powder with average diameter particles size of about 9 nm.

Acknowledgments
Financial support from Bulgarian Academy of Sciences and Bulgarian Ministry of Education (Project DFNI-КП-06-Н27/9, 08/12/2018) is gratefully acknowledged.

References

[1] D. B. Williams and C. B. Carter, (2009) Transmission Electron Microscopy: A Textbook for Materials Science (2nd Ed, Springer Science, NY)
[2] E. Grigorova, M. Khristov, I. Stoycheva, B. Tsyntsarski, D. Nihtianova, P. Markov, Bulg. Chem. Commun., 49 (2017) 109 –114
[3] M. Danaiea, D. Mitlin, J. Alloys Compd., 476 (2009) 590–598
[4] A. Surrey , L. Schultz and B. Rellinghaus, Adv. Struct. Chem. Imag. 2 (2016) 7
[5] Y. Lu, Z. Zhu, D. Su, D. Wang, Z. Liu, R. Schlögl, Carbon 42 (2004) 3199–3207
[6] S. S. Samantaray, S. R. Mangisetti, S.Ramaprabhu, J. Alloys Compd. 789 (2019) 800-804

TEM methods for characterization of encapsulated metal nanoparticles within zeolites framework via 2D to 3D transition

MICHAL MAZUR, YUYAN ZHANG, MARTIN KUBŮ, AND JIŘÍ ČEJKA
Department of Physical and Macromolecular Chemistry, Faculty of Science, Charles University, Prague, Czech Republic

Encapsulation of metal NPs within zeolite cages or channels can protect metal NPs against sintering while maintaining the shape selectivity and provide the novel route to design and synthesize high effective catalysts. Layered zeolite precursors are the materials that blend the advances of layered solids with the properties of zeolites which opens many opportunities in synthesis and modification [1]. One of the methods for introduction of metal NPs into the zeolite system is based on use of two dimensional (2D) layered precursors that are loaded with metal source and consecutively transformed to three dimensional (3D) zeolites [2,3].

Here, we introduced the Pt/Pd nanoparticles into MCM-22P during the swelling process of the lamellar zeolitic precursor followed by calcination, resulting in clusters encapsulation within the 3D framework of **MWW** zeolite. Especially we used a series of surfactants with different carbon chain lengths (C_{12}, C_{14}, C_{16}, C_{18}) as swelling agents and got tunable nanoparticle size within **MWW** framework [4]. Synthesized materials were investigated the shape-selectivity hydrogenation of nitroarenes to anilines, showing high hydrogenation activity for 3-nitrotoluene and almost no activity for 1-nitronaphthalene.

Moreover, we extend this method to other zeolite precursors like IPC-1P *via* ADOR process, we also encapsulated Pt nanoparticles into IPC-2 and IPC-4 materials [5]. All synthesized materials were investigated by PXRD, sorption, ICP-OES, SEM, and TEM methods.

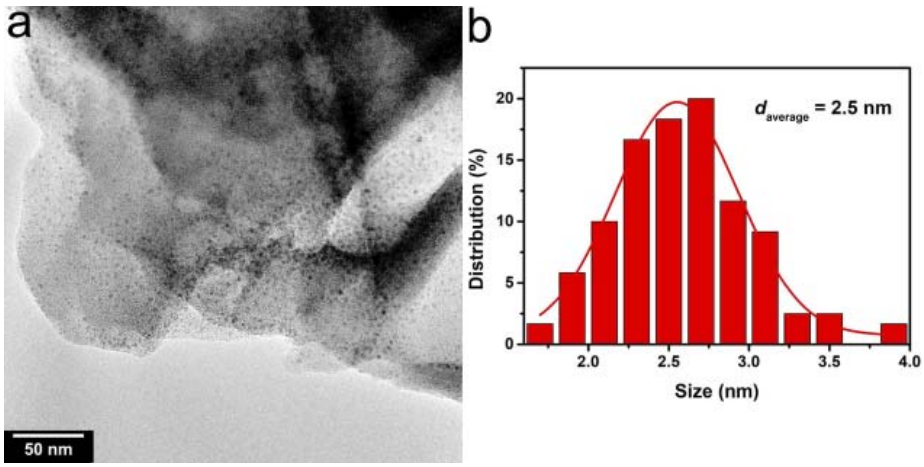

Figure 1. TEM image (a) and Pd NPs size distribution (b) of Pd@MCM-22.

References

[1] W.J. Roth, B. Gil, W. Makowski, B. Marszalek, P. Eliasova., *Chem. Soc. Rev.*, 45, **2016**, 3400-3438.
[2] Z. Zhao, Y. Li, U. Müller, W. Zhang., *ChemCatChem.*, 10, 10, **2018**, 22554-2259.
[3] Liu, L.; Díaz, U.; Arenal, R.; Agostini, P.; Corma, A., *Nat. Mater.*, 16, **2017**, 132-138.
[4] Y. Zhang, M. Kubů, M. Mazur, J. Čejka, *Catal. Today.*, 324, **2019**, 135-143.
[5] Y. Zhang, M. Kubů, M. Mazur, J. Čejka, *Microporous Mesoporous Mater.*, 279, **2019**, 364-370.

Calcium manganite coatings from chemically synthesized powders

JELENA MACAN[1], ANAMARIJA HAVLIČEK[1], SUZANA KRALJ[1], IVANA PANŽIĆ[2], MIRAN ČEH[3] AND ANDREJA GAJOVIĆ[2]

[1] University of Zagreb, Faculty of Chemical Engineering and Technology, Zagreb, Croatia; [2] Ruđer Bošković Institute, Zagreb, Croatia; [3] Institute Jožef Stefan, Ljubljana, Slovenia

Calcium manganite, $CaMnO_3$, is a perovskite which has potential uses in sensing light and various gaseous or volatile compounds, while heterostructures comprising calcium manganite seem to exhibit enhanced photovoltaic and catalytic activities [1,2]. The manganites are both electron and oxygen conductive as well as temperature-resistant and oxidatively stable [3]. Therefore we are investigating appropriate methods to synthesise $CaMnO_3$ powders and prepare thin coatings suitable for these applications.

Calcium manganite powders were synthesised from water solutions of calcium and manganese nitrates by three different methods. Pechini's method includes complexing the metal ions with citric acid, adding ethylene glycol to encourage polyesterification with the acid, and boiling out the water until a sticky gel forms. The gel, due to high nitrate content, energetically self-combusts yielding voluminous ash-like powder. Citrate method is very similar, only ethylene glycol is not added. Despite the lack of possible polyesterification, boiling out the water yields a similar sticky gel and an energetic self-combustion reaction with resulting voluminous ash. Coprecipitation is performed by adding ammonium bicarbonate as a precipitation agent into the nitrate solution, and a white precipitate is formed.

Resulting powders were characterised by Fourier transform infrared spectroscopy (FTIR), X-ray diffraction (XRD) and combined differential scanning calorimetry and thermogravimetric analysis (DSC-TGA). The ash-like powders obtained by Pechini's and citrate methods consisted mostly of crystalline calcium carbonate phase and an amorphous manganese-containing phase which was obvious from typical Mn–O IR bands [4]. Citrate method also yielded some crystalline $CaMnO_3$. Their DSC-TGA curves were also very similar, differing only in the final mass loss, which may well have been caused by uneven intensity of self-combustion reaction in the two cases. The main mass loss occurs at ~700 °C due to thermolysis of calcium carbonate. The precipitate, on the other hand, consisted exclusively of mixed $(Ca,Mn)CO_3$ and thermally degrades in two steps, tentatively ascribed to the thermolysis of manganese-rich part of the precipitate, followed by thermolysis of the remaining carbonates at ~700 °C. To study the crystallization process, raw powders were calcined at 400, 600, 700 and 900 °C for two hours. Full conversion to crystalline $CaMnO_3$ occurs at 900 °C for all cases, but the powders obtained from both Pechini's and citrate method also contain some marokite, $CaMn_2O_4$, while coprecipitation yields XRD-pure $CaMnO_3$. Pechini's and citrate methods also have much poorer yield, resulting in only 25 % of theoretically obtainable quantity of $CaMnO_3$, while coprecipitation has 75 % yield.

Coatings on glass substrates were successfully applied using a doctor blade with 20 and 40 µm gap, from pastes formed by mulling the calcined $CaMnO_3$ powder with 3 % solution of poly(vinylidene fluoride) in 1-methyl-2-pyrrolidone. The coatings were subsequently annealed at 130 °C for 24 h. The powders were characterised by both scanning and transmission electron microscopies (SEM, TEM), while the coatings were characterised by SEM. The ashy powders obtained by Pechini's and citrate methods have very porous, sponge-like morphology (Fig. 1a, b) and are formed from fused smaller crystalline grains, some of which are ~200 nm in diameter (Fig. 2a, b). This morphology is due to intensive gas evolvement during the self-combustion step of the synthesis. Coprecipitation, on the other hand, yields large and porous spherical aggregates of similarly-sized crystalline grains (Fig. 1c, 2c). Due to thickness of the crystallites, it was not possible to characterise them using

high-resolution TEM or selected area electron diffraction. During preparation of the paste for coating application by doctor blade, some of the aggregates and porous structures were broken up into smaller particles, and the level of comminution depended on the mulling time (Fig. 3). Quality and porosity of the coatings can therefore be tailored by careful control of application parameters, including the powder/solvent ratio as well as time and intensity of the paste homogenisation.

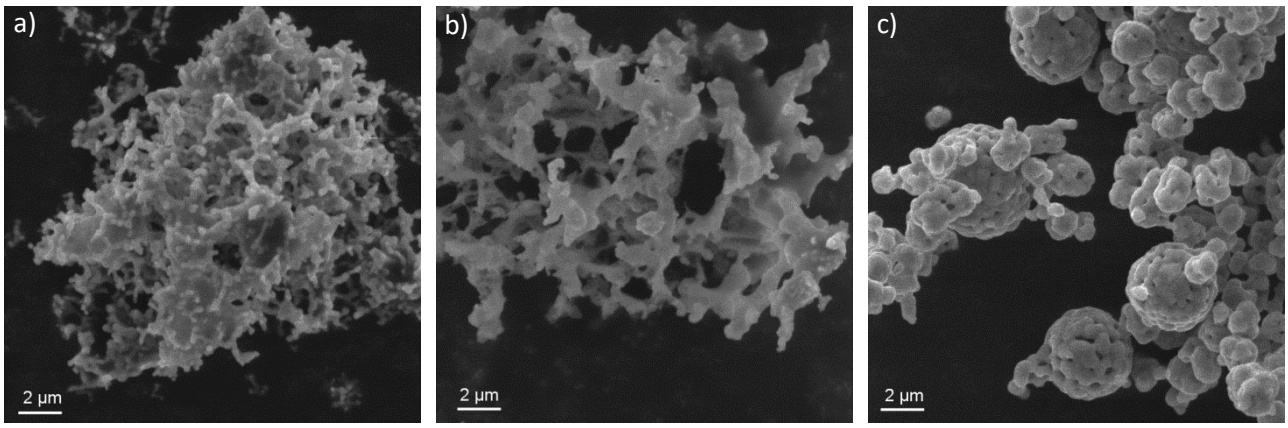

Figure 1. SEM micrographs of $CaMnO_3$ powders obtained by a) Pechini's method, b) citrate method and c) coprecipitation.

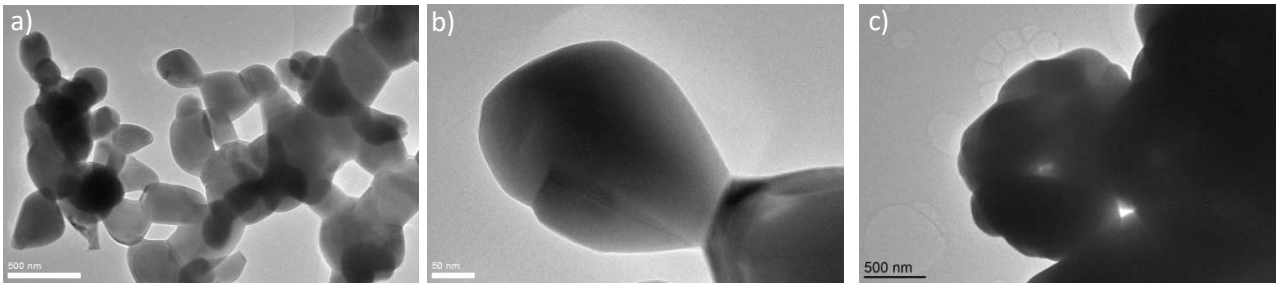

Figure 2. TEM micrographs of $CaMnO_3$ powders obtained by a, b) citrate method and c) coprecipitation.

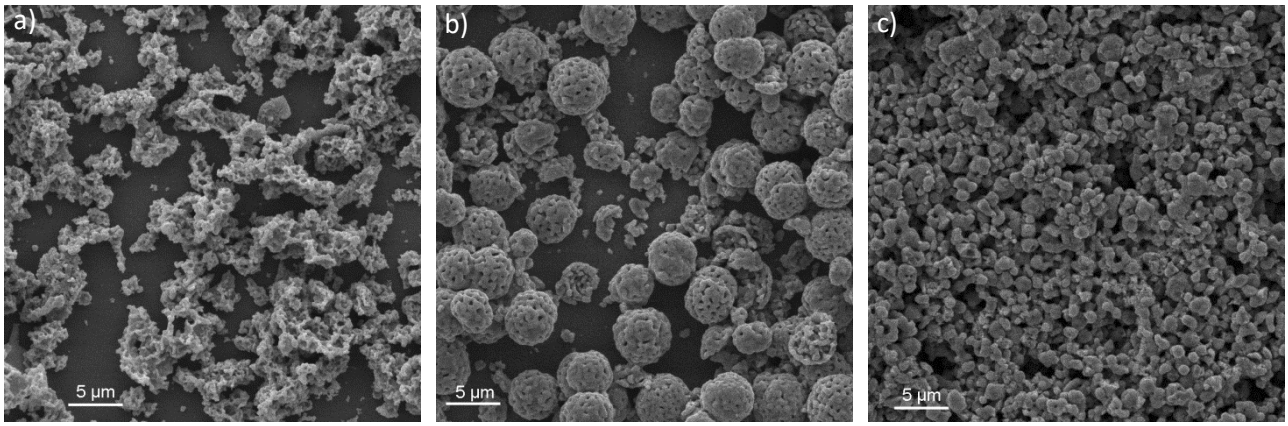

Figure 3. SEM micrographs of $CaMnO_3$ coatings applied by doctor blade: after shorter mulling time from powders obtained by a) citrate method and b) coprecipitation; c) after longer time from powder obtained by coprecipitation.

Acknowledgement
This work has been fully supported by Croatian Science Foundation under the project IP-2018-01-5246.

References
[1] K. A. Stoerzinger, M. Risch, B. Han, Y. Shao-Horn, ACS Catal., 5 (2015) 6021-6031
[2] J. Kim, X. Chen, Y.-T. Pan, P.-C. Shih, H. Yang, J. Electrochem. Soc., 164 (2017) F1074-F1080
[3] K. Zhang, X. Han, Z. Hu, X. Zhang, Z. Tao, J. Chen, Chem. Soc. Rev., 44 (2015) 699-728
[4] S. Liang, F. Teng, G. Bulgan, R. Zong, Y. Zhu, J. Phys. Chem. C, 112 (2008) 5307-5315

Electron Microscopy as an Essential Tool in Electrochemistry: Assessing the Surface Morphology of Al Electrodes

DAVID MOSER[1], SANDRA STEINER[3], BERNHARD GOLLAS[3], GERALD KOTHLEITNER[1,2]

[1] Institute of Electron Microscopy and Nanoanalysis, Graz University of Technology, Graz, Austria; [2] Graz Centre for Electron Microscopy, Graz, Austria; [3] Institute for Chemistry and Technology of Materials, Graz University of Technology, Graz, Austria

The aim of this work is to realize a secondary aluminum battery, using metallic aluminum electrodes in combination with a deep eutectic solvent consisting of $AlCl_3$ and urea as electrolyte [1, 2, 3]. Starting with a natively passivated aluminum surface, the formation of undesired growth morphologies was observed during electrochemical discharge/charge cycling (Figure 1.a). It is suggested, that these flake-like deposits are caused by high local current densities at a limited number of active sites. Extending the period of electrode/electrolyte contact at open circuit potential (stand-by) before subsequent low current cycling, can improve the surface morphology significantly (Figure 1.b). Surface studies of this proposed activation method revealed that cementation (metal deposition by chemical redox reaction) of electrolyte impurities and wrinkling of the surface takes place during stand-by. It could be shown that the change of the surface morphology and composition is time dependent. Wrinkling could be correlated to chlorine uptake (Figure 1.c) and thickness increase of the oxide layer.

Dendritic deposits are unwanted in batteries, because they can cause short circuiting, capacity loss and a decrease in ion mobility [4]. Due to their high surface area, electrodes covered with these morphologies have a low overpotential, which is generally an indicator for good electrochemical performance. This shows that the results of electrochemical measurements can be misleading when encountering passivated surfaces and have to be interpreted alongside morphological studies.

Currently, we are starting to investigate electrochemical deposition and dissolution processes in-situ. A cell suitable for in-situ optical microscopy has been developed.

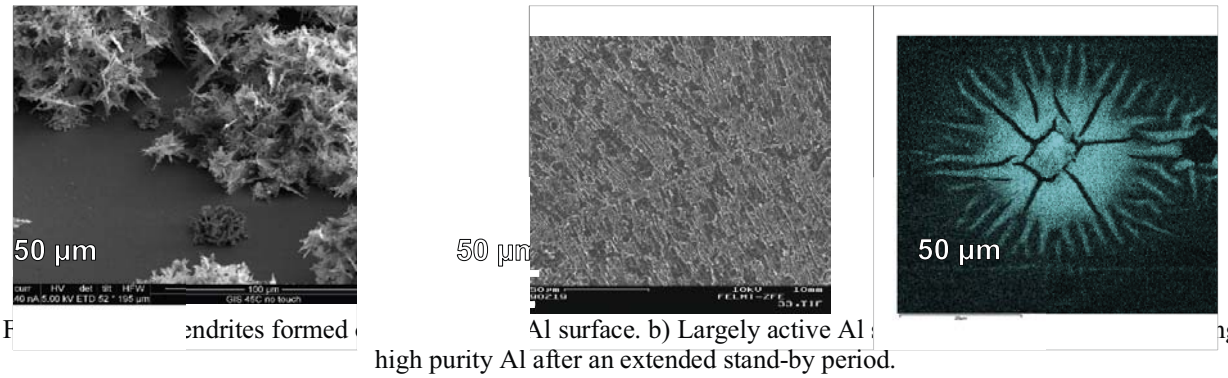

F ndrites formed Al surface. b) Largely active Al ng of high purity Al after an extended stand-by period.

References

[1] Tiemblo *et al*, ACS Sustainable Chem. Eng. 4 (2016), 2114-2121
[2] Passerini *et al*, Adv. Mat. 28 35 (2016), 7564-7579
[3] Gao *et al*, Angew. Chem. 55 (2016), 9898-9901
[4] Chen; *et al*, Mater. Chem. A 5, (2017), 11671–11681

Structural study by Cs-Corrected Electron Microscopy of Luminescent Indium-Zinc Oxides

J. GARCÍA-FERNÁNDEZ[1], A. TORRES-PARDO[1], J. BARTOLOMÉ[2], A. CREMADES[2], J. RAMÍREZ-CASTELLANOS[1] AND J. M. GONZÁLEZ-CALBET[1,3]

[1] Inorganic Chemistry Department, Chemical Sciences Faculty, Universidad Complutense de Madrid, Spain; [2] Materials Physics Department, Physical Sciences Faculty, Universidad Complutense de Madrid, Spain; [3] ICTS National Center for Electronic Microscopy, Universidad Complutense de Madrid, Spain

Transparent semiconducting oxides (TCO) constitute a large field of research due to their excellent carrier nobilities, tunable band-gap and high optical transparency. These features make these materials excellent candidates for several applications as transparent electrodes in transistors, flat panel displays, solar cells, sensors… [1]. In the last years, complex structural of oxides have attracted particular attention due to their chemical features (stability, photocatalysis, ...) and tunable optoelectronic properties as a function of composition and structure.

The main objective of this work is to establish the relationships between the structure and microstructure and luminescent properties in a series of functional oxides $Zn_kIn_2O_{k+3}$ ($3 \leq k \leq 13$) materials. The structure can be described as the ordered intergrowth of one InO_2^- layer where In is octahedrally coordinated and $InZn_kO_{k+1}^+$ blocks with wurtzite structure stacked perpendicular to the c-axis of the crystal, where Zn and In occupy tetrahedral and trigonal bipyramid sites [2]. A detailed study by Cs-Corrected Electron Microscopy along the [010] zone axis shows a gradual shift of the oxygen position, while cationic positions remain constant, in order to keep the polarization neutrality along c axis and allow to the stabilization of the structure. No differences of In distribution inside the wurtzite blocks are visualized. On the other hand, images along the [1-10] zone axis show a zig-zag structural modulation (see figure), where the angles and distances change along the homologous series [3]. Electron energy loss spectroscopy (EELS) confirms the preference site of In^{3+} along this zig zag pattern. Cathodoluminescence signals reveal a main emission band centered at 1.75 eV, which shows an increasing of intensity with *k*, and has been attributed to the existence of randomly distributed Zn vacancies.

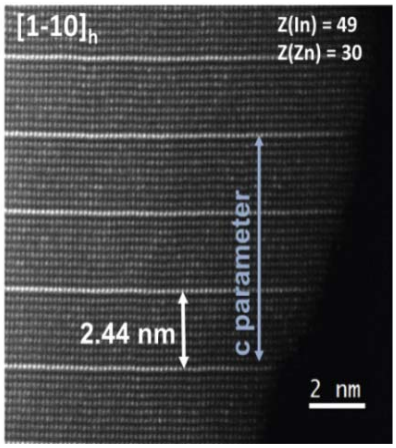

Figure 1.

References

[1] Xinge Yu et al. *Nature Materials* (2016), **15**, 383–396.
[2] T. Moriga et al. *J. Am. Ceram. Soc.* (1998), **81(5)**, 1310-1316.
[3] C. Li et al. *J. Electron Microsc.* (1997), **46**, 119-127.

Identical location TEM for the study of catalyst materials: from single atoms to nanoparticles

FRANCISCO RUIZ-ZEPEDA[1,2], MATIJA GATALO[1,3], PRIMOŽ JOVANOVIČ[1], DAVIDE MENGA[4], TIM-PATRICK FELLINGER[4], LÉONARD JEAN MORIAU[1], ANDRAŽ PAVLIŠIČ[1], NEJC HODNIK[1], MARJAN BELE[1], GORAN DRAŽIĆ[1] AND MIRAN GABERŠČEK[1,3]

[1] National Institute of Chemistry, Ljubljana, Slovenia; [2] Institute of Metals and Technology, Ljubljana, Slovenia; [3] University of Ljubljana, Slovenia; [4] Technische Universität München, Garching, Germany

The performance of catalytic nanoparticles is usually ascribed to the nanostructure, composition and morphology of their surface [1]. It is therefore of great interest to gain insight on the characteristics of these particular components. Furthermore, in order to understand and improve their stability it is necessary to inquire about the behavior and development of such catalyst after being submitted to electrochemical cycling. Specially, due to harsh conditions occurring in a regular workload, metallic catalysts suffer from dissolution or dealloying processes. In this work, we present the study of different metallic catalysts examined by identical location transmission electron microscopy (IL-TEM) [2]. This method allow us to examine the same area of the sample before and after a reaction or an electrochemical proces has taken place. In one of the studies we observed Pt skin $PtCu_3$ nanoparticles being etched preferentially on certain facets, forming pores and reducing in size close to 20% after an electrochemical activation protocol. A second study showed electrochemical induced changes in the structure and morphology of Pt-SnO_2 nanoparticles that would have not been easily visible without an identical location approach. A third study on a binary designed catalyst (ORR/OER) CuPt-Ru-Ir nanoparticles, showed how the catalyst evolved depending on the stage of workflow chosen. Lastly, by adapting the method in a similar way, a study of how atomically dispersed Zn-N-Cs can be used to form atomically dispersed Fe-N-C by a transmetalation process. By tracking these changes it is possible to gain knowledge of the different events involved during the degradation along the lifetime of the catalyst and on the atomically dispersed species. Hence, the IL-TEM approach aims to track important features in processes ocurring *ex-situ,* in one case, by allowing to witness how the dispersion of single atoms happens after transmetalation occurs, and in the case of the electrochemical experiment, to provide a better understanding of the catalyst stability, since allowed us to observe and explore interesting phenomena occurring at the nanoscale during the electrochemical processes in the catalysts.

References

[1] Y. Xia, H. Yang, C. T. Campbell Nanoparticles for Catalysis. Acc. Chem. Res. 46 (2013) 1671–1672.

[2] K. J. J. Mayrhofer, J. C. Meier, S. J. Ashton, G. K. H. Wiberg, F. Kraus, M. Hanzlik, M. Arenz. Fuel cell catalyst degradation on the nanoscale. Electrochem. Commun. 10 (2008) 1144-1147.

Role of lattice oxygen content in the CO oxidation activity of the Ba-Fe-O system

AUREA VARELA[1], ISABEL GÓMEZ-RECIO[1,2], ACHRAF EL HADRI[1], MARÍA HERNANDO[1], MARINA PARRAS[1], JUAN J. DELGADO[2], JOSÉ J. CALVINO[2], JOSÉ M. GONZÁLEZ-CALBET1[3]

[1] Departamento de Química Inorgánica. Facultad de Químicas. Universidad Complutense, Madrid, Spain; [2] Departamento de Ciencia de los Materiales e Ingeniería Metalúrgica y Química Inorgánica. Facultad de Ciencias. Universidad de Cádiz. Campus Río San Pedro, Puerto Real, Spain; [3] Centro Nacional de Microscopia Electrónica. Universidad Complutense, Madrid, Spain

The substitution of so-called critical elements, among which Noble Metals (NM) and some Rare Earths (RE) are included, has become a question of major concern to reach the goal of sustainable development. ABO_3 perovskite related oxides have been essayed as catalysts in a number of reactions, most of them redox processes. The high flexibility of the perovskite structure offers much more opportunities to tailor the oxidation state and the characteristics of the oxygen environment of the catalytically active B element, while preserving a high thermal stability. Lanthanide based Fe, Mn and Co perovskites, $LnBO_3$ (Ln=lanthanide, B=Fe, Co, Mn), have been extensively studied systems, particularly as catalysts in the CO oxidation reaction. Total substitution of La by Ba fits perfectly with the actual demands to replace critical RE since we have investigated the Ba-Fe-O system as catalyst in the CO oxidation process. $BaFeO_{3-\delta}$ ($0.2 < \delta < 0.4$) depicts a 6H perovskite hexagonal structural type with Fe both in III and IV oxidation states and oxygen nonstoichiometry accommodated by random distribution of anionic vacancies [1].

The $BaFeO_{3-\delta}$ catalyst was prepared by a sol-gel method. $BaFeO_{2.78}$ nanoparticles of around 100 nm were obtained. The decrease of the particle size dramatically decreases the temperature of the reduction process of the sample and, under soft conditions (T≈ 200 °C/H_2), nano-$BaFeO_{2.78}$ suffers an easy and reversible reduction process that occurs by a different pathway than that described for $BaFeO_{3-\delta}$ bulk material. The temperature dependence of the redox process has been followed by *in situ* X-ray, Neutron and selected area electron diffraction. Besides, atomically resolved images and chemical maps obtained using different Aberration-Corrected Scanning Transmission Electron Microscopy techniques, have provided a clear picture of the accommodation of oxygen- non-stoichiometry in these materials.

Nano-$BaFeO_{2.78}$ proved to be more active than the above-mentioned $LnFeO_3$ (Ln=La, Sm, Nd) phases. Removal of the lattice oxygen detected in both TPO and TPR diagrams at around 500 K, and which leads to the complete reduction of Fe^{4+} to Fe^{3+}, i.e. to a $BeFeO_{2.50}$ perovskite, decreases significantly the catalytic activity, especially in the low temperature range. The analysis of thermo-gravimetric experiments performed under oxygen and of temperature-programmed reduction (TPR) studies run under CO clearly support the involvement of oxygen lattice in the CO oxidation on these Ba-Fe perovskites, even at the lowest temperatures.

[1] J.M. González-Calbet et al., J. Solid State Chem. 1990, 86, 149-59.

Structural singularities in 2H-related BaNiO phases

D. GUTIÉRREZ-MARTÍN[1], M. HERNANDO[1], A. TORRES-PARDO[1,2], J. M. GONZÁLEZ-CALBET[1,2], A. VARELA[1] AND M. PARRAS[1]

1 Inorganic Chemistry, Department, Universidad Complutense de Madrid, Spain; [2] ICTS National Center for Electronic Microscopy, Universidad Complutense de Madrid, Spain

Establishment of a sustainable energy society has been the driving force to develop low-cost and active catalysts for different reactions. In the particular case of *redox* processes, a number of researches have been focused to the development of perovskite structure catalysts. In this context, we have recently reported the structural and catalytic characterization of a hexagonal perovskite, $BaFeO_{2.78}$, with 6H structure. The obtained results highlight the potential of this oxide as a noble metal and lanthanide free catalyst in the CO oxidation process. The analysis of the thermogravimetric experiments performed under oxygen and of the TPR studies run under CO clearly support the involvement of the lattice oxygen in the CO oxidation on these Ba/Fe perovskites even at low temperatures [1].

Based on these results, we have substituted Fe by Ni and we have investigated the $BaNiO_{3-\delta}$ system in which the Ni oxidation sate and anionic deficiency can be modulated without significant differences of the basic 2H-$BaNiO_3$ structure. These controlled changes can be used to modify the physical and chemical response of the solid, by example its catalytic behavior. In fact, it has been shown that $BaNiO_3$ can be a highly functional catalyst for the evolution reaction in alkaline media [2,3] and the aim of this research is to study this phase as catalyst in the CO oxidation process.

In this work, we show the preparation method and the preliminary results on the structural and microstructural characterization of this system. In a first step, we have tried to prepare $BaNiO_3$ with small particle size by two synthetic methods, sol-gel and solid-state reaction from metallic nitrates as precursors. In both cases, successfully results are obtained and, from X ray diffraction data, the 2H phase seems to be stabilized. However, local structural information, provided by atomically resolved microscopy techniques, shows that $BaNiO_3$ is only attained via solid-state reaction. In the case of the sample obtained by a sol-gel procedure, electron diffraction and transmission electron microscopy suggest the presence of two phases which are not distinguishable by X-ray diffraction. The origin of this phase mixture will be discussed.

References

[1] A. el Hadri et al.ACS Catal. 2017, 7, 8653-63.
[2] J.G. Lee et al., J. Am. Chem. Soc. 2016, 138, 3541-47.
[3] M. Retuerto et al., J. Power Sources, 2018, 404, 56-63.

Surface decorated TiO_2 nanotubes for photocatalytic application

VEDRAN KOJIĆ[1], MARKO RUKAVINA[2], L. RADETIĆ[3], IVANA GRČIĆ[3], ANDREJA GAJOVIĆ[1]

[1] Ruđer Bošković Institute, Zagreb; [2] student at Faculty of Chemical Engineering and Technology, University of Zagreb, Zagreb; [3] Faculty of Geotehnical Engineering, University of Zagreb, Varaždin

1. Introduction

Materials based on nanostructured TiO_2 are among the most prominent materials of the last 40 years, and have been studied for the purpose of use in photocatalysis, photovoltaics, sensors, biomaterials, etc. One of the main limitations for the application of TiO_2 in materials photocatalysis is a wide energy bandgap, Eg = 3.2 eV, so its possible application being limited to UV radiation. In order to increase the efficiency of the TiO_2 nanostructure as a photocatalyst and expand the spectral range in which the photocatalyst is activated, different approaches to modifications of the synthesized nanoparticles of TiO_2 were applied.

In this study, the synthesis of self-assembled TiO_2 nanotubes (NT) was obtained by electrochemical oxidation and decorated by Ag, FeOOH and Fe_2O_3. The photocatalytic properties was studiead using benzoltriazole as model pollutant.

2. Experimental

Self-assembled TiO2 NT was obtained by electrochemical oxidation in organic electrolyte, ethylene glycol with 0.3% NH4F and 12% H2O, at 60V voltage for 3 hours. Surface modification with silver was done by photo-reduction, while decoration with FeOOH/ Fe_2O_3 was achieved by hydrothermal synthesis. SEM, EDS and XRD were applied for characterization, while benzoltriazole was used as model pollutant.

3. Results and discussion

Depending of source of UV light, different size of Ag particled was obtained by photo-reduction (Figure 1), while in the case of decoration with using hydrothermal syntheses FeOOH/ Fe_2O_3 the surface og nanotubes was completely cowered by nanoparticles.

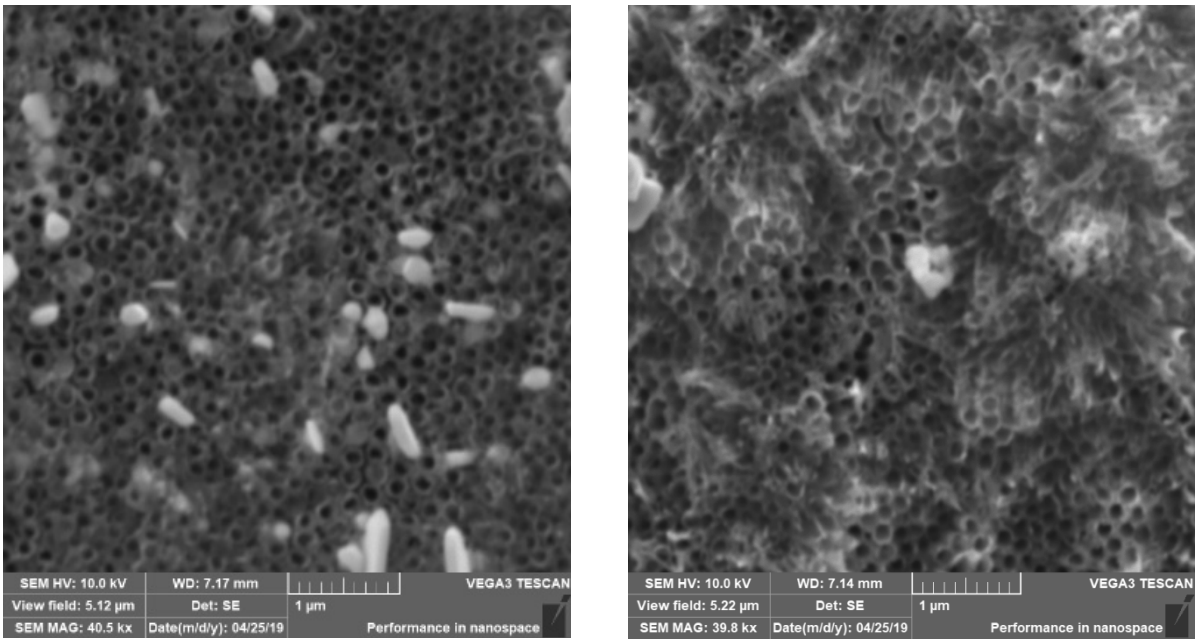

Figure 1. Decoration with silver nanoparticles using: (a) mercury lamp, 366 nm, 80 W, (b) UV LED 365 nm, 4 W.

All the photocatalysts in photocatalytic test behaved on the kinetics of the first order. The best photocatalytic performance, using simulated sun light, was achieved by Ag decorated self-assembled TiO_2 NT, having better performances then commercial TiO_2 P25 (Figure 2).

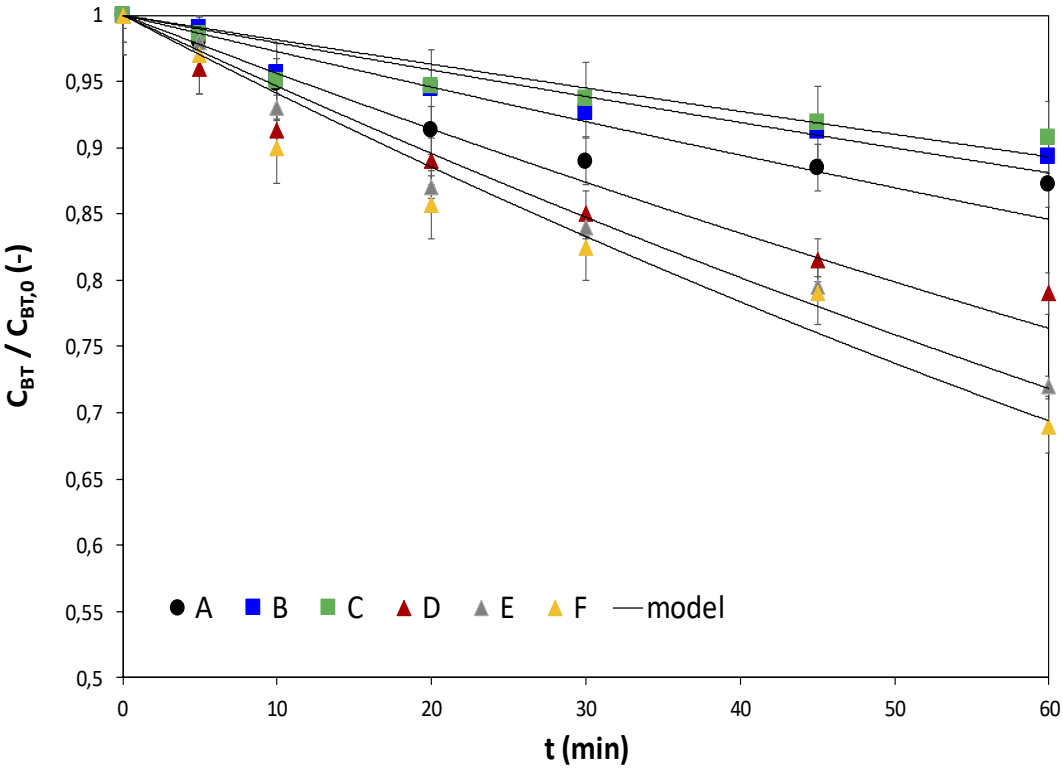

Figure 2. Photocatalytic degradation of benzoltriazole using different catlysts: A (A) P25 on glass (B) TiO_2 NT, (C) TiO_2 NT-polished, (D) TiO_2 NT Fe_2O_3, (E) TiO_2 NT Ag (Hg lamp), (F) TiO_2 NT Ag (LED).

The photocatalytic properties of the synthesized photocatalysts will be discussed considering the morphology, crystal structure and the atomic percentage of the decoration.

Acknowledgments: This work has been fully supported by Croatian Science Foundation under the project IP-2018-01-5246.

Electron Microscopy study of nanocrystalline wurtzite ZnS produced via a co-precipitation technique and its pyroelectric ceramics processed by 2-step-pressureless sintering

RADENKA KRSMANOVIĆ WHIFFEN[1], LORIS PIETRELLI[1], LUCIANO PILLONI[1], GIUSEPPE MAGNANI[2], ELENA SALERNITANO[2], SELENE GRILLI[2], FRANCESCA MAZZANTI[2] AND AMELIA MONTONE[1]

[1] ENEA, CR Casaccia, Rome, Italy; [2] ENEA, CR Faenza, Faenza (RA), Italy

The pyroelectric performances of non-ferroelectric pyroelectrics like wurtzite- based materials (e.g. AlN, GaN, CdS or ZnO) make them important, although not widely used, compared to the current state-of-the-art *ferroelectrics*. Their high chemical and thermal stability allows their use at high temperatures in air, whereas ferroelectrics become ineffective when heated beyond their Curie temperature (T_C). Wurtzite based materials have a *higher thermal conductivity* allowing them to react faster to ambient temperature changes, their raw material *costs are lower* and many of them are *eco-friendly*. Current pyroelectrics applications are limited to portable systems or tasks needing only µW–mW power. To be commercially viable, we must improve the current low efficiency of pyroelectric systems and intrinsically enhance the pyroelectric properties of modern materials through suitable doping or material engineering.

We chose to study hexagonal wurtzite phase of ZnS, among the structurally simplest of pyroelectrics, as a possible energy harvesting material. An easy synthesis method – a co-precipitation technique, was tailored for nanocrystalline wurtzite ZnS production. This method is easy to scale-up and our next step is to build an in-house pilot plant that will produce substantial amounts of wurtzite ZnS nano-powder in an environmentally friendly and cost-effective manner. We further investigated the development of bulk, dense pyroelectric ceramics by the Two-Step Sintering (TSS) fabrication process, using as the precursor material both a micron-sized commercial powder of the ZnS cubic and hexagonal phases mixture, and an in-house produced wurtzite ZnS nanopowder. The TSS was chosen as being a pressureless, simple and cost-effective sintering method for obtaining high density materials with controlled grain growth operating at a lower temperature than the conventiona process. Electron Microscopy techniques helped us to study the microstructure and morphology of both the precursor nanopowders and the obtained ceramics.

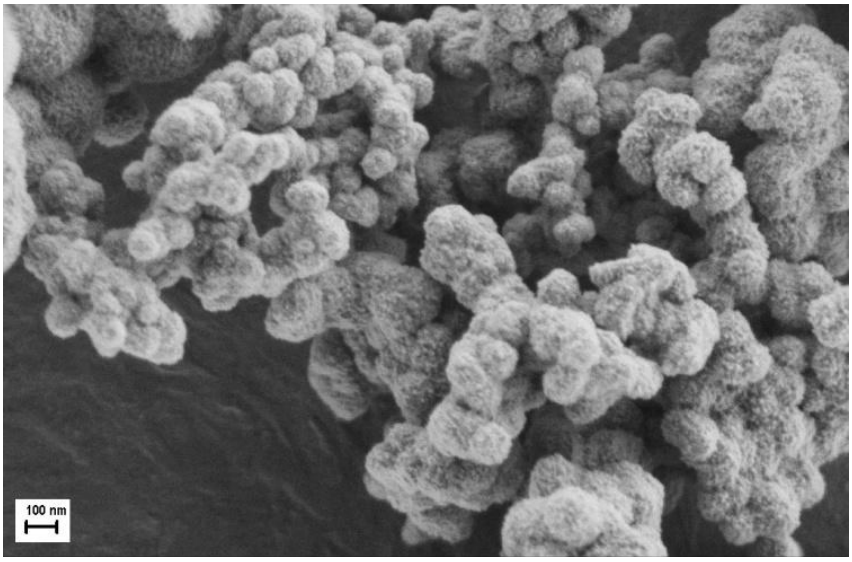

Figure 1. SEM image of the ZnS nanopowder.

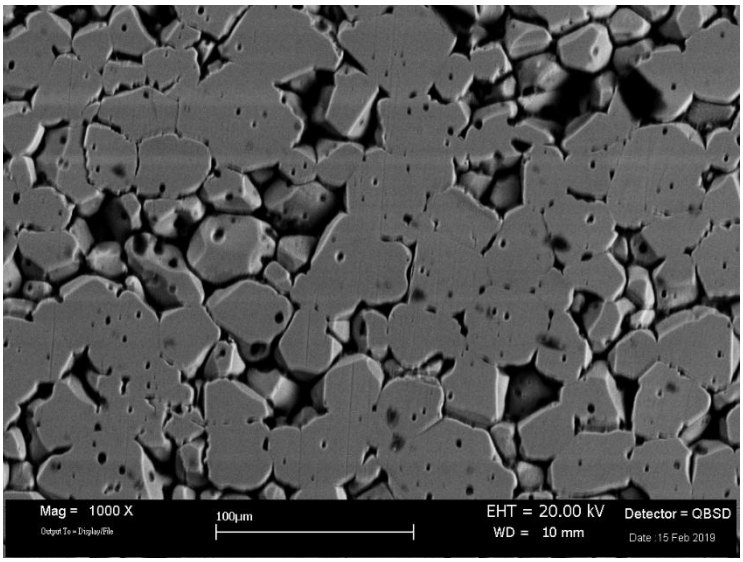

Figure 2. Microstructure of the ZnS sintered sample obtained using the conventional sintering process (d=93% T.D.).

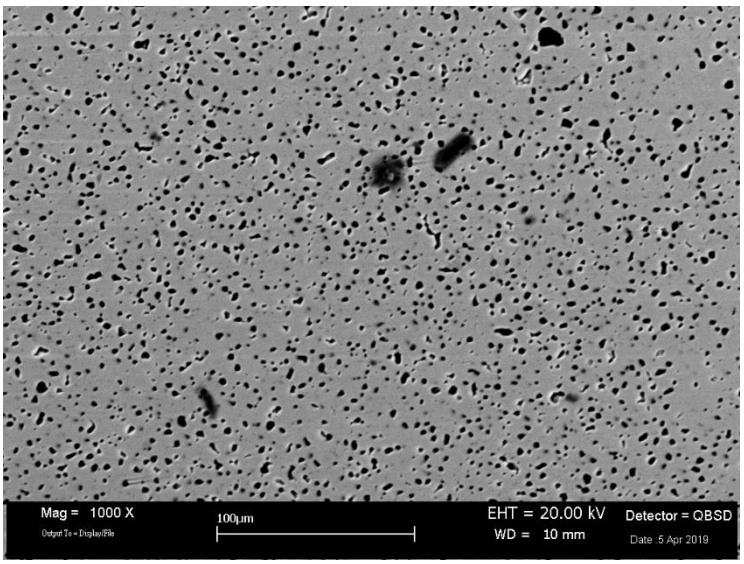

Figure 3. Microstructure of the ZnS sintered sample obtained using the TSS process (d=90% T.D.).

Acknowledgement: This project has received funding from the European Union's Horizon 2020 research and innovation programme under the Marie Skłodowska-Curie grant agreement No. 797951.

Microstructure and thermal behavior of Mg-V thin films for solid state hydrogen storage

T. PANTIĆ[1], K. ZAGAR SODERŽNIK[2], S. ŠTURM[2], S. DREV[2], A. MITROVIĆ[1], S. KURKO[1], B. PASKAŠ MAMULA[1], N. NOVAKOVIĆ[1], J. GRBOVIĆ NOVAKOVIĆ[1], I. MILANOVIĆ[1], S. MILOSEVIĆ GOVEDAROVIĆ[1]

[1] Centre of Excllence for Renewable and Hydrogen Energy – CONVINCE; Vinča Institute of Nuclear Sciences, University of Belgrade, Serbia; [2] Jožef Štefan Institute, Ljubljana, Slovenia

Introduction

The study on hydrogen storage properties of Mg-based thin films is widely conducted due to the fact that they enable controllable design of important properties such as the microstructure, interface, surface and particle size.

The advantages of thin film hydrides over bulk materials and powder [1-3]:

- larger surface area – faster kinetics of dehydrogenation
- lower pressure and temperature of desorption
- composition, interface and crystallinity can be accurately tailored on the nanoscale
- the hydrogen absorption and desorption mechanisms are also easily deduced by modeling and the fitting calculations
- protective coating could be done in order to improve the rate of hydrogenation and reduce the oxygen contamination
- additionaly studied as “switchable mirrors” as they exhibit optical and electrical changes upon hydrogen absorption and desorption
- potential application as hydrogen sensors, energy-efficient windows, solar absorbers…

Experimental:

Nanocrystalline thin films were synthetized by non-equilibrium processing by co-deposition using a multi-source magneton sputtering system Kurt J. Lesker (KJLC CMS-18)

In order to increase hydrogenation rate ion irradiation with H^- and $Xe10^{8+}$ ion has been applied. Irradiation were done on FAMA ion source at Vinca Institute of Nuclear Sciences. Distribution of defects (Frenkel pairs) in the near-surface region was estimated by Monte Carlo simulations

The samples for STEM analysis were prepared by conventional cross-section sample preparation technique. The samples were cut, ground, polished down to approx. 100 µm and, after dimpling, thinned down to electron transparency using Gatan PIPS ion-milling system.
For the structural and compositional studies, we used a probe Cs-corrected scanning transmission electron microscope (Jeol, ARM 200 CF, STEM) operated at 200 kV, equipped with electron dispersive X-ray (EDX) spectrometer (Jeol, Centurion SSD) and electron energy-loss (EEL) spectrometer (Gatan, Quantum ER Dual EELS).

TOF-ERDA measurements were done using 20 MeV $^{127}I^{6+}$ beam. Analysis of TOF-ERDA spectra was done using program Potku.

Results and discussion:

To investigate the microstructure and composition of Mg-V layered structure, STEM with EDX mapping were applied on irradiated and hydrogenated samples. Figure 1 shows Mg-V sample irradiated by H^+ ions. BF-STEM image (Fig. 1(a)) shows layered structure of Mg (appr. 25 nm thick) and V (appr. 1nm thick) which is distorted due to the ion beam direction. The EDX mapping (Fig. 1(b-d)) shows presence of Mg and V elements. During the irradiation the V diffused into Mg.

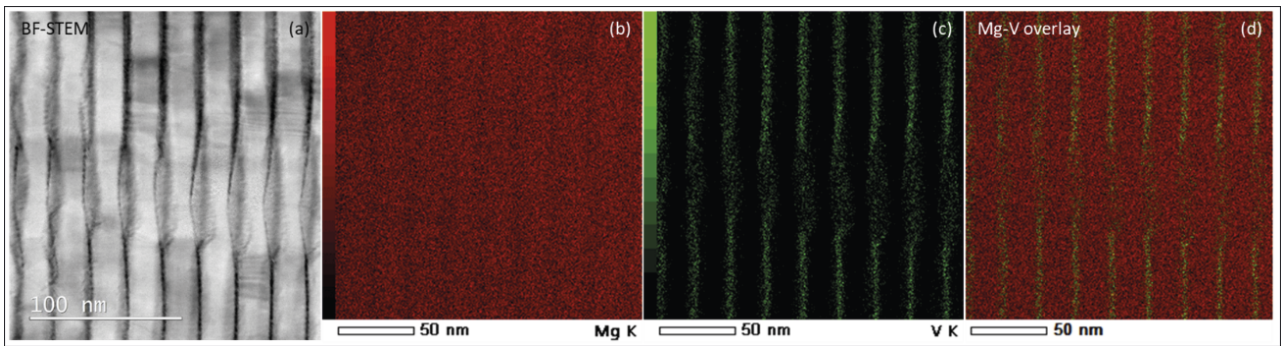

Figure 1. Mg-V irradiated with H^+ ions with fluence of 10^{17}ion/cm^2. (a) BF-STEM image of Mg and V layers. Bright area is Mg layer with thickness of appr. 25 nm, and black layer is V with approx. 1 nm thick layer. (b-c) EDX mapping, with (b) Mg-K line, (c) V-K line and (d) Mg-V overlap.

In contrast to non-hydrogenated sample the BF-STEM image of irradiated and hydrogenated sample shows completely different microstructure (Figure 2(a)). We observed severe microstructural changes. Mg and V layers were transformed to large crystals and the sample became beam sensitive and brittle. The EDX mapping from selected region (Fig. 2(b-d)) shows the presence of Mg, V and O. The samples are oxidized during sample treatment (?), but the results from TOF ERDA analysis shows successful hydrogen diffusion into samples.

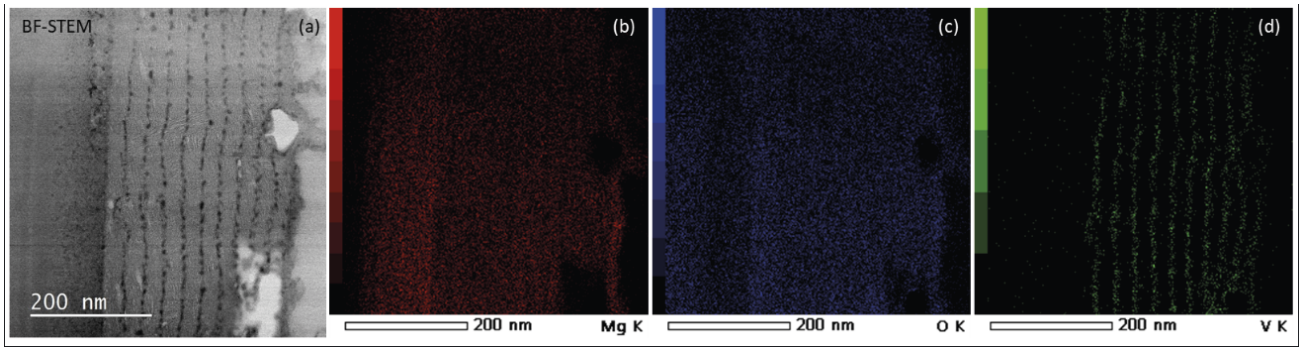

Figure 2. Mg-V irradiated and hydrogenated. (a) BF-STEM image of Mg and V layers. Bright area is Mg layer with thickness of appr. 25 nm, and black layer is V with approx. 1 nm thick layer. (b-c) EDX mapping, with (b) Mg-K line, (c) O-K line and (d) V-K line.

Quantitative depth profiles of TOF-ERDA show difference between irradiated only and irradiated plus hydrogenated films. While in irradiated samples hydrogen is observed on surface, hydrogenated films show hydrogen distribution through whole depth.
Also, after hydrogenation there is mixing between layers and substrate, given that hydrogenation process leads to self-diffusion of metal atoms.

[1] Ž. Rašković Lovre, S. Kurko, N. Ivanović, J. Francisco Fernandez, J.- Ramon Ares, S. Šturm, T. Mongstad, N. Novaković, J. D. Grbovic Novakovic, J.Alloys Compd 695 (2016) 2381-2388

[2] S. Kurko, I. Milanovic, J. Grbovic Novakovic, N. Ivanovic, N Novakovic, Int. J. Hydrogen Energy 39(2) (2014), 862-867

[3] D. Milcius, J. Grobović Novaković, R. Zostautienė, M. Lelis, D. Girdzevicius, M. Urbonavicius. J. Alloys Compd. 647 (2015) 790-796

MS8

Emerging and miscellaneous topics in material sciences

CHAIRPERSONS:

Alena Michalcova, Servet Turan

Photocromic molecular probes for photoacoustic microscopy

FRANCESCO GARZELLA[1,2], PAOLO BIANCHINI[1], ALBERTO DIASPRO[1,3], RANIERI BIZZARRI[4], BARBARA STORTI[4] AND CRISTIANO VIAPPIANI[2]

[1] Istituto Italiano di Tecnologia (Genova, Italy); [2] University of Parma (Parma, Italy); [3] University of Genova (Genova, Italy); [4] NEST, Scuola Normale Superiore and NANO-CNR (Pisa, Italy)

Introduction. The photoacoustic effect is a physical phenomenon involving the generation of sound waves following light absorption in a material sample. Sound waves are generated by irradiating light absorbing systems: photon absorption and subsequent non-radiative relaxation of the chromophores induces a rapid rise in temperature within the sample. When a pulsed laser has a pulse duration shorter than the sample thermal and stress confinement times, then there is not any thermal energy exchanged with the surroundings. The energy deposition occurs on timescales shorter than those needed for mechanical displacements causing strain within the sample to occur. This isochoric heating raises the pressure within the sample by $\Delta p = \Gamma \mu a F$, where Γ is the Grüneisen parameter, μa is the optical absorption coefficient, and F is the incident laser fluence. This pressure rise induces a thermoelastic expansion, and the emission of a pressure wave called a photoacoustic wave[1]. Nowadays, the PA effect has been implemented in several techniques, that have completely improved our way of obtaining in vivo images. Among them, one of the most promising is the Photoacoustic Tomography (PAT). PAT is a technique based on a three-dimensional Photoacoustic Imaging (PAI). PAT can image multi-scale living biological structures, ranging from organelles to organs. Depending on application fields and achievable spatial resolution, PAT is divided into optical-resolution photoacoustic microscopy (OR-PAM), acoustic-resolution microscopy (AR-PAM), photoacoustic computed tomography (PACT) and photoacoustic endoscopy (PAE) [2]. PAI is an innovative imaging approach that overcomes the penetration depth limit of optical imaging methods by acoustically detecting light absorption [3].

Contrast and contrast agent. The contrast in optoacoustic imaging is based on the different absorption coefficients of tissue components like blood, melanin, and lipids or suitable transgene labels in the sample. The method allows high-resolution imaging of tissue to depths of several centimeters [4], [5], and has already proved effective at imaging brain activity, [6], precise cancer localization, [7], cell fate and migration of macrophage [8] or stem cells and it also allows label-free analysis by using endogenous chromophores as contrast agents, which include: hemoglobin in red blood cells (RBC) [9], cytochromes in mitochondria, melanin in melanosomes, and DNA and RNA within the cell nucleus. However, longitudinal, non-invasive studies of live animals, one of the unique capabilities of optoacoustic imaging, are limited by the low number of transgene labels for optoacoustic and their poor signal generation efficiency, which complicates imaging of specific processes at the cellular and subcellular levels. The relatively weak optoacoustic signals generated by illuminating transgene labels at single wavelengths results in weak contrast compared to other strong absorbers like hemoglobin or melanin. Reversibly switchable fluorescent proteins (rsFPs) have had a revolutionizing effect on life science imaging due to their contribution to sub-diffraction-resolution optical microscopy (nanoscopy) as agents able to improve contrast-to-noise ratio and spatial resolution. [10] However, rsFPs show different photophysical behavior in optoacoustics than in optical microscopy because optoacoustics requires pulsed illumination and depends on signal generation via nonradiative energy decay channels. This implies that rsFPs optimized for fluorescence imaging may not be ideal for optoacoustics since light emission and heating are competitive processes in depleting excited states energy [11]. The main aim of this project is the development and study of novel photochromic proteins for photoacoustic microscopy characterized by a lowering of the fluorescence quantum yield. In particular, two different families of photochromic proteins have been considered: GAF3 [12], and two novel mutants of GFPs obtained

adding a fluorescence-decreasing mutation to wildQ and wildQT proteins [13].

Experimental work and preliminary results. GAF3 is the third domain of the protein encoded by the gene slr1393 from the cyanobacterium *Synechocystis sp*. PCC6803 (Slr1393) and the sole domain showing photochromism, by switching between a red-absorbing parental state (GAF3R, λmax = 649 nm) and a green-absorbing photoproduct state (GAF3G, λmax = 536 nm) upon appropriate irradiation (figure 1A). The protein has been tested in a pump and probe system showing a good difference between the peaks height of two forms at 532 nm pulse excitation wavelength which, due to the strong absorption of the red form in the region of the spectrum of the green form, is the one showing lower contrast (figure 1B).

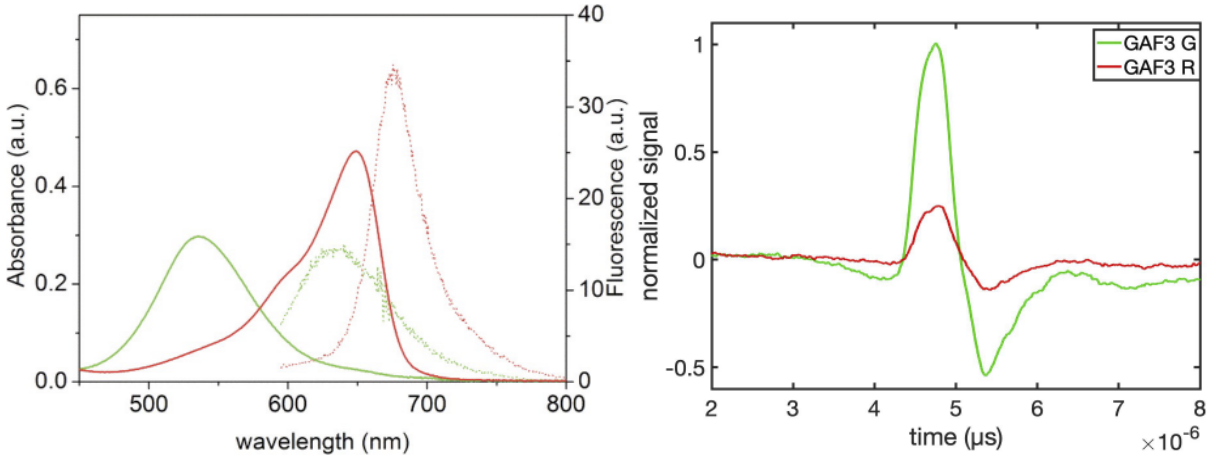

Figure 1. Absorption (A), fluorescence (A) and photoacoustic (B) spectra of the green and red absorbing forms of GAF3.

WildQ and wildQT, respectively E222Q wtGFP and E222Q EGFP, have been used as a starting point for rational mutagenesis involving the addition of Y145W which is supposed to substantially decrease fluorescence quantum yield. The proteins display the predicted behavior with a fluorescence quantum yield which respectively for low-wildQ and low low-wildQT the 20% and 10% of the original wildQ protein (figure 2).

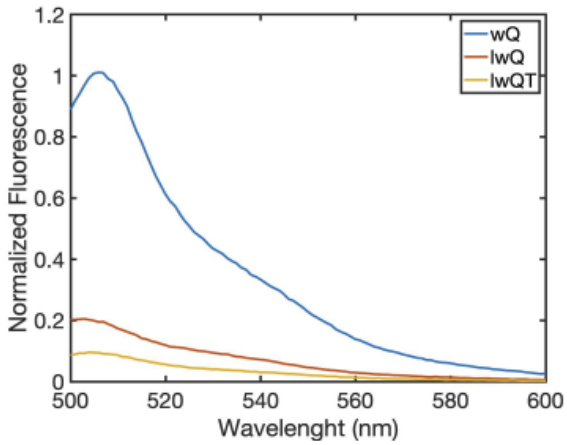

Figure 2. Absorption spectra of wildQ, low-wildQ and low-wildQT.

Further improvements. The next steps of this project will involve the development of a novel photoacoustic selective plane illumination microscope (paSPIM) and the imaging of HEK-spheroids expressing the gene codifying for the proteins.

[1] E. M. Strohm, M. J. Moore, and M. C. Kolios, "Single Cell Photoacoustic Microscopy : A Review," vol. 22, no. 3, 2016.
[2] L. V Wang, "Multiscale photoacoustic microscopy and computed tomography," *Nat. Photonics*, vol. 3, p. 503, Aug. 2009.
[3] A. Taruttis and V. Ntziachristos, "Advances in real-time multispectral optoacoustic imaging and its applications," *Nat. Photonics*, vol. 9, p. 219, Mar. 2015.
[4] J. Weber, P. C. Beard, and S. E. Bohndiek, "Contrast agents for molecular photoacoustic imaging," *Nat. Methods*, vol. 13, p. 639, Jul. 2016.
[5] V. Ntziachristos, "Going deeper than microscopy: the optical imaging frontier in biology," *Nat. Methods*, vol. 7, p. 603, Jul. 2010.
[6] L. Zeng, Z. Piao, S. Huang, W. Jia, and Z. Chen, "Label-free optical-resolution photoacoustic microscopy of superficial microvasculature using a compact visible laser diode excitation," *Opt. Express*, vol. 23, no. 24, pp. 31026–31033, Nov. 2015.
[7] J. V Jokerst, M. Thangaraj, P. J. Kempen, R. Sinclair, and S. S. Gambhir, "Photoacoustic Imaging of Mesenchymal Stem Cells in Living Mice via Silica-Coated Gold Nanorods," *ACS Nano*, vol. 6, no. 7, pp. 5920–5930, Jul. 2012.
[8] N. Beziere *et al.*, "Dynamic imaging of PEGylated indocyanine green (ICG) liposomes within the tumor microenvironment using multi-spectral optoacoustic tomography (MSOT)," *Biomaterials*, vol. 37, pp. 415–424, Jan. 2015.
[9] C. Zhang, K. Maslov, and L. V Wang, "Subwavelength-resolution label-free photoacoustic microscopy of optical absorption in vivo," *Opt. Lett.*, vol. 35, no. 19, pp. 3195–3197, 2010.
[10] P. Vetschera, K. Mishra, J. P. Fuenzalida-werner, A. Chmyrov, V. Ntziachristos, and A. C. Stiel, "Characterization of Reversibly Switchable Fluorescent Proteins in Optoacoustic Imaging," *Anal. Chem.*, vol. 90, pp. 10527–10535, 2018.
[11] T. Gensch and C. Viappiani, "Time-resolved photothermal methods : accessing time-resolved thermodynamics of photoinduced processes in chemistry and biology †," pp. 699–721, 2003.
[12] F. Pennacchietti *et al.*, "Photochromic conversion in a red/green cyanobacteriochrome from Synechocystis PCC6803: quantum yields in solution and photoswitching dynamics in living E. coli cells," *Photochem. Photobiol. Sci.*, vol. 14, no. 2, pp. 229–237, 2015.
[13] B. Storti *et al.*, "Role of Gln222 in Photoswitching of Aequorea Fluorescent Proteins: A Twisting and H-Bonding Affair?," *ACS Chem. Biol.*, vol. 13, no. 8, pp. 2082–2093, 2018.

Pollen *in vitro* germination, viability and morphology of black chokeberry cultivar 'Aronia Nero' (*Aronia melanocarpa* (Michx.) Elliot)

MILENA ĐORĐEVIĆ[1], SVETLANA M. PAUNOVIĆ[1]; MIRA MILINKOVIĆ[1]; RADOSAV CEROVIĆ[2], DRAGAN NIKOLIĆ[3]

[1] Fruit Research Institute, Čačak, Serbia; [2] University of Belgrade, Innovation Centre at Faculty of Technology and Metallurgy, Belgrade, Serbia; [3] Faculty of Agriculture, University of Belgrade, Serbia

1. Introduction

Black-fruited (*Aronia melanocarpa* [Michx.] Elliot) chokeberry belongs to family *Rosaceae*, subfamily *Maloidae* and has origins in eastern North America and East Canada. In the 1900s, chokeberry was transferred to Russian botanic gardens. From there, it spread in the European part of the country [1]. The name chokeberry comes from the astringency of the fruits, and because of that, they are not favoured as 'table fruits'. Black chokeberry is among the richest sources of polyphenols in the plant kingdom and has relatively high values of antioxidant capacity [2]. Experiments so far have shown that *Aronia* species are self-compatible, and may therefore have a mixed breeding system where both outbreeding and self occurs [3]. Some cultivars are bread of true black chokeberry while some are hibrid cultivars (e.g. *Aronia* × *Sorbus*). Little is known, however, about pollen performance *in vitro* of black chokeberry.

The objective of the present investigation was to determine viability, germination and pollen morphology of black chokeberry cultivar 'Nero' (*Aronia melanocarpa* (Michx.) Elliot.).

2. Material and methods

The study was conducted on the black chokeberry cultivar 'Nero' growing at the site of Fruit Research Institute, Čačak. Flowers were picked randomly in late balloon phase. Anthers were separated from flowers in laboratory, placed into paper boxes and dried at 20ºC for 24–28 h until bursting. For the pollen grain germination test, pollen was grown in medium with three different concentration of sucrose (13, 15, and 17%) and 1% agar. Pollen germination was recorded after 1h, 3h and 24 h incubation period. Methods with fluorescin-diacetate [4] and 2,3,5-triphenyl tetrasolium chloride (TTC) [5] were used to determine pollen viability. Observation and photography was performed under an Olympus BX61. For the SEM study, thirty randomly selected pollen grains were used to measure the polar diameter, equatorial diameter and exine sculpturing. Samples were mounted directly on metallic stubs using double-sided adhesive tape and coated with gold in a sputtering chamber (BAL-TEC SCD 005 Sputter Coater). Observation of the prepared samples was carried out with a scanning electron microscope (SEM) JEOL JSM-7100F (Tokyo, Japan) at 15 kV.

3. Results

The results of pollen germination are shown in Table 1. Pollen germination rates were increased with incubation time. The highest germination rates were obtained in medium containing 13% sucrose (Figure 1).

In about 1300 pollen grains viability test was determined by FDA and TTC. Almost two times better pollen viability was obtained by fluorescing diacetate than with TTC (35,70% and 18,22%, respectively) (Figure 2).

Pollen grains of the black chokeberry cultivar 'Nero' can be characterised as isopolar, radially symmetric and tricolporate. Polar view (length) is 44,37 µm, while equatorial diameter (width) is 23,03 µm (Table 2). Germinal furrows (colpus) extended the length of the grain (40,82). The pattern of the exine of the investigated black chokeberry cultivar is striate, perforate and tectate (Table 3; Figure 3).

Table 1 Effect of sucrose medium on agar plate on pollen germination (%) of black chokeberry cultivar 'Nero'.

Sucrose (%)	After 1h incubation time	After 3h incubation time	After 24h incubation time
13	34,55±1,03 a	41,03±1,52 a	41,80±0,21 a
15	32,67±1,65 a	33,94±2,31 b	37,13±2,22 b
17	33,29±1,60 a	33,80±0,83 b	40,57±1,74 a

Figure 1. Pollen germination on medium with 13% sucrose after 1h (A); 3h (B) and 24h (C) incubation time.

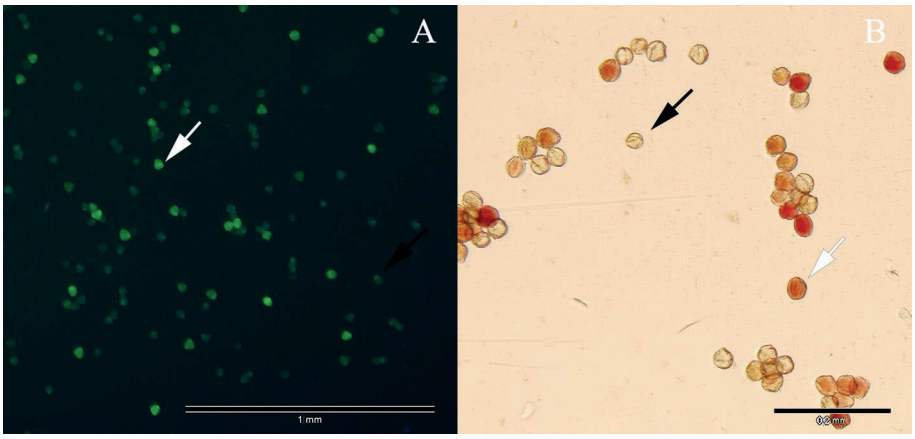

Figure 2. Pollen grain staining with fluorescin-diacetate (A) and (TTC); white arrows= viable pollen grain, black arrows= non viable pollen grain.

Table 2. Morphological characteristic of pollen grains of black chokeberry cultivar 'Nero'.

Cultivar	Pollen length (µm)	Pollen width (µm)	Colpus length (µm)	Colpus width (µm)	Mesocolpium width (µm)
'Nero'	44,37±1,21	23,031±0,93	40,82±0,80	1,51±0,19	11,64±0,57

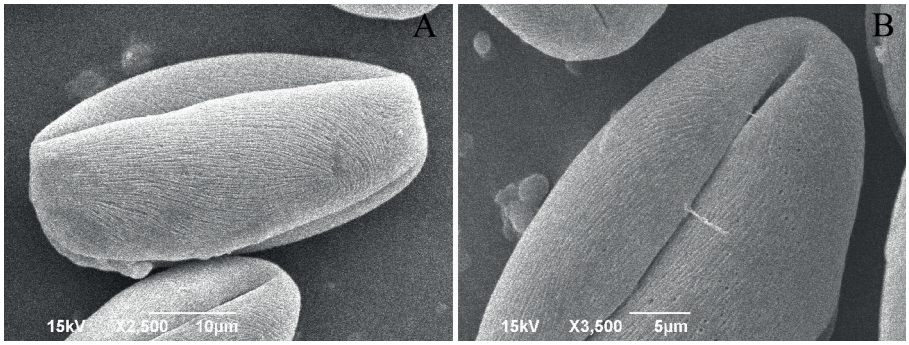

Figure 3. Pollen grain of black chokeberry of the cultivar 'Nero'; A- ×2500; B - × 3500.

Table 3. Exine pattern in black chokeberry of the cultivar 'Nero'.

Cultivar	Ridge width (µm)	Ridge height (µm)	No. of ridges per 100 μm^2 of exine area
'Nero'	0,23±0,007	0,32±0,016	10,33±0,38

References

[1] I. Ochmian, J. Grajkowski, M. Smolik, Notulae Botanicae Horti Agrobotanici, 40 (2012) 253–260
[2] P. Denev, M. Kratchanova, I. Petrova, D. Klisurova, Y. Georgiev, M. Ognyanov, I. Yanafieva, Journal of Chemistry, 2018 Article ID 9574587
[3] H. A. P. Hovmalm, N. Jeppsson, I. V. Bartish, H. Nybom, Hederitas, 141 (2004) 301–312
[4] J. Heslop-Harison, Y. Heslop-Harison, Stain Technol., 45 (1970) 115–120
[5] J. D. Norton, Proc. Amer. Soc. Hort. Sci., 89 (1966) 132–4

Electrochemical sensors based on phyropyilite

ANĐELA MITOVIĆ[1], TIJANA PATNIĆ[1], SIVANA DIMITRIJEVIĆ[2], ALEKSANDRA IVANOVIĆ[2], NIKOLA NOVAKOVIĆ[1], SANDRA KURKO[1], SANJA MILOŠEVIĆ GOVEDAROVIĆ[1], JASMINA GRBOVIĆ NOVAKOVIĆ[1]

[1] University of Belgrade, Vinča Institute of Nuclear Sciences, Centre of Excellence for Hydrogen and Renewable Energy, Belgrade, Serbia; [2] Mining and Metallurgy Institute Bor, Serbia

Pesticides are known as highly toxic chemicals and they are used towards a wide range of organisms has led to its extensively use against pests in a large variety of crops such as bulbs, cereals, fruits, coffee or potato. Determination of pesticides in environmental samples is of great interest due to their toxicity, carcinogenicity and endocrine disrupting effects. Carbendazim (methyl 1H-benzo [d] imidazol-2-yl carbamate) is a benzamidazole fungicide that pays an important role in plant disease control and to prevent some illnesses on bananas, apple, tomatoes, cereals, honey, nuts [1,2]. Carbon paste electrode (CPE) are widely used electrodes in the fields of electrochemistry, due to their attractive advantages, such as low-cost implementation, simple preparation, low background current, wide potential window and these electrode are applicable in the large scale monitoring of electrochemically active environmental pollutants and organic constituents.

Phirophilite carbon paste electrode based on tricresyl phosphate as a binding liquid has been applied as working electrode for the voltammetric characterization and determination of the carbendazim fungicide. To the best of our knowledge, there is no publication with the application CPE based on phyrophilite carbon paste electrode in the field of electroanalytical chemistry. In this work we have tested the use of composite based on phyrophikute on sorption properties of carbendazim. Carbendazim (99% purity) was obtained from Fitofarmacija a.d. (Zemun, Serbia). The stock solution was made 1000 ppm in concentration by dissolving this pesticide in methanol and kept in dark at -18 ^{0}C. Britton-Robinson buffer solutions were prepared mixing solutions of 0.04 mol L^{-1} H_3PO_4, 0.04 mol L^{-1} H_3BO_3 and 0.04 mol L^{-1} CH_3COOH adjusting pH by 0.02 mol L^{-1} NaOH. Methanol, potassium ferrocyanide, sulfuric acid, paraffin oil, tricresyl phosphate, all acids, potassium chloride and NaOH were purchased from Sigma-Aldrich (St. Louise, MO, USA). Deionized water was supplied from Millipore purification system (Bedford, MA, USA). A 797 VA Computrace analyzer (Methrom) controlled by 797 VA Computrace software version 1.2 was applied for all voltammetric measurements. A three-electrode system include Ag/AgCl electrode (saturated with KCl) as a reference electrode, platinum wire as a auxiliary electrode and different types of CPE based on phirophilite carbon paste electrodes with paraffin oil and tricresyl-phosphate as the working electrode. All electrochemical experiments were carried out in conventional voltammetric cell (with operating volume of 10 ml) temperature (23±1 ^{0}C). Before starting the new set of measurements a supporting electrolyte were deaerated by suprapure nitrogen for 5 min. Carbon paste was made by hand mixing of phirophilite carbon paste electrodes with paraffin oil or tricresyl-phosphate as a liquid binder. All pastes homogenized manually using pestle and mortar at the same ratio of 0.25 g of phirophilite, 0.25 g of graphite and 0.11 g of binder and were packed into the Teflon holder (2 mm diameter). Usually before starting a new set of experiments about 0.5 mm carbon paste was mechanically renewed out of electrode holder and polished on a wet filter paper. Morphology and microstructure of phyrophilite has been study by SEM analysis.

Phirophilite carbon paste electrodes have been investigated by cyclic voltammetry measurement in 0.5 M H_2SO_4 as acidic supporting electrolyte, with potential range from -0.5 V to +1.1 V vs Ag/AgCl (saturated KCl) reference electrode. İn addition, 1 mM $K_4Fe(CN)_6$ in 0.1 M KCl was used as redox model compound. Parallel examinations were conducted with carbon paste electrode

(CPE), containing only graphite and liquid binder (paraffin oil (P) and tricresyl phosphate (TCP)). The parameters for CV measurement were as follows: initial potential -0.5 V, end potential 0.8 V, sweep rate 0.1 V/ s, initial purge time 60 s and scan rate 50 mV/s.
Two supporting electrolytes, the acetate-based and 0.1 M phosphate buffer solution were tested as a media of choice for determination of carbendazim. The results have indicated that better shape and higher peak maxima could be obtained in the Briton-Robinson buffer. DPSV was used for quantitative determination of carbendazim in Britton-Robinson buffer pH 4 as supporting electrolyte. The parameters for DPSV measurement were as follows: start potential +0.2 V, end potential +1.2 V, accumulation potential -0.15 V, accumulation time 60 s and scan rate 50 mV/s. Before adding carbendazim, the blank was recorded (supporting electrolyte) under the same conditions. The quantitative DPSV determination of carbendazim at PGTCP is based on the linear relationship between the peak current intensity at +0.9 V in Britton-Robinson buffer solutions pH 4 and carbendazim concentration. As can be seen, carbendazim could be determined by DPSV in the concentration range of 3.2 to 29.2 ng cm^{-3}, with r = 0.999 (Figure 1.) and the limit of detection (LOD) of 1.9 ng cm^{-3}, while the RSD did not exceed 2.3%. The RSD value indicates a relatively good precision of the developed method. The detection limit (LOD) were determined using the 3σ/S, where σ is the estimated standard deviation of the peak height intensity for the lowest measured concentration (6 measurements) and S is the slope of the calibration curve.

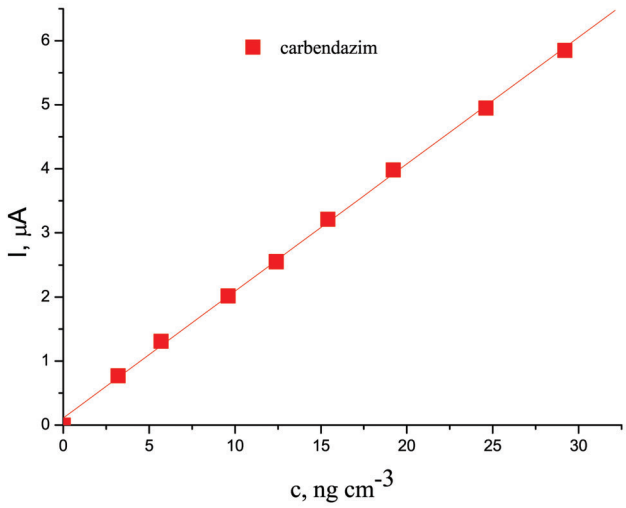

Fig 1. DPSV determination of carbendazim at pyrophilite carbon paste electrode at Britton-Robinson buffer pH = 4 in concentration range from 3.2 to 29.2 ng cm^{-3} and the corresponding calibration plot using the phirophilite carbon paste electrode based on tricresyl phosphate (PGTCP).
Accumulation potential -0.15 V, accumulation time 60 s and scan rate 50 mV/s.

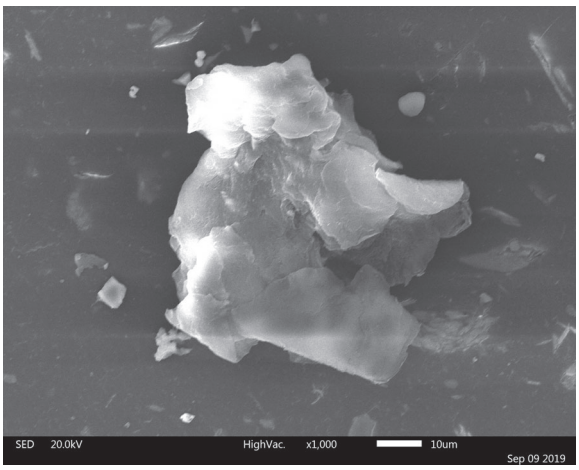

Fig. 2. SEM micrograph of phyrophiilte

Due to enhanced surface properties pyrophilite based electrode can be used as electrochemically active component for application of this material as a carbon paste electrode. The obtained results open a new field for further investigations which concern pyrophilite as a sensor for the detection of water pollutants. An electroanalytical method has been developed for the detection and determination of pesticide carbendazim by DPSV at electrochemically conditioned pyrophilite carbon paste electrode in Britton-Robinson buffer pH = 4 as supporting electrolyte in the

concentration range of 3.2 to 29.2 ng cm^{-3} with LOD of 1.9 ng cm^{-3}. Based on presented results, it can be concluded that the pyrophilite carbon paste electrode can serve as a sensor for the determination of carbendazim in model solution.

Acknowledgments

This study was carried out as part of the projects No III 45006, III45012 and under contract 402-01/2018-010 supported by the Ministry of Education and Science of the Republic of Serbia.

[1] M. D. Pozo, L. Hernández, C. Quintana, Talanta 81 (2010) 1542,
[2] T. A. Zari, A. M. Al-Attar, Euro. Rev. Med. Pharm. Sci. 15 (2011) 413

JEOL

Scientific / Metrology Instruments

Cryo Electron Microscope

CRYO ARM™ 300

Ultimate instrument for Protein/Virus structure study

Cold FEG
Omega energy filter
Phase plate
Single Particle Analysis

www.jeol.com

Thermo Fisher Scientific is the world leader in serving science. Our mission is to enable our customers to make the world healthier, cleaner and safer. We help our customers accelerate life sciences research, solve complex analytical challenges, improve patient diagnostics, deliver medicines to market and increase laboratory productivity. No matter the research field, we supply innovative solutions to take customers from questions to usable data, across scales and modes—through the broadest sample types. Our workflows for 3D electron microscopy imaging and analysis help materials science researchers advance their sample characterization to gain deeper insight into material samples using the latest advances in analytical instruments. Our best-in-class Phenom Desktop SEMs make imaging and analysis at the nanoscale available to every scientist in every lab.

We serve both academic and industrial life sciences researchers, providing an unmatched combination of complete workflow solutions ranging from cryo-EM structural determination of macromolecular complexes and protein sociology, in the native state, to reconstruction of 3D architecture of tissues and cells. Our solutions help researchers unlock the mysteries of underlying protein function and cellular process and bridge the gap between basic science and translational therapeutics.

Our multiscale, multimodal solutions provide the additive manufacturing industry with imaging and characteriza¬tion of powders and parts at nano- to atomic-level resolution. These are supported by helical microCT, plasma FIB/SEM, STEM, 3D visualization software and automated SEMs that simultaneously characterize size, shape and chemistry of powders or surface porosity and inclusions of parts. Our wide range of processing and analytical instruments makes us the only company that can both produce and verify the quality of 3D filaments. Co-rotating twin-screw extruders produce filament for 3D printers with a wide range of raw materials. In-line and off-line IR, Raman and XR instrumentation validates filament uniformity and analyzes final printed parts for potential failure.

The world leader in serving science

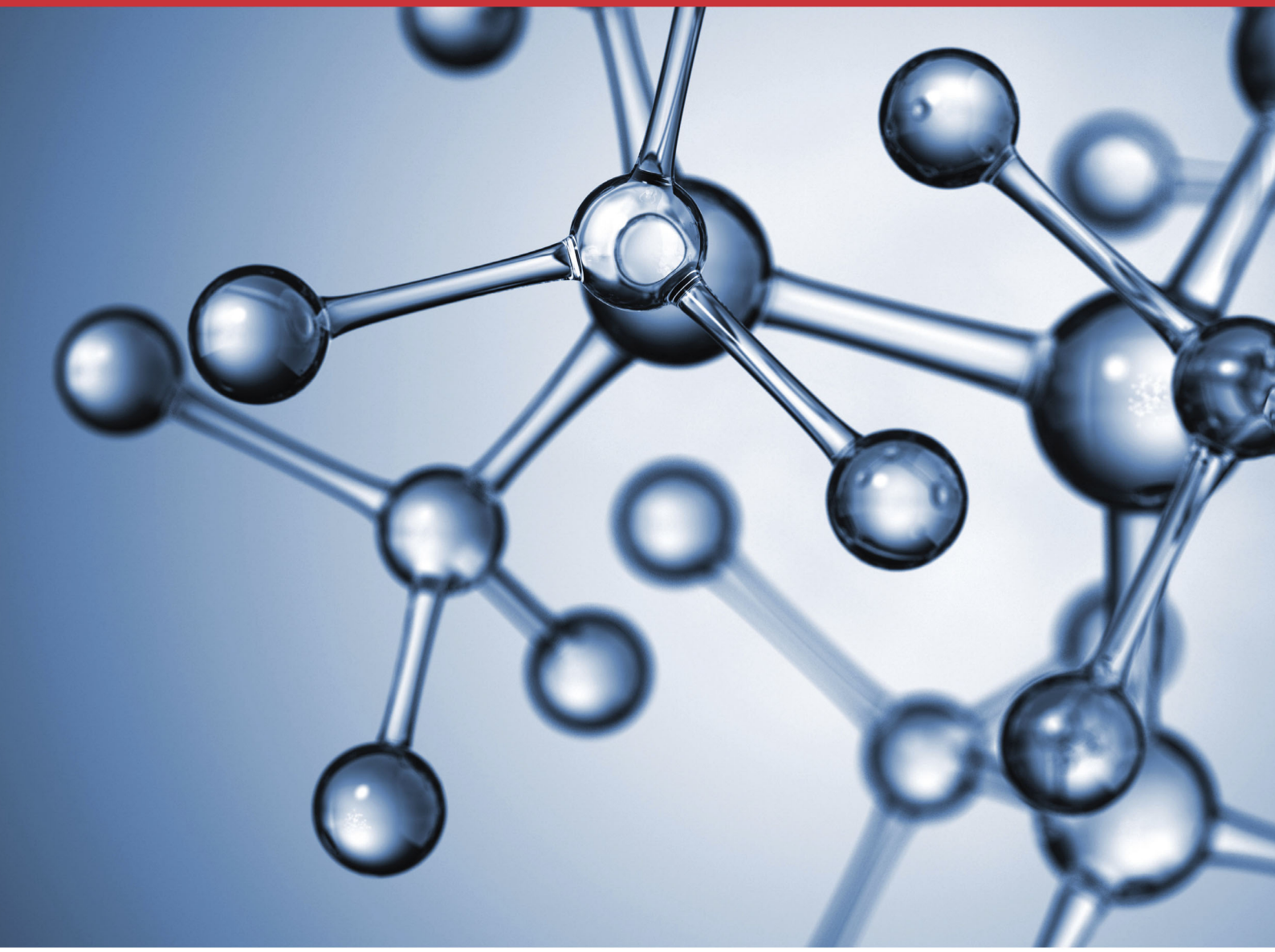

Innovative Electron Microscopy Technologies With Global Reach

Make critical decisions with confidence

Find out more at **thermofisher.com/EM**

ThermoFisher SCIENTIFIC

© 2019 Thermo Fisher Scientific Inc. All rights reserved. All trademarks are the property of Thermo Fisher Scientific and its subsidiaries unless otherwise specified.

Founded in 1949, JEOL aims the development anmanufacture of high-tech scientific equipment. These facilities are essential to the laboratories for research, development and quality control of new products. Its fields of investigation are multiple: sample preparation (cross polisher, ion slicer), nanotechnology (SEM, TEM, Auger, FIB...), the environment, medicine, the life sciences (NMR, EPR, mass spectrometry...). With 3000 employees in more than 80 countries JEOL is the world leader in electron microscopy. This position leads us to constantly innovate in bringing us closer to our customers through dynamic partnerships to meet the upcoming challenges. For more information please visit our web site: www.jeol.fr or http://www.jeol.co.jp/en/

Diatome Ltd, founded 1970, manufactures diamond knives for ultramicrotomy.
In Biology Ultramicrotomy is the recognized technique for achieving ultrathin sections for Transmission Electron Microscopy (TEM), semithin sections for Optical Microscopy, serial sections for Array Tomography, cryo sectioning for immunocytochemistry (Tokuyasu technique), frozen hydrated samples (CEMOVIS). In Materials Research sections of all kinds of polymers and metals, but also brittle materials such as ceramics, semiconductors, crystals, etc, are generated by Ultramicrotomy. Besides the making of ultrathin sections of high quality, Ultramicrotomy also serves for preparing extremely smooth surfaces of a great variety of biological and Materials Research samples.
At the MCM 2019 conference exhibition Diatome displays the entire diamond knife range:
ultra, histo, cryo, semi, ultra sonic, etc. Kindly visit our booth at MCM 2019 and discuss your Ultramicrotomy applications. Our ultramicrotomy specialists are at disposal for any information you might require.

TESCAN is one of the global suppliers of scientific instruments. The company is building its reputation and brand name in the field of designing and manufacturing scanning electron microscopes and system solutions for different applications. The company is focused on research, development and manufacturing of high level SEM, Field Free HR SEM, world–class quality FIB, X-ray micro-CT systems, special vacuum chambers and custom tailor systems, accessories supplementary for SEMs, light optical microscopy and image processing, detection systems, scientific hardware and software development. TESCAN's instrumentation and innovative solutions have won a leading position in the world of nano- and microtechnology. Almost 3,000 SEM installations in more than 80 countries prove the highest technical solution of TESCAN products. Mikrolux is TESCAN representative for the territory of Bosnia and Herzegovina, Bulgaria, Croatia, Kosovo, Macedonia, Monte Negro, Slovenia and Serbia. For more information visit the website: https://www.tescan.com/en-us/ or https://www.mikrolux.hr/

mikrolux
advantageous technologies consulting
general representative
TESCAN
PERFORMANCE IN NANOSPACE

MCM 2019
14th Multinational Congress on Microscopy

September 15-20, 2019
BELGRADE, SERBIA

It is our pleasure to invite you to come and visit us at the 14th Multinational Congress on Microscopy in Belgrade, Serbia.

Check out for the latest news at our booth TESCAN CLARA is one of them...

The new TESCAN CLARA ultra-high-resolution scanning electron microscope (UHR-SEM), based on TESCAN's BrightBeamTM technology, takes materials characterization to the next level

Key Benefits

- Unique In-Beam BSE detector designs allow filtering of signal based on energy and take off angle
- Excellent for imaging of beam-sensitive and non-conductive samples
- Fast setup of electron beam – optimal imaging and analytical conditions guaranteed
- Intuitive and precise live SEM navigation on the sample at low magnification without the need of optical navigation camera
- UHR Field-free characterization of materials at low beam energies for maximum topography
- Intuitive Essence™ software modular platform designed for effortless operation regardless of the user's skill level

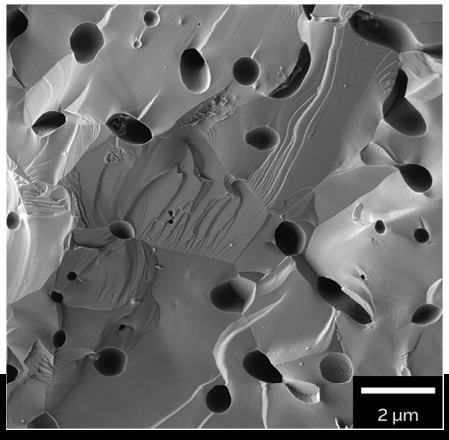

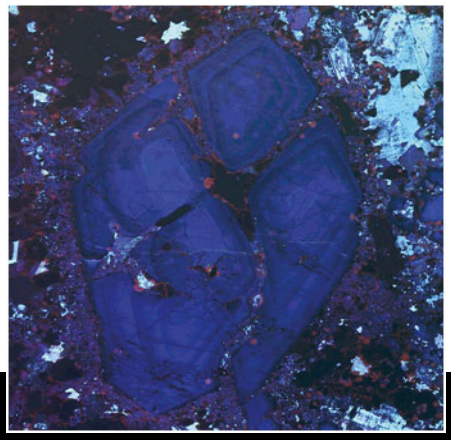

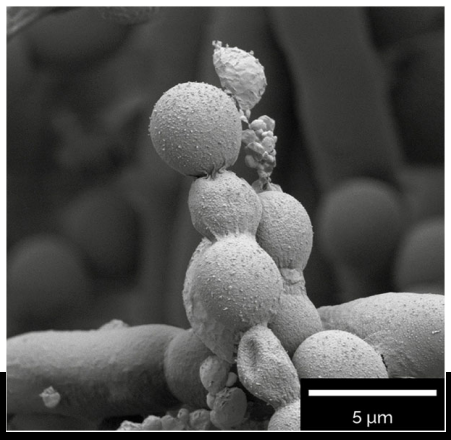

www.tescan.com
www.mikrolux.hr

NanoMEGAS

Advanced Tools for electron diffraction

NanoMEGAS (www.nanomegas.com) founded in Brussels in 2004, is a world leader SME in the development and commercialization of unique transmission electron microscopy (TEM) accessories for several scientific / industrial applications based on precession electron diffraction. NanoMEGAS was the first company to develop and commercialize Precession Electron Diffraction (PED) equipment that is compatible for almost all type of commercial TEM and has been installed in more than 150 laboratories all over the world. Based on PED method that consist a breakthrough in electron diffraction, various applications have been developed the last years. Electron crystallography has been considered as an alternative powerful tool for the structure analysis of crystals of few nm size and many important materials and compounds have been analyzed by TEM. In 2008 in collaboration (common Patent) with CNRS-INP Grenoble-France the Automated Phase-Orientation Mapping application, called "ASTAR", has been launched which allows 1-5 nm resolution maps (EBSD like) for any material (for FEG-TEM). ASTAR received the "Microscopy Today 2011 Innovation Award" during M&M 2011 Congress in USA. NanoMEGAS has also lately developed, in collaboration with NanoMEGAS USA, a Strain Analysis method using TEM that provides results with high strain sensitivity (up to 0.02% of strain) and spatial resolution (up to 1-5 nm when FEG-TEM is used). In September 2015 NanoMEGAS was proudly announced a novel solution in collaboration with Columbia University, for the analysis of amorphous materials using the electron Pair Distribution Function (ePDF) algorithm specifically prepared for data obtained by TEM, reducing dramatically the acquisition time compared to conventional x-ray techniques.
Due to the large number of NanoMEGAS devices and applications installed worldwide, the scientific production on Electron Diffraction applications has been exponentially increased since 2004 with high lever peer reviewed published articles.

BRUKER

Headquartered at Bruker Nano GmbH in Berlin, Bruker Nano Analytics offers solutions for all your nanoscience needs. We develop, manufacture and market systems for the investigation of the composition and structure of materials on the micro and nano scale. This includes a unique range of analysis systems for materials characterization on electron microscopes. Our electron microscope analyzers QUANTAX EDS, QUANTAX WDS, QUANTAX EBSD and QUANTAX Micro-XRF on SEM provide unmatched comprehensive compositional and structural materials analysis. The M-series for mobile and benchtop micro X-ray fluorescence spectrometry, including the M4 TORNADO Micro-XRF spectrometer, adds to our range of nano analysis solutions.

Labena

emsis

Anton Paar

MCLabor

EDAX
Smart Insight

AMETEK
MATERIALS ANALYSIS DIVISION

ZEISS
Seeing beyond

RMC Boeckeler

OXFORD INSTRUMENTS
The Business of Science®

delong instruments
your way to electron microscopy...

SERBIA
National Tourism Organisation of Serbia

CIP – Каталогизација у публикацији
Народна библиотека Србије, Београд

621.385.833.2(082)(0.034.2)
620.187(082)(0.034.2)
66.017/.018(082)(0.034.2)
57+61(082)(0.034.2)
57.086.3(082)(0.034.2)

MULTINATIONAL Congress on Microscopy (14 ; 2019 ; Beograd)
MCM2019 [Elektronski izvor] : proceedings / 14th Multinational Congress on Microscopy, [September 15–20, 2019, Belgrade, Serbia] ; [editors, Jasmina Grbović Novaković, Nataša Nestorović, Dragan Rajnović]. – Belgrade : Serbian Society for Microscopy : Institute for Biological Research "Siniša Stanković" : Serbian Society for Microscopy, 2019 (Beograd : Knjigoveznica i kartonaža Grbović M. Milica). – 1 elektronski optički disk (CD-ROM) ; 12 cm

Sistemski zahtevi: Nisu navedeni. – Nasl. sa naslovne strane dokumenta. – Tiraž 30. – Bibliografija uz svaki rad

ISBN 978-86-80335-11-7 (IBRSS)

a) Електронска микроскопија – Зборници b) Наука о материјалима – Зборници c) Биомедицина - Зборници

COBISS.SR-ID 279354124